

THIS WEEK

EDITORIALS

OBJECTION! The perils of leaving forensic science to the open market **p.548**

WORLD VIEW Colin Macilwain on why nuclear experts fail to convince **p.549**



WATER BORNE Amazonian fish found to carry seeds for miles **p.551**

Lessons from the past

The Chernobyl disaster still has much to tell us about the long-term risks of low-level radiation exposure. But only if the necessary follow-up studies are supported.

As the battle to make safe the Fukushima nuclear reactors continues, the political fallout is spreading across Japan and around the world. Despite reassuring early reports, it is clear that significant amounts of radioisotopes have been released from the plant, and some workers there face severe radiation exposure as they try to cool the overheated nuclear fuel. In response, several governments are reviewing the safety and future of their own nuclear programmes. Fukushima has undoubtedly strengthened the hand of those who oppose nuclear power.

The global reach of the disaster brought an echo from history last week when iodine-131 from Fukushima was detected in Ukraine — home to the Chernobyl power plant, site of the world's worst civilian nuclear disaster. A quarter of a century ago, a flawed safety test at Chernobyl triggered a massive explosion and fire that spread tonnes of radioactive material across Europe, and shredded public confidence in atomic energy.

Like Fukushima, the consequences of Chernobyl were wide ranging. In the satellite countries, resentment of Soviet handling of the disaster contributed to the fall of the Soviet Union. Thousands of children developed thyroid cancer after drinking contaminated milk. Billions of crucial dollars from the economies of Ukraine and Belarus were redirected to remediation, health care and compensation. Every day, some 3,500 workers still labour at the plant to prevent further releases, while decommissioning of the site's four reactors has barely begun. Recovering from a nuclear disaster is the task of generations: it will be another 50 years before Chernobyl is just a memory.

As we report on page 562, the pace of recovery at Chernobyl has been slowed by the reluctance of other countries to pay for it. The shattered reactor 4 still lies beneath a haphazard concrete sarcophagus, erected in the frantic months after the accident. Maintenance work keeps it secure — for now — but the walls are streaked with rust and its roof is in a poor state of repair. Engineers want to build a safe confinement arch to allow them to dismantle the reactor, at an estimated cost of US\$1.4 billion.

The Chernobyl Shelter Fund, managed by the European Bank for Reconstruction and Development, has so far amassed more than \$800 million of that sum, from 30 donors. But funding shortfalls have delayed the project by years and the 2015 target for completion will be difficult to achieve without more money from the international community.

One immediate consequence of the Fukushima disaster should be to encourage this money to flow. Nuclear accidents have global repercussions, and public mistrust of nuclear power demands that its problems not be left to fester. It is in the world's interest to push forward with safe nuclear power — but also to deal properly with its damaging legacy when things go wrong, as they will.

Today, new nuclear power stations are being constructed in more

than a dozen countries. China alone is working on almost half of the 65 reactors currently being built, and there is growing interest in the technology from developing countries. Supporters of the spread of civil nuclear power must acknowledge that some of these countries would be unable to cope alone if faced with a nuclear accident on the scale of Chernobyl.

Nations, particularly those pushing new nuclear build, must invest in bodies such as the International Atomic Energy Agency, to ensure that new and old reactors around the world are sufficiently safe, and that they are fully prepared for the worst. And politicians and the nuclear industry must revisit their relationship with a sceptical public. Being open and transparent about the uncertain costs of new build in countries such as the United Kingdom would be a start. If a public subsidy is required to get them built, then say so. If the industry wants people to believe its assurances that nuclear power is safe, then now is not the time for obfuscation and weasel words, on any aspect of the technology (see page 549).

Governments must also work to present a clear narrative about the health implications of accidents such as Chernobyl and Fukushima. For heroic plant workers exposed to extreme radiation doses — and for those still suffering from Chernobyl's legacy of thyroid cancer — the risks are all too clear. But it is harder to pin down more subtle health effects. There are hints that low-level exposure can raise the risk of cardiovascular disease, breast cancer and other conditions, consistent with the idea that there is no safe threshold for radiation exposure. To clarify the situation, the world needs studies of large numbers of people exposed to very low doses of radiation — and Chernobyl can provide those. Funding such research is vital for those affected by Chernobyl's radiation, but it should also answer some of the questions over the future of nuclear power.

People legitimately ask whether the low levels of radioactivity now drifting across Japan are safe. The current best answer is 'probably'. A better response would be to find out, before another 25 years pass. ■

ANNOUNCEMENT

Nature mentoring awards

Every year, in a selected country or region, *Nature* awards prizes for outstanding scientific mentoring. The competition this year is to be held in France. Two prizes, each of €10,000, will be awarded: for a lifetime of mentoring achievement, and for an outstanding track record at mid-career. The competition is now open. Details of the procedures and nomination forms can be found at www.nature.com/nature/mentoringawards/france. The closing date for nominations is 27 June 2011.

Courtroom drama

Forensic science faces rough justice on both sides of the Atlantic.

Although it is better under the law that ten guilty people go free than that one innocent person be convicted — as eighteenth-century English judge William Blackstone said — it is better still to make as few mistakes as possible. Forensic science is a powerful tool to help achieve this, but many research-based tools are not as fool-proof as they are presented — both in court and in television dramas.

Just over a year ago, this journal stressed the need for more research on forensic techniques (see *Nature* **464**, 340–342, 344–346, 347–348; 2010). In that time, the United States has taken some tentative steps forward, but the United Kingdom is about to stumble backwards.

Britain used to boast one of the great powerhouses of the forensics research world, the Forensic Science Service (FSS). A botched attempt at privatization by the former Labour government left the FSS in an unstable position, and in December last year the coalition government said that the service would close by next March, blaming ongoing losses of £2 million (US\$3.2 million) a month.

The timing is unfortunate, given that in January the UK Home Office asked its chief scientist to conduct a review of research relevant to forensic science. Although that review has asked researchers to confine submissions to a length of 1,000 words — just 200 words per question posed — the inquiry will find plenty of evidence that the loss of the FSS will undermine research on forensic techniques, and ultimately the course of justice. The government's Criminal Cases Review Commission, set up to investigate possible wrongful convictions, has already expressed its unease.

Of particular concern is the fate of the service's unique archive of more than 1.5 million records. These include evidence and forensic samples that could still be valuable for cold-case investigations as techniques improve.

At a parliamentary hearing last week, the research and development manager of the FSS, Gillian Tully, admitted that “at the moment there isn't yet a plan for what's going to happen to the archive”.

In the same week, the Law Commission, an independent body

created to review the laws of England and Wales, called for reform to prevent dubious scientific evidence causing miscarriages of justice. It was prompted to speak out after a number of cases in which forensic evidence used in trials was later discredited.

The commission made some good suggestions, such as allowing judges to call up their own experts to test the reliability of evidence. It is disappointing that they received only a lukewarm response from the government, which suggested that existing laws and procedures are adequate. Even if they were accepted, the Law Commission's

“A botched attempt at privatization left the UK Forensic Science Service in an unstable position.”

suggestions will be useless without a strong base of forensic researchers to subject tests — new and old — to scrutiny. The loss of the FSS will remove this capability. Commercial providers of forensic services do valuable work, but this is one area simply not suited to a fully commercial market. Although a combination of regulation and competition can increase scrutiny and standards, not all

forensic services will be attractive to those who seek a profit.

Also, commercial operators can be reluctant to reveal full details of proprietary techniques used to analyse evidence so that they can be scrutinized by all sides in a case. Such secrecy has already led to objections from defence lawyers, and, in at least one case, a retrial. Basic research must underpin the practice of forensic science, both to bring new, evidence-based tests to market and to use publications in open and peer-reviewed literature to demonstrate the reliability of techniques already in use. It requires financial — and moral — support from the government.

The United States now has a chance to give this support. Two years ago, the US National Academy of Sciences warned of the need to overhaul the country's forensic science base, and recommended the creation of a national institute of forensic science. This idea now looks dead in the water, but earlier this year Senator Patrick Leahy (Democrat, Vermont) proposed legislation that would establish something similar.

Rather than setting up an independent federal agency, Leahy's bill would create an Office of Forensic Science in the Department of Justice. A forensic science board of researchers, lawyers and other players would look at research priorities, and scientists overseen by the National Institute of Standards and Technology would work on research needs in individual disciplines. The idea deserves to be taken seriously. Justice for all takes effort. ■

➤ NATURE.COM
To comment online,
click on Editorials at:
go.nature.com/xhunqv

JOURNAL LAUNCH

Welcome *Nature Climate Change*

Since *Nature Genetics* was founded in 1992, 17 *Nature*-branded research journals have been launched. Most are devoted to specific disciplines (such as immunology or materials research) ranging across all the natural sciences. Some, such as *Nature Photonics*, also have a strong technological component. Others, such as *Nature Nanotechnology*, touch on all the disciplines, sometimes extending into social-science discussions. And one, *Nature Communications*, sets itself, like *Nature*, at no particular discipline or theme.

Nature Climate Change, launched this week, is something of a distinct venture. Climate change is a phenomenon that is relevant, in principle, to all research disciplines. This journal focuses as much on the impacts of climate change as on its origins and mechanisms. And for the first time within the *Nature*-branded stable, the journal is explicitly set up to include the social sciences within

its remit, with a trained social scientist on its staff, and a panel of social-science advisers to help us to penetrate territory that lies beyond our traditional zones of engagement.

The first issue of the journal (see www.nature.com/nclimate) reflects this inclusive strategy. It covers research on aircraft contrails' impact on climate, the effects of climate change on agriculture and health, and how experience of flooding can affect public attitudes to energy use. The issue also includes journalism and commentary on decision-making and on data sharing.

In tackling such issues, *Nature Climate Change* sits alongside *Nature Geoscience* and *Nature*. But this is a complementary relationship and, in line with 'family' tradition, all the journals are editorially independent of each other. *Nature* will continue to publish the most scientifically significant research, and discussions with the broadest impact. *Nature Geoscience* will focus on the relevant Earth and Solar System mechanisms. And *Nature Climate Change* will offer new avenues for those interested in the long-term changes in our atmosphere and their impacts.

Both individually and as a group, we hope the content and influence of these journals will significantly help our planet's inhabitants to anticipate and cope with the global changes ahead. ■



Concerns over nuclear energy are legitimate

Reassurances from 'experts' on the safety of nuclear power will not wash, says **Colin Macilwain**. The Fukushima crisis raises genuine questions.

The unique and almost existential nature of the risk posed by nuclear power has had ample airing over the past three weeks, since the disaster at the Fukushima plant in Japan. Enthusiasm for a global nuclear revival has stalled — and not before time.

The scientific community could yet play a valuable part in the management of this crisis. It could help put events in perspective, and begin the process of drawing out useful regulatory and other lessons. In the United States, this has already begun, with specific suggestions for change coming from former US government science advisers Frank von Hippel and Matthew Bunn. Last week on this page, Charles Ferguson, president of the Federation of American Scientists, did likewise (see C. D. Ferguson *Nature* **471**, 411; 2011).

Less edifying have been the nuclear experts who have popped up in the media to 'inform' the public about the crisis. Individually, their motives may be honourable, but the collective impression has been unconvincing: defensive, selective, condescending towards public fears and, in my view, ultimately counterproductive. Their combined message seems to have been: don't worry, things are under control, and Fukushima is not Chernobyl.

Well, Fukushima is certainly not Chernobyl, but some salient points about what Fukushima actually is, I would argue, deserve wider attention. All are relevant to the future deployment of nuclear power.

One is that Fukushima houses six reactors on one site, despite the fact that even the most basic analysis of failure modes and effects would come out resoundingly against such an arrangement. Not only are all the reactors exposed simultaneously to the same dangers — whether flood, earthquake, war or terrorist attack — but radiation release at one reactor or fuel tank could cripple recovery efforts at the others. Everyone in nuclear engineering knows this. Yet such co-siting is the central organizing principle of current nuclear-build plans in Britain, the United States and elsewhere, because the only communities that will accept new nuclear plants are those that already have them.

The second is an inherent problem with light-water reactors, including boiling-water reactors, as at Fukushima, and pressurized-water reactors (PWRs). These designs are compact and relatively inexpensive, but their potential for meltdown was once obvious enough that Britain spent 30 years trying to develop gas-cooled alternatives. But, now that PWRs are the only viable design for new nuclear build, that extensive search for a safer design seems to have been forgotten by many of those who promote a nuclear future.

A third point is the storage of spent fuel rods in pools of water at power plants. The amount

of fuel held in this way continues to grow relentlessly, particularly in the United States, where the Obama administration's shelving of the Yucca Mountain waste-storage project in Nevada leaves the fuel with nowhere else to go. As in the United Kingdom, such 'interim' storage is the only likely destination for spent fuel from new reactors, ahead of promised deep disposal in an uncoded, unscheduled and uncertain underground repository.

These legitimate technical criticisms of Fukushima, and of planned nuclear build, have been largely drowned out by the flood of technical reassurance offered by nuclear scientists and engineers in the wake of the disaster. For example, reassuring soundbites offered to journalists by the London-based Science Media Centre (which is funded by a variety of scientific bodies and industries, including Nature Publishing Group) in the days immediately after the earthquake contained barely a cautionary note on how serious the situation at Fukushima was set to become.

Instead, the scientific establishment and those whose careers are invested in nuclear power have sought to convince the public that 'science' supports nuclear power. Too many specialists have assured us of the general safety of nuclear power without adequately addressing specific concerns.

Some of this loyalty is deep rooted, I fear, in the development of the atomic bomb, which greatly embellished the standing of the scientific establishment with governments. Not long afterwards, many senior physicists embraced 'atoms for peace'. Having interrogated nature, and established the means to harness some of its terrible powers, they wanted to prove themselves 'useful'. Such a culture influences those who follow — and can take generations to wear off.

Costing and planning of new nuclear power stations will now be carried out in the light of three data points: Three Mile Island in 1979, Chernobyl in 1986 and Fukushima in 2011. In each case, excuses are readily made by supporters of nuclear power. For Three Mile Island, they were that radiation releases were minimal, and that a supposedly unsophisticated American public confused the accident with the plot of *The China Syndrome*. Communist incompetence, we are told, contributed to Chernobyl being as bad as it was. The race is now on to find a narrative that explains away the ugly reality of the Fukushima disaster. The alleged uniqueness of the earthquake and tsunami event is already emerging as the front runner.

Yet the real risk of nuclear power is that active human intervention has to be maintained, come rain, shine, war or political upheaval. That, and the threat of a downside too terrible to contemplate. ■

Colin Macilwain is a contributing correspondent with *Nature*.
e-mail: cfmworldview@gmail.com

THE RISK OF
**NUCLEAR
POWER**
IS THAT ACTIVE
HUMAN INTERVENTION
HAS TO BE
MAINTAINED.

➔ **NATURE.COM**
Discuss this article
online at:
go.nature.com/qfllrr

RESEARCH HIGHLIGHTS

Selections from the
scientific literature

ASTRONOMY

An embarrassment of planets

A system predicted to contain as many as seven planets orbiting a Sun-like star has been discovered 39 parsecs from the Sun — the most populous extrasolar planetary system found so far.

The planets orbit HD 10180 near the southern constellation Hydrus. Christophe Lovis at the University of Geneva in Switzerland and his team used a spectrograph at the European Southern Observatory in Chile to look for a characteristic stellar 'wobble' caused by planets tugging on their parent star. Their results suggest that five planets of a similar mass to Neptune orbit at distances of 0.06–1.4 times the Earth–Sun distance. A possible sixth planet, with a mass similar to that of Saturn, has an orbital period of about 6 years.

The seventh prospective planet could have a mass just 1.4 times that of Earth, making it the smallest extrasolar planet found so far. But with an orbital distance equivalent to just 2% of Earth's, it is likely to be a scorched world.

Astron. Astrophys. 528, A112 (2011)

CHEMISTRY

Vesicles form with pH shift

Lipid bilayers, which make up cell membranes, can change shape in response to external stimuli. To reproduce this behaviour in a synthetic system, Jan van Esch at Delft University of Technology

in the Netherlands and his co-workers have produced a vesicle — a water-filled compartment bounded by a bilayer membrane — that forms and collapses in response to changes in pH.

The system comprises a solution containing a molecule with two 'tails', each of which can form reversible covalent bonds with another molecule. When there is a sufficiently

high number of the molecules, the bonds form and the vesicles spontaneously take shape; conversely, when bonds break, the vesicles eventually collapse (**pictured**). The stability of the bonds is also affected by the solution's pH, with vesicles forming at a pH of more than 7, and dissociating completely when pH falls below 4.

These reversible vesicles might be useful for applications that require controlled encapsulation and delivery.

Angew. Chem. Int. Edn
doi:10.1002/anie.201007401 (2011)

CANCER IMMUNOLOGY

Hide no more, tumour

Deadly pancreatic tumours evade attack by the immune system by developing a stroma — a shell of connective tissue enmeshed with white blood cells that suppress the immune response. Robert Vonderheide at the University of Pennsylvania in Philadelphia and his team now report a way to reverse this immune suppression.

The authors studied



ARCHAEOLOGY

North America's first tool users?

The Clovis people who lived in North America about 13,200 years ago have long been thought to be the continent's first tool-using humans. But the discovery of older human artefacts at a site in Texas is challenging this idea.

In sediments dating from between 13,200 and 15,500 years ago, Michael Waters of Texas A&M University in College Station and his team found 15,528 stone artefacts that seem to have been undisturbed by soil movement. This suggests

that the artefacts, including ancient tools (**pictured**), existed before the Clovis people came to dominate the landscape. A few of the tools have similarities to Clovis ones, but are simpler and still distinct. The authors suggest that a different sort of people was using tools in North America before the Clovis people.

Science 331, 1599–1603 (2011)

For a longer story on this research, see go.nature.com/2sijzo

M. R. WATERS

21 patients undergoing chemotherapy for pancreatic cancer, and added an antibody that stimulates a protein called CD40 to their treatment regimen. CD40 is known to activate certain types of immune cell, including tumour-specific T cells. Tumours in four of the patients regressed.

The scientists repeated the treatment regime in mice genetically engineered to develop similar pancreatic cancers. About 30% of mouse tumours regressed, with holes appearing in the stroma. Surprisingly, the immune cell responsible for killing tumour and stroma cells was not the T cell but the macrophage.

Science 331, 1612–1616 (2011)

For a longer story on this research, see go.nature.com/2ZNMhb

NEUROSCIENCE

No sleep, better mood

Sleep-deprived people are known to have stronger reactions to negative experiences, but some patients with depression seem to perk up with lack of sleep. To resolve this paradox, Matthew Walker at the University of California, Berkeley, and his team used functional magnetic resonance imaging to scan the brains of 14 people who hadn't slept for about 36 hours while presenting them with emotionally neutral and pleasant-looking images.

The volunteers rated a greater proportion of the images as 'pleasant' than did people who had maintained a normal sleep routine. The sleep-deprived individuals also showed increased activation in brain regions that mediate reward-driven behaviour, as well as greater connectivity between certain visual and emotional processing centres.

The results suggest that sleep deprivation can enhance reactivity to both positive and negative stimuli.

J. Neurosci. 31, 4466–4474 (2011)

BIOPHYSICS

Tiny swimmers trapped by lasers

Large, self-propelling microorganisms can be optically trapped with laser beams, a process previously achieved only for smaller motile cells such as sperm and *Escherichia coli*.

Gregor Thalhammer and his colleagues at Innsbruck Medical University in Austria used two opposing laser beams and a system involving a mirror, prism and lenses to capture a variety of organisms. These included protists such as dinoflagellates and *Euglena gracilis*, which measures, on average, 50 micrometres in length. The team's technique avoids creating damaging levels of heat. *Euglena* was held for 13 minutes without showing signs of heat stress. The method could be used to manipulate microbes for imaging, as well as in other experiments, the authors say.

J. Opt. 13, 044024 (2011)



ECOLOGY

Feasting fish scatter seeds

Massive Amazonian characid fish can carry seeds kilometres across jungle flood plains, potentially making them one of the most important seed distributors in this habitat.

Jill Anderson, now at Duke University in Durham, North Carolina, and her colleagues radio-tracked 24 of the animals (*Colossoma macropomum*; pictured) during three flood seasons. They also monitored how long captive fish of this species retained consumed seeds.

COMMUNITY CHOICE

The most viewed papers in science

STEM CELLS

The roots of insulin production

HIGHLY READ
on www.cell.com
19 Feb–21 Mar

The pancreas harbours a small population of insulin-producing stem cells — cells that might one day be harnessed to replace damaged cells in people with diabetes.

Whether new insulin-producing β -cells in the adult pancreas develop from stem cells has been hotly debated. Simon Smukler and his colleagues at the University of Toronto in Ontario, Canada, now report the isolation of 'pancreas-derived multipotent precursor cells' from mouse and human tissue samples. These cells make insulin and can take on various cellular identities, including that of the β -cell. The authors traced the origin of the mouse precursor cells to the embryonic pancreas.

Transplantation of both mouse and human precursor cells into diabetic mice lowered blood sugar levels and reduced diabetes-associated weight loss.

Cell Stem Cell 8, 281–293 (2011)

The authors conclude that wild fish can probably carry seeds up to 5.5 kilometres — one of the longest distances reported for fruit-eating animals — often to habitats where the seeds will germinate once the flood waters recede. However, overfishing has greatly depleted the numbers of larger *C. macropomum*, which carry seeds farther than their smaller counterparts, and may be threatening this mode of seed dispersal.

Proc. R. Soc. B doi:10.1098/rspb.2011.0155 (2011)

For a longer story on this research see go.nature.com/fv4zyd

ARCHAEOLOGY

Early farmers caused floods

Several hundred years before Europeans settled in North America, small Native American farming communities were already having a big impact on eastern flood plains — clearing the land and thus increasing erosion, runoff and flooding.

Gary Stinchcomb of Baylor University in Waco, Texas, and his colleagues dug deep

into the banks of the Delaware River at a site in Pennsylvania looking for prehistoric changes in soil chemistry and sediment particle size, and for ancient plant material. They found increased sediment deposits from AD 1100–1600 — an indicator of elevated erosion — as well as signs that humans had cleared trees around rivers to farm corn. The erosion and flooding were made worse by the wet climate of the Little Ice Age in AD 1450–1530. European settlers later caused further ecological changes to the flood plains as a result of their various land-use practices.

Geology 39, 363–366 (2011)

CORRECTION

The highlight 'Copper makes for selectivity' (*Nature* 471, 413; 2011) stated that selectivity of 90% was achieved using organolithium reagents. In fact, this was achieved by using organolithium reagents in combination with copper-based catalysts.

NATURE.COM

For the latest research published by Nature visit:

www.nature.com/latestresearch

SEVEN DAYS

The news in brief

POLICY

Elections in Canada

Research funding agencies in Canada remain unclear about next year's budget following the toppling of the minority Conservative government. Opposition parties were poised to reject the 2011–12 spending plan, but shortly after it was announced on 22 March, the government was ousted by a vote of no confidence on the grounds of sleaze and financial mismanagement. A federal election will be held on 2 May. See go.nature.com/wsplng for more on science measures in the original budget.

UK budget

A £100-million (US\$160-million) investment in research infrastructure and measures to streamline clinical trials were highlights for scientists from the United Kingdom's 2011–12 budget, announced on 23 March. The boost — which includes £70 million to help companies at existing life-science campuses in Cambridge and Norwich — only slightly softened the blow of deep cuts to science facilities announced last year. The government also announced plans to create a single regulatory agency to cut red tape around clinical-trials research, responding to January recommendations by an Academy of Medical Sciences report. See go.nature.com/ixvuoi for more.

River reserve

Five countries have agreed to create what would be Europe's largest protected river-based ecosystem: a cross-border nature reserve encompassing the Mura, the Drava and the Danube. Austria, Croatia, Hungary, Serbia and Slovenia signed the declaration on 25 March.



AP/PRESS ASSOCIATION IMAGES

Radioactive water slows nuclear cooling

Hundreds of workers trying to restore cooling systems at Japan's crippled Fukushima nuclear power plant have been hindered by radioactive water in flooded turbine buildings and reportedly leaking from reactor units. On 24 March, three workers were exposed to high localized radiation (around 2–3 sieverts in total) while standing in water in a building near reactor 3 to work on electricity cables.

They were hospitalized (pictured, covered by tarpaulin) but released four days later. As *Nature* went to press, Japan's Nuclear and Industrial Safety Agency warned of contaminated water in overflow tunnels from three reactor units, reaching a potentially lethal dose of 1 sievert per hour on its surface. For more on fallout levels around the reactor, see page 555.

Parts of this biodiversity hotspot are already protected in the individual nations, but the group hopes — in two or three years — to have a larger 800,000-hectare area declared a 'biosphere reserve' by the United Nations Educational, Scientific and Cultural Organization in Paris.

China rising

China will be publishing more research papers than the United States by 2020 — and that might happen as soon as 2013 if linear projections hold, a report issued by the UK's Royal Society suggested. The report, which looked at

changing patterns of science production around the world, emphasized that the quality of China's research would not match its quantity. See page 559 for more.

Cloned food

The European Union has been left with no legislation on sales of food and dairy products from cloned animals and their offspring, after last-minute talks in Brussels ended without agreement on 29 March. The European Parliament and the European Council of Ministers had been negotiating for three years on the 'novel foods' legislation,

which also includes the use of nanomaterials in foods. Talks broke down on the feasibility of labelling all food derived from clones' offspring. As a result, 1997 regulations remain in force, and any new proposal for legislating cloned animal products must start from scratch. See go.nature.com/3izkke for more.

BUSINESS

Drug deal dropped

Drug companies Merck & Co., of Whitehouse Station, New Jersey, and Sanofi-aventis, based in Paris, have abandoned plans to form a

joint venture of animal-health units — each generating more than US\$2.5 billion in 2010 sales — that would have created the world's largest animal-health business.

The deal was announced a year ago, but the companies said on 22 March that fair-competition regulations and other aspects of the transaction were too complex to make a merger worthwhile.

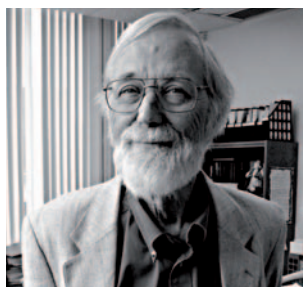
BP's Russian deal

A collaboration announced in January between BP and Russia's state oil company, Rosneft, to drill for oil in the Russian Arctic now seems doubtful after BP's existing Russian partner, TNK-BP, won a court ruling last week to block the deal. The companies had hoped to swap shares and drill in the Arctic waters of the Kara Sea — a venture criticized by environmentalists concerned about the dangers of drilling in the Arctic.

Skin-cancer drug

An eagerly awaited treatment for late-stage melanoma — the deadliest form of skin cancer — was approved by the US Food and Drug Administration on 25 March. Sales of ipilimumab (Yervoy), made by Bristol-Myers Squibb of New York, could reach more than US\$1 billion a year, analysts predict. See page 561 for more.

PEOPLE



Abel award

Mathematician John Milnor, of Stony Brook University in New York, has been awarded this year's Abel Prize in mathematics, worth around US\$1 million and considered as prestigious as the Nobel prizes. A polymath whose work spans topological conundrums, group theory and dynamical systems, Milnor has already won just about every other prize available in his field, including the Fields Medal (1962) and the Wolf prize (1989). See go.nature.com/frdfhh for more.

RESEARCH

Arctic sea ice

Sea-ice cover in the Arctic seems to have peaked this year at the lowest maximum since satellite measurements began in 1979. The US National Snow and Ice Data Center in Boulder, Colorado, declared on 23 March that, with sea ice

retreating, the extent reached on 7 March was probably the winter's peak. On that day, around 14.64 million square kilometres of sea in the Arctic were at least 15% ice-covered, under a measurement system used by the data centre. This ties with 2006 for the lowest maximum recorded by satellite, and is 1.2 million square kilometres below the average extent for the 1979–2000 period.

Tiger census

Heartening news for endangered big cats: India's tiger population has risen by around 16% in the past four years, according to a 2010 census whose results were reported at a conference in New Delhi on 28 March. The government-funded Project Tiger programme estimated the tiger population last year at 1,706 ($\pm 9\%$). Even excluding 70 tigers seen in areas that had not been surveyed before, this is an improvement on the same programme's estimate of 1,411 tigers ($\pm 17\%$) in 2006. Around half of the world's tigers are thought to live in India.

Nuclear opinion

Protests against the use of nuclear power continued last week. Tens of thousands marched in Germany, and hundreds joined an anti-nuclear rally in Tokyo. In the

COMING UP

2–6 APRIL

The American Association for Cancer Research meets in Orlando, Florida. Topics include how best to analyse a flood of newly sequenced cancer genomes.

go.nature.com/yiytk

3–8 APRIL

The European Geosciences Union holds its annual general assembly in Vienna, with discussions on Japan's earthquake and tsunami.

go.nature.com/huj6ko

United States, public support for the increased use of nuclear power has dropped to 39%, with 52% of people opposed to it, reported the Pew Research Center for the People & the Press in Washington DC on 21 March. In comparison, the centre's October 2010 poll found 47% were for nuclear power, and 47% were against. But opinions can swing sharply: the centre said that support for more offshore oil and gas drilling, which dipped after the Gulf of Mexico oil spill, has now rebounded to near its pre-spill level.

Stardust's end

NASA has bade farewell to its comet-chasing Stardust spacecraft. The probe was launched in 1999, and in 2004 collected a canister of dust from comet Wild 2, together with interstellar dust, returning it to Earth two years later. With fuel to spare, Stardust was then sent to take images of the previously examined comet Tempel 1, which it flew past in February this year. On 24 March, Stardust burned up its final fuel and was left to orbit the Sun.

► NATURE.COM

For daily news updates see:

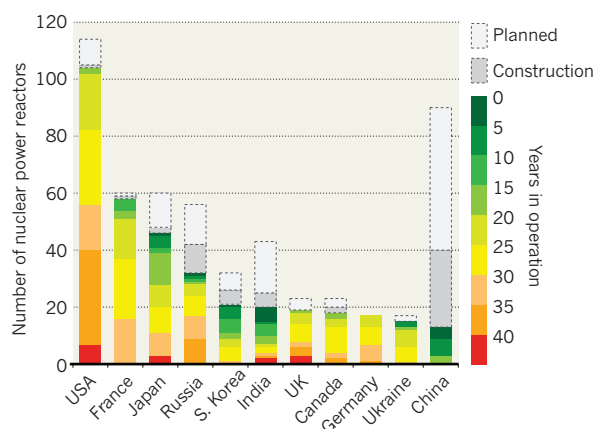
www.nature.com/news

TREND WATCH

If the Fukushima crisis causes expansion of the nuclear power industry outside Japan to slow, the effects will be felt most keenly in China, India and South Korea where, before the disaster, speedy and extensive construction had been planned. Conversely, in the United Kingdom and the United States, which have some of the oldest reactors still in operation, any intended 'renaissance' amounts to little more than replacing those plants that have already seen more than 40 years of service.

THE WORLD'S NUCLEAR POWER PLANTS

The world's newest reactors are mainly being built in Asia.



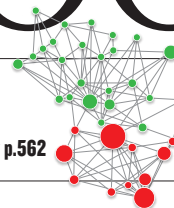
NEWS IN FOCUS

JAPAN How the disaster exposed flaws in earthquake preparations **p.556**

CONSERVATION A mega-deal to preserve Canada's forest may unravel **p.560**

NUCLEAR POWER The Chernobyl disaster casts a long shadow **p.562**

SOCIAL SCIENCE Pentagon tries to forecast conflicts **p.566**



ITSUO INOUE/AP/PRESS ASSOCIATION IMAGES



fishing in the areas worst affected, he says.

It is already clear that Japan's geography has been crucial to reducing the accident's impact. Initial estimates suggest that Fukushima's reactors have emitted one-tenth of all the radioactive material released during the Chernobyl disaster in 1986, and prevailing winds have swept most of the radioactivity over the Pacific Ocean. Austria's Central Institute for Meteorology and Geodynamics in Vienna estimated last week that although Fukushima's radioactive plume has now dispersed across the Northern Hemisphere, negligible levels of volatile radioisotopes such as iodine-131 and caesium-137 (the major components of the plume) have hit countries outside Japan. By contrast, radiation from land-locked Chernobyl spread across much of Europe (see page 562).

Fukushima's plume is still being fed by continued emissions from its damaged reactors, but when these are halted and the plume dissipates, the long-term impact on Japan will depend on which radioisotopes have been deposited on the ground, and in what quantities. Concentrations of caesium-137, which has a half-life of 30 years, are particularly important in determining which areas will be off-limits for settlement or farming, and for how many years.

On Sunday, the International Atomic Energy Agency (IAEA) reported that 16 of Japan's 47 prefectures showed daily deposition rates on the ground of less than 860 becquerels per square metre (Bq m^{-2}) for iodine-131, and 100 Bq m^{-2} for caesium-137. The IAEA also reported that contamination has not increased in 28 of Japan's prefectures over the period 18–25 March. But higher contamination was recorded in Yamagata prefecture, immediately northwest of Fukushima prefecture: $7,500 \text{ Bq m}^{-2}$ of iodine-131 and $1,200 \text{ Bq m}^{-2}$ of caesium-137, which exceeds recommended contamination levels for growing green leafy vegetables. No data were available for Fukushima prefecture itself, where high contamination rates are expected.

Those data are consistent with the results of aerial monitoring of ground radiation carried out by the US Department of Energy. A survey of the region on 22 March showed no increase in deposition of radioactivity compared with a previous survey on 17–19 March, despite the wind blowing inland from the plant for some of that time, suggesting that there had not been a significant additional dump of radioisotopes.

The survey showed that the highest radioactivity doses on the ground (greater than ►

Fears over the spread of radiation from the Fukushima nuclear reactors have sparked protests in Tokyo.

NUCLEAR POWER

Radioactivity spreads in Japan

Fallout is localized, but could persist for years in some regions.

BY DECLAN BUTLER

In a week that has seen little good news about the stricken Fukushima Daiichi nuclear reactors, the latest data on radioisotope fallout from the plant is so far offering a glimmer of hope.

Monitoring efforts are showing that although the reactors have released significant amounts of radiation into the atmosphere, dangerous contamination is mostly localized in a narrow zone northwest of the plant.

Emissions are also lower than immediately after the initial explosions, but radioisotope release continues and trends are unpredictable.

Working through the details is going to take time, and experts are struggling to assess the situation. "We don't have enough data yet, and what we have are still patchy," says Jim Smith, an environmental physicist at the University of Portsmouth, UK. In the meantime, the Japanese authorities are taking many of the right precautions, such as quickly implementing an evacuation zone, and banning farming and

► 0.125 millisieverts per hour; mSv h^{-1}) were restricted to a narrow band within 40 km of the plant, stretching to the northwest (see 'Fukushima's fallout'). No values anywhere exceeded 0.3 mSv h^{-1} , a dose likely to cause adverse health effects in anyone continually exposed for a few months. Still, doses at some sites over the course of a year would top $1,000 \text{ mSv}$, enough to cause symptoms of radiation sickness, including nausea, hair loss and reduced white-blood-cell counts.

Much of the 20-km evacuation zone around the plant had far lower dose levels, below 0.012 mSv h^{-1} . Nevertheless, that corresponds to a potential annual dose of more than 100 mSv , more than five times the annual limit permitted for UK nuclear-industry workers. The patchy distribution of fallout reflects the role of wind patterns and rainfall in washing out radioisotopes to the ground. Overall, Smith says he was "relieved" by the data, as they suggest that contamination around Fukushima will be much lower than that seen around Chernobyl.

But some areas of high contamination seem to lie outside the exclusion zone. Soil samples taken on 20 March from a location 40 km northwest of the plant showed caesium-137 levels of $163,000 \text{ becquerels per kilogram (Bq kg}^{-1})$ and iodine-131 levels of $1,170,000 \text{ Bq kg}^{-1}$, according to Japan's science ministry. Acceptable contamination levels for areas used to grow crops are much lower, typically in the range of a few hundred Bq kg^{-1} . "If there are significant areas of caesium-137 soil concentration of the order of $100,000 \text{ Bq kg}^{-1}$, evacuation of these areas could be effectively permanent," says Smith.

Detailed maps of caesium-137 distribution would help to identify hotspots where people need to be evacuated urgently, he adds. An

estimated 200,000 people have already been evacuated from Fukushima's 20-km zone, and on 25 March, the government encouraged people living in the 10-km radius beyond that to leave voluntarily.

The dispersal of much of the radioactivity over the ocean clearly helped to prevent a worse situation inland, but it is bringing its own problems. Data released last week by Japan's science ministry showed high surface seawater concentrations of $24.9\text{--}76.8 \text{ becquerels per litre (Bq l}^{-1})$ of iodine-131, and $11.2\text{--}24.1 \text{ Bq l}^{-1}$ of caesium-137 some 30 km offshore, although these levels seem to be decreasing. By contrast, the IAEA reported this week that radioactivity levels near the plant's discharge pipes were increasing, with $74,000 \text{ Bq l}^{-1}$ of iodine-131 and

$12,000 \text{ Bq l}^{-1}$ of caesium-134 and caesium-137 combined. Recommended maximum coastal discharges from nuclear power plants are typically lower than $4,000 \text{ Bq l}^{-1}$.

As a result of the nuclear accident, Japan has banned all fishing within 20 km of the Fukushima plant. Seaweeds and other marine organisms can concentrate radioisotopes from the water, and it will be necessary to monitor their transport through the food chain, says Timothy Mousseau, a radioecologist at the University of South Carolina in Columbia. Smith adds: "There has obviously been significant contamination of the marine system, although I would expect that the enormous dilution of the ocean would significantly limit potential doses and impacts."

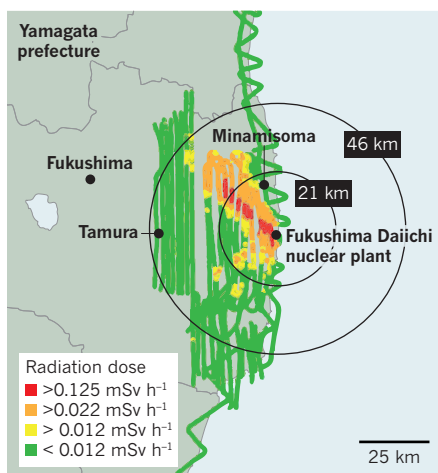
On 27 March, a new threat arose from highly radioactive water flooding the basements of Fukushima's reactors, in some areas delivering a potentially lethal dose of $1,000 \text{ mSv h}^{-1}$. The water is seeping into piping trenches less than 70 metres from the sea shore, raising the spectre of serious contamination of the sea and groundwater in the area. Yukio Edano, Japan's chief cabinet secretary, has promised a massive effort to prevent that from happening.

As long as the reactors continue to release radioisotopes, the human and environmental toll from the Fukushima power plant can only grow. Once emissions are halted, atmospheric radiation levels will fall quickly, as will ground levels of short-lived isotopes. Iodine-131 is responsible for a large share of the total released radioactivity, for example, and has a half-life of just 8 days. But it may be many weeks, or months, before the power plant is tamed — and years before parts of northern Japan tainted by long-lived radioisotopes are habitable again. ■

SOURCE: US DEPT OF ENERGY

FUKUSHIMA'S FALLOUT

Data from air and ground monitoring show that highly radioactive fallout is largely localized within a narrow band northwest of the stricken plant.



DISASTER PREPAREDNESS

Japan faces up to failure of its earthquake preparations

Systems for forecasting, early warning and tsunami protection all fell short on 11 March.

BY DAVID CYRANOSKI IN TOKYO

Japan has the world's densest seismometer network, the biggest tsunami barriers and the most extensive earthquake early-warning system. Its population is drilled more rigorously than any other on what to do in case of earthquakes and tsunamis.

Yet this month's magnitude-9 earthquake surprised the country's forecasters. The grossly underestimated tsunami destroyed the world's deepest tsunami barrier and caught people by

surprise. And the early-warning system for earthquakes largely failed. What went wrong?

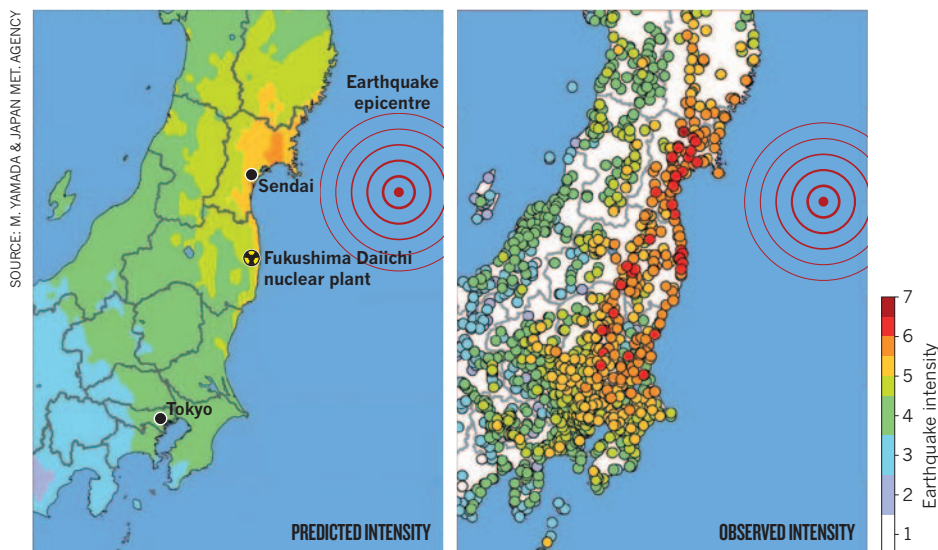
The first problem was the earthquake forecast. Japan's seismic hazard map, the latest version of which was released in March 2009, breaks the offshore area of northeastern Japan into five seismic zones and envisages seven different earthquake scenarios. Each is assigned a probability based on the historical record of earthquakes. The southern Sanriku offshore region, which included the origin of this month's earthquake, was given a 30–40%

chance of rupturing in the next 10 years and a 60–70% chance in the next 20 years.

As earthquake forecasting goes, these are very high numbers. "That basically means it could happen any day," says Yoshinori Suzuki of the Earthquake Disaster Reduction Research Division within the science ministry, which coordinates the map-making. But the fault was expected to unleash an earthquake of around magnitude 7.7 — about as large as any in the historical record for the area (see *Nature* 471, 274; 2011).

FALSE COMFORT

A warning system based on initial seismic signals predicted a limited region of intense shaking. The actual shaking was far more severe and widespread.



SOURCE: M. YAMADA & JAPAN MET. AGENCY

For a separate fault segment offshore from the Fukushima Daiichi nuclear plant, the same forecasting approach postulated only a magnitude-7.4 earthquake, with a less than 2% chance of occurring over the next 10 years and less than 10% over the next 50 years. The government of Fukushima prefecture even refers to the seismic hazard map to boast on its website: “With firm geological foundations and major earthquakes rare, Fukushima is a safe and secure place to do business.” What the risk maps didn’t allow for, however, was the coupling of segments that allowed the rupture to propagate for some 500 kilometres, unleashing an earthquake of magnitude 9.0 (see ‘False comfort’).

Japan’s earthquake forecasting has had its successes. In 2003, the magnitude-8.3 Tokachi-oki earthquake occurred right in the middle of a forecasted hotspot. But for the most part, earthquake forecasting, which really took off in Japan in the 1980s and 1990s, has had mixed results, with many devastating quakes hitting outside the expected zones. “We would like to see more hit the marks,” says Kyoto University’s James Mori.

Despite the surprisingly powerful earthquake, Japan’s earthquake-resistant buildings seemed to hold up well. “There was shaking damage but not much considering how strong the earthquake was,” says Mori. It was the tsunami that did most of the damage, overwhelming barriers and years of preparation.

The world’s deepest tsunami barrier, a 2-kilometre-long edifice at the mouth of Kamaishi Bay on the northeast coast, was completed in 2008 after 30 years, at a cost of more than ¥120 billion (US\$ 1.4 billion). Anchored to the sea floor 63 metres down and rising 8 metres above the water, the 20-metre-thick breakwater was designed to withstand the impact of a tsunami like the one from the 1896 Sanriku earthquake, which produced waves rising to

nearly 40 metres in some areas.

Koji Fujima, a specialist in tsunami wave propagation at the National Defence Academy in Yokosuka, says that this and other structures along the coast gave people a false sense of security. “The region probably gets 2- or 3-metre tsunamis more than once a decade, and people know that the breakwaters will protect them from those,” says Fujima. With the hazard map forecasting earthquakes in the magnitude-7.5 range, people would have anticipated a maximum tsunami of 4–5 metres.

TSUNAMI RISK UNDERESTIMATED

Faith in the barriers seems to have undermined Japan’s legendary tsunami-preparedness drills. In northeastern Japan as elsewhere, university professors, research institutes, non-governmental organizations and local civic groups carried out several drills each year to train people in how and where to evacuate. “We were working as hard as we could to educate people,” says Fujima.

Yet people apparently became relaxed about tsunami risks, says Yoshiaki Kawata, a disaster-management expert at Kansai University. A tsunami originating in Chile last year triggered an evacuation warning to 1.68 million people in northeastern Japan. Only 62,000 sought shelter, says Kawata.

“People thought the breakwater was enough,” says Fujima. But he adds that “there



➔ **NATURE.COM**
For more on the earthquake and nuclear crisis see: go.nature.com/ulsz2n

was no way it could protect them” against the tsunami on 11 March, although it did diminish the wave. Rising an estimated 15–20 metres at sea and 50 metres at some points after hitting the shore, even higher than

the 1896 wave, it destroyed the tsunami barriers at Kamaishi and elsewhere and has killed an estimated 20,000 people who had failed to find safe, higher ground. It also swamped emergency generators at the Fukushima Daiichi plant, disabling the cooling system (see page 555). Built in the 1960s, the plant was designed to withstand a tsunami of no more than 5.7 metres.

The early-warning system operated by the Japan Meteorological Agency, designed to alert people when an earthquake will create shaking at or above level 5 on Japan’s energy intensity scale (severe enough to crack walls), fell short as well. Based on a seismic reading taken a few seconds after an earthquake hits, the system provides up to tens of seconds of warning before the major shaking begins. On 11 March it delivered accurate warnings to areas near the epicentre. But the greater Tokyo region, where many areas experienced level-6 shaking, received no warning. Bullet trains and nuclear reactors, which have their own warning systems, shut down promptly, as designed.

The problem, according to Kyoto University’s Masumi Yamada, was that the system assumes a ‘point source’ for an earthquake. In this case, the point source led to an estimate of a magnitude-7.2 quake. But as the Sanriku rupture ripped hundreds of kilometres of fault line parallel to the coast, unleashing ever more energy and causing slips of 20 metres or more near the Tokyo region, the system didn’t correct itself. The frequent aftershocks also confounded the system, which generated several false alarms and missed large aftershocks.

“The system seems to break down around a magnitude-8 quake,” says Yamada. In April, she will start a three-year collaborative project with the Japan Meteorological Agency

“The system seems to break down around a magnitude-8 quake.”

to convert the point-source warning system to a dynamic one that works in two dimensions.

Japan’s disaster defences can certainly

be improved, says Fujima, but he thinks that people should recognize that there are limits to what can be done against a “once in a thousand or two thousand years earthquake”. Sturdier breakwaters could be built in areas where the tsunamis hit hardest, but they are expensive and could never fully protect against the biggest waves. “People probably should just stop building in the areas where large tsunamis will come,” he says.

Kawata, however, puts his faith in better engineering. He agrees that the most effective way to avoid damage is to have people live out of reach of tsunamis. But he envisages houses (and nuclear plants) built on an artificial coastline supported by 10-metre-high concrete pillars. “There are a lot of things we have to do urgently. If we have a vision and we pool our energies, we can do it.” ■

AP/PRESS ASSOCIATION IMAGES

FUNDING POLICY

NIH firm on grant application rules

Unpopular policy limiting applicants to two submissions has sped up approvals.

BY MEREDITH WADMAN

When does no mean no? The answer for researchers applying for funding from the US National Institutes of Health (NIH) is after the second 'no'. Last week, officials at the biomedical agency stood by that policy despite a 20 February petition from 2,335 scientists urging them to restore a system that allowed three tries per project. Some 400 more researchers have since asked to join the campaign.

The NIH's two-strikes-and-you're-out approach to funding grants was implemented in 2009 in an effort to speed up a dilatory review process. Last week, in a letter to petitioners, Sally Rockey, the agency's chief of extramural research, and principal deputy director Larry Tabak wrote that the policy is working as planned.

Not only has the average time to approve a grant been reduced by almost half a year, they argue, but the proportion of applicants winning funding on their first attempt has "risen dramatically" (see 'Shorter, faster, better?').

Tabak told *Nature* that, under the former system, peer reviewers tended to reject meritorious grants that were being submitted for the first time because they knew that the applicants would have two more attempts at

funding — in effect setting up a queuing system like that of planes lining up for take-off. The two-strikes policy, he says, "is accomplishing what it set out to do, namely to ensure that we support the strongest science as early as possible".

Robert Benezra, the cancer biologist at the Memorial Sloan-Kettering Cancer Center in New York who instigated the petition, is not persuaded. After digesting comments from the first 200 petitioners who wrote to him after he circulated the NIH response, he says, "the overwhelming sentiment is frustration with the fact that the NIH just ignored the central premise of our argument".

That premise is that peer reviewers cannot reliably distinguish between an application scoring in the fifth percentile — near the top — and one in the twentieth percentile. Therefore, in a time when limited resources are squeezing the proportion of fundable projects to as low as 5%, reviewers are effectively choosing at random from too many worthy proposals.

"Removing [second resubmissions] has the effect of eliminating outstanding grants that would otherwise be funded in time. In effect, queuing is the only fair way to go when dollars are so scarce," Benezra wrote to the petitioners on Friday. He recommends that the agency define a threshold — he suggests the 25th percentile — and allow grants that score at this level or better a second resubmission.

One of the petition's signatories, Martin Chalfie, a Nobel-prizewinning neurogeneticist at Columbia University in New York City, says that his deepest concern is the effect of the two-strikes policy on young scientists. "There's

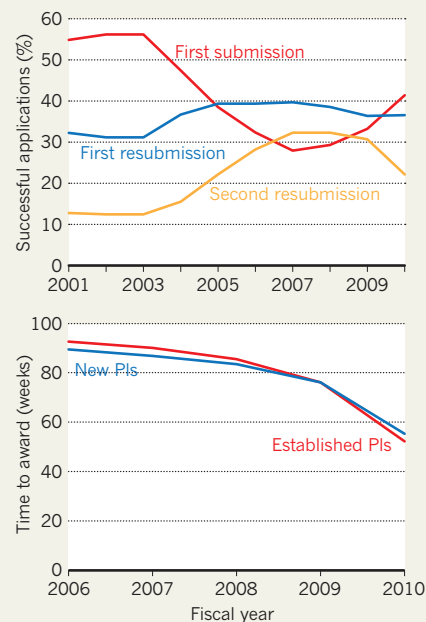


"The NIH just ignored the central premise of our argument."

Robert Benezra

SHORTER, FASTER, BETTER?

Since the NIH implemented its 'two-strikes' policy in 2009, the percentage of successful first-time applications has risen (top) and time to approval has fallen (bottom) for both new and established principal investigators (PIs).



a learning curve" to grant writing, he says, and "for junior people, we are making that learning curve exceptionally steep".

In their response, Rockey and Tabak counter that the new policy "seems not to have had an effect on new or early-career investigators". In fact, they argue, returning to a three-strikes policy might in fact work against young scientists trying to launch independent labs by lengthening the time it takes to get winning grants through the system.

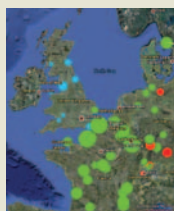
Although "there is little doubt that some great science is not being funded", Rockey and Tabak wrote, that is because budget pressures have forced the agency to fund an ever-diminishing proportion of applications. "Restoring [second resubmissions] will not change that picture."

Despite the groundswell calling for a return to a three-strikes system, some researchers say that even the two-strikes rule does not go far enough. Keith Yamamoto, executive vice-dean of the School of Medicine at the University of California, San Francisco, chaired an advisory committee that recommended that the NIH abolish resubmissions altogether — sparing applicants the time and stress of responding to one set of reviewer criticisms only to be rejected by a new group of reviewers with different opinions. Although the new system is working, says Yamamoto, eliminating resubmissions "would have worked even better".

Tabaka and Rockey note that the agency plans to solicit community opinion on the two-strikes policy in its next survey of extramural grantees late this year. ■

 **MORE ONLINE**

INTERACTIVE MAP



The world's nuclear reactors as you've never seen them before go.nature.com/sgnin3

MORE NEWS

- Offspring of scared birds grow longer wings go.nature.com/kyayan
- Models bolster case for early human effect on greenhouse-gas levels go.nature.com/z1buaz
- 'Virus-eater' discovered in Antarctic lake hints at hidden diversity go.nature.com/toxlzf

COMMUNITY

Research sans frontières

Academy report finds that international collaboration is on the rise, and should not be seen as an 'easy target' for cuts.

BY NATASHA GILBERT

Scientists used to interact with colleagues based abroad mainly at conferences. These days they are increasingly meeting at the lab bench, says a report by the Royal Society, Britain's national academy of science. More than 35% of all articles published in international journals are now the product of such collaboration, an increase of 10% in 15 years, says the study, *Knowledge, Networks and Nations: Global Scientific Collaboration in the 21st Century*.

Collaboration can boost citation impact, spread costs and broaden research horizons. It has, for example, enabled researchers at the International Rice Research Institute in Los Baños, the Philippines, to tackle scientific questions on a scale once thought impossible, says Robert Zeigler, director-general of the institute, which is part of the developing world's network of agricultural research centres — known as the Consultative Group on International Agricultural Research (CGIAR).

The CGIAR used to be “physically isolated from the advanced research institutes” in developed countries, says Zeigler. Today, the centres have partnerships with world-leading labs in Europe and the United States, working on challenging projects such as re-engineering photosynthesis in rice to be more efficient. “This would have been unheard of a decade ago,” says Zeigler.

The Royal Society's study, published on 28 March, finds that collaboration involving US scientists has grown the most during the past 15 years. The number of papers published with lead authors based in the United States and collaborators abroad has risen from about 50,000

in 1996 to around 95,000 in 2008. But the new total represents just 29% of the US research output. By contrast, almost half of all Germany's research output in 2008 involved international collaborations (see ‘A world of collaboration’).

The numbers are not rising across the board, however. Although in China collaboration is increasing overall, it is “not keeping pace with the even more dramatic rise in its overall publication productivity”, according to the report. As a proportion of China's annual national output, papers based on international collaboration fell from around 18% in 1996 to 15% in 2008. Other nations whose science base is growing rapidly, such as Brazil, show similar trends.

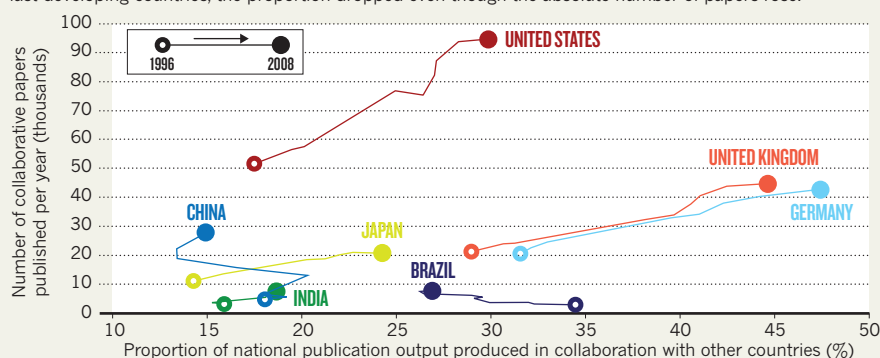
Each collaborating country increases a paper's impact, up to a tipping point of about ten countries, the report says. In some cases, the effect can be dramatic. Compared with papers by authors in Mexico alone, those with authors in both Mexico and Germany had three times the impact. And for authors in Russia, collaboration with researchers in Canada boosted impact by a factor of almost five.

For the traditional science powers, collaborating with up-and-coming countries such as China and Brazil is not just about increasing research impact, says Jonathan Adams, director of research-performance analysts Evidence, part of Thomson Reuters, in Leeds. “It's about keeping in touch with what they are doing,” he says.

The report notes that “the scientific superpowers of the 20th century remain strong”. But it warns these governments against viewing multinational research efforts as “easy targets” for spending cuts during tight fiscal times. Doing so, it says, could isolate national science activities, threatening quality and impact. ■

A WORLD OF COLLABORATION

In developed countries, collaborative papers increased as a proportion of national output. In some fast-developing countries, the proportion dropped even though the absolute number of papers rose.



SOURCE: R. SOC.



A year after it was unveiled, a landmark agreement to protect forests in Canada is not out of the woods.

CONSERVATION

Canadian forest deal at risk

Pact to preserve vast swathe of wilderness faces reluctance from industry and resistance from native groups.

BY CHRISTOPHER PALA

For conservationists, the promise seems almost too good to be true — and some worry that it is. The Canadian Boreal Forest Agreement, a deal between the forestry industry and environmental groups, aims to set aside nearly 30 million hectares of northern wilderness and subject a further 42 million to strict tree-harvesting standards.

Unveiled in May 2010 (see *Nature* **465**, 279; 2010), it would be the single biggest forest-protection deal ever, and has been portrayed by participants as a model of cooperation. At a briefing sponsored by the Canadian Embassy in Washington DC on 9 March, Avrim Lazar, president of the Forest Products Association of Canada in Ottawa, lauded former antagonists for “working together on how to meet the needs of humanity without trashing the environment, our own nest”.

But those close to the negotiations say that the agreement may fall short of its bold vision. With timber companies reluctant to forgo extensive logging rights, and environmentalists adamant that far-reaching protections must be enforced, questions remain over how much forest will actually be preserved. Meanwhile, Canadian aboriginal groups, who were left out of the deal-making process, are threatening to derail it.

“There are differences of expectations that will have to be reconciled,” says Lorne Johnson, co-chairman of the Canadian Boreal Forest Agreement’s secretariat in Ottawa, the body charged with implementing the plan.

Under the agreement, 21 forestry companies and 9 environmental groups are discussing ways to preserve large sections of Canada’s northern forest — a big storehouse of carbon and a crucial habitat for the threatened woodland caribou (*Rangifer tarandus caribou*) — without diminishing lumber and pulp production. The companies that hold the rights to log roughly one-quarter of Canada’s boreal forest have agreed to discuss giving them up in some unspecified areas; in exchange, the environmental groups have stopped urging buyers to boycott the companies’ products. The parties now have one year left to make significant progress on two decision tracks.

In the first track, working groups of company officials and environmentalists in seven provinces are trying to identify areas of caribou habitat to be removed from logging plans. The negotiators will then lobby the aboriginal and provincial governments who have jurisdiction over the regions to turn them into national or provincial parks. “We expect to have draft conservation plans ready to show the provincial and First Nation governments in Quebec, Ontario

and probably Alberta by June,” says Johnson.

In the other track, a three-man panel of forestry auditors is developing new harvesting standards for the remainder of the land. Those standards, which include better mimicking of the natural cycles of forest regeneration through fire and insects, would make the wood produced there “the most environmentally preferable” in the world, said Steven Kallick, director of the International Boreal Conservation Campaign of the Pew Environment Group in Philadelphia, Pennsylvania, at the Washington briefing.

But disagreements have plagued both tracks. Richard Brooks, forests campaign coordinator at Greenpeace Canada in Toronto, who also spoke at the Washington meeting, has said that the agreement “means upwards of 20 million hectares of caribou habitat need to be conserved”. But François Dumoulin, forestry director of AbitibiBowater in Montreal, one of Canada’s largest wood products companies and an industry participant in the agreement, rejects that interpretation. “We never agreed to that,” he says. “What we agreed to do is to increase the protected areas in the caribou range in ways that won’t disrupt the work of our mills.” Dumoulin says that it is too early to predict how much land will be set aside, “but it obviously won’t be close to the total 29 million hectares of caribou habitat”.

The original agreement pledged to respect “the principles of ecosystem-based management”, an approach that takes into account human needs as well as ecological concerns. This would include the needs of aboriginal communities and others who are economically tied to the forest, such as trappers and tourism organizations. But some forestry companies oppose that approach, saying that it infringes on their flexibility, and no decision has yet been taken as to whether people will be included in the agreement’s standards. Brooks says that the final plan must respect “all aspects including human ones” of ecosystem-based management. “If not, the agreement will not be successful,” he says.

Aboriginal groups are unhappy that they have not been included in the dialogue. In December, a special assembly of First Nation chiefs voted to “reject and demand the termination” of the agreement, signalling a major obstacle to the deal in portions of the boreal forest for which aboriginal communities have jurisdiction. Russell Collier, who works for the agreement’s secretariat, says that it was a mistake to leave the First Nations out of the talks, but adds that “an overlap of goals” could still bring native communities on board.

Others hope that the plan will survive, even if in a diminished form. “This is a framework on its way to becoming an agreement,” says Todd Paglia, head of ForestEthics in San Francisco, California, another participating group. “What that destination ends up looking like is still in the air.” ■

CANCER THERAPY

Melanoma drug wins US approval

Therapy is the first to extend lifespan in advanced cases.

BY HEIDI LEDFORD

A drug that takes an unusual approach to harnessing patients' immune systems to fight cancer has been approved by the US Food and Drug Administration (FDA). On 25 March, the FDA cleared ipilimumab, produced by Bristol-Myers Squibb, based in New York, to treat advanced melanoma, a particularly lethal form of skin cancer. Although the drug typically lengthens a patient's life by only 4 months or so, in clinical trials a fraction of patients lived much longer.

Ipilimumab marks success on two fronts: advanced melanoma, which has beaten multiple drug candidates, and cancer immunotherapy, which has had several high-profile disappointments in late-stage clinical trials.

Unlike other cancer immunotherapies on the market, which stimulate the immune system, ipilimumab lifts one of the immune system's restraints. The drug is an antibody that targets the protein cytotoxic T-lymphocyte antigen 4

(CTLA-4). CTLA-4 guards against autoimmune reactions by inhibiting some T cells, but can also keep the immune system from attacking cancers. "The other therapies slam on the immune system's gas pedal," says Patrick Hwu, an oncologist at the MD Anderson Cancer Center in Houston, Texas. "Ipilimumab releases the brakes."

Hwu helped to conduct some of the first clinical trials of the drug more than five years ago. Although patients with advanced melanoma rarely survive more than a year past their diagnosis, some of those initial participants are still alive, he says, years after receiving their final dose of ipilimumab. This stands in stark contrast to the widely hailed genetically targeted melanoma drugs, called BRAF inhibitors, that are currently wending their way through clinical trials. The inhibitors produce dramatic responses in patients whose melanoma has mutations in the BRAF protein, but the cancer becomes resistant

about seven months after starting the drug (see *Nature* **467**, 140–141; 2010).

Although ipilimumab can add years of life, only 20–30% of patients show any benefit at all (F. S. Hodi *et al.* *N. Engl. J. Med.* **363**, 711–723; 2010). "We clearly have to do much better than that," says Hwu. Furthermore, the drug caused severe or fatal side effects in almost 13% of patients, prompting the FDA to qualify its approval with a mitigation strategy.

Ultimately, the key may be to combine ipilimumab with targeted therapies such as the BRAF inhibitors, says James Allison, an immunologist at the Memorial Sloan-Kettering Cancer Center in New York. The targeted therapy would rapidly kill the cancer cells in more patients than would benefit from ipilimumab alone. That wave of destruction might then scatter cellular debris that could catch the attention of an immune system boosted by ipilimumab, yielding a more durable response. "To me this is the area with the most excitement," Allison says. ■

➔ **NATURE.COM**
For more see the
Outlook on cancer
prevention:
go.nature.com/9fqrbn



Ghost from the past: encased in crumbling concrete, the deadly contents of Chernobyl's reactor number 4 still exert a far-reaching effect on the area.

Chernobyl's legacy

Twenty-five years after the nuclear disaster, the clean-up grinds on and health studies are faltering. Are there lessons for Japan?

BY MARK PELOW

The morning train from Slavutych is packed with commuters playing cards, browsing e-readers, or watching the monotonous flood plains pass by. It looks like any other routine journey to work. But rather than facing a crush through subway turnstiles at the end of the 40-minute trip, the workers are met by a row of full-body radiation monitors. It is the start of another day at the Chernobyl power plant, the site of the world's worst civilian nuclear disaster.

As the train trundles through the bleak Ukrainian countryside, another nuclear crisis is unfolding halfway around the world. Barely a week after the partial meltdown at the Fukushima Daiichi nuclear power station, it is no surprise that some of the chatter on the train turns to the incident there. "It looks bad," says one commuter. "But not as bad as Chernobyl," he adds, with a hint of grim pride.

When Chernobyl's reactor number 4 exploded in the early hours of 26 April 1986,

the ensuing blaze spewed 6.7 tonnes of material from the core high into the atmosphere, spreading radioactive isotopes over more than 200,000 square kilometres of Europe (see 'The hottest zone'). Dozens of emergency workers died within months from radiation exposure and thousands of children in the region later developed thyroid cancer. The region around the plant became so contaminated that officials cordoned off a 30-kilometre exclusion zone that straddled Ukraine's border with Belarus. Today, a staff of about 3,500 enters the zone each day to monitor, clean and guard the site, where remediation work will continue for at least another 50 years (see 'Half-life of a disaster').

So far, the Fukushima accident is less severe. Radiation levels measured near the Japanese power plant have been less than those at Chernobyl after the blast there (see 'Exposure in context'). And although radiation has spread from Fukushima, it does not match the amounts that rained down in the region around Chernobyl.

Despite those differences, the quarter-century of work following the Chernobyl disaster will offer some important lessons for Japan as the nation begins to assess the health and environmental consequences of Fukushima. The problems that followed Chernobyl also provide a grim reminder about the value of accurate information. Officials need to tell people immediately how to avoid the initial, most dangerous, exposure; yet in the longer term, scientists and the government must battle against unnecessary concern over low-level doses of radiation, which often causes more harm than the radiation itself.

In some ways, the connection between the two accidents may yield the biggest benefits for Chernobyl. For a brief window of time, the world has again focused attention on the largely overlooked work there. The renewed interest may spur nations to chip in the cash needed to complete the clean-up of the site, and to carry out health studies that have languished for want of proper coordination and funding. "In recent years, Chernobyl has been neglected by funding agencies and, to an extent, the scientific community," says Jim Smith, a radioecologist at the University of Portsmouth, UK, who has studied the consequences of the accident for 20 years. "But there is still more to learn from Chernobyl about decommissioning and the effects of the radiation," says Smith, who is touring the site with a group of other scientists.

After clearing a security checkpoint, the visiting researchers board a bus that heads

HALF-LIFE OF A DISASTER

1986
26 APRIL

Owing to a flawed safety test, Chernobyl's reactor 4 explodes, scattering debris from the core over a wide area.



27 APRIL

A day after the blast, some 44,000 residents are evacuated from Pripjat, just 3 km from the reactor.

5 MAY

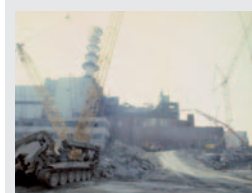
The fire in the reactor is finally extinguished, having released 6.7 tonnes of radioactive material over 200,000 square kilometres.

6 MAY

People and cattle are evacuated from a 30-kilometre exclusion zone around the plant.

AUGUST

4 months after the blast, 28 emergency workers have died from acute radiation sickness, caused by massive doses of radiation.



NOVEMBER

Workers complete a concrete sarcophagus around the shattered reactor to limit further release of radiation.

1991

Cases of thyroid cancer in local children have risen ten-fold from previous levels.



2000

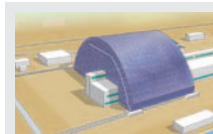
The last of Chernobyl's reactors is switched off.

2005

The United Nations Chernobyl Forum reports that no more than 4,000 people will die from the reactor's fallout.

2011

25th anniversary conference expects to see lobbying for more funds for clean-up and health studies.



2015

New safe confinement shelter projected to be completed.



2020

Remediation efforts at plant's cooling pond scheduled to be completed.

2065

Planned completion of clean-up at Chernobyl.

towards the heart of the ageing power plant. They pass abandoned buildings and bump along potholed roads running beneath archways made of piping; since the accident, pipes have been laid above ground to avoid disturbing contaminated soil.

The visitors stop to look at the most visible reminder of the accident, the concrete sarcophagus that entombs the shattered reactor building. Completed hastily in November 1986, the sarcophagus was built to contain the escaping radiation, but it is now crumbling and streaked with rust. Smith whips a dosimeter out of his rucksack and poses for a photograph in front of the sarcophagus. The reading is $5 \mu\text{Sv h}^{-1}$: about 10 minutes of exposure at that level equals the same dose as an arm X-ray.

The plant's bright main office is a stark contrast to the sarcophagus. Stained-glass windows depict — in glorious socialist-realist style — the harnessing of atomic energy. But the plant has not produced power since 2000, when the last reactor was shut down. Valeriy Seyda, a deputy director of the Chernobyl Nuclear Power Plant, explains that the plant's top priority now is to construct a new confinement shelter for reactor 4 before the sarcophagus becomes too unstable. If it collapses before the new shell is in place, it could throw up a cloud of radioactive particles and expose the deadly remnants of the reactor.

REPLACING THE RUSTING TOMB

The plan is to build an enormous steel arch adjacent to the reactor and slide it along a runway to cover the building. The arch will reach 105 metres high, with a span of 257 metres — the world's largest mobile structure, according to its designers. It is expected to be in place by 2015 and should last for 100 years. It will enable robotic cranes inside to dismantle the sarcophagus and parts of the reactor. Long-term plans call for finishing the clean-up work at Chernobyl by 2065.

Some of the concrete trenches for the project are in place. But the international Chernobyl Shelter Fund that supports the US\$1.4-billion effort still lacks about half of that cash, and the completion date has slipped by almost ten years since the shelter plan was agreed in principle in 2001. One of the key goals of a forthcoming conference — Chernobyl, 25 Years On: Safety for the Future — to be held in Kiev on 20–22 April is to secure more cash commitments from international donors. Meanwhile, Chernobyl is developing long-term storage facilities for the debris that will be hacked out of reactor 4; and for more than 20,000 spent fuel canisters from the site's other reactors, a facility that will cost about €300 million (US\$420 million).

Although all those reactors have been shuttered, the plant continues to generate large amounts of radioactive

waste — partly because of persistent flooding in some of the waste-storage buildings and reactor 4's turbine hall. Every month, at least 300,000 litres of radioactive water must be pumped out of the structures and stored on site.

The main cause of this flooding is Chernobyl's brimming cooling pond, which artificially elevates groundwater levels in the area. Alexander Antropov, a Chernobyl veteran with ice-blue eyes and a cool manner to match, is in charge of a project to decommission the pond. The term 'cooling pond' usually refers to the containers where spent fuel rods are stored until their radiation dissipates enough that they can be put into long-term storage. But Chernobyl's pond is actually a vast reservoir covering 22 square kilometres into which water from the reactor cooling systems was discharged. The pond also contains long-lasting radioactive material such as caesium-137 and strontium-90, which rained down after the explosion. Besides causing flooding at the plant, the high water levels in the cooling pond raise the risk that a weak dyke along its east side will burst, which would send water coursing into the Pripjat River. Radioactivity in the escaping water would be quickly diluted by the river, so although it would not significantly raise exposure levels for people downstream, it could cause panic among the local population.

Antropov says that his team cannot simply lower the water levels in the pond because they don't know what effect microscopic radioactive sediment particles would have if exposed. In the meantime, the team maintains the status quo by pumping water from the Pripjat River into the pond at a cost of a few hundred thousand euros per year. But the long-term plan is to lower the water level by 7 metres to form a patchwork of 10–20 smaller ponds that would keep the most dangerous sediments in place. The project would cost €3 million to €4 million, says Antropov. He is already in discussions with the relevant regulators and is optimistic that the necessary feasibility studies and environmental impact assessments can be completed.

But the effort has been a long time coming. The decommissioning plan is more than a decade old, and was supported by a 2005 survey for the European Commission, led by Smith. Once again, money has been a key factor in the delay. The major parts of Chernobyl's decommissioning plan are paid for by international funds, but the cooling pond project is not. Nor is the research needed to satisfy the regulators. "Most of our own activities come from the Ukrainian budget, and we are not a rich country," says Seyda.

After leaving the cooling pond, the visitors stop at Pripjat, an abandoned town just 3 kilometres from the reactor complex. Some 44,000 residents were evacuated the day after the accident, and many of their belongings still litter the decaying buildings. Antropov once lived here — his daughter was a few months old at the time of the accident — and as deputy

AKG-IMAGES/RIA NOWOSTI

I. KOSTIN/SYGMA/CORBIS

K. DIORIEV/REUTERS/CORBIS

IDÉ/VINCI

M. PEPLAW

➔ **NATURE.COM**
For a slideshow and other extras see:
go.nature.com/bmlu6

THE HOTTEST ZONE

Shifting wind patterns carried radiation from the Chernobyl blast across much of Europe (right). Plant operators are now trying to lower water levels in a massive cooling pond (below) filled with radioactive water and sediments.

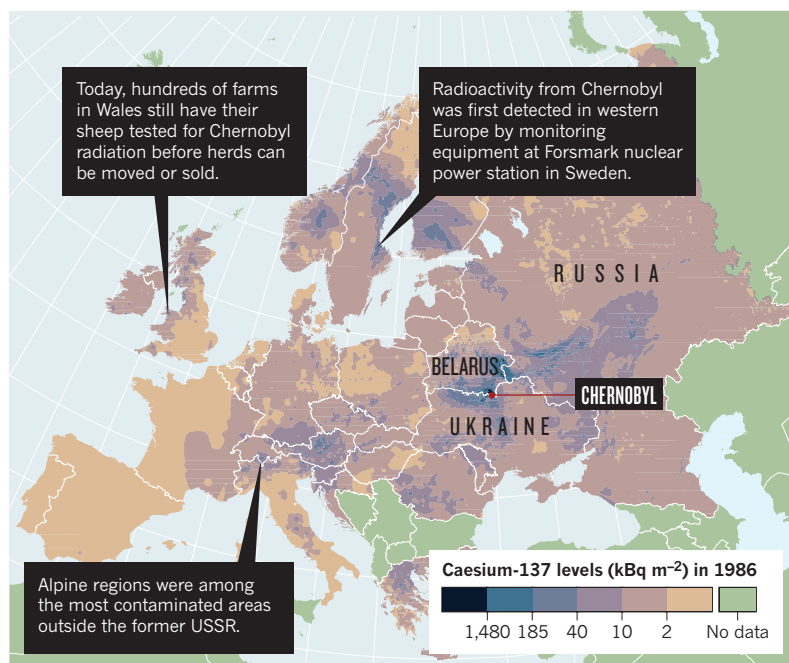
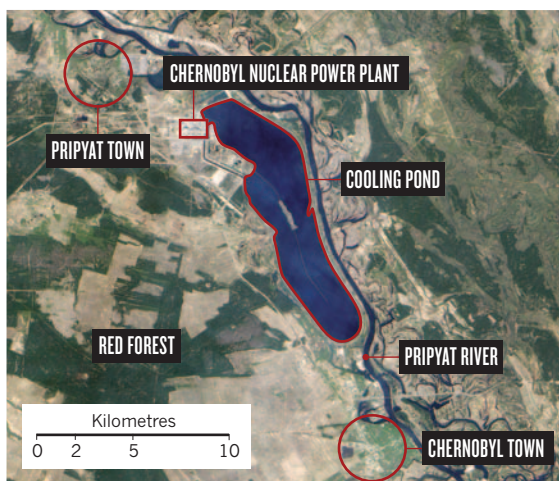


IMAGE CREATED BY J. ALLEN USING EO-1; SOURCE: NASA EO-1 TEAM

chief of the town's Communist party office, he was responsible for evacuating part of the town. Because he worked as a senior engineer at the nuclear plant, he knew that the disaster would have repercussions for decades to come. "I understood that I would never return to live in Pripyat," he says, in an uncharacteristically soft voice. "I still feel some sense of loss."

The evacuees from Pripyat also live with lingering fear about the radiation they were exposed to before fleeing their homes. Along with millions of others from the surrounding regions, they often attribute any sign of ill health to the accident. But pinning down Chernobyl's true public-health impact has proved remarkably difficult.

There is little disagreement about the terrible fate of the workers who brought Chernobyl's stricken reactor under control. Of 134 emergency workers diagnosed with acute radiation sickness, 28 died from their exposure within four months. Another 19 have died since from various causes, and many of the surviving workers now have cataracts and skin injuries.

More than 5,000 cases of thyroid cancer have so far been seen in people who were children at the time of the accident and lived in contaminated areas of the former Soviet Union — a more than ten-fold increase from normal levels (adults were mostly unaffected by the disease). Most of these cases were caused by drinking milk contaminated with radioiodine. Fewer than 20 of these people have died, but the sheer number of cancers, and their rapid onset within 5 years of the accident, surprised many epidemiologists.

This triggered a plethora of thyroid studies, most notably a long-term cohort study of 25,000 people in Ukraine and Belarus who were children in 1986 that is being coordinated by the US National Institutes of Health's

National Cancer Institute (NCI) in Bethesda, Maryland. The latest results from the Ukrainian section of this cohort¹ confirm previous findings that the incidence of thyroid cancer is proportional to the size of the dose, with a particularly high risk seen in younger people and in those who were iodine-deficient due to poor diet. The research is having a direct impact in Japan, where those at risk of exposure are being given potassium iodide tablets to prevent the uptake of radioiodine in their thyroid.

The NCI oversees a second cohort made up of liquidators, a group of more than half a million people sent into the exclusion zone to help clean up and monitor the area after the initial emergency phase of the accident. Liquidators have a slightly raised risk of developing cataracts, and possibly a small increased risk of leukaemia².

LONG-TERM EFFECTS

But what was the impact on the wider population? Various studies have tried to estimate how many deaths Chernobyl will eventually cause across the whole of Europe, but their answers range from a few thousand to hundreds of thousands³. Cancer causes about a quarter of all deaths in Europe, so teasing out Chernobyl's far-reaching influence would probably be impossible, say epidemiologists. Moreover, focusing on such intangible numbers can distract from the much broader social impact of the accident. In Ukraine and Belarus, hit hard by the break-up of the Soviet Union in 1991, lingering fears about radiation are thought to have contributed to a sense of hopelessness that is linked to high rates of alcoholism and smoking — factors that have a much bigger health impact.

"There's tremendous uncertainty for these people," says Elisabeth Cardis, a radiation

epidemiologist at the Centre for Research in Environmental Epidemiology in Barcelona, Spain. "Some think they are doomed because of their radiation exposure." Further research could provide convincing evidence that Chernobyl's radiation did not significantly harm the wider population, but "we won't know unless we look," says Dillwyn Williams, a cancer researcher at the Strangeways Research Laboratory in Cambridge, UK.

A handful of Chernobyl studies have found small increases in rates of breast cancer and cardiovascular disease, but they did not properly account for confounding factors, such as nutrition, alcohol consumption and smoking habits. And although some researchers have claimed to see an increase in genetic mutations in the children of parents irradiated after Chernobyl⁴, there has been no similar evidence of hereditary effects even in the children of Japanese atomic bomb survivors, who on average received much larger radiation doses.

This means that there is still a substantial gap in the overall understanding of Chernobyl's health effects, says Williams. The problem is exacerbated by the piecemeal nature of previous studies. "There has been a failure of European-level coordination on this," he says.

Williams hopes that there is now a chance to establish a Chernobyl Health Effects Research Foundation, which would mirror the highly effective Radiation Effects Research Foundation that monitors the long-term health impacts of the atomic bombs in Japan. Together, the efforts could reveal the differences between the single short-term dose of external radiation delivered by the atomic bombs, and the low-level long-term exposure seen after Chernobyl. Long-term doses were once thought to carry much less risk than the immediate exposure, but evidence is accumulating that the risks

may be much the same⁵. If confirmed, it would mean that people routinely exposed to low-level radiation have a greater chance of health problems than previously thought.

The European Commission has funded Williams, Cardis and a core group of other scientists to develop a research plan, dubbed the Agenda for Research on Chernobyl Health (ARCH), that maps out how the existing cohorts could be used to study a wider range of diseases, such as breast cancer and cardiovascular disease, and to address the questions about the long-term effects of low doses. The liquidator cohort, for example, is six times larger than that of atomic bomb survivors, with a much wider range of exposure doses. It could show how risk varies over that large range of doses and uncover rarer effects at lower doses. It could also help to reassess the threshold dose to prevent nuclear workers from developing problems such as cataracts.

ARCH also suggests testing the feasibility of setting up new cohorts including liquidators' offspring and highly exposed evacuees, along with a tissue bank. The bank may reveal whether people's genetic make-up influences their susceptibility to radiation — key information for determining how individuals are likely to respond to the radiation received during medical procedures such as X-ray scans and radiation treatment.

There are several hurdles, however, to getting ARCH off the ground. The project needs support from the NCI, which stopped funding active clinical monitoring of the thyroid cohort in 2008 because of budgetary constraints. And ARCH's proposals would also require better

access to medical records in Ukraine and more information about participants' lifestyle factors — both potentially tall orders.

The ARCH plan will be presented at the 25th anniversary conference in April, and Cardis hopes that a positive reception will prompt the European Commission to boost its support. It is likely to be difficult to secure a long-term commitment for the studies, which will cost about €3 million to set up, but that cost is minor compared with the billions that will be spent on remediation at Chernobyl, says Williams.

Beyond obtaining the necessary funds, researchers will also require cooperation from participants to expand the cohort studies. That could be difficult. Gennady Laptev, now a hydrologist based at the Ukrainian Hydrometeorological Institute in Kiev, was a liquidator for three years, and says that he stopped attending his medical check-ups about ten years ago because they were too time-consuming. "They never found any major health problems," he says.

Laptev's work involved flying by helicopter from Kiev to Chernobyl twice a week to take radiation readings and collect soil and water samples for analysis. "Nobody forced me to do the work — I did it because it was interesting, and I really enjoyed it," he says. But after three years, he became worried about the risk of working near the plant, so he took a job researching how radioisotopes dispersed in the local water system.

Concerns about radiation exposure continue to plague residents in the region, and the planned studies could provide the answers they so desperately need about Chernobyl's

real health legacy. "I have a house in a village near Slavutych, on contaminated territory," says Antropov during the site visit. "Two of my neighbours died of cancer, and this was probably the result of their radiation doses."

LESSONS FOR JAPAN

It's too early to say how the Chernobyl health studies will help those affected by the Fukushima accident. But Chernobyl has already given the world a lasting lesson on the importance of clear communication during a nuclear disaster, and in the years afterwards.

There was no systematic distribution of prophylactic potassium iodide to the people around Chernobyl, and Pripjat's children were allowed to play outside during the day after the accident, while the reactor continued to burn. "The failure to rapidly communicate radiation risks at Chernobyl led to people receiving higher radiation exposures than was necessary," says Smith.

The Japanese government has been lambasted for not keeping citizens well informed about the accident there. But it was swifter to act than Soviet officials were, ordering the evacuation of people who live near the plant within hours of recognizing the growing nuclear emergency, and expanding that evacuation zone to a radius of 20 kilometres the following day. As well as distributing potassium iodide, the Japanese government banned the sale of food and milk produced in the provinces around the stricken plant. "The Japanese have done exactly the right thing," says Andrew Sherry, director of the Dalton Nuclear Institute at the University of Manchester, UK.

Ultimately, says Smith, Chernobyl's most important lesson for Fukushima is that a nuclear accident haunts a region long after the reactors have cooled. If areas of Japan are significantly contaminated with radioactive caesium-137, which loses half its radioactivity in 30 years, the government may have to maintain an exclusion zone for decades. Decommissioning the Fukushima reactors may also take decades, depending on the extent of damage to their cores. And the uncertainty surrounding the health risks may exact a psychological toll that could surpass the physical harm from the radiation, adds Smith.

Many of the workers at Chernobyl understand those lessons all too well as they shuffle onto the train to Slavutych at the end of their day. The workers will return to tend to the plant tomorrow and the next day — and for many years to come. ■ [SEE EDITORIAL P.547](#)

Mark Peplow is Nature's news editor.

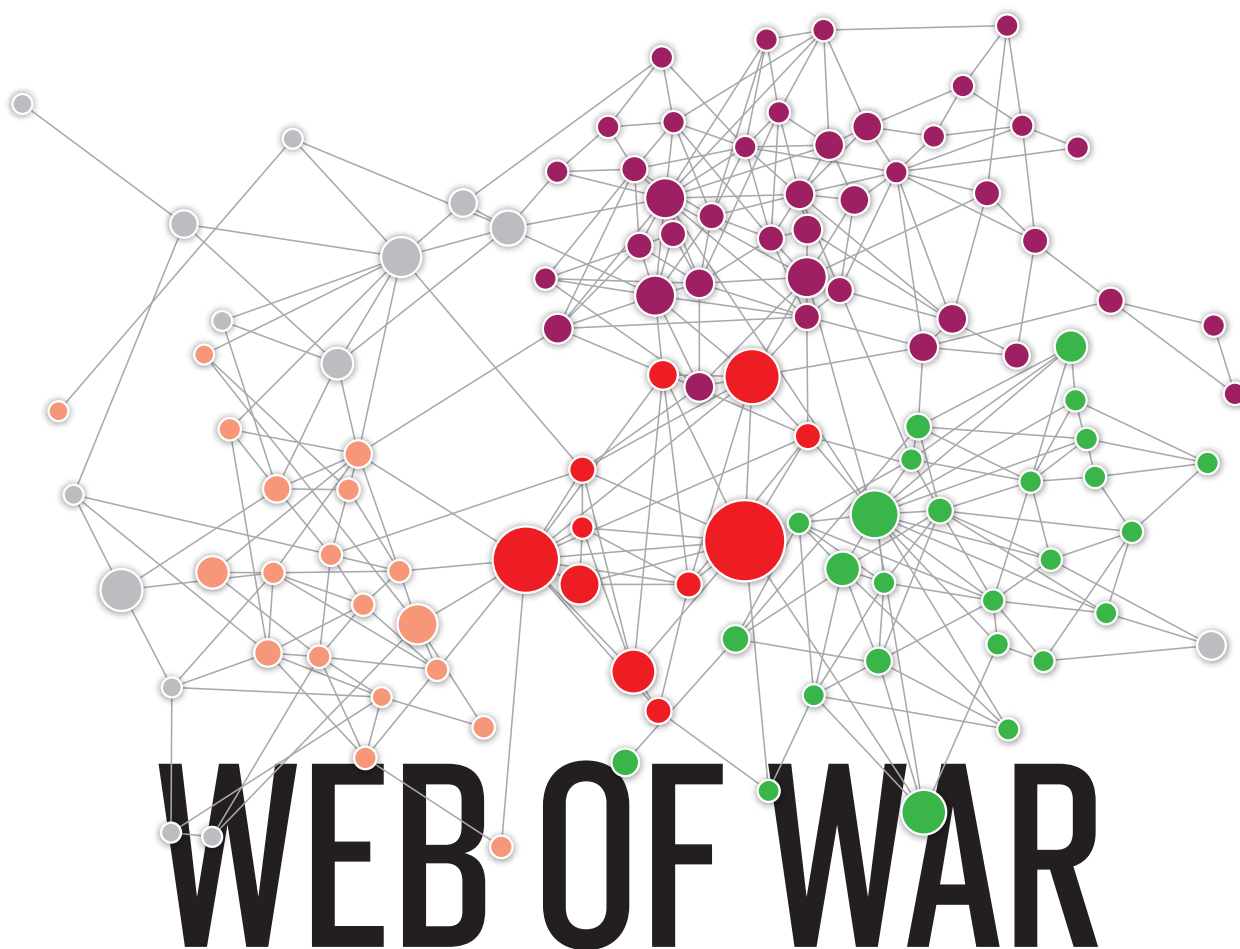
1. Brenner, A. V. *et al. Environ. Health Perspect.* doi:10.1289/ehp.1002674 (2011).
2. Cardis, E. & Hatch, M. *Clin. Oncol.* doi:10.1016/j.clon.2011.01.510 (2011).
3. Peplow, M. *Nature* **440**, 982–983 (2006).
4. Dubrova, Y. E. *et al. Nature* **380**, 683–686 (1996).
5. *Health Risks from Exposure to Low Levels of Ionizing Radiation: BEIR VII Phase 2* (NRC, 2006); available at <http://go.nature.com/r7jeca>.

“Some think they are doomed because of their radiation exposure.”

EXPOSURE IN CONTEXT

Many emergency workers at Chernobyl received lethal doses of radiation, but the broader public, even those living in the contaminated zone, were exposed to levels on a par with some medical procedures.

Dose (mSv)	Source/implication
Up to 5,000	One minute's exposure to Chernobyl core shortly after explosion
1,000	Causes temporary radiation sickness, including nausea and decreased white-blood-cell count
250	Upper annual limit allowed for Fukushima emergency workers
120	Average total dose received by liquidators at Chernobyl (1986–90)
30	Average total dose of external radiation received by evacuees from Chernobyl plant and surrounding area
20	Average annual limit for nuclear-industry workers
9	Total dose received by the 6 million residents in contaminated areas (>37 kBq m ⁻²) in former USSR
9	One computed-tomography (CT) scan
9	Annual exposure of airline crew flying regularly between New York and Tokyo
3	One mammogram
2.4	Average annual background radiation globally
0.3	Total dose received by each resident of Europe for 20 years after Chernobyl



*Can computational social science help to prevent or win wars?
The Pentagon is betting millions of dollars on the hope that it will.*

BY SHARON WEINBERGER

If George Clooney stars in a movie, will it be a hit? Or will it flop, like his 2008 comedy *Leatherheads*?

That question, at least in broad outline, made its way to Ken Comer, deputy director for intelligence at the Joint Improvised Explosive Device Defeat Organization (JIEDDO) of the US defence department, and the man at the centre of the US military's war on roadside bombs. He recently made the time for a briefing by scientists from the US Department of Energy, who were honing their modelling skills by working with a film studio on the formula for a successful blockbuster.

Comer listened to them describe how they had analysed and reanalysed the data that Hollywood vacuums up about its audiences, slicing the results in every way they could think of, only to come to the same conclusion every time: you can't tell. "You can dress George Clooney up," recalls Comer, "you can dress him down, you can put a beard on him, and yet there's no reliable method for predicting whether or not a George Clooney movie is going to be a blockbuster."

And that, says Comer, is a perfect illustration of why the Department of Defense (the Pentagon) is rethinking its data-mining approach to the problem of roadside bombs — not to mention counter-insurgency and other aspects of warfare. "I speak as one who has been swimming in data for three years," he says, referring to the reams of information that the department has compiled about roadside bombs after nearly a decade of war in Iraq and Afghanistan: "Data is not our solution to this problem."

Instead, Comer and other officials are placing their bets on a new generation of computer models that try to predict how groups behave, and how that behaviour can be changed. This work goes under a variety of names, including 'human dynamics' and 'computational social science'. It represents a melding of research fields from social-network analysis to political forecasting and complexity science.

Figures on total funding for this work are difficult to come by. But one of the field's major supporters, the Office of the Secretary of Defense, is planning to spend US\$28 million on it in 2011, almost all on unclassified academic and industrial research. And separate computational social-science programmes are being funded by bodies such as the Defense Advanced Research Projects Agency (DARPA), the Defense Threat Reduction Agency and the research arms of the Army, Navy and Air Force.

The Pentagon's embrace of this work has been so enthusiastic that some scientists have urged a slow-down, for fear that such nascent models will be pushed into operation before they are ready.

NATURE.COM
For more on the
Pentagon's use of
social science, visit:
go.nature.com/phyfjk

In their current state of development, says Robert Albrow, an anthropologist at American University in Washington DC, the models are often a waste of time. "I am not saying that computational social science is voodoo science," says Albrow, a member of the American

Anthropological Association's Commission on the Engagement of Anthropology with the Security and Intelligence Communities. "I'm saying that voodoo science is all too frequently being generated from the work of computational social science."

CLOUDY, WITH AN 80% CHANCE OF WAR

One often-cited inspiration for the current modelling work is an episode in 2003, when coalition forces in Iraq were searching in vain for deposed dictator Saddam Hussein. With conventional methods leading nowhere, a group of US Army intelligence analysts decided to aggregate the available information about Saddam's social network using a link diagram to depict relationships. As they factored in key variables such as trust, the analysts began to realize that the most-wanted government officials — those pictured on the 'personality identification playing cards' that had been widely distributed among US troops — were not necessarily the people whom Saddam trusted most, and were thus not likely to know where he was hiding. Instead, the diagram led the analysts to focus their attention on trusted lower-level associates — including one key bodyguard, whose information led the trackers to the dictator's underground hideaway on a farm near Tikrit.

**"I WOULD SAY
THE WEATHER
GUYS ARE FAR
AHEAD OF
WHERE WE ARE."**

Today's simulations are similar in concept, but with one crucial difference: the Army analysts' diagram was static, constructed by hand and analysed manually. Now the goal is to do all that with algorithms, using computers to integrate vast amounts of data from different sources, and then to keep the results up to date as the data evolve.

A prime example of a system that creates such models is the Organization Risk Analyzer (ORA): a 'dynamic network analysis' program devised by Kathleen Carley, a computer scientist at Carnegie Mellon University in Pittsburgh, Pennsylvania, who has emerged as a leading figure in Pentagon-funded computational social science. "We build the psychohistory models," Carley jokes, referring to the 'science' of group behaviour invented in the 1940s by the science-fiction author Isaac Asimov for his classic Foundation novels. "We are the Foundation!"

To create an ORA model for a politically unstable region such as

Sudan, explains Carley, she uses her own program, AutoMap, to trawl through publicly available news reports and automatically extract names and other key data (see 'The conflict forecast'). The ORA might then use that information to identify people — or, in the lexicon of social-network analysis, nodes — with a high degree of 'betweenness', meaning lots of direct connections to other people within the network. These individuals "are often those that are considered influential because ... they broker information between groups and so on", says Carley.

The same types of model can be used to predict how a terrorist ideology might catch on in the local population and propagate from person to person like a spreading virus. Carley's system can factor in cultural variables, using records of the opinions and attitudes that tend to prevail among specific ethnic groups. The goal, she says, is to produce an effective strategy for stopping the epidemic of radicalization or for destabilizing the terrorist networks by identifying key individuals and groups to be targeted with diplomatic negotiation or military action.

Another example is the Spatial Cultural Abductive Reasoning Engine (SCARE) developed by Venkatramanan Subrahmanian, a computer scientist and co-director of the Laboratory for Computational Cultural Dynamics at the University of Maryland in College Park. Subrahmanian says that SCARE was able to predict the locations of arms caches in Baghdad to within half a mile, using a combination of open-source data on past roadside bomb explosions and constraints based on distance (terrorists didn't want to carry their explosives very far for fear of getting caught) and culture (most of the attacks that they tracked came from Shiite groups with ties to Iran, so the caches were probably not in Sunni neighbourhoods). Subrahmanian says that he has given copies of the program to the military, and "they're clearly trying it out".

Can a model predict a war? The Integrated Crisis Early Warning System (ICEWS) is being developed with DARPA funding by university researchers working with defence giant Lockheed Martin. A revival, at least in part, of a more primitive, 1970s-era DARPA forecasting project, the current incarnation of the ICEWS focuses on predicting political events such as insurgency, civil war, coups or invasions. The system draws its data mainly from the Reuters online news feed, and combines them with models incorporating previous behaviour of ethnic or

THE CONFLICT FORECAST

The US Department of Defense is hoping that a new generation of computer models can help the military to predict how insurgent groups behave, and how that behaviour can be changed.

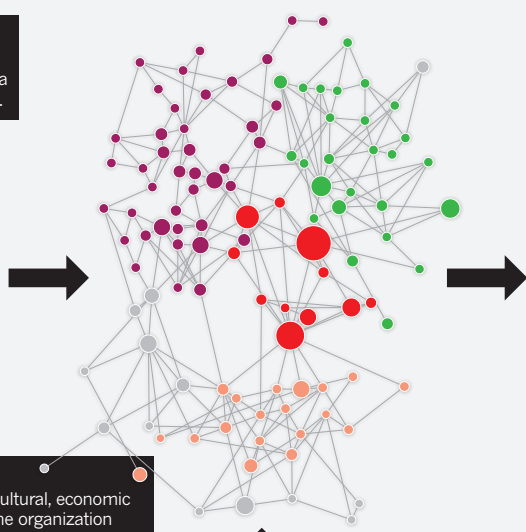
1. DATA GATHERING

Computers automatically extract names, relationships and other data from sources such as news reports.



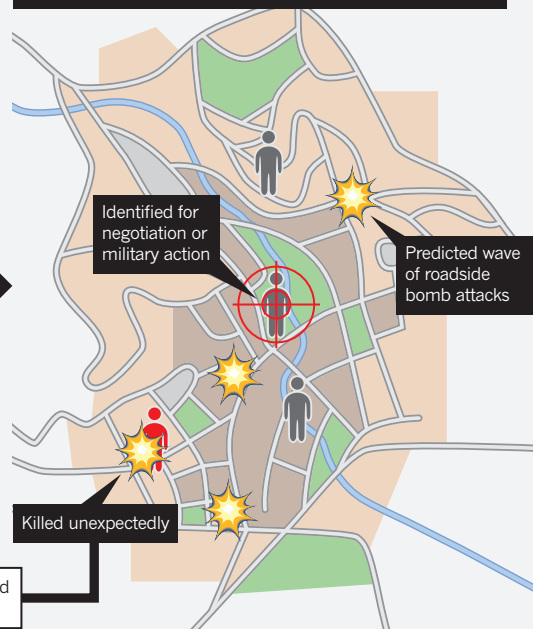
2. MODEL BUILDING

Computers combine the data with cultural, economic and political information to model the organization and behaviour of the target group. One model might identify highly connected individuals critical to the spread of terrorist ideology. Another might predict the locations of weapons caches.



3. REAL-WORLD OUTCOMES

The computer's forecasts are fed to military and intelligence forces on the ground — but few such models have yet proved their worth in real-life situations.



political groups, economic factors such as a country's gross domestic product and geopolitical relationships with neighbouring countries. The result is an ICEWS forecast that might predict, for example, that 'Country X has a 60% probability of civil war'.

The ICEWS has been producing monthly predictions since March 2010, says Sean O'Brien, programme manager for the effort at DARPA. He believes that such models, although imperfect, are already nearing the point at which they can be useful for military leaders. O'Brien has considerable company elsewhere in the Pentagon: the Office of Director of Defense Research and Engineering, for example, is sponsoring its own programme in Human, Social, Cultural and Behavior modeling. And although the office did not provide details, it says that some of its simulations are already being used by the US Special Operations Command and the US Africa Command.

A GENERATION AWAY

Even among researchers working on models with Pentagon funding, there is concern that such enthusiasm may be premature. It seems, for example, that neither computer models nor human analysts were able to precisely predict this year's uprisings in the Middle East.

When it comes to prediction, "I would say the weather guys are far ahead of where we are", says Subrahmanian, who notes that meteorologists are frequently accused of being wrong as much as they are right. "And that might give you some relative understanding of where the science is."

Carley points to the pitfalls of automated data collection. "One of the issues," she says, "is that you will get people who are ... talked about as part of the networks who aren't technically alive." In the ORA model for Sudan, for example, the textual analysis resulted in a network in which one of the key individuals was Muhammad — the Islamic prophet who died in AD 632.

Albro, who has reviewed a number of computational social-science models as part of the US National Research Council's Committee on Unifying Social Frameworks, worries that much of the work is being done by computer scientists, with only token input from social scientists, and that minimal attention is being paid to where the data come from, and what they mean. He points to some models that look for signs of extremist violence by tracking phrases such as "blow up" in online social-media discussions. "There's the constant implication that discursive violence adds up to real violence, and that's crazy," he says.

Robert Axtell, a computational social scientist at the Krasnow Institute for Advanced Study at George Mason University in Fairfax, Virginia, and a pioneer of agent-based modelling, argues that there simply aren't enough accurate data to populate the models. "My personal feeling is that there is a large research programme to be done over the next 20 years, or even 100 years, for building good high-fidelity models of human behaviour and interactions," he says.

Similar notes of caution can be heard within the defence department. "We're at the very beginnings of this," says John Lavery, who manages a programme of complex-systems modelling at the Army Research Office in Research Triangle Park, North Carolina, and who compares the current state of computational social science with physics in the early nineteenth century.

"It's a tool, and if you can leverage it, that's great," agrees Brian Reed, a behavioural scientist at the Network Science Center of the US Military Academy at West Point, New York, who was a key architect of the network analysis that led to Saddam's capture. "But you can get too much information," he warns, "and someone has to provide a focus." Reed cites an example from his own return to Iraq, where he was

deployed from 2008 to 2009 in the province of Diyala. Wanting to stop roadside bomb attacks, he asked his intelligence organization for a network analysis of the insurgent network. They provided an overload of data. "What they crunched, no one at our end could understand," says Reed.

"AS SOON AS THEY DELIVERED IT WE SAID, 'GEE, THANKS. NOW YOU'LL HAVE TO REWRITE THAT FOR AFGHANISTAN.'"

Critics such as Albrow worry that too many researchers are unaware of the real limitations of their work. Many of the models that Albrow has seen focus on verification — ensuring that the simulations are internally consistent — but give short shrift to validation, or making sure that they correlate to something in the real world. The models might provide an interpretative tool that allows policy-makers or military leaders to think critically about a problem, he suggests, but the technique's limitations are sometimes overlooked. "It does not answer our questions for us," says Albrow. "It does not solve that dilemma of what decision I need to make."

Indeed, it is often far from clear whether the current generation of models is telling people anything that an expert in the relevant subject wouldn't already know. Carley recalls a conference at which she presented her results about the key individuals whom her ORA model had identified in Sudan. "Yeah," came the response from the regional specialists in the audience, "we kind of knew most of this."

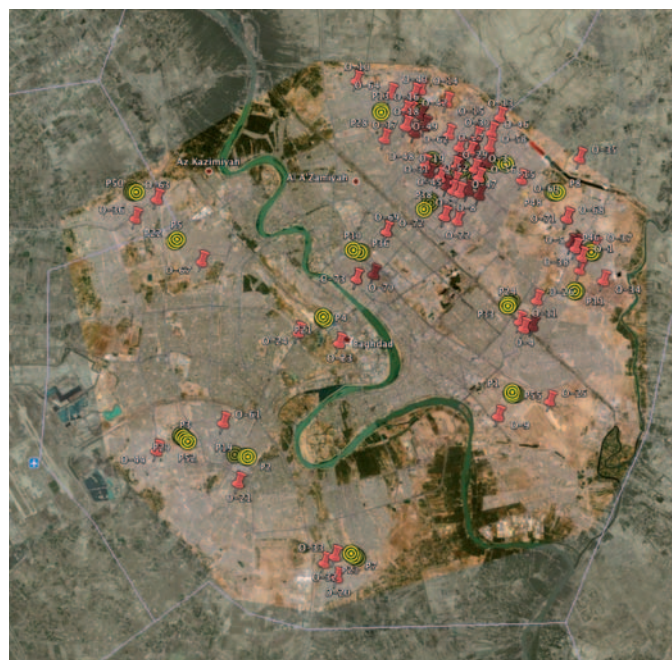
For all the caveats, however, the need to help soldiers on the ground carries an acute sense of urgency back at JIEDDO headquarters. "We have a few instances of models that have docked with the data successfully," says Comer, citing an agent-based simulation of the Iraqi city of Samarra, which was funded by JIEDDO. "The big magic trick is to move those models to a point where they can be predictive."

The model of Samarra was able to match specific changes in US military strategy to decreases or increases in the incidence of roadside bombs, but it was specific to that city. The researchers "did a great model and it was really useful," says Comer. "Just as soon as they delivered it we said, 'Gee, thanks. Now you'll have to rewrite that for Afghanistan.'"

Comer acknowledges the irony that as the world's most technologically advanced military spends tens of millions of dollars on sophisticated computer tools to predict insurgent behaviour, the insurgents in question are busy building crude bombs with little more than fertilizer and basic electronics.

"The enemy is holding his own," says Comer, "not only without the data, but without the computer power, without the Internet, without the databases — and without the science." ■

Sharon Weinberger is an Alicia Patterson Foundation Fellow based in Washington DC.



Models used bomb attacks in Iraq (red) to predict weapons caches (yellow).

COMMENT

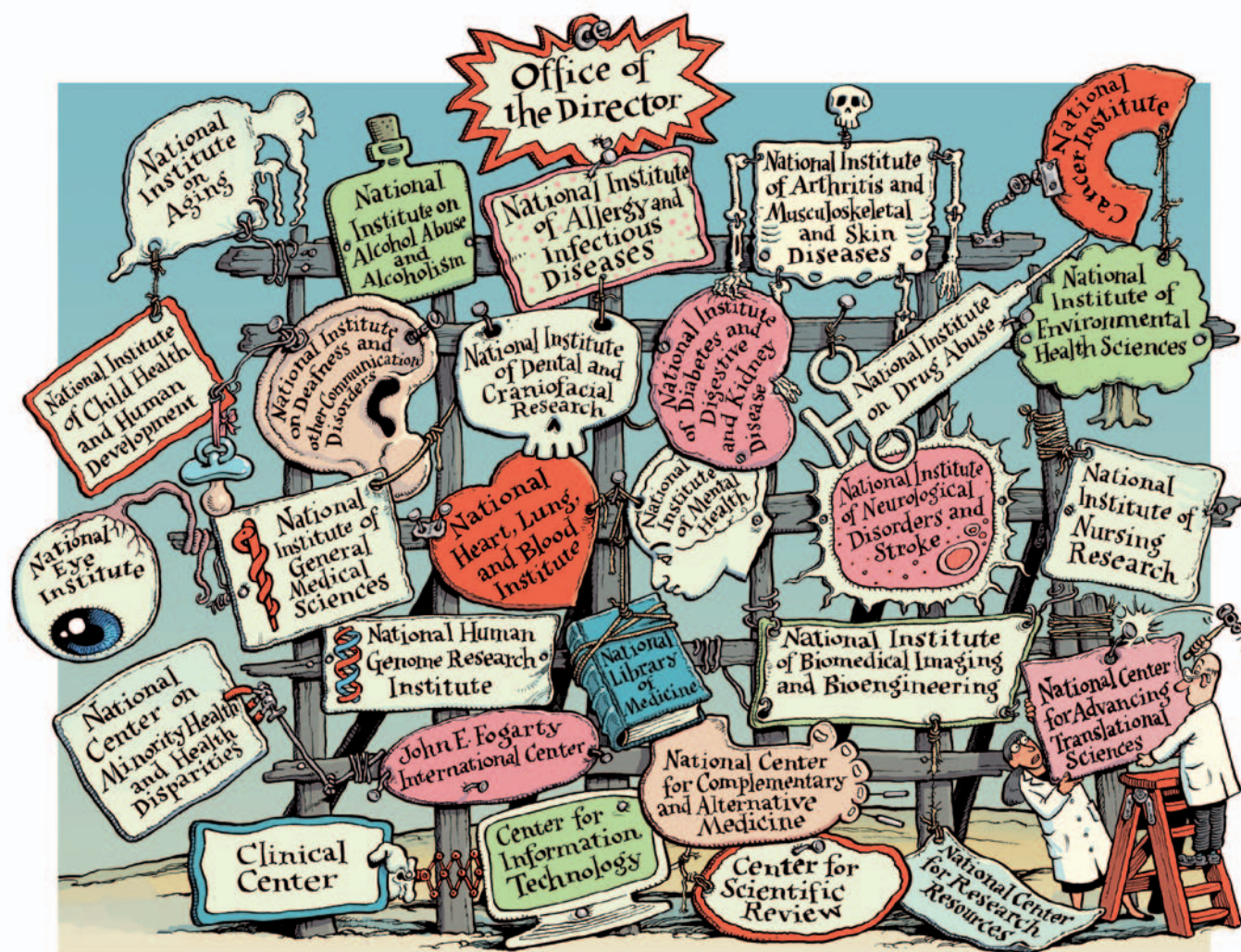
GEOSCIENCE The meteorite, from Roman reverence to dinosaur doomsday **p.573**



COOKING Nathan Myhrvold on molecular gastronomy and Microsoft **p.575**

MUSEUMS A call to unify Germany's university collections **p.576**

ENVIRONMENT Integrated research programme needed for contaminants **p.577**



Time to rethink the NIH

A radical restructure is the only way to solve the systemic problems of the world's biggest funder of biomedical research, argues **Michael M. Crow**.

The United States bets around US\$30 billion a year that advances in basic research will yield improvements in national health care. Yet the nation's global leadership in biomedical science spending has not translated into leadership in health.

Francis Collins, the director of the US National Institutes of Health (NIH) in

Bethesda, Maryland, recently determined that a new centre will help the agency's numerous other institutes and centres better convert 'blue-sky' research into treatments and diagnostics¹.

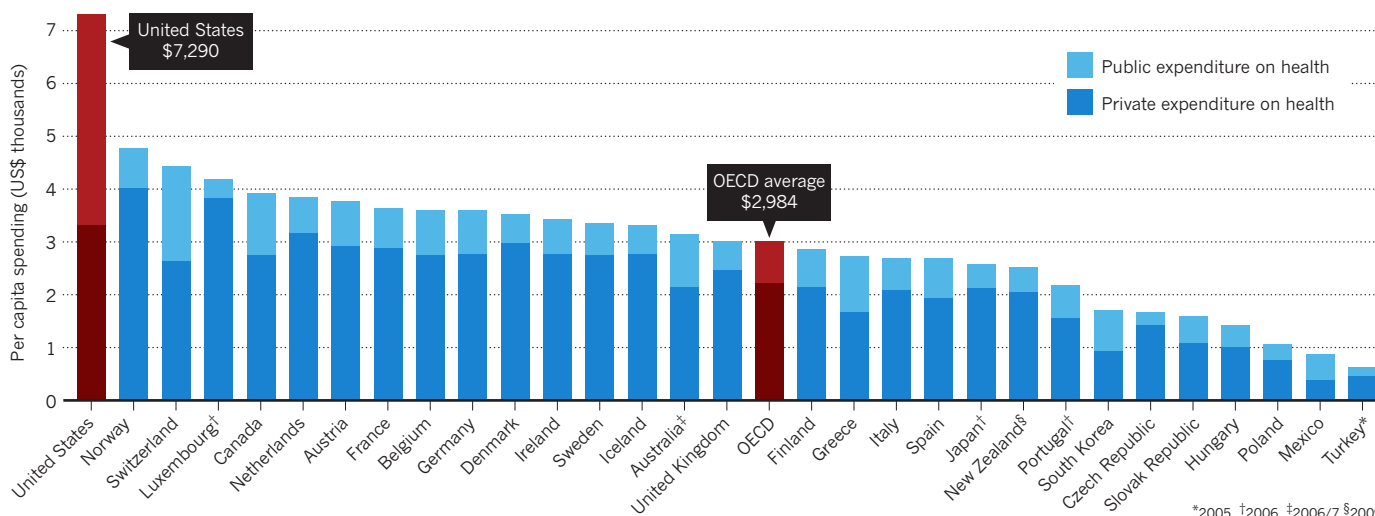
A firestorm of discussion has erupted since Collins announced his plans for the National Center for Advancing Translational Sciences (NCATS) in December^{2,3}.

Much of the debate reflects concerns about what the move will mean for existing programmes and budgets. In my view, Collins's NCATS plan perpetuates the same outmoded beliefs that have led to the current disconnect between the laboratory and the clinic, and sidesteps an opportunity to address the fundamental limitations of the NIH. Therefore I ►

ILLUSTRATIONS BY DAVID PARKINSON

BIG SPENDER

The US health spend is almost 2.5 times the average for Organisation for Economic Co-operation and Development (OECD) countries, but the country scores middling to poor on a range of health measures including infant mortality and cancer survival rates (data from 2007 unless otherwise stated).



*2005 †2006 ‡2006/7 §2009

► shall not weigh in on the debate about NCATS.

Instead, I propose a thought experiment. If the United States were to start from scratch, what institutional arrangement would do a better job of improving the health and well-being of its citizens for \$30 billion of annual expenditure? I base this experiment on three decades of experience designing large-scale knowledge enterprises — such as the Earth Institute at Columbia University in New York City and the recently reorganized Arizona State University.

Researchers, policy-makers and the government have failed to recognize that progress in health care results from a complex integration of scientific advances with technological, behavioural, social and cultural shifts. To improve clinical outcomes, the NIH needs to be reconfigured around the many determinants of health — with fundamental research as an important component, but integrated and co-equal with others.

THE ROAD TO HERE

In 1945, Vannevar Bush, the director of the Office of Scientific Research and Development under US presidents Franklin Roosevelt and Harry Truman, issued his science policy manifesto *Science: The Endless Frontier*, which set the stage for US government support of science in exchange for scientists securing national defence, economic prosperity and a healthy life for the American people. Influenced by this, and especially by the success of the scientific contribution to victory in the Second World War, the government expanded its investment in all forms of science but mainly in defence and health.

NIH funding in 1939 totalled less than

\$500,000 a year, a sum that supported just one institute. Adjusting for inflation, the budget has since increased nearly 4,000-fold — and now funds a Byzantine array of 27 institutes and centres, most of which focus on a particular group of diseases. That the NIH budget has grown at such a rate reflects the strong belief of political supporters, including scientists, activist groups and other constituencies, that more science inevitably leads to more social good.

This model for discovery and application in health care is failing to deliver. A 2009 report⁴ found that the United States ranked highest in health spending among the 30 countries that made up the Organisation for Economic Co-operation and Development (OECD) in 2007, both as a share of gross domestic product and per capita. In fact, the country spent 2.5 times the OECD average (see 'Big spender'). Yet life expectancy in the United States ranked 24th of

the 30 countries⁴ (see 'Poor returns'). And on numerous other measures — including infant mortality, obesity, cancer survival rates, length of patient stays in hospital and the discrepancy between the care of high- versus low-income groups — the country fares middling to poor.

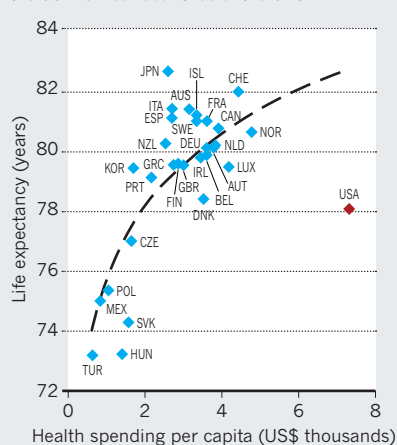
What is missing is not 'translational' research, but stronger links between all types of knowledge-generating activities related to health, and a focus on outcomes beyond science.

A cluster of studies from public-health and research-and-development economists indicates that progress in treating diseases results from complex feedbacks between a range of academic disciplines, technological innovation and clinical practice⁵. Take, for example, the advances in treating and preventing cardiovascular disease, which account for most of the gains in life expectancy in the United States during the past half-century. About one-third of the reduction in mortality has been traced to high-tech invasive treatments, such as coronary bypass surgery; one-third has been linked to medications that treat conditions such as hypertension; and one-third to behavioural changes — shifts in smoking habits, diet and exercise — achieved through education and clinical trials revealing the risks of, say, a high-fat, high-salt diet⁶.

Another example illustrates the cost of letting scientific momentum alone drive research strategies. According to the NIH's National Cancer Institute, more than 220,000 people in the United States were diagnosed with cancer of the lung and bronchus last year. Between 80% and 90% of lung cancers have been linked to smoking tobacco. Yet of the \$2.45 billion that the NIH has spent on trying to find a cure during the

POOR RETURNS

In 2007, US life expectancy was ranked 24th of the 30 member countries of the OECD.



past decade, most has been directed towards the discovery of molecular and genetic causes and treatments rather than on establishing how to modify people's behaviour. Thirty-two years of data⁷ show that lung-cancer death rates overall are worse than they were in the early years of the 'war on cancer', initiated by US president Richard Nixon in the early 1970s.

THE ROAD AHEAD

What if the NIH were reconfigured to reflect what we know about the drivers of innovation and progress in health care?

This new NIH should be structured around three institutes. A fundamental biomedical systems research institute could focus on the core questions deemed most crucial to understanding human health in all its complexity — from behavioural, biological, physical, environmental and sociological perspectives.

Take, for instance, the 'obesity pandemic'. In the United States, medical costs related to obesity (currently around \$160 billion a year) are projected to double within the decade. And by some estimates, indirect spending associated with obesity by individuals, employers and insurance payers — for example on absenteeism, decreased productivity or short-term disability, exceeds direct medical costs by nearly threefold⁸. The NIH conducts and supports leading research on numerous factors relevant to obesity, but efforts are fragmented: 27 NIH components are associated with the NIH Obesity Research Task Force, a programme established to speed up progress in obesity research.

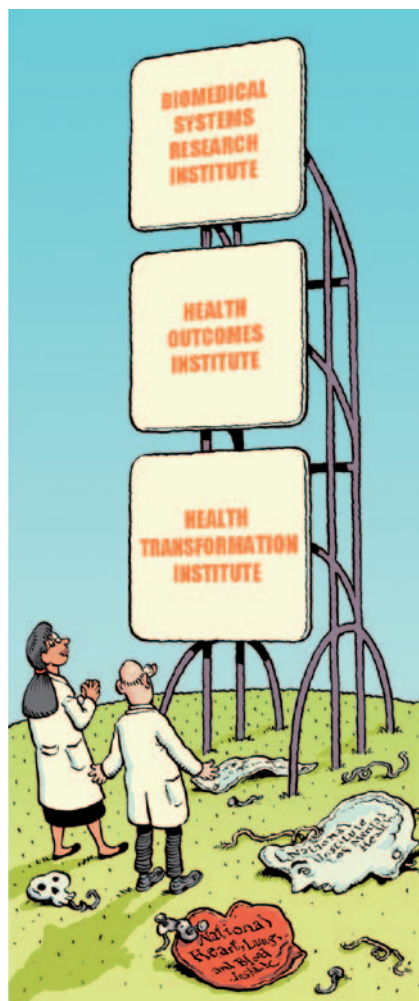
Within a systems research institute, scientists could better integrate investigations of drivers as diverse as genetics, psychological forces, sedentary lifestyles and the lack of availability of fresh fruit and vegetables in socioeconomically disadvantaged neighbourhoods.

A second institute should be devoted to research on health outcomes, that is, on measurable improvements to people's health. This should draw on behavioural sciences, economics, technology, communications and education as well as on fundamental biomedical research. Existing NIH research in areas associated with outcomes could serve as the basis for expanded programmes that operate within a purpose-built organization. If the aim is to reduce national obesity levels — currently around 30% of the US population is obese — to less than 10% or 15% of the population, for example, project leaders would measure progress against that goal rather than according to some scientific milestone such as the discovery of a genetic or microbial driver of obesity.

The third institute, a 'health

transformation' institute, should develop more sustainable cost models by integrating science, technology, clinical practice, economics and demographics. This is what corporations have to do to be successful in a competitive high-tech world. Rather than be rewarded for maximizing knowledge production, this institute would receive funding based on its success at producing cost-effective public-health improvements.

This kind of tripartite reorganization would limit the inevitable Balkanization that has come from having separate NIH units dedicated to particular diseases.



Indeed, such a change would reflect today's scientific culture, which is moving towards convergence — especially in the life sciences, where collaboration across disciplines is becoming the norm, advances in one field influence research in others, and emerging technologies are frequently relevant across different fields.

What remains unclear is how to bring about the change in mindset that is needed to focus scientific research and technological innovation on outcomes that benefit society. A committee of the National Research Council considered the question

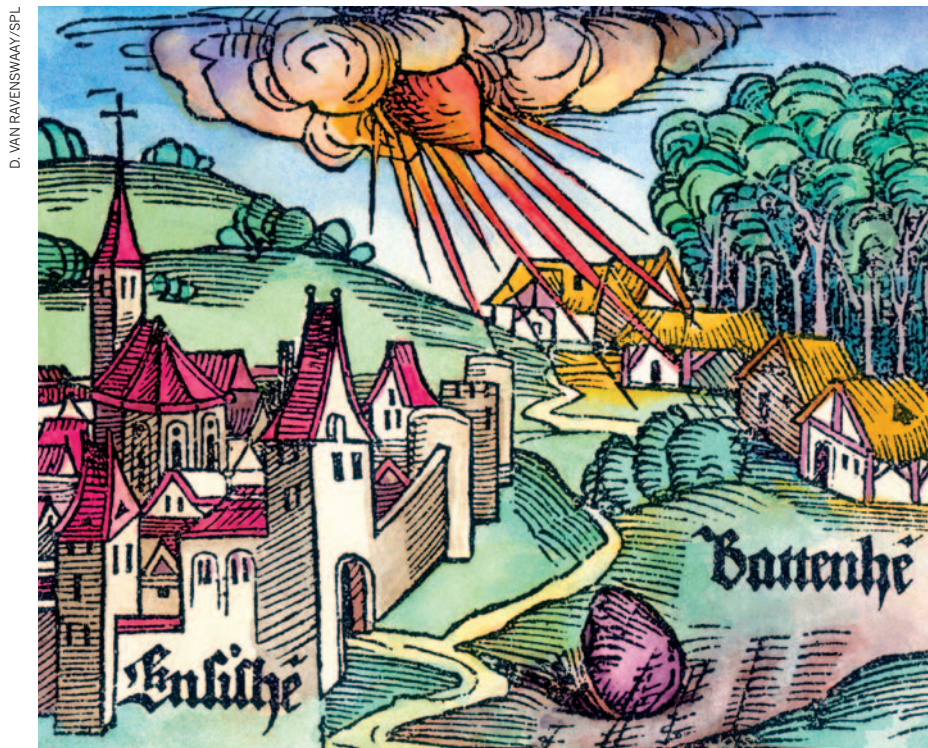
of whether to rethink the organization of the NIH in 2003. This committee concluded⁹ that despite its "theoretical attractiveness", restructuring would be difficult because the structure of the NIH is the "result of a set of complex evolving social and political negotiations among a variety of constituencies including the Congress, the administration, the scientific community, the health advocacy community and others interested in research, research training and public policy related to health."

Shifting the mindset of scientists and policy-makers alike must begin with transdisciplinary undergraduate and graduate curricula that stress the importance of societal outcomes. The US Mayo Clinic and Arizona State University, for instance, are jointly developing a master's degree in the 'science of health-care delivery' — a concept initiated by the Mayo Clinic, whose Center for the Science of Health Care Delivery designs and evaluates best practice in areas such as health maintenance.

As Harold Varmus, former director of the NIH, put it in 2001, the perception that the NIH represents the "jewel in the crown of the federal government" has led to "new facets being added without much thought to overall design"¹⁰. Especially in these recessionary times, spending \$30 billion effectively requires that the accretions of the past be replaced with a framework that better addresses the health-care priorities of the twenty-first century. ■

Michael M. Crow is president of Arizona State University, Tempe, Arizona 85287-7705, USA. He previously served as executive vice-provost and professor of science policy at Columbia University. e-mail: michael.crow@asu.edu

1. NIH Scientific Management Review Board Report on Translational Medicine and Therapeutics (2010); available at <http://go.nature.com/fxygkj>
2. <http://go.nature.com/wsq92>
3. Kaiser, J. Fourteen More Senators Question NIH Reorganization. *Science Insider* (17 February 2011); available at <http://go.nature.com/zuprcf>
4. *Health at a Glance* OECD Indicators (OECD, 2009); available at <http://go.nature.com/rcbqtf>
5. Sampat, B. N. in *The New Economics of Technology Policy* (ed. Foray, D.) 148–162 (Edward Elgar, 2009).
6. Cutler, D. M. & Kadiyala, S. in *Measuring the Gains from Medical Research: An Economic Approach* (eds Murphy, K. M. & Topel, R. H.) 110–162 (Univ. Chicago Press, 2003).
7. <http://go.nature.com/vbzvan>
8. Algazy, J., Gipstein, S., Riahi, F. & Tryon, K. J. *Health International* **10**, 88–101 (2010).
9. Committee on the Organizational Structure of the National Institutes of Health. *Enhancing the Vitality of the National Institutes of Health: Organizational Change to Meet New Challenges* (National Research Council, 2003).
10. Varmus, H. *Science* **291**, 1903–1905 (2001).



A woodcut of the 1492 Ensisheim meteorite fall, perhaps one of the earliest witnessed in the West.

EARTH SCIENCE

Mind your head

From Roman reverence to dinosaur extinctions, **Birger Schmitz** is riveted by a history of the meteorite.

In the third century AD, the Roman empire briefly worshipped a meteorite. A blackened rock that had fallen from the skies in Syria was given godly status by the transsexual priest-emperor Elagabalus. In one ceremony, Elagabalus walked backwards before a horse-drawn chariot that carried the stone, his eyes fixed upon it, with gold dust strewn at his feet. Sadly, after Elagabalus began to dress in women's clothes, married a Vestal virgin and requested a sex change from the imperial surgeons, he was dismembered and thrown into the Tiber. The fate of the meteorite is not known.

This fascinating episode can be found alongside many others in Ted Nield's latest book, *Incoming!*, which charts how our ideas about stones falling from the skies have developed over millennia. Rich in detail, informative and entertaining, it challenges the stereotype that heavenly bodies hitting Earth are bad omens or doomsday triggers.

The book is in three parts. The first

section describes the transition from humankind's belief that these unusual stones were either terrestrial or came from God, to the modern scientific understanding of their origins in the Solar System. The second section relates the discovery by physicist Luis Alvarez and his geologist son Walter in 1980 of the huge meteorite that hit Earth 65 million years ago, now widely held to have wiped out the dinosaurs. In the third part, Nield explores today's research frontier, describing evidence that a storm of meteorites hit Earth around 470 million years ago and coincided, not with a mass extinction, but with a dramatic rise in biodiversity.

Nield describes the fall of the Ensisheim



Incoming! Or, Why We Should Stop Worrying and Learn to Love the Meteorite
TED NIELD
Granta: 2011.
288 pp. £20

meteorite in what was then Germany (now Alsace in northeastern France) in 1492. The event was interpreted by the royal advisers to Maximilian I of Habsburg as a sign of good fortune for his conflicts with the Turks and the French — a prediction that held true. Locals wrapped the miraculous stone in heavy chains inside Ensisheim's church to prevent it from shooting off again. We also learn about how the evolution of our scientific understanding of meteorites was linked with transitions to more liberal and democratic societies in Europe. The physicist, musician and inventor Ernst Chladni (1756–1827) is usually held as the father of modern meteoritics, but Nield describes many illustrious characters who laid the foundation for the paradigm shift triggered by Chladni's slim 1794 paper, in which he correctly identifies the nature of meteorites.

“Locals wrapped the miraculous stone in heavy chains inside Ensisheim's church to prevent it from shooting off again.”

One such character is the great French chemist Antoine-Laurent de Lavoisier, who in the 1770s analysed the chemistry of a newly fallen meteorite and noted its anomalous nature compared with other rocks. But he insisted that meteorites formed by the action of lightning in the upper atmosphere. Lavoisier was executed at the guillotine — the Revolutionary judge cut short his final appeal, saying: “The Republic needs neither scientists nor chemists.”

Nield explains how his and others' opinion of dinosaur extinctions has changed over the years, having written in the past of his doubt that a meteorite impact was mainly responsible. He has now moved towards the majority view that the Alvarez group basically got it right. That is, the impact of an asteroid measuring some 10–15 kilometres across triggered the extinction of most of Earth's animal species, including all the dinosaurs, at the transition of the Cretaceous to Tertiary periods. This hypothesis, now tested in hundreds of studies, has gained almost universal acceptance. A notable exception is Princeton University palaeontologist Gerta Keller, who has combated the idea for decades. Nield argues for a compromise — that a big impact did harm nature, but that the extinctions had more varied causes.

Compromises belong in politics, not in science. I started my career in the 1980s as a non-believer of the impact theory, and even published with Keller. But I have now seen the Cretaceous–Tertiary boundary clay layer at about 50 geological sites

➤ **NATURE.COM**

For more on the Alvarez theory of dinosaur extinction:
go.nature.com/8wroxk

worldwide. In the marine records, this thin, iridium-enriched clay bed always occurs exactly at the level at which the microscopic foraminifera typical of Cretaceous oceans disappear almost completely.

Foraminifera are single-celled creatures with a calcite shell. Hundreds can be found fossilized within just one cubic centimetre of marine sedimentary rock. It would have required a cataclysmic catastrophe to obliterate billions of them across the world's ocean. And we know for sure, on the basis of many mineralogical and chemical studies, that the iridium layer originates from a major meteorite impact. The precise coincidence of these two events is so compelling that it is difficult to understand how anyone can doubt a direct relationship between them. Nevertheless, on the whole, Nield gives a credible account of this major scientific discovery.

"For 2 million years, shards of a shattered asteroid bombarded Earth."

The rest of the book deals with the recent finding of more than 90 fossil meteorites — all of which are a stony form called L-chondrites, measuring 1–20 cm in diameter — buried in a quarry of Ordovician marine limestone in Sweden. The meteorites that fell on that ancient sea floor can be linked by isotopic and geochemical analyses to the largest known break-up in the asteroid belt in the past few billion years. The L-chondrite parent body, measuring more than 100 km across, was hit 470 million years ago, possibly by a comet from outer space that shattered it into billions of pieces.

For 2 million years afterwards, shards of it bombarded Earth. One or two of the meteorites may have been almost as large as the body that took out the dinosaurs. Yet strangely, this bombardment coincides with the Great Ordovician Biodiversification Event, when biodiversity on Earth rapidly increased from an all-time low to modern levels. Although researchers are still uncertain as to how this happened, Nield gives an insightful account of the ways these events can be related.

On my night table there is a pile of books in which the bookmark never made it beyond page 60. From these, I've derived a personal definition of a good book: one where I can't stop reading until the end. *Incoming!* is just such a book. ■

Birger Schmitz is professor of geology at the University of Lund, Sweden.
e-mail: birger.schmitz@geol.lu.se

GASTRONOMY

A visual feast

Felice Frankel grapples with a 20-kilogram cookbook.

It took me 40 minutes to unpack *Modernist Cuisine*. The 6-volume, 2,400-page set of books by culinary experimenters Nathan Myhrvold, Chris Young and Maxime Bilet weighs more than 20 kilograms and arrives wrapped in clean white paper and encased in a clear plastic box, from which each of the five main volumes can be retrieved: History and Fundamentals; Techniques and Equipment; Animals and Plants; Ingredients and Preparations; and Plated-Dish Recipes. The sixth volume, Kitchen Manual, is a simpler spiral-bound handbook intended for use in the kitchen, containing some 1,500 recipes referred to in the larger volumes.

The care given to the packaging of this collection foreshadows the precision that went into its production. It is a masterwork filled with historical references and scientific explanations of why, for example, thickening liquids is important for taste, or why food browns during cooking. Nothing is left out, it seems. The pages are designed to form a monumental narrative and visual story, written and illustrated with passion and an obsession with getting it right. The authors' expertise blends science and cuisine: Myhrvold is a former physicist, Microsoft scientist and now entrepreneur with a lifelong interest in cooking (see page 575); Bilet and Young trained under innovative British chef Heston Blumenthal;

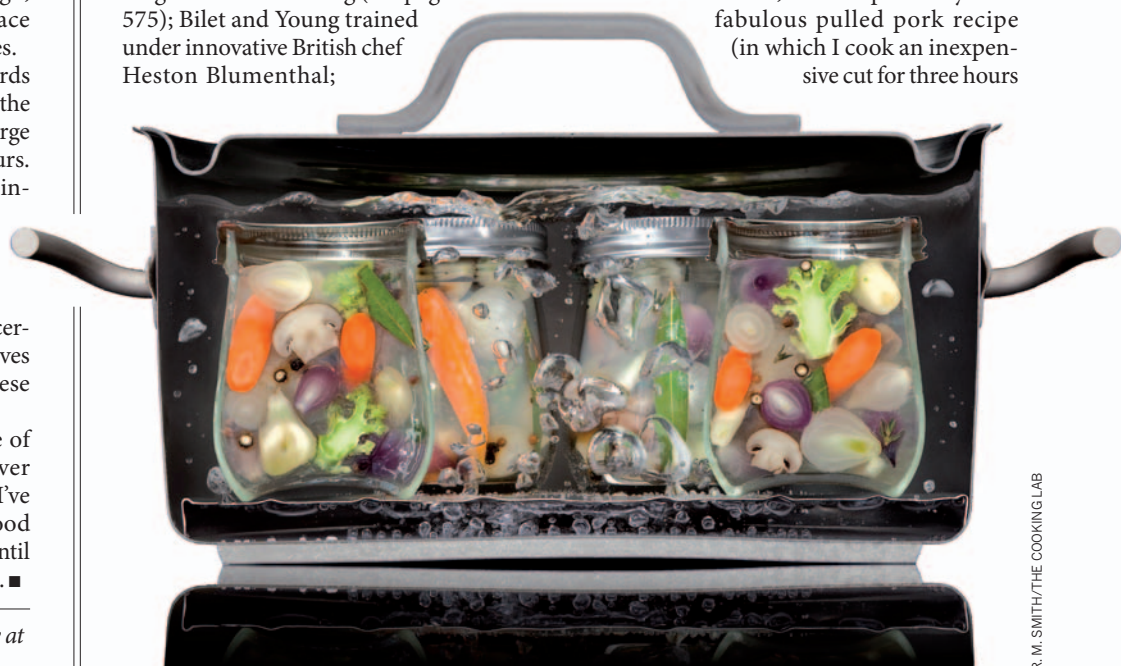
and Young also holds degrees in mathematics and biochemistry.

Photography is used to powerful effect. Myhrvold is a serious photographer, and he and Ryan Matthew Smith have created technically remarkable, often breathtaking and informative photographs. Some are purely decorative, such as their high-speed camera image of a bullet passing through six eggs. But the most innovative technique they have developed is the cutaway. To show what was happening inside food as it cooked, the team literally cut pots, woks and pans in half and cooked recipes in them. The cross-sectional images are laid out and annotated with scientific information, such as labels for zones of conduction, condensation and convection. Each image is a marvel.

I haven't yet tested the recipes. And I am not sure I will ever feel the urge to try the Edible Soap Bar with Honey Bubbles, for instance, or to replace my own fabulous pulled pork recipe (in which I cook an inexpensive cut for three hours



Modernist Cuisine: The Art and Science of Cooking
NATHAN MYHRVOLD,
CHRIS YOUNG AND
MAXIME BILET
The Cooking Lab:
2011. 2,438 pp.
\$625, £395



A cutaway image from the *Modernist Cuisine* cookbook.

R. M. SMITH/THE COOKING LAB

with leeks, Worcestershire sauce, garlic, sugar, wine and vinegar, among other ingredients) with the *sous vide* version in *Modernist Cuisine*. This technique — in which ingredients are vacuum-sealed in a plastic bag before being cooked at low temperature in a water bath or combi oven — plays a major part in the set, and the authors go to great lengths to argue its value. I have tasted meats cooked this way, and am unconvinced that it is essential to home cooking. But I am willing to give the pasta marinara a shot. It calls for tomato water, which I was happy to discover could be produced with a simple wine filter (to separate the flavourful water from the pulp after first processing the tomatoes in a juicer) rather than with the preferred piece of kitchen equipment in *Modernist Cuisine*, the centrifuge.

The format of the recipes will also challenge most cooks. Because the authors consider that “volume measurements are not sufficiently accurate”, all ingredients, even liquids, are measured by weight in grams. One recipe, for example, calls for 100 g of wine — good luck with that. The amounts of ingredients are also presented in the baker’s percentage system, in which the weight ratios of each are scaled to a reference ingredient. Having to weigh liquids and work with percentages will mystify most non-professional cooks, and will probably vex scientists who want to relax at the end of a long day in the lab.

So who is the audience for *Modernist Cuisine*? In its present form, the volumes will be bought by those who can afford their three-figure price tag and have time for slow, precise cooking — people who are already familiar with the chefs and cognoscenti mentioned in volume I: Blumenthal, Ferran Adrià and Harold McGee, among others. Purchasers will also need space to store the bulky set, and a table on which to rest the book to delve into its pages. The volumes are so heavy and large that they are difficult to hold open.

Modernist Cuisine is too important to be offered only to an elite audience. The stunning visual impact of the printed volumes supports the publisher’s choice to produce the initial work on paper. Still, I hope the authors bring out the book in an electronic form, so that a larger audience can explore its many layers of information. Like a good meal, this remarkable effort needs to be shared. ■

Felice Frankel is a research scientist at the Massachusetts Institute of Technology, Cambridge, Massachusetts 02139, USA. She is an author, science photographer and serious amateur cook. e-mail: felice@felicefrankel.com

Q&A Nathan Myhrvold Steakhouse science

Nathan Myhrvold trained as a quantum cosmologist with Stephen Hawking and was chief technology officer of Microsoft before founding Intellectual Ventures, a US company that funds inventors and acquires patents. As he publishes a six-volume work on the science of cooking, Myhrvold explains why chemistry techniques could soon be seen in every restaurant.

Why did you write a six-volume scientific cookbook?

When I was two years old, I told my mother that I would be a scientist; when I was nine I insisted on cooking Thanksgiving dinner. In the mid-1990s, I took a leave of absence from Microsoft and went to culinary school in France, and got back into cooking with a vengeance. The only way to learn about modern cooking techniques now is to work at a cutting-edge restaurant. I saw an opportunity to write a book that would cover modern techniques and the science behind them [see page 574]. I hired a team and we kept getting more ambitious. I think ours is the only cookbook in the world to cover prion science and quorum sensing in cells. We could have gone further. We decided not to include pastry and desserts.

Can you see science-driven cooking catching on?

Yes. Chocolate cake with a liquid centre was once a novelty, but is now in every shopping mall in the United States. Some of these techniques are incredibly convenient and tasty. We have a chapter on emulsions, with an indestructible vinaigrette, and a rapid soufflé recipe. I think most steakhouses should use *sous vide* cooking [slow cooking in an airtight plastic bag immersed in a low-temperature water bath]. You can get the steak done perfectly without worrying about timing, and cheaper cuts are just as tender as a prime filet mignon. I think science-based cooking will be in every US steakhouse within a few years. Once you explain the science, people will find uses for the techniques.

You have many interests, including palaeontology and wildlife photography. How do your pursuits fit together?

Each makes a good diversion from the other, and occasionally they filter back into my work at Intellectual Ventures. Wildlife photography is about travelling to a beautiful place and taking pictures. Palaeontology is about going into the desert and walking around until you find a bone sticking out of the ground. Our chapter on meat opens with



R. M. SMITH/THE COOKING LAB

a picture that I took of a lion cub eating a wildebeest. Some of the technical solutions that we cover in the cookbook have led us to consider inventions to improve food safety in developing countries, where adequate sanitation is often lacking.

In 2000, you pledged US\$1 million to help Microsoft co-founder Paul Allen fund the Allen Telescope Array in California. Why do you believe in the private funding of science?

Venture capital has grown faster than government science funding. If you can show that you can make money rather than begging for a grant, people will compete to fund you. I’m not suggesting this is a panacea. Outside the life sciences, people don’t tend to fund things with a level of technical risk. We’ve created Intellectual Ventures to do just this. We invest in existing patents, help institutions to develop new technologies, and fund inventors and scientists to come up with new ideas. If we could find a way to fund more science and innovation at venture-capital growth rates, that would be a wonderful thing.

What makes an invention successful?

The best way to stimulate invention is to get the right set of smart people in a room talking to each other. What separates successful from unsuccessful inventions is not the quality of the idea. To be successful, an invention needs to have a passionate advocate. It requires the initial flash of genius — then believing and investing in it. ■

INTERVIEW BY JASCHA HOFFMAN

➔ **NATURE.COM**
For a Q&A with molecular chef and chemist Hervé This: go.nature.com/wdrmrcc



Some of the scientific riches confined to storage at the Berlin Medical Historical Museum.

MUSEUMS

Out of the cellar

Thomas Schnalke calls on Germany to turn its historical scientific collections into centres for object research.

Many universities in Germany are centuries old. Their institutes, labs and clinics are treasure troves of historical objects, from eighteenth-century gynaecological instruments and nineteenth-century wax moulages of diseases used for clinical teaching, to pathology specimens spanning 300 years. Often these collections are locked away in dark and dusty cellars. There is little space for scholars to work with them, or for the public to view them. The riches are hidden.

A huge opportunity to change this situation has arisen with the recommendations of the German Council of Science and Humanities on using scientific collections for broader research (see *Nature* 470, 5–6; 2011). Realizing these recommendations is the central topic of a national collections conference to be held next week at the Phyletic Museum in Jena. The council has provided helpful suggestions for how to improve matters. It suggests: determining the status of each collection on the basis of defined criteria; installing a collections spokesperson in each university; developing concepts for a systematic continuation of collecting; generating a self-organized network among the collections; developing instruments to finance and support scientific collections; and developing common standards for analysing, managing

and conserving the collections.

These suggestions are welcome, but we must think bigger. The decentralized nature of these university collections hinders many improvements. The stocks must be brought together within each university — virtually and physically. Object archives, analogous to those for text and images, need to be established in universities with rich collections, such as those in Berlin.

One model is Museum Boerhaave in Leiden, the Netherlands. It holds some 40,000 objects, ranging from late-medieval herbals to modern electron microscopes. Just 6% of the entire collection is on display. But three years ago, the 94% not on show moved to a huge, research-friendly, centrally located depot. And a number of objects are searchable on the museum's website.

Similarly, the Whipple Museum of the History of Science at the University of Cambridge, UK, makes good use of its 7,000-plus objects — mainly sundials, mathematical instruments and early electrical apparatus. Since 1944, they have been on public display and used for undergraduate and graduate teaching by the university's history and philosophy of science departments. Its

website (go.nature.com/cb7cwg) features articles, images and interactive displays.

To get such institutions of material studies going, ambitious research programmes should be embedded within associated graduate schools. One model is the object-research community established at the Deutsches Museum in Munich. Since 2004, the museum has run a scholar-in-residence programme for four researchers at a time to work on their holdings for up to a year. The scholars benefit from a thriving academic atmosphere, working alongside some 50 conservators, archivists and librarians, and with around 50 other scholars from the Munich Centre for the History of Science and Technology close by.

SHOW AND TELL

What are the features of an object archive? First, an institution must have an online database for a researcher to consult — such as those provided at the Boerhaave museum or at the Deutsches Hygiene Museum in Dresden. Researchers can then come and physically inspect objects that are of interest to them. Larger objects are consulted in established depots; smaller artefacts are brought from the archive's storage rooms. After signing a form promising good handling practice, the researcher is left to study their chosen objects in an adequately equipped study chamber. Just as in a conventional text and picture archive, researchers can handle, observe, describe, measure, take pictures and make notes. A good object archive also provides associated sources such as technical drawings, photographs, handwritten manuscripts and letters, and printed primary and secondary literature such as related company catalogues, patents, historical journals and monographs.

What object might one study in such an archive? At Berlin's Charité, it might be a gallstone in a labelled glass jar from around 1796, originally from the private Berlin Anatomical Museum of Johann Gottlieb Walter and his son Friedrich August Walter. The anatomists cut the stone in half, categorized it using their own classification system according to its beautifully striped inner surface, and interpreted its growth from the still-visible darkish central density. The attached label links the stone to a catalogue, revealing the Walters' interest in combining humoral thinking — based on ancient medical concepts — with modern chemical experiments.

At my institution, the Berlin Medical Historical Museum, also at the Charité, one can examine the first functioning photocystoscope — an instrument designed for internal examination of the bladder. Developed in the early 1890s by Berlin urologist Max Nitze, the endoscope is equipped with a cylindrical camera that shot 10 round photographs, each 3 millimetres across, on bromide gelatine plates. Although the first

NATURE.COM
For more hidden
treasures in Europe's
science collections:
go.nature.com/v52qt5

images, published by Nitze in 1894, were just a cloudy mix of light and shade, one can see why he was pleased with the “objective representation of reality” in his images.

In Germany, such archives would be possible in various university cities beyond Berlin. Jena, Halle, Tübingen and Erlangen, for instance, all hold unique stocks from archaeology to zoology. Plugging these collections into a network of similar existing or soon-to-be established institutions in Cambridge, Leiden, London, Paris and Boston, Massachusetts, would be a great boon to the study of material culture in the history of the sciences, medicine and the humanities.

A pilot project in Berlin would need a large building with, say, four floors measuring 1,000 square metres each. Converting an existing building would probably cost around €15 million (about US\$21 million); a new building would cost double that. Another €1 million a year would be necessary to maintain the building, with a team of at least 15 professionals to run the archive. All this would have to be provided by a joint venture of top research-funding organizations, such as the Deutsche Forschungsgemeinschaft (DFG), the Fritz Thyssen Foundation and the Volkswagen Foundation. Experience at the Boerhaave and the Whipple museums shows that the job may take as little as three to five years.

At the same time, there needs to be an impulse to implement research with objects on a wider scale. A good path to take here, aside from linking object archives with related university departments and institutes, would be to establish or engage associated graduate schools, which would encourage multidisciplinary work on and with objects. Structures developed successfully at the Berlin Max Planck Institute for the History of Science could serve as a model. Its research-network project in the history of scientific objects, which ran from 2005 until 2010, linked 18 scholars worldwide. The institute also recruited 15 pre- and postdocs to participate in an eight-week ‘wandering seminar’ on scientific objects in 2006, touring through substantial museums and collections within Europe. The seminar produced essays, an exhibition, a conference and an informative website (go.nature.com/4farzy).

The first step towards realizing this ambitious overhaul of Germany’s hidden collections will require the universities and the research-funding organizations to discuss setting up one or more pilot projects. If these can be funded, the universities will need to act quickly to develop workable concepts — otherwise, their holdings might be lost to research for ever. ■

Thomas Schnalke is director of the Berlin Medical Historical Museum at the Charité.
e-mail: thomas.schnalke@charite.de

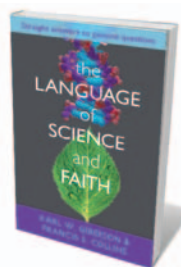
Books in brief



The Sorcerer's Apprentices: A Season at elBulli

Lisa Abend SIMON AND SCHUSTER 304 pp. £18.99 (2011)

Similar to star scientists, top chefs are an exacting breed. So what is it like to work in the kitchen of the restaurant voted as the world's best for three years in a row? In a behind-the-scenes peek, Lisa Abend relates her experience of enrolling in chef Ferran Adrià's culinary laboratory at his restaurant elBulli in Catalonia, Spain. Abend describes how she adapted to the innovative and technological cooking techniques, and how she and other apprentices learned to push themselves to the extreme of their abilities in order to achieve perfection night after night.



The Language of Science and Faith: Straight Answers to Genuine Questions

Karl Giberson & Francis Collins SPCK PUBLISHING 224 pp. £12.99 (2011)

For scientists who hold religious beliefs, it can be hard to disentangle the two world views. Geneticist Francis Collins follows on from his 2006 best-seller *The Language of God* (Free Press), in which he reconciled his scientific knowledge with his Christian faith, joining with physicist Karl Giberson to answer questions about Charles Darwin, evolution and the age of Earth and the Universe. Pointing out that the Bible is not a scientific text, they aim to satisfy the spiritual mainstream while challenging atheists and creationists.



Britain's War Machine: Weapons, Resources and Experts in the Second World War

David Edgerton ALLEN LANE 464 pp. £25 (2011)

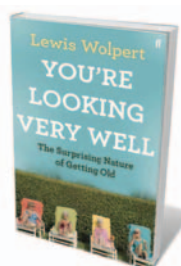
By putting resources, machines and experts at the centre of a global story of the Second World War, historian of science David Edgerton paints a different picture of British military success in the mid-twentieth century. Far from being the plucky underdog, the wealthy nation was a great power at the heart of a global production system. Strategic in its thinking about technology, and ruthless in the pursuit of its interests with formidable arms, Britain's victory was ultimately a cheap one, Edgerton argues.



Chinnovation: How Chinese Innovators are Changing the World

Yinglan Tan WILEY 288 pp. £19.99 (2011)

It is often said that China makes products but does not invent them. Business professor Yinglan Tan dispels that myth through case studies of Chinese companies that are leading the way in entrepreneurship. Businesses in technology-related fields are overcoming barriers to innovation, scaling up rental networks of hybrid cars nationwide or offering user-led travel and restaurant guide websites. He discusses harnessing resources, navigating legal restrictions, dealing with risk and the attraction and retention of talent in China.



You're Looking Very Well: The Surprising Nature of Getting Old

Lewis Wolpert FABER AND FABER 256 pp. £14.99 (2011)

Considering it is something we must all endure, most of us know remarkably little about ageing. In researching his book, developmental biologist and octogenarian Lewis Wolpert admits that much of it came as a surprise even to him. He explores the implications of an ageing population, explains why we age through cellular wear and tear and examines attitudes to death and euthanasia. He also raises concerns that we are not doing enough to plan for our old age, either individually or as a society.

CORRESPONDENCE

Unite to assess contaminant risk

There is an urgent need for a globally coordinated research programme to evaluate the risks to human health and the environment posed by contaminants of emerging concern, or CECs.

CECs are natural or synthetic chemicals that can affect an organism's ability to communicate with and respond to its environment. Well-known examples of their adverse biological effects include intersex phenotypes in wildlife, and poor sperm quality and quantity in humans (see also R. W. Stahlhut *et al. Environ Health Perspect.* 115, 876–882; 2007).

Field studies have so far been unsuccessful in predicting CEC effects. This is partly because of the complex interactions and multiple stressors that occur in nature, but also because such investigations often focus on a single chemical or chemical class, or on a specific mechanism or organism, or use environmentally unrealistic experimental exposure levels.

A coordinated programme should integrate new and ongoing research into the sources and fates of CECs, and the exposure risks associated with them. This would replace the present scattershot approach and would provide solutions and reliable information for policy-makers.

Paige J. Novak and 14 co-authors*, University of Minnesota, USA.
novak010@umn.edu

*A full list of authors is online at <http://dx.doi.org/10.1038/471578a>.

Funding studies of the unpredictable

The unpredictability of extreme weather events calls for a mechanism for mobilizing research funds at short notice, so

that an event can be investigated while it is still going on.

At the local and national levels, authorities could create a consortium of respected scientists as standby funding recipients. International contributions might be coordinated by a body such as the Intergovernmental Panel on Climate Change, which could set up a worldwide agreement on data and information sharing.

Besides investigations such as model validation, funding bids would need to cover basic research into these extreme weather events. Allocation would have to be decided within days, and research results fed promptly to a United Nations panel.

Such measures could minimize the cost of disastrous weather events over the medium to long term and help to lessen their socioeconomic, cultural and environmental effects.

Brajesh K. Singh University of Western Sydney, Penrith, Australia. b.singh@uws.edu.au

Turkey's research council clarifies role

Some points you raise about TÜBİTAK, Turkey's scientific and technological research council, need clarification (*Nature* 470, 436; 2011).

As the main government agency for research management, funding and conduct, TÜBİTAK aims to create optimal conditions for Turkey's scientific and technological development. It is therefore concerned about the association of several notable scientists with the trial surrounding the Ergenekon organization, which is accused by the Turkish chief prosecutor of plotting against the democratically elected government.

TÜBİTAK has chosen to remain silent out of respect for the principle of judicial independence (as specified in the country's

Criminal Code 5237).

You are incorrect in saying that TÜBİTAK was involved in the appointment of supporters of Turkey's ruling Justice and Development Party to key academic positions. Most of the scientists in TÜBİTAK's senior management were working at the agency for many years before the ruling party took over. The organization has insisted on transparent recruitment procedures since 2006.

Regarding the allegation of Darwin being removed from the cover of TÜBİTAK's popular-science magazine *Bilim ve Teknik* (*Nature* 458, 259; 2009), the magazine published a special issue on Darwin in June 2009, as originally scheduled. There was never any censorship, as confirmed by the Ankara Fifth Criminal Court.

Nüket Yetiş TÜBİTAK, Ankara, Turkey. nuket.yetis@tubitak.gov.tr

Microbial sequences benefit health now

We are still waiting for widespread health-care improvements resulting from sequencing of the human genome (*Nature* 470, 140; 2011), but microbial genome sequences are already generating important clinical applications.

Hospital laboratory sequencing is set to become an invaluable tool for the delineation, tracking and control of infections such as methicillin-resistant *Staphylococcus aureus* (MRSA) and *Streptococcus pneumoniae* (see, for example, S. R. Harris *et al. Science* 327, 469–474; 2010, and N. J. Croucher *et al. Science* 331, 430–434; 2011). It will also be crucial for monitoring antibiotic resistance and emerging pathogens such as those responsible for severe acute respiratory syndrome (SARS), H5N1 and H1N1 influenza.

The use of routine sequencing in diagnostic laboratories will

revolutionize our understanding of infectious diseases. By reducing the need for microbiological reference laboratories, there will be fewer delays in delivering information. Sequencing will provide the ultimate source of clinically relevant information on responses to vaccines and microbial drug resistance, for example, as well as useful public-health data. It will also help to direct research by enabling real-time tracking of pathogens.

Edward J. P. Cartwright University of Cambridge, UK.
Claudio U. Köser Health Protection Agency, Cambridge; and University of Cambridge, UK.
Sharon J. Peacock The Wellcome Trust Sanger Institute; Health Protection Agency, Cambridge; and University of Cambridge, UK.
sharon@tropmedres.ac

Career postdocs increase scrap heap

Jennifer Rohn's solution to the problems of postdoctoral careers does not add up (*Nature* 471, 7; 2011).

Most fields of science are at a steady state of funding, or worse, so paying for new professional postdocs would require cuts to training postdoc positions. But a career spans 30–40 years, so each career postdoc would replace 6–20 training postdocs. If there were enough professional postdoc positions to make a difference, there would be a huge reduction in the number of training postdocs. The scrap heap would be larger: each rescued professional postdoc would be replaced by several new PhDs with no chance of finding a postdoc position.

The only other way to avoid a scrap heap would be to restrict the number of people who start PhDs, which raises a host of other complex issues.

Robert Insall Beatson Institute for Cancer Research, Glasgow, UK.
r.insall@beatson.gla.ac.uk

ASTROPHYSICS

The inner lives of red giants

The natural pulse of a red-giant star provides crucial insight into what makes it shine. Observations of red giants by the Kepler space telescope shed light on a previously untested prediction of stellar evolution theory. [SEE LETTER P.608](#)

TRAVIS S. METCALFE

Just as in Hollywood, the age of a star is not always obvious if you look only at the surface. During certain phases in a star's life, its size and brightness are remarkably constant, even while profound transformations are taking place deep inside. For most of their existence, stars shine from the energy released by nuclear reactions that convert hydrogen into helium, but eventually they begin to burn the helium in their cores to synthesize heavier elements, such as carbon and oxygen. On page 608 of this issue, Bedding *et al.*¹ demonstrate a new technique for distinguishing between these life stages, using continuous 'starquakes' to probe the deepest regions, where the changes are most dramatic.

The objects examined by Bedding and colleagues are known as red giants, the bloated fate of stars such as our Sun as they begin to exhaust their primary source of energy — the hydrogen near the centre that powers nuclear fusion. The resulting helium accumulates in the core, forcing hydrogen in a surrounding shell to burn more vigorously than before. About 5 billion years from now, these processes will gradually cause our own star to expand to more than 100 times its present size, becoming a red giant and destroying some of the inner planets in the Solar System². Stars that were born before the Sun, as well as heavier stars (which evolve more quickly), have already reached this phase of stellar evolution.

Like the Sun, the surface of a red giant seems to boil as convection brings heat up from the interior and radiates it into the coldness of outer space. These turbulent motions act like continuous starquakes, creating sound waves that travel down through the interior and back to the surface. Some of the sounds have just the right tone — a million times lower than the audible range for humans — to set up standing waves (known as solar-like oscillations) that cause the entire star to change its brightness regularly over hours and days, depending on its size. Inferring the properties of stars from these periodic brightness changes is a technique known as asteroseismology³.

The sound waves generated near the surface of a red giant can interact with buoyancy waves (rather like the waves in the ocean) that

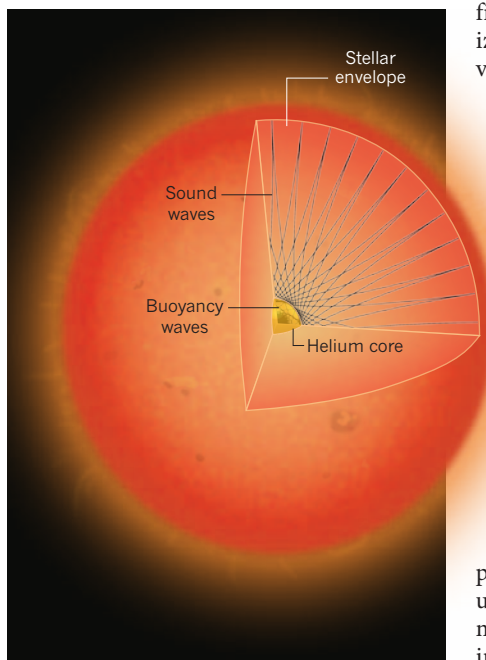


Figure 1 | Red-giant oscillations. Turbulent motions inside a red-giant star act like continuous starquakes, creating sound waves that travel down through the interior and back to the surface. Under the right conditions, these standing waves can couple with buoyancy waves trapped inside the helium core. Bedding *et al.*¹ identify these 'mixed' oscillation modes in hundreds of red giants observed by the Kepler space telescope, providing unique tests of stellar evolution theory.

are trapped inside the helium core. Under the right conditions, the two types of waves can couple to each other, changing the regularity of the brightness changes at the surface. These 'mixed' oscillation modes are much more sensitive to structure in the core than are the uncoupled sound waves that sample only the stellar envelope (Fig. 1).

The innovation that allowed Bedding *et al.*¹ to distinguish between red giants at different life stages emerged from precise observations by the Kepler space telescope. Launched in March 2009, Kepler stares at a large patch of sky near the constellation Cygnus, monitoring the brightness of more than 156,000 stars with the goal of detecting Earth-like planets. The mission has been extremely successful at

finding alien worlds⁴, but it is also revolutionizing the study of stellar oscillations by providing many months of continuous data for thousands of stars^{5,6}. Earlier efforts to study red giants from ground-based telescopes were hampered by both the daily interruptions of sunlight and the limited duration of the monitoring.

As mentioned before, the trouble with red giants is that they all look nearly the same on the outside, regardless of their mass and age. Bedding and colleagues¹ sought to determine these properties for the hundreds of red giants observed by the Kepler satellite, to measure precisely when stars of a given mass would shift from burning hydrogen in a shell to helium in the core. The regular pattern of standing waves is insufficient to pinpoint which energy source makes a particular red giant shine, but the mixed oscillation modes exhibit a unique pattern⁷. By deciphering this pattern, Bedding *et al.*¹ demonstrate how the two life stages of red giants can be separated using asteroseismology.

The life story of a red giant theoretically depends not only on its age but also on its mass, with stars smaller than about twice the mass of the Sun experiencing a sudden ignition known as a helium flash. The temperature required to fuse helium is significantly higher than that needed for hydrogen, and in low-mass stars the helium accumulates in the core at very high density until it reaches a critical size and ignites almost instantaneously. In more massive stars, the transition to helium core burning is gradual, so the stars exhibit a wider range of core sizes and never experience a helium flash. Bedding and colleagues show how these two populations can be distinguished observationally using their oscillation modes, providing new data to validate a previously untested prediction of stellar evolution theory.

This extraordinary peek into the inner lives of red giants was made possible by just the first year of observations from the Kepler mission, which is scheduled to operate for at least 3.5 years and might be extended by NASA for a further 2.5 years. The picture that emerges from asteroseismology will steadily improve as the observations continue, so

we can expect even better results for the stars examined by Bedding *et al.*¹, as well as similar measurements for other red giants, in the near future. ■

Travis S. Metcalfe is at the High Altitude Observatory, National Center for Atmospheric Research, Boulder, Colorado 80307-3000, USA. e-mail: travis@ucar.edu

IMMUNOLOGY

Cross-dressers turn on T cells

Memory T cells remember viruses from previous infections, providing immunity by facilitating the killing of infected cells. For this, they exploit cross-dressing, the transfer of antigens between antigen-presenting cells. [SEE LETTER P.629](#)

JONATHAN W. YEWDELL & BRIAN P. DOLAN

As their name suggests, antigen-presenting cells flag up the presence of foreign molecules (antigens) to killer T cells of the immune system, triggering the appropriate immune response. The cells generally acquire antigens in one of two ways: by direct presentation, in which the cell itself is infected with the antigen it presents; and by cross-presentation, in which the presenting cell engulfs components of an infected cell and then processes and presents the associated antigen. A third mechanism — cross-dressing — has also been postulated^{1–3}, in which an antigen-presenting cell acquires the requisite processed antigen directly from another infected antigen-presenting cell. On page 629 of this issue, Wakim and Bevan⁴ report the strongest evidence yet for the relevance of cross-dressing, showing in mice that this process is required for an effective antiviral response.

Humans possess some 100 billion versions of killer (cytotoxic) T cells, each of which carries a T-cell receptor on its cell membrane that recognizes a specific set of antigens. Antigenic peptides of 8–10 residues are presented to T cells as complexes with MHC class I molecules of the immune system. Unnecessary T-cell responses can gravely damage the host by triggering autoimmune effects, so safeguards are in place to prevent this. The most important safeguard is that naive T cells — those that have not previously been exposed to an antigen — must initially be activated by dendritic cells, a type of antigen-presenting cell. Dendritic cells are present in immune tissues such as the spleen and lymph nodes, and sample the blood and lymphatic system respectively for antigens. They are derived from the bone marrow and specialize in

1. Bedding, T. R. *et al. Nature* **471**, 608–611 (2011).
2. Silvotti, R. *et al. Nature* **449**, 189–191 (2007).
3. Aerts, C., Christensen-Dalsgaard, J., Cunha, M. & Kurtz, D. W. *Sol. Phys.* **251**, 3–20 (2008).
4. Borucki, W. J. *et al. Astrophys. J.* **728**, 117–137 (2011).
5. Gilliland, R. *et al. Publ. Astron. Soc. Pacif.* **122**, 131–143 (2010).
6. Chaplin, W. J. *et al. Science* (in the press).
7. Beck, P. G. *et al. Science* doi:10.1126/science.1201939 (2011).

presenting viral and tumour antigens to T cells.

Once activated, T cells replicate at an astonishing speed (a 4–6-hour division time), leading to a 10,000-fold increase in effector-cell numbers within a few days. The effector cells live for weeks, but a subset called memory cells, which constitute only 1% of the cytotoxic T cells in the body, can live for decades. Having run the gauntlet of the activation safeguards as naive cells, memory cells' safeguards for preventing autoimmunity are relaxed, so they can respond more rapidly to an infection. Wakim and Bevan⁴ report that memory T cells can be activated through cross-dressing.

If viruses infect dendritic cells, the direct presentation of processed viral proteins can efficiently activate T cells (Fig. 1a). Many viruses, however, infect only one or a few cell types. They could therefore potentially avoid recognition by not infecting dendritic cells. To prevent this — and to be able to present tumour antigens — dendritic cells use cross-presentation, whereby they acquire antigens from extracellular fluids through the process of endocytosis, or from infected cells either by engulfing them or by the diffusion of antigenic peptides through 'gap junctions' formed between the cells (Fig. 1b). Cross-presentation seems to be essential for cytotoxic T-cell responses to many viruses⁵.

Cross-presentation can also occur by a process called trogocytosis — the transfer of cell-membrane patches or individual proteins between cells^{6,7} (Fig. 1c). This allows antigen presentation by acceptor dendritic cells to occur immediately, without any processing. Such cross-dressing has been demonstrated in proof-of-principle experiments^{2,3}, and Wakim and Bevan confirm that dendritic cells in culture transfer MHC class I–antigen peptide complexes by trogocytosis. Nonetheless,

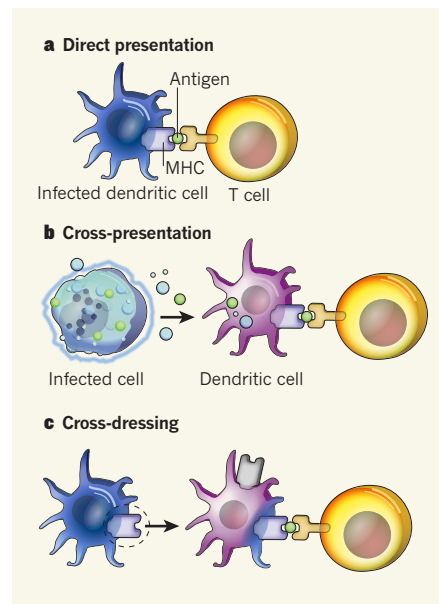


Figure 1 | Pathways to antigen presentation. **a**, Direct presentation occurs when an antigen-presenting cell such as a dendritic cell is infected, and displays processed antigenic peptides in complex with MHC class I molecules on its surface, thereby activating T cells. **b**, In cross-presentation, dendritic cells acquire antigens obtained by infected cells through endocytosis and phagocytosis, and — with or without some processing — load them onto class I molecules for presentation to T cells. **c**, In a third pathway, called cross-dressing, dendritic cells acquire preformed MHC class I molecules in complex with antigens from other cells by the process of trogocytosis or through gap junctions. Wakim and Bevan⁴ show that cross-dressing is used to activate memory T cells, but not naive T cells, in response to viral infection.

convincingly extending such findings to situations more like those encountered *in vivo* has remained notoriously difficult. Wakim and Bevan elegantly do just that using chimaeric mice that had received transplanted bone marrow.

To generate the chimaeric animals, the authors used γ -irradiation to destroy short-lived bone-marrow-derived cells — including the resident dendritic cells of the spleen and lymph nodes — in normal mice. They then transferred bone-marrow-derived stem cells to these animals from a variety of genetically manipulated mice. In this way, they could distinguish dendritic cells that generate MHC class I–peptide complexes from dendritic cells presenting the class I–peptide complexes to T cells. This revealed that cross-dressed dendritic cells (cells that had acquired the complexes) have a crucial role in activating memory, but not naive, T cells.

How can this selectivity be explained? One possibility is that memory T cells specifically interact with a subset of dendritic cells that are specialized for cross-dressing-based activation. Although Wakim and Bevan show that, in

frozen sections of chimaeric spleens, memory and naive cells have a similar anatomical distribution, imaging the tissues of living animals might reveal differences in T-cell localization or behaviour relating to their immunological experience. However, the authors favour another explanation, which indeed seems more likely: that naive T cells, with their high activation threshold, disfavour cross-dressing, which involves the presentation of vanishingly small numbers of MHC class I–antigen complexes.

Whatever the explanation, it will be essential to characterize cross-dressed dendritic cells in more detail, particularly because they belong to a subset of immune cells (CD8⁺) that are less adept at many types of cross-presentation than their cytotoxic (CD8⁺) counterparts. What's more, cross-dressing may prove particularly important in cancer immunology, because the

killing of infiltrating cross-presenting immune cells by T cells may be crucial for tumour eradication⁸.

Although these elegant experiments highlight the biological relevance of cross-dressing, it is likely that, under many circumstances, the standard direct-presentation and cross-presentation pathways are more prevalent. Nevertheless, Wakim and Bevan⁴ raise a noteworthy, yet largely neglected, issue: how the activation of memory and naive T cells differs for immune responses ranging from those to acute (sporadic) pathogens such as influenza virus and rotavirus, to persistent pathogens including HIV and hepatitis B and C viruses, and to tumours, where the rules are likely to differ altogether. More generally, their findings illustrate the astounding ability of the immune system to use minimal packets of information

to control pathogens that seek to exploit the slightest chinks in our immune armour. ■

Jonathan W. Yewdell and Brian P. Dolan are in the Laboratory for Viral Diseases, NIAID, Bethesda, Maryland 20892, USA.
e-mail: jyewdell@niaid.nih.gov

1. Yewdell, J. W. & Haeryfar, S. M. M. *Annu. Rev. Immunol.* **23**, 651–682 (2005).
2. Dolan, B. P., Gibbs, K. D. Jr & Ostrand-Rosenberg, S. *J. Immunol.* **177**, 6018–6024 (2006).
3. Qu, C., Nguyen, V. A., Merad, M. & Randolph, G. J. *J. Immunol.* **182**, 3650–3659 (2009).
4. Wakim, L. M. & Bevan, M. J. *Nature* **471**, 629–632 (2011).
5. Yewdell, J. W. *Curr. Opin. Immunol.* **22**, 402–410 (2010).
6. Joly, E. & Hudrisier, D. *Nature Immunol.* **4**, 815 (2003).
7. Herrera, O. B. et al. *J. Immunol.* **173**, 4828–4837 (2004).
8. Schietinger, A., Philip, M., Liu, R. B., Schreiber, K. & Schreiber, H. *J. Exp. Med.* **207**, 2469–2477 (2010).

sequence of the miRNA, possibly disrupting normal regulation.

Is it realistic to suppose that a single-base mismatch could have any sizeable effect on an organism's fitness by this mechanism? Two pieces of evidence suggest that it can. Often, miRNA binds, not in the protein-coding body of the mRNA, but in an untranslated region at the terminus of the mRNA. Single mutations in this region are known to modify miRNA-based repression and in turn to be associated with disease^{8,9}. Second, when miRNA binding is within the body of the gene, synonymous positions involved in miRNA–mRNA binding tend to be highly sequence-conserved between species¹⁰, as would be expected if mutations in the binding residues significantly reduce fitness. In a study of Crohn's disease, Brest and colleagues² now provide evidence that silent mutations contribute to disease in this manner.

Crohn's disease is a complex inflammatory disorder of the intestine, and is influenced by many genes. One of these, *IRGM*, specifies a protein involved in the intracellular removal of bacteria; the persistence of bacteria in cells of the gut lining is a feature of the disease. At a leucine-encoding sequence in this gene, there are two silent variants: CTG or TTG, the C form being the common and ancestral form. In European populations, the T variant is repeatedly associated with Crohn's disease¹¹, but why this might be is unknown.

Brest *et al.*² report that a family of miRNAs is highly expressed in the lining of the intestine when there is a gut infection. These miRNAs bind in the part of the mRNA of *IRGM* that specifies the leucine and thus covers the C/T mutation. The miRNA is a good match for the C variant and hence, usually, the miRNA–mRNA binding has the effect of turning down the level of *IRGM* protein, allowing precise control of the process of intracellular bacterial digestion. However, the T version is not turned down.

By constructing an artificial version of the

MOLECULAR GENETICS

The sound of silence

There are various ways in which apparently 'silent' DNA mutations — those that don't result in a change in the encoded protein — have untoward consequences. A striking example has emerged in a study of Crohn's disease.

LAURENCE D. HURST

Because of the structure of the genetic code, many mutations in genes will not obviously affect the resultant protein and are hence considered 'silent'. If they don't affect the protein, silent mutations cannot cause genetic disease. Or can they? There is evidence for a variety of mechanisms¹ whereby these apparently innocuous mutations can be harmful, if not lethal. In a paper in *Nature Genetics*, Brest and colleagues² provide evidence of an example of disruption in which a silent mutation affects the regulation, through microRNA, of the process of making the protein.

To produce a protein, the run of nucleotide bases (A, C, T and G) in DNA that makes up a gene is transcribed into a single-stranded messenger RNA (mRNA). This in turn is translated, by the ribosome, into the string of amino acids that constitute the protein. The mRNA is read in blocks of three bases (codons). The codon TTG, for example, translates as the amino-acid leucine. As there are 64 possible codons but only 20 amino acids encoded, different codons can specify the same amino acid. For example, CTG is also translated as leucine. Silent (synonymous) mutations change one codon to another that specifies the same amino acid (for example CTG ↔ TTG).

Unlike mutations that change a protein, synonymous mutations are typically not considered as possible causes of genetic disease, in part because there is, at first sight, no reason

why so seemingly benign a change should have so serious an effect. Indeed, genome-wide searches for disease-causing mutations commonly ignore synonymous changes in functional follow-up studies. This seems reasonable, given that natural selection eliminates new amino-acid-changing mutations from populations much more commonly than it does new synonymous mutations.

Silent mutations can, however, be highly deleterious. Many affect regulatory domains hidden within the mRNA, commonly those controlling splicing — the process in which the mRNA must first be cut up, then resectioned, before translation³. Synonymous mutations also influence the way the mRNA folds, which can in turn perturb the translation process^{4,5}. They can affect how fast or how accurately the mRNA is translated⁶, although whether this is a disease-causing mechanism is unknown. Synonymous changes may even change the way the protein folds⁷.

A further possible mode of disruption involves a process in which an mRNA is down-regulated by being bound by a short, untranslated RNA. These microRNAs (miRNA) have a sequence that is complementary to a small section of the target mRNA, thereby making, after binding, a small section of double-stranded RNA. RNA with a double-strand section is usually destroyed or otherwise prevented from being translated. A single base mutation in a gene's miRNA pairing region, even if synonymous, would cause a mismatch with the

miRNA, one complementary to the T, not the C, Brest and colleagues show that sequence matching at the C/T site is crucial. In individuals with the T variant, the miRNA downregulation fails, IRGM levels remain high, and the process of bacterial digestion is uncontrolled. This, the authors suggest, explains the abnormal persistence of intracellular bacteria in affected individuals and the conservation of the silent C between species. To support this idea, they manipulate levels of the key players and show that such manipulation affects the process of bacterial digestion and in turn bacterial numbers within cells. Consistently high levels of the miRNA in inflamed tissue in patients with Crohn's disease suggest that the cells are constantly trying, but, in the case of those with the T variant, failing, to control the digestion of intracellular bacteria.

One curiosity is that the T variant maintains high levels of IRGM, which might be expected to result in ultra-efficient clearance of bacteria. Perhaps a reduced level of IRGM is needed to control the flow of bacteria through the system, in much the same way as a reduced speed limit on a motorway during peak times lessens traffic jams.

It also remains to be seen why mutations in the *IRGM* gene are not associated with Crohn's disease in Japan¹², although a higher normal expression level of the protein in Japanese people compared with Europeans may be relevant¹³. That the same T variant is associated with susceptibility to tuberculosis¹⁴, at least among African Americans, hints at the possibility of a broader link between this synonymous variant and bacterial persistence.

More generally, understanding how and how often silent mutations affect fitness is important not only for the hunt for disease-causing mutations¹⁵, but also for estimating the mutation rate, for identifying positive selection and for gene manipulation. ■

Laurence D. Hurst is in the Department of Biology and Biochemistry, University of Bath, Bath BA2 7AY, UK.
e-mail: l.d.hurst@bath.ac.uk

1. Chamary, J. V., Parmley, J. L. & Hurst, L. D. *Nature Rev. Genet.* **7**, 98–108 (2006).
2. Brest, P. et al. *Nature Genet.* **43**, 242–245 (2011).
3. Cartegni, L., Chew, S. L. & Krainer, A. R. *Nature Rev. Genet.* **3**, 285–298 (2002).
4. Nackley, A. G. et al. *Science* **314**, 1930–1933 (2006).
5. Kudla, G., Murray, A. W., Tollervey, D. & Plotkin, J. B. *Science* **324**, 255–258 (2009).
6. Plotkin, J. B. & Kudla, G. *Nature Rev. Genet.* **12**, 32–42 (2011).
7. Kimchi-Sarfaty, C. et al. *Science* **315**, 525–528 (2007).
8. Yu, Z. et al. *Nucleic Acids Res.* **35**, 4535–4541 (2007).
9. Abelson, J. F. et al. *Science* **310**, 317–320 (2005).
10. Hurst, L. D. *J. Mol. Evol.* **63**, 174–182 (2006).
11. Parkes, M. et al. *Nature Genet.* **39**, 830–832 (2007).
12. Yamazaki, K. et al. *Gut* **58**, 228–232 (2009).
13. Prescott, N. J. et al. *Hum. Molec. Genet.* **19**, 1828–1839 (2010).
14. King, K. Y. et al. *PLoS ONE* **6**, e16317 (2011).
15. Chen, R., Davydov, E. V., Sirota, M. & Butte, A. J. *PLoS ONE* **5**, e13574 (2010).

BIOCHEMISTRY

How two amino acids become one

Twenty amino acids form the basis of all proteins, but another two genetically encoded amino acids have also been discovered. The biosynthesis of one of these, pyrrolysine, has now been elucidated. [SEE LETTER P.647](#)

STEPHEN W. RAGSDALE

The first genetically encoded amino acid was identified more than two centuries ago, but new ones are still being found. The most recently reported one — the twenty-second — is pyrrolysine (Pyl), which was found^{1,2} in 2002 at the active sites of methyltransferase enzymes obtained from a methane-producing archaeon. Like the 20 common amino acids that are incorporated into cellular proteins, Pyl is synthesized in the cytoplasm and incorporated at a specific position in a growing polypeptide chain during translation³. However, it was the only genetically encoded amino acid for which a biosynthetic pathway had not been established. On page 647 of this issue, Krzycki and colleagues⁴ report that the essential amino acid lysine is the sole precursor of Pyl, and they define the enzymatic steps for

the conversion of two L-lysine molecules into one molecule of L-Pyl.

Translation occurs on ribosomes, and involves decoding a series of nucleotide triplets (codons) on a messenger RNA strand into a corresponding series of amino acids. Prior to translation, an aminoacyl-tRNA synthetase enzyme catalyses the attachment of each amino acid to a transfer RNA, forming an aminoacyl-tRNA molecule. During translation, the ribosome transfers the growing protein chain carried on the preceding tRNA (the peptidyl-tRNA) to the next incoming aminoacyl-tRNA. Translation continues stepwise in this way until the ribosome reaches a stop codon, which triggers specific factors to release the polypeptide chain into the cell.

In previous studies^{1,2}, Krzycki and co-workers found that, surprisingly, a specific stop codon (UAG) in the sequence of

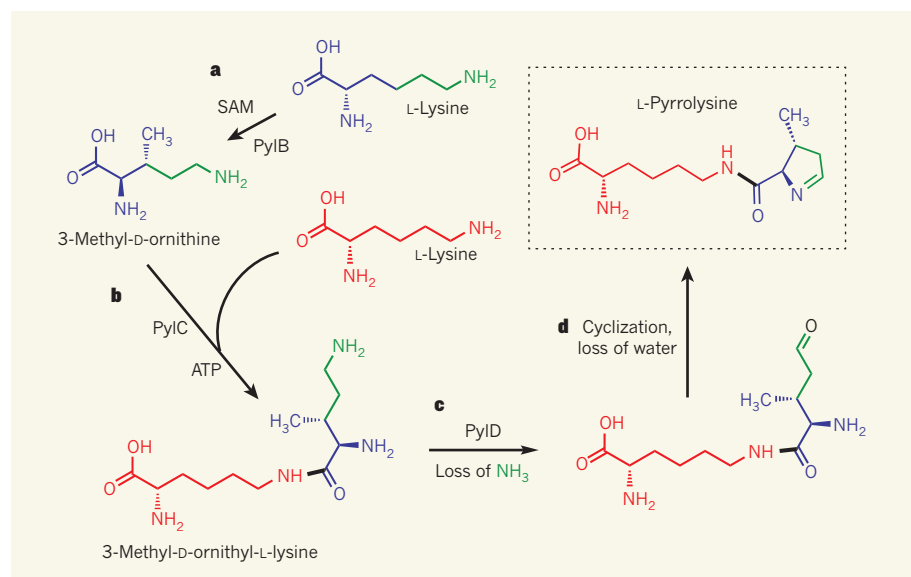


Figure 1 | Proposed biosynthesis of pyrrolysine. Krzycki and colleagues⁴ report that L-pyrrolysine forms from two L-lysine molecules in archaea, and propose the following biosynthetic pathway. **a**, In the presence of a cofactor (S-adenosylmethionine, SAM), the protein PylB catalyses the conversion of L-lysine to 3-methyl-D-ornithine, a molecular-rearrangement reaction. **b**, PylC then catalyses the ATP-dependent combination of 3-methyl-D-ornithine with another L-lysine to make 3-methyl-D-ornithyl-L-lysine (ATP is an energy-carrying cofactor). **c**, **d**, Finally, PylD catalyses an oxidative deamination reaction (in which an NH₂ group is eliminated as ammonia, NH₃), which is followed by cyclization and dehydration steps to yield L-pyrrolysine. It is not currently clear whether PylD catalyses the transformation shown in **d**, or whether this is a spontaneous process. Fragments of the molecules are colour-coded to make the reactions easier to follow.

methyltransferase enzymes from methanogenic archaea encodes Pyl. They went on to show⁵ that the biological machinery associated with Pyl's synthesis and incorporation into proteins is encoded by the *pylTSBCD* cluster of genes, which can be thought of as a genetic-code expansion cassette — a gene cluster that, when transferred into an organism, enables that organism's ribosomes to recognize UAG and translate it into Pyl. The ribosome therefore 'reads through' this stop codon and catalyses a reaction between the Pyl-tRNA and the preceding peptidyl-tRNA to insert Pyl into a protein. The protein PylS was found to be the Pyl-tRNA synthetase⁶, whereas PylT was identified⁷ as the Pyl-tRNA. The remaining *pylBCD* genes in the cassette were therefore expected to encode the enzymatic pathway for Pyl biosynthesis.

It has been proposed that Pyl derives from lysine and some other cellular compound — possibly one of the amino acids D-ornithine⁸, D-glutamate⁹, D-isoleucine⁸ or D-proline^{5,8}. But Krzycki and colleagues⁴ have now demonstrated that the protein products of the *pylBCD* genes catalyse the synthesis of Pyl from two lysines using the pathway shown in Figure 1.

The authors began by genetically engineering a common laboratory strain of the bacterium *Escherichia coli* to include the *pylTSBCD* expansion cassette from the archaeon *Methanosarcina acetivorans* and the methyltransferase gene *mtmB1* from another archaeon, *Methanosarcina barkeri*. The mRNA sequence of *mtmB1* contains the UAG stop codon that specifies Pyl. Krzycki *et al.* then provided the engineered *E. coli* with lysine in which all six carbon atoms and both nitrogen atoms were isotopically labelled, and later purified the methyltransferase produced by the organism.

To decipher the biosynthetic pathway for Pyl, the authors used mass spectrometry to accurately measure the masses of peptide fragments (produced *in situ* in the mass spectrometer) of the purified methyltransferase. By comparison with a similar analysis of methyltransferase purified from engineered *E. coli* grown in unlabelled lysine, they identified a single labelled Pyl-containing peptide fragment. Further mass spectrometry experiments unambiguously revealed that all 12 carbon atoms in the Pyl residue and all three of its nitrogen atoms were isotopically labelled. Because lysine contains six carbons and two nitrogens, the results conclusively demonstrated that two molecules of lysine combine to produce Pyl, and that one of the lysines eliminates a nitrogen atom during the PylBCD-catalysed biosynthetic pathway (Fig. 1). In other words, no precursor other than lysine is used in the biosynthesis of Pyl.

These results are surprising in light of a report⁸ that D-ornithine stimulates UAG read-through in an *E. coli* strain similarly engineered to contain the *pylTSBCD* expansion cassette — a finding that suggests that

D-ornithine is a precursor of Pyl. To investigate the apparent disparity, Krzycki and co-workers⁴ performed mass spectrometric analysis of the methyltransferase obtained from engineered *E. coli* cultures grown in a medium supplemented with both unlabelled D-ornithine and labelled lysine. They discovered that some of this methyltransferase contained labelled Pyl, as before. However, part of the protein contained desmethylpyrrolysine, an amino acid in which the methyl group of Pyl has been replaced by a hydrogen atom. Desmethylpyrrolysine can be made from one lysine and one D-ornithine, suggesting that D-ornithine was charged onto Pyl-tRNA by the Pyl-tRNA synthetase and thereby misincorporated into the methyltransferase. This implies that the Pyl biosynthetic cassette could be used to incorporate useful modified amino-acid residues into proteins — something that is of interest to many research laboratories.

One limitation of Krzycki and colleagues' study⁴ is that the *pylBCD*-encoded proteins were not purified and used to demonstrate their proposed activities. But on the basis of the similarity of the amino-acid sequences of PylB, PylC and PylD to other proteins whose functions are known, the biosynthetic pathway proposed by the authors is reasonable and chemically feasible. The door is now open for enzymologists to study the Pyl biosynthetic pathway in detail. A prime target

for investigation is the PylB-catalysed lysine mutase reaction, in which an aminoethyl group ($\text{CH}_2\text{CH}_2\text{NH}_2$) shifts from one part of the molecule to another (Fig. 1a). This is particularly interesting because the amino-acid sequence of PylB suggests that it is a member of the radical S-adenosylmethionine protein family¹⁰, which is not currently known to catalyse this reaction. More broadly, these findings will help us to better understand the relationship between the evolution of the genetic code and of amino-acid biosynthetic pathways. ■

Stephen W. Ragsdale is in the Department of Biological Chemistry, University of Michigan Medical School, Ann Arbor, Michigan 48109-0606, USA.
e-mail: swagsdal@umich.edu

1. Hao, B. *et al.* *Science* **296**, 1462–1466 (2002).
2. Srinivasan, G., James, C. M. & Krzycki, J. A. *Science* **296**, 1459–1462 (2002).
3. Rother, M. & Krzycki, J. A. *Archaea* **2010**, 453642 doi:10.1155/2010/453642 (2010).
4. Gaston, M. A., Zhang, L., Green-Church, K. B. & Krzycki, J. A. *Nature* **471**, 647–650 (2011).
5. Longstaff, D. G. *et al.* *Proc. Natl Acad. Sci. USA* **104**, 1021–1026 (2007).
6. Polycarpo, C. *et al.* *Proc. Natl Acad. Sci. USA* **101**, 12450–12454 (2004).
7. Blight, S. K. *et al.* *Nature* **431**, 333–335 (2004).
8. Namy, O. *et al.* *FEBS Lett.* **581**, 5282–5288 (2007).
9. Krzycki, J. A. *Curr. Opin. Chem. Biol.* **8**, 484–491 (2004).
10. Frey, P. A., Hegeman, A. D. & Ruzicka, F. J. *Crit. Rev. Biochem. Mol. Biol.* **43**, 63–88 (2008).

CLIMATE

Cold winters from warm oceans

Winters are colder in northeastern North America and Asia than in other regions at the same latitude. Previous explanations may be incomplete, having overlooked the radiation of atmospheric wave energy. SEE LETTER P621

WILLIAM R. BOOS

Barcelona and London both lie north of New York, yet winters in these two European cities are warmer than winters in the northeastern United States (Fig. 1). It would seem easy to attribute this difference simply to the fact that Europe lies downwind of the warm North Atlantic Ocean. But Kaspi and Schneider (page 621 of this issue)¹ put forward the counter-intuitive argument that the northeastern parts of North America, and also of Asia, are instead cooled in winter by heat released from oceans just off their coasts.

No exotic thermodynamics is needed to create continental cold from oceanic warmth. Instead, Kaspi and Schneider show that heat emitted by a warm swathe of mid-latitude

ocean can set up a pattern of north–south flow that draws cold Arctic air into regions immediately upstream of the heat source. Waters just east of Asia and North America do indeed emit large amounts of heat into the atmosphere during winter, when prevailing eastward winds draw cold continental air over the warm waters of the Gulf Stream and the Kuroshio, Asia's analogous continental boundary current.

Two main processes were previously thought to create the wintertime thermal contrast across the Atlantic, the first of which is the warming of Europe by heat drawn out of the ocean by prevailing eastward winds². The North Atlantic itself is kept warm in winter by storage of the previous summer's heat and by ocean currents that transport heat from lower latitudes. There has been some excitement in



Figure 1 | Winter temperature asymmetry. This image of snow cover over North America and Europe was taken on 23 March 2003 by NASA's Terra satellite using the MODIS instrument. Approximate latitudes at 30° N, 45° N, 60° N and 75° N are marked. Note that northeastern North America is almost entirely snow covered between 45° N and 60° N, but that there is little snow at the same latitudes in western Europe. Also shown is sea-ice surface temperature (imaged by the MODIS instrument on NASA's Aqua satellite): pink, temperatures between 0 °C and -15 °C; purple, temperatures between -15 °C and -28 °C; white (in the deep Arctic), temperatures colder than -28 °C. Kaspi and Schneider¹ invoke the influence of Rossby-wave plumes as a partial explanation of this transatlantic asymmetry.

the popular press over the idea that Europe might be plunged into a deep freeze if northward ocean heat transport were to weaken as the planet warms³, but simulations of such an ocean circulation decline suggest that it would merely counteract part of the warming that Europe would otherwise experience because of an increase in greenhouse-gas emissions⁴. The issue has been further muddled by conflation of the density-driven ocean circulation that transports heat, which might be altered by redistribution of ocean salinity in a changed climate, with the Gulf Stream, a wind-driven current that owes its existence to the less mutable principle of the conservation of angular momentum on a rotating planet⁵.

The other accepted cause of Europe's relative winter warmth, and one that seems less challenged by Kaspi and Schneider's result¹, is the steady pattern of wind set up by mountains. As eastward mid-latitude winds impinge on the Rocky Mountains, the downstream flow is perturbed to blow southward over the northeastern United States and northward over Europe, drawing cold and warm air, respectively, into those regions^{2,6}. Mountains perturb the flow by creating a particular type of wave that exists in planetary oceans and atmospheres, called a Rossby wave, which also happens to be central to the east-coast cooling mechanism proposed by Kaspi and Schneider.

Waves in general exist because some force accelerates a disturbed medium back towards its equilibrium position, with gravity providing the restoring force for the familiar example of ripples on the surface of a pond. In Earth's Northern Hemisphere, the Coriolis force

accelerates moving masses to the right, and this force can produce waves that typically span thousands of kilometres and involve almost entirely horizontal motions⁷. These are Rossby waves, and they are peculiar in that their crests propagate only westward relative to the flow in which they are embedded. When Rossby waves are triggered by eastward winds hitting mountains, some waves travel against the flow fast enough to be stationary relative to Earth's surface. The north-south flow set up by these stationary waves creates temperature contrasts downstream of mountains by transporting air from distant latitudes.

Kaspi and Schneider¹ show that Rossby waves can also induce southward winds upstream of a mid-latitude heat source by a mechanism quite distinct from that involving flow over mountains. Rossby waves are dispersive, meaning that different frequencies travel at different speeds, and as waves of different frequencies pass through each other, they create envelopes of wave energy. Rossby-wave energy emitted by an atmospheric heat source can propagate upstream faster than the mid-latitude eastward flow, producing horizontal circulations that spread out to the west of the wave source in elongated plumes⁷. Although such Rossby-wave plumes had been known to exist in both the atmosphere and the ocean, it seems that, until now, no one had looked for them in this mid-latitude atmospheric context.

Using an idealized numerical model of an atmosphere over an entirely water-covered planet, Kaspi and Schneider¹ studied the response to a mid-latitude heat source that

had a spatial scale similar to that of the Gulf Stream or the Kuroshio. In their model, a cold region formed upstream of the heating owing to the southward transport of air from more polar regions, and the width of this cold region increased with the rotation rate of their model planet in a manner consistent with the existing theory of Rossby-wave plumes. Kaspi and Schneider argue that upstream cooling by these plumes would explain why the coldest regions of eastern Asia and North America have similar horizontal extents despite large differences in the topography and size of the respective continents.

Many questions remain, one of which is whether signatures of this upstream cooling mechanism can be found in observations and in numerical models with more realistic representations of continents and oceans. It is also unclear how much of the temperature contrast across the Pacific and Atlantic can be explained by Rossby-wave plumes. The authors estimate that these plumes might account for

about half, a fraction not inconsistent with a previous finding² that the north–south flow patterns set up by mountains account for almost half of these temperature contrasts.

As to whether northeastern North America might warm if oceanic northward heat transport wanes with global warming, that seems unlikely. Simulations using climate models suggest that poleward ocean heat transport warms nearly all longitudes of the extratropical Northern Hemisphere^{2,4}, and those models should include the Rossby-wave-plume mechanism, even though it may have gone unrecognized. Perhaps even when ocean heat transport is reduced, cold and dry continental air still extracts abundant thermal energy from the warmer ocean just off eastern coasts. Or perhaps the dynamics are relatively insensitive to climate change because the Gulf Stream and Kuroshio are wind-driven.

Kaspi and Schneider's work¹ provides fresh insight into processes that create a notable asymmetry in Earth's climate. It also raises

numerous issues regarding how east-coast Rossby-wave plumes might be involved in the seasonal cycle, interannual variability, and climate change over centennial and longer timescales. ■

William R. Boos is in the Department of Geology and Geophysics, Yale University, New Haven, Connecticut 06520, USA.
e-mail: william.boos@yale.edu

1. Kaspi, Y. & Schneider, T. *Nature* **471**, 621–624 (2011).
2. Seager, R. *et al.* *Q. J. R. Meteorol. Soc.* **128**, 2563–2586 (2002).
3. Leake, J. *The Sunday Times* 8 May 2005.
4. Cubasch, U. *et al.* in *Climate Change 2001: The Scientific Basis* (eds Houghton, J. T. *et al.*) 525–582 (Cambridge Univ. Press, 2001).
5. Stommel, H. *Trans. Am. Geophys. Union* **29**, 202–206 (1948).
6. Held, I. M., Ting, M. & Wang, H. J. *Clim.* **15**, 2125–2144 (2002).
7. Rhines, P. B. in *Encyclopedia of Atmospheric Sciences* 2nd edn (eds Holton, J. *et al.*) 1923–1939 (Elsevier, 2002).

in a stem-cell zone — which encompasses the LRCs and is characterized by the expression of the marker protein CD34 — and in the secondary germ, which lies below it (Fig. 1).

The stem-cell zone is a component of the permanent follicle, whereas the secondary germ is a transient structure incorporated into the regenerating lower follicle. Notably, there is substantial flux of keratinocytes out of and into the stem-cell zone, not only in response to injury, but also with each cycle of regeneration and degeneration^{3–5}. Despite all this movement, zones of gene expression and correlated biological properties are maintained. In this context, local cues might be expected to play an essential part in sustaining this follicular architecture.

Fujiwara *et al.*¹ set out to test the function of proteins produced by stem cells and selectively deposited in the basement membrane of the bulge region. They chose nephronectin, a protein that keratinocyte stem cells deposit in the extracellular matrix of the bulge. They found that nephronectin guides the attachment of APM cells to the bulge by binding with high affinity to the $\alpha 8 \beta 1$ integrin receptor on the surface of these cells.

The authors report that mice lacking either nephronectin or the $\alpha 8$ integrin chain in their skin still form the APM in most of their follicles. But when the gene encoding nephronectin is mutated, the APM most frequently attaches slightly higher than normal on the follicle. Similarly, although in $\alpha 8$ -deficient mice the APM usually finds its normal attachment site, it attaches higher up on the follicle more frequently than in normal animals. APM attachment close to its normal site in both mutants may be explained by the presence above the bulge of EGFL6 — another ligand that binds to the $\alpha 8 \beta 1$ integrin receptor, albeit

DEVELOPMENTAL BIOLOGY

A hair-raising tale

Signals from the external microenvironment or 'niche' determine the fate of stem cells. In the hair follicle, stem cells themselves seem to act as a niche for the adjoining muscle cells that cause goosebumps.

BRUCE A. MORGAN

When you are angry, cold or scared, your hairs stand up. This response is mediated by the arrector pili muscle, which runs from the bulge — the permanent portion of the hair follicle — to the skin surface. The muscle's contraction shifts the angle of the hair relative to the skin. Piloerection, or goosebumps, makes the hair a better insulator, and alters its appearance to send a message, gruff or bluff. Writing in *Cell*, Fujiwara *et al.*¹ describe how the stem cells of the bulge act as a niche for these smooth muscle cells, coordinating their differentiation and ensuring their correct localization with high reproducibility. Although piloerection still seems to occur even when the muscle cells are not attached in precisely the right position, these data provide valuable insight into stem-cell biology.

The hair follicle has become a focus of research, in part because, in adults, its lower portion undergoes cycles of degeneration and regeneration. The keratinocytes that regenerate the follicle and hair shaft are derived from a stem-cell population housed in the bulge (Fig. 1).

Early observations suggested a simple model in which label-retaining cells (LRCs) — the

most quiescent population of stem cells in the follicular epithelium — lie at the base of a stem-cell/progenitor-cell hierarchy². At the outset of the regeneration phase, LRCs were thought to undergo asymmetrical division, generating transient amplifying cells — cells with less proliferative and developmental potential that ultimately form the differentiated cell types of the lower follicle and hair shaft. The LRCs reside in the bulge region that is adjacent to the attachment site of the arrector pili muscle (APM), and the APM was speculated to serve as a niche to maintain follicular stem cells.

Direct analysis of keratinocyte dynamics in the follicle has revealed a more complicated story that further emphasizes the potential importance of a niche. For instance, the most quiescent LRCs have a more restricted function in follicular regeneration (perhaps serving as a 'reserve' stem-cell pool), whereas other keratinocyte precursors in the permanent follicle have more active roles in the cyclical regeneration process³.

Moreover, asymmetrical division does not seem to be the mechanism that generates a fate-restricted progenitor that is distinct from the stem cell. Instead, position within the follicle seems to have a more essential role in the retention of stem-cell character. The cells that actively maintain the follicle are arranged both

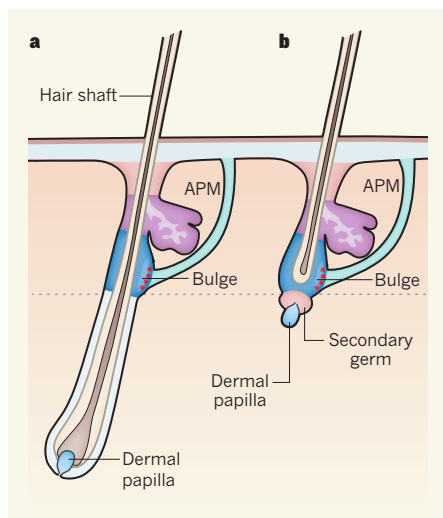


Figure 1 | The anatomy of hair. The hair follicle during the growth phase (a) and in the resting phase — between the end of the degeneration phase and the start of a new growth phase (b). Stem cells reside in the CD34-expression zone (dark blue), which is generally more quiescent than surrounding regions. The most quiescent cells, LRCs (red), are preferentially found on the posterior side, near the site of attachment of the arrector pili muscle (APM). Fujiwara *et al.*¹ find that, in the nephronectin mutant, the APM usually attaches above the stem-cell zone (not shown). The dashed line separates the permanent portion of the follicle from the portion that is replaced in each cycle.

with lower affinity — in nephronectin mutants, and by α v integrins on the APM, which can bind to nephronectin in the α 8 mutant.

This beautifully executed analysis provides a clear picture of how APM attachment is directed to the nascent bulge. It is equally noteworthy, however, that the authors detected no defects in stem-cell activity in these mutants. (Note that this analysis was limited to the normal expression of a few markers preferentially expressed in bulge keratinocytes.)

Two questions arise from this observation. First, do these mutants shed light on the significance of relative quiescence within the stem-cell hierarchy? This question might once have seemed heretical, when quiescence was routinely assumed to be a defining character of stem cells. But as our understanding of stem cells in the follicle evolves, it is reasonable to ask if the LRCs really lie at the root of the stem-cell hierarchy. How does the abnormal location, or absence, of the APM affect LRCs? Do LRCs continue to co-localize with the APM wherever it attaches? And does relative quiescence of these cells have more to do with their interaction with the APM than with their 'stemness'? If the most quiescent cells co-localize with the APM in the nephronectin mutant, it would be worthwhile evaluating the properties displayed by these cells when they reside outside the 'normal' stem-cell zone.

The second question is, if the APM is not a

niche for stem cells, what other cues maintain the stem-cell population in the bulge region? Perhaps the answer lies in the basement membrane. Proteins that are preferentially expressed by bulge keratinocytes and are deposited in the extracellular matrix are candidates to leave an adhesion marker in the bulge — to assist with the sorting of cells that return to the bulge region during the degeneration phase. Or perhaps they leave an instructive marker to promote resumption of the appropriate surface-marker profile and cell behaviour for cells that return to the bulge. Although nephronectin does not seem to fit these criteria, more rummaging in the basement membrane may identify other components that do.

It may also be worth delving deeper. The APM was one candidate for a mesenchymal niche for stem cells. The dermal papilla is the other well-characterized cluster of mesenchymal cells in the hair follicle, the activity of which is crucial for regulating follicular regeneration and morphogenesis⁶. However,

it is physically separated from the bulge with each growth cycle and cannot serve as a niche for stem cells (Fig. 1).

Is there a third specialized group of mesenchymal cells that helps to maintain the bulge, or is this a function that is handled in the epidermis itself? Further analysis of the follicular basement membrane may provide the answer. ■

Bruce A. Morgan is in the Cutaneous Biology Research Center, Massachusetts General Hospital, Charlestown, Massachusetts 02129, USA.

e-mail: bruce.morgan@cbr2.mgh.harvard.edu

1. Fujiwara, H. *et al.* *Cell* **144**, 577–589 (2011).
2. Sun, T.-T., Costasarelis, G. & Lavker, R. M. *J. Invest. Dermatol.* **96**, 77S–78S (1991).
3. Hsu, Y. C., Pasolli, H. A. & Fuchs, E. *Cell* **144**, 92–105 (2011).
4. Ito, M., Kizawa, K., Toyoda, M. & Morohashi, M. *J. Invest. Dermatol.* **119**, 1310–1316 (2002).
5. Jaks, V. *et al.* *Nature Genet.* **40**, 1291–1299 (2008).
6. Enshell-Seijffers, D., Lindon, C., Kashiwagi, M. & Morgan, B. A. *Dev. Cell* **18**, 633–642 (2010).

CONDENSED-MATTER PHYSICS

Transitions on triangles

An exquisitely sensitive technique shows that a magnetic field only a few hundred times greater than Earth's can bring an exotic phase of matter known as a quantum spin liquid to an ordered magnetic state. SEE LETTER P.612

THOMAS F. ROSENBAUM

Contrary to expectation and experience, cooling a material will not always freeze it, no matter how low the temperature falls. Two factors can act to preserve the liquid state even down to absolute zero: fluctuations away from order and towards disorder, which are especially important when atoms are confined to sheets and chains; and geometrical frustration, a failure to simultaneously satisfy all the constraints imposed by interactions between neighbouring atoms. On page 612 of this issue, Pratt *et al.*¹ probe a model two-dimensional frustrated system that has magnetic spins as stand-ins for atoms and a quantum spin-liquid phase that is stable down to the lowest temperatures accessible. This is the layered molecular system denoted κ -(BEDT-TTF)₂Cu₂(CN)₃.

When a system is precariously balanced between solid and liquid, or more generally between order and disorder, and the temperature hovers just above absolute zero, the range and impact of quantum fluctuations grow and the fundamental nature of the system's ground (minimal-energy) state becomes apparent. Moreover, low-energy excitations, collective and widespread, become accessible in new ways. Pratt and colleagues find¹ that small

magnetic fields applied to the model spin-liquid system tip the balance from disorder to order by exciting and condensing collective modes of spins. Ramping up the magnetic field disrupts the collective magnetic order and induces the possibility of shorter-range spin pairings.

Quantum spin liquids touch on some of the central themes of condensed-matter physics: correlations, competition between ground states, frustration, fluctuations, and protected degrees of freedom. The model system discussed here¹ allows these themes to be explored quantitatively. Its magnetic properties are determined by the fact that its lattice consists of linked, corner-sharing triangles with electronic ($S = 1/2$) spins at each of the corners². Think of the spins as compass needles that want to line up antiparallel to each other: an antiferromagnetic ground state. If the needle at the apex of the triangle points north, then each of the other two needles should point south to satisfy the constraint provided by interacting with the apex. But the two needles at the base of the triangle also interact with each other and impose the incompatible constraint of one needle pointing north and one pointing south. Each needle switches from north to south with little cost in energy. The spins can continue to fluctuate even at

extremely low temperatures, refusing to order into the antiferromagnet³, just as atoms in a liquid fluctuate away from the lattice positions that they would assume in an ordered solid.

Significantly, the effects of these spin fluctuations are amplified because of the effective two-dimensional nature of the material. Consider the following analogy: a few spectators queuing to enter a football stadium can step out of line and easily dissolve that (one-dimensional) line, and a small number of band members stepping out of position at the half-time show will disrupt the (two-dimensional) formation, but a good portion of the total stadium attendance must leave their seats for (three-dimensional) order to be disturbed. Combined with the well-defined geometry of a spin-1/2, frustrated triangular antiferromagnet, the reduced dimensionality leads to an interesting and complex phase diagram⁴.

Pratt *et al.*¹ show that the native spin-liquid state can be frozen and become ordered by the application of a magnetic field of 14 millitesla, which is only a few hundred times stronger than Earth's magnetic field. Given that the external magnetic field points in one direction and the spins at the corners of the triangles want to point in opposite directions, this ordering is not as simple as just aligning the spins with the applied field. Rather, the magnetic field provides the means to excite spins to energies above their ground state. The excitations then collectively condense into the long-range, ordered, antiparallel configuration of antiferromagnetism, following a scenario analogous to Bose–Einstein condensation in superfluid helium.

How are Pratt and colleagues able to deduce all this information? They use an exquisitely sensitive technique called muon spin rotation — which, as its name implies, is performed with subatomic particles known as muons — and their samples are cooled to a few hundredths of a degree above absolute zero. The muons are injected into the material with their own spins aligned along one direction, and are then used to sample the local magnetic environment and to communicate the presence of order or disorder by decaying within microseconds. Not only does the quantum phase transition between spin liquid and weak antiferromagnet — ‘weak’ because the ordered state still feels the disruption of fluctuations — show up clearly, but there is also evidence for a transition to another ordered state at much higher applied magnetic fields. Unfortunately, the local nature of the information obtained from the muon-spin-rotation technique makes it difficult to identify definitively the character of the high-field order.

Pratt and colleagues' work¹ provides a compelling opportunity for serious confrontation between theory and experiment, including determination of the critical exponents that define the fundamental and generalizable character of the quantum spin liquid. More

generally, it illuminates the ramifications of frustration, a concept useful in fields as diverse as economics, computer design and physics. In three-dimensional magnetic solids, order and disorder can mix, and geometrically frustrated states can exist in which only a fraction of the magnetic spins can change direction with little cost in energy. These blocks of spins are surrounded by frozen neighbours, but protected from them⁵. They not only offer the opportunity to probe the general structure of the state, but also, if they can be preferentially accessed, may serve to encode and manipulate information⁶. ■

MICROBIOLOGY

Dicing defence in bacteria

A newly discovered variation in the process by which bacteria resist invasion by foreign nucleic acids provides an intriguing parallel between the defence mechanisms of the different domains of life. [SEE ARTICLE P.602](#)

SUSAN GOTTESMAN

Viruses and mobile genetic elements such as plasmids pose a threat to the genomic integrity of organisms from all domains of life, whether they be eukaryotes (organisms with discrete cell nuclei, for example plants and animals), bacteria or archaea. Some of the most exciting findings made over the past 15 years have been the RNA-based defence systems of eukaryotes (RNA interference, or RNAi) and of bacteria and archaea (CRISPR systems). In both cases, RNA transcripts are processed by endonuclease enzymes into short guide RNAs that then target invaders that have complementary nucleic-acid sequences. The Dicer endonuclease is essential for RNAi processing¹. On page 602 of this issue, Deltcheva *et al.*² describe a processing pathway for CRISPR RNA that has intriguing similarities to the RNAi pathway, including dependence on the bacterial equivalent of Dicer, RNase III. A *trans*-acting RNA, *tracrRNA*, targets the cleavage process that ultimately produces mature guide RNAs.

The sequencing of bacterial and archaeal genomes led to recognition of clustered, regularly interspaced short palindromic repeats (CRISPR). These palindromic repeats are separated by unique spacers that are frequently homologous to portions of bacteriophage or plasmid genomes (Fig. 1). The spacers function as a bacterial memory of past invasions, and endow the cell with the ability to restrict a second invasion by the same phage or plasmid.

Spacers arise through the capture of

Thomas F. Rosenbaum is at the James Franck Institute and the Department of Physics, University of Chicago, Chicago, Illinois 60637, USA.

e-mail: t-rosenbaum@uchicago.edu

1. Pratt, F. L. *et al.* *Nature* **471**, 612–616 (2011).
2. Shimizu, Y. *et al.* *Phys. Rev. Lett.* **91**, 107001 (2003).
3. Aeppli, G. & Chandra, P. *Science* **275**, 177–178 (1997).
4. Xu, C. & Sachdev, S. *Phys. Rev. B* **79**, 064405 (2009).
5. Laughlin, R. B. & Pines, D. *Proc. Natl Acad. Sci. USA* **97**, 28–31 (2000).
6. Ghosh, S., Rosenbaum, T. F. & Aeppli, G. *Phys. Rev. Lett.* **101**, 157205 (2008).

invading sequences, with short regions of the invader's genome being incorporated between repeats to create the CRISPR array (acquisition step, Fig. 1; see refs 3, 4 for reviews). The CRISPR region is transcribed as a single, long RNA. As with RNAi, the effective RNA species for the CRISPR defence system is not the initial transcript, but a short, processed piece. For CRISPR, the processed RNA contains the sequence-specific spacer and some of the flanking repeats. This guide RNA is then used to direct the destruction of invading nucleic acids (DNA in some cases, RNA in others)^{5,6}.

How does processing occur? The CRISPR arrays are associated with genes that encode a set of CRISPR-associated proteins (Cas). One of the difficulties in untangling the CRISPR pathway is the variability between species — and even strains — in the multiple families of associated proteins, implying multiple variants in the machinery for the acquisition step and subsequent immunity⁷. Some organisms have 20 proteins at a CRISPR locus, whereas others have only four. Purified Cas proteins from the bacteria *Escherichia coli* and *Pseudomonas aeruginosa*, and from the archaeon *Pyrococcus furiosus*, can all cleave the precursor RNA within the spacers to generate guide RNAs (processing steps, Fig. 1); therefore, specific Cas proteins are necessary and sufficient for RNA cleavage in these organisms^{8–10}.

Streptococcus pyogenes, the organism studied by Deltcheva *et al.*², has a CRISPR system with only four Cas-protein genes and none of the protein families that have been implicated in processing in other systems. Instead,

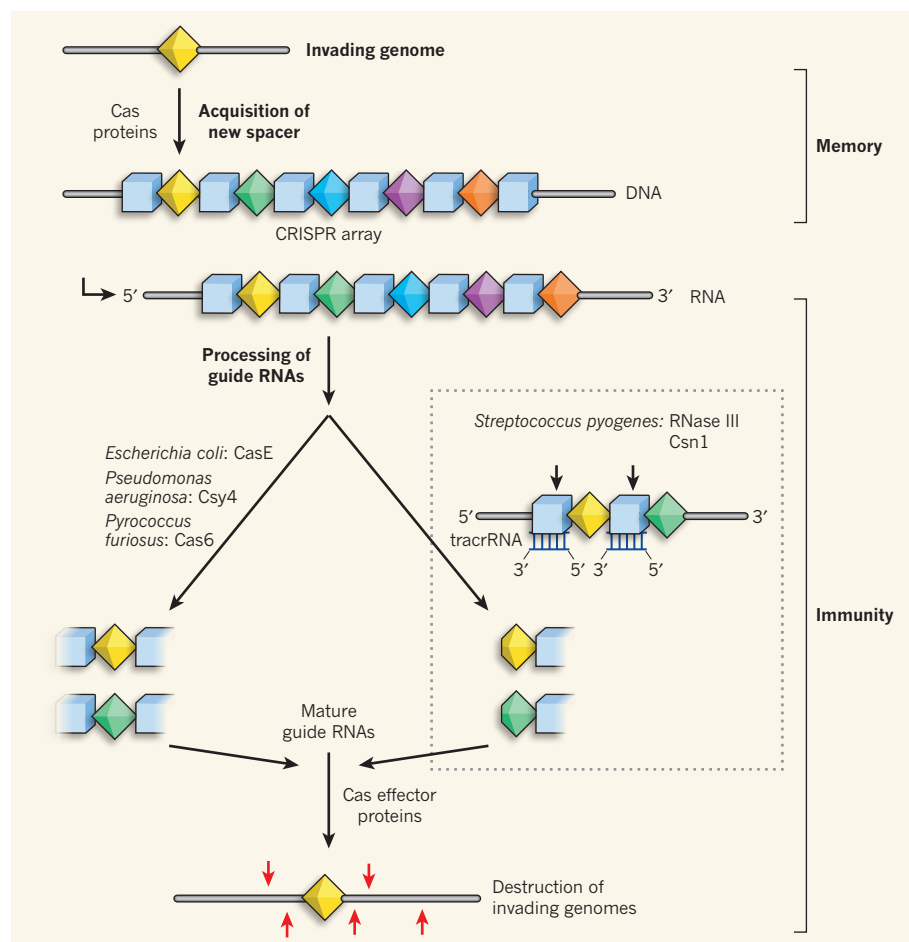


Figure 1 | Flexibility in CRISPR processing systems. In CRISPR arrays of DNA, conserved repeats (squares) alternate with variable spacers (diamonds). During the acquisition/memory step, new spacers are incorporated as a result of invasion of the cell by a phage or plasmid. During the processing steps required to confer immunity, RNA transcripts of the CRISPR array are cleaved to give mature guide RNAs, which then target for destruction invading genomes that match the spacer. The related proteins CasE, Csy4 and Cas6 carry out the initial processing step in many organisms. Deltcheva *et al.*² describe a different pathway for guide-RNA maturation that operates in *Streptococcus pyogenes* and certain other bacteria (boxed area). This pathway involves a *trans*-acting RNA (tracrRNA) that hybridizes with the spacers, leading to cleavage by RNase III. Csn1 aids in the process, and an undefined step yields mature guide RNAs.

the authors find that *S. pyogenes* uses the bacterial RNase III to process CRISPR RNA; targeting of cleavage is determined by an antisense RNA, tracrRNA, with complementarity to the CRISPR spacer (boxed area in Fig. 1).

RNase III is a conserved endonuclease that cleaves double-stranded RNA and is involved in the maturation of ribosomal RNA. It is also the bacterial equivalent of the Dicer endonuclease. The new work² demonstrates the flexibility in CRISPR systems and, for the first time, links RNase III to the bacterial CRISPR defence system. Finally, the use of a core RNase rather than a Cas-specific protein provides a clear example of crosstalk between the CRISPR system and bacterial metabolism.

The antisense RNA that plays an important part here was identified when Deltcheva and colleagues' deep sequencing of *S. pyogenes* revealed abundant short RNAs all containing a region of complementarity to the CRISPR repeat. These antisense RNAs were encoded

close to the CRISPR cluster but on the opposite strand. Deleting the gene for the antisense RNA prevented processing of the CRISPR RNA. *In vitro*, this antisense RNA can anneal to CRISPR RNA, making a double-stranded RNA that is a substrate for RNase III. *In vivo*, cleavage requires RNase III and Csn1, one of the Cas proteins specific to this family of CRISPR clusters; Csn1 may facilitate pairing of tracrRNA and CRISPR RNA, and also a second processing step. Finally, Deltcheva *et al.* find that all of these elements (tracrRNA, Csn1 and RNase III) are necessary for immunity — that is, for *S. pyogenes* to destroy an invading plasmid containing sequences complementary to the CRISPR spacer.

When the family of CRISPRs containing Csn1 was first defined, Haft *et al.*⁷ noted that "A characteristic feature of this subtype is a single copy of the repeat (sometimes direct, sometimes inverted), which appears upstream of the first gene in the locus". Now we know that Csn1

is essential, as is the nearby upstream repeat, to this unique pathway for guide RNA maturation. The many bacterial species containing this family of proteins all express tracrRNA², and so are highly likely to use this RNA, and RNase III, to mature their CRISPR RNAs.

We do not yet know whether this CRISPR variant is an evolutionary remnant, predating the acquisition of dedicated Cas proteins, or a more recent variation. Certainly the small number of Cas proteins necessary for the *S. pyogenes* system to work, coupled with the enticing similarity of the tracrRNA-dependent processing pathway to the eukaryotic Dicer pathway, favours this as an ancestral minimal system. Curiously, all of the species that harbour the genes in this pathway are associated with vertebrates, either as pathogens or commensals⁷. Perhaps this is a system that has evolved to deal not only with phage invaders, but also with invasion by eukaryotic RNAs (possibly microRNAs).

The recognition of CRISPR was a direct outcome of the sequencing of multiple microbial genomes. Now, deep sequencing² of the RNA complement of *S. pyogenes* has demonstrated the existence of a novel pathway for an antisense RNA in CRISPR maturation. We can expect many more roles for regulatory RNAs to emerge as this approach continues to be applied to eukaryotes, bacteria and archaea. ■

Susan Gottesman is in the Laboratory of Molecular Biology, National Cancer Institute, Bethesda, Maryland 20892, USA.
e-mail: susang@helix.nih.gov

1. Jaskiewicz, L. & Filipowicz, W. *Curr. Top. Microbiol. Immunol.* **320**, 77–97 (2008).
2. Deltcheva, E. *et al. Nature* **471**, 602–607 (2011).
3. Karginov, F. V. & Hannon, G. J. *Mol. Cell* **37**, 7–19 (2010).
4. Marraffini, L. A. & Sontheimer, E. J. *Nature Rev. Genet.* **11**, 181–190 (2010).
5. Marraffini, L. A. & Sontheimer, E. J. *Science* **322**, 1843–1845 (2008).
6. Hale, C. R. *et al. Cell* **139**, 945–956 (2009).
7. Haft, D. H., Selengut, J., Mongodin, E. F. & Nelson, K. E. *PLoS Comput. Biol.* **1**, e60 (2005).
8. Brouns, S. J. J. *et al. Science* **321**, 960–964 (2008).
9. Carte, J., Wang, R., Li, H., Terns, R. M. & Terns, M. P. *Genes Dev.* **22**, 3489–3496 (2008).
10. Haurwitz, R. E. *et al. Science* **329**, 1355–1358 (2010).

CLARIFICATION

"Reproductive biology: Progesterone's gateway into sperm" by Steve Publicover and Christopher Barratt (*Nature* **471**, 313–314; 2011). The following sentence in this article — "The second, more recent, advance was the development of a method for applying to sperm the technique of whole-cell patch clamping, which records ionic currents across the entire plasma membrane of a cell" — should have been accompanied by a reference to P. V. Lishko, I. L. Botchkina, A. Fedorenko & Y. Kirichok *Cell* **140**, 327–337 (2010).

Linear ubiquitination prevents inflammation and regulates immune signalling

Björn Gerlach^{1,2*}, Stefanie M. Cordier^{1*}, Anna C. Schmukle^{1*}, Christoph H. Emmerich^{1,2*}, Eva Rieser^{1*}, Tobias L. Haas^{2,3*}, Andrew I. Webb^{4*}, James A. Rickard⁵, Holly Anderton⁵, Wendy W.-L. Wong⁵, Ueli Nachbur⁵, Lahiru Gangoda⁵, Uwe Warnken⁶, Anthony W. Purcell⁴, John Silke⁵ & Henning Walczak^{1,2}

Members of the tumour necrosis factor (TNF) receptor superfamily have important functions in immunity and inflammation. Recently linear ubiquitin chains assembled by a complex containing HOIL-1 and HOIP (also known as RBCK1 and RNF31, respectively) were implicated in TNF signalling, yet their relevance *in vivo* remained uncertain. Here we identify SHARPIN as a third component of the linear ubiquitin chain assembly complex, recruited to the CD40 and TNF receptor signalling complexes together with its other constituents, HOIL-1 and HOIP. Mass spectrometry of TNF signalling complexes revealed RIP1 (also known as RIPK1) and NEMO (also known as IKK γ or IKBKG) to be linearly ubiquitinated. Mutation of the *Sharpin* gene (*Sharpin*^{*cpdm/cpdm*}) causes chronic proliferative dermatitis (*cpdm*) characterized by inflammatory skin lesions and defective lymphoid organogenesis. Gene induction by TNF, CD40 ligand and interleukin-1 β was attenuated in *cpdm*-derived cells which were rendered sensitive to TNF-induced death. Importantly, *Tnf* gene deficiency prevented skin lesions in *cpdm* mice. We conclude that by enabling linear ubiquitination in the TNF receptor signalling complex, SHARPIN interferes with TNF-induced cell death and, thereby, prevents inflammation. Our results provide evidence for the relevance of linear ubiquitination *in vivo* in preventing inflammation and regulating immune signalling.

Members of the TNF receptor superfamily (TNFRSF) exert pleiotropic effects in immune and non-immune tissues¹ and their signalling is regulated by different types of ubiquitin chains^{2–4}. We and others recently showed that pro-survival signalling by TNF receptor 1 (TNFR1) was compromised in cells deficient in HOIL-1 or HOIP and that these cells were sensitized to TNF-induced cell death^{5,6}. Together, HOIL-1 and HOIP form the linear ubiquitin chain assembly complex (LUBAC) which catalyses the formation of a peptide bond between the amino-terminal methionine (M1) of one ubiquitin molecule and the carboxy-terminal glycine (G76) of the next. Therefore, linear ubiquitin linkage is also referred to as M1 linkage. LUBAC is recruited to the TNF receptor signalling complex (RSC)⁵ and its linear-ubiquitin-chain-generating activity is required in the TNF-RSC for efficient gene activation and prevention of apoptosis induction by TNF^{5,6}. This has been suggested to be due to LUBAC-mediated linear ubiquitination of NEMO⁶. NEMO can bind both lysine 63 (K63)-linked and linear ubiquitin chains^{7–9}. Therefore we proposed that LUBAC and its linear-ubiquitin-chain-forming activity are important for efficient NEMO recruitment to, and retention in, the TNF-RSC and consequent TNF-induced gene activation⁵. The relevance of LUBAC and linear ubiquitination *in vivo*, however, remains unknown and contested¹⁰.

SHARPIN is recruited to CD40- and TNF-RSCs

We recently reported on the identification of HOIL-1 and HOIP as novel components of the TNF-RSC by tandem-mass-spectrometry following isolation of this protein complex by modified tandem affinity purification (moTAP)⁵. We developed a similar moTAP approach for

CD40L (also known as CD154 or CD40LG; Supplementary Fig. 1a–c) and purified the native CD40-RSC (Fig. 1a). This analysis revealed HOIL-1, HOIP as well as SHARPIN as potential novel components of the CD40-RSC (Supplementary Fig. 2a). SHARPIN was also the only other novel protein, apart from HOIL-1 and HOIP⁵, for which peptides were identified by mass-spectrometry following moTAP of the TNF-RSC (Supplementary Fig. 2b). Using a SHARPIN-specific monoclonal antibody (Supplementary Fig. 3a) we next showed that SHARPIN was indeed recruited to both, the CD40-RSC and the TNF-RSC in a ligand- and time-dependent manner, with similar kinetics as HOIL-1 and HOIP (Fig. 1b and Supplementary Fig. 3b). We showed previously that recruitment of HOIL-1 and HOIP to the TNF-RSC depended on the presence and E3 activity of cellular inhibitor of apoptosis proteins (cIAPs)⁵. We therefore tested whether SHARPIN recruitment also required cIAPs by using the Smac (also known as DIABLO)-mimetic compound SM-164 (ref. 11). Treatment of cells with SM-164 resulted in rapid and complete depletion of cIAPs over the entire time course of the experiment (Fig. 1c, d). This pre-treatment prevented RIP1 ubiquitination in TNF-treated cells (Fig. 1d) and almost completely abolished recruitment of HOIL-1, HOIP and SHARPIN to both the CD40-RSC (Fig. 1c) and the TNF-RSC (Fig. 1d and ref. 5).

Complexes of SHARPIN, HOIL-1 and HOIP generate linear ubiquitin chains

In addition to the sequence similarity between SHARPIN and HOIL-1 (Supplementary Fig. 3c), these results indicated that SHARPIN may be recruited to the CD40- and TNF-RSCs together with HOIP and/or

¹Tumour Immunology Unit, Department of Medicine, Imperial College London, W12 0NN London, UK. ²Division of Apoptosis Regulation, German Cancer Research Center (DKFZ), 69120 Heidelberg, Germany. ³Department of Experimental Oncology, Mediterranean Institute of Oncology, 95029 Viagrande, Italy. ⁴Department of Biochemistry, Bio21 Melbourne University, Melbourne, VIC 3010, Australia. ⁵Department of Biochemistry, La Trobe University, Melbourne, VIC 3086, Australia. ⁶Protein Analysis Core Facility, German Cancer Research Center (DKFZ), 69120 Heidelberg, Germany.

*These authors contributed equally to this work.

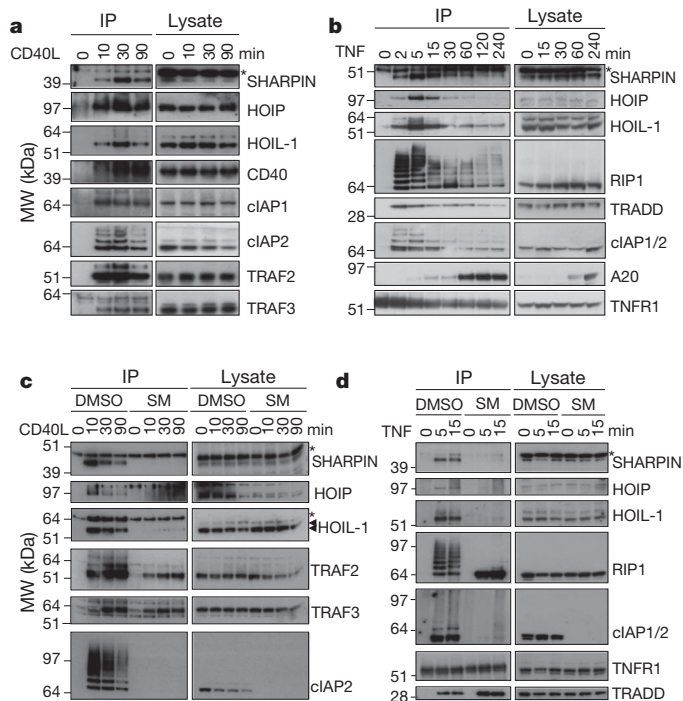


Figure 1 | SHARPIN is recruited to the native CD40- and TNF-RSCs. **a, b**, SHARPIN, HOIL-1 and HOIP are recruited to the native CD40- and TNF-RSC in Raji B cells (**a**) and HeLa cells (**b**), respectively. **c, d**, Raji (**c**) and HeLa (**d**) cells were pre-treated for 2 h with SM-164 (SM) before the CD40- (**c**) and TNF-RSCs (**d**) were precipitated at the indicated times. IP, immunoprecipitation; *, unspecific bands.

HOIL-1 and possibly cooperates with them functionally. To test this hypothesis we examined the possibility of endogenous complex formation between SHARPIN and HOIL-1/HOIP. Gel filtration analysis showed that the three endogenous proteins eluted together in the same high-molecular-weight fractions, with SHARPIN being shifted away from a strongly reactive but unspecific band that remained in the low-molecular-weight fractions (Fig. 2a). In addition, co-immunoprecipitation experiments showed that the endogenous proteins were also bound to each other independently of TNF stimulation (Fig. 2b). These results strongly indicate the existence of a tripartite protein complex consisting of HOIP, SHARPIN and HOIL-1, but do not rule out the existence of additional functionally active complexes consisting of other combinations of these proteins.

We next investigated the functionality of SHARPIN interactions with HOIL-1 and/or HOIP. SHARPIN was unable to activate NF- κ B when expressed alone, or when combined with HOIL-1, yet when combined with HOIP, NF- κ B was activated to a similar level as when HOIL-1 and HOIP were co-expressed. Overexpression of all three components together resulted in the strongest NF- κ B activation (Fig. 2c). This pointed to an essential role for HOIP in the functional activity of the different combinations. Using deletion and point mutants of SHARPIN and HOIP (Supplementary Fig. 4a) we determined that the interaction between these two proteins is primarily due to the ubiquitin-like (UBL) domain of SHARPIN binding to the second Npl4 zinc-finger domain (NZF2) of HOIP (Supplementary Fig. 4b–d and Supplementary Fig. 5a, b). In addition, via its NZF domain SHARPIN binds to ubiquitin (Supplementary Fig. 6a, b), preferring M1- and K63- over K48-linked ubiquitin tetramers (Supplementary Fig. 6c).

Activation of NF- κ B by simultaneous overexpression of HOIL-1 and HOIP correlates with their ability to generate linear ubiquitin chains⁶. We therefore tested the ability of recombinant SHARPIN in combination with recombinant HOIL-1 and/or HOIP to generate M1-linked ubiquitin chains. In accord with their respective abilities

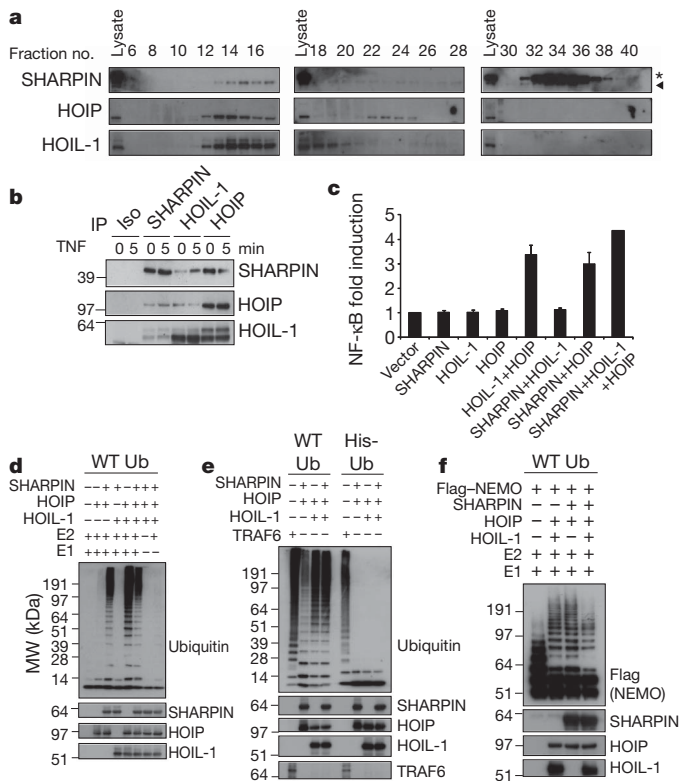


Figure 2 | SHARPIN forms a tripartite complex with HOIP and HOIL-1 that is capable of forming linear ubiquitin chains. **a**, SHARPIN, HOIL-1 and HOIP co-elute in high molecular weight S100 cytosolic fractions in HeLa cells. *, unspecific band. **b**, SHARPIN, HOIL-1 and HOIP form a stimulation-independent complex. Iso, isotype control. **c**, SHARPIN activates NF- κ B when co-expressed with HOIP or HOIP and HOIL-1. Proteins were overexpressed in 293-NF- κ B cells and a luciferase-reporter assay was performed ($n = 4$). Data are presented as mean \pm s.e.m. **d, e** SHARPIN contributes to linear ubiquitin chain formation when complexed with HOIP or HOIP and HOIL-1. Ub, ubiquitin; WT, wild type. **f**, HOIP in combination with SHARPIN and/or HOIL-1 attaches ubiquitin chains to NEMO.

to activate NF- κ B, combinations of SHARPIN–HOIP–HOIL-1, SHARPIN–HOIP and HOIP–HOIL-1, but not of SHARPIN–HOIL-1, were capable of forming ubiquitin chains (Fig. 2d). His-tagged ubiquitin (His-ubiquitin) is blocked at the N terminus and capable of contributing to all ubiquitin chain linkages except for linear ones. Accordingly, TRAF6, a control E3 that forms nonlinear chains, was capable of using both wild-type and His-ubiquitin to generate polyubiquitin chains (Fig. 2e). The three active LUBAC combinations were, however, capable of generating ubiquitin chains only with wild-type but not His-ubiquitin (Fig. 2e). This demonstrates that, in addition to the LUBAC consisting of HOIL-1 and HOIP described previously, a second dimeric LUBAC consisting of SHARPIN and HOIP, as well as a third LUBAC, the tripartite complex consisting of SHARPIN, HOIP and HOIL-1, exclusively generate linear ubiquitin chains.

RIP1 and NEMO are linearly ubiquitinated in the TNF-RSC

To test whether the three different LUBAC versions may share and/or act differentially on various possible targets, we investigated their ability to modify components of the CD40- and TNF-RSCs *in vitro*. This analysis revealed that all three LUBAC versions were capable of ubiquitinating NEMO *in vitro* (Fig. 2f). Yet none of the eight other CD40- and/or TNF-RSC components tested were modified to any significant extent (Supplementary Figs 7 and 8), except RIP1 on which subtle modification was detected. To investigate the *in vivo* relevance of these findings we developed a highly specific and sensitive method to enable the analysis of isolated, individual RSC components

(Supplementary Figs 9 and 10) by combining moTAP with fluorescence protein labelling, two-dimensional (2D) separation, fluorescence-guided robotic spot picking, tryptic digestion and multiple reaction monitoring (MRM) mass spectrometry. This moTAP-2D-MRM approach (Fig. 3) showed that both RIP1 and NEMO are linearly ubiquitinated in the native TNF-RSC (Fig. 3 and Supplementary Figs 11 and 12). In each of two individual RIP1-containing spots, in addition to the signature peptide of linear ubiquitin linkage (Ub-M1), we also identified signature peptides identifying K11-, K48- and K63-linked ubiquitin (Fig. 3a, c, Supplementary Figs 11 and 12 and data not shown for RIP1 spot B). The NEMO spot we analysed, however, contained exclusively M1-linked ubiquitin (Fig. 3b, d and Supplementary Figs 11 and 12). Thus, RIP1 and NEMO reside as linearly ubiquitinated proteins in the native TNF-RSC.

SHARPIN is required for TNF, CD40L and IL-1 β signalling

We next assessed whether any one of the three LUBAC components was required for LUBAC recruitment to the TNF-RSC. Suppression of HOIL-1 resulted in only slight reduction of SHARPIN and HOIP in the TNF-RSC (Supplementary Fig. 13a), indicating that HOIL-1 is not required for their recruitment. Suppression of HOIP on the other hand completely abrogated recruitment of HOIL-1 and SHARPIN to the TNF-RSC (Fig. 4a). To test the role of SHARPIN, we took advantage of the chronic proliferative dermatitis (*cpdm*) strain of BL/6 mice that carry a spontaneous mutation in the *Sharpin* gene¹². Although murine embryonic fibroblasts (MEFs) generated from *Sharpin*^{*cpdm/cpdm*} (*cpdm*) mice expressed less HOIL-1 and HOIP than wild-type MEFs (Supplementary Fig. 14a), recruitment of HOIL-1 and HOIP to the TNF-RSC still occurred, albeit at a lower level than in wild-type MEFs (Supplementary Fig. 13b). Importantly, reduced protein levels of HOIL-1 and HOIP in *cpdm* MEFs was not due to decreased mRNA levels for these proteins (Supplementary Fig. 14b), indicating that SHARPIN stabilizes HOIL-1 and HOIP at the protein level. This finding provides further indirect evidence for the existence of a tripartite LUBAC. Taken together, neither HOIL-1 nor SHARPIN are required for LUBAC recruitment to the TNF-RSC, but HOIP as the central component is. Interestingly, the recruitment of SHARPIN

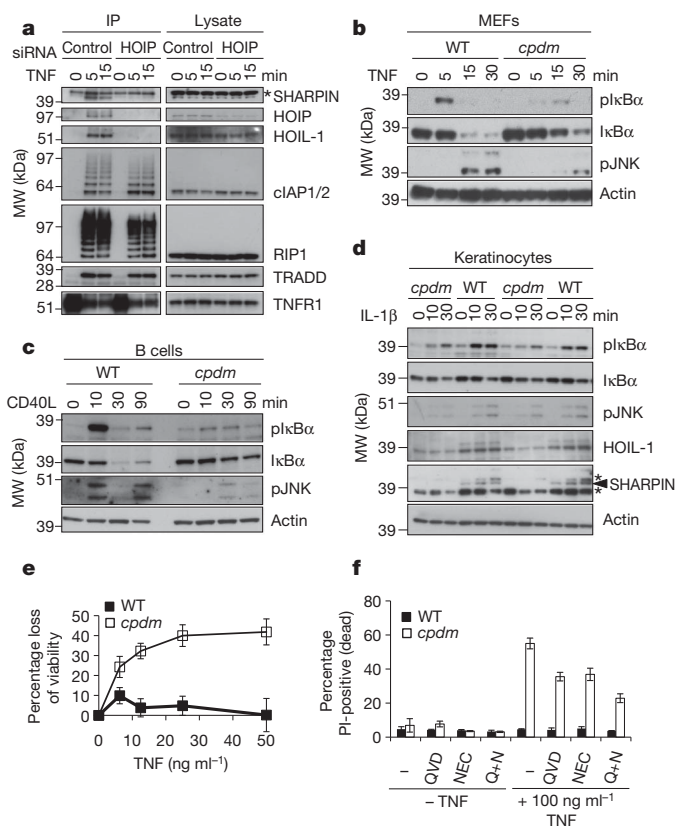


Figure 4 | SHARPIN is required for full TNF-, CD40L- and IL-1 β -induced activation of NF- κ B and JNK and to prevent TNF-induced cell death.

a, Recruitment of the HOIP–HOIL-1/SHARPIN complex to the TNF-RSC is mediated by HOIP. **b–d**, SHARPIN is required for efficient TNF- (**b**), CD40L- (**c**) and IL-1 β -induced (**d**) NF- κ B and JNK activation. pl κ B α and pJNK, phosphorylated I κ B α and JNK. **e**, **f**, Absence of SHARPIN sensitises MEFs to TNF-induced cell death as determined by (**e**) cell viability measurement ($n = 4$) and (**f**) propidium iodide (PI) incorporation ($n = 6$). Data are presented as mean \pm s.e.m.

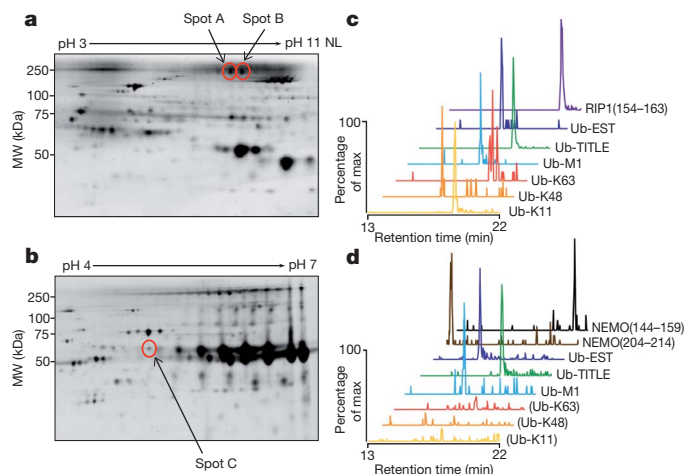


Figure 3 | NEMO and RIP1 are linearly ubiquitinated in the native TNF-RSC. **a**, **b**, Fluorescence images of 2D gels of moTAP-purified CyDye-stained TNF-RSC. U937 cells (3×10^6 , **a**; and 1.8×10^{10} , **b**) were stimulated with moTAP-TNF before tandem purification of the TNF-RSC, fluorescence labelling and 2D separation. Red circles indicate spots in which RIP1 and ubiquitin (**a**) and NEMO and ubiquitin (**b**) were detected, respectively. **c**, Extracted ion chromatograms (XICs) for all peptides detected in spot A. Enhanced product ion (EPI) spectra, confirming the MRM transition, were observed for all peptides shown (Supplementary Fig. 7). **d**, XICs for all peptides detected in spot C. EST and TITL, the ubiquitin-derived tryptic peptides ESTLHLVLR and TITLVEPSDTIENVK.

and HOIP in HOIL-1-suppressed cells, and of HOIL-1 and HOIP in SHARPIN-deficient cells (Supplementary Fig. 13a, b), shows that at least in the absence of the respective third component, complexes of the other two exist and can be recruited to RSCs.

Mutation of the *Sharpin* gene is causative for the *cpdm* phenotype^{12–14}. In addition to the skin, many other tissues including liver, lung, forestomach and oesophagus, are also inflamed in *cpdm* mice¹³. *Cpdm* mice also present with a prominent immunological phenotype characterized by lymphoid dysregulation, splenomegaly, defects in T_H1 cytokine production and various lymphoid developmental and structural abnormalities^{13–15}.

Therefore, we next examined immune cytokine signalling in cells obtained from *cpdm* mice. We showed previously that suppression of HOIL-1 and HOIP negatively affected activation of the NF- κ B and JNK pathways as well as gene induction following TNF stimulation⁵. Consistent with this, we found that *cpdm* MEFs also activated NF- κ B poorly in response to TNF. In particular, these cells showed decreased phosphorylation and degradation of I κ B α (Fig. 4b), impaired and delayed nuclear translocation of the NF- κ B subunit p65 (Supplementary Fig. 15a, b) and reduced induction of TNF target genes when compared to wild-type MEFs (Supplementary Fig. 16a). Intriguingly, induction of I κ B α was substantially less affected than that of other target genes (Supplementary Fig. 16a). This might be explained by a recent finding showing that induction of certain NF- κ B target genes, for example, I κ B α , was relatively independent of signal strength and occurred even at low doses of TNF, whereas that of others required high doses and a strong TNF response¹⁶. The additional reduction of

JNK activation in TNF-stimulated *cpdm* MEFs (Fig. 4b) indicates that genes which require cooperation between NF- κ B and JNK for their expression will be particularly affected by defective LUBAC recruitment or absence of LUBAC components. Our findings in TNF-stimulated *cpdm* MEFs are corroborated by defective CD40L-induced NF- κ B and JNK activation in splenic *cpdm* B cells (Fig. 4c and Supplementary Fig. 17a, b). Importantly, in primary keratinocytes obtained from the skin of 2-week-old non-diseased *cpdm* mice (skin being the tissue most strongly affected by loss of SHARPIN) activation of NF- κ B and JNK by both IL-1 β and TNF was also attenuated (Fig. 4d and Supplementary Fig. 18). By contrast, CD40L- and TWEAK (also known as TNFSF12)-induced processing of p100 to p52 were not significantly altered in *cpdm*-derived B-cells and MEFs, respectively (Supplementary Fig. 17b, c and Supplementary Fig. 19). However, given the similarity in lymphoid organogenesis defects between *cpdm* mice and mice in which non-canonical NF- κ B is defective¹⁷, on the basis of these results we do not rule out the possibility that in cells responsible for proper lymphoid organ development non-canonical NF- κ B activity might be negatively affected, either directly or indirectly, by the absence of SHARPIN.

Additional suppression of HOIL-1 in *cpdm* MEFs further decreased TNF-induced destabilization and phosphorylation of I κ B α compared to *cpdm* MEFs (Supplementary Fig. 15c). However, activation of NF- κ B still occurred. This demonstrates that SHARPIN and, consequently, LUBAC activity are not essential for TNF-induced activation of NF- κ B but that they are important for regulating the strength

of signal transduction and hence gene expression following TNF stimulation.

Given our previous finding that suppression of HOIL-1 or HOIP by RNA interference sensitises cells to TNF-induced death⁵, we next tested whether the *cpdm* mutation also had an impact on survival following TNF stimulation. We found that *cpdm* MEFs were highly sensitive to TNF-induced cell death (Fig. 4e, f). This cell death was partially blocked by the apoptosis inhibitor Q-Val-Asp(non-O-methylated)-Oph (QVD) and the necroptosis inhibitor necrostatin-1 (NEC) and most efficiently inhibited by a combination thereof (Fig. 4f). Thus, TNF-induced cell death in *cpdm* MEFs includes an apoptotic (Supplementary Fig. 20) as well as a necroptotic component. Taken together, these results demonstrate that loss of SHARPIN results in a gene-induction-inhibitory dysregulation of cytokine signalling and sensitisation to TNF-induced cell death.

Ablation of TNF rescues *cpdm* skin phenotype

Increased rates of keratinocyte cell death have been described in the skin of *cpdm* mice^{14,18}. Given that our analysis of TNF signalling pathways in *cpdm* MEFs revealed sensitisation to TNF-induced cell death we reasoned that removal of TNF might alleviate or even prevent inflammation in *cpdm* mice. We therefore crossed *cpdm* mice with TNF-deficient mice. Strikingly, we found that deletion of only one allele of the *Tnf* gene prevented the occurrence of macroscopic and microscopic skin lesions in *cpdm* mice (Fig. 5a, b and Supplementary Fig. 21). In contrast to the rescue of the skin phenotype, many other

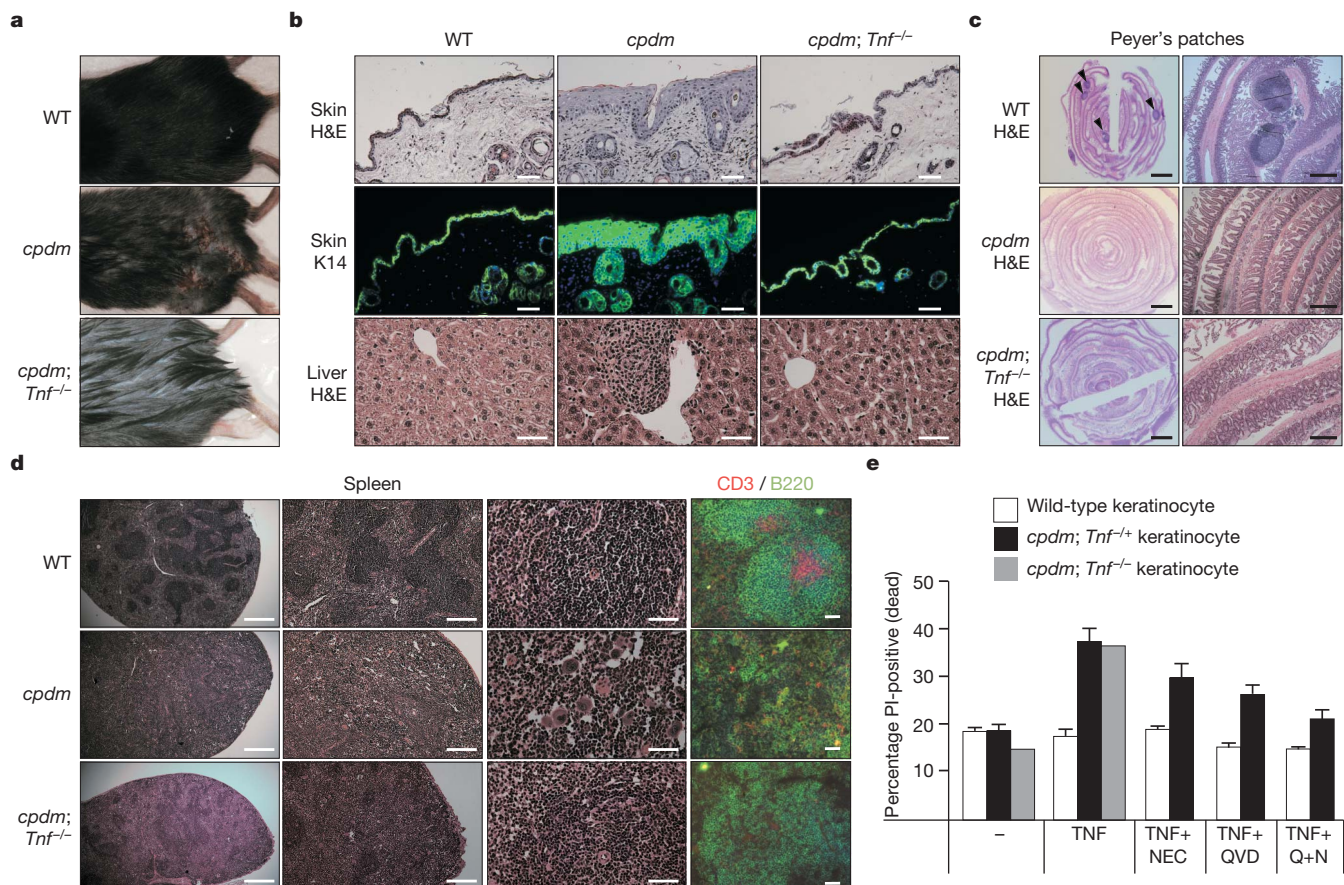


Figure 5 | Genetic ablation of TNF rescues the skin phenotype and reduces inflammation in *cpdm* mice but does not revert the immunological distortion. **a**, Loss of TNF restores normal skin morphology in *cpdm* mice. **b**, Inflammatory skin and liver lesions do not develop in *cpdm; Tnf^{-/-}* mice as shown by haematoxylin and eosin (H&E) and K14-fluorescence stained skin sections. Scale bars, 50 μ m. **c**, Peyer's patches are present in the small intestine of wild-type (WT) but not of *cpdm* or *cpdm; Tnf^{-/-}* mice as shown by 'Swiss

roll' preparations. Scale bars, 2.5 mm (left panels), 500 μ m (right panels). **d**, Spleen architecture of *cpdm* mice is not rescued by additional TNF ablation. Red, CD3; green, B220; blue, nuclei. Scale bars, (from left to right) 500 μ m, 200 μ m, 50 μ m and 50 μ m. **e**, SHARPIN-deficient primary keratinocytes are sensitive to TNF-induced cell death. Wild type $n = 6$, *cpdm; Tnf^{-/-}* $n = 2$, *cpdm; Tnf^{-/-}* $n = 4$, except TNF+NEC, TNF+QVD and TNF+NEC+QVD, where $n = 3$.

aspects of the immunological phenotype of *cpdm* mice were unaltered in *cpdm;Tnf^{+/-}* and *cpdm;Tnf^{-/-}* mice; Peyer's patches remained absent (Fig. 5c and Supplementary Fig. 22a), spleens remained without marginal zones (Fig. 5d) and enlarged, albeit, on average, to a somewhat lesser degree than the *cpdm* spleens (Supplementary Fig. 22b). In addition, the blood cell counts of various leukocyte populations also remained abnormal in TNF-deficient *cpdm* mice (Supplementary Fig. 22c). Hence, the inflammatory phenotype of *cpdm* mice is corrected by genetic ablation of TNF, identifying it as TNF-dependent, whereas the immunological phenotype of *cpdm* mice remains unaltered by TNF deficiency.

Given that skin inflammation is so pivotal in the inflammatory manifestation of the *cpdm* phenotype, we examined the skin phenotype of *cpdm;Tnf^{-/-}* mice in more detail. Histological examination of the skin revealed that, as previously reported¹³, *cpdm* mice have hyperkeratosis with some parakeratosis (Fig. 5b). In *cpdm;Tnf^{+/-}* (Supplementary Fig. 21), and particularly in *cpdm;Tnf^{-/-}* mice, this was almost completely absent (Fig. 5b). Likewise, the immune cell infiltrate, readily apparent in sections from livers of *cpdm* mice and present as nodular lymphocyte aggregates distributed around the central vein branches, was absent in *cpdm;Tnf^{+/-}* (not shown) and *cpdm;Tnf^{-/-}* mice (Fig. 5b). Combined with our observations that *cpdm* MEFs were more susceptible to TNF-induced cell death and that genetic ablation of TNF corrected the inflammatory phenotype in *cpdm* mice, including the inflammatory skin disease, we reasoned that one potential explanation for the inflammatory phenotype could be increased sensitivity of *cpdm* keratinocytes to TNF-induced cell death. This hypothesis was further supported by our finding that TNF-induced NF- κ B and JNK activation were reduced in *cpdm*-derived keratinocytes (Supplementary Fig. 18) and by a report describing increased rates of keratinocyte cell death observed in the skin of *cpdm* mice¹⁴. We found that primary keratinocytes derived from lesion-free *cpdm;Tnf^{-/-}* and *cpdm;Tnf^{+/-}* mice were sensitive to TNF-induced cell death, whereas keratinocytes derived from wild-type mice were not (Fig. 5e). As for *cpdm* MEFs, the cell death induced by TNF in SHARPIN-deficient keratinocytes was partially apoptotic and partially necroptotic. This result immediately suggests an explanation for the initiation and subsequent worsening of the skin phenotype, namely that *cpdm* keratinocytes are prone to die when exposed to TNF in the skin, some of them by necroptosis, some of them by apoptosis which may also lead to secondary necrosis. Because necroptosis and secondary necrosis are pro-inflammatory forms of cell death they initiate the vicious circle of inflammation and the inflammatory phenotype progressively worsens over time.

Discussion

We show that SHARPIN is recruited to native TNF- and CD40-RSCs, forms part of the tripartite LUBAC and is required for this complex's stability. SHARPIN also has a physiological role in lymphoid system development and suppression of inflammation. The genetic ablation of TNF completely resolved skin lesions in *cpdm* mice, demonstrating that the inability of *cpdm* cells to signal properly in response to TNF results in inflammation. It was recently shown that genetic ablation of the IL-1 receptor accessory protein (IL-1RAcP) reduced, but did not prevent, skin inflammation in these mice¹⁹. Our data show that, like TNF signalling, IL-1 β -induced NF- κ B and JNK activation is also impaired in *cpdm*-derived keratinocytes. One model that integrates both findings would be that dying *cpdm* keratinocytes stimulate increased production of IL-1 β or related cytokines that require the IL-1RAcP for signalling^{20,21}. These cytokines could contribute to inflammatory lesions in *cpdm* mice directly or by promoting the production of additional pro-inflammatory cytokines. This highly inflammatory milieu, caused by TNF-induced cell death, promotes inflammation despite the observed reduction in the absolute signalling capacity of IL-1 β in *cpdm*-derived primary keratinocytes. However, more work will be required to dissect and fully comprehend the disease process.

K48- and K63-linked ubiquitin chains and their physiological roles in protein degradation or intracellular signalling, respectively, are well established⁴. However, recent data claimed active roles also for other ubiquitin chain linkages, particularly for M1-linked chains on NEMO^{5,6,22–24}. We now demonstrate the presence of M1-linked ubiquitin chains on RIP1 and NEMO in the native TNF-RSC. *In vitro* LUBAC can add linear ubiquitin chains to NEMO, but only very inefficiently to RIP1. LUBAC may therefore preferentially linearly ubiquitinate pre-existing ubiquitin moieties on RIP1 or, alternatively, RIP1 only serves as a LUBAC substrate in a properly composed TNF-RSC. It is possible that other proteins, in addition to RIP1 and NEMO, could be targeted by LUBAC in this and other signalling complexes. The determination of the exact ubiquitination pattern and timing of these modifications on individual components of signalling complexes will be required to understand better how signalling from receptor-associated and intracellular signalling complexes is controlled^{25,26}. We believe that the application of the moTAP-2D-MRM technique is likely to contribute to this endeavour.

Our findings point towards a complex network of interactions between proteins modified by ubiquitin and proteins recruited to specific ubiquitin linkages. Presence of certain linkage types, such as linear ubiquitin chains, may promote recruitment of factors such as NEMO. However, absence of a linkage like linear ubiquitin does not imply that recruitment of these factors will not occur. For example, NEMO binds to M1-linked but can also bind to K63-linked chains, albeit with lower affinity⁷ or different topology²⁷. Additionally, NEMO has been shown recently to bind to K11-linked chains²⁸ which, incidentally, we identified on TNF-RSC-recruited RIP1. Adjusting levels of particular ubiquitin chains does, however, suggest a mechanism by which signal strength can be adjusted and, as demonstrated here for SHARPIN mutants, may lead to significant alterations in physiological outcome. Thus, the regulated expression of factors that generate a particular linkage type, for example, of LUBAC components, may enable a versatile fine-tuning of signalling output with respect to the differentiation stage and/or cell type, and dysregulation of such a factor may lead to a patho-physiological outcome. We therefore predict that germ-line mutations in human genes encoding LUBAC components will cause auto-inflammatory manifestations reminiscent of the *cpdm* phenotype. Patients with auto-inflammatory disease with unknown aetiology should therefore be screened for such mutations and, if found, our data further suggest that inhibition of TNF may alleviate many of their symptoms.

Along the same line of thought, our results also provide a possible alternative explanation for the aetiology of autoimmune diseases and the therapeutic effect of TNF inhibitors in treating them, even in cases when other, non-specific anti-inflammatory drugs fail²⁹. The current concept is that TNF inhibitors work in rheumatoid arthritis, Crohn's disease, psoriasis and other auto-immune diseases by interfering with the gene-inducing arm of TNF signalling, that is, the part of the pathway which is so far thought to be the source of pro-inflammatory signals induced by this cytokine³⁰. Based on our data an alternative explanation could be, however, that dysregulated expression or somatic mutation of a TNF signalling pathway component, for example, of one of the LUBAC components or a cIAP, would unbalance TNF signalling output in favour of pro-inflammatory cell death. This would then cause TNF to induce inflammation and, consequently, autoimmunity. If this were the case, TNF inhibition would exert its therapeutic effect by inhibiting TNF-induced pro-inflammatory cell death as the disease-initiating principle. It will be interesting to test this provocative hypothesis experimentally, both for our understanding of the basic mechanisms of immune signalling and in our quest for new therapeutic options in autoimmunity and possibly also in inflammation-associated cancer^{31–33}.

METHODS SUMMARY

Fluorescence-labelling of moTAP-purified TNF-RSC components, two-dimensional electrophoresis and MRM mass spectrometry. The moTAP-purified

TNF-RSC was eluted in two sequential steps, each performed with 2D lysis buffer. Eluted proteins were minimally fluorescently labelled by incubation with Cydyes 2, 3 or 5 (GE Healthcare). Labelling was stopped by addition of L-lysine. Labelled proteins were adjusted to 20 mM DTT and 1% IPG buffer, before cup loading onto either pH 3–11 NL or pH 4–7 rehydrated Immobiline Drystrips (GE Healthcare), and separated on an Ettan IPGphor II (GE Healthcare). After IEF, the Immobiline strip was washed with equilibration buffer (65 mM DTT) and then equilibration buffer (135 mM iodoacetamide) before second dimension electrophoresis (Bio-Rad Criterion). Fluorescence images of the resulting 2D gels (Typhoon Trio, GE Healthcare) were used to guide robotic spot picking (Ettan spot picker, GE Healthcare). Proteins contained in picked spots were digested with trypsin and analysed using MRM with a 4000 QTRAP mass spectrometer. In the first part of this MS analysis, the instrument was used as a triple quadrupole mass spectrometer to perform MRM analyses to screen for specific proteins and ubiquitin (including linkage-specific tryptic peptides that contain the Gly-Gly motif bound to the ϵ -amino group of lysine residues, or N-terminal Gly-Gly for the M1 linear peptide). The second phase of the analysis uses the third quadrupole as a linear ion trap for product ion detection to confirm peptide identification.

Full Methods and any associated references are available in the online version of the paper at www.nature.com/nature.

Received 8 April 2010; accepted 11 January 2011.

- Ware, C. F. The TNF superfamily. *Cytokine Growth Factor Rev.* **14**, 181–184 (2003).
- Bianchi, K. & Meier, P. A tangled web of ubiquitin chains: breaking news in TNF-R1 signaling. *Mol. Cell* **36**, 736–742 (2009).
- Silke, J. & Brink, R. Regulation of TNFRSF and innate immune signalling complexes by TRAFs and cIAPs. *Cell Death Differ.* **17**, 35–45 (2010).
- Wertz, I. E. & Dixit, V. M. Ubiquitin-mediated regulation of TNFR1 signaling. *Cytokine Growth Factor Rev.* **19**, 313–324 (2008).
- Haas, T. L. *et al.* Recruitment of the linear ubiquitin chain assembly complex stabilizes the TNF-R1 signaling complex and is required for TNF-mediated gene induction. *Mol. Cell* **36**, 831–844 (2009).
- Tokunaga, F. *et al.* Involvement of linear polyubiquitylation of NEMO in NF- κ B activation. *Nature Cell Biol.* **11**, 123–132 (2009).
- Rahighi, S. *et al.* Specific recognition of linear ubiquitin chains by NEMO is important for NF- κ B activation. *Cell* **136**, 1098–1109 (2009).
- Lo, Y. C. *et al.* Structural basis for recognition of diubiquitins by NEMO. *Mol. Cell* **33**, 602–615 (2009).
- Komander, D. *et al.* Molecular discrimination of structurally equivalent Lys 63-linked and linear polyubiquitin chains. *EMBO Rep.* **10**, 466–473 (2009).
- Xu, M., Skaug, B., Zeng, W. & Chen, Z. J. A ubiquitin replacement strategy in human cells reveals distinct mechanisms of IKK activation by TNF α and IL-1 β . *Mol. Cell* **36**, 302–314 (2009).
- Cossu, F. *et al.* Structural basis for bivalent Smac-mimetics recognition in the IAP protein family. *J. Mol. Biol.* **392**, 630–644 (2009).
- Seymour, R. E. *et al.* Spontaneous mutations in the mouse *Shardin* gene result in multiorgan inflammation, immune system dysregulation and dermatitis. *Genes Immun.* **8**, 416–421 (2007).
- HogenEsch, H. *et al.* A spontaneous mutation characterized by chronic proliferative dermatitis in C57BL mice. *Am. J. Pathol.* **143**, 972–982 (1993).
- HogenEsch, H., Janke, S., Boggess, D. & Sundberg, J. P. Absence of Peyer's patches and abnormal lymphoid architecture in chronic proliferative dermatitis (*cpdm/cpdm*) mice. *J. Immunol.* **162**, 3890–3896 (1999).
- HogenEsch, H. *et al.* Increased expression of type 2 cytokines in chronic proliferative dermatitis (*cpdm*) mutant mice and resolution of inflammation following treatment with IL-12. *Eur. J. Immunol.* **31**, 734–742 (2001).
- Tay, S. *et al.* Single-cell NF- κ B dynamics reveal digital activation and analogue information processing. *Nature* **466**, 267–271 (2010).
- Senftleben, U. *et al.* Activation by IKK α of a second, evolutionary conserved, NF- κ B signaling pathway. *Science* **293**, 1495–1499 (2001).
- Gijbels, M. J., HogenEsch, H., Bruijnzeel, P. L., Elliott, G. R. & Zurcher, C. Maintenance of donor phenotype after full-thickness skin transplantation from mice with chronic proliferative dermatitis (*cpdm/cpdm*) to C57BL/Ka and nude mice and vice versa. *J. Invest. Dermatol.* **105**, 769–773 (1995).
- Liang, Y., Seymour, R. E. & Sundberg, J. P. Inhibition of NF- κ B signaling retards eosinophilic dermatitis in SHARPin-deficient mice. *J. Invest. Dermatol.* **131**, 141–149 (2011).
- Martin, M. U. & Wesche, H. Summary and comparison of the signaling mechanisms of the Toll/interleukin-1 receptor family. *Biochim. Biophys. Acta* **1592**, 265–280 (2002).
- Arend, W. P., Palmer, G. & Gabay, C. IL-1, IL-18, and IL-33 families of cytokines. *Immunol. Rev.* **223**, 20–38 (2008).
- Huang, H. *et al.* K33-linked polyubiquitination of T cell receptor- ζ regulates proteolysis-independent T cell signaling. *Immunity* **33**, 60–70 (2010).
- Matsumoto, M. L. *et al.* K11-linked polyubiquitination in cell cycle control revealed by a K11 linkage-specific antibody. *Mol. Cell* **39**, 477–484 (2010).
- Arimoto, K. *et al.* Polyubiquitin conjugation to NEMO by tripartite motif protein 23 (TRIM23) is critical in antiviral defense. *Proc. Natl Acad. Sci. USA* **107**, 15856–15861 (2010).
- Ikeda, F., Crosetto, N. & Dikic, I. What determines the specificity and outcomes of ubiquitin signaling? *Cell* **143**, 677–681 (2010).
- Liu, S. & Chen, Z. J. Expanding role of ubiquitination in NF- κ B signaling. *Cell Res.* **21**, 6–21 (2011).
- Laplanche, E. *et al.* NEMO specifically recognizes K63-linked poly-ubiquitin chains through a new bipartite ubiquitin-binding domain. *EMBO J.* **28**, 2885–2895 (2009).
- Dynek, J. N. *et al.* c-IAP1 and UbcH5 promote K11-linked polyubiquitination of RIP1 in TNF signalling. *EMBO J.* **29**, 4198–4209 (2010).
- Taylor, P. C. & Feldmann, M. Anti-TNF biologic agents: still the therapy of choice for rheumatoid arthritis. *Nature Rev. Rheumatol.* **5**, 578–582 (2009).
- Sacre, S. M., Andreakos, E., Taylor, P., Feldmann, M. & Foxwell, B. M. Molecular therapeutic targets in rheumatoid arthritis. *Expert Rev. Mol. Med.* **7**, 1–20 (2005).
- Mantovani, A., Allavena, P., Sica, A. & Balkwill, F. Cancer-related inflammation. *Nature* **454**, 436–444 (2008).
- Pikarsky, E. *et al.* NF- κ B functions as a tumour promoter in inflammation-associated cancer. *Nature* **431**, 461–466 (2004).
- Griennikov, S. I., Greten, F. R. & Karin, M. Immunity, inflammation, and cancer. *Cell* **140**, 883–899 (2010).

Supplementary Information is linked to the online version of the paper at www.nature.com/nature.

Acknowledgements We thank M. Miasari for developing the cIAP2 antibody, M. Leverkus for advice on skin histology, J. Lokan for advice on liver histology, C. Rappl, N. Barboza, S. Kupka, D. Heinze, J. Zipprich, J. Corbin, S. Wiegmann and A. Bankovacki for excellent technical assistance, M. Bolognesi and P. Seneci for SM-164, H. Koerner for *Tnf^{-/-}* mice, and all past and present members of the Walczak and Silke laboratories for continuous stimulating scientific discussions and support. Research in the Walczak lab is supported by grants from Cancer Research UK, AICR, BBSRC (ERASysBio PLUS), Ovarian Cancer Action and the EU Marie Curie Research Training Network ApoptoTRAIN. Work in the Silke lab is supported by NHMRC grants 541901, 541902 and 602516. Work in the Purcell lab is supported by the NHMRC (Senior Research Fellowships for A.W.P. and a C. J. Martin Overseas Biomedical Fellowship to A.I.W.), and by grants from the NHMRC and ARC. U.W. is funded by HGF/SBCancer. E.R. and T.L.H. are ApoptoTRAIN fellows and U.N. is supported by the Schweizer Nationalfonds (SNF).

Author Contributions T.L.H. and H.W. conceived the moTAP procedure. B.G., E.R., H.W. and U.W., and T.L.H. determined the composition of the CD40- and TNF-RSC, respectively. B.G. performed all other experiments involving CD40L, A.C.S. and C.H.E. cloned and purified all recombinant proteins, determined the molecular interaction between the LUBAC components and performed the *in vitro* ubiquitination assays. B.G., S.M.C., A.C.S., C.H.E. and E.R. provided moTAP-purified TNF-RSCs for 2D-MRM analysis which was conceived by A.I.W. and H.W., performed by A.I.W., and analysed by A.I.W. and A.W.P.; J.S. and H.W. planned and J.A.R., H.A., U.N., W.W.-L.W., L.G., B.G., S.M.C. and E.R. performed the analyses of cells, tissues and blood samples obtained from all mouse strains used in this study. H.W. and J.S. wrote the manuscript assisted by B.G., S.M.C., A.C.S., C.H.E., E.R. and A.I.W.

Author Information Reprints and permissions information is available at www.nature.com/reprints. The authors declare competing financial interests: details accompany the full-text HTML version of the paper at www.nature.com/nature. Readers are welcome to comment on the online version of this article at www.nature.com/nature. Correspondence and requests for materials should be addressed to H.W. (h.walczak@imperial.ac.uk).

METHODS

Reagents. Antibodies used were: anti-CD40 (H-120), anti-I κ B α (C-15), anti-p65 (A), anti-TNFR1 (H-5), anti-TRADD (H-278), anti-TRAF2 (C-20), anti-TRAF3 (H122), anti-TRAF6 (D10) and anti-V5 (sv5-pk) from Santa Cruz Biotechnology; anti-Ub (FK1 and FK2) and anti-PARP (C-2-10) from Biomol; anti-Ub (#07-375) from Millipore; anti-Bid (#2002), anti-JNK (56G8), anti-NIK (4994), anti-p100 (4882), anti-pI κ B α (5A5) and anti-pJNK (98F2) from Cell Signaling; anti-myc (9E10) and anti-TNFR1 (ab19139) from Abcam; anti-cIAP Pan (MAB3400) from R&D Systems; anti-Caspase 8 (ALX-804-429) from Axxora life sciences; anti-RIP1 (#610459), anti-TRADD (clone37) and anti-mouse FITC-conjugated (554334) from BD Biosciences; anti-GST from Amersham, anti-HA (3F10) and anti-His (BMG-His-1) from Roche Applied Science; anti-A20 (59A426) from Imgenex and anti-Actin (A5441), anti-Flag (M2) from Sigma. Anti-cIAP1 monoclonal antibodies and anti-cIAP2 mAbs were generated as described³⁴. Anti-HOIL-1 and anti-HOIP antibodies were previously described⁵. SM-164 (Smac059) was synthesized and provided by P. Seneci and L. Manzoni¹¹. Murine B cells were isolated from the spleen with CD43 (Ly-48) MicroBeads according to the manufacturer's protocol (Miltenyi Biotec). Primary murine keratinocytes were stimulated with recombinant IL-1 β from Enzo Life Sciences.

Generation of SHARPIN antibody. A monoclonal antibody specific for SHARPIN was generated from 8-week-old Balb/c \times C57BL/6 mice which were immunised with KLH-coupled peptide (GPDAEAQLRRLQLSADC).

Cell lines. Wild-type and *cpdm* MEFs were generated from E15 embryos in accordance with standard procedures and were infected with SV40 large T antigen-expressing lentivirus. HEK293-NF- κ B cells were purchased from Panomics.

Mice. *Tnfr*^{-/-} mice³⁵ were a gift from H. Körner and *cpdm* mice were obtained from The Jackson Laboratory. Colonies were kept under conventional conditions. *Cpdm* mice were crossed with *Tnfr*^{-/-} mice and typed by PCR and sequencing.

Expression and purification of recombinant proteins. The extracellular portion of CD40L was cloned into the pCDNA3.1 expression vector (Invitrogen) in which a new N-terminal moTAP tag, consisting of a double Flag epitope, a PreScission cleavage site (LEVLFQ/GP) and a human Fc-portion, was integrated. Recombinant moTAP-CD40L was expressed in HEK293T cells and collected 24 and 48 h after transfection.

His-Flag-TNF (HF-TNF)³⁶ and moTAP-TNF⁵ were generated as described. Unless stated otherwise, the TNF used in this study was HF-TNF.

HOIP-V5/His and its mutants (HOIP Δ C terminus (residues 1–654), Δ UBA (deletion of residues 564–615), Δ N terminus (residues 494–end)) were previously described⁵. Untagged or V5/His-tagged versions of SHARPIN were generated by PCR and cloned into pCDNA3.1 (Invitrogen). The following mutants were used: SHARPIN Δ UBL (deletion of residues 219–289), SHARPIN Δ NZF (deletion of residues 348–377), SHARPIN NZFmut1 (point mutations of cysteines 353 and 356 to serine) and SHARPIN NZFmut2 (point mutations of cysteines 367 and 370 to serine). The specific point-mutants were obtained by site-directed mutagenesis. All mutations and deletions were verified by sequencing.

Recombinant SHARPIN, HOIL-1, HOIP, SHARPIN-UBL-only (residues 218–314), HOIP-ZnF-only (residues 298–329), HOIP-NZF1-only (residues 350–379), HOIP-NZF2-only (residues 408–438) and TRAF6 were expressed from a pGEX-6P2-vector (GE Healthcare Life Sciences) in *Escherichia coli* BL21(DE3) pLysS (Invitrogen) after addition of 1 μ M IPTG and 200 μ M ZnSO₄ at 18 °C overnight. The proteins were purified with GSTrap FF columns according to the manufacturer's protocol (GE Healthcare Life Sciences). The GST-tag was removed by incubation with PreScission protease (GE Healthcare Life Sciences) and quality was controlled by SDS-PAGE and Coomassie staining.

Western blotting. Western blot analyses were performed as previously described⁵. The quantification of western blots was done with ImageJ software. Briefly, the background was subtracted of the 8-bit greyscale image with a rolling ball radius of 50. The image was inverted and the rectangular selection tool used to frame the band tight on each side. Every lane was selected and analysed. The remaining background was cut off with the straight line selection tool and the area selected with the magic wand. Each p100 band was standardised to its respective actin control levels.

Precipitation of the TNF-RSC. Analytical and preparative precipitation of the TNF-RSC as shown in Fig. 1b was performed as described previously⁵.

Tandem affinity purification of the CD40-RSC. Raji cells (3.5×10^9) were stimulated with 50 ml moTAP-CD40L-containing supernatant (approximately 50 μ g ml⁻¹) at 37 °C for 10 min. Cells were washed twice with ice-cold PBS and lysed in 1.2 ml IP-lysis buffer/10⁸ cells with 0.5% NP-40 at 4 °C for 30 min. The detergent-insoluble fraction was pelleted (30 min; 15,000g) and the cell lysate was incubated with 4 μ l M2 beads per 10⁸ cells (Sigma) for 8 h. Beads were washed four times with 1 ml IP-lysis buffer and subsequently incubated in 1 ml lysis buffer containing 5 U ml⁻¹ PreScission (GE Healthcare Life Sciences) and 250 μ g ml⁻¹ Flag-peptide (Sigma) for 12 h. Protein complexes were eluted from the

beads, and the beads were rinsed once with 500 μ l IP-lysis buffer. The second precipitation step was carried out using 25 μ l Protein G-coupled beads (GE Healthcare Life Sciences) at 4 °C for 6 h. The beads were washed four times and proteins were directly eluted with 3 \times LDS buffer. The purified CD40-RSC was loaded on a NuPAGE gel. The gel was silver-stained using a mass-spectrometry compatible protocol (Invitrogen) and photo-documented before the lane containing the CD40-RSC was cut into 24 pieces of equal size. The gel pieces were then destained according to the manufacturer's protocol, subjected to tryptic digest as previously described⁵ and used for mass spectrometric analysis.

Liquid chromatography tandem mass spectroscopy (LC-MS/MS). The peptide mixtures from the purified receptor complexes in Supplementary Fig. 2 were separated on-line with a split free nano AQUITTY UPLC (Waters) using a Symmetry 5 μ m C₁₈ 20 \times 0.18 mm precolumn and a 1.7 μ m BEH130 C₁₈ 100 \times 0.1 mm column (Waters) at a flow rate of 400 nl min⁻¹ using a 60 min 5–90% acetonitrile/water gradient. Both gradient solvents were spiked with 0.1% formic acid. The electrospray voltage was set to 2.4 kV. Peptides were analysed using a linear trap/Orbitrap (LTQ-Orbitrap) hybrid mass spectrometer (Thermo Electron). Peptide precursor ion scans were acquired with the Orbitrap mass analyser, the resolving power was set at 60,000 ($m/\Delta m_{50\%}$ at m/z 400). Simultaneously, six MS/MS spectra of the most abundant peptide precursor ions were acquired in the LTQ. Dynamic exclusion was used with two repeat counts, 20 s repeat duration, and 30 s exclusion duration. Mass-spectrometric analysis of the TNF-RSC as shown in Fig. 1b was performed as described previously⁵.

Protein identification. Processed data were searched against the National Center for Biotechnology Information (NCBI) non-redundant database (2010-02-03; 1,039,027 sequences total) using the Mascot algorithm version v2.2.0 (Matrix Science). The algorithm was set to use *Homo sapiens* as taxonomy (229,496 protein sequences). The following search parameters were selected: fixed carbamidomethyl modification on cysteine side chain, variable modification due to methionine oxidation, deamidation to asparagine and glutamine, glycine dipeptide modification on lysine, one missed cleavage site in the case of incomplete trypsin hydrolysis. The mass tolerance was set to 5 p.p.m. for precursor ions and 0.6 Da for fragment ions. A fragment ions score cut-off of 20 was applied when performing the search. Protein hits were taken as identified if the individual scoring value of at least one peptide match exceeded the Mascot identity threshold (typically a score of ≥ 36 ; $P \leq 0.05$). Repeated matches of the same peptide in different forms (charge state or modifications) were combined into one single hit.

Generation of MRM transitions. The acquisition method consisted of an enhanced MS scan (EMS) with a scan rate of 1,000 Da s⁻¹ and four enhanced product ion (EPI) scans with 4,000 Da s⁻¹ scan rate. Each of EPI scans had a linear ion trap fill time of 80 ms with unit Q1 resolution, and either doubly or triply charged masses of each peptide were selected as the target masses. The mass range for EMS analysis was 400 to 1,000 Da and 60 to 1,000 Da for the EPI scans. To determine the best collision energy (CE) to use to achieve the optimum multiple reaction monitoring (MRM) transitions for each of the peptides, the collision energy (CE) for the scans were ramped from 16 to 40 eV with an increment of 4 eV. The three highest intensity fragment ions from the MS/MS spectrum obtained with the optimum CE for each peptide were selected as the Q3 mass for the MRM scanning method. All MRM transitions were combined into a single acquisition method for sample analysis. Refer to Supplementary Fig. 10 for a list of all peptide MRM transitions.

CyDye labelling and 2D gel electrophoresis. TNF-RSC was eluted from Protein G beads with 100 μ l of 2D lysis buffer, which contains 7 M urea, 2 M thiourea, 4% CHAPS and 40 mM Tris buffered to pH 8.5 at 4 °C. Cydyes 2, 3 or 5 (100 pmol each, GE Healthcare) were used to minimally label eluted proteins for 30 min on ice. L-lysine (1 μ l of 10 mM) was then added for a further 10 min. Labelled proteins were adjusted to 20 mM DTT and 1% IPG buffer, before being loaded by cup loading onto either pH 3–10 or pH 4–7 rehydrated 11 cm Immobiline Drystrip (GE Healthcare) and run using manufacturer's recommended settings. The Immobiline strip was then washed with equilibration buffer (GE Healthcare) containing 65 mM DTT and 135 mM Iodoacetamide for 15 min each. Equilibrated gel strips were then loaded and run on 8–16% gradient Criterion Tris-HCl gel (Bio-Rad). 2D gels were then imaged on a Typhoon Trio (GE Healthcare) using default settings for CyDyes. Protein-containing spots were identified and selected using ImageMaster 2D Platinum v7.0 software (GE Healthcare) and were robotically excised by an Ettan Spot Picker (GE Healthcare). Gel pieces were washed using 100 mM TEAB (triethylammonium bicarbonate, pH 8.5) in 50% (v/v) acetonitrile. Gel pieces were dehydrated using 100% (v/v) acetonitrile and air-dried. Dried gel pieces were rehydrated in the presence of 250 ng sequencing grade trypsin (Sigma) in 50 mM TEAB. Digests were allowed to proceed overnight at 37 °C.

MRM mass spectrometry. Chromatographic separation of peptides picked from 2D gels (Fig. 3) was performed before MS analysis using a Shimadzu Prominence UPLC coupled with a pre-packed 300 μ m internal diameter \times 10 mm ReproSil

C18-AQ 5 µm trap column (SGE) and a 15 µm tip internal diameter, 75 µm capillary internal diameter, 360 µm OD fused-silica PicoFrit nano analytical column (New objective) packed with 15 cm of ReproSil-Pur C18-AQ 5 µm resin (Dr. Maisch). Gel digests were loaded onto the trap column using the auto-sampler with a flow rate of 100 µl min⁻¹ 0.1% formic acid and separated using a step gradient with mobile phase A consisting of 0.1% formic acid and mobile phase B consisting of 95% acetonitrile and 0.1% formic acid. Peptides eluting off the reverse-phased column were analysed using a 4000 Q TRAP hybrid triple quadrupole-linear ion trap-mass spectrometer (AB SCIEX) in positive ion mode. The acquisition method was set to perform a MRM scanning experiment and an information-dependent acquisition (IDA) of a full mass MS/MS spectrum in EPI mode triggered by MRM transitions that exceeded 200 counts. An AB SCIEX nanospray II ion source was used for ionisation with the ion spray voltage (IS) set at 2,200 V, curtain gas (CUR) at 22, ion source gas (GS1) at 25, high collision gas (CAD), and an interface heater temperature setting of 90. For the SRM transitions, the dwell time for each transition was fixed at 40 ms with the resolution of the first (Q1) and third (Q3) quadrupole operating at unit resolution. A scan rate of 1000 Da s⁻¹ was used for the EPI scan with a scanning *m/z* range of 70 to 1,500 Da, a fixed LIT fill time of 80 ms, and the Q1 resolution set to unit.

Gel filtration. HeLa cells were lysed in lysis buffer containing 50 mM Tris-HCl, pH 7.5, 1 mM MgCl₂, 1 mM DTT and a protease inhibitor cocktail (Complete EDTA-free, Roche) by repeated passing through a syringe needle. After adding an equal volume of lysis buffer containing 300 mM NaCl, lysates were centrifuged at 100,000g for 60 min to obtain S100 lysates. S100 lysates were separated via a Superdex 200 10/300 GL column (GE Healthcare Life Sciences) in 50 mM Tris-HCl pH 7.5, 150 mM NaCl using an ÄKTA chromatography system (GE Healthcare Life Sciences).

NF-κB luciferase assay. HEK293-NF-κB cells were transfected with plasmids encoding the indicated proteins using Eugene6 (Roche Applied Science). Cells were lysed in passive lysis buffer (Promega Corporation) 16 h post transfection and luminescence was measured using a microplate reader (Mithras LB940; Berthold Technologies). Viability was controlled by MTT (3-[4,5-dimethyl thiazol-2-yl]-2,5-diphenyltetrazolium] bromide) measurement.

In vitro transcription/translation. For *in vitro* binding assays, SHARPIN, HOIP and their respective mutants were generated *in vitro* using the TNT Quick Coupled Transcription/Translation System (Promega Corporation) according to the manufacturer's instructions. Equal protein production was controlled by western blotting.

In vitro ubiquitination assay. For *in vitro* ubiquitination assays, 0.8 µg recombinant HOIP, HOIL-1 and GST-SHARPIN were incubated with 5 µg ubiquitin, 200 ng E1 (UBE1), 300 ng E2 (UbcH5c), 1 × ERS (Boston Biochem) in ubiquitination buffer (20 mM Tris-HCl pH 7.5, 2 mM DTT, 5 mM MgCl₂). After 2 h incubation at 37 °C the reaction was stopped by adding reducing sample buffer (RSB). The samples were analysed by western blotting.

For *in vitro* ubiquitination of potential targets 293T cells were transfected with plasmids encoding a tagged version of the respective protein using calcium phosphate and proteins were immunoprecipitated using beads coupled to antibodies specific for either the tag or the protein itself. The beads were washed, dried and added to the reaction mix. The assay was performed as described above.

Interaction mapping. *In vitro*: 10 µg of recombinant protein were immobilised on Protein G beads using specific antibodies, bound to glutathione beads using their GST-tag or precipitated via their V5-tag using anti-V5-agarose resin (Sigma). The beads were washed three times before *in-vitro*-translated versions of the possible interaction partner, 2 µg of tetra-ubiquitin chains or of the recombinant interaction partner were added, respectively. Co-immunoprecipitation occurred overnight at 4 °C.

In vivo: 7.5 × 10⁶ HEK293T cells were transfected with 5 µg of the respective expression plasmids by standard calcium phosphate transfection. Cells were harvested 24 h post transfection, lysed and immunoprecipitations were performed at 4 °C for 16 h using anti-V5-agarose resin (Sigma). Interactions with ubiquitin were mapped using agarose beads coupled to ubiquitin (Boston Biochem).

Quantitative real-time PCR. RNA purification, cDNA synthesis and quantitative real-time PCR were performed as described previously⁵. The following gene-specific primers were used: 5'-CCCACGCTACCTCTGCTC-3' and 5'-GATGGA TACCTGAGCATCACC-3' (*ICAM-1*), 5'-ACGAGCAAATGGTGAAGGAG-3' and 5'-ATGATTGCCAAGTGCAGGA-3' (*IκBα*), 5'-TGCCTATGTCTCAGCC TCTTC-3' and 5'-GAGGCCATTGGGAACCTTCT-3' (*TNF*), 5'-GCTCAACTG

TGTGTCGTGAAG-3' and 5'-ATGAGGCAGTTTCCATCACC-3' (*A20*), 5'-CTG TGCATTACACCGACAAC-3' and 5'-CACTACCAGTTCCCACTCCAG-3' (*CyclinD2*), 5'-CCCAGTGTCAACGACCTTC-3' and 5'-CCTCACAACCTCCG TCCTCTG-3' (*HOIP*), 5'-TCTCCCCAACACAGGACATC-3' and 5'-AAATGG TGACGGTGTGCAT-3' (*HOIL-1*).

Staining cells for confocal microscopy. Cells were seeded onto cover slips and starved for 6 h before TNF-treatment. After stimulation (50 ng ml⁻¹ TNF), cells were washed twice with ice-cold PBS and fixed with 4% paraformaldehyde/PBS for 20 min. Cell membranes were permeabilized with 0.2% Triton in PBS for 5 min. Unspecific binding was blocked with 1% BSA/PBS for 1 h and cells were stained with anti-p65 in a wet chamber at 4 °C overnight. Next, cells were washed three times and incubated with Alexa488-coupled anti-rabbit antibodies (Invitrogen) for 1 h at room temperature. Cells were washed again and nuclei were stained with ProLong Gold antifade reagent containing DAPI (Invitrogen). The p65-positive nuclear area was quantified with the Leica Application Suite software.

Cell death/viability assessment. MEF cells (1 × 10⁵ or 1 × 10⁴) were seeded per 12-well or 96-well, respectively, pre-treated with medium, 10 µM Q-Val-Asp(non-O-methylated)-OPH (QVD; R&D Systems) and/or 30 µM necrostatin-1 (NEC; Biomol) before addition of TNF. The percentage of cell death was assessed by propidium iodide (PI) uptake 24 h later. Alternatively, cell viability was measured by Cell Titer Glo (Promega) according to the manufacturer's instructions.

Cytosol/nuclear fractionation. Splenocytes from wild-type and *cpdm* mice (3.5 × 10⁶) were stimulated for different time points with TAP-CD40L-containing supernatant and washed with ice-cold PBS. Cytosolic and nuclear fractions were prepared with NE-Per Nuclear Cytosol Extraction kit (Thermo Fisher Scientific) where the manufacturer protocol was strictly followed.

Histology. For haematoxylin and eosin stain tissues were fixed in 4% paraformaldehyde in PBS. Tissues were embedded in paraffin and sections were stained with haematoxylin and eosin.

For fluorescence stains spleens were frozen in Tissue Tek OCT compound (Sakura). Sections (6 µm) were cut using a CM8500 cryostat (Leica), fixed in acetone and blocked overnight with 3% normal horse serum (SAFC Biosciences). Slides were stained with the following antibodies: anti-CD3e-biotin (eBio500A2, eBiosciences) and anti-B220-FITC (BD Pharmingen). Biotinylated antibodies were detected with streptavidin-Alexa Fluor 555 (Invitrogen). Hoechst (Invitrogen) staining was used to visualize nuclei. Slides were analysed with an Olympus BX-50 fluorescence microscope using ×10 and ×20 objective lenses and the SPOT Advance software. For immunofluorescence stainings of the skin, sections were stained with polyclonal rabbit anti-keratin 14 (Covance) and Alexa-fluor 594 goat-anti-rabbit (Invitrogen). Nuclei were visualized using Hoechst (Invitrogen). Images were acquired using SPOT Advance and processed using ImageJ software.

Keratinocyte culture and cell death assays. Murine tail skin was incubated in keratinocyte serum free media (Invitrogen) supplemented with 50 µg ml⁻¹ gentamicin and 2.1 U ml⁻¹ dispase II (Roche) at 4 °C overnight. The epidermis was then removed and incubated in TrypLE Express trypsin (Invitrogen) for 10 min with agitation to isolate keratinocytes. Cells were seeded in 24-well plates in keratinocyte media and cultured to at least 70% confluency. Cells were then left untreated or pre-treated with 50 µM Necrostatin-1 (Tetralogics) and/or 10 µM QVD (SM Biochemicals LLC) for 1 h before addition of 100 ng ml⁻¹ human Fc-TNFα for a further 24 h. Death was quantified by FACS analysis of PI uptake.

Swiss roll. For Swiss rolls, the intestinal tract from stomach to caecum was harvested and fixed overnight in 4% buffered paraformaldehyde. Intestines were then cut open longitudinally, cleaned from faeces and rolled. The rolls were embedded in paraffin and processed as other tissue slides³⁷.

34. Silke, J. *et al.* Determination of cell survival by RING-mediated regulation of inhibitor of apoptosis (IAP) protein abundance. *Proc. Natl Acad. Sci. USA* **102**, 16182–16187 (2005).
35. Körner, H. *et al.* Distinct roles for lymphotoxin-α and tumor necrosis factor in organogenesis and spatial organization of lymphoid tissue. *Eur. J. Immunol.* **27**, 2600–2609 (1997).
36. Diessenbacher, P. *et al.* NF-κB inhibition reveals differential mechanisms of TNF versus TRAIL-induced apoptosis upstream or at the level of caspase-8 activation independent of cIAP2. *J. Invest. Dermatol.* **128**, 1134–1147 (2008).
37. Moolenaar, C. & Ruitenberg, E. J. The 'Swiss roll': a simple technique for histological studies of the rodent intestine. *Lab. Anim.* **15**, 57–59 (1981).

Habenular $\alpha 5$ nicotinic receptor subunit signalling controls nicotine intake

Christie D. Fowler¹, Qun Lu¹, Paul M. Johnson¹, Michael J. Marks² & Paul J. Kenny¹

Genetic variation in *CHRNA5*, the gene encoding the $\alpha 5$ nicotinic acetylcholine receptor subunit, increases vulnerability to tobacco addiction and lung cancer, but the underlying mechanisms are unknown. Here we report markedly increased nicotine intake in mice with a null mutation in *Chrna5*. This effect was ‘rescued’ in knockout mice by re-expressing $\alpha 5$ subunits in the medial habenula (MHb), and recapitulated in rats through $\alpha 5$ subunit knockdown in MHb. Remarkably, $\alpha 5$ subunit knockdown in MHb did not alter the rewarding effects of nicotine but abolished the inhibitory effects of higher nicotine doses on brain reward systems. The MHb extends projections almost exclusively to the interpeduncular nucleus (IPN). We found diminished IPN activation in response to nicotine in $\alpha 5$ knockout mice. Further, disruption of IPN signalling increased nicotine intake in rats. Our findings indicate that nicotine activates the habenulo–interpeduncular pathway through $\alpha 5$ -containing nAChRs, triggering an inhibitory motivational signal that acts to limit nicotine intake.

Tobacco smoking results in more than 5 million deaths each year and accounts for almost 90% of all deaths from lung cancer¹. Nicotine is the principal reinforcing component in tobacco smoke responsible for addiction². Nicotine acts in the brain through neuronal nicotinic acetylcholine receptors (nAChRs), which are ligand-gated ion channels consisting of five membrane-spanning subunits³. Twelve neuronal nAChR subunits have been identified: nine α subunits ($\alpha 2$ – $\alpha 10$) and three β subunits ($\beta 2$ – $\beta 4$)³. The predominant nAChR subtypes in mammalian brain that have been heavily implicated in regulating the addictive properties of nicotine are those containing $\alpha 4$ and $\beta 2$ subunits^{4–8}. A major advance in our understanding of smoking behaviour is the finding that allelic variation in the $\alpha 5/\alpha 3/\beta 4$ nAChR subunit gene cluster located in chromosome region 15q25 significantly increases risk of tobacco addiction^{9–11}. In particular, polymorphisms in the $\alpha 5$ subunit gene (*CHRNA5*), which result in decreased function of the subunit, increase vulnerability to tobacco addiction^{12,13}. Nevertheless, mechanisms through which nAChRs that contain the $\alpha 5$ subunit (denoted as $\alpha 5^*$ nAChRs) may influence smoking behaviour are unclear. Genetic variability in *CHRNA5* is also a major risk factor for lung cancer and chronic obstructive pulmonary disease (COPD) in smokers^{14–16}, which may reflect higher levels of tobacco dependence in individuals carrying risk alleles and consequently greater exposure to carcinogens contained in tobacco smoke¹⁷, although the precise role of $\alpha 5^*$ nAChRs in lung cancer and COPD is unknown.

$\alpha 5^*$ nAChRs control nicotine intake

Here we investigated the role of $\alpha 5^*$ nAChRs in the reinforcing properties of nicotine. We found that wild-type mice and mice with a null mutation in $\alpha 5$ subunits, which therefore did not express $\alpha 5^*$ nAChRs, responded for intravenously self-administered nicotine infusions according to an inverted U-shaped dose–response curve, consistent with previous reports in humans¹⁸, non-human primates¹⁹, dogs²⁰ and rats²¹. However, the knockout mice responded far more vigorously than wild-type mice for nicotine infusions, especially when higher unit doses were available (Fig. 1a). Increased responding for nicotine in knockout mice was not secondary to alterations in operant performance or the motivational salience of reward-paired conditioned stimuli

(Supplementary Fig. 1). When we calculated the total amount of nicotine consumed at each dose available for self-administration, we found that wild-type mice titrated their responding to consume $\sim 1.5 \text{ mg kg}^{-1}$ per session (Fig. 1b); which achieves plasma concentrations of nicotine comparable to those detected in humans after 5 h of smoking their preferred brand of cigarette^{23,24}. In contrast, knockout mice did not titrate their responding and consumed greater amounts of nicotine as the dose increased (Fig. 1b). Knockout mice also had greater motivation to seek and obtain nicotine when tested under a progressive ratio schedule of reinforcement, an effect most apparent again at high doses (Supplementary Fig. 2). Enhanced responding for nicotine as the unit dose increases is thought to reflect an intensification of the reinforcing properties of the drug, thereby motivating higher levels of intake²⁵. Diminished responding as the dose increases reflects greater restraint over intake to avoid the increasingly aversive effects of higher drug doses^{18,25} or more rapid development of drug satiation^{25,26}. Our findings indicate, therefore, that deletion of $\alpha 5^*$ nAChRs has a dissociable effect on the motivational drives that control nicotine intake. The stimulatory effects of nicotine on brain reinforcement systems

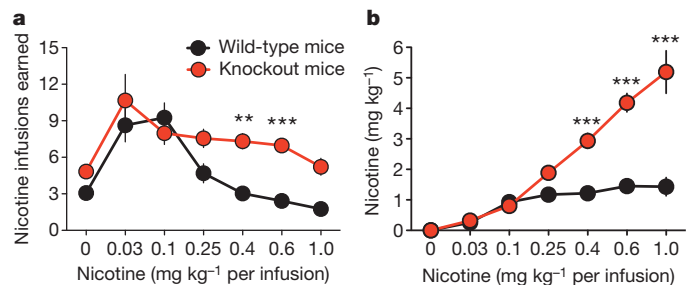


Figure 1 | Increased nicotine intake in $\alpha 5^*$ knockout mice. **a**, Data are presented as mean (\pm s.e.m.) number of nicotine infusions earned across a range of nicotine doses. Two-way ANOVA: genotype, $F_{(1,91)} = 28.57$, $P < 0.0001$; dose, $F_{(6,91)} = 13.69$, $P < 0.0001$; interaction, $F_{(6,75)} = 2.55$, $P < 0.05$; $n = 10$ – 11 per group. **b**, Data from **a** are presented as mean (\pm s.e.m.) total nicotine intake at each dose. Genotype, $F_{(1,91)} = 67.98$, $P < 0.0001$; dose, $F_{(6,91)} = 39.06$, $P < 0.0001$; interaction, $F_{(6,791)} = 14.25$, $P < 0.0001$. ** $P < 0.01$, *** $P < 0.001$ compared with wild-type mice at the same nicotine dose.

¹Laboratory for Behavioral and Molecular Neuroscience, Department of Molecular Therapeutics, The Scripps Research Institute—Scripps Florida, Jupiter, Florida 33458, USA. ²Institute of Behavioral Genetics, University of Colorado, Boulder, Colorado 80309, USA.

(ascending portion of dose–response curve) are unaltered by $\alpha 5$ subunit knockout, as the wild-type and knockout mice responded for nicotine at a similar maximal rate. Instead, deficient $\alpha 5^*$ nAChR signalling seems to attenuate the negative effects of nicotine that limit its intake (descending portion of dose–response curve); see also ref. 22. These findings are highly consistent with the increased vulnerability to tobacco addiction in human smokers carrying *CHRNA5* risk alleles that result in less functional $\alpha 5^*$ nAChRs^{12,13}.

Habenular $\alpha 5^*$ nAChRs control nicotine intake

The $\alpha 5$ nAChR subunit has a restricted distribution profile in the brain, with dense expression in the habenulo-interpeduncular pathway, deep layers of the cortex and hippocampus, and lower expression in the ventral tegmental area (VTA) and substantia nigra²⁷. The MHb projects almost exclusively to the IPN via the fasciculus retroflexus²⁸. Functional $\alpha 5^*$ nAChRs are expressed on MHb afferents to the IPN²⁹, and high but not low nicotine doses activate the habenulo-interpeduncular tract, as measured by increased local glucose utilization in rats³⁰. The habenulo-interpeduncular tract regulates avoidance of noxious substances³¹ and regulates somatic aspects of nicotine withdrawal³². However, little is known of its role in drug-taking behaviour³³. Intriguingly, the lateral habenula (LHb) has an inhibitory influence on VTA dopamine neurons³⁴, is activated by aversive stimuli or omission of anticipated reward, and is considered to be a source of negative motivational signals in the brain³⁴. We proposed therefore that nicotine-induced stimulation of $\alpha 5^*$ nAChRs in the habenulo-interpeduncular pathway triggers an inhibitory motivational signal that limits consumption of the drug. In knockout and wild-type mice that received injections of a control lentivirus expressing green-fluorescent protein (GFP; Lenti-Control) into the MHb, we

again found that knockout mice self-administered far greater amounts of nicotine when a high unit dose was available (Fig. 2a), replicating the earlier findings. However, nicotine intake was indistinguishable in knockout versus wild-type mice after injection of a lentivirus vector (Lenti-CHRNA5) into the MHb to rescue $\alpha 5^*$ nAChR in the habenulo-interpeduncular tract (Fig. 2b and Supplementary Fig. 3). GFP immunostaining to confirm MHb delivery of virus was carried out for the majority of the mice. Responding for nicotine (0, 0.1 and 0.4 mg kg⁻¹ per infusion) in the subset of Lenti-CHRNA5-treated mice used for immunostaining was 3.6 \pm 0.83, 8.8 \pm 1.4 and 4.86 \pm 1.0, respectively, for wild types and 4.53 \pm 0.85, 7.72 \pm 0.68 and 4.53 \pm 1.4, respectively, for knockouts. GFP immunostaining confirmed that virus-infected cells were detected almost exclusively in the habenulo-interpeduncular tract of Lenti-CHRNA5 knockout mice, with little detectable staining in other brain areas that could potentially affect self-administration behaviour (Fig. 2c, d, e and Supplementary Fig. 4). The remaining mice not used for immunostaining were used to verify that the Lenti-CHRNA5 virus was effective at ‘rescuing’ $\alpha 5$ subunit expression in the knockout mice. Real-time polymerase chain reaction (PCR) verified that $\alpha 5$ subunit mRNA was detectable only in the MHb (Supplementary Fig. 5) and IPN (Supplementary Fig. 6) of the Lenti-CHRNA5-treated knockout mice, indicating that $\alpha 5$ subunit mRNA is transported from the MHb along the fasciculus retroflexus and into the IPN. Wild-type mice treated with the Lenti-CHRNA5 vector did not demonstrate increased $\alpha 5$ subunit mRNA above baseline levels in the MHb (Supplementary Fig. 5), indicating that strict regulatory mechanisms control $\alpha 5$ subunit expression levels in the habenulo-interpeduncular pathway.

Using radiolabelled rubidium (⁸⁶Rb⁺) efflux as a functional measure of nAChR signalling, we found that acetylcholine-evoked ⁸⁶Rb⁺ efflux was markedly attenuated in synaptosomes prepared from the MHb

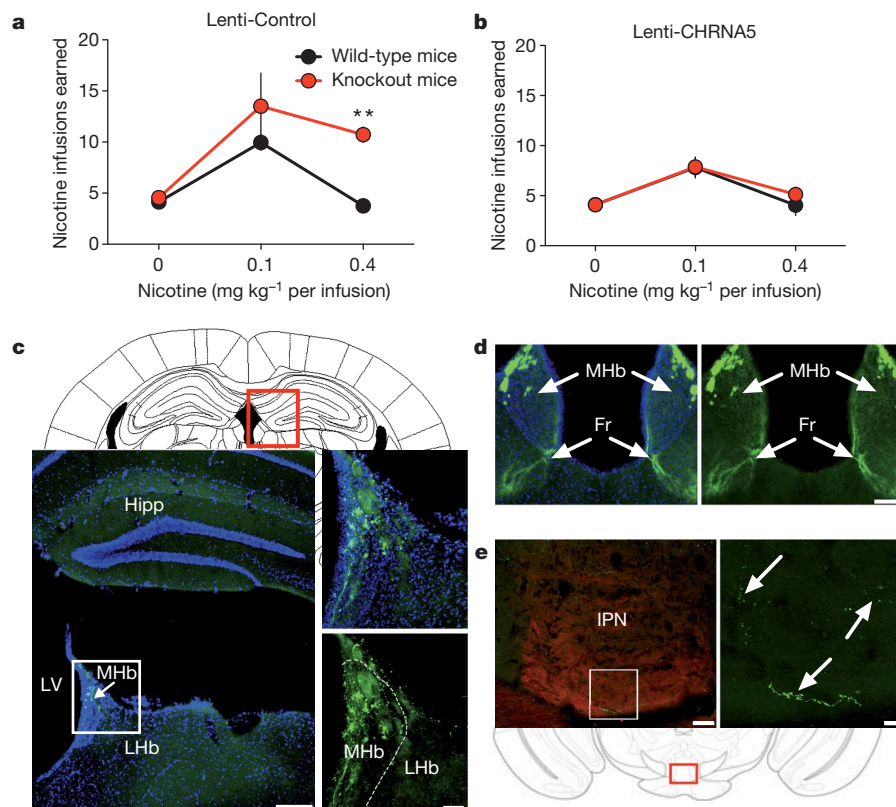


Figure 2 | ‘Rescue’ of $\alpha 5^*$ nAChRs in the habenulo-interpeduncular tract normalizes nicotine intake. **a**, Mean (\pm s.e.m.) nicotine infusions in Lenti-Control mice. Genotype, $F_{(1,22)} = 7.70$, $P < 0.05$; dose, $F_{(2,22)} = 19.34$, $P < 0.0001$; interaction, $F_{(2,22)} = 3.75$, $P < 0.05$. ****** $P < 0.01$ between genotypes. **b**, Mean (\pm s.e.m.) nicotine infusions in Lenti-CHRNA5 mice. Genotype, $F_{(1,28)} = 0.17$, not significant (NS); dose, $F_{(2,28)} = 16.05$, $P < 0.0001$; interaction, $F_{(2,28)} = 0.36$, NS; $n = 6$ –9 per group. **c**, GFP immunostaining

confirmed MHb virus delivery. Hipp, hippocampus; LHb, lateral habenula; LV, lateral ventricle; MHb, medial habenula. Scale bars, 500 μ m (left), 200 μ m (right). **d**, GFP-labelled cells in MHb, 4’,6-diamidino-2-phenylindole (DAPI)-counterstained in left panel, extend into the fasciculus retroflexus (Fr). Scale bar, 200 μ m. **e**, GFP-positive axons detected in IPN. Left panel is labelled with vesicular acetylcholine transporter (VACHT) (red) to identify the IPN. Scale bars, 50 μ m (left), 10 μ m (right).

and IPN, but not the cortex or hippocampus, of a separate cohort of knockout versus wild-type mice (Supplementary Fig. 7). Consistent with a recent report,⁸⁶Rb⁺ efflux was also attenuated in synaptosomes from the thalamus of knockout mice³⁵ (Supplementary Fig. 7). Injections of Lenti-CHRNA5 into the MHb attenuated the deficits in ⁸⁶Rb⁺ efflux in the IPN, but not in the MHb or thalamus, of knockout mice (Supplementary Fig. 8). These findings demonstrate that $\alpha 5^*$ nAChRs have a critical role in regulating nAChR transmission in the habenulo-interpeduncular tract, and confirm that the Lenti-CHRNA5 vector rescues not only expression, but also function, of $\alpha 5^*$ nAChRs in the habenulo-interpeduncular pathway. These data also reveal three additional insights. First, $\alpha 5$ subunits produced in MHb are predominantly incorporated into $\alpha 5^*$ nAChRs expressed presynaptically on afferents to the IPN. Second, injection of the Lenti-CHRNA5 vector into MHb rescued local $\alpha 5$ subunit mRNA expression, but not deficits in MHb ⁸⁶Rb⁺ efflux. This indicates that nAChR signalling in the MHb may be derived from $\alpha 5^*$ nAChRs located presynaptically on afferent inputs from brain sites not infected by the virus. Third, although the Lenti-CHRNA5 vector attenuated the deficits in nAChR signalling detected in the IPN of knockout mice, this rescue was only partial (Supplementary Fig. 8). Hence, postsynaptically localized $\alpha 5^*$ nAChRs on IPN neurons, or perhaps presynaptic $\alpha 5^*$ nAChRs on afferent inputs that originate from brain sites other than the MHb, also have a major role in nAChR transmission in the IPN.

Next, we developed and validated a lentivirus vector to deliver a short hairpin RNA against the $\alpha 5$ nAChR subunit (Lenti- $\alpha 5$ -shRNA; Supplementary Fig. 9). Then we microinjected the Lenti- $\alpha 5$ -shRNA vector into the MHb of rats to knockdown habenulo-interpeduncular $\alpha 5^*$ nAChRs (Supplementary Fig. 10). As expected, Lenti-Control rats responded for nicotine according to an inverted U-shaped dose-response curve (Fig. 3a). There was a marked increase in nicotine consumption across the dose-response curve in the Lenti- $\alpha 5$ -shRNA rats that was most apparent at high unit doses (Fig. 3a). When total nicotine intake at each dose was calculated, we found that Lenti-Control rats titrated their responding to consume ~ 0.75 – 1 mg kg⁻¹ nicotine per session (Supplementary Fig. 10). In contrast, the knockdown rats showed little evidence of titration and continued to increase their consumption as the unit dose increased. We obtained similar effects on nicotine intake using a second lentivirus vector that expressed an shRNA targeting a different portion of $\alpha 5$ subunit mRNA (Supplementary Fig. 11). Overall, these findings in rats recapitulate those in the $\alpha 5$ knockout mice and confirm that $\alpha 5^*$ nAChRs in the habenulo-interpeduncular pathway regulate levels of nicotine intake across species.

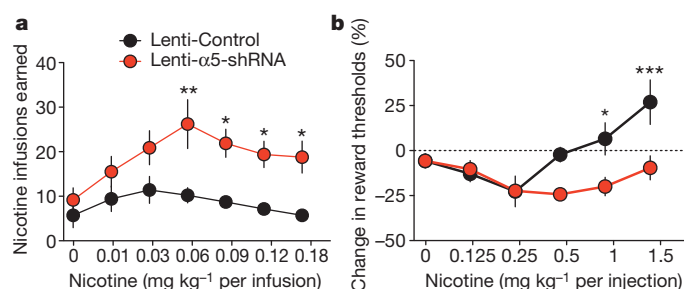


Figure 3 | $\alpha 5^*$ nAChRs in the habenulo-interpeduncular tract control nicotine intake and its reward-inhibiting effects in rats. **a**, Nicotine self-administration in rats injected with Lenti-Control or Lenti- $\alpha 5$ -shRNA in the MHb. Data are presented as mean (\pm s.e.m.) number of nicotine infusions earned. Lentivirus, $F_{(1,60)} = 21.07$, $P < 0.01$; dose, $F_{(6,60)} = 3.84$, $P < 0.01$; interaction, $F_{(6,60)} = 1.57$, NS; $n = 5$ – 7 per group. **b**, Intracranial self-stimulation thresholds in rats. Data are presented as mean (\pm s.e.m.) percentage change from baseline reward threshold. Lentivirus, $F_{(1,60)} = 13.23$, $P < 0.001$; dose, $F_{(5,60)} = 6.38$, $P < 0.0001$; interaction, $F_{(5,60)} = 4.19$, $P < 0.01$. * $P < 0.05$, ** $P < 0.01$ and *** $P < 0.001$ indicate statistically significant differences between groups; $n = 6$ – 8 per group.

$\alpha 5^*$ nAChRs inhibit brain reward function

Next we examined the effects of nicotine on brain-stimulation reward (BSR) thresholds in rats after knockdown of $\alpha 5^*$ nAChRs in the habenulo-interpeduncular pathway. In the BSR procedure, rats respond vigorously to obtain rewarding electrical self-stimulation via an intracranial stimulating electrode, with the minimal stimulation intensity that maintains self-stimulation behaviour termed the reward threshold. Low doses of nicotine (~ 0.25 mg kg⁻¹) that condition a place preference in rats also lower BSR thresholds³⁶, reflecting drug-induced enhancement of brain reward activity. Conversely, higher doses of nicotine (≥ 1 mg kg⁻¹) that condition a place aversion can raise the BSR thresholds in rats³⁷. Importantly, rats regulate their pattern of nicotine self-administration behaviour at a level that achieves maximal lowering of BSR thresholds³⁶, indicating that obtaining the stimulatory effects of nicotine on brain reward circuits, while avoiding its negative effects, determines the amounts of nicotine consumed by rats. We found that low doses of nicotine (0.125 – 0.25 mg kg⁻¹; free base; injected subcutaneously) lowered BSR thresholds by a similar magnitude in the Lenti-Control and Lenti- $\alpha 5$ -shRNA rats (Fig. 3b). However, as the dose of nicotine was increased (1 – 1.5 mg kg⁻¹; free base; injected subcutaneously), BSR thresholds were raised above baseline in Lenti-Control rats, but continued to be lowered below baseline levels in Lenti- $\alpha 5$ -shRNA rats (Fig. 3b). These data demonstrate that the stimulatory effects of nicotine on brain reward systems, which probably provide a crucial source of reinforcement that maintains the tobacco smoking habit³⁸, are unaltered by deficits in $\alpha 5^*$ nAChRs in the habenulo-interpeduncular pathway. Instead, the inhibitory effects of higher nicotine doses on the activity of reward circuitries, which probably determine the amounts of nicotine that can be consumed, are greatly attenuated by knockdown of $\alpha 5^*$ nAChRs in this pathway.

Habenular $\alpha 5^*$ nAChRs regulate IPN activation

The earlier ⁸⁶Rb⁺ efflux data indicate that $\alpha 5$ subunits transcribed in the MHb are incorporated into presynaptic $\alpha 5^*$ nAChRs in the IPN where they may regulate neurotransmitter release. Acetylcholine and glutamate are the major neurotransmitters produced by MHb neurons innervating the IPN³⁹, and presynaptic $\alpha 5^*$ nAChRs are thought to regulate glutamate but not acetylcholine release in the IPN^{29,40,41}. Interestingly, glutamatergic transmission at the habenulo-interpeduncular synapse is increased in response to the nicotine concentrations probably achieved in the brains of smokers⁴². Therefore, we proposed that deficient $\alpha 5^*$ nAChR signalling in the habenulo-interpeduncular tract may decrease nicotine-evoked glutamatergic transmission in the IPN and thereby attenuate a negative motivational signal that limits its intake. Consistent with this hypothesis, an aversive higher dose of nicotine (1.5 mg kg⁻¹)⁴³, but not a rewarding lower dose (0.5 mg kg⁻¹)⁴³, robustly activated the IPN in wild-type mice, reflected in increased Fos immunoreactivity (Fig. 4a, b). This effect of the high nicotine dose was almost completely abolished in knockout mice. Wild-type and $\alpha 5$ knockout mice showed similar Fos immunoreactivity in the ventromedial hypothalamus (Supplementary Fig. 12), a region in which Fos induction is highly stress responsive⁴⁴, indicating that altered stress responses in knockout mice did not account for this effect. Nicotine-induced increases in Fos immunoreactivity in the VTA, which controls the reinforcing effects of nicotine, were similar in wild-type and $\alpha 5$ knockout mice (Supplementary Fig. 13). Nevertheless, there was a non-statistically significant trend towards lower VTA Fos immunoreactivity in the knockout mice in response to the high nicotine dose. Considering that the VTA can also regulate aversive responses to nicotine⁴⁵, it is possible that $\alpha 5^*$ nAChRs in the VTA may differentially regulate activation of this structure in response to aversive but not rewarding doses of nicotine. Taken together, these findings are consistent with our behavioural data in which the reinforcing effects of nicotine, probably involving VTA activation, are substantially conserved in the knockout mice. However,

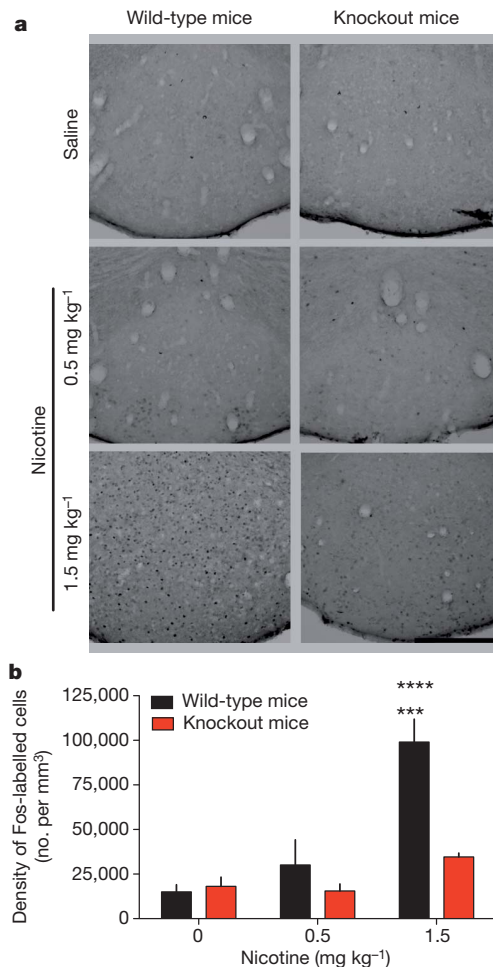


Figure 4 | Nicotine-induced activation of the IPN in mice.

a, Photomicrograph of IPN showing Fos immunoreactivity in wild-type (left) and $\alpha 5$ knockout (right) mice following saline (top), 0.5 mg kg⁻¹ nicotine (centre), or 1.5 mg kg⁻¹ nicotine (bottom); $n = 5$ per group. Scale bar, 100 μ m. **b**, Cell density was quantified with unbiased stereology. Data are presented as the mean (\pm s.e.m.) density of Fos-immunoreactive cells (number per mm³). Genotype, $F_{(1,24)} = 13.50$, $P < 0.01$; drug, $F_{(2,24)} = 21.13$, $P < 0.0001$; interaction, $F_{(2,24)} = 8.64$, $P < 0.01$. *** $P < 0.001$ compared with saline treatment; **** $P < 0.001$ compared with knockout mice at the same nicotine dose.

recruitment of an aversive/satiety pathway by nicotine overconsumption, involving habenular-driven activation of IPN, is diminished in animals with deficient $\alpha 5^*$ nAChR signalling.

Habenulo-interpeduncular activity limits nicotine intake

Next we examined the effects of reversible inactivation of the habenulo-interpeduncular tract on nicotine self-administration behaviour in rats, accomplished by direct microinjection of lidocaine into targeted brain sites. Lidocaine-induced inactivation of the IPN increased responding for nicotine (0.03 mg kg⁻¹ per infusion) (Fig. 5a and Supplementary Fig. 14), further supporting a role for nicotine-induced activation of the IPN in restricting nicotine intake. Conversely, inactivation of the VTA profoundly decreased nicotine intake (0.03 mg kg⁻¹ per infusion) (Supplementary Figs 15 and 16). Inactivation of the MHb increased nicotine intake similarly to IPN inactivation (Fig. 5b), but this effect was only detected when rats self-administered a higher (0.12 mg kg⁻¹ per infusion) unit dose of nicotine (Supplementary Figs 17 and 18). This effect is consistent with habenular-mediated activation of the IPN preferentially occurring when higher nicotine doses are consumed. Next we investigated the role of glutamate-mediated transmission in these brain sites in regulating nicotine intake. Microinjection of the competitive NMDA (*N*-methyl-D-aspartate) glutamate receptor

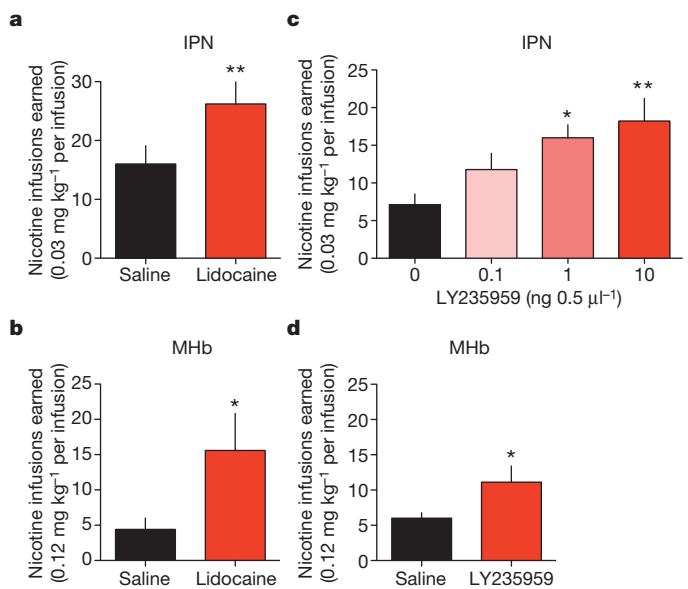


Figure 5 | Disruption of IPN or MHb signalling increases nicotine intake in rats. **a–d**, All data are presented as mean (\pm s.e.m.) number of nicotine infusions earned. **a**, Lidocaine infused into the IPN increased nicotine intake in rats; ** $P < 0.01$. **b**, Lidocaine into the MHb increased nicotine intake in rats self-administering a high unit dose (0.12 mg kg⁻¹ per infusion); * $P < 0.05$. **c**, LY235959 infused into the IPN increased nicotine intake in rats ($n = 9$). $F_{(3,24)} = 6.08$, $P < 0.01$. * $P < 0.05$ and ** $P < 0.01$ compared to control. **d**, LY235959 (10 ng per side) into the MHb increased nicotine intake in rats responding for a high unit dose (0.12 mg kg⁻¹ per infusion; $n = 5$); * $P < 0.05$.

antagonist LY235959 (ref. 46) into the IPN dose-dependently increased nicotine self-administration (Fig. 5c). LY235959 infused into the MHb also increased nicotine intake at the higher unit dose of nicotine, whereas infusion into the VTA decreased nicotine intake (Fig. 5d and Supplementary Fig. 16). Taken together, these data support a conceptual framework in which high levels of nicotine intake stimulate the habenulo-interpeduncular tract through $\alpha 5^*$ nAChRs and thereby enhance NMDA-receptor-mediated glutamatergic transmission in the IPN. This nicotine-induced enhancement of IPN activity relays an inhibitory motivational signal that limits further drug intake. Deficient $\alpha 5^*$ nAChR signalling diminishes the magnitude of this inhibitory motivational signal, permitting larger amounts of nicotine to be consumed (Supplementary Fig. 19).

Our findings reveal the habenulo-interpeduncular pathway as a key neurocircuit controlling nicotine intake. This circuit acts in a manner opposite to the mesoaccumbens 'positive reward' pathway and instead transmits an inhibitory motivational signal that limits nicotine intake. There are reciprocal projections between the MHb and portions of the caudomedial VTA (interfascicular nucleus), with the VTA and IPN projecting to many common brain areas including the dorsal tegmental nucleus, raphe nuclei and dorsomedial nucleus of thalamus. Hence, it will be important to determine if direct cross-talk between VTA and IPN, or integration of reward-related information from these structures at downstream brain sites⁴⁷, is responsible for regulating the motivational salience of nicotine and coordinating behavioural output. Our data indicate that individuals carrying risk alleles for tobacco dependence resulting in deficient $\alpha 5^*$ nAChR function are relatively insensitive to inhibitory effects of nicotine on reward pathways, consequently extending the range of nicotine doses that have net stimulatory effects on reward systems. Such a scenario is likely to be most important in the acquisition of the tobacco habit in which experiencing a negative effect of nicotine on reward pathways may decrease the likelihood of repeatedly engaging in smoking behaviour⁴⁸. As such, these findings have important implications for understanding the high incidence of lung cancer and COPD in individuals carrying *CHRNA5* risk alleles, indicating that far higher levels of nicotine can be tolerated

in these individuals, probably resulting in greater exposure to carcinogens contained in tobacco smoke.

We have established a new framework for understanding the motivational drives that control nicotine intake. These findings are a key advance in our understanding of brain systems that regulate vulnerability to tobacco addiction, and reveal the importance of $\alpha 5^*$ nAChRs as targets for the development of novel smoking cessation therapeutics.

METHODS SUMMARY

Mice with null mutation in the $\alpha 5$ nAChR subunit gene and their wild-type littermates, or male Wistar rats (Charles River Laboratories), were surgically prepared with silastic catheters in the jugular vein and trained to respond on an 'active' lever for food pellets under a fixed ratio 5 time-out 20 s (FR5TO20) schedule of reinforcement. Mice and rats then responded for nicotine infusions on the FR5TO20 reinforcement schedule during 1-h daily testing sessions. Nicotine hydrogen tartrate salt was dissolved in sterile saline solution (0.9% w/v). Each nicotine reward earned resulted in the delivery of a nicotine infusion (0.033-ml injection volume delivered over 3 s in mice; 0.1 ml delivered over 1 s in rats) and initiated a 20-s time-out period signalled by a light cue located above the active lever during which responding on the lever was without consequence.

Full Methods and any associated references are available in the online version of the paper at www.nature.com/nature.

Received 25 February 2010; accepted 10 January 2011.

Published online 30 January 2011.

- Mokdad, A. H., Marks, J. S., Stroup, D. F. & Gerberding, J. L. Actual causes of death in the United States, 2000. *J. Am. Med. Assoc.* **291**, 1238–1245 (2004).
- Stolerman, I. P. & Jarvis, M. J. The scientific case that nicotine is addictive. *Psychopharmacology* **117**, 2–10 (1995).
- Le Novère, N., Corringer, P. J. & Changeux, J. P. The diversity of subunit composition in nAChRs: evolutionary origins, physiologic and pharmacologic consequences. *J. Neurobiol.* **53**, 447–456 (2002).
- Picciotto, M. R. et al. Acetylcholine receptors containing the $\beta 2$ subunit are involved in the reinforcing properties of nicotine. *Nature* **391**, 173–177 (1998).
- Tapper, A. R. et al. Nicotine activation of $\alpha 4^*$ receptors: sufficient for reward, tolerance, and sensitization. *Science* **306**, 1029–1032 (2004).
- Corrigall, W. A., Franklin, K. B., Coen, K. M. & Clarke, P. B. The mesolimbic dopaminergic system is implicated in the reinforcing effects of nicotine. *Psychopharmacology* **107**, 285–289 (1992).
- Ikemoto, S., Qin, M. & Liu, Z. H. Primary reinforcing effects of nicotine are triggered from multiple regions both inside and outside the ventral tegmental area. *J. Neurosci.* **26**, 723–730 (2006).
- Maskos, U. et al. Nicotine reinforcement and cognition restored by targeted expression of nicotinic receptors. *Nature* **436**, 103–107 (2005).
- Berrettini, W. et al. $\alpha 5/\alpha 3$ nicotinic receptor subunit alleles increase risk for heavy smoking. *Mol. Psychiatry* **13**, 368–373 (2008).
- Saccone, S. F. et al. Cholinergic nicotinic receptor genes implicated in a nicotine dependence association study targeting 348 candidate genes with 3713 SNPs. *Hum. Mol. Genet.* **16**, 36–49 (2007).
- Liu, J. Z. et al. Meta-analysis and imputation refines the association of 15q25 with smoking quantity. *Nature Genet.* **42**, 436–440 (2010).
- Bierut, L. J. et al. Variants in nicotinic receptors and risk for nicotine dependence. *Am. J. Psychiatry* **165**, 1163–1171 (2008).
- Kuryatov, A., Berrettini, W. & Lindstrom, J. Acetylcholine receptor (AChR) $\alpha 5$ subunit variant associated with risk for nicotine dependence and lung cancer reduces ($\alpha 4\beta 2$) $\alpha 5$ AChR function. *Mol. Pharmacol.* **79**, 119–125 (2011).
- Hung, R. J. et al. A susceptibility locus for lung cancer maps to nicotinic acetylcholine receptor subunit genes on 15q25. *Nature* **452**, 633–637 (2008).
- Wang, Y., Broderick, P., Matakidou, A., Eisen, T. & Houlston, R. S. Role of 5p15.33 (*TERT-CLPTM1L*), 6p21.33 and 15q25.1 (*CHRNA5-CHRNA3*) variation and lung cancer risk in never-smokers. *Carcinogenesis* **31**, 234–238 (2010).
- Amos, C. I. et al. Genome-wide association scan of tag SNPs identifies a susceptibility locus for lung cancer at 15q25.1. *Nature Genet.* **40**, 616–622 (2008).
- Le Marchand, L. et al. Smokers with the *CHRNA* lung cancer-associated variants are exposed to higher levels of nicotine equivalents and a carcinogenic tobacco-specific nitrosamine. *Cancer Res.* **68**, 9137–9140 (2008).
- Henningfield, J. E. & Goldberg, S. R. Nicotine as a reinforcer in human subjects and laboratory animals. *Pharmacol. Biochem. Behav.* **19**, 989–992 (1983).
- Le Foll, B., Wertheim, C. & Goldberg, S. R. High reinforcing efficacy of nicotine in non-human primates. *PLoS ONE* **2**, e230 (2007).
- Risner, M. E. & Goldberg, S. R. A comparison of nicotine and cocaine self-administration in the dog: fixed-ratio and progressive-ratio schedules of intravenous drug infusion. *J. Pharmacol. Exp. Ther.* **224**, 319–326 (1983).
- Corrigall, W. A. & Coen, K. M. Nicotine maintains robust self-administration in rats on a limited-access schedule. *Psychopharmacology* **99**, 473–478 (1989).
- Jackson, K. J. et al. Role of $\alpha 5$ nicotinic acetylcholine receptors in pharmacological and behavioral effects of nicotine in mice. *J. Pharmacol. Exp. Ther.* **334**, 137–146 (2010).
- Matta, S. G. et al. Guidelines on nicotine dose selection for *in vivo* research. *Psychopharmacology* **190**, 269–319 (2007).
- Russell, M. A., Wilson, C., Patel, U. A., Feyerabend, C. & Cole, P. V. Plasma nicotine levels after smoking cigarettes with high, medium, and low nicotine yields. *BMJ* **2**, 414–416 (1975).
- Lynch, W. J. & Carroll, M. E. Regulation of drug intake. *Exp. Clin. Psychopharmacol.* **9**, 131–143 (2001).
- Lynch, W. J. & Carroll, M. E. Regulation of intravenously self-administered nicotine in rats. *Exp. Clin. Psychopharmacol.* **7**, 198–207 (1999).
- Marks, M. J. et al. Nicotine binding and nicotinic receptor subunit RNA after chronic nicotine treatment. *J. Neurosci.* **12**, 2765–2784 (1992).
- Herkenham, M. & Nauta, W. J. Efferent connections of the habenular nuclei in the rat. *J. Comp. Neurol.* **187**, 19–47 (1979).
- Grady, S. R. et al. Rodent habenulo-interpeduncular pathway expresses a large variety of uncommon nAChR subtypes, but only the $\alpha 3\beta 4^*$ and $\alpha 3\beta 3\beta 4^*$ subtypes mediate acetylcholine release. *J. Neurosci.* **29**, 2272–2282 (2009).
- London, E. D., Connolly, R. J., Szikszay, M., Wamsley, J. K. & Dam, M. Effects of nicotine on local cerebral glucose utilization in the rat. *J. Neurosci.* **8**, 3920–3928 (1988).
- Donovick, P. J., Burright, R. G. & Zuromski, E. Localization of quinine aversion within the septum, habenula, and interpeduncular nucleus of the rat. *J. Comp. Physiol. Psychol.* **71**, 376–383 (1970).
- Salas, R., Sturm, R., Boulter, J. & De Biasi, M. Nicotinic receptors in the habenulo-interpeduncular system are necessary for nicotine withdrawal in mice. *J. Neurosci.* **29**, 3014–3018 (2009).
- Glick, S. D., Ramirez, R. L., Livi, J. M. & Maisonneuve, I. M. 18-Methoxycoronaridine acts in the medial habenula and/or interpeduncular nucleus to decrease morphine self-administration in rats. *Eur. J. Pharmacol.* **537**, 94–98 (2006).
- Matsumoto, M. & Hikosaka, O. Lateral habenula as a source of negative reward signals in dopamine neurons. *Nature* **447**, 1111–1115 (2007).
- Brown, R. W., Collins, A. C., Lindstrom, J. M. & Whiteaker, P. Nicotinic $\alpha 5$ subunit deletion locally reduces high-affinity agonist activation without altering nicotinic receptor numbers. *J. Neurochem.* **103**, 204–215 (2007).
- Kenny, P. J. & Markou, A. Nicotine self-administration acutely activates brain reward systems and induces a long-lasting increase in reward sensitivity. *Neuropsychopharmacology* **31**, 1203–1211 (2006).
- Schaefer, G. J. & Michael, R. P. Task-specific effects of nicotine in rats: intracranial self-stimulation and locomotor activity. *Neuropharmacology* **25**, 125–131 (1986).
- Kenny, P. J. Brain reward systems and compulsive drug use. *Trends Pharmacol. Sci.* **28**, 135–141 (2007).
- Qin, C. & Luo, M. Neurochemical phenotypes of the afferent and efferent projections of the mouse medial habenula. *Neuroscience* **161**, 827–837 (2009).
- Hussain, R. J., Taraschenko, O. D. & Glick, S. D. Effects of nicotine, methamphetamine and cocaine on extracellular levels of acetylcholine in the interpeduncular nucleus of rats. *Neurosci. Lett.* **440**, 270–274 (2008).
- Girod, R., Barazangi, N., McGehee, D. & Role, L. W. Facilitation of glutamatergic neurotransmission by presynaptic nicotinic acetylcholine receptors. *Neuropharmacology* **39**, 2715–2725 (2000).
- McGehee, D. S., Heath, M. J., Gelber, S., Devay, P. & Role, L. W. Nicotine enhancement of fast excitatory synaptic transmission in CNS by presynaptic receptors. *Science* **269**, 1692–1696 (1995).
- Rauhut, A. S., Hawrylak, M. & Mardekian, S. K. Bupropion differentially alters the aversive, locomotor and rewarding properties of nicotine in CD-1 mice. *Pharmacol. Biochem. Behav.* **90**, 598–607 (2008).
- Gavrilov, Y. V., Perekrst, S. V., Novikova, N. S. & Korneva, E. A. Stress-induced changes in cellular responses in hypothalamic structures to administration of an antigen (lipopolysaccharide) (in terms of c-Fos protein expression). *Neurosci. Behav. Physiol.* **38**, 189–194 (2008).
- Lavolette, S. R., Alexson, T. O. & van der Kooy, D. Lesions of the tegmental pedunculopontine nucleus block the rewarding effects and reveal the aversive effects of nicotine in the ventral tegmental area. *J. Neurosci.* **22**, 8653–8660 (2002).
- Kenny, P. J., Chartoff, E., Roberto, M., Carlezon, W. A. Jr & Markou, A. NMDA receptors regulate nicotine-enhanced brain reward function and intravenous nicotine self-administration: role of the ventral tegmental area and central nucleus of the amygdala. *Neuropsychopharmacology* **34**, 266–281 (2009).
- Hong, L. E. et al. A genetically modulated, intrinsic cingulate circuit supports human nicotine addiction. *Proc. Natl Acad. Sci. USA* **107**, 13509–13514 (2010).
- Schlaepfer, I. R. et al. The *CHRNA5/A3/B4* gene cluster variability as an important determinant of early alcohol and tobacco initiation in young adults. *Biol. Psychiatry* **63**, 1039–1046 (2008).

Supplementary Information is linked to the online version of the paper at www.nature.com/nature.

Acknowledgements This work was supported by the National Institute on Drug Abuse (DA020686 to P.J.K.; DA026693 to C.D.F.; P30DA015663 to M.J.M.) and The James and Esther King Biomedical Research Program, Florida Department of Health (07KN-06 to P.J.K.).

Author Contributions C.D.F., Q.L., P.M.J. and M.J.M. performed all experiments; M.J.M. also provided essential reagents and assisted in manuscript editing; C.D.F. and P.J.K. designed the experiments, performed the statistical analyses and wrote the manuscript.

Author Information Reprints and permissions information is available at www.nature.com/reprints. The authors declare no competing financial interests. Readers are welcome to comment on the online version of this article at www.nature.com/nature. Correspondence and requests for materials should be addressed to P.J.K. (pjkenny@scripps.edu).

METHODS

Animals. Male and female mice with null mutations of the $\alpha 5$ nAChR subunit gene *Chrna5* ($\alpha 5$ knockout) and their wild-type littermates were bred in our animal facilities. Brain structure and baseline behavioural measures were determined between the knock-out mice and wild-type littermates⁴⁹. The mutant mice had been bred for more than ten generations onto a C57BL6 background. Breeding was conducted by mating heterozygous pairs. All mice were housed in cages of 1–3 and were at least 6 weeks of age at the beginning of each experiment. Male Wistar rats weighing 275–300 g were purchased from Charles River Laboratories and housed 1–2 per cage. Mice and rats were maintained in an environmentally controlled vivarium on a 12 h:12 h reversed light:dark cycle, and food and water were provided *ad libitum* until behavioural training commenced. During self-administration procedures, mice and rats were food restricted to 85–90% of their free-feeding body weight, but water was maintained without restriction. All procedures were conducted in strict accordance with the National Institutes of Health Guide for the Care and Use of Laboratory Animals and were approved by the Institutional Animal Care and Use Committee of The Scripps Research Institute, Florida.

Genotyping. Around 21 days of age, mouse pups were weaned and their tails were clipped for genetic analysis. DNA was extracted with a tissue DNA extraction kit purchased from Biomiga. Primers for the $\alpha 5$ wild-type and mutant genes were: $\alpha 5$ wild-type forward, 5'-CACTGTCACTTGGACGACGCC-3'; $\alpha 5$ wild-type reverse, 5'-GTTCCCTTGTCTCCCATTCG-3'; Neo-1, 5'-CTTTTGTCAAGACCGACCTGTCCG-3'; and Neo-2, 5'-CTCGATGCGATGTTTCGCTTGGTG-3'. Samples were processed for genetic amplification with PCR and subsequently run on a 1% agarose gel with ethidium bromide. The band for the $\alpha 5$ wild-type gene was at 190 bp, and the $\alpha 5$ mutant gene was at 290 bp.

Drugs. For self-administration experiments in mice and rats, (–)-nicotine hydrogen tartrate salt (Sigma) was dissolved in 0.9% sterile saline. All doses of nicotine refer to the free-base form. The NMDA antagonist LY235959 (Tocris) or lidocaine (2%; Sigma) was microinjected at a volume of 0.5 μ l for over 1 min, and the injector remained in place for an additional 2 min to allow for diffusion. The pH of solutions was adjusted to ~7.4.

Surgery. Mice and rats were anaesthetized with an isoflurane (1–3%)/oxygen vapour mixture and prepared with intravenous catheters. Briefly, the catheters consisted of a 6 cm (mice) or 12 cm (rats) length of silastic tubing fitted to guide cannula (Plastics One) bent at a curved right angle and encased in dental acrylic. The catheter tubing was passed subcutaneously from the animal's back to the right jugular vein, and a 1-cm (mice) or 2.5-cm (rats) length of the catheter tip was inserted into the vein and tied with surgical silk suture. Catheters were flushed daily with physiological sterile saline solution (0.9% w/v) containing heparin (10–60 USP units ml^{−1}). Catheter integrity was tested with the ultra short-acting barbiturate anaesthetic Brevital (methohexital sodium; Eli Lilly).

Intravenous self-administration. Mice and rats were mildly food restricted to 85–90% of their free-feeding body weight and trained to press a lever in an operant chamber (Med Associates) for food pellets (20 mg pellets for mice; 45 mg food pellets for rats; TestDiet) under a fixed-ratio 5 time out 20 s (FR5TO20) schedule of reinforcement before catheter implantation. Once stable responding was achieved (>30 pellets per session in mice; >90 pellets per session in rats), subjects were catheterized as described earlier. The animals were allowed at least 48 h to recover from surgery, then permitted to respond for food reinforcement again under the FR5TO20 schedule. Once food responding criteria were re-established, subjects were permitted to acquire intravenous nicotine self-administration by autoshaping during 1-h daily sessions, 7 days per week. Nicotine was delivered through the tubing into the intravenous catheter by a Razel syringe pump (Med Associates). Each nicotine self-administration session was performed using two retractable levers (one active, one inactive) that extend 1 cm into the chamber. Completion of the response criteria on the active lever resulted in the delivery of an intravenous nicotine infusion (0.03 ml infusion volume for mice; 0.1 ml for rats). Responses on the inactive lever were recorded but had no scheduled consequences. For dose–response studies (fixed and progressive ratio schedules), animals were presented with each dose of nicotine for at least 5 days (mice) or 3 days (rats); the mean intake over the last 3 (mice) or 2 (rats) sessions for each dose was calculated and used for statistical analysis. In between each dose, subjects were placed back on the training dose for at least 2 days or until their intake returned to baseline levels before being tested on the next dose.

Surgical procedures for microinjections and electrode placement. Animals were anaesthetized as described earlier and positioned in a stereotaxic frame (Kopf Instruments). Unless otherwise noted, the incisor bar was set to the 'flat-skull' position. To test the efficacy of the re-expressing and knockdown viruses *in vivo*, bilateral injections were made into the hippocampus of mice or rats, respectively. This area was chosen based on the constitutive expression of the $\alpha 5$ nAChR subunit

mRNA in wild-type animals. In mice, six bilateral injections (1 μ l each at a flow rate of 1 μ l per min) were made at the following coordinates: anterior-posterior (AP), −1.7 mm from bregma; medial-lateral (ML), ± 0.75 mm from midline; dorsal-ventral (DV), −2.05 mm, −1.80 mm and −1.35 mm from brain surface⁵⁰. Virus injections into mouse medial habenula were aimed at the following coordinates: AP, −1.94 mm from bregma; ML, ± 1.06 mm from midline; DV, −2.37 from dura. In rats, the six hippocampal injections (three 2- μ l injections per side at a flow rate of 1 μ l per min) were made at the following coordinates: AP, −3.3 mm from bregma; ML, ± 1.1 mm from midline; DV, −3.6 mm, −3.0 mm and −2.4 mm from brain surface⁵¹. For habenular injections in mice, the needle was angled 20° towards midline, and bilateral injections (0.375 μ l each) were administered at a rate of 0.375 μ l per min. For habenular injections in rats, the lentivirus was injected bilaterally based on previously published coordinates⁵². The incisor bar was set to 5 mm above plane, and the injector needle was at a 10° angle towards midline (AP: −2.2 mm from bregma; ML: ± 1.5 mm from midline; DV: −4.9 mm from brain surface). The bilateral injections (1 μ l each) were administered at a rate of 1 μ l per min. For all of the injections, the injector needle was left in place for a minimum of 2 min after injection. For IPN and VTA microinjections in rats, guide cannulae (Plastics One) were implanted as follows: IPN (flat skull; 10° angle towards midline; AP, −6.72 mm from bregma; ML, ± 1.6 mm from midline; DV, −6.5 mm from brain surface) or VTA (bilateral; flat skull; 6° angle towards midline; AP, −5.4 mm from bregma; ML, ± 1.3 mm from midline; DV, −7.0 mm from skull)⁵¹. The MHB guide cannula coordinates were the same as for the lentiviral injections, except with DV at −2.9 mm from brain surface. For all of the cannulae, injector needles extended 2 mm below the tip of the cannula for placement into the brain region. For the intracranial self-stimulation electrode, a stainless steel bipolar electrode (Plastics One) was implanted into the lateral hypothalamus (AP, −0.5 mm from bregma; ML, ± 1.7 mm from midline; DV, −8.3 mm from brain surface)⁵¹.

BSR behavioural procedure. Rats were trained to respond according to a modification of the discrete-trial current-threshold BSR procedure of Kornetsky and Esposito^{53,54} in an operant box equipped with a wheel manipulandum and intracranial self-stimulation stimulator (Med Associates). Briefly, a trial was initiated by the delivery of a non-contingent electrical stimulus. This electrical reinforcer had a duration of 500 ms and consisted of 0.1-ms rectangular cathodal pulses that were delivered at a frequency of 50–100 Hz. The frequency of the stimulation was selected for individual rats so that threshold elevation and lowering may be detected, and this frequency was held constant throughout the experiment. A one-quarter turn of the wheel manipulandum within 7.5 s of the delivery of the non-contingent stimulation resulted in the delivery of an electrical stimulus identical in all parameters to the non-contingent stimulus that initiated the trial. After a variable inter-trial interval (7.5–12.5 s, mean of 10 s), another trial was initiated with the delivery of a non-contingent electrical stimulus. Failure to respond to the non-contingent stimulus within 7.5 s resulted in the onset of the inter-trial interval. Responding during the inter-trial interval delayed the onset of the next trial by 12.5 s. In each testing session, current levels were varied in alternating descending ($\times 2$) and ascending ($\times 2$) series in 5- μ A steps. A set of five trials was presented for each current intensity. The threshold for each series is defined as the midpoint between two consecutive current intensities that yield 'positive scores' (animals respond for at least three of the five trials) and two consecutive current intensities that yield 'negative scores' (animals do not respond for three or more of the five trials). The overall threshold for the session is defined as the mean of the thresholds for the four individual series. Threshold data are presented as per cent of baseline values due to inter-subject variability in baseline rates.

Generation of lentivirus. For $\alpha 5$ subunit re-expression studies, the mouse $\alpha 5$ nAChR subunit gene, *Chrna5*, was cloned into the pCDF1 lentivirus expression vector containing copGFP (GFP cloned from copepod *Pontellina plumata*) from Systems Biosciences. For $\alpha 5$ subunit knockdown studies, two different shRNAs directed against the rat *Chrna5* gene were designed using the Genscript online construct builder (see Supplementary Figures for shRNA sequence). The shRNAs were cloned into the pRNAT-U6.2/Lenti construct containing GFP (GenScript). Control vectors were identical to the expression constructs, but without the gene insert.

Generation of lentivirus. To generate lentivirus supernatant, HEK 293FT packaging cells (3.75×10^6 293TN cells per 10-cm plate) were transfected with the vectors, along with the pPACKF1TM Lentiviral Packaging Kit using lipofectamine reagent and plus reagent (Invitrogen) according to the manufacturer's instructions. Medium containing virus particles (~10 ml) was harvested 48–60 h after transfection by centrifugation at 76,755g at room temperature (22 °C) for 5 min to pellet cell debris and filtered through 0.45 mm PVDF (polyvinylidene difluoride) filters (Millex-HV). To concentrate the viral supernatant for intrastriatal administration, supernatants were centrifuged at 32,000g for 90 min at

4 °C, and the precipitate re-suspended in 100 µl cold PBS. Supernatants were aliquoted into 100 µl volumes and stored at −80 °C until use.

Estimation of lentivirus titre. Viral supernatant titres were determined using the Lentivector Rapid Titer Kit from System Biosciences, according to the manufacturer's instructions. The number of infectious units per ml of supernatant (IFU ml^{−1}) was calculated as follows. Multiplicity of infection (MOI) of the sample × the number of cells in the well upon infection × 1,000 / µl of viral supernatant used.

Tissue dissection. Mice and rats were killed by inhalation of CO₂, brains were rapidly removed and frozen on dry ice. Tissues were stored at −80 °C until dissection. Brains were sliced on a cryostat, and bilateral dissections were made for the hippocampus, MHb, IPN and/or VTA with a scalpel. Samples were pooled across multiple subjects owing to the small size of selected brain areas and stored at −80 °C until processing for RNA isolation.

RNA isolation and real-time RT-PCR. Cells grown in monolayer or dissected tissue were homogenized in RNA-STAT60 (Tel-Test) using a 27-gauge needle. After homogenization, 250 µl of chloroform was added and the samples were vortexed for 1 min. Samples were then centrifuged for 15 min at 12,000g at 4 °C, and the upper aqueous RNA-containing layer was removed for an additional RNASTAT60/chloroform extraction. The RNA was precipitated with 2× volume of isopropanol overnight at −20 °C and centrifuged for 30 min at 12,000g. The RNA pellets were washed twice with 70% ethanol/RNase-free water and subsequently resuspended in RNasecure (Ambion/Applied Biosystems), and ~10 µg of RNA from each sample was treated with Turbo DNase (Ambion/Applied Biosystems) for 60 min at 37 °C to degrade residual genomic DNA. To assess RNA levels, samples were reverse transcribed into complementary DNA with the TaqMan High Capacity cDNA Reverse Transcription kit (Applied Biosystems). Thereafter, they were processed with the TaqMan Universal PCR kit with the mouse or rat *Chrna5* gene expression assay (Applied Biosystems); controls consisted of either β-actin or 18S. Samples were quantified by real-time RT-PCR (7900 Real-Time PCR system; Applied Biosystems). All data were normalized in accordance with the mean housekeeping messenger RNA expressing levels as an internal control. Comparison between groups was made using the method of $2^{-\Delta\Delta Ct}$.

Brain perfusion and fixation. Subjects were anaesthetized with sodium pentobarbital (0.1 mg per 10 g body weight) and perfused through the ascending aorta with 0.9% saline, followed by 4% paraformaldehyde in 0.1 M PBS (pH 7.4). Brains were harvested, postfixed for 2 h in 4% paraformaldehyde, and then stored in 30% sucrose in PBS. All brains were cut into 30–40-µm coronal sections on a microtome, and the floating sections were stored in 0.1 M PBS with 0.01% sodium azide at 4 °C until processing for immunocytochemistry.

Fluorescence immunolabelling. Floating sections were processed for GFP fluorescent immunostaining. To localize the GFP-tagged lentivirus-infected cells in mice, we used a rabbit polyclonal IgG that recognizes copGFP. To localize the lentivirus tagged with GFP in rats, we used a chicken polyclonal IgG that recognizes a 27 kDa protein derived from the jellyfish *Aequorea victoria*. Further, to identify IPN we used a guinea pig polyclonal IgG that recognizes VACHT. Sections were rinsed in 0.1 M PBS, pH 7.4, with 0.3% Triton-X 100 (PBT) and then blocked in 10% normal donkey serum/PBT. Thereafter, sections were incubated in the primary antibody in PBT at 4 °C overnight. The primary antibodies were diluted as follows: rabbit anti-copGFP (1:2,000; Evrogen), chicken anti-GFP (1:2,000; Millipore) or guinea pig anti-VACHT (1:500; Millipore). On day 2, the sections were rinsed and incubated in Alexa 488 donkey anti-rabbit (1:400; Invitrogen), DyLight 488 donkey anti-chicken (1:400; Jackson ImmunoResearch) and/or DyLight 594 or 647 donkey anti-guinea pig (1:500; Jackson ImmunoResearch) secondary antibodies in 0.3% PBT for 2 h. Next, the sections were rinsed, mounted on slides with vectashield (with or without DAPI) (Vector Labs), and coverslipped. Controls included processing the secondary antibodies alone to verify background staining, processing each primary with the secondary antibody to verify laser-specific excitation, examining for autofluorescence in an alternate laser channel with tissue lacking that laser-specific probe, and using sequential scanning. For subsequent fluorescent images, only the brightness and/or contrast levels were adjusted after acquisition and were imposed across the entire image.

⁸⁶Rb⁺ efflux. ⁸⁶RbCl (average initial specific activity 15 Ci mg^{−1}) as well as Optiphase Supermix scintillation cocktail was purchased from Perkin-Elmer

NEN. The α5 knockout mice were injected with either the Lenti-CHRNA5 or Lenti-Control vector as previously described. After an incubation period of at least 3 weeks, mice were killed and synaptosomes were generated from the IPN, MHb, hippocampus, striatum, thalamus and cortex as described previously⁵⁵. Samples were loaded with ⁸⁶Rb⁺ and acetylcholine-stimulated ⁸⁶Rb⁺ efflux was measured as described previously⁵⁵, with each sample stimulated only once. ⁸⁶Rb⁺ efflux was expressed as the increase in signal above basal efflux. A non-linear least-squares curve fit to a first-order equation ($C_t = C_0 \times e^{-kt}$), where C_t is the basal efflux counts at time t , C_0 is the estimated efflux counts at $t = 0$ s, and k is the first-order decay constant) was used to estimate basal efflux for each sample. Counts in fractions preceding and following the peak were used for curve fitting. Acetylcholine-stimulated efflux was calculated by summing the counts in the fractions exceeding basal efflux during acetylcholine exposure and dividing by the corresponding basal efflux counts. This value represents total peak relative to baseline.

Fos procedure. Wild-type and α5 subunit knockout mice were injected subcutaneously with nicotine (0.5 or 1.5 mg kg^{−1}, free base) or saline. The moderate dose of nicotine is known to be rewarding in these mice, reflected in the conditioning of a place preference²². The higher dose of nicotine is aversive, reflected in the induction of a conditioned taste aversion in wild-type mice⁵⁶. After 2 h, each subject was perfused and brains were removed and stored as described earlier. Brain sections were cut at 30 µm on a cryostat and stored in 0.1 M PBS with 0.01% sodium azide until processing. For Fos immunolabelling, sections were rinsed in 0.1 M PBS (pH 7.4), treated with 0.3% H₂O₂-PBS for 15 min, rinsed in PBS, and then blocked in 10% normal goat serum and 0.5% Triton X-100 in PBS for 1 h. Thereafter, sections were incubated in rabbit anti-cFos IgG (1:500 dilution; Abcam) in 0.5% Triton-PBS overnight at 4 °C. The following day, sections were incubated at room temperature (22 °C) for 2 h, rinsed in PBS, and then incubated in a 1:300 dilution of goat anti-rabbit secondary IgG (Vector Labs) in 0.5% Triton X-100 in PBS for 2 h. After rinsing, sections were incubated in ABC Elite (Vector Labs) for 90 min, rinsed in PBS, and immunoreactivity was revealed by using 3-diaminobenzidine (DAB) with nickel (Vector Labs). To reduce variability in the background and to standardize the staining, sections from subjects across groups were processed concurrently. Sections were mounted and coverslipped with Permount (Fisher Scientific). Cell numbers and region volumes for the IPN, VTA and ventromedial hypothalamus were quantified under ×40 magnification using unbiased stereological methods and the optical fractionator probe with Stereo Investigator software (MicroBrightField). This method of assessing total volume and cell number has been validated and used in many previous studies. Total cell counts and area measurements were determined for each brain area, and cell density (number of cells per cubic millimetre) was calculated for each subject.

Statistical analyses. All data were analysed by one- or two-way analysis of variance (ANOVA) or *t*-test using Graphpad Prism software. Significant main or interaction effects were followed by Bonferroni or Newman-Keuls post-hoc tests as appropriate. The criterion for significance was set at $P < 0.05$.

49. Salas, R. *et al.* The nicotinic acetylcholine receptor subunit α5 mediates short-term effects of nicotine *in vivo*. *Mol. Pharmacol.* **63**, 1059–1066 (2003).
50. Paxinos, G. & Franklin, K. B. J. *The Mouse Brain in Stereotaxic Coordinates* 2nd edn (Academic, 2001).
51. Paxinos, G. & Watson, C. *The Rat Brain in Stereotaxic Coordinates* 3rd edn (Academic, 1997).
52. Lecourtier, L., Neijt, H. C. & Kelly, P. H. Habenula lesions cause impaired cognitive performance in rats: implications for schizophrenia. *Eur. J. Neurosci.* **19**, 2551–2560 (2004).
53. Kornetsky, C., Esposito, R. U., McLean, S. & Jacobson, J. O. Intracranial self-stimulation thresholds: a model for the hedonic effects of drugs of abuse. *Arch. Gen. Psychiatry* **36**, 289–292 (1979).
54. Huston-Lyons, D. & Kornetsky, C. Effects of nicotine on the threshold for rewarding brain stimulation in rats. *Pharmacol. Biochem. Behav.* **41**, 755–759 (1992).
55. Marks, M. J. *et al.* Two pharmacologically distinct components of nicotinic receptor-mediated rubidium efflux in mouse brain require the β2 subunit. *J. Pharmacol. Exp. Ther.* **289**, 1090–1103 (1999).
56. Shoaib, M. *et al.* The role of nicotinic receptor beta-2 subunits in nicotine discrimination and conditioned taste aversion. *Neuropharmacology* **42**, 530–539 (2002).

CRISPR RNA maturation by *trans*-encoded small RNA and host factor RNase III

Elitza Deltcheva^{1,2}, Krzysztof Chylinski^{1,2*}, Cynthia M. Sharma^{3*}, Karine Gonzales², Yanjie Chao^{3,4}, Zaid A. Pirzada², Maria R. Eckert², Jörg Vogel^{3,4} & Emmanuelle Charpentier^{1,2}

CRISPR/Cas systems constitute a widespread class of immunity systems that protect bacteria and archaea against phages and plasmids, and commonly use repeat/spacer-derived short crRNAs to silence foreign nucleic acids in a sequence-specific manner. Although the maturation of crRNAs represents a key event in CRISPR activation, the responsible endoribonucleases (CasE, Cas6, Csy4) are missing in many CRISPR/Cas subtypes. Here, differential RNA sequencing of the human pathogen *Streptococcus pyogenes* uncovered *tracrRNA*, a *trans*-encoded small RNA with 24-nucleotide complementarity to the repeat regions of crRNA precursor transcripts. We show that *tracrRNA* directs the maturation of crRNAs by the activities of the widely conserved endogenous RNase III and the CRISPR-associated Csn1 protein; all these components are essential to protect *S. pyogenes* against prophage-derived DNA. Our study reveals a novel pathway of small guide RNA maturation and the first example of a host factor (RNase III) required for bacterial RNA-mediated immunity against invaders.

Organisms of all kingdoms of life have evolved RNA-guided immunity mechanisms to protect themselves against genome invaders^{1–6}. In bacteria and archaea, CRISPR/Cas (clustered, regularly interspaced short palindromic repeats/CRISPR-associated proteins) constitutes an adaptive RNA-mediated defence system which targets invading phages or plasmids in three steps: (1) adaptation via integration of viral or plasmid DNA-derived spacers into the CRISPR locus, (2) expression of short guide CRISPR RNAs (crRNAs) consisting of unique single repeat-spacer units and (3) interference with the invading cognate foreign genomes by mechanisms that are yet to be fully understood^{7–27}. A key event in CRISPR activation is the maturation of the active crRNAs from the CRISPR precursor transcript (pre-crRNA)^{28,29}. Three Cas proteins, Cse3 (CasE), Cas6 and Csy4, have been identified as endoribonucleases that cleave within the repeat sequences of pre-crRNA to generate the mature crRNAs^{28–31}. However, their homologues are missing in many CRISPR/Cas subtypes, suggesting the existence of alternate crRNA maturation pathways involving other Cas proteins and/or fundamentally different RNA processing events. Here, our study of the human pathogen *Streptococcus pyogenes* uncovered a new pathway of CRISPR activation wherein a *trans*-encoded small RNA, the host endoribonuclease III and the CRISPR-associated Csn1 protein are responsible for the production of the active crRNAs.

CRISPR/Cas systems in *S. pyogenes*

Our analysis of *S. pyogenes* genome sequences revealed the presence of two CRISPR/Cas loci of two different subtypes, CRISPR01 (system II, Nmeni/CASS4 subtype) and CRISPR02 (system I-C, Dvulg/CASS1 subtype)^{32,33}, each having a distinct set of repeats and *cas* genes (Fig. 1a, Supplementary Fig. 1 and Supplementary Table 1). Almost all of the associated CRISPR spacers show homology to chromosomal prophage sequences^{34–38} (Supplementary Tables 2–5), indicating that the CRISPR/Cas systems of *S. pyogenes* target lyso-genic phages.

To examine the *in vivo* expression of CRISPR01 and CRISPR02, we analysed *S. pyogenes* strain SF370 (M1 serotype) by differential RNA sequencing (dRNA-seq)³⁹. The most abundantly recovered small RNA species were CRISPR01 crRNAs originating from a ~511-nucleotide pre-crRNA (Fig. 1a; Supplementary Fig. 2a, b and Supplementary Table 6), confirming that the CRISPR01 locus is active. In contrast, the CRISPR02 locus seems not to be expressed (Supplementary Fig. 3).

We detected six crRNAs from CRISPR01 which were 39 to 42 nucleotides in length and probably were processed species, as judged by their depletion in the dRNA-seq library for primary transcripts. The individual crRNAs appeared to result from double cleavage, one within the repeat and the other within the spacer, and carry a 20-nucleotide spacer-derived 5'-guide sequence and a 19–22 nucleotides repeat-derived 3'-sequence (Supplementary Fig. 2a, b). The latter sequence is distinct from the crRNA-tag (8 nucleotides of the upstream repeat sequence) located in 5' of mature crRNAs produced by the Cse3 (CasE) and Cas6-encoding CRISPR/Cas subtypes of *Escherichia coli*, *Pyrococcus furiosus* and *Staphylococcus epidermidis*^{28,31}, providing evidence for the diversity of crRNA-tags among CRISPR/Cas systems and perhaps also for the underlying crRNA maturation and immunity mechanisms.

tracrRNA directs pre-crRNA processing

Strikingly, dRNA-seq also detected abundant RNA species transcribed 210 nucleotides upstream, on the opposite strand of the CRISPR01-associated genes and the leader-repeat-spacer array (Fig. 1a, b, Supplementary Fig. 4a, b and Supplementary Table 6); we refer to these abundant transcripts as *tracrRNA* (*trans*-activating CRISPR RNA). Northern blot probing detected four *tracrRNA* forms with approximate lengths of 171, 89, 75 and 65 nucleotides, all of which were present throughout growth, notwithstanding a slightly decreased abundance of the longer transcripts in late stationary phase (Fig. 1c and Supplementary Fig. 4b–d). According to our dRNA-seq data, the 171- and 89-nucleotide forms corresponded to primary transcripts whereas the

¹The Laboratory for Molecular Infection Medicine Sweden (MIMS), Umeå Centre for Microbial Research (UCMR), Department of Molecular Biology, Umeå University, S-90187 Umeå, Sweden. ²Max F. Perutz Laboratories, University of Vienna, A-1030 Vienna, Austria. ³ZINF Research Center for Infectious Diseases, University of Würzburg, D-97080 Würzburg, Germany. ⁴RNA Biology Group, Institute for Molecular Infection Biology, University of Würzburg, D-97080 Würzburg, Germany.

*These authors contributed equally to this work.

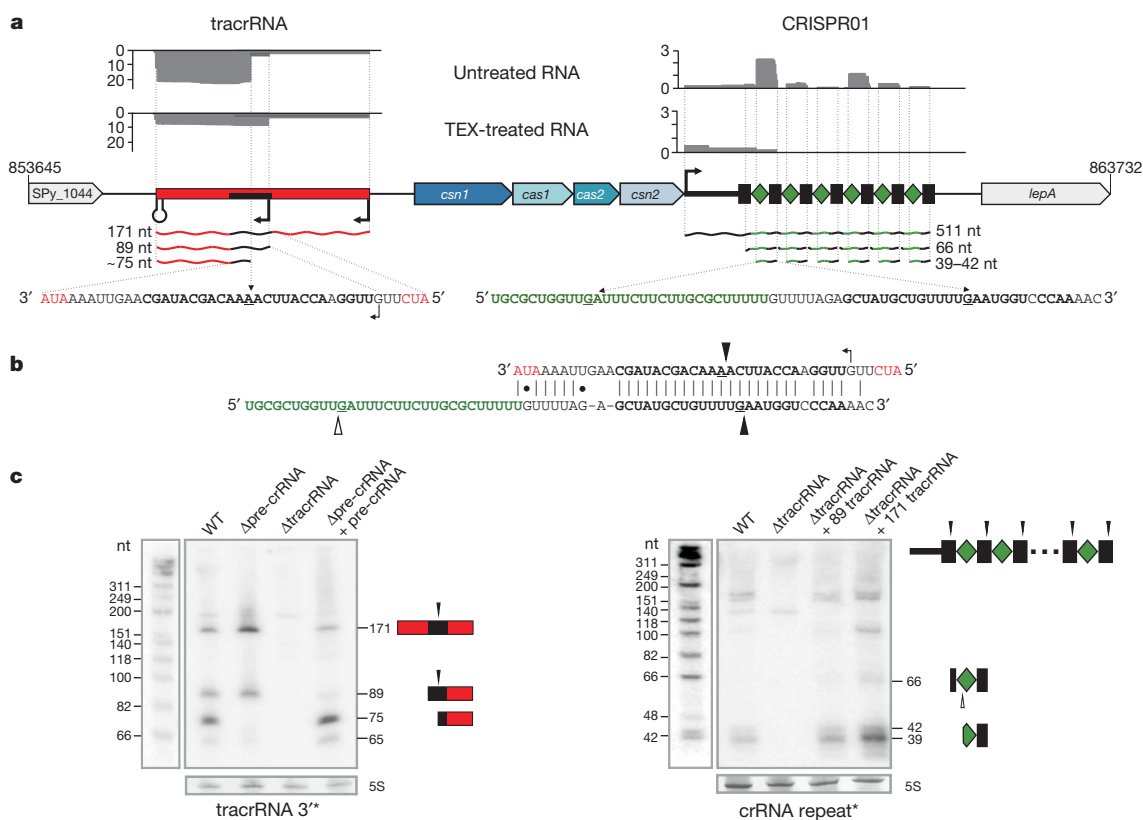


Figure 1 | A newly identified tracrRNA is required for crRNA maturation in *S. pyogenes*. **a**, dRNA-seq reveals expression of tracrRNA and crRNAs. Sequence reads of cDNA libraries derived from untreated and terminator 5'-phosphate-dependent exonuclease (TEX)-treated total RNA are shown. Vertical axis, relative amounts of sequenced cDNAs. The absence of ~75 nucleotides (nt) tracrRNA form and 39–42 nt crRNA fragments in the TEX-treated cDNA library indicates that they are generated by processing. Genomic organization of tracrRNA and CRISPR01/Cas (*csn1-cas1-cas2-csn2*) loci. Transcriptional start sites and a terminator are indicated. (Left) tracrRNA (red) is encoded on the minus strand and detected as 171, 89 and ~75 nt tracrRNA species. Black rectangle, 36-nt sequence stretch complementary to CRISPR01 repeat. (Right) pre-crRNA is encoded on the plus strand. Rectangles,

CRISPR01 repeats; diamonds, CRISPR01 spacers; 511, 66 and 39–42 nt, pre-crRNA and processed crRNAs. **b**, Base-pairing of tracrRNA with a CRISPR01 repeat is represented. Cleavages observed by dRNA-seq and leading to the formation of short overhangs at the 3' ends of the processed RNAs are indicated by black arrows. Open arrow, cleavage in the spacer sequence. **c**, tracrRNA and pre-crRNA are co-processed *in vivo*. Northern blot analysis of *S. pyogenes* total RNA: strains and probes are indicated (Supplementary Figs 2 and 4). Left panel: processing of tracrRNA into the ~75-nt form is abolished in Δ pre-crRNA and re-established upon complementation with pre-crRNA. Right panel: processing of pre-crRNA into mature crRNA forms (39–42 nt) is abrogated in Δ tracrRNA. Trans-complementation of Δ tracrRNA with 171 or 89 nt tracrRNA restores the processing.

shorter ~75-nucleotide species resulted from processing of those longer tracrRNAs (Fig. 1a and Supplementary Fig. 4b).

Remarkably, both the 171- and 89-nucleotide tracrRNAs contain a 25-nucleotide stretch with almost perfect (one mismatch) complementarity to all repeats of CRISPR01 (Fig. 1b and Supplementary Fig. 5), predicting their potential base-pairing with pre-crRNA. Moreover, the tracrRNA and pre-crRNA processing sites detected by dRNA-seq fell in the putative RNA duplex region, indicative of co-processing of the two RNAs upon pairing. In support of this prediction, tracrRNA processing into the ~75-nucleotide form was absent in a Δ pre-crRNA mutant. Conversely, we did not detect mature crRNAs in a Δ tracrRNA strain, indicating that tracrRNA is essential for the processing of pre-crRNA (Fig. 1c, Supplementary Figs 2c and 4c). Trans-complementation with the long tracrRNA species restored pre-crRNA processing in Δ tracrRNA bacteria, and showed that the 89-nucleotide form of tracrRNA suffices for co-processing (Fig. 1c and Supplementary Fig. 2c). Together, these findings reveal a novel function of a bacterial non-coding RNA such that a trans-encoded small RNA (tracrRNA) directs the maturation of another non-coding RNA (pre-crRNA) to yield the active species (crRNAs).

crRNA maturation requires RNase III and Csn1

According to our dRNA-seq data, the co-processed tracrRNA and pre-crRNA carry short 3' overhangs reminiscent of cleavage by the

endoribonuclease RNase III^{22,40–44} or the related eukaryotic Dicer and Drosha enzymes^{1,4–6,45}. Because none of the Cas proteins of CRISPR01 contains an RNase III-like motif, we hypothesized that the endogenous RNase III—a general RNA processing factor^{40,42,46} encoded by the conserved *rnc* gene of the host—was recruited to cleave tracrRNA and pre-crRNA upon base pairing. In support of our prediction, tracrRNA and pre-crRNA co-processing was abrogated in a Δ rnc mutant of *S. pyogenes* (Fig. 2), yet restored by trans-complementation of RNase III expression (Supplementary Fig. 6).

To demonstrate directly that the paired RNAs are substrates of this nuclease, tracrRNA and pre-crRNA were synthesized, annealed *in vitro* and incubated with *E. coli* RNase III. Whereas neither of the two RNAs alone was cut by the nuclease, their annealing promoted the expected singular RNase III cleavage in either RNA (Fig. 3a–c). Consistent with their shared complementarity to CRISPR01 repeats, both the 171-nucleotide and 89-nucleotide tracrRNAs promoted RNase III cleavage of pre-crRNA within the repeat to produce intermediate crRNA species, and both were converted to the ~75-nucleotide tracrRNA species in the process (Fig. 3b, c). Mutations in the complementary regions of tracrRNA or pre-crRNA hindered co-processing with the respective wild-type RNA partner, yet RNase III cleavage was fully restored when the compensatory tracrRNA and crRNA mutants were combined (Supplementary Fig. 7), corroborating that RNA duplex formation underlies the observed processing. Others have

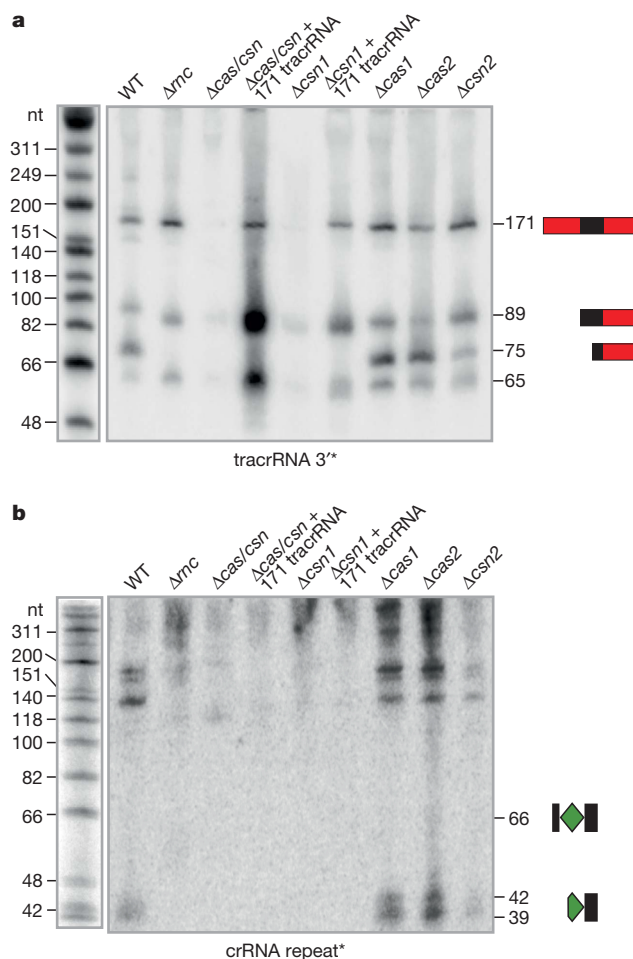


Figure 2 | Co-processing of tracrRNA and pre-crRNA requires both endogenous RNase III and Csn1 *in vivo*. **a, b,** Northern blot analysis of tracrRNA (**a**) and pre-crRNA (**b**) expression: strains and probes are indicated (Supplementary Figs 6 and 8). Processing of tracrRNA (**a**) into a ~75-nt form and pre-crRNA (**b**) into 39–42 nt mature crRNA forms is abolished in Δnrc , $\Delta cas/csn$ and $\Delta csn1$ (refer to Supplementary Figs 6 and 8).

noticed that the repeats of CRISPR/Cas subtype II (Nmeni/CASS4) lack the potential to form stem-loop structures⁴⁷; our findings suggest that tracrRNA overcomes this deficiency by providing an intermolecular RNA structure for pre-crRNA processing. Taken together, RNase III serves as a host factor in tracrRNA-mediated crRNA maturation, and constitutes the first example of a non-Cas protein that is recruited to CRISPR activity.

Next, we entertained the possibility that—in addition to RNase III—Cas proteins facilitate the co-processing of the duplex RNA *in vivo*. Intriguingly, deletion of the *csn1-cas1-cas2-csn2* operon impaired the processing of both tracrRNA and pre-crRNA (Fig. 2 and Supplementary Fig. 8a). In-frame deletions of any of the operon's four genes then revealed Csn1 as the only Cas protein required for the production of mature crRNAs and concomitant tracrRNA cleavage. This was further supported by restored tracrRNA and pre-crRNA processing upon ectopic expression of Csn1 in $\Delta cas-csn$ or $\Delta csn1$ mutants (Fig. 2 and Supplementary Fig. 8b–d).

Csn1 (or COG3513) is a large, likely multi-domain protein^{32,33} of unknown function except that it is essential for CRISPR-mediated immunity in *Streptococcus thermophilus*⁸. Here, we propose a model wherein Csn1 acts as a molecular anchor facilitating the base-pairing of tracrRNA with pre-crRNA for subsequent recognition and cleavage of pre-crRNA repeats by the host RNase III (Fig. 4). Because Csn1 has predicted motifs of RuvC-like (RNase H fold) and McrA/HNH nucleases^{32,33}, it might also mediate the second cleavage to occur at

a fixed distance within the spacers. Furthermore, Csn1 might help protect tracrRNA and pre-crRNA against other host RNases, as suggested by the strongly reduced accumulation of tracrRNA in the absence of *csn1* (Fig. 2 and Supplementary Fig. 8a, b). Collectively, our results show that in the absence of Cse3 (CasE), Cas6 or Csy4 proteins, CRISPR01 crRNA maturation is achieved by the concerted action of three novel factors, a *trans*-encoded small RNA, a host-encoded RNase and a Cas protein previously not implicated in pre-crRNA cleavage.

CRISPR immunity against prophage sequences

To investigate further the role of tracrRNA in CRISPR01-mediated immunity, we developed a plasmid-based read-out system that mimics infection with protospacer-containing lysogenic phages (a protospacer is a DNA target sequence that matches a CRISPR spacer). We assayed transformation rates of a plasmid carrying a protospacer of the *speM* exotoxin gene, expected to be a target because of 100% identity to the second spacer of CRISPR01 (Spyo1h_002; Supplementary Table 2). Consistent with this protospacer being recognized by CRISPR01, wild-type *S. pyogenes* was protected from plasmids containing the *speM* gene, with or without its endogenous promoter region. Protection was specific because the wild-type strain was readily transformed with variants of the parental backbone plasmid as control (Fig. 5 and Supplementary Fig. 9). Importantly, in contrast to the wild-type strain, the $\Delta pre-crRNA$, $\Delta tracrRNA$, Δnrc and $\Delta csn1$ mutants invariably tolerated the *speM* plasmid (Fig. 5 and Supplementary Fig. 9). Together, these results demonstrate that tracrRNA, RNase III and Csn1 are essential in CRISPR01-mediated immunity of *S. pyogenes* against lysogenic phages, and further indicate that the tracrRNA/CRISPR01/Cas system, in concert with the host RNase III, limits horizontal virulence gene transfer among pathogenic streptococcal species^{34–38}.

tracrRNA homologues in CRISPR/Cas systems

How widely spread is the tracrRNA-mediated CRISPR activation? Sequence analysis revealed anti-CRISPR repeat sequences, thus candidate tracrRNA homologues, in the vicinity of system II (Nmeni/CASS4) CRISPR/Cas loci of other bacterial genomes (Supplementary Table 7). We probed selected loci of *Listeria innocua*, *Neisseria meningitidis*, *Streptococcus mutans* and *S. thermophilus* (Fig. 6 and Supplementary Figs 12–16) and consistently observed both expression and processing of the homologous tracrRNAs and respective pre-crRNAs (Supplementary Figs 12–16). In addition, our analysis indicates potential co-evolution of the tracrRNA anti-repeat and CRISPR repeat sequences (Supplementary Table 7 and Supplementary Fig. 11). Thus, RNA base-pairing might generally determine crRNA maturation in type II CRISPR/Cas systems, and based on RNA probing results, these systems seem to be constitutively activated to target and affect the maintenance of invader genomes.

No putative tracrRNA homologue was found in the vicinity of other CRISPR/Cas subtypes, and the two additional degenerated repeats identified near the type III-A (Mtube/CASS6) CRISPR/Cas locus in *S. epidermidis* RP62a²⁵ lacked a corresponding tracrRNA homologue (Supplementary Fig. 17). Thus, the requirement of a *trans*-encoded small RNA for pre-crRNA processing into active crRNAs is a general RNA maturation mechanism shared by the type II (Nmeni/CASS4) CRISPR/Cas systems that lack the *cse3* (*casE*), *cas6* or *csy4* gene but possess *csn1*. Whether all of the type II CRISPR/Cas loci require RNase III as a host factor remains to be seen.

In summary, *trans* RNA-mediated activation of crRNA maturation to confer sequence-specific immunity against parasite genomes represents a novel RNA maturation pathway, and highlights the remarkable diversity and complexity of molecular mechanisms of CRISPR/Cas systems^{9–14,26,28,29}. Importantly, CRISPR loci have been generally regarded as autonomous genetic units, encoding all the proteins and RNAs required for their activity. Our identification of RNase III as the

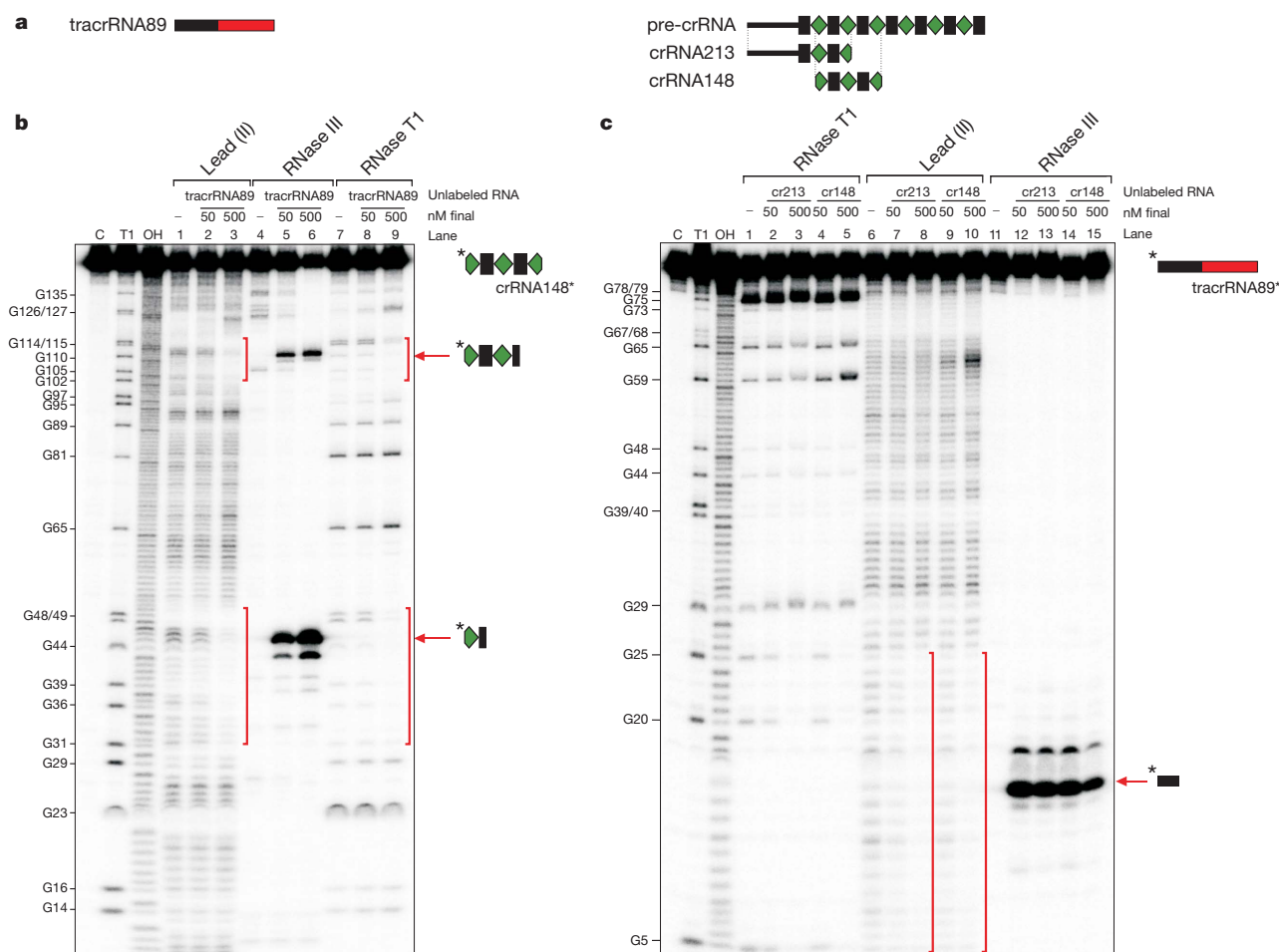
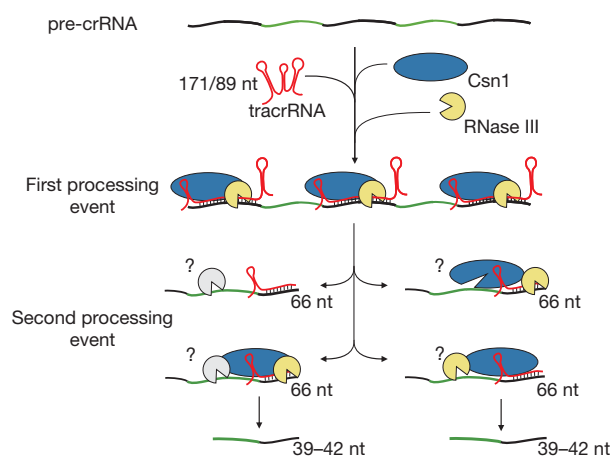


Figure 3 | tracrRNA directs pre-crRNA cleavage by RNase III *in vitro*. **a**, Schematic representation of tracrRNA89 corresponding to 89-nt-long tracrRNA, and crRNA213 and crRNA148 corresponding to a 213-nt-long leader-repeat-spacer1-repeat-spacer2 fragment and a 148-nt-long spacer1-repeat-spacer2-repeat-spacer3 fragment, respectively. **b**, Identification of tracrRNA89 binding sites on crRNA148*. 5' end-labelled crRNA148* (~10 nM) was subjected to lead(II), RNase III and RNase T1 cleavage in the absence (lanes 1, 4, 7) and presence of cold tracrRNA89 (final concentration in lanes 2, 5, and 7: ~50 nM; lanes 3, 6, and 9: ~500 nM). Lane C: untreated crRNA148*; lane T1: RNase T1 digest of crRNA148* under denaturing

conditions; lane OH: alkaline ladder; cleaved G residues are labelled. Vertical bars: crRNA148 region protected by tracrRNA89. Arrows denote specific RNase III cleavages in the two repeat regions of crRNA148 in the presence of tracrRNA89. **c**, Identification of crRNA148 and crRNA213 binding sites on tracrRNA89*. 5' end-labelled tracrRNA89* (~10 nM) was subjected to RNase T1, lead(II) and RNase III cleavage in the absence (lanes 1, 6, 11) and presence of cold crRNA148 or crRNA213 (final concentration in lanes 2, 4, 7, 9, 12 and 14: ~50 nM; lanes 3, 5, 8, 10, 13 and 15: ~500 nM). Lanes C, T1 and OH, positions of cleaved G residues and vertical bars: as above but referring to tracrRNA89* in the presence of cold crRNA148 or crRNA213.

first host factor in CRISPR activity raises the exciting possibility that a recruitment of non-Cas proteins from the host chromosome might contribute to the rapid evolutionary diversification of CRISPR/Cas systems.



We suggest that Csn1 together with RNase III forms a microprocessor complex responsible for tracrRNA-mediated pre-crRNA processing (Fig. 4). As such, the requirement of RNase III in the process seems reminiscent of the key roles of related nucleases (Dicer, Drosha) in eukaryotic RNA-protein complexes that mediate the production of small interfering RNAs and maturation of microRNAs. However, the eukaryotic pathways employing RNase III-like enzymes for pre-RNA processing do not rely on *trans*-encoded RNA factors. More studies are needed to determine whether an RNase III-mediated activation of a small effector RNA by co-processing with a *trans*-acting non-coding RNA is also used in other biological systems.

Figure 4 | Model for tracrRNA-mediated crRNA maturation involving RNase III and Csn1. Black, repeat; green, spacer. tracrRNA can bind with almost perfect complementarity to each repeat sequence of the pre-crRNA. The resulting RNA duplex is recognized and site-specifically diced by RNase III in the presence of Csn1, releasing the individual repeat-spacer-repeat units (first processing event). The generated units undergo further processing within the spacer sequences resulting in mature crRNA species consisting of unique spacer-repeat sequences (second processing event) by a yet-to-be elucidated mechanism. Csn1 may also be involved in the silencing of invading sequences.

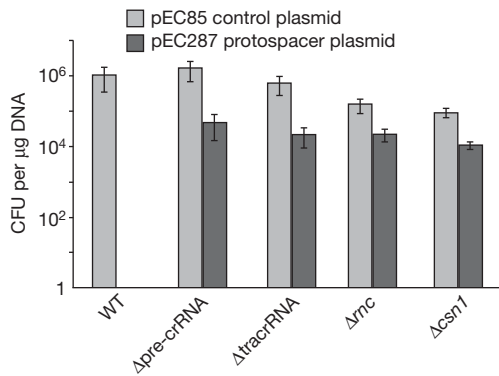


Figure 5 | Both tracrRNA and pre-crRNA confer immunity against acquisition of a protospacer gene derived from a lysogenic phage.

Transformation efficiencies of *S. pyogenes* with *speM* protospacer containing plasmid (pEC287) and reference 'backbone' plasmid (pEC85) (Supplementary Fig. 9). Strains: *S. pyogenes* wild type (WT; SF370), Δpre-crRNA, ΔtracrRNA, ΔtrnG and Δcsn1. Graph bars, mean values of colony forming units (CFU) per µg of plasmid DNA; error bars, s.d.; $n \geq 3$. pEC287 is tolerated by the Δpre-crRNA, ΔtracrRNA, ΔtrnG and Δcsn1 mutants but not by the WT strain. As control, transformants in all strains were obtained with the backbone plasmid (Supplementary Fig. 9).

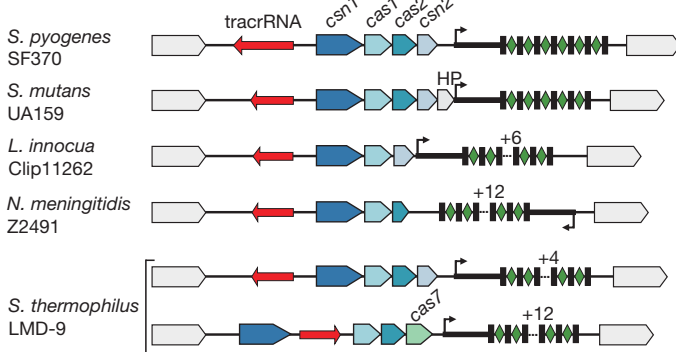


Figure 6 | tracrRNA-mediated crRNA maturation is conserved among different bacterial species. tracrRNA-mediated crRNA maturation is inherent to the type II (Nmeni/CASS4) CRISPR/Cas systems. Type II (Nmeni/CASS4) loci from *S. pyogenes* SF370, *S. mutans* UA159, *L. innocua* Clip11262, *N. meningitidis* Z2491 and *S. thermophilus* LMD-9 (Nmeni/CASS4a); red, tracrRNA; rectangles, repeats; diamonds, spacers.

METHODS SUMMARY

Details of bacteria (culture conditions, transformation), DNA (biocomputational analysis, plasmid construction, in-frame gene deletion mutants) and RNA manipulation (cDNA library construction (vertis Biotechnologie), RNA expression analysis, RNA structure probing and hydrolysis) are provided as Supplementary Information^{34,39,48}. In brief, half of DNase I-treated SF370 total RNA was enriched for primary transcripts by treatment with Terminator 5'-phosphate-dependent exonuclease (TEX) (Epicentre), which degrades RNAs with a 5' P (processed RNAs) but not primary transcripts with a 5' PPP RNA³⁹. cDNA libraries were constructed from both untreated and TEX-treated RNA³⁹. Following 454 pyrosequencing, cDNAs were mapped to the SF370 genome and visualized using the Affymetrix Integrated Genome Browser³⁹. Strains, plasmids and primers are listed in Supplementary Tables 8, 9 and 10, respectively.

Full Methods and any associated references are available in the online version of the paper at www.nature.com/nature.

Received 9 September 2010; accepted 28 January 2011.

1. Aliyari, R. & Ding, S. W. RNA-based viral immunity initiated by the Dicer family of host immune receptors. *Immunol. Rev.* **227**, 176–188 (2009).

- Carthew, R. W. & Sontheimer, E. J. Origins and mechanisms of miRNAs and siRNAs. *Cell* **136**, 642–655 (2009).
- Filipowicz, W., Bhattacharyya, S. N. & Sonenberg, N. Mechanisms of post-transcriptional regulation by microRNAs: are the answers in sight? *Nature Rev. Genet.* **9**, 102–114 (2008).
- Jinek, M. & Doudna, J. A. A three-dimensional view of the molecular machinery of RNA interference. *Nature* **457**, 405–412 (2009).
- Malone, C. D. & Hannon, G. J. Small RNAs as guardians of the genome. *Cell* **136**, 656–668 (2009).
- Meister, G. & Tuschl, T. Mechanisms of gene silencing by double-stranded RNA. *Nature* **431**, 343–349 (2004).
- Andersson, A. F. & Banfield, J. F. Virus population dynamics and acquired virus resistance in natural microbial communities. *Science* **320**, 1047–1050 (2008).
- Barrangou, R. et al. CRISPR provides acquired resistance against viruses in prokaryotes. *Science* **315**, 1709–1712 (2007).
- Deveau, H., Garneau, J. E. & Moineau, S. CRISPR/Cas system and its role in phage-bacteria interactions. *Annu. Rev. Microbiol.* **64**, 475–493 (2010).
- Horvath, P. & Barrangou, R. CRISPR/Cas, the immune system of bacteria and archaea. *Science* **327**, 167–170 (2010).
- Koonin, E. V. & Makarova, K. S. CRISPR-Cas: an adaptive immunity system in prokaryotes. *F1000 Biol. Rep.* **1**, 95 (2009).
- Marraffini, L. A. & Sontheimer, E. J. CRISPR interference: RNA-directed adaptive immunity in bacteria and archaea. *Nature Rev. Genet.* **11**, 181–190 (2010).
- Sorek, R., Kunin, V. & Hugenoltz, P. CRISPR—a widespread system that provides acquired resistance against phages in bacteria and archaea. *Nature Rev. Microbiol.* **6**, 181–186 (2008).
- van der Oost, J., Jore, M. M., Westra, E. R., Lundgren, M. & Brouns, S. J. CRISPR-based adaptive and heritable immunity in prokaryotes. *Trends Biochem. Sci.* **34**, 401–407 (2009).
- Mojica, F. J., Diez-Villasenor, C., Garcia-Martinez, J. & Soria, E. Intervening sequences of regularly spaced prokaryotic repeats derive from foreign genetic elements. *J. Mol. Evol.* **60**, 174–182 (2005).
- Bolotin, A., Quinquis, B., Sorokin, A. & Ehrlich, S. D. Clustered regularly interspaced short palindromic repeats (CRISPRs) have spacers of extrachromosomal origin. *Microbiology* **151**, 2551–2561 (2005).
- Pourcel, C., Salvignol, G. & Vergnaud, G. CRISPR elements in *Yersinia pestis* acquire new repeats by preferential uptake of bacteriophage DNA, and provide additional tools for evolutionary studies. *Microbiology* **151**, 653–663 (2005).
- van der Oost, J. & Brouns, S. J. RNAi: prokaryotes get in on the act. *Cell* **139**, 863–865 (2009).
- Jansen, R., Embden, J. D., Gaastra, W. & Schouls, L. M. Identification of genes that are associated with DNA repeats in prokaryotes. *Mol. Microbiol.* **43**, 1565–1575 (2002).
- Mojica, F. J., Ferrer, C., Juez, G. & Rodriguez-Valera, F. Long stretches of short tandem repeats are present in the largest replicons of the Archaea *Haloferax mediterranei* and *Haloferax volcanii* and could be involved in replicon partitioning. *Mol. Microbiol.* **17**, 85–93 (1995).
- Nakata, A., Amemura, M. & Makino, K. Unusual nucleotide arrangement with repeated sequences in the *Escherichia coli* K-12 chromosome. *J. Bacteriol.* **171**, 3553–3556 (1989).
- Waters, L. S. & Storz, G. Regulatory RNAs in bacteria. *Cell* **136**, 615–628 (2009).
- Makarova, K. S., Aravind, L., Grishin, N. V., Rogozin, I. B. & Koonin, E. V. A DNA repair system specific for thermophilic Archaea and bacteria predicted by genomic context analysis. *Nucleic Acids Res.* **30**, 482–496 (2002).
- Garneau, J. E. et al. The CRISPR/Cas bacterial immune system cleaves bacteriophage and plasmid DNA. *Nature* **468**, 67–71 (2010).
- Marraffini, L. A. & Sontheimer, E. J. CRISPR interference limits horizontal gene transfer in staphylococci by targeting DNA. *Science* **322**, 1843–1845 (2008).
- Hale, C. R. et al. RNA-guided RNA cleavage by a CRISPR RNA-Cas protein complex. *Cell* **139**, 945–956 (2009).
- Marraffini, L. A. & Sontheimer, E. J. Self versus non-self discrimination during CRISPR RNA-directed immunity. *Nature* **463**, 568–571 (2010).
- Carte, J., Wang, R., Li, H., Terns, R. M. & Terns, M. P. Cas6 is an endoribonuclease that generates guide RNAs for invader defense in prokaryotes. *Genes Dev.* **22**, 3489–3496 (2008).
- Brouns, S. J. et al. Small CRISPR RNAs guide antiviral defense in prokaryotes. *Science* **321**, 960–964 (2008).
- Haurwitz, R. E., Jinek, M., Wiedenheft, B., Zhou, K. & Doudna, J. A. Sequence- and structure-specific RNA processing by a CRISPR endonuclease. *Science* **329**, 1355–1358 (2010).
- Carte, J., Pfister, N. T., Compton, M. M., Terns, R. M. & Terns, M. P. Binding and cleavage of CRISPR RNA by Cas6. *RNA* **16**, 2181–2188 (2010).
- Haft, D. H., Selengut, J., Mongodin, E. F. & Nelson, K. E. A guild of 45 CRISPR-associated (Cas) protein families and multiple CRISPR/Cas subtypes exist in prokaryotic genomes. *PLOS Comput. Biol.* **1**, e60 (2005).
- Makarova, K. S., Grishin, N. V., Shabalina, S. A., Wolf, Y. I. & Koonin, E. V. A putative RNA-interference-based immune system in prokaryotes: computational analysis of the predicted enzymatic machinery, functional analogies with eukaryotic RNAi, and hypothetical mechanisms of action. *Biol. Direct* **1**, 7 (2006).
- Vojtek, I. et al. Lysogenic transfer of group A *Streptococcus* superantigen gene among streptococci. *J. Infect. Dis.* **197**, 225–234 (2008).
- Fischetti, V. A. In vivo acquisition of prophage in *Streptococcus pyogenes*. *Trends Microbiol.* **15**, 297–300 (2007).
- Brussow, H., Canchaya, C. & Hardt, W. D. Phages and the evolution of bacterial pathogens: from genomic rearrangements to lysogenic conversion. *Microbiol. Mol. Biol. Rev.* **68**, 560–602 (2004).

37. Banks, D. J., Beres, S. B. & Musser, J. M. The fundamental contribution of phages to GAS evolution, genome diversification and strain emergence. *Trends Microbiol.* **10**, 515–521 (2002).
38. Aziz, R. K. *et al.* Mosaic prophages with horizontally acquired genes account for the emergence and diversification of the globally disseminated M1T1 clone of *Streptococcus pyogenes*. *J. Bacteriol.* **187**, 3311–3318 (2005).
39. Sharma, C. M. *et al.* The primary transcriptome of the major human pathogen *Helicobacter pylori*. *Nature* **464**, 250–255 (2010).
40. Drider, D. & Condon, C. The continuing story of endoribonuclease III. *J. Mol. Microbiol. Biotechnol.* **8**, 195–200 (2004).
41. Huntzinger, E. *et al.* *Staphylococcus aureus* RNAIII and the endoribonuclease III coordinately regulate *spa* gene expression. *EMBO J.* **24**, 824–835 (2005).
42. Nicholson, A. W. Function, mechanism and regulation of bacterial ribonucleases. *FEMS Microbiol. Rev.* **23**, 371–390 (1999).
43. Vogel, J., Argaman, L., Wagner, E. G. & Altuvia, S. The small RNA IstR inhibits synthesis of an SOS-induced toxic peptide. *Curr. Biol.* **14**, 2271–2276 (2004).
44. Opdyke, J. A., Fozo, E. M., Hemm, M. R. & Storz, G. RNase III participates in GadY-dependent cleavage of the *gadX-gadW* mRNA. *J. Mol. Biol.* **406**, 29–43 (2010).
45. Carmell, M. A. & Hannon, G. J. RNase III enzymes and the initiation of gene silencing. *Nature Struct. Mol. Biol.* **11**, 214–218 (2004).
46. Condon, C. Maturation and degradation of RNA in bacteria. *Curr. Opin. Microbiol.* **10**, 271–278 (2007).
47. Kunin, V., Sorek, R. & Hugenholtz, P. Evolutionary conservation of sequence and secondary structures in CRISPR repeats. *Genome Biol.* **8**, R61 (2007).
48. Mangold, M. *et al.* Synthesis of group A streptococcal virulence factors is controlled by a regulatory RNA molecule. *Mol. Microbiol.* **53**, 1515–1527 (2004).

Supplementary Information is linked to the online version of the paper at www.nature.com/nature.

Acknowledgements We thank D. Veit for technical help. This work was funded by the European Community (FP6, BACRNAs-018618; E.C.), the Austrian Science Fund (FWF, P17238-B09 (E.C.) and W1207-B09 (E.C., K.C.)), the Austrian Agency for Research Promotion (FFG, 812138-SCK/KUG; E.C.), the Theodor Körner Fonds (E.C.), Umeå University (E.C.), the Swedish Research Council (E.C.), IMPRS-IDI (Y.C.), the German Research Council (DFG Priority Program “Sensory and Regulatory RNAs in Prokaryotes” SPP1258, Vo875/4; J.V.), and the German Ministry of Education and Research (BMBF, 01GS0806/JV-BMBF-01 and 0315836; J.V.).

Author Contributions E.D., K.C., C.M.S., K.G., J.V. and E.C. designed the research; E.D., K.C., C.M.S., K.G., Z.A.P., Y.C. and M.R.E. conducted the experiments; E.D., K.C., C.M.S., K.G., J.V. and E.C. analysed and interpreted the data; E.C. wrote the paper which E.D., K.C., C.M.S. and J.V. commented on, and supervised the project. Author information and raw data are available from E.D., K.C., C.M.S., J.V. and E.C.

Author Information Reprints and permissions information is available at www.nature.com/reprints. The authors declare no competing financial interests. Readers are welcome to comment on the online version of this article at www.nature.com/nature. Correspondence and requests for materials should be addressed to E.C. (emmanuelle.charpentier@mims.umu.se).

METHODS

Bacterial strains and culture conditions. Bacterial strains used in the study are listed in Supplementary Table 8. *Streptococcus pyogenes* and *Streptococcus mutans* were cultured in THY medium (Todd Hewitt Broth (THB, Bacto, Becton Dickinson) supplemented with 0.2% yeast extract (Oxoid)) or on TSA (trypticase soy agar, BBL, Becton Dickinson) supplemented with 3% sheep blood. BHI broth (brain heart infusion) and BHI agar were used for growth of *Listeria innocua* and *Staphylococcus epidermidis*. *Streptococcus thermophilus* was grown in M17 broth supplemented with 0.5% (w/v) lactose (LM17)⁴⁹ or on BHI agar. *Escherichia coli* was cultured in Luria–Bertani (LB) medium and agar. *Neisseria meningitidis* cells were grown on GC-agar and in PPM liquid medium including 1% vitamin-mix and 0.5% NaHCO₃. Cultures of *S. mutans*, *S. pyogenes* and *S. thermophilus* were incubated at 37 °C (*S. mutans*, *S. pyogenes*) or 42 °C (*S. thermophilus*) in an atmosphere supplemented with 5% CO₂ without shaking. Strains of *E. coli*, *L. innocua*, *N. meningitidis* and *S. epidermidis* were grown aerobically at 37 °C with shaking. Whenever required, suitable antibiotics were added to the medium at the following final concentrations: ampicillin, 100 µg ml⁻¹ for *E. coli*; kanamycin, 25 µg ml⁻¹ for *E. coli* and 300 µg ml⁻¹ for *S. pyogenes*. Bacterial cell growth was monitored periodically by measuring the absorbance (A) of culture aliquots at 620 nm using a microplate reader (SLT Spectra Reader).

Bacterial transformation. Transformation of *E. coli* with plasmid DNA was carried out according to standard protocols⁵⁰. Transformation of *S. pyogenes* was performed as previously described⁵¹ with some modifications. For the transformation read-out experiment, *S. pyogenes* electrocompetent cells were equalized to the same A_{620 nm} and subsequently used for electroporation with 500 ng of plasmid. Transformations were done in triplicate with the same batch of electrocompetent cells. Each transformation was plated three to four times. Experiments were performed at least three times independently for statistical analysis. Transformation efficiencies were calculated as colony-forming units per µg of DNA. Mock and control transformations were done with sterile dH₂O and backbone ‘empty’ plasmid pEC85, respectively.

DNA manipulations. DNA manipulations including DNA preparation, amplification, digestion, ligation, purification, agarose gel electrophoresis and Southern blot analysis were performed according to standard techniques⁵⁰ with some modifications. Site-directed mutagenesis in plasmid inserts was done using QuickChange II XL kit (Stratagene). Kits (Peqlab Biotechnology and Qiagen) were used for plasmid preparation and DNA purification with minor modifications. Synthetic oligonucleotides used in this study were supplied by VBC-Biotech Services and Sigma-Aldrich and are listed in Supplementary Table 10. When required (for example, further use in cloning experiments, verification of in-frame gene deletion mutants), PCR-generated DNA fragments and plasmid inserts were sequenced at VBC-Biotech Services and LGC Genomics. All plasmids generated in this study are listed in Supplementary Table 9.

In-frame gene deletion in *S. pyogenes*. The following procedure was used for the generation of Δ tracrRNA, Δ pre-crRNA, Δ csn1-cas1-cas2-csn2, Δ csn1, Δ cas1, Δ cas2, Δ csn2 and Δ rnc mutants in *S. pyogenes* wild-type (WT) SF370 (M1 serotype). Briefly, we constructed the shuttle vector pEC214 that includes a thermosensitive origin of replication (pWV01-*repA*) specific for Gram-positive bacteria⁴⁸, the ColE1 replicon specific for *E. coli*⁵², a kanamycin resistance cassette (*aphIII*) for plasmid selection in both *E. coli* and Gram-positive bacteria⁵², a thermostable β -galactosidase cassette (*bgaB*) under the control of the *Staphylococcus aureus* *clpB* promoter for plasmid loss selection⁵³ and a multiple-cloning site (MCS)⁵² (Supplementary Table 9). For each in-frame gene deletion, DNA fragments located upstream and downstream of the gene of interest were amplified by PCR using genomic DNA of *S. pyogenes* SF370 and primers containing flanking restriction sites (Supplementary Table 10). The amplified fragments were then cloned in the MCS of pEC214, thus generating thermosensitive plasmids containing a DNA region with in-frame deletion of the gene of interest (Supplementary Table 9). Each recombinant plasmid was introduced in *S. pyogenes* SF370 by electroporation at the permissive temperature (28 °C). A series of incubation at the non-permissive temperature (37 °C) and the permissive temperature (28 °C)⁴⁸ led to the selection of in-frame gene deletion mutants sensitive to kanamycin (Supplementary Table 8). Kanamycin-sensitive wild-type (WTs) clones issued from the same temperature shift procedure were also kept for comparative analysis. In this study, the phenotypes of all control WTs strains were identical to that of the wild-type (WT) strain. This indicated that the phenotypes observed in the in-frame gene deletion mutants were not caused by mutations, which would have occurred somewhere else on the chromosome during the recombination procedure (Supplementary Table 8). The correct deletion and non-deletion events in selected clones were verified by PCR, sequencing and Southern blot analyses (Supplementary Table 10). Reverse transcription–PCR (RT–PCR) analysis of the in-frame Δ rnc, Δ csn1, Δ cas1, Δ cas2 and Δ csn2 mutants demonstrated that each deletion of the single genes did not affect the expression of the other genes in the operons

(operon *rnc-smc*, Supplementary Fig. 6, and operon *csn1-cas1-cas2-csn2*, Supplementary Fig. 8) (data not shown). RT–PCR analysis also showed *rnc* expression in Δ csn1 and *csn1* expression in Δ rnc (data not shown).

Construction of plasmids for complementation studies in *S. pyogenes*. Plasmid pEC85 containing an origin of replication specific for Gram-positive bacteria (*repDEG*-pAM β 1)⁵⁴, the ColE1 replicon specific for *E. coli*⁵², a kanamycin resistance cassette (*aphIII*) for selection in both *E. coli* and Gram-positive bacteria⁵², and an expanded MCS⁵⁴ was used as vector for complementation studies. For tracrRNA, CRISPR01 pre-crRNA and *rnc* complementation plasmids, a RNA-(tracrRNA and pre-crRNA) or protein-(*rnc*) encoding DNA fragment of interest under the control of the native promoter was cloned in pEC85 (Supplementary Tables 9, 10). For *csn1*, *cas1*, *cas2* and *csn2* complementation plasmids, a DNA fragment containing the coding sequence of the gene of interest under the control of the promoter of the *csn1-cas1-cas2-csn2* operon was cloned in pEC85 (Supplementary Tables 9, 10). The generated recombinant plasmids were introduced in *S. pyogenes* mutant strains selecting for kanamycin resistant clones (Supplementary Table 8). The integrity of plasmids was verified by plasmid digestion and sequencing analysis. In addition, RT–PCR analysis was conducted to verify that the genes (encoding RNAs or proteins) in the inserts of the recombinant plasmids were expressed in the recombinant *S. pyogenes* strains (data not shown).

Construction of plasmids for transformation studies in *S. pyogenes*. Plasmid pEC85 described above was used as vector for transformation studies. A control DNA fragment and DNA fragments containing wild-type and mutated protospacers were cloned in pEC85 (Supplementary Tables 9, 10). The integrity of the cloned plasmids was verified by enzymatic digestion and sequencing analysis. The generated recombinant plasmids were introduced in *S. pyogenes* wild-type and mutant strains, selecting for kanamycin resistant clones (Supplementary Table 8). The integrity of plasmids was verified in selected clones by plasmid digestion and northern blot analysis of protospacer expression (Supplementary Table 10 and Supplementary Fig. 9).

RNA preparation. Total RNA from streptococcal, staphylococcal, listerial and neisserial cells was prepared from culture samples collected at different time points during growth^{48,54,55}, using the TRIzol reagent (Sigma-Aldrich) with some modifications. The total RNA samples were treated with DNase I (Fermentas) according to the manufacturer's instructions. The concentration of RNA in each sample was further normalized following spectrophotometry measurements using NanoDrop.

cDNA library for differential RNA sequencing (dRNA-seq) and 454 pyrosequencing. In brief, total RNA from *S. pyogenes* SF370 (M1 serotype) cells grown until mid-logarithmic phase was treated with DNase I to remove any residual genomic DNA³⁹. The RNA was submitted to a new treatment protocol to deplete processed transcripts and thereby enrich for primary transcripts by using Terminator 5'-phosphate-dependent exonuclease (TEX) (Epicentre)³⁹. A cDNA library from the TEX-treated and untreated RNA was constructed by Vertis Biotechnologie and a total of 38,468 DNAs was sequenced. After 5'-end-linker and poly(A)-tail clipping, cDNAs longer than 17 nucleotides (87%) were mapped to the *S. pyogenes* M1 GAS genome (NC_02737) using WU-BLAST 2.0 (<http://blast.wustl.edu/>) as previously described⁵⁶. Afterwards, mapping data were visualized using the ‘Integrated Genome Browser’ (Affymetrix). Small RNA candidates were selected on the basis of the following criteria: encoded in intergenic regions, size ranging from 50 to 500 nucleotides, presence of a putative promoter (BPROM software) and/or Rho-independent transcription terminator (TransTermHP (v2.04) program) (see below for references).

Northern blot analysis. Northern blot analysis was carried out essentially as described elsewhere^{55,57,58}. RNAs separated on 10 or 12% polyacrylamide gels containing 8 M urea were blotted onto Hybond-N+ or Hybond-XL membranes (General Electric Healthcare) and then hybridized with specific probes. In general, ³²P-labelled primers specific to the RNAs of interest were used as probes (Supplementary Table 10). For primer labelling, 40 pmol of oligonucleotide were denatured for 5 min at 95 °C and then mixed with 20 µCi of ³²P- γ -ATP and 10 U of T4 polynucleotide kinase (Fermentas). Labelled probes were purified before hybridization using G25 columns (GE Healthcare) in order to remove unincorporated nucleotides. For all northern blots, 5S rRNA served as loading control.

RNA metabolic stability analysis. The metabolic stability of RNAs was determined as previously described⁵⁹ with minor modifications. Cells were grown until mid-logarithmic phase, at which time point rifampicin (250 µg ml⁻¹, Sigma-Aldrich) was added. Aliquots of cells were collected before treatment (control), immediately after (0 min) and at defined time points after addition of rifampicin. A mixture of ice-cold acetone-ethanol (vol:vol, 1:1) was added and cells were frozen immediately at -80 °C. Total RNA was prepared and analysed by northern blot analysis as described above. RNA half-life (*t*_{1/2}) was calculated by automated pixel counting using the ImageQuant v5.1 software, referring to 5S rRNA as loading control. To ensure absence of rifampicin-resistant bacteria, serial

dilutions of the rifampicin-treated cells were plated on TSA blood plates with or without rifampicin ($250 \mu\text{g ml}^{-1}$), incubated overnight at 37°C and then visualized for the possible appearance of colonies.

RT-PCR analysis. RT-PCR analysis of RNA samples was done using the OneStep RT-PCR Kit (Qiagen) according to the manufacturer's instructions and primers listed in Supplementary Table 10. For the semiquantitative analysis, RNA samples were serial-diluted before reverse transcription and PCR. DNase I-treated RNA samples (8 ng to $1 \mu\text{g}$; TURBO DNA-free, Ambion) were used. Quantification of RT-PCR fragments was done using 5S rRNA or transfer-messenger RNA (tmRNA) as loading control.

RNA mapping. Head-to-tail RNA circularization and/or primer extension were used to map the RNA termini. (1) Head-to-tail RNA circularization: this method and its suitability to simultaneously map the 5' and 3' ends of RNAs was described elsewhere⁶⁰. Briefly, total RNA was treated with tobacco acid pyrophosphatase (TAP, Epicentre Biotechnologies) according to the supplier's instructions and the treated RNA was purified by acid:phenol:chloroform (Ambion) extraction and precipitation. RNAs were circularized using T4 RNA Ligase I (New England Biolabs) followed by purification using acid phenol:chloroform extraction and precipitation. The purified circularized RNAs were reverse transcribed and amplified by PCR using inward RNA-specific primers (Supplementary Table 10) and the OneStep RT-PCR Kit (Qiagen). The generated PCR fragments were cloned into pCR2.1-TOPO vector using TOPO TA cloning kit (Invitrogen) and the inserts of three to five clones were sequenced. (2) Primer extension: 5 to $10 \mu\text{g}$ of total RNA were denatured in presence of 5' radiolabelled reverse primer. Reverse transcription was done using ThermoScript Reverse Transcriptase (Invitrogen) following the manufacturer's instructions. The reverse transcription reaction was subsequently separated on 8% polyacrylamide/8 M urea gel and analysed in reference to the PhiX174/HinfI ladder (Fermentas).

In vitro transcription, purification and 5' end labelling of RNA. DNA templates carrying a T7 promoter sequence for *in vitro* transcription were generated by PCR using genomic DNA of *S. pyogenes* SF370 and primers listed in Supplementary Table 10. RNA was *in vitro* transcribed, gel-purified and quality-checked as described earlier⁶¹. 5' labelling of RNA was done according to a previously published protocol⁶².

In vitro RNA structure mapping and footprinting. Secondary structure probing and mapping of RNA complexes was conducted on 5'-end-labelled RNA ($\sim 0.1 \text{ pmol}$) in $10 \mu\text{l}$ reactions. RNA was denatured 1 min at 95°C and chilled on ice for 5 min, upon which $1 \mu\text{g}$ yeast RNA and $10\times$ structure buffer (0.1 M Tris pH 7, 1 M KCl, 0.1 M MgCl_2 , Ambion) were added. Concentrations of unlabelled tracrRNA/crRNA fragments added to the reactions are given in the figure legends. Following incubation for 10 min at 37°C , $2 \mu\text{l}$ of a fresh solution of lead(II) acetate (25 mM; Fluka), or $2 \mu\text{l}$ of RNase T1 ($0.05 \text{ U } \mu\text{l}^{-1}$; Ambion) were added and incubated for 1 and 3 min at 37°C , respectively. RNase III cleavage reactions contained 1 mM DTT and 0.0026 units ($1 \mu\text{l}$ of a 1:500 dilution of the $1.3 \text{ U } \mu\text{l}^{-1}$ enzyme stock) enzyme (RNase III from *E. coli*, New England Biolabs), and were incubated for 3 min at 37°C . Reactions were stopped by direct addition of $12 \mu\text{l}$ loading buffer on ice. RNase T1 ladders were obtained by incubating labelled RNA ($\sim 0.2 \text{ pmol}$) in $1\times$ sequencing buffer (Ambion) for 1 min at 95°C . Subsequently, $1 \mu\text{l}$ RNase T1 ($0.1 \text{ U } \mu\text{l}^{-1}$) was added and incubation was continued at 37°C for 5 min. OH ladders were generated by 5 min incubation of 0.2 pmol labelled RNA in alkaline hydrolysis buffer (Ambion) at 95°C . Reactions were stopped with $12 \mu\text{l}$ loading buffer II (Ambion). Samples were denatured for 3 min at 95°C before separation on 6% or 8% polyacrylamide/7 M urea sequencing gels in $1\times$ TBE. Gels were dried and analysed using a PhosphorImager (FLA-3000 Series, Fuji) and AIDA software (Raytest).

Computational analysis of DNA and protein sequences. Gene annotations are according to NCBI genome browser and KEGG (Kyoto Encyclopedia of Genes and Genomes; <http://www.genome.jp/kegg/>). DNA sequence analysis for genetic locus organization and plasmid generation was done using the Vector NTI software (Invitrogen). Comparative sequence analysis of DNA and putative proteins was done using BLAST (<http://www.ncbi.nlm.nih.gov/BLAST/>). ClustalW2 (<http://www.ebi.ac.uk/Tools/clustalw2/index.html>) and AlignX (Invitrogen) were used for sequence alignments. Putative rho-independent transcription terminators (RITs) were annotated using the TransTermHP (v2.04) program (<http://transterm.cbcb.umd.edu/>)⁶³. Putative promoters were predicted using the BPROM software (<http://www.softberry.com/>) and BDGP Neural Network Promoter Prediction NNPP version 2.2 (http://www.fruitfly.org/seq_tools/promoter.html).

Computational predictions of RNA structure and co-folding. Computational predictions were done using algorithms of the Vienna RNA package^{64,65}. RNA secondary structures were predicted with RNAfold, co-folding was done using RNAcofold and co-folded secondary structures were drawn using VARNA⁶⁶.

49. Deveau, H. *et al.* Phage response to CRISPR-encoded resistance in *Streptococcus thermophilus*. *J. Bacteriol.* **190**, 1390–1400 (2008).
50. Sambrook, J., Fritsch, E. F. & Maniatis, T. *Molecular Cloning: a Laboratory Manual* 2nd edn (Cold Spring Harbor Laboratory Press, 1989).
51. Caparon, M. G. & Scott, J. R. Genetic manipulation of pathogenic streptococci. *Methods Enzymol.* **204**, 556–586 (1991).
52. Charpentier, E. *et al.* Novel cassette-based shuttle vector system for gram-positive bacteria. *Appl. Environ. Microbiol.* **70**, 6076–6085 (2004).
53. Arnaud, M., Chastanet, A. & Debarbouille, M. New vector for efficient allelic replacement in naturally nontransformable, low-GC-content, gram-positive bacteria. *Appl. Environ. Microbiol.* **70**, 6887–6891 (2004).
54. Siller, M. *et al.* Functional analysis of the group A streptococcal *luxS*/AI-2 system in metabolism, adaptation to stress and interaction with host cells. *BMC Microbiol.* **8**, 188 (2008).
55. Urban, J. H. & Vogel, J. Translational control and target recognition by *Escherichia coli* small RNAs *in vivo*. *Nucleic Acids Res.* **35**, 1018–1037 (2007).
56. Sittka, A. *et al.* Deep sequencing analysis of small noncoding RNA and mRNA targets of the global post-transcriptional regulator, Hfq. *PLoS Genet.* **4**, e1000163 (2008).
57. Herbert, S., Barry, P. & Novick, R. P. Subinhibitory clindamycin differentially inhibits transcription of exoprotein genes in *Staphylococcus aureus*. *Infect. Immun.* **69**, 2996–3003 (2001).
58. Pall, G. S. & Hamilton, A. J. Improved northern blot method for enhanced detection of small RNA. *Nature Protocols* **3**, 1077–1084 (2008).
59. Roberts, C. *et al.* Characterizing the effect of the *Staphylococcus aureus* virulence factor regulator, SarA, on log-phase mRNA half-lives. *J. Bacteriol.* **188**, 2593–2603 (2006).
60. Britton, R. A. *et al.* Maturation of the 5' end of *Bacillus subtilis* 16S rRNA by the essential ribonuclease YkqC/RNase J1. *Mol. Microbiol.* **63**, 127–138 (2007).
61. Sittka, A., Pfeiffer, V., Tedin, K. & Vogel, J. The RNA chaperone Hfq is essential for the virulence of *Salmonella typhimurium*. *Mol. Microbiol.* **63**, 193–217 (2007).
62. Papenfort, K. *et al.* SigmaE-dependent small RNAs of *Salmonella* respond to membrane stress by accelerating global *omp* mRNA decay. *Mol. Microbiol.* **62**, 1674–1688 (2006).
63. Kingsford, C. L., Ayanbule, K. & Salzberg, S. L. Rapid, accurate, computational discovery of Rho-independent transcription terminators illuminates their relationship to DNA uptake. *Genome Biol.* **8**, R22 (2007).
64. Denman, R. B. Using RNAfold to predict the activity of small catalytic RNAs. *Biotechniques* **15**, 1090–1095 (1993).
65. Hofacker, I. L. & Stadler, P. F. Memory efficient folding algorithms for circular RNA secondary structures. *Bioinformatics* **22**, 1172–1176 (2006).
66. Darty, K., Denise, A. & Ponty, Y. VARNA: Interactive drawing and editing of the RNA secondary structure. *Bioinformatics* **25**, 1974–1975 (2009).

Gravity modes as a way to distinguish between hydrogen- and helium-burning red giant stars

Timothy R. Bedding¹, Benoit Mosser², Daniel Huber¹, Josefina Montalbán³, Paul Beck⁴, Jørgen Christensen-Dalsgaard⁵, Yvonne P. Elsworth⁶, Rafael A. García⁷, Andrea Miglio^{3,6}, Dennis Stello¹, Timothy R. White¹, Joris De Ridder⁴, Saskia Hekker^{6,8}, Conny Aerts^{4,9}, Caroline Barban², Kevin Belkacem¹⁰, Anne-Marie Broomhall⁶, Timothy M. Brown¹¹, Derek L. Buzasi¹², Fabien Carrier⁴, William J. Chaplin⁶, Maria Pia Di Mauro¹³, Marc-Antoine Dupret³, Søren Frandsen⁵, Ronald L. Gilliland¹⁴, Marie-Jo Goupil², Jon M. Jenkins¹⁵, Thomas Kallinger¹⁶, Steven Kawaler¹⁷, Hans Kjeldsen⁵, Savita Mathur¹⁸, Arlette Noels³, Victor Silva Aguirre¹⁹ & Paolo Ventura²⁰

Red giants are evolved stars that have exhausted the supply of hydrogen in their cores and instead burn hydrogen in a surrounding shell^{1,2}. Once a red giant is sufficiently evolved, the helium in the core also undergoes fusion³. Outstanding issues in our understanding of red giants include uncertainties in the amount of mass lost at the surface before helium ignition and the amount of internal mixing from rotation and other processes⁴. Progress is hampered by our inability to distinguish between red giants burning helium in the core and those still only burning hydrogen in a shell. Asteroseismology offers a way forward, being a powerful tool for probing the internal structures of stars using their natural oscillation frequencies⁵. Here we report observations of gravity-mode period spacings in red giants⁶ that permit a distinction between evolutionary stages to be made. We use high-precision photometry obtained by the Kepler spacecraft over more than a year to measure oscillations in several hundred red giants. We find many stars whose dipole modes show sequences with approximately regular period spacings. These stars fall into two clear groups, allowing us to distinguish unambiguously between hydrogen-shell-burning stars (period spacing mostly ~50 seconds) and those that are also burning helium (period spacing ~100 to 300 seconds).

Oscillations in red giants, like those in the Sun, are thought to be excited by near-surface convection. The observed oscillation spectra are indeed remarkably Sun-like, with a broad range of radial and non-radial modes in a characteristic comb pattern^{7–11}. However, theoretical models of red giants^{12–16} reveal a more complicated story for the non-radial modes (those with angular degree $l \geq 1$), and it has been suggested that this offers a means to determine the evolutionary states of these stars¹⁵. Owing to the large density gradient outside the helium core, a red giant is effectively divided into two cavities. In the envelope, the oscillations have properties of acoustic pressure modes (p modes), but in the core, they behave like gravity modes (g modes), with buoyancy as the restoring force. The models predict a very dense spectrum of these so-called mixed modes for each value of l (except $l = 0$, as radial g modes do not exist). Most mixed modes have a much larger amplitude in the core than in the envelope, and we refer to them as g-dominated mixed modes. Like pure g modes, they are approximately equally spaced in period^{17,18}, and measuring their average period spacing (ΔP) would give a valuable new asteroseismic probe of the cores of

red giants. Unfortunately, they have very high inertias (the total interior mass that is affected by the oscillation), which leads to a very low amplitude at the stellar surface and makes them essentially impossible to observe. However, because of resonant coupling between the two cavities, some of the mixed modes have an enhanced amplitude in the envelope, making them more like p modes. These p-dominated mixed modes have a lower inertia than the g-dominated mixed modes, and so their amplitudes can be high enough to render them observable. We expect their frequencies to be shifted from the regular asymptotic spacing, a feature known as ‘mode bumping’¹⁹.

Figure 1a shows theoretical oscillation frequencies in a red giant of mass $1.5 M_{\odot}$ (where M_{\odot} is the solar mass). The dashed lines show the radial modes ($l = 0$), whose frequencies decrease with time as the envelope of the star expands. These are pure p modes and are approximately equally spaced in frequency, with a separation of $\Delta \nu$. The solid lines show the much denser spectrum of dipole modes ($l = 1$). The g-dominated mixed modes appear as upward-sloping lines whose frequencies increase with time as the stellar core contracts. These modes are approximately equally spaced in period. The downward-sloping features that run parallel to the $l = 0$ modes are produced by mode bumping: the p-dominated mixed modes, with frequencies decreasing with age, undergo avoided crossings¹⁹ with the g-dominated mixed modes. A similar pattern of mode bumping and avoided crossings is seen in models of subgiant stars^{13,20}.

In Fig. 1b we show the period spacings between adjacent $l = 1$ modes in one of the models, indicated in Fig. 1a with the vertical line. The dips in Fig. 1b correspond to bumped modes that are squeezed together. The period spacing of the g-dominated modes (ΔP_g) can be measured from the upper envelope but cannot be observed directly because only the bumped modes have enough p-mode character to be detected, by virtue of their reduced mode inertias^{6,12–14}. Observations will detect only a few modes in each p-mode order, and the average spacings of those observable sequences (ΔP_{obs}) will be less than the true g-mode spacing by up to a factor of two (the actual value depends on the number of modes detected, which is a function of the signal-to-noise ratio in the data, and on the strength of the coupling between the g- and p-mode cavities²⁰). Figure 1c shows the mode frequencies of the model in Fig. 1b displayed in échelle format, where the spectrum has been divided into segments that are stacked one above the other. Note

¹Sydney Institute for Astronomy (SIfA), School of Physics, University of Sydney, New South Wales 2006, Australia. ²LESIA, CNRS, Université Pierre et Marie Curie, Université Denis Diderot, Observatoire de Paris, 92195 Meudon cedex, France. ³Institut d'Astrophysique et de Géophysique de l'Université de Liège, Allée du 6 Août 17, B 4000 Liège, Belgium. ⁴Instituut voor Sterrenkunde, KU Leuven, Celestijnenlaan 200D, 3001 Leuven, Belgium. ⁵Danish Asteroseismology Centre (DASC), Department of Physics and Astronomy, Aarhus University, DK-8000 Aarhus C, Denmark. ⁶School of Physics and Astronomy, University of Birmingham, Birmingham B15 2TT, UK. ⁷Laboratoire AIM, CEA/DSM-CNRS, Université Paris 7 Diderot, IRFU/SAP, Centre de Saclay, 91191 Gif-sur-Yvette, France. ⁸Astronomical Institute 'Anton Pannekoek', University of Amsterdam, Science Park 904, 1098 XH Amsterdam, The Netherlands. ⁹IMAPP, Department of Astrophysics, Radboud University Nijmegen, PO Box 9010, 6500 GL Nijmegen, The Netherlands. ¹⁰Institut d'Astrophysique Spatiale, UMR 8617, Université Paris XI, Bâtiment 121, 91405 Orsay Cedex, France. ¹¹Las Cumbres Observatory Global Telescope, Goleta, California 93117, USA. ¹²Eureka Scientific, 2452 Delmer Street Suite 100, Oakland, California 94602-3017, USA. ¹³INAF – IASF, Istituto di Astrofisica Spaziale e Fisica Cosmica, Via del Fosso del Cavaliere 100, 00133 Roma, Italy. ¹⁴Space Telescope Science Institute, 3700 San Martin Drive, Baltimore, Maryland 21218, USA. ¹⁵SETI Institute/NASA Ames Research Center, MS 244-30, Moffett Field, California 94035, USA. ¹⁶Department of Physics and Astronomy, University of British Columbia, 6224 Agricultural Road, Vancouver, British Columbia V6T 1Z1, Canada. ¹⁷Department of Physics and Astronomy, Iowa State University, Ames, Iowa 50011, USA. ¹⁸High Altitude Observatory, NCAR, PO Box 3000, Boulder, Colorado 80307, USA. ¹⁹Max-Planck-Institut für Astrophysik, Karl-Schwarzschild-Str. 1, 85748 Garching, Germany. ²⁰INAF – Osservatorio Astronomico di Roma, Via Frascati 33, 00040 Monte Porzio Catone (RM), Italy.

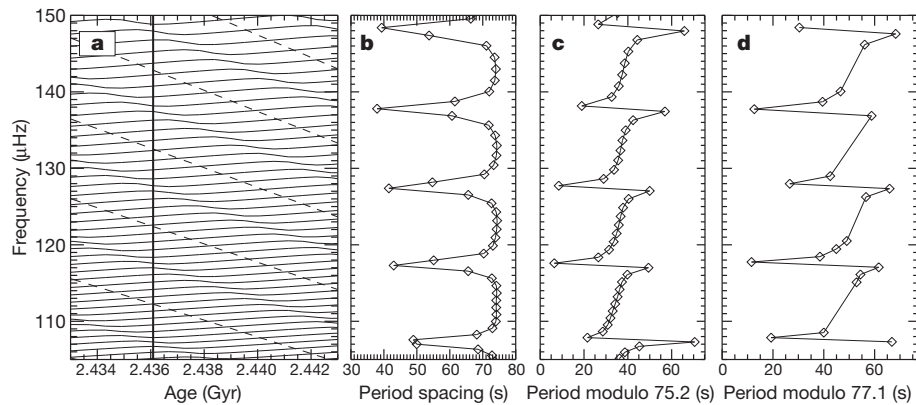


Figure 1 | Mixed modes and avoided crossings in red giant stars.

a, Evolution with time of oscillation frequencies in a model of a hydrogen-shell-burning red giant with a mass of $1.5M_{\odot}$ and solar metallicity, calculated using the Aarhus stellar evolution code ASTEC²⁷. Dashed lines show radial modes ($l=0$) and solid lines show dipole modes ($l=1$). The models span ranges in radius and luminosity of $6.3\text{--}6.7R_{\odot}$ and $19.1\text{--}21.4L_{\odot}$, respectively (here R_{\odot} is the solar radius, and L_{\odot} the solar luminosity). **b**, Period spacings between adjacent $l=1$ modes for the model marked with a vertical line in **a**. The period spacing of the g-dominated modes (ΔP_g) can be seen from the maximum values to be about 75 s. Note that model frequencies were not corrected for near-

surface effects^{6,28}, which would have a small effect on the period spacings.

c, Échelle diagram of $l=1$ modes for the same model as shown in **b**. Here, the oscillation spectrum has been divided into segments of fixed length that are stacked one above the other. Note that the abscissa is the period modulo the g-mode period spacing, ΔP_g (whereas a conventional échelle diagram plots frequencies modulo the p-mode frequency spacing, $\Delta\nu$). **d**, Échelle diagram of observed $l=1$ frequencies in the star KIC 6928997. We conclude that the true g-mode spacing is $\Delta P_g = 77.1$ s, whereas the average spacing of the observed modes⁶ was found to be $\Delta P_{\text{obs}} \approx 55$ s.

that the abscissa shows the period modulo ΔP_g (that is, the remainder after dividing by ΔP_g), whereas a conventional échelle diagram plots frequencies modulo the p-mode frequency spacing, $\Delta\nu$.

Sequences of $l=1$ modes with approximately constant period spacings were first observed in the red giant KIC 6928997 (ref. 6), and we have found similar patterns in several hundred more stars. The observations were obtained with the Kepler satellite over the first 13 months of its mission and were sampled every 29.4 min in the long-cadence mode²¹. Figure 1d shows the period échelle diagram for KIC 6928997, and allows us to estimate the spacing of the g-dominated modes to be $\Delta P_g = 77.1$ s, which is the value required to produce a vertical alignment. Remarkably, we have been able to estimate ΔP_g despite the fact that g-dominated modes are not observed (the average spacing of the observed modes⁶ is $\Delta P_{\text{obs}} \approx 55$ s).

Figure 2 compares observed power spectra of two red giants that have similar p-mode spacings ($\Delta\nu \approx 8\text{ }\mu\text{Hz}$) but very different $l=1$ period spacings. We note that the outermost peaks in each $l=1$ cluster

(values of l are given above the peaks), which we expect to be the closest in character to the g-dominated modes, appear to be the narrowest. This observation is consistent with theoretical calculations of mode inertias and lifetimes^{13–16}. Once again, we have detected enough modes to determine ΔP_g unambiguously using échelle diagrams (right panels). We find ΔP_g for the two stars to differ by about a factor of two, implying they have very different core properties.

Inferring ΔP_g in this way using the period échelle diagram is not possible for most of the stars in our sample, because it requires at least 3–4 modes to be detected in several of the $l=1$ clusters, which is only possible for the stars with the best signal-to-noise ratio. Therefore, we have instead measured the average period spacing of the observed $l=1$ modes (ΔP_{obs}) by using the power spectrum of the power spectrum. In this method, the power spectrum was first expressed in period rather than frequency and then set to zero in regions not containing power from the $l=1$ modes, as determined using the methods of ref. 10. The power spectrum of this power spectrum was then calculated in order to

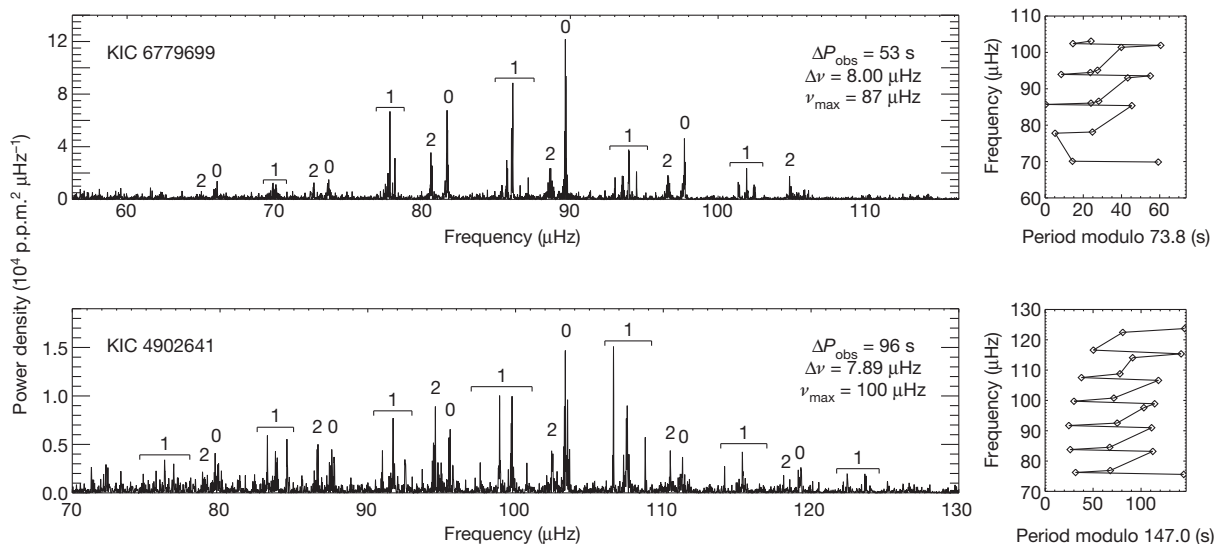


Figure 2 | Oscillation power spectra and échelle diagrams of two red giant stars observed with Kepler. Top, KIC 6779699; bottom, KIC 4902641: left, power spectra; right, échelle diagrams. The difference in the spacings of the $l=1$ modes indicates that KIC 6779699 is undergoing hydrogen-shell-burning

on the red giant branch, while KIC 4902641 is also burning helium in its core (see Fig. 3). Observations of KIC 6779699 were made over the first 13 months of the Kepler mission (Q0–Q5, where Q indicates the quarter), while those of KIC 4902641 were made over the first 10 months (Q0–Q4).

determine the most prominent period spacing. For the reasons mentioned above, we expect ΔP_{obs} to be less than ΔP_g and we have measured the ratio between them to be in the range 1.3–1.6 in the few cases where ΔP_g can be estimated unambiguously. Two other methods to

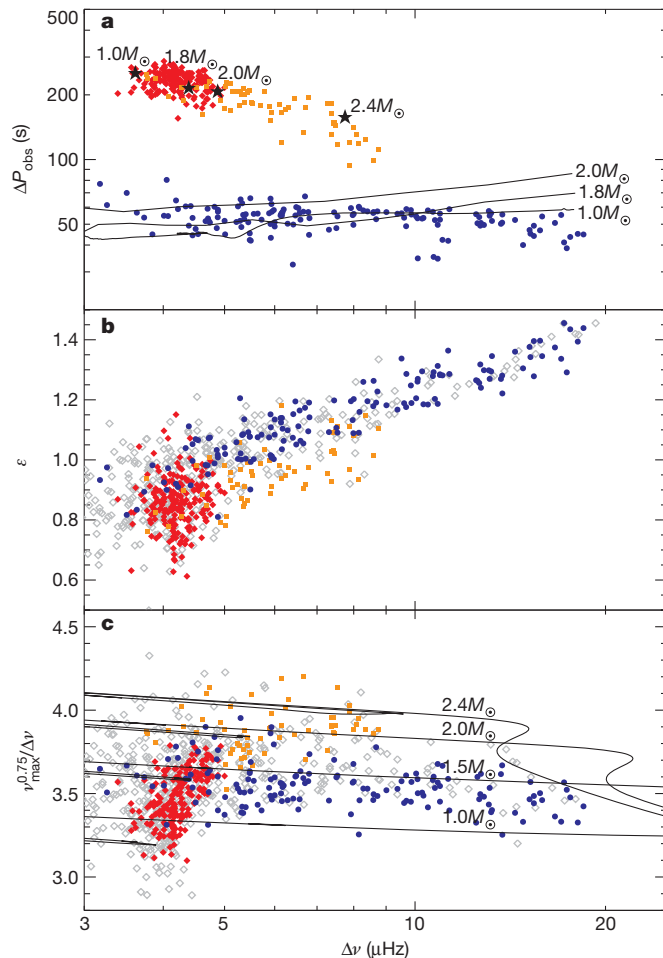


Figure 3 | Asteroseismic diagrams for red giants observed with Kepler. The abscissa is the p-mode large frequency separation. **a**, Filled symbols show period spacings measured from observations (Supplementary Table). The stars divide into two clear groups, with blue circles indicating hydrogen-shell-burning giants (143 stars), while the remainder are helium-core-burning stars (193 red diamonds and 61 orange squares, divided on the basis of panel c). The solid lines show average observable period spacings for ASTEC²⁷ models of hydrogen-shell-burning giants on the red giant branch as they evolve from right to left, calculated from the central three modes in the $l = 1$ clusters. The black stars show theoretical period spacings calculated in the same way, for four models of helium-core-burning stars that are midway through that phase (core helium fraction 50%). The $2.4-M_{\odot}$ model was calculated with ASTEC²⁷ and commenced helium-burning without passing through a helium flash. The other three models, which did undergo a helium flash, were computed using the ATON code^{15,29} (J.M. *et al.*, manuscript in preparation). Solar metallicity was adopted for all models, which were computed without mass loss. **b**, The quantity ε , which specifies the absolute frequency of the p-mode comb pattern^{10,11}. We see a systematic difference between the hydrogen- and helium-burning stars. The open grey diamonds are stars for which a reliable period spacing could not be measured (391 stars). Many of these had high signal-to-noise but lacked a clear structure that would indicate regular period spacings. **c**, The quantity $\nu_{\text{max}}^{0.75}/\Delta\nu$, which is approximately independent of luminosity¹⁰ (here ν_{max} and $\Delta\nu$ are in μHz). Helium-burning stars that we identify as belonging to the red clump, based on their positions in this diagram, are marked with red diamonds. The remainder, which presumably belong to the secondary clump, are marked with orange squares. The lines show model calculations based on scaling relations²⁶ for $\Delta\nu$ and ν_{max} applied to solar-metallicity BASTI models³⁰ with the mass loss efficiency parameter set to $\eta = 0.2$.

measure ΔP_{obs} gave comparable results. The first was simply to measure pairwise separations of the strongest $l = 1$ peaks in the power spectrum. The other was to calculate the autocorrelation of the time series²² with narrow filters centred on the $l = 1$ clusters.

Observed period spacings for about 400 stars are shown in Fig. 3a, which clearly demonstrates the existence of two distinct populations with different core properties. A comparison with model calculations confirms that the two groups coincide with hydrogen-shell-burning stars on the red giant branch (blue circles) and those that are also burning helium in the core (red diamonds and orange squares). We conclude that ΔP_{obs} is an extremely reliable parameter for distinguishing between stars in these two evolutionary stages, which are known to have very different core densities¹⁵ but are otherwise very similar in their fundamental properties (mass, luminosity and radius). We note that other asteroseismic observables, such as the small p-mode separations, are not able to do this^{10,15}.

Our ability to distinguish between hydrogen- and helium-burning stars makes it possible to investigate their properties as separate populations. One example is the parameter ε , which specifies the absolute position of the p-mode comb pattern^{10,11}. As shown in Fig. 3b, there is a systematic offset between the two populations. This may indicate a difference in the surface layers, given that ε is sensitive to the upper turning point of the modes²³. However, the difference may also arise because the envelope of oscillation power is centred at different frequencies in the two types of stars (see below). This result is clearly worthy of further study.

A very important application for the helium-burning stars is to distinguish between the so-called red clump and the secondary clump^{24,25}. The red clump comprises low-mass stars that suffered from electron degeneracy in their hydrogen-shell-burning phase and ignited helium in a flash (that is, all the helium ignited more or less simultaneously) once the core attained a critical mass. This common core mass explains why the red clump (known as the horizontal branch when seen in metal-poor clusters) spans a very narrow range of luminosities. The secondary-clump stars, meanwhile, are too massive to have undergone a helium flash and so have a range of core masses, and hence of luminosities. The mass threshold that divides these two populations depends on metallicity, and also on core overshoot²⁴ (the phenomenon in which the motion of convection cells extends beyond the nominal boundary of the convective zone).

Among the helium-burning stars in Fig. 3a we can indeed see this division into a compact group (the red clump; red diamonds) and a dispersed group (the secondary clump; orange squares). It is even more apparent when we examine the quantity $\nu_{\text{max}}^{0.75}/\Delta\nu$, which is approximately independent of luminosity¹⁰ (ν_{max} is the frequency at which the oscillation envelope has its maximum²⁶). This quantity is shown in Fig. 3c, and the comparison with evolutionary models having solar metallicity implies a helium-flash threshold of around $2M_{\odot}$. Refinement of this result, using data from more detailed studies of individual stars near the boundary between the red clump and the secondary clump, should test predictions of convective-core overshoot.

Received 24 December 2010; accepted 16 February 2011.

- Schwarzschild, M. & Härm, R. Red giants of population II. *Astrophys. J.* **136**, 158–165 (1962).
- Iben, I. Jr. Low-mass red giants. *Astrophys. J.* **154**, 581–595 (1968).
- Sweigart, A. V. & Gross, P. G. Evolutionary sequences for red giant stars. *Astrophys. J. Suppl. Ser.* **36**, 405–437 (1978).
- Charbonnel, C. in *Cosmic Abundances as Records of Stellar Evolution and Nucleosynthesis* (eds Barnes, T. G. & Bash, F. N.) 119–130 (Vol. 336, Astronomical Society of the Pacific Conference Series, 2005).
- Aerts, C., Christensen-Dalsgaard, J. & Kurtz, D. W. *Asteroseismology* (Springer, 2010).
- Beck, P. G. *et al.* Detection of gravity-mode period spacings in red giant stars by the Kepler Mission. *Science* (in the press).
- De Ridder, J. *et al.* Non-radial oscillation modes with long lifetimes in giant stars. *Nature* **459**, 398–400 (2009).
- Kallinger, T. *et al.* Oscillating red giants in the CoRoT exo-field: asteroseismic radius and mass determination. *Astron. Astrophys.* **509**, A77 (2010).

9. Bedding, T. R. *et al.* Solar-like oscillations in low-luminosity red giants: first results from *Kepler*. *Astrophys. J.* **713**, L176–L181 (2010).
10. Huber, D. *et al.* Asteroseismology of red giants from the first four months of *Kepler* data: global oscillation parameters for 800 stars. *Astrophys. J.* **723**, 1607–1617 (2010).
11. Mosser, B. *et al.* The universal red-giant oscillation pattern. An automated determination with CoRoT data. *Astron. Astrophys.* **525**, L9 (2011).
12. Dziembowski, W. A., Gough, D. O., Houdek, G. & Sienkiewicz, R. Oscillations of α UMa and other red giants. *Mon. Not. R. Astron. Soc.* **328**, 601–610 (2001).
13. Christensen-Dalsgaard, J. Physics of solar-like oscillations. *Sol. Phys.* **220**, 137–168 (2004).
14. Dupret, M. *et al.* Theoretical amplitudes and lifetimes of non-radial solar-like oscillations in red giants. *Astron. Astrophys.* **506**, 57–67 (2009).
15. Montalbán, J., Miglio, A., Noels, A., Scuflaire, R. & Ventura, P. Seismic diagnostics of red giants: first comparison with stellar models. *Astrophys. J.* **721**, L182–L188 (2010).
16. Di Mauro, M. P. *et al.* Solar-like oscillations from the depths of the red-giant star KIC 4351319 observed with *Kepler*. *Mon. Not. R. Astron. Soc.* (submitted).
17. Tassoul, M. Asymptotic approximations for stellar nonradial pulsations. *Astrophys. J. Suppl. Ser.* **43**, 469–490 (1980).
18. Miglio, A., Montalbán, J., Eggenberger, P. & Noels, A. Gravity modes and mixed modes as probes of stellar cores in main-sequence stars: from solar-like to β Cep stars. *Astron. Nachr.* **329**, 529–534 (2008).
19. Aizenman, M., Smeyers, P. & Weigert, A. Avoided crossing of modes of non-radial stellar oscillations. *Astron. Astrophys.* **58**, 41–46 (1977).
20. Deheuvels, S. & Michel, E. New insights on the interior of solar-like pulsators thanks to CoRoT: the case of HD 49385. *Astrophys. Space Sci.* **328**, 259–263 (2010).
21. Jenkins, J. M. *et al.* Initial characteristics of *Kepler* long cadence data for detecting transiting planets. *Astrophys. J.* **713**, L120–L125 (2010).
22. Mosser, B. & Appourchaux, T. On detecting the large separation in the autocorrelation of stellar oscillation times series. *Astron. Astrophys.* **508**, 877–887 (2009).
23. Gough, D. O. in *Hydrodynamic and Magnetodynamic Problems in the Sun and Stars* (ed. Osaki, Y.) 117–143 (Univ. Tokyo Press, 1986).
24. Girardi, L. A secondary clump of red giant stars: why and where. *Mon. Not. R. Astron. Soc.* **308**, 818–832 (1999).
25. Miglio, A. *et al.* Probing populations of red giants in the galactic disk with CoRoT. *Astron. Astrophys.* **503**, L21–L24 (2009).
26. Kjeldsen, H. & Bedding, T. R. Amplitudes of stellar oscillations: the implications for asteroseismology. *Astron. Astrophys.* **293**, 87–106 (1995).
27. Christensen-Dalsgaard, J. ASTEC – the Aarhus STellar Evolution Code. *Astrophys. Space Sci.* **316**, 13–24 (2008).
28. Kjeldsen, H., Bedding, T. R. & Christensen-Dalsgaard, J. Correcting stellar oscillation frequencies for near-surface effects. *Astrophys. J.* **683**, L175–L178 (2008).
29. Ventura, P., D'Antona, F. & Mazzitelli, I. The ATON 3.1 stellar evolutionary code. A version for asteroseismology. *Astrophys. Space Sci.* **316**, 93–98 (2008).
30. Pietrinferni, A., Cassisi, S., Salaris, M. & Castelli, F. A large stellar evolution database for population synthesis studies. I. Scaled solar models and isochrones. *Astrophys. J.* **612**, 168–190 (2004).

Supplementary Information is linked to the online version of the paper at www.nature.com/nature.

Acknowledgements We acknowledge the entire Kepler team, whose efforts made these results possible. We thank M. Biercuk for comments. Funding for this Discovery mission was provided by NASA's Science Mission Directorate. T.R.B. and D.S. were supported by the Australian Research Council; P.B. and C.A. were supported by European Community's 7th Framework Programme (PROSPERITY); S.H. was supported by the Netherlands Organisation for Scientific Research (NWO). The National Center for Atmospheric Research is sponsored by the National Science Foundation.

Author Contributions T.R.B., B.M., P.B., Y.P.E., R.A.G., S.H., C.A., A.-M.B. and F.C. measured and interpreted period spacings; B.M., D.H., R.A.G., S.H., T.K., W.J.C., C.B., D.L.B. and S.M. calculated power spectra and measured large frequency separations; J.M., J.C.-D., A.M., D.S., T.R.W., K.B., M.P.D.M., M.-A.D., M.-J.G., S.K., A.N., V.S.A. and P.V. calculated and interpreted theoretical models; J.D.R., S.H., S.F., Y.P.E., D.S., T.M.B., H.K., J.C.-D. and R.L.G. contributed to the coordination of the project, including the acquisition and distribution of the data; and J.M.J. constructed the photometric time series from the original Kepler pixel data. All authors discussed the results and commented on the manuscript.

Author Information Reprints and permissions information is available at www.nature.com/reprints. The authors declare no competing financial interests. Readers are welcome to comment on the online version of this article at www.nature.com/nature. Correspondence and requests for materials should be addressed to T.R.B. (t.beddington@physics.usyd.edu.au).

F. L. Pratt¹, P. J. Baker¹, S. J. Blundell², T. Lancaster², S. Ohira-Kawamura³, C. Baines⁴, Y. Shimizu⁵, K. Kanoda⁶, I. Watanabe⁷
& G. Saito^{8†}

Field-induced magnetic moments were first detected in κ -(BEDT-TTF)₂Cu₂(CN)₃ in the broadening of the NMR linewidth at low temperatures⁷. The static moment associated with this broadening is very weak, corresponding to just a few per cent of the full moment expected from the $S = 1/2$ spin of each BEDT-TTF dimer. In the present study, we use the muon spin rotation (μ SR) technique¹² to extend measurements of this low-moment magnetism to a much wider range of fields, revealing a detailed phase diagram (Fig. 1). An example scan of the transverse-field μ SR linewidth at 120 mK is shown in Fig. 2a. The root mean squared width of the internal field distribution experienced by the muon, B_{rms} , is obtained from the damping of the muon precession signal (see Supplementary Fig. 1 for example raw data). At low fields, the system is in a quantum critical phase where the electronic contribution to the relaxation is relatively weak and nuclear dipole fields dominate the width. When the applied magnetic field, H , is above a critical value, H_c , where $\mu_0 H_c = 14$ mT (μ_0 is the permeability of free space), the width increases rapidly, signifying the onset of a field-induced

To determine the detailed phase boundary for this transition, the position of $H_c(T)$ has been measured for a series of temperatures, T , ranging between 20 mK and 8 K (Fig. 2b). A scaling analysis of the phase boundary, $T_c \propto (H - H_0)^\phi$, gives $\phi = 0.94(1)$, and the position of the $T = 0$ quantum critical point (QCP) is $\mu_0 H_0 = 5.2(3)$ mT, where $H_0 = H_c(T = 0)$. Because $\phi = 2/d$ for Bose-Einstein condensation¹³ (BEC) with dimensionality $d \geq 2$, this suggests an effective

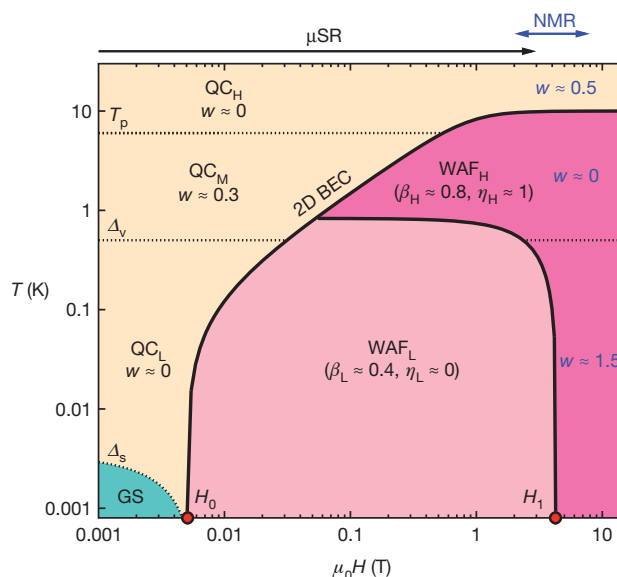


Figure 1 | Phase diagram for κ -(BEDT-TTF) $_2$ Cu $_2$ (CN) $_3$. The finite-temperature H - T phase diagram obtained from the current μ SR experiments, taken in conjunction with previously reported NMR and thermodynamic measurements. The respective field ranges for the μ SR and NMR techniques are indicated. The dominant feature of the phase diagram is the presence of two quantum critical points at the well-separated field values H_0 and H_1 . The boundaries between phases and the critical properties of these phases are obtained from a series of H scans at constant T . The properties of the quantum critical phase are obtained from a T scan at $H = 0$. The quantum critical (QC) and WAF regions are subdivided on the basis of the behaviour of their characteristic critical parameters, β , η and w as functions of T or H (L, low; M, intermediate; H, high). GS is the gapped-spin-liquid regime, where $T < \Delta_s(H)$.

¹ISIS Facility, Rutherford Appleton Laboratory, Chilton OX11 0QX, UK. ²Department of Physics, University of Oxford, Clarendon Laboratory, Parks Road, Oxford OX1 3PU, UK. ³Neutron Science Section, J-PARC Center, Japan Atomic Energy Agency, 2-4 Shirane, Shirakata, Tokai, Ibaraki 319-1195, Japan. ⁴Paul Scherrer Institut, Laboratory for Muon-Spin Spectroscopy, CH-5232 Villigen, Switzerland. ⁵Institute for Advanced Research, Nagoya University, Nagoya 464-8601, Japan. ⁶Department of Applied Physics, University of Tokyo, Bunkyo-ku, Tokyo 113-8656, Japan. ⁷Meson Science Laboratory, RIKEN, 2-1 Hirosawa, Wako, Saitama 351-0198, Japan. ⁸Division of Chemistry, Graduate School of Science, Kyoto University, Oiwakekyo, Kitashirakawa, Sakyo-ku, Kyoto 606-8502, Japan. †Present address: Research Institute, Meijo University, Nagoya 468-8502, Japan.

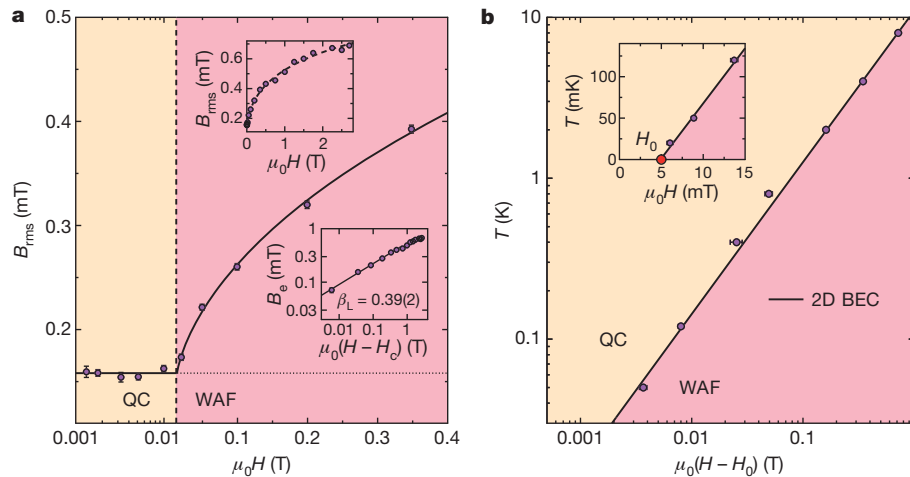


Figure 2 | Low-field QPT and phase boundary. **a**, Field dependence of the transverse-field μ SR linewidth measured at 120 mK. The onset of the field-dependent broadening is seen above a critical field, $\mu_0 H_c(120 \text{ mK}) = 14(2) \text{ mT}$, which reflects the QPT between the quantum critical phase and the WAF phase at this temperature. The linewidth in the quantum critical phase, B_0 , primarily reflects the nuclear dipole contribution. Upper inset, high-field behaviour; lower inset, critical scaling analysis of the field-induced magnetic broadening, $B_c = (B_{\text{rms}}^2 - B_0^2)^{0.5}$, with a fit for fields below 0.4 T that gives the value

dimensionality that is close to two and that the physics of the two-dimensional (2D) layers determines the phase boundary in the manner recently observed for BEC in the ‘Han purple’ layered, spin-1/2 dimer system¹² $\text{BaCuSi}_2\text{O}_6$, where frustration of the interlayer coupling leads to an effective dimensionality of $d = 2$ for the BEC at low temperatures^{13,14}. Although our system lacks the perfect interlayer frustration of $\text{BaCuSi}_2\text{O}_6$, the interlayer coupling is expected to be extremely weak. The T_c for BEC in this situation is expected to follow a Kosterlitz–Thouless-like form¹⁴

$$T_c \propto \frac{\mu \ln(t_{\parallel}/\mu)}{\ln(\ln(t_{\parallel}/\mu))} \quad (1)$$

where $\mu \propto H - H_0$ is the chemical potential and t_{\parallel} is the transfer integral governing the dispersion of the spin excitations in the plane of the layers. Analysis of the phase boundary using equation (1) gives a marginally better fit than the simple scaling analysis, with a virtually identical position for the $T = 0$ QCP, $\mu_0 H_0 = 5.2(2) \text{ mT}$. The size of the spin gap can be estimated as $\Delta_s = gS(\mu_B \mu_0 / k_B) H_0 = 3.5(1) \text{ mK}$, where μ_B is the Bohr magneton, k_B is Boltzmann’s constant and we take $S = 1/2$ and $g = 2$. This gap is nearly five orders of magnitude weaker than J , and strongly suggests an emergent low-energy scale for the bosons that condense to form the magnetic state.

Because this field-induced BEC transition points directly to the presence of gapped spin excitations, albeit with a very small gap, quantum spin liquid (QSL) models that include the possibility of a gap are necessary for describing the low-temperature properties. Gap behaviour is intrinsic to models with bosonic spins, but fermionic spin models with spinon Fermi surfaces can also produce bosons and gap behaviour if there is a pairing instability below some temperature, T_p (refs 15, 16). Such a pairing leading to conversion of fermions to bosons may be partial, and models that allow for the coexistence of fermionic and bosonic spin excitations¹⁷ may then be appropriate. Many properties of $\kappa\text{-(BEDT-TTF)}_2\text{Cu}_2(\text{CN})_3$ show characteristic features around 6 K, such as a partial drop in the magnetic susceptibility⁶ and a peak in the specific heat^{9,11}. These could be interpreted as the result of a fraction of the fermionic spins forming bosonic pairs at $T_p \approx 6 \text{ K}$.

If we focus on the gapped spins revealed by the low-temperature experiments, the spin-liquid model of refs 18, 19 may be particularly relevant. This model involves both bosonic spinons and bosonic topological vortex objects called visons that arise as spinless excitations

$\beta_L = 0.39(2)$ for the low- T , low- H critical exponent associated with the magnetic order parameter. **b**, Field-dependent scans of the transverse-field linewidth at different temperatures give a series of $H_c(T)$ points that determine the phase boundary between the quantum critical and WAF phases. A 2D BEC model gives the best fit, with the phase boundary following equation (1), and the location of the QCP at $T = 0$ is found to be $\mu_0 H_0 = 5.2(2) \text{ mT}$. Inset, linear plot of the low- T region. Error bars, s.e. of the fitted parameters (further discussion of errors is given in Supplementary Information).

of the valence bond structure²⁰. Various phases are found in the model: a Z_2 gapped spin liquid, a valence-bond solid, and collinear and non-collinear WAF states. QPTs between these phases are controlled by microscopic coupling parameters. Field-induced magnetic phases arise in this model as BEC of the gapped bosonic spinons and the closeness to a QCP leads to strong suppression both of the spinon gap, Δ_s , in the gapped-spin-liquid phase and of the magnetic moment in the WAF phase; these features all tie in well with the present experimental results, although this does not preclude other possible theoretical interpretations. In this type of model, a quantum critical region is expected for temperatures above the ordering temperature in the WAF phase or above Δ_s in the gapped-spin-liquid phase (see Supplementary Fig. 2 for further background details of the system and Supplementary Fig. 3 for a possible interpretation of the present data within the theoretical framework of refs 18, 19).

Local spin probes such as μ SR or NMR are sensitive to spin fluctuations and can be used to characterize the various phases by measuring the temperature dependence of the spin fluctuation rate, $\Gamma(T)$, which can in general be described by a power law, $\Gamma(T) \propto T^w$, over a given temperature range. For the specific case of a 2D, frustrated QSL, the quantum critical fluctuations seen in NMR spin-lattice relaxation are predicted to follow a T^w power law¹⁹ where w equals η , the anomalous-dimension critical exponent that reflects the wavevector dependence of critical correlations at the critical point.

The measured temperature dependence of the electronic contribution to the μ SR relaxation at $H = 0$ is shown in Fig. 3. A number of crossovers are seen in the effective w value. The first crossover occurs around 0.5 K, at the point labelled Δ_v , with $w \approx 0$ in the lower region, labelled QC_L , and $w = 0.27(5)$ in an intermediate region, labelled QC_M . A similar characteristic temperature, of 0.44 K, is seen in the thermal conductivity data¹⁰, which was originally assigned to a spin gap. However, the gap is known to be independent of field below 4 T, suggesting that it is associated with a spinless excitation, and it was subsequently reinterpreted as a vison gap¹⁹. Our results would be consistent with such an interpretation (although a valence-bond-solid transition corresponding to vison condensation is another possibility that cannot be excluded completely¹⁸). We note that the characteristic energy Δ_v is around two orders of magnitude larger than Δ_s .

In the region labelled QC_H in Fig. 3, the behaviour changes again, with notable structure appearing in the region between 5 and 80 K.

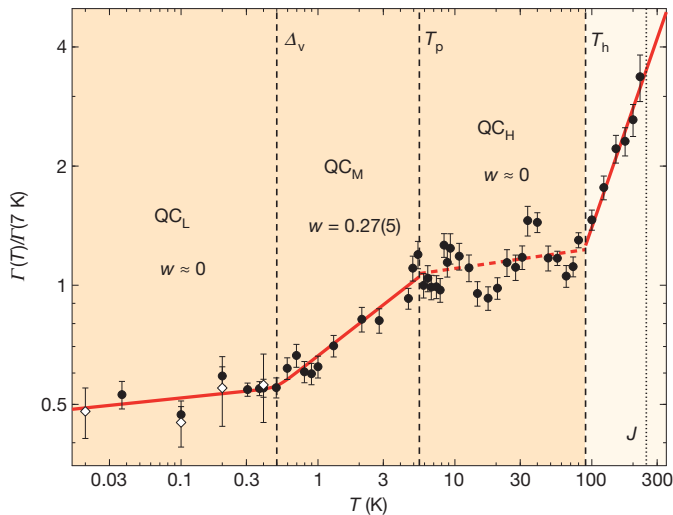


Figure 3 | Electronic spin fluctuation rate. Temperature-dependent data within the quantum critical phase are obtained from μ SR with $H = 0$. Data have been combined from several experiments to provide a very wide T range (black circles). White diamonds show additional low- T data from a previous μ SR study⁸. A crossover in the power-law exponent w is seen at around 0.5 K. Very weak scaling ($w \approx 0$) is seen below this point, in the QC_L region. A significant w value of 0.27(5) is seen in the intermediate, QC_M , region, between Δ_v and T_p . In the QC_H region, between T_p and T_h , the temperature dependence becomes more structured, but the underlying trend is again weak (dashed red line). Finally, as T approaches J , the fluctuation rate crosses over to linear behaviour. Error bars, s.e. of the fitted parameters (Supplementary Information).

This structure may be related to suggested higher-energy features in the spin excitation spectrum, such as the roton-like minima³ or the onset of excitations related to the charge degree of freedom, but the underlying power-law exponent, w , seems to return to a low value, as in the QC_L region. Finally, above 100 K, where T approaches J , a well-defined temperature-linear regime sets in. Power laws are also observed in NMR relaxation⁷; these have crossovers at temperatures

similar to those in the μ SR data, but the absolute values of w in the various regions are quite different (Fig. 1).

For field scans made at temperatures between 0.6 and 0.8 K, a second set of field-induced transitions has been detected. Example data for $T = 0.8$ K are shown in Fig. 4a. For fields below 0.6 T, B_c scales with an exponent β consistent with the value of β_L obtained at 120 mK. However, above this field there is a dramatic crossover to a stronger field dependence, characterized by $\beta_H = 0.83(4)$. This larger exponent would be compatible with the value expected for models with deconfined spin excitations (as discussed below) and therefore suggests a field-induced deconfinement transition, where the character of the spin fluctuations crosses over from that of normal $S = 1$ spin waves to that of freely propagating $S = 1/2$ spinons. We note that this increase in exponent is consistent with the broadening of the NMR linewidth⁷, which is close to linear in field over the measured field range, 2 to 8 T, for temperatures down to 1.6 K. There is also complementary evidence for a similar transition at high fields in the thermal conductivity⁹, which shows a sudden rapid increase above 4 T at low temperatures. Such an increase could be interpreted as the onset of an additional spinon contribution above a deconfinement transition. The overall phase boundary for the high-field transition (Fig. 4a, inset) defines a second QCP of the system, at $\mu_0 H_1 \approx 4$ T. A comparable field-induced increase in thermal conductivity was recently seen at 2 T in another molecular QSL system, $\text{EtMe}_3\text{Sb}[\text{Pd}(\text{dmit})_2]_2$ (ref. 21). This system is believed to lie even closer to the ideal, symmetrical triangular-lattice case than κ -(BEDT-TTF)₂Cu₂(CN)₃, suggesting that the extent of the low-field ‘confined’ region characterized by H_1 may scale with the degree of departure of each system from the ideal lattice.

Distinguishing experimentally between the many subtle theoretical possibilities for the nature of a QSL state is a significant challenge. Inelastic neutron scattering has historically been a powerful tool for studying spin excitations and could in principle be very helpful in distinguishing between the different types of spinon dispersion predicted by various 2D QSL models. However, current crystal growth methods have not been able to produce crystals that are large enough for inelastic neutron scattering. In these circumstances, the most practical method of

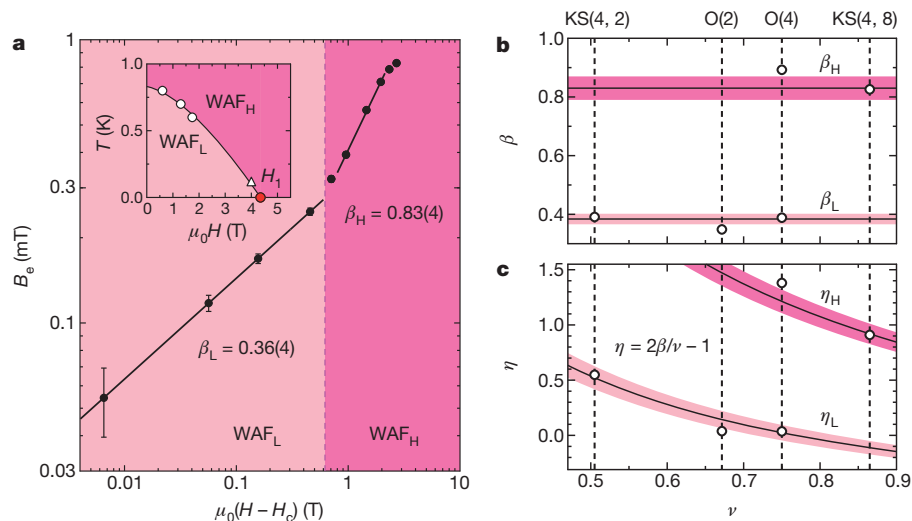


Figure 4 | High-field QPT and critical exponents. **a**, Field dependence of B_c at $T = 0.8$ K. The low-field exponent, β_L , is consistent with that obtained at 120 mK (Fig. 2a), but above 0.6 T a crossover to a higher value, β_H , is seen, consistent with the enhancement expected for deconfined spinons in models with non-collinear spin correlations. Inset, this transition measured at several temperatures (white circles), along with the transition of similar character seen in the low-temperature thermal conductivity¹⁰ (triangle); the line is a suggested common phase boundary for the spinon deconfinement transition, terminating in a QCP at H_1 (red circle). Error bars, s.e. of the fitted parameters (Supplementary Information). **b**, **c**, Comparison between the measured critical parameters and those of $O(N)$ class models^{22,23}, along with the model of ref. 17,

$\text{KS}(N_b, N_f)$, which involves N_b bosons coexisting with N_f fermions. The symbols show the computed exponents β (**b**) and η (**c**) for each model, plotted against the correlation-length exponent, ν . Solid lines and shaded bands respectively indicate the values and uncertainties of the exponents measured using μ SR. We find good agreement between β_L and the normal critical exponents of the $O(4)$ model. For β_H , a fair agreement is obtained with the enhanced value for an $O(4)$ complex order parameter, but the best overall agreement with experiment is found with $\text{KS}(4, 8)$ for β_H and with $\text{KS}(4, 2)$ for β_L . A more detailed comparison of the results with the various models is given in Supplementary Information.

discriminating between potential models of the QSL state is to focus on the critical behaviour associated with the state and its QPTs, measured using currently available techniques, such as μ SR, and compare it with the known critical behaviour of specific models.

To this end, the μ SR-determined exponents β , the corresponding exponents η and their ranges of uncertainty are set out in Fig. 4b along with some theoretical model values (further details and model comparisons are provided in Supplementary Information). The critical exponents are plotted against the relevant correlation-length exponent, ν , for each model. A simple planar-magnet XY spin system would be expected to have O(2) exponents. Within a frustrated spin model, however, non-collinearity leads to an enlarged order-parameter dimension, giving an O(4) class¹⁸. Furthermore, the complex non-collinear spin correlations in such a system with deconfined spinons are predicted to lead to enhanced exponents that are significantly modified from their normal values: in the O(4) class it is found that η increases from 0.036 to 1.38 (refs 22, 23), and β correspondingly increases from 0.39 to 0.89. These two O(4) values are found to agree well with the experimental results (Fig. 4b) in the low- and high-field phases, β_L and β_H .

The more elaborate model of ref. 17 can provide an even closer match to the experimental values. This model allows N_f species of fermions and N_b species of bosons to contribute to the criticality and might be appropriate to describe a system in which part of a spinon Fermi surface has undergone pairing. The best agreement with experiment is found by taking $N_b = 4$ and $N_f = 8$ for the WAF_H phase and $N_b = 4$ and $N_f = 2$ for the WAF_L phase. More details of the model of ref. 17 and a possible interpretation of the parameter values are given in Supplementary Information, although it should be noted that the accuracy of the numerical values of this theory is not as well established as those of the O(N) models. Even if not yet fully conclusive, these comparisons with experiment give an indicator of the type of model that would be consistent with the measured field dependence in the two phases. Such comparisons between experiment and theory are also valuable in highlighting directions for further experimental and theoretical work.

In considering the field-dependent behaviour, we note that other field-induced phenomena have recently been proposed for Mott insulators that involve coupling to orbital currents^{24–26}. These would produce effects that are linear in the applied field (that is, $\beta = 1$), and this might be a possible alternative picture for the high-field phase, where β is found to be closer to one. However, in contrast to the BEC model, no mechanism is provided in these theories for producing a finite, temperature-dependent threshold field for the induced moments. Neither do these theories account for the WAF_L phase, with its definite sublinear scaling ($\beta \approx 0.4$), and an overall interpretation in terms of orbital currents is very difficult to reconcile with the experimental phase diagram.

Since the NMR data first showed the emergence of inhomogeneous moments, attention has been given to the possible effect of impurities in nucleating staggered moments in QSL systems and leading to the inhomogeneous distribution of magnetic order that is linear in applied field^{7,27}. However, the current data clearly show that, regardless of any inhomogeneity in the distribution of the order, the spatial average of the order parameter, as measured by μ SR, simply follows the criticality of a QCP separating the gapped-spin-liquid and WAF phases. Here the small size of the moment relative to the total spin provides a serious problem for most standard methods of probing an antiferromagnetic state. However, the sensitivity and flexibility of μ SR allows the subtle WAF phase to be readily revealed in this system.

The primary result of this study of the model spin-liquid system κ -(BEDT-TTF)₂Cu₂(CN)₃ is the phase diagram showing a QCP at a low threshold field and a second QCP at a much higher field. The presence of transitions and critical behaviour associated with these QCPs strongly favours low-energy models with weak spin gaps over models that are based on a completely ungapped spinon Fermi surface

or models based on orbital currents or impurity-induced moments. Although at zero field the magnetism is fully suppressed by the presence of the QCP, closure of this weak spin gap by the application of field provides a natural explanation for the field-induced re-emergence of static magnetic moments.

The present system should be placed in the broader context of various other examples of QSL systems². The kagome lattice provides an alternative, but rather more complex, example of a frustrated 2D system, whereas the hyperkagome and pyrochlore lattices provide examples of highly frustrated three-dimensional structures². The pyrochlores can act as hosts for spin-ice behaviour and emergent magnetic monopoles, which have been the focus of much recent attention². Both the kagome and the hyperkagome systems show a combination of dispersive and localized, non-dispersive spin excitations that can lead to some novel properties²⁸. The hyperkagome system Gd₃Ga₅O₁₂ is notable also for having a field-induced transition from a spin-liquid phase to an antiferromagnetic phase²⁹. However, the spin and the threshold field there are significantly greater than in the molecular system studied here, suggesting that the physics there has a different character. Overall, the triangular lattice provides the simplest prototype of a frustrated-lattice spin liquid, and the improved understanding of the triangular-lattice QSL provided by examples such as the one studied here should offer a good basis for interpreting the more complex manifestations of spin liquids in the kagome and hyperkagome lattices.

METHODS SUMMARY

The muon measurements reported here were carried out at the Swiss Muon Source and at the ISIS and RIKEN-RAL muon facilities in the UK. Data analysis was carried out using the WiMDA program³⁰. Further experimental details of the sample and the muon measurements and analysis procedures are included in Supplementary Information.

Received 16 September 2010; accepted 7 February 2011.

- Anderson, P. W. Resonating valence bonds: a new kind of insulator? *Mater. Res. Bull.* **8**, 153–160 (1973).
- Balents, L. Spin liquids in frustrated magnets. *Nature* **464**, 199–208 (2010).
- Zheng, W., Fjaerestad, J. O., Singh, R. R. P., McKenzie, R. H. & Coldea, R. Excitation spectra of the spin 1/2 triangular-lattice Heisenberg antiferromagnet. *Phys. Rev. B* **74**, 224420 (2006).
- Motrunich, O. I. Variational study of triangular lattice spin-1/2 model with ring exchanges and spin liquid state in κ -(ET)₂Cu₂(CN)₃. *Phys. Rev. B* **72**, 045105 (2005).
- Pratt, F. L. Using Shubnikov-de Haas data to estimate the magnetic frustration parameter t'/t in the spin-liquid system κ -ET₂Cu₂(CN)₃. *Physica B* **405**, S205–S207 (2010).
- Shimizu, Y. *et al.* Spin liquid state in an organic Mott insulator with a triangular lattice. *Phys. Rev. Lett.* **91**, 107001 (2003).
- Shimizu, Y. *et al.* Emergence of inhomogeneous moments from spin liquid in the triangular-lattice Mott insulator κ -(ET)₂Cu₂(CN)₃. *Phys. Rev. B* **73**, 140407(R) (2006).
- Ohira, S. & Shimizu, Y., Kanoda, K. & Saito, G. Spin liquid state in κ -(BEDT-TTF)₂Cu₂(CN)₃ studied by muon spin relaxation method. *J. Low Temp. Phys.* **142**, 153–158 (2006).
- Yamashita, S. *et al.* Thermodynamic properties of a spin-1/2 spin-liquid state in a κ -type organic salt. *Nature Phys.* **4**, 459–462 (2008).
- Yamashita, M. *et al.* Thermal-transport measurements in a quantum spin-liquid state of the frustrated triangular magnet κ -(BEDT-TTF)₂Cu₂(CN)₃. *Nature Phys.* **5**, 44–47 (2009).
- Manna, R. S. *et al.* Lattice effects and entropy release at the low-temperature phase transition in the spin-liquid candidate κ -(BEDT-TTF)₂Cu₂(CN)₃. *Phys. Rev. Lett.* **104**, 016403 (2010).
- Blundell, S. J. Spin-polarized muons in condensed matter physics. *Contemp. Phys.* **40**, 175 (1999).
- Sebastian, S. E. *et al.* Dimensional reduction at a quantum critical point. *Nature* **441**, 617–620 (2006).
- Schmalien, J. & Batista, C. D. Emergent symmetry and dimensional reduction at a quantum critical point. *Phys. Rev. B* **77**, 094406 (2008).
- Lee, S.-S., Lee, P. A. & Senthil, T. Amperean pairing instability in the U(1) spin liquid state with Fermi surface and application to κ -(BEDT-TTF)₂Cu₂(CN)₃. *Phys. Rev. Lett.* **98**, 067006 (2007).
- Galitski, V. & Kim, Y. B. Spin-triplet pairing instability of the spinon Fermi surface in a U(1) spin liquid. *Phys. Rev. Lett.* **99**, 266403 (2007).
- Kaul, R. K. & Sachdev, S. Quantum criticality of U(1) gauge theories with fermionic and bosonic matter in two spatial dimensions. *Phys. Rev. B* **77**, 155105 (2008).

18. Xu, C. & Sachdev, S. Global phase diagrams of frustrated quantum antiferromagnets in two dimensions: doubled Chern-Simons theory. *Phys. Rev. B* **79**, 064405 (2009).
19. Qi, Y., Xu, C. & Sachdev, S. Dynamics and transport of the Z_2 spin liquid: application to κ -(ET)₂Cu₂(CN)₃. *Phys. Rev. Lett.* **102**, 176401 (2009).
20. Senthil, T. & Fisher, M. P. A. Z_2 gauge theory of electron fractionalization in strongly correlated systems. *Phys. Rev. B* **62**, 7850–7881 (2000).
21. Yamashita, M. *et al.* Highly mobile gapless excitations in a two-dimensional candidate quantum spin liquid. *Science* **328**, 1246–1248 (2010).
22. Ballasteros, H. G., Fernandez, L. A., Martin-Mayor, V. & Munoz Sudupe, A. Finite size effects on measures of critical exponents in $d = 3$ O(N) models. *Phys. Lett. B* **387**, 125–131 (1996).
23. Isakov, S. V., Senthil, T., & Kim, Y. B. Ordering in Cs₂CuCl₄: possibility of a proximate spin liquid. *Phys. Rev. B* **72**, 174417 (2005).
24. Motrunich, O. I. Orbital magnetic field effects in spin liquid with spinon Fermi sea: possible application to κ -(ET)₂Cu₂(CN)₃. *Phys. Rev. B* **73**, 155115 (2006).
25. Bulaevskii, L. N., Batista, C. D., Mostovoy, M. V. & Khomskii, D. I. Electronic orbital currents and polarization in Mott insulators. *Phys. Rev. B* **78**, 024402 (2008).
26. Al-Hassanieh, K. A., Batista, C. D., Ortiz, G. & Bulaevskii, L. N. Field-induced orbital antiferromagnetism in Mott insulators. *Phys. Rev. Lett.* **103**, 216402 (2009).
27. Gregor, K. & Motrunich, O. I. Nonmagnetic impurities in a $S = 1/2$ frustrated triangular antiferromagnet: broadening of ¹³C NMR lines in κ -(ET)₂Cu₂(CN)₃. *Phys. Rev. B* **79**, 024421 (2009).
28. Ghosh, S., Rosenbaum, T. F. & Aeppli, G. Macroscopic signature of protected spins in a dense frustrated magnet. *Phys. Rev. Lett.* **101**, 157205 (2008).
29. Schiffer, P., Ramirez, A. P., Huse, D. A. & Valentino, A. J. Investigation of the field induced antiferromagnetic phase transition in the frustrated magnet: gadolinium gallium garnet. *Phys. Rev. Lett.* **73**, 2500–2503 (1994).
30. Pratt, F. L. WiMDA: a muon data analysis program for the Windows PC. *Physica B* **289–290**, 710–714 (2000).

Supplementary Information is linked to the online version of the paper at www.nature.com/nature.

Acknowledgements We acknowledge discussions with S. Sachdev, J. Schmalian and T. Senthil. Part of this work was performed at the Swiss Muon Source, Paul Scherrer Institute, Villigen, Switzerland. This work is supported by EPSRC (UK).

Author Contributions F.L.P. and S.O.-K. planned the experiments. F.L.P., P.J.B., S.J.B., T.L., S.O.-K., C.B. and I.W. contributed to the measurements. Y.S., G.S. and K.K. supplied the sample material and supporting NMR measurements. F.L.P. analysed the data and wrote the paper. All authors critically reviewed the paper.

Author Information Reprints and permissions information is available at www.nature.com/reprints. The authors declare no competing financial interests. Readers are welcome to comment on the online version of this article at www.nature.com/nature. Correspondence and requests for materials should be addressed to F.L.P. (francis.pratt@stfc.ac.uk).

Controlling inelastic light scattering quantum pathways in graphene

Chi-Fan Chen¹, Cheol-Hwan Park¹, Bryan W. Boudouris^{2,3}, Jason Horng¹, Baisong Geng¹, Caglar Girit¹, Alex Zettl^{1,3}, Michael F. Crommie^{1,3}, Rachel A. Segalman^{2,3}, Steven G. Louie^{1,3} & Feng Wang^{1,3}

Inelastic light scattering spectroscopy has, since its first discovery^{1,2}, been an indispensable tool in physical science for probing elementary excitations, such as phonons³, magnons⁴ and plasmons⁵ in both bulk and nanoscale materials. In the quantum mechanical picture of inelastic light scattering, incident photons first excite a set of intermediate electronic states, which then generate crystal elementary excitations and radiate energy-shifted photons⁶. The intermediate electronic excitations therefore have a crucial role as quantum pathways in inelastic light scattering, and this is exemplified by resonant Raman scattering⁶ and Raman interference^{7,8}. The ability to control these excitation pathways can open up new opportunities to probe, manipulate and utilize inelastic light scattering. Here we achieve excitation pathway control in graphene with electrostatic doping. Our study reveals quantum interference between different Raman pathways in graphene: when some of the pathways are blocked, the one-phonon Raman intensity does not diminish, as commonly expected, but increases dramatically. This discovery sheds new light on the understanding of resonance Raman scattering in graphene. In addition, we demonstrate hot-electron luminescence⁹ in graphene as the Fermi energy approaches half the laser excitation energy. This hot luminescence, which is another form of inelastic light scattering, results from excited-state relaxation channels that become available only in heavily doped graphene.

Graphene, a two-dimensional carbon sheet^{10,11}, is an attractive system in which to explore novel inelastic light scattering phenomena. Raman scattering from few-layer graphene is readily observable, and has been widely used to distinguish layer thickness¹², characterize quality^{13–15}, and probe electron–phonon interactions^{16,17}. At the same time, graphene has unique optical transitions that can be tuned through electrostatic gating^{18–20}. However, using electrostatic doping to control quantum pathways of inelastic light scattering has presented a challenge, because it requires the modification of intermediate excited states with transition energies close to the laser photon energy. Here we achieve this goal by combining highly efficient ion-gel gating (Methods) and near-infrared laser excitation. This combination enables us to control intermediate optical transition pathways and reveal interesting new optical phenomena. We show that, counter-intuitively, the one-phonon Raman signal increases dramatically when certain quantum pathways are blocked. This represents a notable manifestation of quantum interference between different Raman scattering pathways. On the other hand, the two-phonon Raman signal decreases monotonically with reduced quantum channels. In addition, we observe the emergence of hot luminescence⁹ when the Fermi energy (E_F) approaches half the value of the photon excitation energy. This hot luminescence in graphene arises from new dynamic relaxation channels of the photo-excited states.

The excitation pathways in graphene samples are controlled through electrostatic doping using a high-capacitance ion-gel gate dielectric^{21,22}. Figure 1a displays a diagram of a typical device. The carrier concentration in graphene is controlled by the top gate voltage

(V_g). The doping dependence of electrical transport, optical transmission and inelastic light scattering are measured on the same graphene devices. Figure 1b shows the electrical resistance curve of a graphene device, which has a charge neutral point (CNP) at 1.2 V. The resistance decreases from the CNP value on both electron and hole doping. A lower resistance, corresponding to a higher carrier concentration and a larger shift of Fermi energy, is achieved in the hole-doping region; such hole doping in graphene will be the focus of our study.

To determine the gate-induced Fermi energy shift in graphene samples, we use infrared transmission spectroscopy^{18,19}. This approach is based on the fact that an optical transition can be blocked by hole doping when the initial state has an energy higher than the Fermi level and is not occupied (Fig. 1c). Figure 1d displays the gate-induced change in the real part of graphene optical conductivity ($\Delta\sigma'$) at different gate biases. The spectra exhibit distinct step-like behaviour,

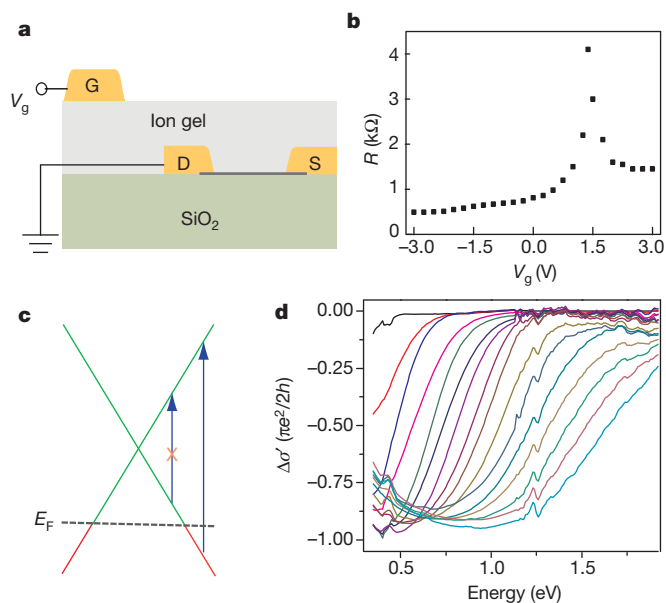


Figure 1 | Controlling the optical transitions in graphene with ion-gel gating. **a**, Illustration of an ion-gel-gated graphene device on a SiO_2 substrate. G, gate; D, drain; S, source. **b**, Graphene resistance (R) as a function of gate voltage, V_g ; R has a maximum at the charge neutral point $V_{\text{CNP}} = 1.2$ V. The largest resistance decrease, corresponding to the highest carrier density, occurs at $V_g = -3$ V with hole doping. **c**, Illustration of gate-induced change in graphene absorption. Electronic states are filled (red line) below E_F and empty (green line) above E_F . Electronic transitions (blue arrows) from zero energy to $2|E_F|$ get blocked by hole doping due to empty initial states. **d**, Change in the real part of optical conductivity, $\Delta\sigma'$, when $V_g - V_{\text{CNP}}$ is varied from -0.25 to -4 V in steps of 0.25 V. The optical conductivity is reduced for optical excitation energies below $2|E_F|$, which increases with gating strength. $2|E_F|$ values up to 1.8 eV are achieved using the ion-gel gate. (The feature around 1.3 eV is an artefact due to a minimum spectral density of our lamp light source at this energy.)

¹Department of Physics, University of California at Berkeley, Berkeley, California 94720, USA. ²Department of Chemical and Biomolecular Engineering, University of California at Berkeley, Berkeley, California 94720, USA. ³Materials Science Division, Lawrence Berkeley National Laboratory, Berkeley, California 94720, USA.

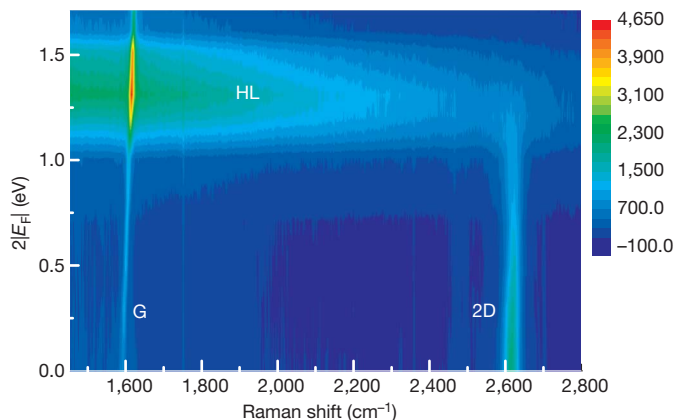


Figure 2 | Controlling inelastic light scattering with electrostatic doping. Graphene inelastic light scattering intensity (colour scale, arbitrary units) is plotted as a function of Stokes Raman redshift and $2|E_F|$ for 1.58-eV laser excitation energy (E_{ex}). G-mode Raman intensity (G; $\sim 1,600 \text{ cm}^{-1}$) is strongly enhanced as $2|E_F|$ approaches E_{ex} , thus blocking some of the Raman quantum pathways. In contrast, the 2D-Raman peak (2D; $\sim 2,600 \text{ cm}^{-1}$) is suppressed and eventually disappears with increasing $2|E_F|$. Broadband hot luminescence (HL) emerges when $2|E_F|$ is lower than but close to E_{ex} .

with reduced optical conductivity below the threshold energy, $2|E_F|$. The transition width of the threshold is due largely to the lifetime broadening from the excited state, and the transition centre yields the $2|E_F|$ value with an uncertainty less than 100 meV. From these spectra, we can also determine the carrier concentration $n = (E_F/\hbar v_F)^2/\pi$ (refs 10, 11), where v_F is the Fermi velocity. With ion-gel gating, vertical electronic transitions with excitation energies as high as 1.8 eV can be blocked. This corresponds to an induced carrier concentration of $6 \times 10^{13} \text{ cm}^{-2}$.

This large gate-induced shift in Fermi energy with ion-gel gating not only allows for controlled optical absorption, but also enables control over inelastic light scattering by varying the allowed intermediate excitations. Using a 785-nm excitation laser (that is, $E_{\text{ex}} = 1.58 \text{ eV}$),

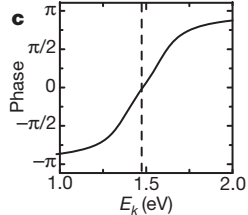
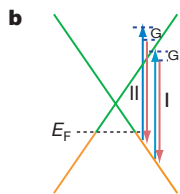
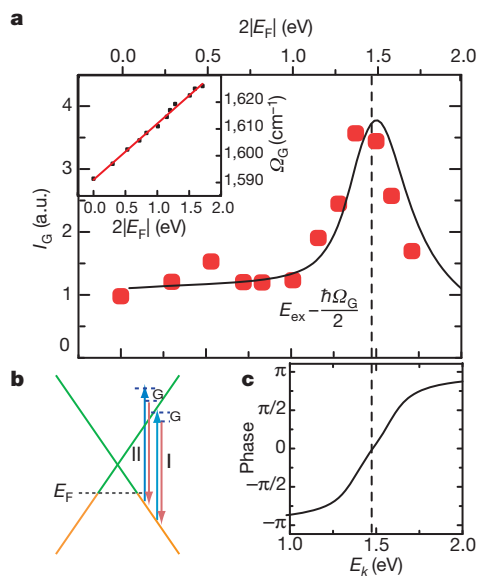
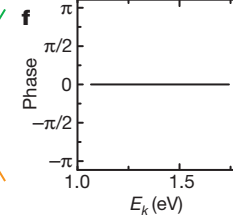
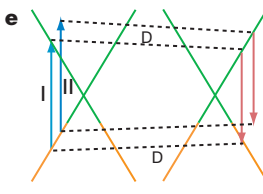
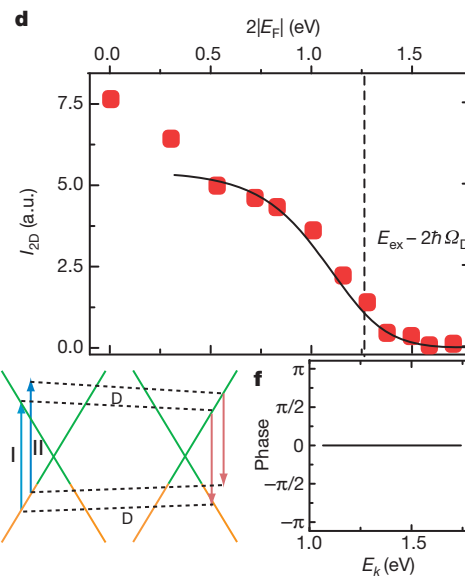


Figure 3 | Quantum interference between graphene Raman pathways. **a**, G-mode Raman intensity as a function of $2|E_F|$ (symbols). A large enhancement is observed when some of the Raman pathways are blocked, which is a hallmark of quantum interference. Black line, theoretical prediction. Inset, doping dependence of G-mode frequency. **b**, Illustration of two representative G-mode Raman pathways (I and II) through two different intermediate excited states. **c**, Quantum phase of Raman pathway amplitude illustrated as a function of intermediate excitation energy. Raman pathways with intermediate excitation energy above and below $E_{\text{ex}} - \hbar\Omega_G/2$ (dashed

we examine the evolution of inelastic light scattering spectra as $2|E_F|$ is varied from 0 to 1.8 eV. Figure 2 shows the inelastic emission intensity as a function of the Raman shift and of $2|E_F|$. At low doping, the spectra are characterized by prominent G-mode ($\sim 1,600 \text{ cm}^{-1}$) and 2D-mode ($\sim 2,600 \text{ cm}^{-1}$) phonon Raman peaks, as observed in previous studies¹². But two new features emerge when $2|E_F|$ becomes large enough to significantly alter intermediate-state pathways. (1) With larger $2|E_F|$ blocking part of the Raman quantum pathways, the G-mode Raman intensity does not decrease as one might expect, but increases and reaches a much higher peak value. This behaviour is in contrast to 2D-mode Raman intensity, the intensity of which does decrease monotonically as the resonant Raman pathways are blocked. (2) Photoluminescence over a wide spectral range emerges when $2|E_F|$ is slightly below the laser excitation energy. This hot-electron luminescence from continuous-wave laser excitation is quite unexpected, and it is distinctly different from recently observed nonlinear photoluminescence using femtosecond laser excitations^{23,24}.

We start our investigation by examining the unusual behaviour of G-mode phonon Raman intensity. The measured Raman peak position Ω_G blue-shifts linearly with Fermi energy as $\Delta\Omega_G = |E_F| \times 42 \text{ cm}^{-1} \text{ eV}^{-1}$ (Fig. 3a inset). This blue shift is due to phonon renormalization from non-adiabatic electron-phonon coupling, and has been well-studied previously^{16,17}. The behaviour of the integrated G-mode Raman intensity with $2|E_F|$ (Fig. 3a), however, has not been observed before. Increased event probability with reduced pathways, as observed in the G-mode Raman intensity here, is a canonical signature of destructive quantum interference. This result highlights the quantum nature of Raman scattering, and provides a valuable probe for microscopic Raman processes in graphene.

G-phonon Raman scattering has been extensively studied for characterizing graphitic materials^{12,13,25}, and is widely assumed to be a resonant Raman scattering process dominated by pathway I depicted in Fig. 3b (ref. 13). This picture, although appealing, cannot account for our observation. The possibility of enhancement in the Raman G signal on doping because of quantum interference between different Raman pathways was discussed in a recent theoretical study⁸. The



line) have an average phase difference of π and interfere destructively. Blocking pathways below $E_{\text{ex}} - \hbar\Omega_G/2$ therefore leads to large enhancement of G-mode Raman scattering. **d**, Doping dependence of 2D-mode Raman intensity (symbols). It drops quickly to zero when $2|E_F|$ approaches $E_{\text{ex}} - 2\hbar\Omega_D$ (dashed line), and agrees well with two-phonon Raman scattering theory (black line). **e**, Two representative pathways for the 2D Raman mode. **f**, Two-phonon scattering pathways illustrated in **e** have the same phase and interfere constructively. Blocking these pathways diminishes the intensity of 2D Raman scattering.

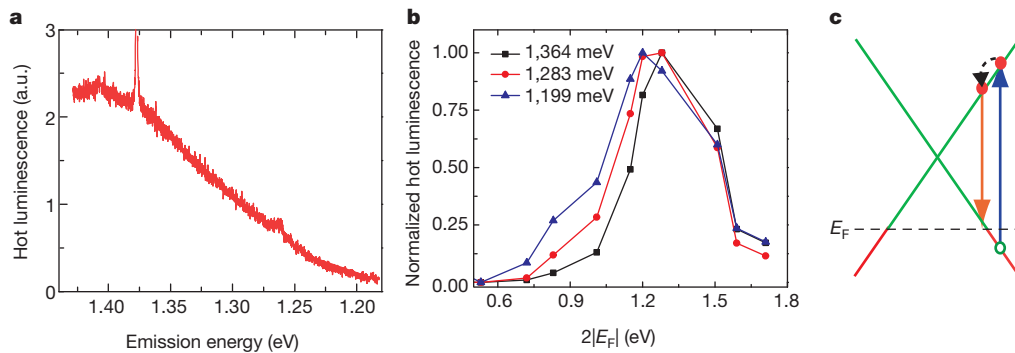


Figure 4 | Hot luminescence in graphene. **a**, Hot luminescence at $2|E_F| = 1.4$ eV shows a broad emission spectrum. It has an integrated intensity (in the range 1.2–1.4 eV) more than 100 times stronger than phonon Raman scattering. **b**, Normalized luminescence intensity as a function of $2|E_F|$ for three different excitation energies. Higher energy photon emissions have higher onset values for $2|E_F|$. **c**, Illustration of the hot luminescence generation mechanism. Red and green

Raman pathways in graphene can be on resonance (I in Fig. 3b), close to resonance (II in Fig. 3b), or off resonance. For a given final state of excitation (that is, emission of an optical phonon with defined momentum and polarization), pathways involving different intermediate states are indistinguishable. Therefore, all the pathways having different quantum mechanical amplitudes (that is, phase and magnitude) will interfere with each other. As such, blocking one quantum pathway can not only decrease but also increase the Raman intensity, depending on its phase relative to other pathways.

G-mode Raman intensity for any specific final one-phonon and one-photon state can be described by⁶:

$$I = \left| \sum_k C_k R_k \right|^2$$

and

$$R_k = \frac{1}{(E_{\text{ex}} - E_k - i\gamma)(E_{\text{ex}} - \hbar\Omega_G - E_k - i\gamma)}. \quad (1)$$

Here C_k and R_k are the matrix element and resonance factor, respectively, for a Raman pathway through a vertical electronic transition at wavevector k . E_k is the transition energy, E_{ex} the excitation energy, Ω_G the G-phonon frequency, and γ the energy broadening of the excited state. Phase differences between different pathways come mainly from the resonance factor R_k . For example, R_k for pathways resonant with incident light ($E_k = E_{\text{ex}}$) and scattered light ($E_k = E_{\text{ex}} - \hbar\Omega_G$) have opposite sign for small γ , and their Raman amplitudes largely cancel one other. In Fig. 3c we plot the phase of quantum pathways, $\Phi = \arg(R_k)$, through different intermediate electronic transitions for $E_{\text{ex}} = 1.58$ eV. We have set $\gamma = 0.2$ eV, which is estimated from the energy broadening in optical absorption spectra. The phase varies rapidly close to the resonance condition $E_k \approx E_{\text{ex}}$. In particular, pathways with transition energy E_k above and below energy $E_{\text{ex}} - \hbar\Omega_G/2$ have an average phase difference of π . They interfere destructively if all quantum pathways are allowed, and this leads to a weak overall Raman signal. When $2|E_F|$ is increased to block pathways with transition energies below $E_{\text{ex}} - \hbar\Omega_G/2$, the destructive interference is eliminated, and this leads to the observed large enhancement of Raman intensity. When $2|E_F|$ is increased further, more in-phase pathways are blocked and the Raman intensity starts to decrease. A quantitative evaluation of the matrix elements and a summation of all quantum pathways with $\gamma = 0.2$ eV was performed following ref. 8, and the result (black line in Fig. 3a) fits our experimental data (red squares) well. Because the cancellation from destructive interference from different Raman pathways is not perfect with energy dependent transition matrix elements and density of states, the G-mode Raman signal is still observable in undoped graphene. Nevertheless, the Raman intensity with all resonant pathways blocked ($2|E_F| = 1.8$ eV) is approximately the same

as when every pathway is allowed ($2|E_F| = 0$). It shows that the simple picture of G-mode graphene Raman scattering, in which only the on-resonance pathways are considered, is invalid.

The integrated intensity of the 2D-mode Raman peak, which results from simultaneous excitation of two phonons with wavevector close to the K-point in the graphene Brillouin zone, exhibits a doping dependence completely different from that of the integrated intensity of the G-mode Raman peak. Figure 3d shows the 2D-mode Raman intensity as a function of $2|E_F|$. The 2D intensity decreases slowly with increased doping when $2|E_F|$ is relatively small, which was observed previously¹⁴ and can be explained theoretically through the excited state broadening^{14,26}. Here we focus on the behaviour when $2|E_F|$ approaches E_{ex} . Instead of an enhanced scattering intensity as in G-mode Raman, the 2D-mode intensity drops quickly at the threshold energy $2|E_F| = E_{\text{ex}} - 2\hbar\Omega_D$, where Ω_D is the zone-boundary phonon frequency.

The intensity of 2D-mode Raman scattering is also determined by quantum interference between different pathways. Figure 3e illustrates two representative Raman pathways, including one satisfying the double resonance condition (pathway I)¹². Such two-phonon Raman pathways have one more virtual transition than one-phonon processes, and it has a profound effect on the Raman interference behaviour. Quantitatively, quantum interference in 2D-mode Raman for a specific final two-phonon and one-photon state is described by⁶:

$$I = \left| \sum_k D_k R_k \right|^2, \quad (2)$$

$$R_k = \frac{1}{(E_{\text{ex}} - E_k - i\gamma)(E_{\text{ex}} - \hbar\Omega_D - E_k - i\gamma)(E_{\text{ex}} - 2\hbar\Omega_D - E_{k'} - i\gamma)}$$

Here D_k is the matrix element of 2D-mode Raman scattering for a pathway starting at transition k . E_k , $E_{k'}$ and $E_{k''}$ are the energies of the three intermediate states. The resonance factor R_k determines the relative phase between different pathways. Figure 3f plots the phase of quantum pathways, involving the emission of two phonons with a specific wavevector, as a function of first-intermediate-state energy E_k for processes similar to those depicted in Fig. 3e (see also Supplementary Information). All the different pathways have the same phase and they interfere constructively. As a result, any reduction in quantum pathways leads to decreased Raman intensity, and when all resonant channels are blocked, the 2D-mode Raman signal becomes negligible. In Fig. 3d we show a more quantitative comparison between this theoretical picture (black line) and experimental results (symbols).

Last, we examine the graphene hot luminescence. Figure 4a shows the hot luminescence spectrum at $2|E_F| = 1.4$ eV, which is characterized by a broadband emission. To investigate the effect of carrier doping, we plot in Fig. 4b the normalized luminescence intensity as a function of

$2|E_F|$ for several emission energies (symbols). The luminescence is distinctly different from electronic Raman scattering²⁷ because zero-momentum electron-hole pair excitations required for the electronic Raman scattering do not exist in the strongly doped graphene. The peak observed in the hot luminescence when $2|E_F|$ approaches E_{ex} also has a different physical origin compared with that in G-mode phonon Raman. Instead of being an interference phenomenon from blocked Raman quantum pathways, the hot luminescence maximum is a consequence of newly opened dynamic pathways for photo-excited hot carriers.

We depict this dynamic process in Fig. 4c. An incident photon generates an electron and a hole, which then relax to the Fermi level through interactions with low-energy electrons and phonons. During the relaxation process, a hot electron has a finite probability of emitting a photon, but requires the final valence band state to be empty because of Pauli blocking (Fig. 4c). This pathway is opened up only when $2|E_F|$ exceeds the light emission energy, and defines a threshold doping level for hot luminescence generation. The qualitative features observed in Fig. 4b can be understood using this picture: hot luminescence emerges when the energy $2|E_F|$ is higher than an onset value that increases with the emission photon energy. When $2|E_F|$ is further increased to a value greater than the laser energy, hot luminescence at all energies suddenly disappears as the initial photoexcitations are blocked. Because the hot luminescence arises from radiative decay of excited electrons right after photoexcitation, it could become a valuable probe for ultrafast electron dynamics in graphene⁹.

Our study shows that inelastic light scattering phenomena can be explored by controlling the intermediate excited states. In graphene, it enables us to demonstrate the critical role of quantum interference in Raman scattering, and to reveal a new broadband hot luminescence. Such inelastic light scattering control could also be applied to general nanoscale material research, because electronic transitions in many nanostructures can be modified in a controlled fashion (for example, electrostatic gating of carbon nanotubes²⁸ and electrochemically tuned semiconductor quantum dots²⁹). This control will make inelastic light scattering a more powerful tool for probing novel nanoscale physics. It could also lead to optimized inelastic light scattering in nanomaterials for biological sensors and optoelectronic applications.

METHODS SUMMARY

In this study we use large area graphene grown by chemical vapour deposition³⁰. Graphene is grown on copper films using CH_4 as the feed gas, which was then transferred with poly(methyl methacrylate) (PMMA) support to a fused silica substrate after wet-etching to remove the copper film by FeCl_3 . The PMMA support is dissolved in acetone solution. Subsequently, Ti (10 nm) and Au (40 nm) were deposited in vacuum through stencil masks onto the graphene sample for the source, drain and gate electrodes.

The ionic liquid, 1-ethyl-3-methylimidazolium bis(trifluoromethylsulfonyl)imide ([EMIM][TFSI]), was purchased from EMD Chemicals. The ionic liquid was dried at $T = 100^\circ\text{C}$ under vacuum (~ 200 mtorr) for 3 days and then transferred to an inert-atmosphere glove box. Polystyrene-*b*-poly(ethylene oxide)-*b*-polystyrene (PS-PEO-PS) triblock copolymer was purchased from Polymer Source and used as received. The quoted molecular weights of the block copolymer moieties were 10–44–10 kg mol^{-1} for the PS-PEO-PS blocks, respectively (PEO volume fraction = 0.67). The physically crosslinked, ionic liquid/triblock copolymer gel (ion gel) was produced in the following manner. In an inert atmosphere glove box, 0.55 g of [EMIM][TFSI] were dissolved with 21 mg of PS-PEO-PS in 2 ml of dry dichloromethane. The solution was stirred overnight at room temperature. The ion gel was removed from the glove box and spin-coated on the graphene sample at a rate of 4,000 r.p.m.

Infrared transmission measurements were performed with a Fourier transform infrared spectrometer at the Advanced Light Source, Lawrence Berkeley National Laboratory. Inelastic light scattering was measured with a micro-Raman set-up with a 785-nm excitation laser. The Raman set-up has a spectral resolution of 1 cm^{-1} . All measurements were performed in air and at 300 K.

Received 1 September 2010; accepted 18 January 2011.

Published online 16 March 2011.

1. Raman, C. V. A change of wave-length in light scattering. *Nature* **121**, 619 (1928).

- Landsberg, G. & Mandelstam, L. Eine neue Erscheinung bei der Lichtzerstreuung in Kristallen. *Naturwissenschaften* **16**, 557 (1928).
- Rao, A. M. *et al.* Diameter-selective Raman scattering from vibrational modes in carbon nanotubes. *Science* **275**, 187–191 (1997).
- Devereaux, T. P. & Hackl, R. Inelastic light scattering from correlated electrons. *Rev. Mod. Phys.* **79**, 175–233 (2007).
- Gofri, A. R. *et al.* One-dimensional plasmon dispersion and dispersionless intersubband excitations in GaAs quantum wires. *Phys. Rev. Lett.* **67**, 3298–3301 (1991).
- Cardona, M. *Light Scattering in Solids I* 2nd edn (Springer, 1982).
- Ralston, J. M., Wadsack, R. L. & Chang, R. K. Resonant cancellation of Raman scattering from CdS and Si. *Phys. Rev. Lett.* **25**, 814–818 (1970).
- Basko, D. M. Calculation of the Raman G peak intensity in monolayer graphene: role of Ward identities. *N. J. Phys.* **11**, 095011 (2009).
- Elsaesser, T., Shah, J., Rota, L. & Lugli, P. Initial thermalization of photoexcited carriers in GaAs studied by femtosecond luminescence spectroscopy. *Phys. Rev. Lett.* **66**, 1757–1760 (1991).
- Novoselov, K. S. *et al.* Two-dimensional gas of massless Dirac fermions in graphene. *Nature* **438**, 197–200 (2005).
- Zhang, Y. B., Tan, Y. W., Stormer, H. L. & Kim, P. Experimental observation of the quantum Hall effect and Berry's phase in graphene. *Nature* **438**, 201–204 (2005).
- Ferrari, A. C. *et al.* Raman spectrum of graphene and graphene layers. *Phys. Rev. Lett.* **97**, 187401 (2006).
- Pimenta, M. A. *et al.* Studying disorder in graphite-based systems by Raman spectroscopy. *Phys. Chem. Chem. Phys.* **9**, 1276–1291 (2007).
- Das, A. *et al.* Monitoring dopants by Raman scattering in an electrochemically top-gated graphene transistor. *Nature Nanotechnol.* **3**, 210–215 (2008).
- Dresselhaus, M. S., Jorio, A., Hofmann, M., Dresselhaus, G. & Saito, R. Perspectives on carbon nanotubes and graphene Raman spectroscopy. *Nano Lett.* **10**, 751–758 (2010).
- Pisana, S. *et al.* Breakdown of the adiabatic Born-Oppenheimer approximation in graphene. *Nature Mater.* **6**, 198–201 (2007).
- Yan, J., Zhang, Y. B., Kim, P. & Pinczuk, A. Electric field effect tuning of electron-phonon coupling in graphene. *Phys. Rev. Lett.* **98**, 166802 (2007).
- Li, Z. Q. *et al.* Dirac charge dynamics in graphene by infrared spectroscopy. *Nature Phys.* **4**, 532–535 (2008).
- Wang, F. *et al.* Gate-variable optical transitions in graphene. *Science* **320**, 206–209 (2008).
- Zhang, Y. *et al.* Direct observation of a widely tunable bandgap in bilayer graphene. *Nature* **459**, 820–823 (2009).
- Cho, J. H. *et al.* Printable ion-gel gate dielectrics for low-voltage polymer thin-film transistors on plastic. *Nature Mater.* **7**, 900–906 (2008).
- Kim, B. J. *et al.* High-performance flexible graphene field effect transistors with ion gel gate dielectrics. *Nano Lett.* **10**, 3464–3466 (2010).
- Lui, C. H., Mak, K. F., Shan, J. & Heinz, T. F. Ultrafast photoluminescence from graphene. Preprint at (<http://arxiv.org/abs/1006.5769>) (2010).
- Stoehr, R. J., Kolesov, R., Pflaum, J. & Wrachtrup, J. Fluorescence of laser created electron-hole plasma in graphene. Preprint at (<http://arxiv.org/abs/1006.5434>) (2010).
- Dresselhaus, M. S., Dresselhaus, G., Saito, R. & Jorio, A. Raman spectroscopy of carbon nanotubes. *Phys. Rep.* **409**, 47–99 (2005).
- Basko, D. M., Pisanec, S. & Ferrari, A. C. Electron-electron interactions and doping dependence of the two-phonon Raman intensity in graphene. *Phys. Rev. B* **80**, 165413 (2009).
- Kashuba, O. & Fal'ko, V. I. Signature of electronic excitations in the Raman spectrum of graphene. *Phys. Rev. B* **80**, 241404(R) (2009).
- Ilani, S., Donev, L. A. K., Kindermann, M. & McEuen, P. L. Measurement of the quantum capacitance of interacting electrons in carbon nanotubes. *Nature Phys.* **2**, 687–691 (2006).
- Wang, C. J., Shim, M. & Guyot-Sionnest, P. Electrochromic nanocrystal quantum dots. *Science* **291**, 2390–2392 (2001).
- Li, X. S. *et al.* Large-area synthesis of high-quality and uniform graphene films on copper foils. *Science* **324**, 1312–1314 (2009).

Supplementary Information is linked to the online version of the paper at www.nature.com/nature.

Acknowledgements This work was supported by the US Department of Energy, Laboratory Directed Research and Development Program of Lawrence Berkeley National Laboratory under contract no. DE-AC02-05CH11231 (C.-F.C. and F.W.), by the Office of Basic Energy Sciences under contract nos DE-AC02-05CH11231 (B.W.B. and R.A.S.), DE-AC03-76SF0098 (Materials Science Division) (C.G., A.Z.) and DE-AC02-05CH11231 (Advanced Light Source), and by ONR MURI award N00014-09-1-1066 (J.H., C.-H.P., S.G.L., M.F.C.). C.-F.C. also acknowledges fellowship support from the National Science Council and National Tsing Hua University, Taiwan, under awards NSC98-2811-M-007-008 and NSC98-2120-M-007-004.

Author Contributions F.W. designed the experiment; C.-F.C. and J.H. carried out optical measurements; B.G., C.G. and B.W.B. contributed to sample growth and fabrication; and C.-H.P., S.G.L. and F.W. performed theoretical analysis. All authors discussed the results and wrote the paper together.

Author Information Reprints and permissions information is available at www.nature.com/reprints. The authors declare no competing financial interests. Readers are welcome to comment on the online version of this article at www.nature.com/nature. Correspondence and requests for materials should be addressed to F.W. (fengwang76@berkeley.edu).

Winter cold of eastern continental boundaries induced by warm ocean waters

Yohai Kaspi¹ & Tapio Schneider¹

In winter, northeastern North America and northeastern Asia are both colder than other regions at similar latitudes. This has been attributed to the effects of stationary weather systems set by elevated terrain (orography)¹, and to a lack of maritime influences from the prevailing westerly winds². However, the differences in extent and orography between the two continents suggest that further mechanisms are involved. Here we show that this anomalous winter cold can result in part from westward radiation of large-scale atmospheric waves—nearly stationary Rossby waves—generated by heating of the atmosphere over warm ocean waters. We demonstrate this mechanism using simulations with an idealized general circulation model^{3–5}, with which we show that the extent of the cold region is controlled by properties of Rossby waves, such as their group velocity and its dependence on the planetary rotation rate. Our results show that warm ocean waters contribute to the contrast in mid-latitude winter temperatures between eastern and western continental boundaries not only by warming western boundaries, but also by cooling eastern boundaries.

In middle latitudes, the eastern boundaries of Northern Hemisphere continents are colder than other regions at similar latitudes. Northeastern North America in winter is up to 20 K colder than similar latitudes in Europe, and northeastern Asia is similarly cold in comparison to northwestern North America (Fig. 1a). This anomalous cold has been attributed to several factors. The mean atmospheric flow in middle latitudes is westerly (eastward), so northeastern regions are farthest downstream from the warmer oceans, which may contribute to their coldness². However, although Asia is much wider than North America, the longitudinal extent of the two continents' coldest regions is similar (Fig. 1a), so this cannot be the sole contributing factor. The pattern of stationary weather systems, such as the Icelandic low over the Atlantic and the Aleutian low over the Pacific, also contributes to the advection of cold polar air over the eastern continental regions (Fig. 1b). The positions and strength of these weather systems are controlled by orography and the distribution of diabatic heating in the atmosphere^{6,7}. Orography has been posited as the principal factor controlling the temperature contrasts between eastern and western continental boundaries, in particular between North America and Europe, by generating stationary weather systems that drive warm and moist air towards Europe¹. However, although the American and Asian regions of extreme cold polewards of 30° N have a similar structure (Fig. 1a), the North American and Asian orographies are very different. This suggests that yet further mechanisms contribute to the formation of the cold regions.

By sharp contrast, the western boundaries of oceans adjacent to the cold regions are characterized by strong, warm currents such as the Gulf Stream off the North American coast and the Kuroshio off the Asian coast. These boundary currents carry large amounts of heat polewards⁸, leading to large heat fluxes (mainly latent heat fluxes) from the warm oceans into the atmosphere (Fig. 1c). Here we show that atmospheric heating above warm ocean waters generates nearly stationary Rossby waves^{7,9}, which cause an anomalously cold region immediately to the

west of the heating region. The size of this cold region is not set by the length scale of stationary waves⁹, but is controlled by the distance over which wave groups are radiated westwards before they dissipate.

To demonstrate this mechanism we use a three-dimensional general circulation model (GCM) with an active hydrological cycle^{3–5}. The GCM is idealized, in that radiative transfer and moist convection are represented in a simplified manner, and processes not essential to the mechanism we study (for example, cloud-radiative feedbacks) are ignored. To represent heat fluxes from warm ocean waters, we added a localized ocean heat-flux convergence in the Northern Hemisphere; as a control, we added the same zonal-mean heat-flux convergence in the Southern Hemisphere, spread in a zonally symmetric fashion over all longitudes. The triangular heating region in the Northern Hemisphere (Fig. 2) roughly mimics the shape of the Asian and North American shorelines and the adjacent western boundary currents, with the western side of the triangle loosely representing the land–ocean boundary. The magnitude of the heat-flux convergence is set to resemble observed measurements (Fig. 1c), but the mechanism discussed here does not depend on details such as the magnitude or shape of the heating. See the Methods for details of the model.

To analyse systematically how heating leads to upstream cooling, we performed a series of simulations with planetary rotation rates between 0.25 Ω_e and 10 Ω_e , where Ω_e is Earth's rotation rate. This allows us to discriminate between wave mechanisms that depend in different ways on the planetary rotation rate. We begin by looking at a simulation with Earth's rotation rate (Fig. 2, left column).

The localized surface heating induces a region of strong temperature gradients, and therefore strong baroclinicity, downstream (Supplementary Fig. 2). It also creates a region of strong atmospheric diabatic heating. Both factors contribute to the formation of a region of enhanced transient eddy kinetic energy downstream (Fig. 2a). Furthermore, the localized heating creates a stationary low-pressure system (cyclone) to its east and a stationary high-pressure system (anticyclone) to its west (Fig. 2d), resembling in structure and magnitude the pattern of stationary weather systems observed in nature (Fig. 1b). This pattern of stationary weather systems arises because, in the middle latitudes, atmospheric heating is primarily balanced by horizontal advection of cooler air, and this advection must be in approximate geostrophic balance with the pressure field^{10,11}. The stationary circulation induced by localized heating causes equatorward advection of cold polar air towards the heating region and westward of it, and poleward advection of warm low-latitude air eastward of it (Fig. 2b).

The surface highs and lows are manifestations of stationary Rossby waves, which are induced by the localized heating^{6,7,9,10,12–14}. These stationary waves can be described well by barotropic dynamics¹⁰, and can be seen clearly in the vertically averaged meridional velocity (Fig. 2c). The frequency of barotropic Rossby waves, ω , is given by

$$\omega = \bar{u}k - \frac{\beta k}{k^2 + l^2} \quad (1)$$

where β is the planetary vorticity gradient, k is the zonal wave number, l is the meridional wave number and \bar{u} is the mean zonal velocity¹⁵. For

¹California Institute of Technology, Pasadena, California 91125, USA.

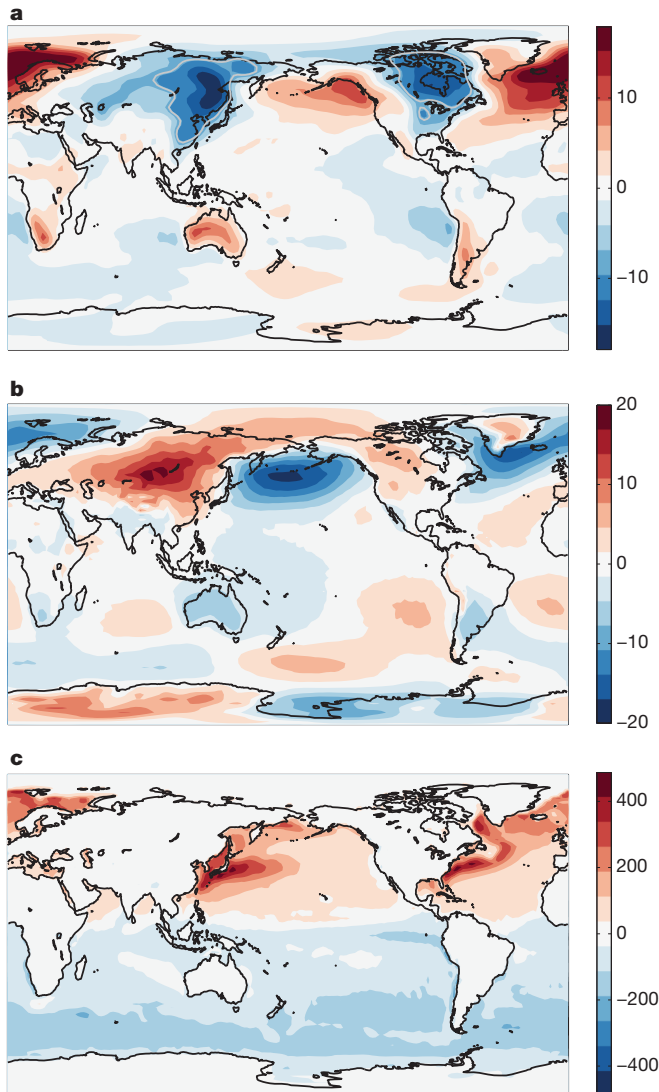


Figure 1 | Observational data for Northern Hemisphere winter months (December–February), averaged between 1970 and 2009. **a**, Surface-temperature deviation (K) from zonal mean (-8 K contour shown in grey, pointing to the similarity between the width of the cold regions in America and Asia). **b**, Interpolated sea-level pressure deviation from zonal mean (hPa). **c**, Implicit ocean heat-flux convergence (W m^{-2}) given by $Lh + Sh + LW - SW$, where Lh is the latent heat flux, Sh is the sensible heat flux and LW and SW are the net upward longwave and downward shortwave radiative fluxes at the surface. This implicit ocean heat-flux convergence contains contributions from the actual ocean heat-flux convergence and the seasonal release of stored heat. (Based on reanalysis data from the US National Centers for Environmental Prediction²².)

isotropic waves ($k = l$), this gives a length scale of $\lambda = 2\pi(\bar{u}/\beta)^{1/2}$ when $\omega = 0$ (that is, for stationary waves). For $\Omega = \Omega_e$ and a typical mid-latitude value of $\bar{u} \approx 20 \text{ m s}^{-1}$, this gives wavelengths of about 7,000 km, corresponding to about 4 wave crests over a latitude circle, similar to the length scales seen in nature and in the simulations (Figs 1b and 2c). One might thus infer that the longitudinal extent of the region of upstream cooling is set by the stationary Rossby wavelength.

However, when the planetary rotation rate is changed, it becomes clear that the extent of the region of upstream cooling is set by different dynamics. The extent of the cooling region increases with rotation rate (Fig. 2b), whereas the stationary Rossby wavelength decreases (Fig. 2c). Thus, it is not simply the phase of the stationary wave that controls the extent of the cold region upstream of the heating. As the rotation

rate increases, both the energy-containing length scale¹⁶ and the stationary wavelength become smaller, whereas—counterintuitively—the cold region upstream expands.

The extent of the upstream cold region is controlled by the group dynamics of nearly stationary Rossby waves. Dispersive waves can have a non-zero group velocity ($\vec{c}_g = \partial\omega/\partial(k, l)$) even when they are stationary¹⁷. The dispersion relation equation (1) implies the group velocity

$$\vec{c}_g = [c_{gx}, c_{gy}] = \left[\bar{u} - \frac{\beta}{l^2}, 0 \right] \quad (2)$$

in the nearly stationary limit ($\omega \rightarrow 0$) of zonally elongated waves ($k \rightarrow 0$)^{18,19}. This zonal group velocity is westward for waves with a sufficiently large meridional scale, such that $\bar{u} < \beta/l^2$. Features such as an anticyclonic vorticity anomaly to the west of a localized heating can be then radiated farther westwards at this group velocity, forming a plume^{18–20}. The extent of this plume is limited by the scale over which the nearly stationary Rossby wave groups propagate zonally. If the waves are damped on a time scale τ , the plume can be expected to extend over a zonal scale $L \sim c_{gx}\tau = (\bar{u} - \beta/l^2)\tau$, which depends on \bar{u} , β and the meridional scale of the localized heating, $2\pi/l$ ^{18,19}. To the extent that variations in \bar{u} and τ are relatively small, this length scale increases linearly with planetary rotation rate.

This is borne out in our simulations. The scale of the cold region upstream of the heating does indeed increase approximately linearly with rotation rate from $0.5 \Omega_e$ to $10 \Omega_e$ (Fig. 3). (The strength of the mid-tropospheric zonal flow \bar{u} varies by less than a factor of 2 in the range of rotation rates we have explored, and therefore does not strongly affect the approximately linear dependence between c_{gx} and Ω .) For a meridional wave number $l \approx 5$ corresponding to the scale of our heating region, $\beta/l^2 \approx 28 \text{ m s}^{-1}$ in middle latitudes for Earth's rotation rate, and this velocity increases with rotation rate. Therefore, for all cases in which $\Omega \geq \Omega_e$ (for which $\bar{u} \lesssim 20 \text{ m s}^{-1}$ in the mid-troposphere), we have $\bar{u} < \beta/l^2$, and so the group velocity is westwards. The extent of the upstream cooling region is controlled by the westward radiation of nearly stationary Rossby wave groups, which decay over τ . The variations in \bar{u} are weak relative to those in the rotation rate, so τ can be inferred from the slope of the line of extent plotted against rotation rate (Fig. 3). It is of the order of days in our simulations. The damping time scale inferred from the regression of the extent of the cold region on the estimated group velocity of the waves varies by less than a factor of 2 as the rotation rate is varied, whereas the group velocity varies from about 10 to 250 m s^{-1} . (An exact determination is difficult because it is unclear at precisely which level \bar{u} should be evaluated to obtain the group velocity.)

It happens that for Earth's rotation rate and the typical meridional scales of the heating regions over western boundary currents, the group velocity is such that the extent of the cold region upstream is similar to the length scale of a stationary Rossby wave. But the extent of the cold region is in fact controlled by different dynamics. Although downstream features of the circulation (for example, the eddy kinetic energy) may be controlled by stationary wave length scales²¹, the upstream cooling is controlled by the group velocity of nearly stationary, zonally elongated waves, as the simulations with different rotation rates show. Even when compared with a simulation without any extra heating (whether localized or spread out longitudinally in middle latitudes), the simulations with localized mid-latitude heating exhibit an anomalously cold region upstream.

Ref. 1 posited that winter temperature contrasts between mid-latitude eastern and western continental boundaries were controlled mostly by stationary weather systems caused by orography, as opposed to heating over oceans. However, this inference was based on eliminating all ocean heat transports in a GCM simulation, including tropical and subtropical transports, which resulted in widespread and large extra-tropical atmospheric cooling, with concomitant large atmospheric

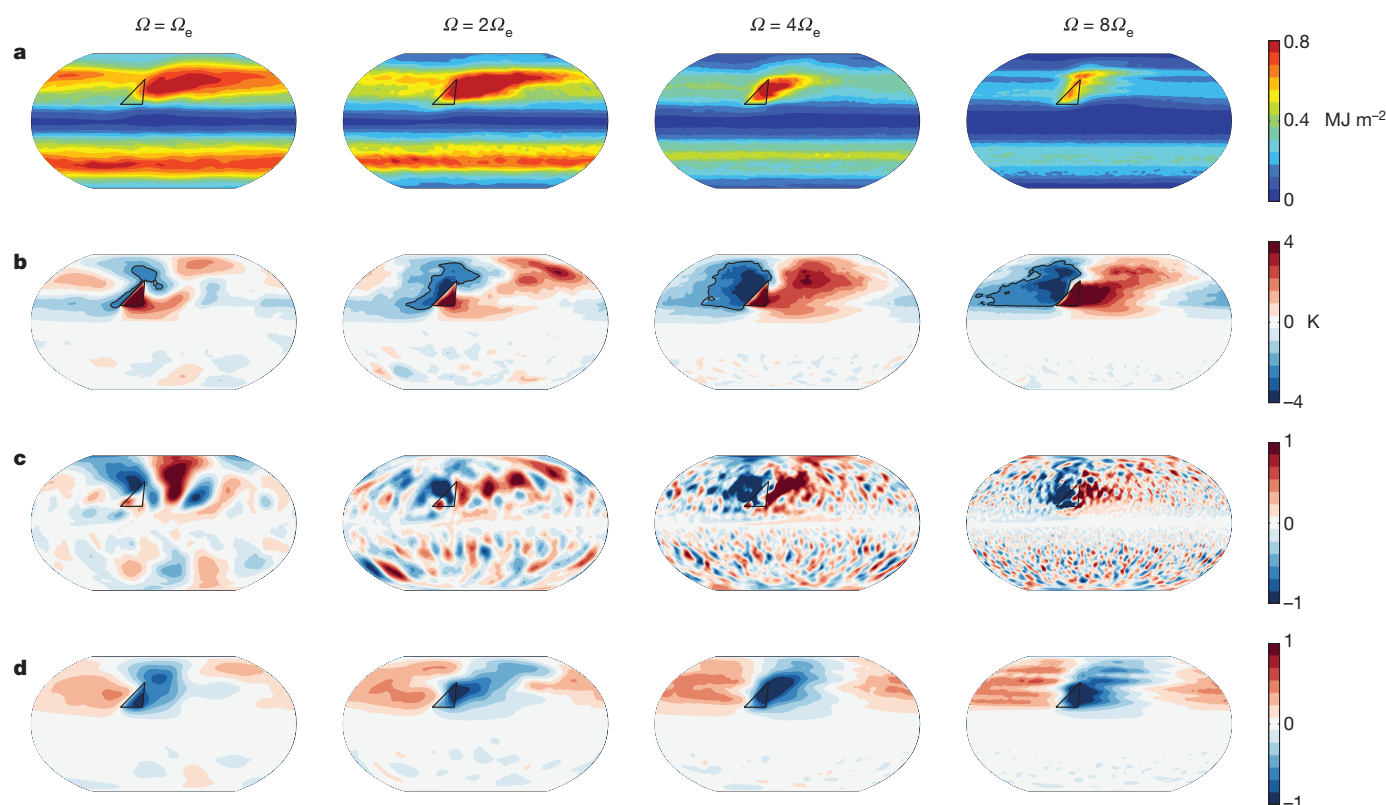


Figure 2 | Time-averaged fields simulated with the idealized GCM for planetary rotation rates of Ω_e , $2\Omega_e$, $4\Omega_e$ and $8\Omega_e$. **a**, Vertically integrated tropospheric transient eddy kinetic energy. **b**, Surface-temperature deviation from zonal mean. **c**, Vertically averaged tropospheric meridional velocity deviation from zonal mean. The units are non-dimensional, with 1 corresponding to 2.5 m s^{-1} (for Ω_e), 1.5 m s^{-1} ($2\Omega_e$), 0.75 m s^{-1} ($4\Omega_e$) and 0.6 m s^{-1} ($8\Omega_e$), respectively. **d**, Surface-pressure deviation from zonal mean. The units are non-dimensional, with 1 corresponding to 10 hPa (for Ω_e), 15 hPa

($2\Omega_e$), 20 hPa ($4\Omega_e$) and 25 hPa ($8\Omega_e$), respectively. In all figures, the heating region is marked with a triangle and has a uniform heat-flux convergence of 500 W m^{-2} , similar to observations. The upstream cooling increases linearly with the heat-flux convergence; see Supplementary Fig. 1. As the rotation rate increases, the eddy kinetic energy maximum becomes zonally more confined, whereas the upstream cold region expands. The stationary waves are evident in the meridional velocity (c).

circulation changes. This does not rule out the local importance of extratropical ocean heat fluxes for stationary weather systems.

We propose, then, that the anomalous winter cold of eastern continental boundaries can result at least in part from radiation of nearly stationary Rossby wave groups off the regions of large surface heat fluxes over the warm waters in oceanic western boundary currents. We have demonstrated this mechanism in the idealized GCM, with heat fluxes of similar magnitude to those observed over the western boundary currents, and with a climate similar to that of Earth in winter

(Supplementary Fig. 2). The GCM produces a stationary cyclone–anticyclone pair and a cold region upstream, with surface-pressure ($\sim 10 \text{ hPa}$) and temperature ($\sim 4 \text{ K}$) deviations from the zonal mean and from the mean over regions far downstream that are about half those observed on Earth (compare Figs 1 and 2). Thus, the Rossby-wave mechanism is probably quantitatively significant in producing the cold regions over eastern continental boundaries on Earth. Topography has already been shown to contribute¹, and other factors ignored in the idealized GCM, such as land–ocean contrasts, effects of continentality and clouds probably also play a role. Nevertheless, the dynamics we have described are large-scale and robust. They provide a plausible answer to the question of why the eastern continental boundaries of both Asia and North America are so cold, and why the extent of the cold regions on both continents is similar.

METHODS SUMMARY

The idealized GCM is based on the Flexible Modelling System of the US National Oceanic and Atmospheric Administration's Geophysical Fluid Dynamics Laboratory. It is a three-dimensional model of a spherical aquaplanet, and solves the primitive equations for an ideal-gas atmosphere^{3–5}. We use a horizontal spectral resolution of T85 and 30 vertical levels. For simulations with planetary rotation rates Ω greater than $4\Omega_e$ we use the higher resolution of T127 to resolve the smaller energy-containing eddies. The lower boundary is a uniform slab ocean. Radiative transfer is represented by a two-stream grey radiation scheme. Moist convection is represented by a quasi-equilibrium convection scheme⁴, which relaxes temperatures towards a moist adiabat and water vapour towards a profile with fixed relative humidity relative to a moist adiabat. To damp small scales, strongly scale-selective hyperdiffusion is included in the vorticity, divergence and temperature equations.

Zonal asymmetries to initiate stationary waves are introduced by imposing a localized ocean heat-flux convergence in a triangular mid-latitude region. This is

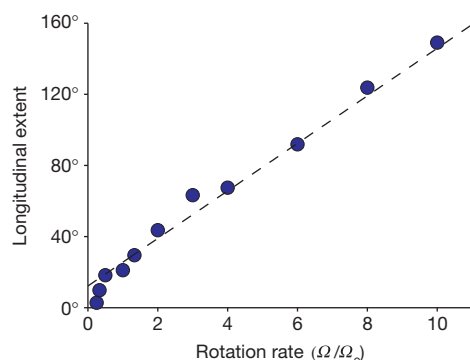


Figure 3 | Extent of upstream cold region as a function of planetary rotation rate. The extent of the upstream cold region is the longitudinal distance between the centre of the triangle and the westernmost extent of the bold -2 K contour in Fig. 2b; the planetary rotation rate is given in multiples of Ω_e . The dashed line represents the linear least-squares fit.

an idealized representation of the area of warm ocean waters and strong atmospheric diabatic heating in the Gulf Stream or Kuroshio western boundary currents. The magnitude of the heat flux convergence (500 W m^{-2}) is chosen to be similar to the observed heat fluxes (Fig. 1c). Our results do not depend qualitatively on the particular shape, size or magnitude of the imposed heat-flux convergence; the magnitude of the upstream cooling increases approximately linearly with the imposed heat-flux convergence (Supplementary Fig. 1). All simulation results presented are averages of flow fields sampled 4 times a day for at least 4 years, after a long spin-up period in which the GCM statistics reached a steady state.

Full Methods and any associated references are available in the online version of the paper at www.nature.com/nature.

Received 30 August 2010; accepted 10 February 2011.

- Seager, R. *et al.* Is the Gulf Stream responsible for Europe's mild winters? *Q. J. R. Meteorol. Soc.* **128**, 2563–2586 (2002).
- Hartmann, D. L. *Global Physical Climatology* (Academic Press, 1994). Ch. 7.4.
- Frierson, D. M. W., Held, I. M. & Zurita-Gotor, P. A gray-radiation aquaplanet moist GCM. Part I: static stability and eddy scale. *J. Atmos. Sci.* **63**, 2548–2566 (2006).
- Frierson, D. M. W. The dynamics of idealized convection schemes and their effect on the zonally averaged tropical circulation. *J. Atmos. Sci.* **64**, 1959–1976 (2007).
- O'Gorman, P. A. & Schneider, T. The hydrological cycle over a wide range of climates simulated with an idealized GCM. *J. Clim.* **21**, 3815–3832 (2008).
- Held, I. M. in *Large-scale Dynamical Processes in the Atmosphere* (eds Hoskins, B. & Pearce, R.) 127–168 (1983).
- Held, I. M., Ting, M. & Wang, H. Northern winter stationary waves: theory and modeling. *J. Clim.* **15**, 2125–2144 (2002).
- Hsiung, J. Estimates of global oceanic meridional heat transport. *J. Phys. Oceanogr.* **15**, 1405–1413 (1985).
- Smagorinsky, J. The dynamical influence of large-scale heat sources and sinks on the quasi-stationary mean motions of the atmosphere. *Q. J. R. Meteorol. Soc.* **79**, 342–366 (1953).
- Hoskins, B. J. & Karoly, D. J. The steady linear response of a spherical atmosphere to thermal and orographic forcing. *J. Atmos. Sci.* **38**, 1179–1196 (1981).
- Held, I. M. & Ting, M. Orographic versus thermal forcing of stationary waves: the importance of the mean low-level wind. *J. Atmos. Sci.* **47**, 495–500 (1990).
- Lau, N. C. The observed structure of tropospheric stationary waves and the local balances of vorticity and heat. *J. Atmos. Sci.* **36**, 996–1016 (1979).
- Grose, W. L. & Hoskins, B. J. On the influence of orography on large-scale atmospheric flow. *J. Atmos. Sci.* **36**, 223–234 (1979).
- Cook, K. H. & Held, I. M. The stationary response to large-scale orography in a general circulation model and a linear model. *J. Atmos. Sci.* **49**, 525–539 (1992).
- Pedlosky, J. *Geophysical Fluid Dynamics* 2nd edn (Springer-Verlag, 1987).
- Schneider, T. & Walker, C. C. Self-organization of atmospheric macroturbulence into critical states of weak nonlinear eddy–eddy interactions. *J. Atmos. Sci.* **63**, 1569–1586 (2006).
- Lighthill, M. J. On waves generated in dispersive systems by travelling forcing effects, with applications to the dynamics of rotating fluids. *J. Fluid Mech.* **27**, 725–752 (1967).
- Rhines, P. B. in *Dynamics in Astrophysics and Geophysics* (ed. Lebovitz, N. R.) 3–58 (1983).
- Rhines, P. B. *Rossby Waves, Encyclopedia of Atmospheric Sciences* (Academic Press, 2002).
- Rhines, P. B. Jets and orography: idealized experiments with tip jets and Lighthill blocking. *J. Atmos. Sci.* **64**, 3627–3639 (2007).
- Kaspi, Y. & Schneider, T. Downstream self-destruction of storm tracks. *J. Atmos. Sci.* (in the press) (2011).
- Kalnay, E. *et al.* The NCEP/NCAR 40-year reanalysis project. *Bull. Am. Meteorol. Soc.* **77**, 437–470 (1996).

Supplementary Information is linked to the online version of the paper at www.nature.com/nature.

Acknowledgements We thank D. Abbot, I. Eisenman, X. Levine and T. Merlis for comments. This research was supported by the National Oceanic and Atmospheric Administration Climate and Global Change Postdoctoral Fellowship administered by the University Corporation for Atmospheric Research (Y.K.), by a David and Lucile Packard Fellowship (T.S.), and by a grant from the National Science Foundation (AGS-1019211). The simulations were performed on the California Institute of Technology's Division of Geological and Planetary Sciences Dell cluster.

Author Contributions Y.K. and T.S. designed the study and wrote the paper; Y.K. performed the numerical simulations and data analyses.

Author Information Reprints and permissions information is available at www.nature.com/reprints. The authors declare no competing financial interests. Readers are welcome to comment on the online version of this article at www.nature.com/nature. Correspondence and requests for materials should be addressed to Y.K. (yohai@alum.mit.edu).

METHODS

The idealized GCM is based on the Flexible Modelling System of the US National Oceanic and Atmospheric Agency's Geophysical Fluid Dynamics Laboratory. It is a three-dimensional model of a spherical aquaplanet, and solves the primitive equations for an ideal-gas atmosphere^{3–5}. It does not take into account factors that are not essential to the mechanism, such as clouds, aerosols, sea-ice, water-vapour feedback and the diurnal and seasonal cycles.

Resolution. The GCM solves the hydrostatic primitive equations in vorticity-divergence form, using the spectral-transform method in the horizontal and finite differences in the vertical. The horizontal spectral resolution is T85 (corresponding to about $1.4^\circ \times 1.4^\circ$ resolution of the transform grid). The vertical coordinate is $\sigma = p/p_s$ (pressure p normalized by surface pressure p_s), and has 30 discrete levels. For simulations with planetary rotation rates Ω greater than $4\Omega_e$, we use the higher resolution of T127 to resolve the smaller energy-containing eddies.

Radiative transfer. Radiative transfer is represented by a two-stream grey radiation scheme with longwave and shortwave optical depths that depend only on latitude and pressure. The longwave optical thickness τ is given by

$$\tau = [f_l \sigma + (1 - f_l) \sigma^4] [\tau_e + (\tau_p - \tau_e) \sin^2 \phi],$$

where ϕ is latitude and $f_l = 0.2$. The linear and quadratic terms in σ roughly represent absorption by a well mixed absorber (with weight f_l) and by water vapour (with weight $1 - f_l$), respectively^{3,5}. The term τ_e represents the longwave optical thickness at the equator, and is equal to 4.8; τ_p is the longwave optical thickness at the pole, and is 1.2. These are chosen to result roughly in a winter-hemisphere meridional temperature distribution. Solar radiative fluxes are imposed equally between hemispheres and are given by

$$S = \frac{S_0}{4} \left[1 + \frac{\Delta_s}{4} (1 - 3 \sin^2 \phi) \right] \exp(-\tau_s \sigma^2),$$

where $S_0 = 1,360 \text{ W m}^{-2}$ is the solar constant, $\Delta_s = 1.2$ controls the pole–equator insolation gradient and $\tau_s = 0.22$ is the optical thickness for solar radiation.

Moist convection and large-scale condensation. Moist convection is represented by a quasi-equilibrium convection scheme⁴, which relaxes temperatures towards a moist adiabat with a time scale of 2 h, and water vapour towards a profile with fixed humidity of 70% relative to the moist adiabat, whenever a parcel lifted from the lowest model level is convectively unstable. Large-scale condensation removes water vapour from the atmosphere when the specific humidity on the grid scale exceeds saturation.

Moist thermodynamics. Water vapour is advected with a finite-volume scheme on the transform grid. A large-scale (grid-scale) condensation scheme ensures that the mean relative humidity in a grid cell does not exceed 100%. Only the vapour–liquid phase change is considered, and the saturation vapour pressure e_s is calculated from a simplified Clausius–Clapeyron relation given by

$$e_s(T) = e_0 \exp \left[-\frac{L}{R_v} \left(\frac{1}{T} - \frac{1}{T_0} \right) \right],$$

where $R_v = 461.5 \text{ J kg}^{-1} \text{ K}^{-1}$ is the gas constant for water vapour, $L = 2.5 \times 10^6 \text{ J kg}^{-1}$ is a fixed latent heat of vaporization, and $e_0 = 610.78 \text{ Pa}$ is the vapour pressure and $T_0 = 273.16 \text{ K}$ the temperature at the triple point of water.

Boundary layer. The lower boundary of the GCM is uniform and water covered, with an albedo of 0.38. A planetary boundary-layer scheme with Monin–Obukhov surface fluxes, which depend on the stability of the boundary layer, links atmospheric dynamics to surface fluxes of momentum, latent heat and sensible heat. The roughness length for momentum, moisture and heat fluxes is $1 \times 10^{-3} \text{ m}$, and an additive gustiness term of 1 m s^{-1} is added to surface velocities in bulk aerodynamic formulae to represent subgrid-scale wind fluctuations. These values allow us to obtain energy fluxes and a climate similar to Earth's in the aquaplanet setting of our simulations. Our results are not very sensitive to the choice of these parameters.

Subgrid-scale dissipation. Above the boundary layer, horizontal ∇^8 hyperdiffusion in the vorticity, divergence and temperature equations is the only dissipative process. The hyperdiffusion coefficient is chosen to give a damping time scale of 12 h at the smallest resolved scale.

Surface energy balance. The surface temperature evolves according to the surface energy balance of a homogeneous slab, with temperature tendencies balanced by insolation, thermal radiative fluxes and the surface fluxes of sensible heat and latent heat. The precise value of the heat capacity (or thickness) of the slab does not substantially affect our results, which are for statistically steady states. In our simulations, the slab has a heat capacity corresponding to a 1-m layer of water.

Spin-up. All simulations have been spun-up to statistically steady state for at least 3,000 simulation days. The results presented here have been averaged over at least 4 years of simulation time beyond spin-up, and are all in a statistically steady state.

Zonal Asymmetries. Zonal asymmetries are introduced by imposing a localized heat-flux convergence in a triangular mid-latitude region. This is an idealized representation of the area of warm ocean waters and strong atmospheric heating in the Gulf Stream or Kuroshio western boundary currents. The localized heating is applied between latitudes 25° N and 50° N . The magnitude of the heat-flux convergence (500 W m^{-2}) is chosen to be similar to the observed heat fluxes from the surface (Fig. 1c). Our results do not depend qualitatively on the particular shape, size or magnitude of the imposed heat-flux convergence. The upstream cooling increases approximately linearly with the magnitude of the heating (Supplementary Fig. 1). As a control case, we impose in the Southern Hemisphere a heat-flux convergence that is equal in the zonal mean to that in the Northern Hemisphere, but is spread zonally symmetrically over all longitudes. (The deviations from the local zonal mean in the Northern Hemisphere shown in Fig. 2 are very similar to the corresponding deviations from the Southern Hemisphere zonal mean.)

A eudicot from the Early Cretaceous of China

Ge Sun^{1,2}, David L. Dilcher^{1,2,3}, Hongshan Wang^{1,4} & Zhiduan Chen⁵

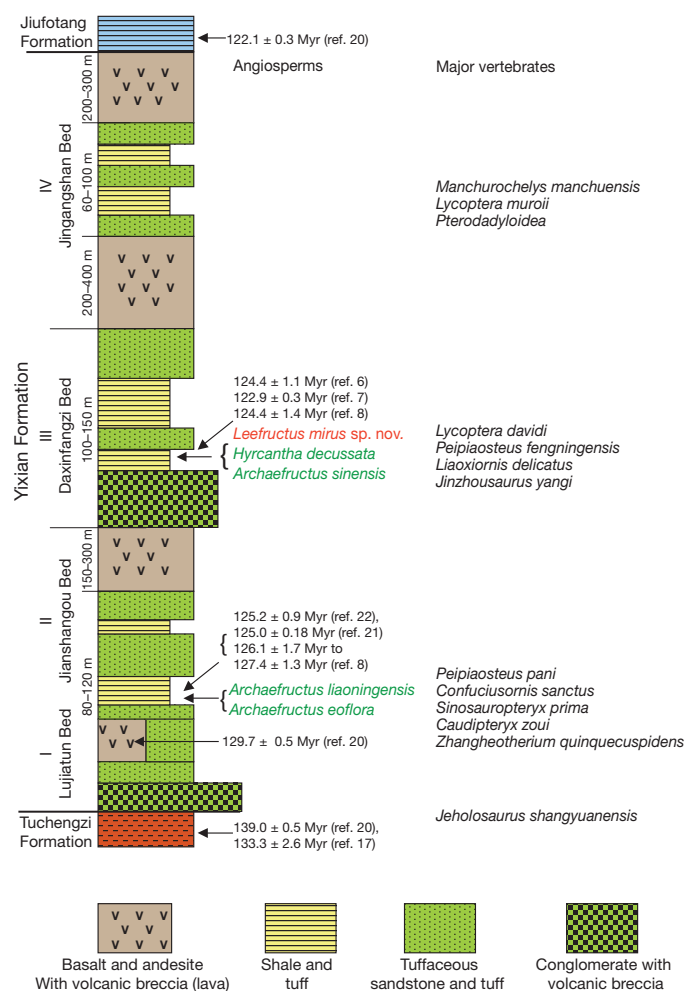
The current molecular systematics of angiosperms¹ recognizes the basal angiosperms and five major angiosperm lineages: the Chloranthaceae, the magnoliids, the monocots, *Ceratophyllum* and the eudicots, which consist of the basal eudicots and the core eudicots². The eudicots form the majority of the angiosperms in the world today. The flowering plants are of exceptional evolutionary interest because of their diversity of over 250,000 species and their abundance as the dominant vegetation in most terrestrial ecosystems, but little is known of their very early history. In this report we document an early presence of eudicots during the Early Cretaceous Period. Diagnostic characters of the eudicot fossil *Leefructus* gen. nov. include simple and deeply trilobate leaves clustered at the nodes in threes or fours, basal palinactinodromous primary venation, pinnate secondary venation, and a long axillary reproductive axis terminating in a flattened receptacle bearing five long, narrow pseudo-syncarpous carpels. These morphological characters suggest that its affinities are with the Ranunculaceae, a basal eudicot family. The fossil co-occurs with *Archaeofructus sinensis*³ and *Hyracantha decussata*⁴ whereas *Archaeofructus liaoningensis*⁵ comes from more ancient sediments. Multiple radiometric dates of the Lower Cretaceous Yixian Formation place the bed yielding this fossil at 122.6–125.8 million years old^{6–8}. The earliest fossil records of eudicots are 127 to 125 million years old, on the basis of pollen^{9,10}. Thus, *Leefructus* gen. nov. suggests that the basal eudicots were already present and diverse by the latest Barremian and earliest Aptian.

The evolutionary history of the angiosperms is still being revealed since their Early Cretaceous or possible earlier origin and their rapid radiations during the mid-Cretaceous^{2,11,12,13}. Here we present a new fossil plant from the Jehol Biota. The Jehol Biota is preserved mainly in

the Yixian Formation of northeast China (Figs 1 and 2), which has yielded rich assemblages of animals and plants. Early birds, feathered dinosaurs, placental mammals and a variety of invertebrate fossils have been found^{14–16} as well as several angiosperms, including *Archaeofructus* and *Hyracantha*^{3–5}. The presence of *Archaeofructus* at about 125 Myr ago¹⁷ clearly documents the presence of basal angiosperms in the megafossil record of the Early Cretaceous and now we also document the presence of basal eudicots from the same stratigraphic horizon. These early angiosperms are followed by diverse and abundant fossils



Figure 1 | Fossil locations. The map shows the Dawangzhangzi locality in Lingyuan where the fossil *Leefructus mirus* gen. et sp. nov. was collected (1) and the Huangbanjigou locality in Beipiao where *Archaeofructus liaoningensis* was collected (2). The inset map shows the location of Liaoning Province in northeast China (star indicates Beijing).



¹Paleontological Institute of Shenyang Normal University, Shenyang 110034, China. ²Research Center of Paleontology, Jilin University, Changchun 130026, China. ³Department of Biology, Indiana University, Bloomington, Indiana 47405, USA. ⁴Florida Museum of Natural History, University of Florida, Gainesville, Florida 32611-7800, USA. ⁵State Key Laboratory of Systematic and Evolutionary Botany, Institute of Botany, Chinese Academy of Sciences, Beijing 100093, China.

of all major angiosperm taxa in sediments of the late Aptian and the Albian ages (112 to 100 Myr ago). Much of the record of early angiosperm diversity and their subsequent middle to late Albian radiations come to us from fossils that encompass a complete range of preserved plant organs such as pollen, mesofossils and megafossils^{11,12}. We follow the Angiosperm Phylogeny Group¹⁸ to classify the fossil.

Angiosperms
Eudicots

Ranunculales (compare Family stem lineage to the Ranunculaceae)

Leefructus Sun, Dilcher, Wang et Chen, gen. nov.

Leefructus mirus Sun, Dilcher, Wang et Chen, sp. nov.

Generic diagnosis: The plant consists of a shoot bearing leaves at distinct nodes. The leaf is simple, petiolate, and deeply trilobate with each lobe further dissected. Leaves clustered at the nodes in threes or fours are attached in a tight spiral at each node. Primary venation is basal palinactinodromous. Secondary venation is pinnate, with secondary vein branches bracing the leaf sinuses and then producing conspicuous looping veins near the leaf margin. The long reproductive axis is axillary, terminating in a flattened receptacle bearing five long, narrow, pseudo-syncarpous carpels.

Etymology: *Lee* is given in honour of Shiming Li of Shenyang, China; *fructus* for fruiting. The species epithet *mirus* is from the Latin word *mira*, meaning beautiful.

Specific diagnosis: The specific diagnosis is the same as for the generic diagnosis because of limited material at this time.

Holotype: PISNU-0701 (Fig. 3), deposited in the Paleontological Institute of Shenyang Normal University, Shenyang, China.

Age and horizon: Early Cretaceous, Daxinfangzi Bed, Yixian Formation.

Description and interpretation: The whole shoot is 16 cm long, consisting of a stem with two nodes, each bearing leaves and one fertile branch. The major stem appears herbaceous (see Fig. 4 for a reconstruction, and Figs 3 and 5c), robust, multistranded, with a prominent node, 55 mm long by 2–2.5 mm wide, bearing leaves, fruit and a vegetative shoot. The leaf scar and leaf attachment at the node appear to be helical. Three or four leaves are clustered at each node. Proximal leaves

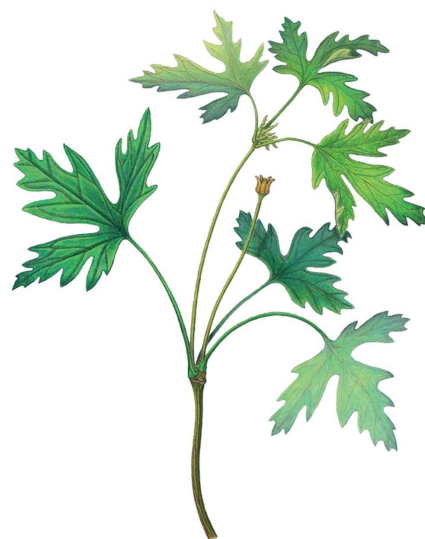


Figure 4 | Reconstruction of *Leefructus mirus* Sun, Dilcher, Wang et Chen. Diagram by S. Trammel and D.L.D.

are larger with lateral lobes about 20–35 mm long by 11–12 mm wide and medial lobes are about 35–40 mm long by 15–22 mm wide. Leaves are simple, estipulate, and deeply trilobate with each lobe further pinnately lobed with non-glandular lobules gradually decreasing in



Figure 3 | Holotype specimen of *Leefructus mirus* Sun, Dilcher, Wang et Chen. The fossil shows multistranded stems, several leaves clustered at two distinct nodes, three-lobed leaves, and a single reproductive auxiliary shoot. Scale bar, 1 cm. Photograph by C. T. Li.

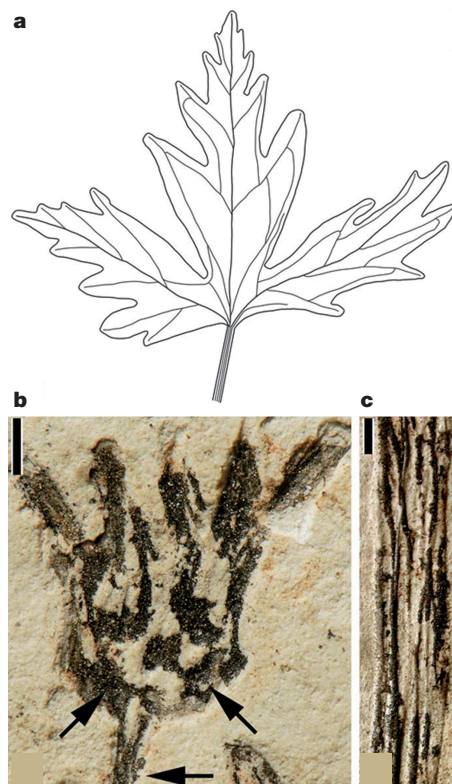


Figure 5 | Details of *Leefructus mirus* Sun, Dilcher, Wang et Chen. a, Line diagram of the leftmost leaf seen in Fig. 3 to show venation. Scale bar, 5 mm. (Diagram by D.L.D.) b, Enlargement of the fruit in Fig. 3 to show five pseudo-syncarpous elongate carpels loosely fused and slightly enclosed by a flat receptacle that has faint oval basal scars (indicated by arrows), and a faint scar 3 mm below the receptacle (indicated by the horizontal arrow). Scale bar, 1 mm. c, Enlargement of the main axis in Fig. 3 to show the multistranded stem. Scale bar, 1 mm.

size distally, resulting in a toothed appearance on the distal leaf margin (Fig. 5a). The petioles of proximal leaves are elongate, about 37–40 mm long by 1.3–1.5 mm wide, multistranded and broadly attached at the node. There may be one abscission scar present at the node. The petioles of distal leaves are short, 10–15 mm long. Primary venation is basal palinactinodromous with three major and two minor primary veins diverging at the extreme base of the leaf lamina from the petiole. One major primary vein forms the medial vein in each major lobe; each of the minor secondary veins form sub-marginal veins in the basal portion of the medial lobes and extend into the basal marginal lobes, then loop to join superadjacent secondary veins and successive marginal lobes (Fig. 5a). Secondary venation is pinnate with an irregular branching pattern. Secondary veins branch and produce conspicuous looping secondary or tertiary veins near the leaf margin; these branches form intramarginal veins extending to and fusing with the next distal secondary veins, or extending into the apex of the lobules but diminishing before reaching the leaf margin. An axillary solitary inflorescence terminates an elongate pedicle 50 mm long by 0.5 mm wide with a faint scar 1 mm below the receptacle. The fruit (Fig. 5b) is 6 mm long by 4 mm wide, pseudo-syncarpous with the basal two-thirds of the five elongate carpels loosely fused, the carpels sitting on and slightly enclosed by a flat receptacle. Elongate tips are present on each carpel, suggesting long stigmatic tips. The receptacle has several faint oval scars (Fig. 5b) that may represent scars of deciduous stamens.

The geological age of the Yixian Formation has received considerable attention over the past two decades¹⁹. The main focus has been on the two horizons (beds) yielding early angiosperms: (1) the Daxinfangzi Bed in Lingyuan and (2) the Jianshangou Bed in Beipiao (Fig. 2).

The Daxinfangzi Bed of the Yixian Formation in Lingyuan is an important horizon for early angiosperms, including *Archaeofructus sinensis*, *Hyrantha decussata* and *Leeffructus mirus* gen. et sp. nov. This bed has been dated as 122.9 ± 0.3 Myr old⁷, 124.4 ± 1.4 Myr old⁸ and 124.4 ± 1.1 Myr old⁶. We consider the Daxinfangzi Bed to range in age from 122.6 to 125.8 Myr. The lowest volcanic beds of the Lujiatun Bed have been dated at 133.3 ± 2.6 Myr (ref. 17) and 129.7 ± 0.5 Myr (ref. 20). The Jiufotang Formation, which conformably overlies the Yixian Formation, was dated as 122.1 ± 0.3 Myr old^{17,20} (Fig. 2). These dates indicate that the entire Yixian Formation ranges in age from 121.8 to 135.9 Myr, lasting a total of about 7 to 14 Myr (refs 17 and 20).

The Jianshangou Bed in Beipiao is also an important horizon for the age of early angiosperms including *Archaeofructus liaoningensis* and *A. eoflora*. Since 2001 this bed is dated as 125.0 ± 0.18 Myr old²¹ or 125.2 ± 0.9 Myr old²², which is close to the Barremian–Aptian boundary. Recently, further dating using both ⁴⁰Ar/³⁹Ar and U–Pb methods yielded ages of 127.4 ± 1.3 to 126.1 ± 1.7 Myr (ref. 8). According to these radiometric dates, the age of the Jianshangou Bed can be considered to range from 124.3 to 128.7 Myr.

Wang *et al.*²³ have examined basal eudicot phylogeny and evolution with a large generic and species sampling including all seven families of Ranunculales (105 taxa including 42 new sequences, 129 genera of Ranunculales and 99 genera of Ranunculaceae) using both a 65-character morphological data set and molecular data from four genomic regions—the plastids *rbcL*, *matK*, *trnL-F* and nuclear ribosomal 26S ribosomal DNA. They present their results using both maximum parsimony and Bayesian inference, which give strong support for the monophyletic nature of three main clades, the family Eupteleaceae (two species), the family Papaveraceae (750 species) and the core Ranunculales, the latter consisting of the five families Circaeasteraceae (two species), Lardizabalaceae (50 species), Menispermaceae (450), Berberidaceae (650 species) and Ranunculaceae (2,000 species). The number of species in these families is very uneven, but the combination of molecular and morphological character states resulted in well-resolved cladograms²³.

The morphological characters of *Leeffructus mirus* gen. et sp. nov. are well preserved. These characters include multistranded and possible herbaceous upright stems, several leaves clustered at two distinct nodes,

three-lobed leaves with the lobe margins further lobed and a unique venation pattern. The fossil leaves resemble the venation patterns and forms of *Delphinium* leaves, typical of the Ranunculaceae. The fossil shoot has a simple reproductive auxiliary long pedicle terminating in a collection of five basally fused follicles sitting on a flattened receptacle (Figs 3–5), which appears to have several small scars around its base. Several genera of the Ranunculaceae have two to five multilobed leaves and carpels borne on flattened receptacles at the ends of long axillary pedicles. The small circular scars on the receptacle may represent attachment scars of stamens (Fig. 5b). Because many of the fossil characters occur in extant genera of the Ranunculaceae, we suggest the fossil *Leeffructus mirus* gen. et sp. nov. to be an extinct taxon along the stem lineage of this extant family.

The term eudicot was proposed in 1991 as a “putatively monophyletic group” using tricolpate pollen to define the clade⁹. This clade was recognized at the Barremian–Aptian boundary from sediments in Gabon²⁴ and from the early Albian of the Potomac Group in North America²⁵. Hughes¹⁰ recognized tricolpate pollen from Bed 35 at the base of the Vectis Formation that Hughes considered to be “Phase 4”, which is at the Barremian–Aptian boundary. This current understanding of the fossil record places the earliest fossils of the eudicots at this Barremian–Aptian boundary age of about 125 Myr. The distribution of this pollen type from cores taken off the coast of Gabon and from England suggests that eudicot plants were already distributed widely by about 125 Myr ago and probably had an earlier origin.

The early fossil record of basal eudicot evolution is incomplete, so each fossil that can be placed in this clade provides new and important information about early angiosperms. Previous fossil angiosperms reported from the Yixian Formation include *Archaeofructus* and *Hyrantha*^{3–5}. It is possible that *Hyrantha* could also be considered within the stem lineage of the Ranunculaceae^{4,26}, and *Archaeofructus* is considered to be basal to all angiosperms^{3,26}.

Molecular studies during the past decade have helped to push the age of the first angiosperms earlier than the Early Cretaceous^{27–30}. The basalmost ANITA (*Amborella*, *Nymphaea*, *Illicium*, *Trimenia* and *Austrobaileya*) grade must have existed before mesangiosperms (magnoliids, Chloranthaceae, *Ceratophyllum*, monocots and eudicots). The presence of the megafossils, *Leeffructus mirus* gen. et sp. nov. and *Hyrantha decussata*^{4,26}, which also has possible Ranunculales/Ranunculaceae affinities, documents eudicot evolution early in angiosperm history. Both the fossil record and molecular data suggest the early presence of basal eudicots, which encourages us to consider seriously the probable pre-Cretaceous evolution of the angiosperms.

METHODS SUMMARY

Leeffructus mirus gen. et sp. nov. was collected from the Daxinfangzi Bed (previously known as Dawangzhangzi Bed) of the middle part of the Yixian Formation exposed in Dawangzhangzi Village (41°09′961″N, 119°16′298″E) about 15 km south of Lingyuan City in western Liaoning Province (Figs 1 and 2). Lithologically the Daxinfangzi bed is mainly composed of yellowish grey and grey sandstone intercalated with grey silt stone and tuffaceous silt and fine-grained sandstone. The Daxinfangzi bed is dated as 122.6–125.8 Myr old^{6–8,14,17}. *Leeffructus mirus* gen. et sp. nov. is preserved as an impression in the intercalated yellowish grey siltstone. Only one part of the impression was collected and studied. On the same slab, *Leeffructus mirus* gen. et sp. nov. co-occurs with the fish, *Lycoperon davidi* Sauvage. Several small samples were removed from the same slab and macerated in hopes of finding pollen, spores or cuticular material but we had no success. Small dark pigmented flakes were removed and examined with the scanning electron microscope for organic remains. These were found to consist of iron-stained matrix and no original organic material is preserved.

Received 14 April 2010; accepted 6 January 2011.

1. Qiu, Y.-L. *et al.* The earliest angiosperms: evidence from mitochondrial, plastid and nuclear genomes. *Nature* **402**, 404–407 (1999).
2. Moore, M. J. *et al.* Using plastid genome-scale data to resolve enigmatic relationships among basal angiosperms. *Proc. Natl Acad. Sci. USA* **104**, 19363–19368 (2007).

3. Sun, G. *et al.* Archaeofractaceae, a new basal angiosperm family. *Science* **296**, 899–904 (2002).
4. Dilcher, D. L. *et al.* An early infructescence *Hyracanthia decussata* (comb. nov.) from the Yixian Formation in northeastern China. *Proc. Natl Acad. Sci. USA* **104**, 9370–9374 (2007).
5. Sun, G. *et al.* In search of the first flower: a Jurassic angiosperm, *Archaeofructus*, from Northeast China. *Science* **282**, 1692–1695 (1998).
6. Zhang, H. *et al.* U-Pb isotopic age of the Lower Yixian Formation in Lingyuan of western Liaoning and its significance. *Geol. Rev.* **52**, 63–71 (2006).
7. Swisher, C. C. *et al.* Cretaceous age for the feathered dinosaurs of Liaoning, China. *Nature* **400**, 58–61 (1999).
8. Meng, F. X., Gao, S. & Liu, X. M. U-Pb zircon geochronology and geochemistry of volcanic rocks of the Yixian Formation in the Lingyuan area, western Liaoning, China. *Geol. Bull. China* **27**, 364–373 (2008).
9. Doyle, J. A. & Hottel, C. L. in *Pollen and Spores: Patterns of Diversification* (eds Blackmore, S. & Barnes, S. H.) 169–195 (Clarendon Press, 1991).
10. Hughes, N. F. *The Enigma of Angiosperm Origins* (Cambridge University Press, 1994).
11. Crepet, W. L., Nixon, K. C. & Gandolfo, M. A. Fossil evidence and phylogeny: the age of major angiosperm clades based on mesofossil and macrofossil evidence from Cretaceous deposits. *Am. J. Bot.* **91**, 1666–1682 (2004).
12. Anderson, C. L., Bremer, K. & Friis, E. M. Dating phylogenetically basal eudicots using rbcL sequences and multiple fossil reference points. *Am. J. Bot.* **92**, 1737–1748 (2005).
13. Taylor, T. N., Taylor, E. L. & Krings, M. *Paleobotany: The Biology and Evolution of Fossil Plants* (Elsevier Science and Technology, 2008).
14. Chang, M. M. (ed). *Jehol Biota* [in Chinese] (Shanghai Sci. Tech. Press, 2001).
15. Ren, D. *et al.* Flower-associated brachycera flies as fossil evidence for Jurassic angiosperm origins. *Science* **280**, 85–88 (1998).
16. Zhou, Z., Barrett, P. M. & Hilton, J. An exceptionally preserved Lower Cretaceous ecosystem. *Nature* **421**, 807–814 (2003).
17. Peng, Y. D. *et al.* $^{40}\text{Ar}/^{39}\text{Ar}$ and K-Ar dating of the Yixian Formation volcanic rocks, western Liaoning Province, China. *Geochimica* **32**, 427–435 (2003).
18. Angiosperm Phylogeny Group. An update of the Angiosperm Phylogeny Group classification for the orders and families of flowering plants: APG III. *Bot. J. Linn. Soc.* **161**, 105–121 (2009).
19. Barrett, P. M. Evolutionary consequences of dating the Yixian Formation. *Trends Ecol. Evol.* **15**, 99–103 (2000).
20. Chang, S.-C. *et al.* High-precision $^{40}\text{Ar}/^{39}\text{Ar}$ age for the Jehol Biota. *Palaeogeogr. Palaeoclimatol. Palaeoecol.* **280**, 94–104 (2009).
21. Swisher, C. C. *et al.* Further support for a Cretaceous age for the feathered-dinosaur beds of Liaoning, China: New dating of the Yixian and Tuchengzi Formations. *Chin. Sci. Bull.* **47**, 136–139 (2002).
22. Wang, S. S. *et al.* Further discussion on the geological age of Sihetun vertebrate assemblage in western Liaoning, China: evidence from Ar-Ar dating. *Acta Petrol. Sin.* **7**, 663–668 (2001).
23. Wang, W. *et al.* Phylogeny and classification of Ranunculales: evidence from four molecular loci and morphological data. *Perspect. Plant Ecol. Evol. Syst.* **11**, 81–110 (2009).
24. Doyle, J. A. *et al.* Angiosperm pollen from the pre-Albian Lower Cretaceous of equatorial Africa. *Bull. Centres Recherches Exploration-Production Elf-Aquitaine* **1**, 451–473 (1977).
25. Doyle, J. A. Cretaceous angiosperm pollen of the Atlantic Coastal Plain and its evolutionary significance. *J. Arnold Arb.* **50**, 1–35 (1969).
26. Leng, Q. & Friis, E. M. *Sinocarpus decussates* gen. et sp. nov., a new angiosperm with basally syncarpous fruits from the Yixian Formation of Northeast China. *Plant Syst. Evol.* **241**, 77–88 (2003).
27. Wikström, N., Savolainen, V. & Chase, M. W. Evolution of the angiosperms: calibrating the family tree. *Proc. R. Soc. Lond.* **268**, 2211–2220 (2001).
28. Bell, C. D., Soltis, D. E. & Soltis, P. S. The age of the angiosperms: a molecular timescale without a clock. *Evolution* **59**, 1245–1258 (2005).
29. Bell, C. D., Soltis, D. E. & Soltis, P. S. The age and diversification of the angiosperms re-revisited. *Am. J. Bot.* **97**, 1296–1303 (2010).
30. Smith, S. A., Beaulieu, J. M. & Donoghue, M. J. An uncorrelated relaxed-clock analysis suggests an earlier origin for flowering plants. *Proc. Natl. Acad. Sci. USA* **107**, 5897–5902 (2010).

Acknowledgements We acknowledge the support of the Key Lab of Evolution of Past Life and Environment in Northeast Asia, Ministry of Education, China, and Project “111” of China, NSFC project number 40842002, and the President Special Fund of Shenyang Normal University to carry out this research project during 2008–2009. Many thanks to S. M. Li and L. X. Wang for their help in collecting the fossil specimen. We thank Y. Duan, C. T. Li, Y. S. Liu, D. M. Jarzen, T. Lott, S. Trammel and W. Wang for their assistance in analysis, computer work, photography and artwork. We also thank P. and D. Soltis, K. Nixon, M. Moore and J. Doyle for suggestions.

Author Contributions G.S. and D.L.D. designed the research plan. G.S., D.L.D., H.W. and Z.C. performed analysis. G.S., D.L.D. and H.W. wrote the manuscript. All authors discussed and commented on the manuscript.

Author Information Reprints and permissions information is available at www.nature.com/reprints. The authors declare no competing financial interests. Readers are welcome to comment on the online version of this article at www.nature.com/nature. Correspondence and requests for materials should be addressed to G.S. (sunge@synu.edu.cn) and D.L.D. (dilcher@indiana.edu).

Cross-dressed dendritic cells drive memory CD8⁺ T-cell activation after viral infection

Linda M. Wakim¹ & Michael J. Bevan¹

After an infection, cytotoxic T lymphocyte precursors proliferate and become effector cells by recognizing foreign peptides in the groove of major histocompatibility complex (MHC) class I molecules expressed by antigen-presenting cells (APCs)¹. Professional APCs specialized for T-cell activation acquire viral antigen either by becoming infected themselves (direct presentation) or by phagocytosis of infected cells, followed by transfer of antigen to the cytosol, processing and MHC class I loading in a process referred to as cross-presentation². An alternative way, referred to as 'cross-dressing', by which an uninfected APC could present antigen was postulated to be by the transfer of preformed peptide-MHC complexes from the surface of an infected cell to the APC without the need of further processing³. Here we show that this mechanism exists and boosts the antiviral response of mouse memory CD8⁺ T cells. A number of publications have demonstrated sharing of peptide-loaded MHC molecules *in vitro*^{4–7}. Our *in vitro* experiments demonstrate that cross-dressing APCs do not acquire peptide-MHC complexes in the form of exosomes released by donor cells. Rather, the APCs and donor cells have to contact each other for the transfer to occur. After a viral infection, we could isolate cross-dressed APCs able to present viral antigen *in vitro*. Furthermore, using the diphtheria toxin system to selectively eliminate APCs that could only acquire viral peptide-MHC complexes by cross-dressing, we show that such presentation can promote the expansion of resting memory T cells. Notably, naive T cells were excluded from taking part in the response. Cross-dressing is a mechanism of antigen presentation used by dendritic cells that may have a significant role in activating previously primed CD8⁺ T cells.

We investigated the capacity of dendritic cells to use peptide-MHC I complexes acquired from other cells to drive CD8⁺ T-cell activation and expansion. Bone-marrow-derived dendritic cells (BMDCs) from B6.SJL-Ptprc^aPep3/BoyJ (B6.SJL) mice pulsed with SIINFEKL peptide (donor) were mixed with BMDCs from B6.GFP mice (recipient). After a 4-h incubation period the dendritic cell populations were separated using the markers CD45.1 and green fluorescent protein (GFP) to distinguish donor and recipient populations (Supplementary Fig. 1). Sorted dendritic cells were cultured with carboxyfluorescein diacetate succinimidyl ester (CFSE)-labelled OT-I TCR transgenic cells, which express a TCR recognizing SIINFEKL in the context of H-2K^b (Fig. 1a). Although only the CD45.1⁺ donor dendritic cells were pulsed with peptide, both dendritic cell populations could drive OT-I division (Fig. 1b). Fixation of the recipient dendritic cells before mixing with peptide-loaded donor dendritic cells abolished their ability to drive OT-I division (Fig. 1c). Antigen transfer could also occur when recipient dendritic cells were deficient in transporter associated with antigen processing (TAP), indicating that it is not conventional cross-presentation (Fig. 1d).

It was unclear whether the recipient dendritic cells were merely acquiring free peptide from the culture or if they were 'stealing' an intact MHC I-peptide complex. Thus, we repeated the above experiment only this time B6.SJL peptide-loaded dendritic cells were mixed with dendritic cells from H-2K^{bm1} mice (Supplementary Fig. 2).

H-2K^{bm1} mice bear a mutation in the K^b molecule and although SIINFEKL can bind it is not recognized by OT-I T cells (Fig. 1e). Nonetheless, culturing H-2K^{bm1} dendritic cells with peptide-loaded B6.SJL donor dendritic cells for a short period before purification resulted in OT-I T cell division (Fig. 1f). Once again, fixation of H-2K^{bm1} dendritic cells before mixing with peptide-loaded donor dendritic cells abolished their ability to drive T-cell division, indicating that it was not simply contaminating donor dendritic cells that initiated OT-I expansion (Supplementary Fig. 3). Therefore it seems that H-2K^{bm1} dendritic cells drive OT-I division due to their ability to acquire peptide-loaded class I molecules from other dendritic cells. Titrating the amount of peptide used to load donor dendritic cells showed that the recipient 'cross-dressed' dendritic cells were about three orders of magnitude less efficient than the donor dendritic cells in driving naive and memory T-cell proliferation (Fig. 1g, h and Supplementary Fig. 4).

Exosomes are membrane vesicles of endocytic origin that are secreted by a range of cell types, including dendritic cells. Fusion of exosomes with a target cell membrane could facilitate the exchange of membrane proteins between two cell types^{8,9}. We explored if exosomes served as the means by which dendritic cells acquired loaded class I molecules in culture. Exosomes isolated from the supernatants of SIINFEKL peptide-loaded BMDCs were attached to beads and their phenotype assessed by flow cytometry. Exosomes stained positive for CD9, a member of the tetraspanin protein family routinely found on the surface of dendritic-cell-derived exosomes and MHC class II molecules. An antibody that recognizes SIINFEKL in the groove of H-2K^b revealed that they also express peptide-loaded MHC class I molecules (Supplementary Fig. 5). Exosomes recovered from the supernatant of B6 dendritic cells pulsed with SIINFEKL peptide were added to cultures containing CFSE-labelled OT-I cells and either B6 or H-2K^{bm1} dendritic cells. Exosomes alone as well as exosomes in the presence of B6 dendritic cells resulted in OT-I division (Fig. 2a). Interestingly, the addition of H-2K^{bm1} dendritic cells to the exosome-T-cell culture resulted in the ablation of OT-I division. We speculate that this is due to the H-2K^{bm1} dendritic cells engulfing exosomes and degrading the contents or reloading the peptide onto their own, non-presenting class I molecule. To explore this possibility further, we isolated exosomes from the supernatant of peptide-pulsed H-2K^{bm1} dendritic cells. Exosomes from H-2K^{bm1} dendritic cells alone failed to drive OT-I division (Fig. 2a). However, feeding these exosomes to B6 dendritic cells resulted in OT-I T cell division, indicating that dendritic cells can use exosomes as a source of antigen but do this by reloading the peptide onto their endogenous MHC class I molecules. Hence, exosomes are not the means by which intact MHC class I-peptide complexes are picked up by dendritic cells, but may serve as an effective means to transfer peptide antigen between cells.

Dendritic cells may acquire preformed peptide-MHC complexes from neighbouring cells using a mechanism termed trogocytosis^{10–13}. Consistent with a previous study¹², we visualized membrane transfer during live imaging of cultures containing dendritic cells labelled with either a membrane (red) or a cytoplasmic dye (green) (Fig. 2b and

¹Department of Immunology, Howard Hughes Medical Institute, University of Washington, Box 357370, Seattle, Washington 98195, USA.

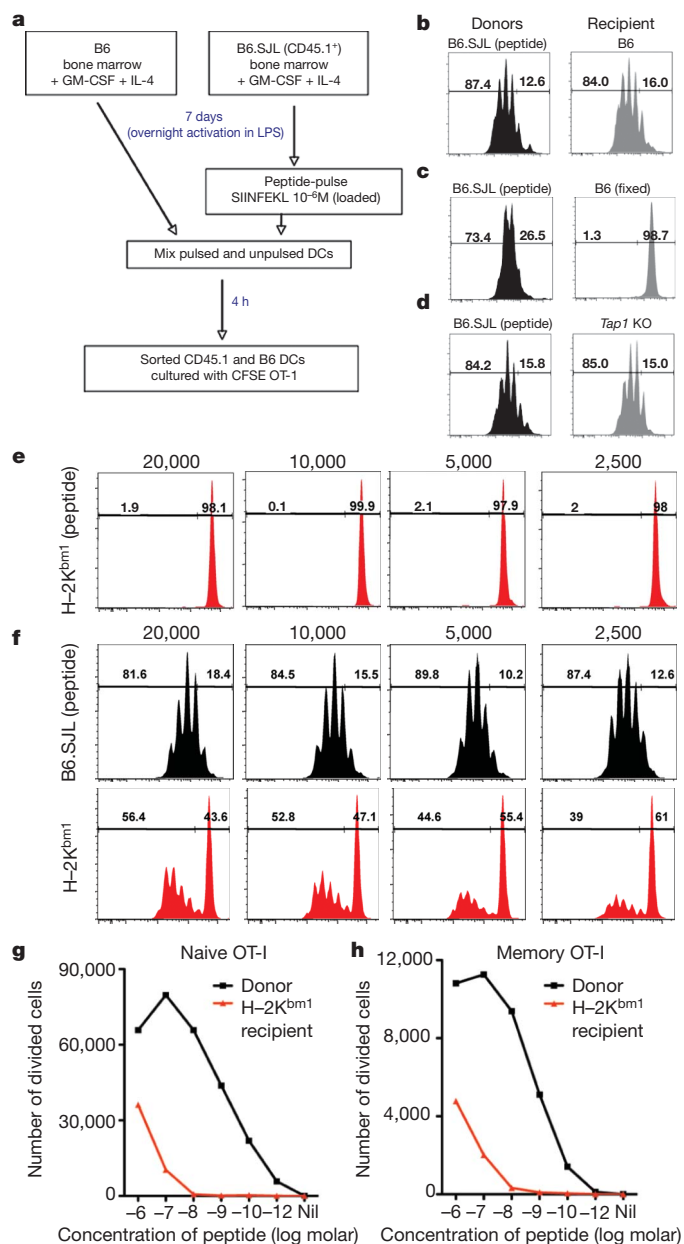


Figure 1 | Transfer of peptide-loaded class I molecules between dendritic cells *in vitro*. **a**, Scheme of the experiment. DC, dendritic cell; GM-CSF, granulocyte macrophage colony-stimulating factor. **b–d**, *In vitro*-generated bone-marrow-derived B6.SJL dendritic cells were peptide pulsed and cultured with unloaded bone-marrow-derived B6.GFP dendritic cells (**b**), fixed B6.GFP dendritic cells (**c**) or *Tap1*^{-/-} dendritic cells (**d**). Dendritic cells were separated by cell sorting and 2×10^4 cells were cultured with CFSE-labelled OT-I cells for 60 h. Representative flow cytometry profiles are depicted. **e**, H-2K^{bmi} dendritic cells were pulsed with peptide before culture with CFSE-labelled OT-I cells. **f**, Peptide-pulsed B6.SJL dendritic cells were cultured with unloaded H-2K^{bmi} dendritic cells. Dendritic cells were then separated and cultured with CFSE-labelled OT-I cells. Representative flow cytometry profiles are shown. The numbers above the plots indicate the number of dendritic cells cultured per well. Bone-marrow-derived B6.GFP dendritic cells were pulsed with varying concentrations of SIINFEKL peptide and cultured with unloaded H-2K^{bmi} dendritic cells. **g**, **h**, Dendritic cells were then separated and 4×10^4 cells were cultured with CFSE-labelled naive (**g**) or memory (**h**) OT-I cells for 60 h. The absolute numbers of divided cells are shown.

Supplementary Movie 1). To investigate whether trogocytosis was the means by which dendritic cells acquired peptide-loaded MHC class I molecules, we used a transwell system with peptide-loaded B6 dendritic cells in one chamber and unloaded H-2K^{bmi} dendritic cells in the

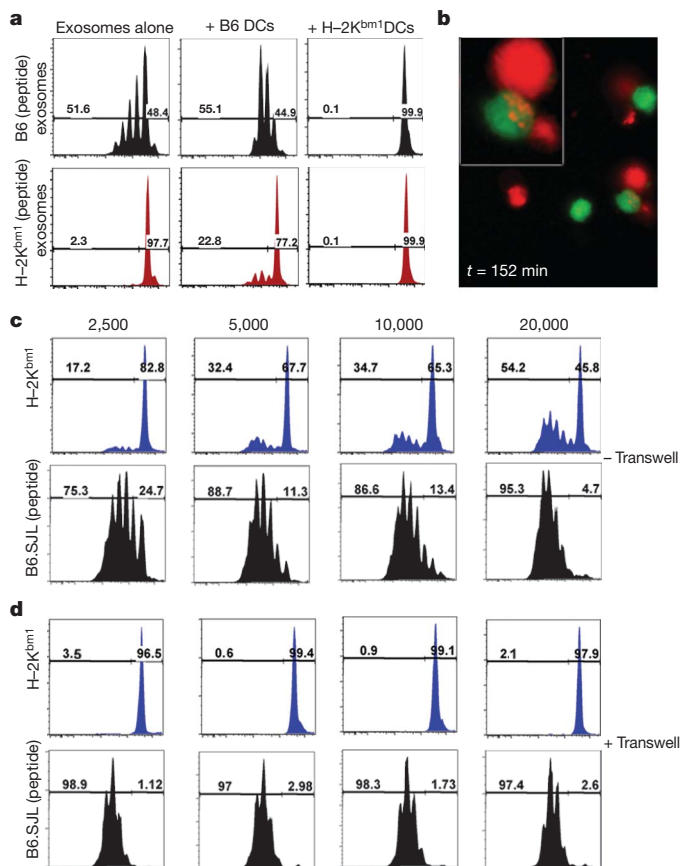


Figure 2 | MHC I-peptide transfer does not require exosomes but does require cell contact between donor and recipient cells. **a**, Exosomes recovered from the supernatants of peptide-pulsed B6 or H-2K^{bmi} dendritic cells were incubated alone (exosomes alone) or with B6 dendritic cells or H-2K^{bmi} dendritic cells and cultured with CFSE-labelled OT-I cells for 60 h. Representative flow cytometry profiles are shown. **b**, Dendritic cells labelled with either CMFDA (cytoplasmic dye (green)) or Dil (membrane dye (red)) were cultured together. A representative frame is shown. **c**, **d**, B6.SJL peptide-pulsed dendritic cells were cultured with unloaded H-2K^{bmi} dendritic cells mixed together (**c**; -transwell) or separated by a transwell (**d**; +transwell). Dendritic cells were then separated by cell sorting and cultured with CFSE-labelled OT-I cells for 60 h. Representative flow cytometry profiles are shown. The numbers above the plots indicate the number of dendritic cells cultured per well.

other to see if this separation would alter the ability of the H-2K^{bmi} dendritic cells to drive OT-I division. Physical separation of donor and recipient dendritic cells prevented MHC I-peptide acquisition by the H-2K^{bmi} dendritic cells (Fig. 2c, d). Hence, dendritic cells acquire MHC class I-peptide complexes capable of driving CD8⁺ T-cell activation via a mechanism that requires cell contact.

We next wanted to determine if dendritic cells could act as cross-dressing APCs *in vivo* by acquiring class I-peptide complexes derived during a viral infection. We generated bone marrow chimaeras where we injected B6.GFP bone marrow into lethally irradiated F₁[BALB/c \times C57BL/6] mice. In this chimaera, bone-marrow-derived cells are of B6 origin and can be readily identified and sorted based on GFP expression, whereas the parenchyma cells are of F₁ origin and express both B6 and BALB/c MHC molecules. F₁[BALB/c \times C57BL/6] mice receiving B6.GFP bone marrow were infected with lymphocytic choriomeningitis virus (LCMV) and on day 2 and 3 after infection CD11c⁺GFP⁺ cells were sorted from the spleen and cultured with a T-cell hybridoma specific for the BALB/c H-2L^d restricted LCMV epitope NP(118–226). As negative and positive controls, respectively, CD11c⁺ cells were sorted from B6 mice receiving B6.GFP bone marrow and from BALB/c mice. CD11c⁺GFP⁺ dendritic cells isolated from LCMV-infected F₁[BALB/c \times C57BL/6] mice receiving B6.GFP bone marrow could drive IL-2

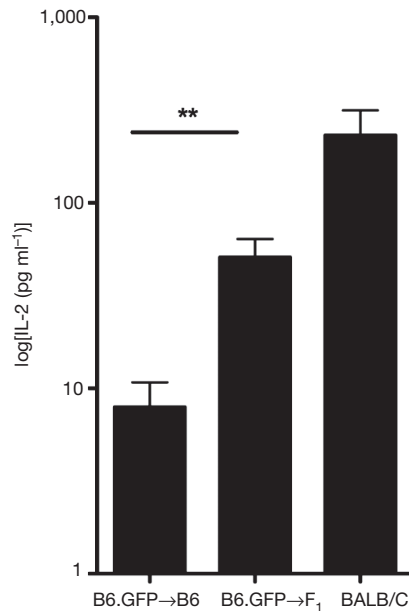


Figure 3 | Dendritic cells can acquire MHC I–peptide *in vivo* after viral infection. B6 mice receiving B6.GFP bone marrow (B6.GFP→B6), F₁(BALB/c × B6) mice receiving B6.GFP bone marrow (B6.GFP→F₁), and BALB/c mice were infected with LCMV and on day 2 after infection CD11c⁺ cells were sorted from the spleen and cultured with an L^d-NP(118–226)-specific hybridoma. The amount of IL-2 produced was determined by ELISA. Error bars represent the mean + s.e.m. pooled from eight independent experiments.

production to a level 6-fold above background levels generated when CD11c⁺ cells were recovered from LCMV-infected B6 mice receiving B6.GFP bone marrow (where there is no available source of H-2L^d) (Fig. 3 and Supplementary Fig. 6a). This ability to present to the hybridoma was limited to CD11c⁺ cells, as isolated CD11c⁺GFP⁺ cells from the same animals were unable to stimulate the L^d restricted hybridoma (Supplementary Fig. 6b, c). Furthermore, dendritic cell subsets sorted from LCMV-infected F₁[BALB/c × C57BL/6] mice receiving B6.GFP bone marrow revealed that CD8α⁺ dendritic cells were superior to their CD8α⁺ counterparts at antigen presentation via cross-dressing (Supplementary Fig. 7), which is consistent with previous *in vitro* studies⁷.

To investigate whether cross-dressing functions to drive a CD8⁺ T-cell response *in vivo*, we generated another set of bone marrow chimaeras. BALB/c.CD11cDTR bone marrow was used to reconstitute lethally irradiated F₁[BALB/c × C57BL/6] mice, creating a setting where dendritic cells are of BALB/c origin, express only H-2^d class I molecules and are removable with diphtheria toxin treatment, whereas the parenchyma is of F₁ origin and expresses both H-2^d and H-2^b MHC molecules. After reconstitution we adoptively transferred equal numbers of naive OT-I.CD45.1 and memory OT-I.GFP⁺ T cells into these mice. The mice were infected with recombinant vesicular stomatitis virus that expresses ovalbumin (VSV-OVA) and either treated with diphtheria toxin to ablate CD11c⁺ BALB/c-derived cells or left untreated. On day 7 after infection we determined if the H-2K^b-restricted OT-I T cells expanded in an environment where bone-marrow-derived APCs are of BALB/c origin.

Memory OT-I T cells expanded markedly in the intact, virus-infected F₁[BALB/c × C57BL/6] mice receiving BALB/c.CD11cDTR bone marrow, with the OT-I cells accumulating to ~8.5% of the total CD8⁺ T-cell population in the spleen (Fig. 4a, b). Importantly, this expansion was not the result of direct antigen presentation by infected F₁ parenchyma cells or due to direct or classical cross-presentation by radio-resistant F₁ APCs, because when we ablated the BALB/c

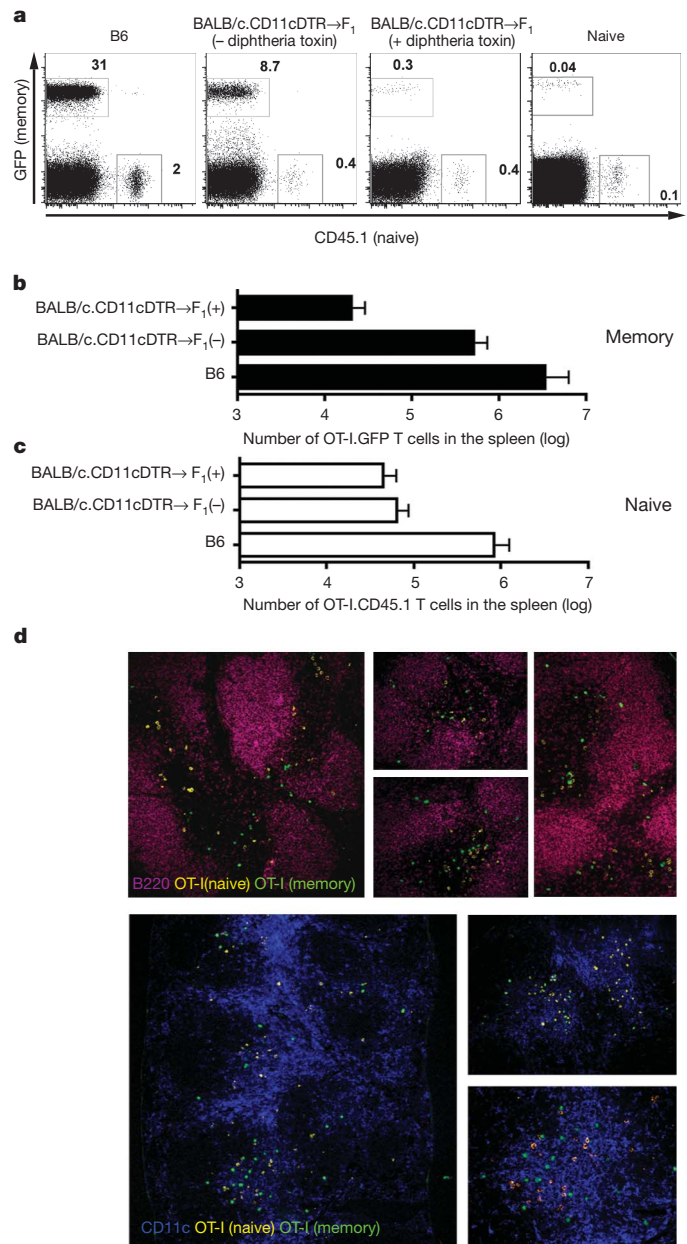


Figure 4 | Cross-dressed dendritic cells in VSV-infected mice stimulate memory CD8⁺ T cells. B6 mice or F₁(BALB/c × B6) mice receiving BALB/c.CD11cDTR bone marrow (BALB/c.CD11cDTR→F₁) were seeded with naive OT-I.CD45.1 and memory OT-I.GFP T cells before infection with VSV-OVA. BALB/c.CD11cDTR→F₁ chimaeras were treated with diphtheria toxin (+) or were left untreated (–). On day 7 after infection, spleens were recovered and the proportion of OT-I cells of the total CD8⁺ T-cell population was determined by flow cytometry. **a**, Representative flow cytometry profiles of the spleen gated on CD8⁺ T cells. **b**, **c**, The absolute numbers of memory OT-I.GFP (**b**) and naive OT-I.CD45.1 (**c**) T cells in the spleen on day 7 after infection are shown. Data are pooled from two independent experiments with 4–5 mice per group. Shown is the mean + s.e.m. **d**, Naive (CD45.1) or memory (GFP⁺) OT-I T cells were adoptively transferred into mice before infection with VSV-OVA. Representative pictures of the spleen on day 2 after infection showing staining for B220 (purple), CD11c (blue), CD45.1 (naive OT-I; yellow) and GFP (memory OT-I; green) are shown.

bone-marrow-derived CD11c⁺ cells using diphtheria toxin treatment, OT-I expansion was greatly attenuated. It is unlikely that this effect is due to the acquisition of the diphtheria toxin receptor (DTR) either by the T cells themselves or by non-professional APCs capable of stimulating memory T cells, because *in vitro* co-cultures of peptide-loaded CD11cDTR dendritic cells with DTR⁺ dendritic cells, or with naive or

memory OT-I T cells, did not render the non-transgenic cells susceptible to diphtheria toxin (Supplementary Fig. 8).

Remarkably, naive OT-I T-cell numbers in the same animals were not affected by the presence or absence of BALB/c APCs (Fig. 4a, c). The naive T cells may be activated by recognizing antigen expressed either on residual, radio-resistant F₁ dendritic cells or on infected parenchymal cells. But it is clear that the naive CD8⁺ T cells are not able to respond to cross-dressed antigen presentation in this *in vivo* model. This was not due to the naive T cells being out-competed by memory OT-I T cells because even when we transferred the naive T cells alone they failed to respond to this form of presentation (Supplementary Fig. 9). Although memory and naive OT-I T cells seem to reside in similar locations within the spleen in this experimental set-up (Fig. 4d and Supplementary Fig. 10), memory T cells may be more responsive to cross-dressed antigen presentation due to more frequent and productive interactions with the dendritic cell subset actively engaged in trogocytosis. In addition, the differential response of naive and memory T cells may reflect a disparity in their epitope density requirements for activation *in vivo*, considering that cross-dressed antigen presentation is likely to be extremely low density (see Supplementary Fig. 4).

Cross-dressing serves as an alternative mode of antigen presentation to memory T cells during viral infection. It eliminates the need for antigen processing by the presenting dendritic cell and allows the prompt presentation of peptide epitopes that very accurately reflect those expressed on infected cells.

METHODS SUMMARY

Bone-marrow-derived dendritic cells were generated and matured as described¹⁴. Dendritic cells loaded with OVA peptide (donors) were mixed at a 1:1 ratio with unloaded dendritic cells (recipient) for 4 h at 37 °C. Dendritic cells were separated by cell sorting and cultured with 2×10^4 CFSE-labelled naive OT-1CD45.1 T cells. Cultures were analysed for proliferation after 60 h.

Naive OT-I cells were purified from pooled spleen and lymph node prepared from OT-I mice by depletion of non-CD8⁺ cells using a MACs CD8 enrichment kit (Miltenyi Biotec) following the manufacturer's instructions.

Mice were infected intranasally with 5×10^4 plaque-forming units (p.f.u.) of recombinant vesicular stomatitis virus that expresses GFP and a truncated form of OVA¹⁵. The lymphocytic choriomeningitis virus (LCMV) Armstrong 53b was grown and titred as described previously¹⁶. Mice were infected intraperitoneally with 2×10^5 p.f.u. of LCMV Armstrong 53b.

Exosomes were isolated following the procedure described in detail previously¹⁷.

To visualize membrane transfer, dendritic cells were labelled with the lipophilic probe 1'-dioctadecyl-3,3,3',3'-tetramethylindocarbocyanine perchlorate (DiI; Molecular probes) or the thiol-reactive chloromethyl probe 5-chloromethylfluorescein diacetate (CMFDA; Invitrogen). A mixture of cells labelled with DiI or CMFDA were introduced into an ibiTreat, 35-mm μ -Dish (Ibidi GmbH) and images were collected every 4 min for each of the illumination conditions.

The T-cell hybridoma specific for the L^d restricted NP(118–226) LCMV immunodominant epitope was prepared by fusing T cells from LCMV-primed BALB/c mice with BWZ.36/CD8 (ref. 18). For analysis of antigen presentation, 1×10^5 dendritic cells were cultured with 1×10^5 hybridoma cells in a U-bottom 96-well plate. Secretion of IL-2 was measured by ELISA.

Received 4 November 2010; accepted 19 January 2011.

1. Vyas, J. M., Van der Veen, A. G. & Ploegh, H. L. The known unknowns of antigen processing and presentation. *Nature Rev. Immunol.* **8**, 607–618 (2008).
2. Lin, M. L., Zhan, Y., Villadangos, J. A. & Lew, A. M. The cell biology of cross-presentation and the role of dendritic cell subsets. *Immunol. Cell Biol.* **86**, 353–362 (2008).
3. Yewdell, J. W. & Haeryfar, S. M. Understanding presentation of viral antigens to CD8⁺ T cells *in vivo*: the key to rational vaccine design. *Annu. Rev. Immunol.* **23**, 651–682 (2005).
4. Dolan, B. P., Gibbs, K. D. Jr & Ostrand-Rosenberg, S. Dendritic cells cross-dressed with peptide MHC class I complexes prime CD8⁺ T cells. *J. Immunol.* **177**, 6018–6024 (2006).
5. Dolan, B. P., Gibbs, K. D. Jr & Ostrand-Rosenberg, S. Tumor-specific CD4⁺ T cells are activated by "cross-dressed" dendritic cells presenting peptide-MHC class II complexes acquired from cell-based cancer vaccines. *J. Immunol.* **176**, 1447–1455 (2006).
6. Qu, C., Nguyen, V. A., Merad, M. & Randolph, G. J. MHC class I/peptide transfer between dendritic cells overcomes poor cross-presentation by monocyte-derived APCs that engulf dying cells. *J. Immunol.* **182**, 3650–3659 (2009).
7. Smyth, L. A. *et al.* The relative efficiency of acquisition of MHC:peptide complexes and cross-presentation depends on dendritic cell type. *J. Immunol.* **181**, 3212–3220 (2008).
8. Théry, C. *et al.* Indirect activation of naive CD4⁺ T cells by dendritic cell-derived exosomes. *Nature Immunol.* **3**, 1156–1162 (2002).
9. Théry, C., Ostrowski, M. & Segura, E. Membrane vesicles as conveyors of immune responses. *Nature Rev. Immunol.* **9**, 581–593 (2009).
10. Joly, E. & Hudrisier, D. What is trogocytosis and what is its purpose? *Nature Immunol.* **4**, 815 (2003).
11. Davis, D. M. Intercellular transfer of cell-surface proteins is common and can affect many stages of an immune response. *Nature Rev. Immunol.* **7**, 238–243 (2007).
12. Harshyne, L. A., Watkins, S. C., Gambotto, A. & Barratt-Boyes, S. M. Dendritic cells acquire antigens from live cells for cross-presentation to CTL. *J. Immunol.* **166**, 3717–3723 (2001).
13. Matheoud, D. *et al.* Cross-presentation by dendritic cells from live cells induces protective immune responses *in vivo*. *Blood* **115**, 4412–4420 (2010).
14. Wakim, L. M., Woodward-Davis, A. & Bevan, M. J. Memory T cells persisting within the brain after local infection show functional adaptations to their tissue of residence. *Proc. Natl Acad. Sci. USA* **107**, 17872–17879 (2010).
15. Turner, M. J., Jellison, E. R., Lingenheld, E. G., Puddington, L. & Lefrançois, L. Avidity maturation of memory CD8 T cells is limited by self-antigen expression. *J. Exp. Med.* **205**, 1859–1868 (2008).
16. Sun, J. C., Williams, M. A. & Bevan, M. J. CD4⁺ T cells are required for the maintenance, not programming, of memory CD8⁺ T cells after acute infection. *Nature Immunol.* **5**, 927–933 (2004).
17. Thery, C., Amigorena, S., Raposo, G. & Clayton, A. Isolation and characterization of exosomes from cell culture supernatants and biological fluids. *Curr. Protoc. Cell Biol.* **3**, Unit 3.22, (2006).
18. Sanderson, S. & Shastri, N. LacZ inducible, antigen/MHC-specific T cell hybrids. *Int. Immunol.* **6**, 369–376 (1994).

Supplementary Information is linked to the online version of the paper at www.nature.com/nature.

Acknowledgements This work was supported by the Howard Hughes Medical Institute and National Institutes of Health. L.M.W. is supported by an Overseas Biomedical Fellowship from the National Health and Medical Research Council of Australia.

Author Contributions L.M.W. and M.J.B. devised experiments and wrote the paper. L.M.W. performed the work.

Author Information Reprints and permissions information is available at www.nature.com/reprints. The authors declare no competing financial interests. Readers are welcome to comment on the online version of this article at www.nature.com/nature. Correspondence and requests for materials should be addressed to M.J.B. (mbevan@u.washington.edu).

SHARPIN is a component of the NF- κ B-activating linear ubiquitin chain assembly complex

Fuminori Tokunaga^{1*}, Tomoko Nakagawa^{1*}, Masaki Nakahara¹, Yasushi Saeki², Masami Taniguchi¹, Shin-ichi Sakata¹, Keiji Tanaka², Hiroyasu Nakano³ & Kazuhiro Iwai^{1,4}

Cpdm (chronic proliferative dermatitis) mice develop chronic dermatitis and an immunodeficiency with increased serum IgM^{1–3}, symptoms that resemble those of patients with X-linked hyper-IgM syndrome and hypohydrotic ectodermal dysplasia (XHM-ED), which is caused by mutations in NEMO (NF- κ B essential modulator; also known as IKBKG)^{4–6}. Spontaneous null mutations in the *Sharpin* (SHANK-associated RH domain interacting protein in postsynaptic density)⁷ gene are responsible for the *cpdm* phenotype in mice⁸. SHARPIN shows significant similarity to HOIL-1L (also known as RBCK1)^{8,9}, a component of linear ubiquitin chain assembly complex (LUBAC), which induces NF- κ B activation through conjugation of linear polyubiquitin chains to NEMO^{10–13}. Here, we identify SHARPIN as an additional component of LUBAC. SHARPIN-containing complexes can linearly ubiquitinate NEMO and activated NF- κ B. Thus, we re-define LUBAC as a complex containing SHARPIN, HOIL-1L, and HOIP (also known as RNF31). Deletion of SHARPIN drastically reduced the amount of LUBAC, which resulted in attenuated TNF- α - and CD40-mediated activation of NF- κ B in mouse embryonic fibroblasts (MEFs) or B cells from *cpdm* mice. Considering the pleomorphic phenotype of *cpdm* mice, these results confirm the predicted role of LUBAC-mediated linear polyubiquitination in NF- κ B activation induced by various stimuli, and strongly suggest the involvement of LUBAC-induced NF- κ B activation in various disorders.

NF- κ B is a transcription factor involved in various functions, including inflammation and cell survival. NF- κ B is shown to be activated by various stimuli^{14–16}. CD40-mediated degradation of inhibitor of κ B α (I κ B α , also known as NFKBIA) leads to the activation of NF- κ B. This pathway is severely impaired, but not completely abolished, in patients with XHM-ED, a syndrome caused by mutations in NEMO^{5,6}, a crucial regulator of the canonical NF- κ B pathway¹⁷. CD40-mediated degradation of I κ B α was impaired, but not completely abolished in splenic B cells from *cpdm* mice carrying the *Sharpin* null mutation^{1–3,8} (Fig. 1a), which indicated that loss of SHARPIN impairs, but does not completely abolish NF- κ B activation. The ubiquitin-like (UBL) and NPL4 zinc-finger (NZF) domains of SHARPIN showed significant similarity to those of HOIL-1L, a component of LUBAC that has a crucial role in TNF- α -mediated NF- κ B activation^{9–12} (Fig. 1b and Supplementary Fig. 1). TNF- α -induced activation of I κ B kinase (IKK), phosphorylation and degradation of I κ B α , and nuclear localization of the p65 subunit of NF- κ B, which are hallmarks of NF- κ B activation, were impaired, but not completely abolished, in *cpdm* MEFs (Fig. 1c–e). In addition, expression of NF- κ B targets was markedly reduced in *cpdm* MEFs (Supplementary Fig. 2). These results clearly indicated that deletion of *Sharpin* also attenuates TNF- α -induced NF- κ B activation.

The UBL domain of HOIL-1L is critical for complex formation with HOIP, the catalytic component of the linear polyubiquitination^{10,11}. We proposed that SHARPIN forms a ubiquitin ligase complex with

HOIP (SHARPIN–HOIP) and activates NF- κ B¹⁰. Indeed, SHARPIN co-immunoprecipitated with HOIP, but not HOIL-1L (Supplementary Fig. 3). Introduction of SHARPIN–HOIP, but not SHARPIN alone or SHARPIN and HOIL-1L, induced NF- κ B transcriptional activity (Supplementary Fig. 4a). Nuclear translocation of p65 was observed in HEK293T cells expressing SHARPIN–HOIP (Supplementary Fig. 4b). Furthermore, SHARPIN–HOIP showed linear polyubiquitination activity in an *in vitro* polyubiquitination assay, and the SHARPIN UBL domain was indispensable for HOIP binding and ubiquitination activity (Supplementary Figs 5 and 6). The NZF domain of SHARPIN seemed to be indispensable for NF- κ B activation, but not for linear ubiquitination, and the UBA and RING-IBR-RING regions of HOIP were crucial for NF- κ B activation mediated by SHARPIN–HOIP (Supplementary Figs 5d and 6). Given that UBA and RING-IBR-RING domains have crucial roles in HOIP binding to SHARPIN and in linear polyubiquitination, these results indicated that the SHARPIN–HOIP complex can activate NF- κ B via linear polyubiquitination. In fact, SHARPIN–HOIP catalysed linear polyubiquitination of NEMO almost as efficiently as HOIL-1L–HOIP when overexpressed in HEK293T cells, as assessed by mass spectrometry and an anti-linear chain specific antibody (Supplementary Fig. 7).

We have noticed that NF- κ B was more strongly activated in 293T cells expressing SHARPIN–HOIL-1L–HOIP as compared to cells co-expressing HOIL-1L–HOIP or SHARPIN–HOIP (Supplementary Fig. 4a). Co-immunoprecipitation assays to determine whether SHARPIN formed a ternary complex with HOIL-1L and HOIP showed that SHARPIN co-immunoprecipitated with both HOIP and HOIL-1L when co-expressed with either protein (Supplementary Fig. 3). Moreover, immunoprecipitation of endogenous LUBAC from HEK293T cells revealed that endogenous SHARPIN forms complexes with both HOIP and HOIL-1L (Fig. 2a). In HEK293T and Jurkat cells, SHARPIN co-fractionated primarily with HOIL-1L and HOIP in the relative molecular mass ~600,000 fraction (M_r 600K; Fig. 2b). Sequential precipitation of the ~600K fraction from HEK293 cells that stably expressed Flag–HOIP, HOIL-1L–His₆–haemagglutinin (HA), and Myc–SHARPIN confirmed that HOIL-1L, HOIP and SHARPIN form a ternary complex (Supplementary Fig. 8). These results conclusively indicated that SHARPIN forms a ternary complex with HOIL-1L and HOIP, and we re-defined LUBAC as a 600K complex containing HOIL-1L and/or SHARPIN together with HOIP. Sequential precipitation of HEK293T cells expressing Flag–HOIP, His₆–HOIP and Myc–HOIP showed that there were at least three HOIP molecules per LUBAC complex (Supplementary Fig. 9). SHARPIN–HOIP formed complexes with HOIL-1L–HOIP more efficiently than SHARPIN alone (Supplementary Fig. 10). Thus, LUBAC seems to be composed of a mixture of HOIL-1L–HOIP and SHARPIN–HOIP complexes, although we cannot exclude the possibility that LUBAC may break down into HOIL-1L–HOIP and

¹Department of Biophysics and Biochemistry, Graduate School of Medicine, Osaka University, Suita, Osaka 565-0871, Japan. ²Laboratory of Protein Metabolism, Tokyo Metropolitan Institute of Medical Science, Setagaya-ku, Tokyo 156-8506, Japan. ³Department of Immunology, Juntendo University School of Medicine, Bunkyo-ku, Tokyo 113-8421, Japan. ⁴Cell Biology and Metabolism Group, Graduate School of Frontier Biosciences, Osaka University, Suita, Osaka 565-0871, Japan.

*These authors contributed equally to this work.

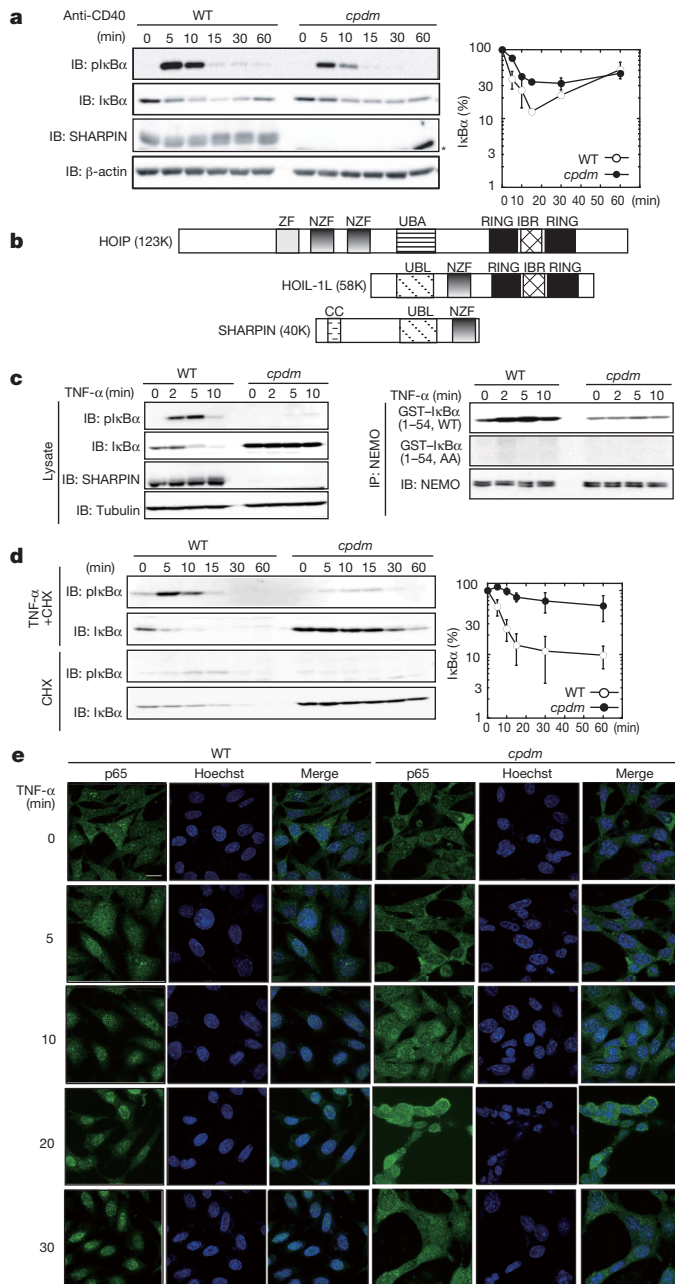


Figure 1 | Ablation of *Sharpin* causes impaired NF-κB signalling.

a, Immunoblot (IB) showing impaired CD40-signalling in *cpdm* B cells. Splenic B cells were treated with an anti-CD40 antibody. *, non-specific signal. Relative amounts of IkBα are shown (mean ± s.d., *n* = 3). pIkBα, phosphorylated IkBα. **b**, Domain structures of HOIP, HOIL-1L, and SHARPIN. **c**, Reduced IKK activity in *cpdm* MEFs. Shown is IKK activity in anti-NEMO immunoprecipitates (IP) from TNF-α-treated MEFs and corresponding immunoblots. AA, IkBα (1–54) mutant S32/36A. **d**, Reduced TNF-α-mediated NF-κB activation in *cpdm* MEFs treated with cycloheximide (CHX) and TNF-α. **e**, Reduced TNF-α-induced nuclear translocation of p65 in *cpdm* MEFs. Cells were stained with anti-p65 antibodies and Hoechst 33258. Bar, 20 μm.

SHARPIN–HOIP sub-complexes under certain conditions. Both baculovirally purified SHARPIN-containing and endogenous LUBAC had linear polyubiquitination activity (Supplementary Fig. 11). LUBAC bound to NEMO in the IKK complex, and assembled linear polyubiquitin chains on NEMO (Fig. 2c and Supplementary Figs 12 and 13a). The minimal regions necessary for ubiquitination of NEMO by LUBAC mapped to amino acids 241–344 and 293–419 (Supplementary Fig. 13b, c). Notably, TNF-α-induced linear polyubiquitination of endogenous NEMO was attenuated in *cpdm* MEFs (Fig. 2d). These

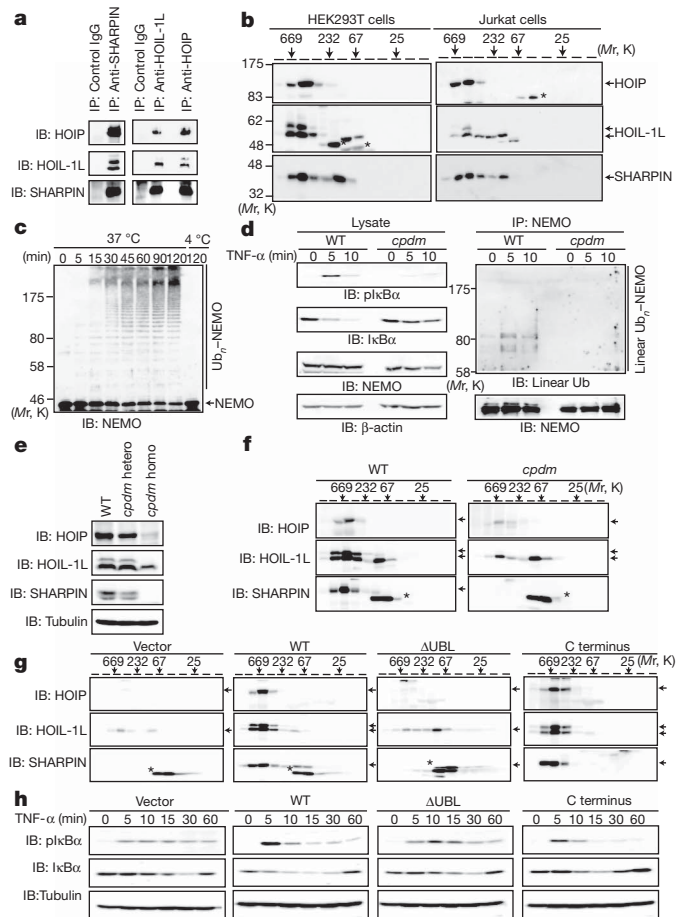


Figure 2 | Linear-ubiquitination of NEMO by SHARPIN-containing LUBAC activates NF-κB. **a**, Endogenous SHARPIN associates with HOIP and HOIL-1L. **b**, SHARPIN co-elutes with HOIP and HOIL-1L in fractionated HEK293T and Jurkat cell lysates. **c**, *In vitro* ubiquitination of NEMO by LUBAC. **d**, Decreased TNF-α-induced linear ubiquitination of NEMO in *cpdm* MEFs. **e**, HOIP and HOIL-1L are reduced in *cpdm* MEFs. **f**, *Sharpin* ablation reduces ~600K LUBAC levels in *cpdm* MEFs. **g**, SHARPIN restores ~600K LUBAC levels. Shown are *cpdm* MEFs expressing wild-type SHARPIN or various SHARPIN mutants. **h**, TNF-α-induced NF-κB activation is restored by wild-type SHARPIN. *, nonspecific signals (**b**, **f**, **g**).

results indicated that linear polyubiquitination of NEMO by SHARPIN-containing LUBAC may be involved in NF-κB activation.

Trace amounts of HOIP and HOIL-1L were detected in *cpdm* MEFs (Fig. 2e). In addition, gel filtration of MEF lysates (Fig. 2f) or brain homogenates (Supplementary Fig. 14) from *cpdm* mice revealed small amounts of HOIL-1L and HOIP in the ~600K fraction. Retroviral transduction of wild-type SHARPIN or a C-terminal SHARPIN fragment (C term), both of which can bind to HOIP, increased the amounts of HOIP and HOIL-1L in the ~600K fraction (Fig. 2g and Supplementary Fig. 15). Moreover, TNF-α induced the phosphorylation and degradation of IkBα in MEFs expressing wild-type or C-term SHARPIN, but not SHARPIN ΔUBL, which cannot bind to HOIP (Fig. 2h). These results clearly indicated that the lack of SHARPIN in *cpdm* mice reduces the level of LUBAC and attenuates NF-κB activation. Trace amounts of SHARPIN and HOIP were also detected in the ~600K fraction from HOIL-1L^{-/-} MEFs (Fig. 3a, b). Furthermore, SHARPIN and HOIL-1L present in the ~600K fraction of HOIL-1L^{-/-} MEFs and *cpdm* MEFs, respectively, formed complexes with HOIP (Fig. 3c). In *cpdm* MEFs transfected with a small interfering RNA (siRNA) specific for HOIL-1L, expression of HOIL-1L and HOIP was severely suppressed and TNF-α-mediated IkBα degradation was almost completely abolished (Fig. 3d). Given that HOIL-1L–HOIP¹¹ and SHARPIN–HOIP can activate NF-κB, these results

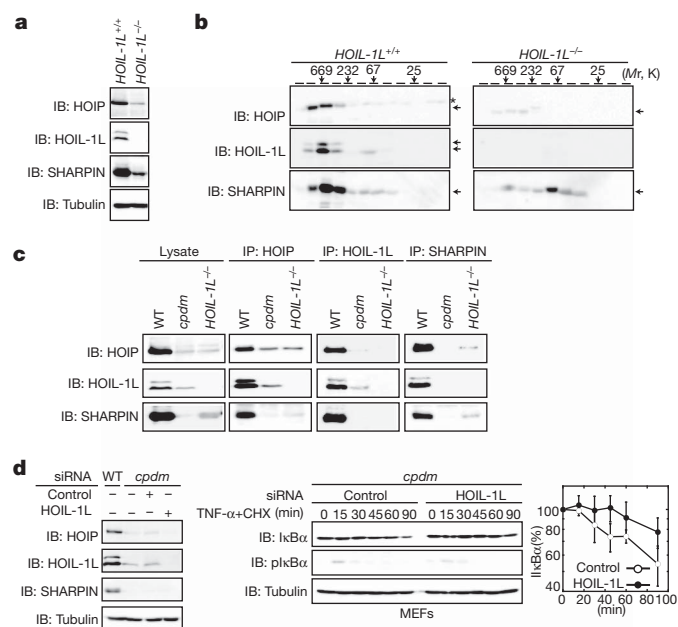


Figure 3 | SHARPIN affects the stability of LUBAC. **a**, Reduction of HOIP and SHARPIN in *HOIL-1L*^{-/-} MEFs. Lysates of *HOIL-1L*^{+/+} and *HOIL-1L*^{-/-} MEFs were analysed by immunoblotting. **b**, Reduced levels of ~600K LUBAC in *HOIL-1L*^{-/-} MEFs. **c**, HOIL-1L-HOIP and SHARPIN-HOIP complex formation in *cpdm* and *HOIL-1L*^{-/-} MEFs, respectively. The ~600K fractions from wild-type, *HOIL-1L*^{-/-}, or *cpdm* MEFs were subjected to immunoprecipitation and then analysed by immunoblotting, as indicated. **d**, Knockdown of HOIL-1L in *cpdm* MEFs almost completely abolished TNF- α -induced NF- κ B activation. *cpdm* MEFs transfected with control or HOIL-1L-specific siRNAs were analysed.

strongly indicated that the residual NF- κ B activity in cells from *cpdm* mice, and also perhaps in cells from *HOIL-1L*^{-/-} mice¹¹, is due to the presence of residual amounts of HOIL-1L-HOIP or SHARPIN-HOIP, respectively.

Although HOIP was present only in the ~600K fraction, small amounts of SHARPIN and HOIL-1L were also present in the lower molecular weight fractions of HOIL-1L KO or *cpdm* cell lysates, respectively (Figs 2f and 3b). The level of HOIP was greatly increased in *cpdm* MEFs expressing wild-type SHARPIN, but not SHARPIN Δ UBL (Fig. 2h), whereas the level of HOIP messenger RNA was almost identical (Supplementary Fig. 16a). The reduced amount of HOIP in cells lacking SHARPIN seemed to be due in part to degradation of HOIP, because the proteasome inhibitor MG132 increased HOIP levels in *cpdm* MEFs expressing SHARPIN Δ UBL (Supplementary Fig. 16b). These results indicated that HOIL-1L and SHARPIN are necessary for HOIP stability and LUBAC formation, but SHARPIN and/or HOIL-1L may also be present outside of HOIP complexes. We also observed a slower migrating HOIL-1L variant (upper arrow) that was present only in the ~600K fraction (Fig. 2b). Thus, post-translational modification of HOIL-1L may be involved in LUBAC stabilization, although the nature of the modification is currently unknown.

LUBAC components, including SHARPIN, were abundantly expressed in thymus and spleen, and expression of these components was high in splenic B and T cells (Supplementary Fig. 17), in accordance with the important function of NF- κ B in the immune system^{15,18}. The amounts of HOIP and HOIL-1L were similarly reduced in B and T cells from *cpdm* mice (Supplementary Fig. 17). Several of the immunological features of *cpdm* mice, including the lack of Peyer's patches², are often observed in mice with defects in non-canonical NF- κ B activation pathways³. Non-canonical CD40- or BAFF (also known as TNFSF13B)-mediated activation of NF- κ B, as monitored by p100 processing into p52, was not affected in *cpdm* B cells (Fig. 4a and Supplementary Fig. 18). Non-canonical lymphotoxin- β receptor (LT- β R)-mediated activation

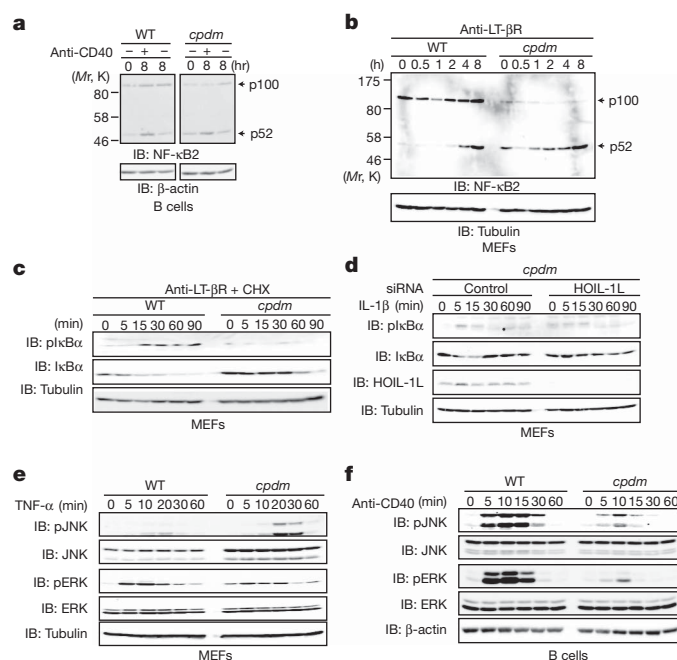


Figure 4 | Involvement of LUBAC in NF- κ B activation induced by various stimuli. **a**, **b**, Non-canonical NF- κ B activation was not affected in *cpdm* cells. Wild-type- and *cpdm*-derived B cells (**a**) or MEFs (**b**) were analysed. **c**, Reduced LT- β R-mediated canonical NF- κ B activation in *cpdm* MEFs. Wild-type and *cpdm* MEFs were treated as indicated. **d**, Knockdown of HOIL-1L in *cpdm* MEFs strongly impaired IL-1 β -induced NF- κ B activation. *cpdm* MEFs transfected with indicated siRNAs were treated with IL-1 β (10 ng ml⁻¹). **e**, **f**, Effect of *Sharpin* deletion on JNK/ERK activation. Wild-type- and *cpdm*-derived MEFs (**e**) or B cells (**f**) were treated as indicated.

of NF- κ B was not also suppressed in *cpdm* MEFs (Fig. 4b). Thus, loss of SHARPIN does not seem to affect non-canonical pathways of NF- κ B activation overtly. Mice in which non-canonical NF- κ B pathways are abolished, including NIK-mutated alymphoplasia (aly) mice or RelB KO mice, do not have lymph nodes¹⁹. In contrast, lymph nodes are present in *cpdm* mice³. The lack of Peyer's patches, however, has been reported in mice carrying a defect only in the canonical NF- κ B pathway²⁰. More importantly, lymphotoxins have crucial roles in the development of secondary lymphoid organs, including lymph nodes²¹. Canonical LT- β R-induced NF- κ B activation was impaired in *cpdm* MEFs (Fig. 4c); thus, the abnormal structure of secondary lymphoid organs in *cpdm* mice may be due to attenuated canonical activation of NF- κ B via LT- β R.

LUBAC clearly has a crucial role in canonical pathways of NF- κ B activation by TNF- α , CD40 and LT- β R. IL-1 β -mediated IKK α degradation was strongly impaired in *cpdm* MEFs transfected with an siRNA specific for HOIL-1L (Fig. 4d), indicating that LUBAC-mediated linear polyubiquitination also has a crucial role in IL-1 β -induced NF- κ B activation. Although IL-1 β -induced NF- κ B was significantly suppressed in *HOIL-1L*^{-/-} MEFs¹¹, it was only mildly affected in *cpdm* MEFs (Supplementary Fig. 19). Loss of HOIL-1L may have a more profound effect on the association of LUBAC with K63-linked chains, because K63-linked ubiquitin chains have a crucial role in IL-1 β , but not TNF- α -mediated IKK activation²². Although *HOIL-1L*^{-/-} mice do not display an obvious phenotype¹¹, *cpdm* mice exhibit severe chronic dermatitis and immune deficiency^{1-3,23}. The phenotypic differences between these mice may result in part from differential effects on IL-1 β -induced NF- κ B activation and TNF- α -induced caspase 3 activation, both of which were higher in *cpdm* MEFs than in *HOIL-1L*^{-/-} MEFs (Supplementary Fig. 20). The symptoms observed in patients with NEMO mutations are quite diverse²⁴. Thus, phenotypic differences between these two mice may be due to differences in NF- κ B activation mediated by residual levels of HOIL-1L-HOIP and SHARPIN-HOIP. Alternatively, the different phenotypes could be

due to differences in the levels of binding proteins, for example, protein(s) involved in recruitment of LUBAC to the IL-1 β receptor, and/or differences in the levels of LUBAC ubiquitination substrates. Further analyses will be needed to clarify mechanisms underlying these phenotypic differences between *cpdm* and *HOIL-1L*^{-/-} mice.

In addition to activating NF- κ B, TNF- α and CD40 also activate the JNK/ERK pathway. TNF- α -induced JNK/ERK activation was slightly higher in *cpdm* MEFs than wild-type MEFs (Fig. 4e), as observed in *HOIL-1L* KO MEFs¹¹. However, CD40-mediated JNK/ERK activation was mildly suppressed in both *cpdm* and *HOIL-1L*^{-/-} B cells (Fig. 4f and Supplementary Fig. 21). Therefore, our results do not conclusively support a role for LUBAC in JNK/ERK activation. Elucidation of the role of LUBAC in JNK/ERK activation awaits further study.

In summary, we have identified SHARPIN as a novel component of LUBAC. SHARPIN-containing LUBAC assembled linear polyubiquitin chains on NEMO, leading to NF- κ B activation. These results do not rule out the presence of other targets of LUBAC-mediated linear polyubiquitination. Given the pleomorphic phenotype of *cpdm* mice^{1-3,23}, linear polyubiquitination by LUBAC may be involved in several disorders, including chronic dermatitis and immunodeficiency. Enhanced expression of SHARPIN has been reported in various human cancers²⁵. Enhanced expression of LUBAC increases NF- κ B activation (Supplementary Fig. 22), indicating that overexpression of LUBAC may be involved in tumorigenesis through activation of the anti-apoptotic function of NF- κ B.

METHODS SUMMARY

***Cpdm* mice, purification of B and T cells, and preparation of MEFs.** *Cpdm* mice were obtained from the Jackson Laboratory. For genotyping of *cpdm* mice, exon 1 of the *Sharpin* gene was amplified by PCR and analysed by direct sequencing to identify a guanine deletion⁸. All animal experiments were approved by the Animal Research Committee of the Graduate School of Medicine, Osaka University. B and T cells were isolated from splenic single-cell suspensions by positive selection with anti-B220 or anti-Thy1 magnetic beads, respectively (Miltenyi Biotec). Cell purity was typically more than 95% for both B220⁺ and Thy1⁺ cells, as assessed by flow cytometry. MEFs of *cpdm* mice were prepared from embryonic day 12.5 (E12.5) embryos. MEFs were transfected with pEF321-T plasmid and transformed clones were isolated.

Full Methods and any associated references are available in the online version of the paper at www.nature.com/nature.

Received 25 January 2010; accepted 11 January 2011.

- Gallardo Torres, H. I., Gijbels, M. J., HogenEsch, H. & Kraal, G. Chronic proliferative dermatitis in mice: neutrophil-endothelium interactions and the role of adhesion molecules. *Pathobiology* **63**, 341–347 (1995).
- HogenEsch, H., Janke, S., Boggess, D. & Sundberg, J. P. Absence of Peyer's patches and abnormal lymphoid architecture in chronic proliferative dermatitis (*cpdm/cpdm*) mice. *J. Immunol.* **162**, 3890–3896 (1999).
- Seymour, R., Sundberg, J. P. & HogenEsch, H. Abnormal lymphoid organ development in immunodeficient mutant mice. *Vet. Pathol.* **43**, 401–423 (2006).
- Zonana, J. et al. A novel X-linked disorder of immune deficiency and hypohidrotic ectodermal dysplasia is allelic to incontinentia pigmenti and due to mutations in *IKK-gamma* (*NEMO*). *Am. J. Hum. Genet.* **67**, 1555–1562 (2000).

- Jain, A. et al. Specific missense mutations in NEMO result in hyper-IgM syndrome with hypohidrotic ectodermal dysplasia. *Nature Immunol.* **2**, 223–228 (2001).
- Jain, A. et al. Specific NEMO mutations impair CD40-mediated c-Rel activation and B cell terminal differentiation. *J. Clin. Invest.* **114**, 1593–1602 (2004).
- Lim, S. et al. Sharpin, a novel postsynaptic density protein that directly interacts with the shank family of proteins. *Mol. Cell. Neurosci.* **17**, 385–397 (2001).
- Seymour, R. E. et al. Spontaneous mutations in the mouse Sharpin gene result in multiorgan inflammation, immune system dysregulation and dermatitis. *Genes Immun.* **8**, 416–421 (2007).
- Yamanaka, K. et al. Identification of the ubiquitin-protein ligase that recognizes oxidized IRP2. *Nature Cell Biol.* **5**, 336–340 (2003).
- Kirisako, T. et al. A ubiquitin ligase complex assembles linear polyubiquitin chains. *EMBO J.* **25**, 4877–4887 (2006).
- Tokunaga, F. et al. Involvement of linear polyubiquitylation of NEMO in NF- κ B activation. *Nature Cell Biol.* **11**, 123–132 (2009).
- Iwai, K. & Tokunaga, F. Linear polyubiquitination: a new regulator of NF- κ B activation. *EMBO Rep.* **10**, 706–713 (2009).
- Haas, T. L. et al. Recruitment of the linear ubiquitin chain assembly complex stabilizes the TNF-R1 signaling complex and is required for TNF-mediated gene induction. *Mol. Cell* **36**, 831–844 (2009).
- Karin, M. Nuclear factor- κ B in cancer development and progression. *Nature* **441**, 431–436 (2006).
- Vallabhapurapu, S. & Karin, M. Regulation and function of NF- κ B transcription factors in the immune system. *Annu. Rev. Immunol.* **27**, 693–733 (2009).
- Bhoj, V. G. & Chen, Z. J. Ubiquitylation in innate and adaptive immunity. *Nature* **458**, 430–437 (2009).
- Yamaoka, S. et al. Complementation cloning of NEMO, a component of the I κ B kinase complex essential for NF- κ B activation. *Cell* **93**, 1231–1240 (1998).
- Hayden, M. S. & Ghosh, S. Shared principles in NF- κ B signaling. *Cell* **132**, 344–362 (2008).
- Gerondakis, S. et al. Unravelling the complexities of the NF- κ B signalling pathway using mouse knockout and transgenic models. *Oncogene* **25**, 6781–6799 (2006).
- Piao, J. H. et al. TNF receptor-associated factor 2-dependent canonical pathway is crucial for the development of Peyer's patches. *J. Immunol.* **178**, 2272–2277 (2007).
- Koni, P. A. et al. Distinct roles in lymphoid organogenesis for lymphotoxins α and β revealed in lymphotoxin β -deficient mice. *Immunity* **6**, 491–500 (1997).
- Xu, M., Skaug, B., Zeng, W. & Chen, Z. J. A Ubiquitin replacement strategy in human cells reveals distinct mechanisms of IKK activation by TNF α and IL-1 β . *Mol. Cell* **36**, 302–314 (2009).
- Renninger, M. L., Seymour, R. E., Whiteley, L. O., Sundberg, J. P. & HogenEsch, H. Anti-IL5 decreases the number of eosinophils but not the severity of dermatitis in Sharpin-deficient mice. *Exp. Dermatol.* **19**, 252–258 (2009).
- Smahi, A. et al. The NF- κ B signalling pathway in human diseases: from incontinentia pigmenti to ectodermal dysplasias and immune-deficiency syndromes. *Hum. Mol. Genet.* **11**, 2371–2375 (2002).
- Jung, J. et al. Newly identified tumor-associated role of human Sharpin. *Mol. Cell. Biochem.* **340**, 161–167 (2010).

Supplementary Information is linked to the online version of the paper at www.nature.com/nature.

Acknowledgements We thank T. Kitamura, S. Sugano, P. Rennert and J. Browning for reagents; O. Takeuchi for comments; and K. Kamei and K. Fukunaga for technical assistance. This work was partly supported by Grants-in-Aid from the Ministry of Education, Culture, Sports, Science, and Technology of Japan (F.T. and K.I.).

Author Contributions F.T., T.N., M.N., Y.S., M.T., S.-i.S. and H.N. performed experiments. K.T. and K.I. coordinated the study, and F.T. and K.I. wrote the manuscript. All authors discussed the results and commented on the manuscript.

Author Information Reprints and permissions information is available at www.nature.com/reprints. The authors declare no competing financial interests. Readers are welcome to comment on the online version of this article at www.nature.com/nature. Correspondence and requests for materials should be addressed to K.I. (e-mail: kiwai@cellbio.med.osaka-u.ac.jp).

METHODS

RT-PCR and plasmids. The open reading frames of human and mouse *Sharpin* were amplified by RT-PCR. The human SHARPIN mutants were as follows: wild-type (amino acids 1–387), Δ NZF (1–348), Δ UBL (deletion of amino acids 230–304), N terminus (1–239), and C terminus (240–387). The mouse SHARPIN mutants were as follows: wild-type (1–387), Δ NZF (1–347), Δ UBL (deletion of amino acids 233–305), N terminus (1–162), and C terminus (163–387). The N terminus (1–300) and C terminus (701–1066) fragments of mouse HOIP were amplified by PCR. Other cDNAs were prepared as described previously^{10,11}. cDNAs were ligated to the appropriate epitope sequences and then cloned into pcDNA3.1, pVL1393 (Invitrogen), pMAL-c2x (New England Biolabs), pGEX-6P-1 (GE Healthcare), pT7-7, or pMXs-IP (gifts from T. Kitamura). pEF321-T, which includes the SV40 large T antigen, was supplied by S. Sugano.

Antibodies and reagents. Human GST-SHARPIN N terminus was expressed in *Escherichia coli* and then purified using glutathione Sepharose (GE Healthcare). Purified recombinant fusion protein was used to immunize rabbits. Affinity-purified anti-SHARPIN IgG was prepared from antisera using protein A Sepharose (GE Healthcare) followed by affinity chromatography using immobilized recombinant MBP-SHARPIN N-term-Sepharose. Similarly, the anti-mouse-HOIP antibody was purified from sera of rabbits immunized with bacterially expressed recombinant MBP-mouse HOIP using protein A Sepharose and immobilized GST-HOIP Sepharose column chromatography. Anti-ERK and anti-phospho-ERK antibodies were purchased from Cell Signaling, and the anti-CD40 antibody was obtained from BD Pharmingen. The anti mouse-LT- β R was provided by P. Rennert and J. Browning. Anti-Lys 48- and anti-Lys 63-specific polyubiquitin antibodies were obtained from Millipore. Cycloheximide and BAFF were purchased from Calbiochem and PeproTech, respectively. Other antibodies and reagents were obtained as described previously^{10,11}.

Retroviral expression. Flag-tagged wild-type and mutant mouse *Sharpin* cDNAs were ligated into pMXs-IP, and the plasmids were transfected into Plat E packaging cells, as described¹¹. The resultant retrovirus was used to infect *cpdm* MEFs, and the stable clones were selected by puromycin resistance.

IKK kinase assay. Wild-type or *cpdm* MEFs were lysed with buffer containing 20 mM Tris-HCl, pH 7.5, 10 mM EGTA, 10 mM MgCl₂, 60 mM β -glycerophosphate, 1 mM Na₃VO₄, 20 mM NaF, 2 mM DTT, 1% Triton X-100, and protease and phosphatase inhibitor cocktails (Sigma). Where indicated, TNF- α (10 ng ml⁻¹) was added to the cells before lysis. Anti-NEMO immunoprecipitates were incubated with 5 μ g of GST-I κ B α (1–54) or GST-I κ B α -AA (1–54, S32/36A), and 3.7 kBq of [γ -³²P]-ATP (Perkin Elmer) at 37 °C for 20 min. Samples were visualized with a BAS5000 Image Analyser (Fuji Film).

***Cpdm* mice, purification of B and T cells, and preparation of MEFs.** *Cpdm* mice were obtained from the Jackson Laboratory. For genotyping of *cpdm* mice, exon 1 of the *Sharpin* gene was amplified by PCR and analysed by direct sequencing to identify a guanine deletion⁸. All animal experiments were approved by the Animal Research Committee of the Graduate School of Medicine, Osaka University. B and T cells were isolated from splenic single-cell suspensions by positive selection with anti-B220 or anti-Thy1 magnetic beads, respectively (Miltenyi Biotec). Cell purity was typically more than 95% for both B220⁺ and Thy1⁺ cells, as assessed by flow cytometry. MEFs of *cpdm* mice were prepared from embryonic day 12.5 (E12.5) embryos. MEFs were transfected with pEF321-T plasmid and transformed clones were isolated.

Cell culture and transfection. MEFs derived from wild-type and *cpdm* mice and HEK293T cells were grown in DMEM plus 10% fetal bovine serum, 100 IU ml⁻¹ penicillin G and 100 μ g ml⁻¹ streptomycin. Splenic B cells from wild-type or *cpdm* mice were grown in RPMI1640 plus 10% fetal bovine serum, 100 IU ml⁻¹ penicillin G and 100 μ g ml⁻¹ streptomycin. As indicated, cells were treated with TNF- α (10 ng ml⁻¹), cycloheximide (20 μ g ml⁻¹), IL-1 β (10 ng ml⁻¹), anti-CD40 (0.5 μ g ml⁻¹) or anti-LT- β R (1 μ g ml⁻¹). Transfections were performed using Lipofectamine2000 (Invitrogen) or ExGen500 (Fermentas).

Immunoprecipitation and immunoblotting. Cells were lysed with lysis buffer containing 50 mM Tris-HCl, pH 7.5, 150 mM NaCl, 1% Triton X-100, and 2 mM PMSF. For immunoprecipitation, lysates were incubated with the appropriate

antibodies for 1 h on ice, followed by incubation with rmp protein A Sepharose (GE Healthcare). Samples were separated by SDS-PAGE and then transferred to a PVDF membrane. After blocking in TBS containing 0.1% Tween 20 and 5% skimmed milk, the membrane was incubated with the appropriate primary antibody, followed by incubation with horseradish peroxidase-conjugated secondary antibody (GE Healthcare). Immunoreactive proteins were visualized using enhanced chemiluminescence. For the detection of linear polyubiquitin chains, cell lysates were heated at 90 °C for 15 min in 1% SDS to eliminate noncovalent binding. Tenfold dilutions were prepared using buffer containing 1% Triton X-100, 50 mM Tris-HCl, pH 7.5 and 150 mM NaCl and then subjected to immunoprecipitation with an anti-NEMO monoclonal antibody. After electrophoresis, samples were transferred to a nitrocellulose membrane (BA83, Schleicher & Schunell), autoclaved with distilled water at 121 °C for 30 min, and then autoclaved again for 15 min without water, as described¹¹. Membranes were incubated with an anti-linear ubiquitin antibody¹¹. Immunoblots were quantified using a LAS3000 or LAS4000 Mini-Imaging Analyzer (Fuji Film).

Luciferase assay. The luciferase reporter plasmids pSP-6xNF- κ B-Luc and pSV40-Renilla-Luc were previously described¹¹. Following transfection for 24 h with the appropriate plasmids, cells were lysed and then luciferase activity was measured in a Lumat luminometer (Berthold) using the Dual-Luciferase Reporter or Bright-Glo Luciferase assay system (Promega).

Gel filtration. Cells were lysed in lysis buffer containing 50 mM Tris-HCl, pH 7.5, 1 mM MgCl₂, 1 mM DTT, 1 mM PMSF, and a protease inhibitor cocktail (Complete EDTA-free, Roche) by passage through polycarbonate filters (Whatman)¹¹. After adding an equal volume of lysis buffer containing 300 mM NaCl, lysates were centrifuged at 100,000g for 30 min to obtain S100 lysates. S100 lysates were injected on a Superdex 200 HR (10/30) column (GE Healthcare) and fractionated in 50 mM Tris-HCl pH 7.5, containing 150 mM NaCl using an ÄKTA chromatography system (GE Healthcare).

Preparation of recombinant proteins and *in vitro* ubiquitination assays. Recombinant His₆-HOIP-HOIL-1L complexes, Myc-IKK α -His₆-IKK β -Flag-NEMO complexes, GST-NEMO mutants, E1, and E2 were prepared as previously described^{10,11}. Recombinant baculoviruses encoding Myc-SHARPIN were generated using the Bac-PAK6 baculovirus expression system (BD Biosciences), and the recombinant Myc-SHARPIN-His₆-HOIP-HOIL-1L complex was purified as described previously²⁶. *In vitro* ubiquitination assays were performed as previously described using UbcH5c as an E2 (refs 10, 11).

Mass spectrometry. CBB-stained protein bands were excised from an SDS-polyacrylamide gel, destained, and then treated with 0.1% RapiGest (Waters) in AMBC to improve tryptic digestion. After dehydration, proteins were subjected to in-gel digestion with 10 μ g ml⁻¹ of modified trypsin (Trypsin Gold, Mass Spec Grade, Promega) for 12 h at 37 °C. The resulting peptides were desalted with ZipTipC18 (Millipore) and then analysed using an ABI4800 MALDI-TOF/TOF Proteomics Analyzer. MS and MS/MS spectra were analysed by ProteinPilot software 3.0 (Applied Biosystems).

RNAi. A double-stranded stealth siRNA for mouse *HOIL-1L* and the corresponding scrambled control RNA were prepared by Invitrogen. The sequences were as follows: *HOIL-1L*, 5'-GAUGAACAGGCGUCUAUCAAGUAUG-3'; and *HOIL-1L* control (scrambled), 5'-GAUACACGGCGUUAUACUGGAAUG-3'. Cells were transfected with stealth siRNAs as described¹¹.

Semi-quantitative and quantitative RT-PCR. Semi-quantitative RT-PCR analysis and oligonucleotides for A20 and β -actin were used as described previously¹¹. *I κ B α* and *ICAM* were amplified using the following oligonucleotides: *I κ B α* sense, 5'-CACGAAGAGAAGCCGCTGACCATGGAA-3' and *I κ B α* anti-sense, 5'-TG GATAGAGGCTAGGTGCAGACACG-3'; *ICAM* sense, 5'-CAACTGGAAGCT GTTTGAGCTG-3' and *ICAM* anti-sense, 5'-TAGCTGGAAGATCGAAAGTC CG-3'. Quantitative real time PCR was performed using a Step-One-Plus PCR system (Applied Biosystems) with inventoried TaqMan probes for mouse *HOIP* and β_2 -microglobulin, according to the manufacturer's specifications.

26. Iwai, K. *et al.* Identification of the von Hippel-Lindau tumor-suppressor protein as part of an active E3 ubiquitin ligase complex. *Proc. Natl Acad. Sci. USA* **96**, 12436–12441 (1999).

SHARPIN forms a linear ubiquitin ligase complex regulating NF- κ B activity and apoptosis

Fumiyo Ikeda¹, Yonathan Lissanu Deribe^{1*}, Sigrid S. Skånland^{1*}, Benjamin Stieglitz², Caroline Grabbe^{1,3}, Mirita Franz-Wachtel⁴, Sjoerd J. L. van Wijk¹, Panchali Goswami¹, Vanja Nagy⁵, Janos Terzic⁶, Fuminori Tokunaga⁷, Ariadne Androulidaki⁸, Tomoko Nakagawa⁷, Manolis Pasparakis⁸, Kazuhiro Iwai^{7,9}, John P. Sundberg¹⁰, Liliana Schaefer¹¹, Katrin Rittinger², Boris Macek⁴ & Ivan Dikic^{1,6}

SHARPIN is a ubiquitin-binding and ubiquitin-like-domain-containing protein which, when mutated in mice, results in immune system disorders and multi-organ inflammation^{1,2}. Here we report that SHARPIN functions as a novel component of the linear ubiquitin chain assembly complex (LUBAC) and that the absence of SHARPIN causes dysregulation of NF- κ B and apoptotic signalling pathways, explaining the severe phenotypes displayed by chronic proliferative dermatitis (*cpdm*) in SHARPIN-deficient mice. Upon binding to the LUBAC subunit HOIP (also known as RNF31), SHARPIN stimulates the formation of linear ubiquitin chains *in vitro* and *in vivo*. Coexpression of SHARPIN and HOIP promotes linear ubiquitination of NEMO (also known as IKK β), an adaptor of the I κ B kinases (IKKs) and subsequent activation of NF- κ B signalling, whereas SHARPIN deficiency in mice causes an impaired activation of the IKK complex and NF- κ B in B cells, macrophages and mouse embryonic fibroblasts (MEFs). This effect is further enhanced upon concurrent downregulation of HOIL-1L (also known as RBCK1), another HOIP-binding component of LUBAC. In addition, SHARPIN deficiency leads to rapid cell death upon tumour-necrosis factor α (TNF- α) stimulation via FADD- and caspase-8-dependent pathways. SHARPIN thus activates NF- κ B and inhibits apoptosis via distinct pathways *in vivo*.

In addition to the established roles of K63- and K48-linked ubiquitin chains, linear ubiquitin chains have recently emerged as important regulators of the NF- κ B pathway, controlling immune responses, as well as cell survival, proliferation, and development^{3–8}.

Linear ubiquitin conjugation relies on two RING-between-RING (RBR) domain-containing proteins, HOIL-1L (longer isoform of hemoxidized iron-regulatory protein 2 ubiquitin ligase-1) and HOIP (HOIL-1L interacting protein), which together form the E3 ligase complex LUBAC (linear ubiquitin chain assembly complex)⁹. We became interested in SHARPIN (SHANK-associated RH domain-interacting protein) because of the significant sequence homology of its C-terminal region, enclosing a ubiquitin-like (UBL) domain and a putative ubiquitin-binding NPL4 zinc-finger domain (NZF), with the N-terminal region of HOIL-1L^{9,10} (Fig. 1a). Initially, we established SHARPIN as a bona fide ubiquitin-binding protein by mapping the ubiquitin binding site to the NZF domain (Supplementary Fig. 1). A direct NZF-dependent interaction of SHARPIN with mono-ubiquitin, linear, and K63 ubiquitin chains was confirmed by pull-down assays (Supplementary Fig. 1b–d) and isothermal titration calorimetry (ITC) (Fig. 1b). Mutagenesis of two key residues surrounding the zinc coordination site of the NZF (T358L, F359V) abolished ubiquitin binding

(Supplementary Fig. 1a, c). The isolated NZFs of SHARPIN, HOIL-1L and HOIP interact with mono-ubiquitin with similar affinities (Fig. 1b), recognizing the classical hydrophobic patch surrounding I44, as indicated by the absence of any interaction with mutant I44A ubiquitin (Fig. 1b) and display no specificity for different chain types (Fig. 1b and Supplementary Fig. 1c). These data are consistent with binding assays employing a panel of HOIP and HOIL-1L protein variants expressed in transfected cells or in *in vitro* ubiquitin binding experiments (Supplementary Fig. 1e–h).

We next investigated whether SHARPIN directly associates with the LUBAC complex in cells. Tagged versions of HOIP, HOIL-1L and SHARPIN were readily immunoprecipitated from lysates of transiently transfected HEK293T cells (Fig. 1c). Likewise, the interaction of endogenous SHARPIN, HOIP and HOIL-1L was confirmed in primary mouse embryonic fibroblasts (MEFs) (Fig. 1d). The interaction between SHARPIN and HOIP is mediated by the UBL domain of SHARPIN, which recognizes the NZF2 domain of HOIP (Supplementary Fig. 1i, j). In agreement, the interaction between HOIP and SHARPIN was abolished in response to either deletion or mutation (I272A) of the UBL domain of SHARPIN, but was not affected in the ubiquitin-binding deficient mutant of SHARPIN NZF (Supplementary Fig. 2a). On the other hand, purified HOIL-1L did not interact with full-length SHARPIN in *in vitro* binding assays (Supplementary Fig. 2b). Thus, HOIP has the capacity to interact with either SHARPIN or HOIL-1L or both of them. Indeed, endogenous HOIP can form a complex with only HOIL-1L or SHARPIN in the absence of the other, because in SHARPIN- or HOIL-1L-deficient MEFs, HOIP can coprecipitate with residual HOIL-1L or SHARPIN, respectively (Fig. 1d). Interestingly, the deficiency of either SHARPIN or HOIL-1L led to a partial destabilization of the other protein (Fig. 1d). Together these findings indicate the existence of three putative LUBAC complexes: dimeric complexes, HOIP–HOIL-1L (LUBAC-I) and SHARPIN–HOIP (LUBAC-II), and a trimeric SHARPIN–HOIP–HOIL-1L complex (Supplementary Fig. 2c).

The purified SHARPIN–HOIP complex stimulated the *in vitro* assembly of linear ubiquitin chains (Fig. 2a), similar to the ligase activity of a HOIP–HOIL-1L complex (Supplementary Fig. 3a). We thus extended our studies to investigate whether SHARPIN and HOIP can induce linear ubiquitination of proteins in cells. The UBL domain of ABIN-1 (also known as TNIP1), known to bind linear ubiquitin chains preferentially^{11,12}, was used as an affinity matrix to pull down cellular proteins modified by linear ubiquitination upon overexpression of SHARPIN and HOIP (Fig. 2b and Supplementary

¹Frankfurt Institute for Molecular Life Sciences and Institute of Biochemistry II, Goethe University School of Medicine, Theodor-Stern-Kai 7, D-60590 Frankfurt (Main), Germany. ²MRC-National Institute for Medical Research, The Ridgeway, London NW7 1AA, UK. ³Department of Molecular Biology, Umeå University, Building 6L, 901 87 Umeå, Sweden. ⁴Proteome Center Tübingen, Interfaculty Institute for Cell Biology, University of Tübingen, Auf der Morgenstelle 15, 72076 Tübingen, Germany. ⁵IMBA-Institute of Molecular Biotechnology of the Austrian Academy of Sciences, Dr. Bohrergasse 3, 1030 Vienna, Austria. ⁶School of Medicine, University of Split, Soltanska 2, Split, HR-21000, Croatia. ⁷Department of Biophysics and Biochemistry, Graduate School of Medicine, Osaka University, Suita, Osaka 565-0871, Japan. ⁸Institute for Genetics, Centre for Molecular Medicine (CMMC), and Cologne Excellence Cluster on Cellular Stress Responses in Aging-Associated Diseases (CECAD), University of Cologne, Zùlpicher Str. 47a, 50674 Cologne, Germany. ⁹Cell Biology and Metabolism Group, Graduate School of Frontier Biosciences, Osaka University, Suita, Osaka 565-0871, Japan. ¹⁰The Jackson Laboratory, Bar Harbor, Maine 04609, USA. ¹¹Allgemeine Pharmakologie und Toxikologie, Division Nephropharmakologie, Klinikum der Goethe Universität, Theodor-Stern Kai 7, 60590 Frankfurt, Germany.

*These authors contributed equally to this work.

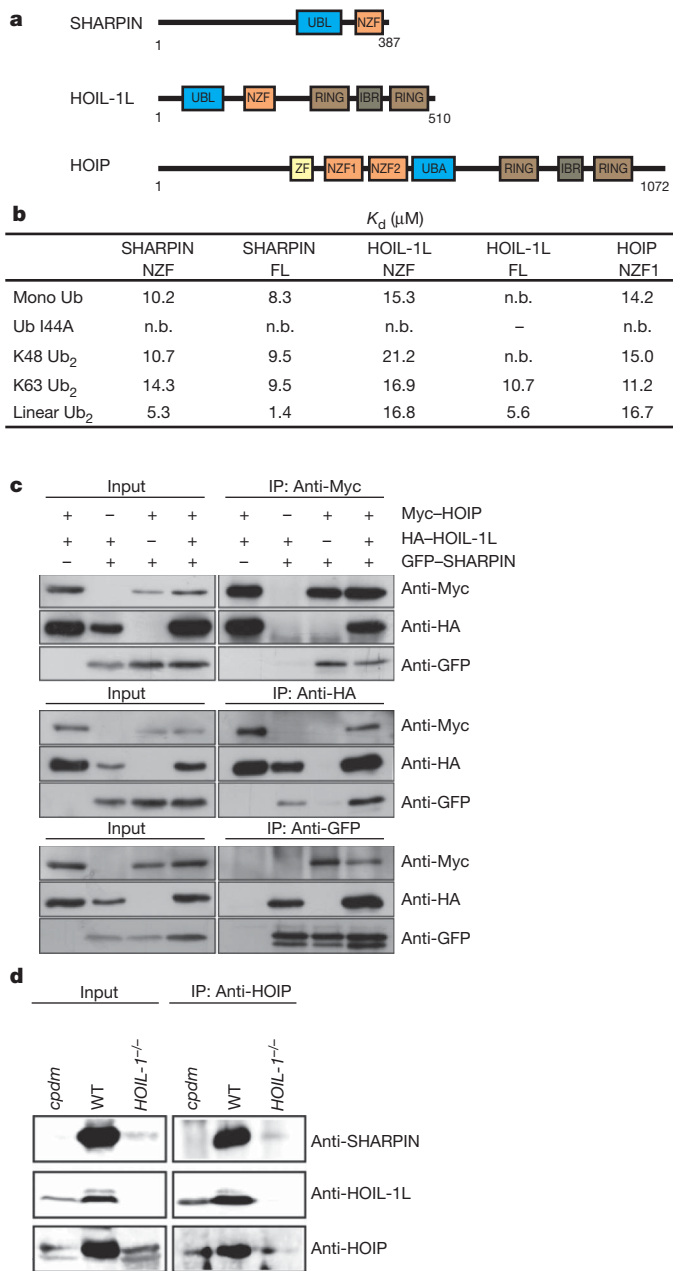


Figure 1 | SHARPIN is a novel component of the LUBAC complex.

a, Schematic representation of the domain architecture of SHARPIN, HOIL-1L and HOIP. **b**, Quantitative assessment of the binding of SHARPIN, HOIL-1L and HOIP to a panel of ubiquitin species using isothermal titration calorimetry (ITC). The obtained equilibrium dissociation constants of individual measurements are listed. n.b., no binding observed; Ub, ubiquitin. **c**, **d**, Formation of a trimeric complex between SHARPIN, HOIL-1L and HOIP in HEK293T cells (**c**) or MEFs (**d**) transfected with Myc–HOIP, haemagglutinin (HA)–HOIL-1L and green fluorescent protein (GFP)–SHARPIN. Lysates were immunoprecipitated (IP) and analysed by western blot.

Fig. 3f). Both the NZF and UBL domains of SHARPIN were essential for this activity, because neither the SHARPIN-NZF (T358L, F359V), nor the SHARPIN-UBL (I272A) mutant showed any ability to induce linear ubiquitination *in vivo* (Fig. 2b). Similarly, the ABIN-1-UBAN D485A mutant, which is unable to bind linear polyubiquitin, did not pull down any ubiquitin conjugates (Fig. 2b and Supplementary Fig. 3d, e). A specific enrichment of linear ubiquitination in cells overexpressing SHARPIN and HOIP was further confirmed by tandem mass spectrometry (MS/MS) analysis. In samples transfected with SHARPIN–HOIP

as well as HOIP–HOIL-1L the linear ubiquitin peptide GGMQIFVK was detected (Fig. 2c). MS-based quantification (employing the AQUA approach described in Supplementary Fig. 4a) detected an increase in the absolute amounts of ubiquitin present in linear chains compared to the total pool of ubiquitin (measured by the TITLEVEPSDTIENVK peptide) in cells expressing wild-type SHARPIN–HOIP, in contrast to cells expressing an inactive SHARPIN–HOIP complex (Supplementary Fig. 4b–e). We next performed a stable isotope labelling using amino acids in cell culture (SILAC)-based quantitative MS/MS analysis on immunoprecipitated NEMO upon co-transfection with either wild-type or inactive SHARPIN–HOIP (experimental design is shown in Supplementary Fig. 5a, b). The measured intensity of linear ubiquitin peptides on immunoprecipitated NEMO was >25 times higher in cells transfected with wild-type SHARPIN–HOIP compared to cells expressing inactive SHARPIN–HOIP mutants (Fig. 2d, e). In the same sample we detected 13 ubiquitination sites on NEMO, of which 11 were increased following transfection with wild-type versus mutated SHARPIN–HOIP (Supplementary Fig. 5c), indicating that NEMO is a substrate of LUBAC II.

SHARPIN-deficient (*Sharpin*^{cpdm/cpdm}, abbreviated to *cpdm*) mice exhibit diverse phenotypes in the immune system, which resemble the phenotypes of genetically engineered mouse models with impaired NF- κ B activation^{7,8}. As linear ubiquitination is important for activation of the NF- κ B pathway^{3,11,13,14} we speculated that the SHARPIN–HOIP LUBAC complex might have a critical role in regulation of the NF- κ B pathway. Consistent with this hypothesis, co-transfection of SHARPIN and HOIP increased transcription of a luciferase-based NF- κ B reporter, similar to the effect of HOIP and HOIL-1L co-expression (Fig. 2f), whereas no activation of NF- κ B was detected when cells were transfected with SHARPIN, HOIL-1L or HOIP alone (Fig. 2f), or a combination of mutant forms of NZF or UBL domains in SHARPIN together with HOIP (Fig. 2g).

Based on the finding that TNF- α stimulated formation of a signalling complex between SHARPIN–HOIP and NEMO (Supplementary Fig. 6), we reasoned that the SHARPIN–HOIP complex might act as an upstream regulator of IKK activation. *In vitro* IKK kinase assay showed that TNF- α rapidly enhanced IKK kinase activity in wild-type MEFs, which was delayed and reduced in cells lacking SHARPIN (Fig. 3a). Upon additional abrogation of HOIL-1L expression in *cpdm* MEFs by stably expressing short hairpin RNA (shRNA) against HOIL-1L (*cpdm* shHOIL-1L) IKK activation was further inhibited (Fig. 3a). Moreover, downstream events of IKK activation, such as phosphorylation and subsequent degradation of I κ B α (also known as NFKBIA), as well as nuclear translocation of p65 (also known as RELA), were also reduced in *cpdm* MEFs and further impaired in response to shRNA-mediated downregulation of HOIL-1L (Fig. 3b, c and Supplementary Fig. 7a) or overexpression of an I κ B α super-repressor mutant (Supplementary Fig. 7b).

Given the plethora of evidence presented above that SHARPIN modulates the NF- κ B pathway, we further assessed the functional role of SHARPIN in NF- κ B activation *in vivo* using cells isolated from the *cpdm* mice. The absence of SHARPIN in *cpdm* splenic B cells stimulated with soluble CD40L (also known as CD40LG) resulted in impaired activation of the NF- κ B pathway, evaluated by phosphorylation and degradation of I κ B α , compared to wild-type B cells (Fig. 3d). Similar findings were obtained in thioglycollate-induced peritoneal macrophages from *cpdm* mice, which in response to bacterial lipopolysaccharide (LPS) stimulation failed to induce an efficient phosphorylation and degradation of I κ B α (Fig. 3e), proper nuclear translocation of the NF- κ B transcription factor p65 (Supplementary Fig. 8a) or secretion of TNF- α and MCP-1 (Fig. 3f, g). Furthermore, IL-1 β (also known as IL1B) stimulation-induced NF- κ B activation was delayed in SHARPIN-deficient MEFs (Supplementary Fig. 8b). Similarly, we observed partial impairment of JNK activation in response to TNF- α , CD40L or LPS in *cpdm* MEFs, B cells or macrophages, respectively, compared to wild-type cells (Fig. 3e and Supplementary Fig. 8c–e).

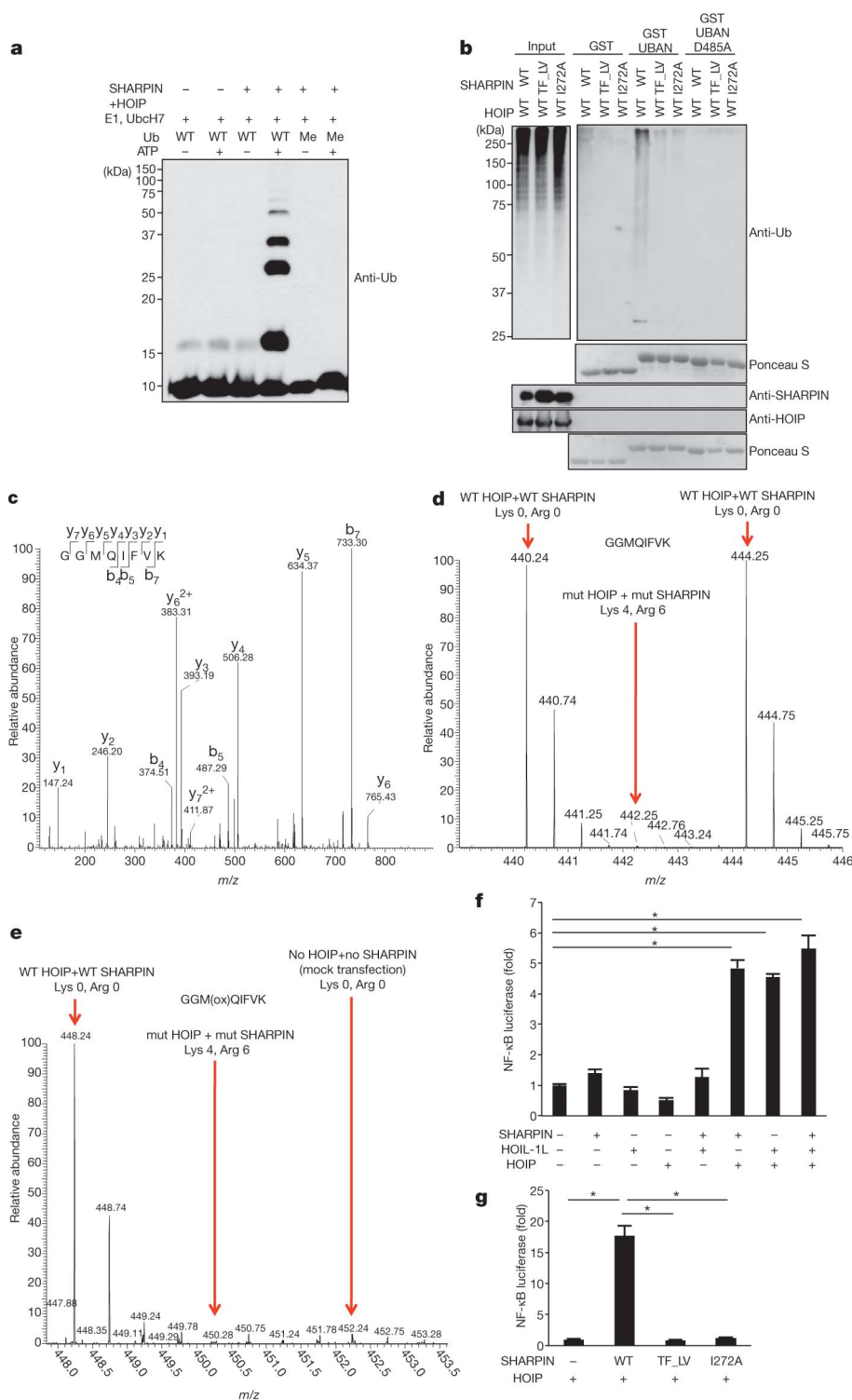


Figure 2 | SHARPIN and HOIP form a novel LUBAC complex with the ability to induce linear ubiquitination and NF- κ B activation. **a**, *In vitro* linear ubiquitin chain synthesis by purified SHARPIN and HOIP. **b**, Stimulation of linear ubiquitination by SHARPIN and HOIP *in vivo*. Immobilised GST-ABIN-1-UBAN domain was used to detect linear ubiquitination of proteins. **c**, MS/MS spectrum of the prototypic linear ubiquitin peptide present *in vivo*. **d**, **e**, SILAC experiments comparing relative

An interesting feature of *cpdm* mice is the combination of epidermal hyperplasia and inflammation with the presence of apoptotic bodies in keratinocytes and increased cell death in the skin¹⁵. Moreover, inhibition of TNF- α -induced NF- κ B signalling in keratinocytes results in inflammatory skin lesions as observed in genetically engineered mouse

levels of linear ubiquitin on immunoprecipitated NEMO induced by HOIP and SHARPIN (**d**) or HOIP-mut (C699/702S, C871/874S)-SHARPIN-mut(T358L, F359V)(Lys 8, Arg 10) (**e**). **f**, **g**, Generation of NF- κ B transcriptional activity by SHARPIN and HOIP *in vivo*. NF- κ B-Luciferase assays using the indicated combinations of SHARPIN, HOIL-1L, and HOIP were performed. Results are shown as means and s.e.m. ($n = 4$). * $P < 0.0001$, determined by the Student's *t*-test.

models, as well as in human diseases such as incontinentia pigmenti⁷. Using a highly sensitive impedance-based real-time cell analyser, we found that *cpdm* MEFs were extremely sensitive to rapid TNF- α -induced cell death (Fig. 4a). This correlated with an appearance of typical apoptotic cell morphology (Supplementary Fig. 9a) and early

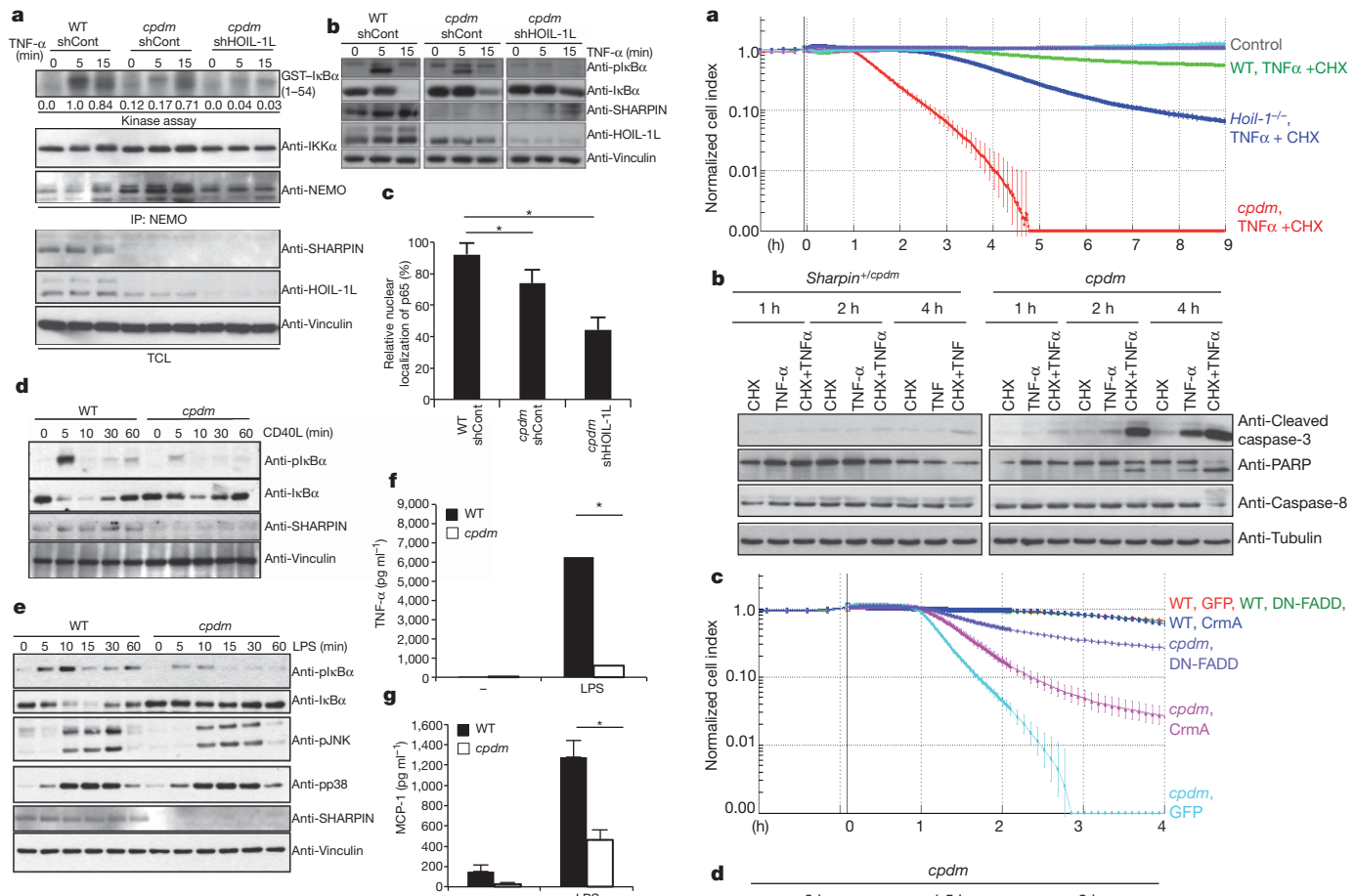
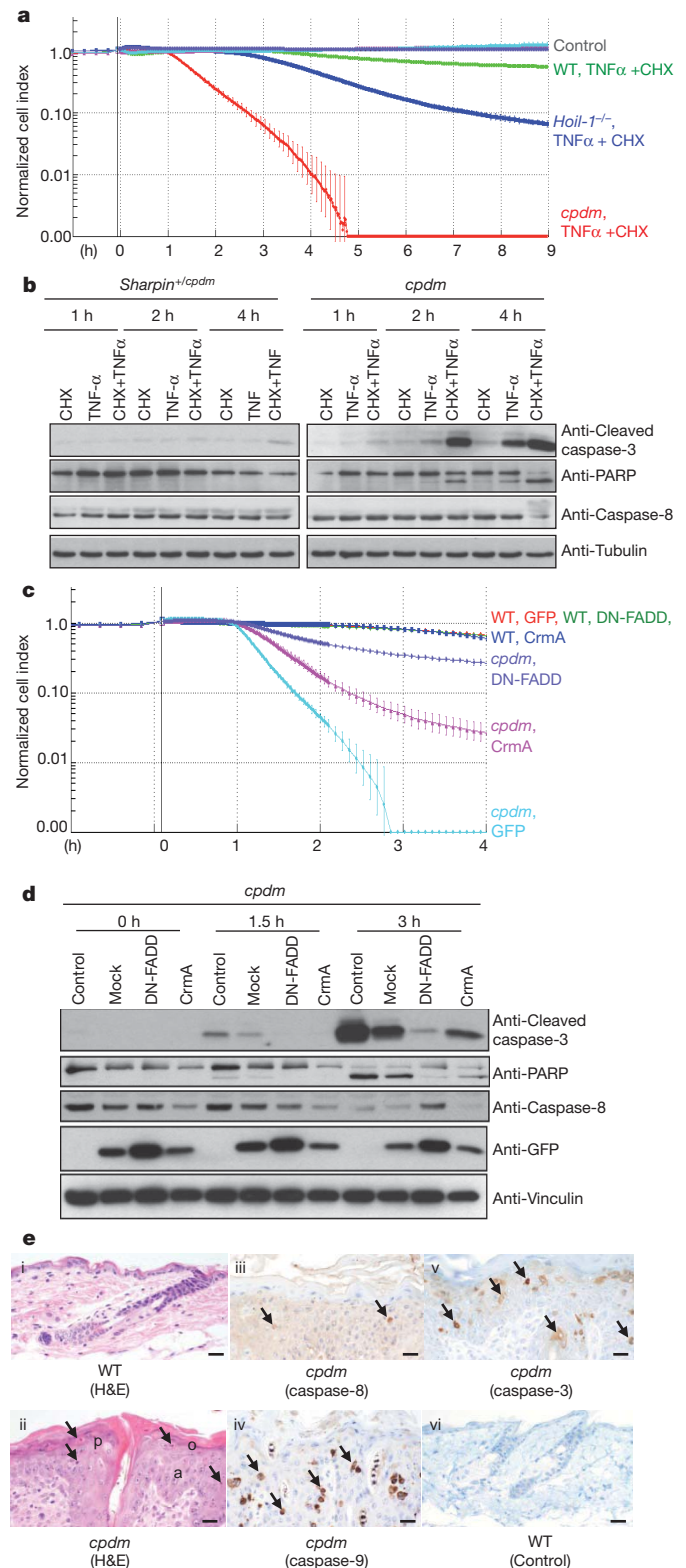


Figure 3 | SHARPIN and HOIL-1L are essential for full activation of IKK and NF- κ B. **a**, *In vitro* IKK-kinase activity in TNF- α -treated *cpdm* MEFs stably transduced with non-targeting (control) or HOIL-1L shRNA. **b**, **c**, Defect of TNF- α -induced I κ B α phosphorylation (pI κ B α), degradation and translocation of p65 in *cpdm* MEFs stably transduced with HOIL-1L shRNA. **d**, **e**, Impaired NF- κ B activation in primary B cells or macrophages of *cpdm* stimulated with CD40L (**d**) or LPS (**e**). **f**, **g**, Reduced capacity of *cpdm* macrophages to secrete TNF- α and MCP-1 in response to LPS. TNF- α ELISA (**f**); $n = 5$, MCP-1 ELISA (**g**); $n = 4$. Results in **c**, **f** and **g** are shown as means and s.e.m. * $P < 0.0001$, determined by the Student's *t*-test.

signs (2–4 h after TNF- α stimulation) of apoptotic signalling, including proteolytic cleavage of the initiator caspase, caspase-8, the effector caspase, caspase-3, as well as PARP (also known as PARP1), a substrate of caspase-3 (Fig. 4b). In agreement with a requirement for caspase activity for the induction of apoptosis, pre-treatment of *cpdm* cells with the general caspase inhibitor zVAD-FMK abolished the observed cell death in response to TNF- α (Supplementary Fig. 9b). When performing the reciprocal experiments on MEFs derived from *HOIL-1* null

Figure 4 | Loss of SHARPIN sensitizes cells to FADD- and caspase-8-mediated apoptosis **a**, Increased susceptibility to TNF- α -induced apoptosis in SHARPIN-deficient MEFs. Cell detachment and death were measured continuously in real-time using an impedance-based real-time cell analyser (RTCA). **b**, Increased caspase activation by TNF- α and CHX in SHARPIN-deficient MEFs. **c**, **d**, Cell death caused by loss of SHARPIN via FADD and caspase-8 dependent apoptotic signalling. MEFs were retrovirally transduced with indicated proteins and treated with TNF- α . **e**, Increased apoptotic cell death in the skin of *cpdm* mice. Normal epidermis (i) and *cpdm* (ii) skin samples were immunostained for caspase-8 (iii), caspase-9 (iv) and caspase-3 (v). None of these markers were present in control mouse epidermis (vi). H&E; haematoxylin and eosin. Scale bars, 2 μ m. Results in **a** and **c** are shown as means and s.e.m. ($n = 3$).



mice¹⁴, we observed a delayed and significantly weaker induction of the apoptotic response in cells stimulated with TNF- α and cycloheximide (CHX) (Fig. 4a). In accordance, we were unable to detect rapid activation of caspase-3 and caspase-8 upon TNF- α or TNF- α + CHX treatment of HOIL-1L-deficient MEFs (Supplementary Fig. 9c). Moreover, additional downregulation of HOIL-1L in *cpdm* MEFs did not further increase TNF- α -induced apoptosis or caspase activation (Supplementary Fig. 9d), whereas a combined lack of SHARPIN and HOIL-1L had a strong additive effect on the inhibition of the NF- κ B pathway

(Fig. 3a–c). Cell death in *cpdm* MEFs was not upregulated by other stress stimuli, including staurosporine, brefeldin A and doxorubicin (Supplementary Fig. 9e–g).

TNF- α -induced cell death is known to proceed through the cytosolic TNFR1 signalling complex II that is composed of TRADD, TRAF2, RIP1 (also known as RIPK1), caspase-8/10, and the death domain containing protein FADD, which together serve as a cell death checkpoint control in TNF-sensitive cells^{16,17}. The apoptotic cell death displayed by *cpdm* MEFs occurs through the FADD and caspase-8-containing TNFR1 (also known as TNFRSF1A) complex II, because retroviral transduction of either a dominant negative mutant of FADD or CrmA, a cowpox-virus-derived serine protease inhibitor (serpin) of caspase-8, markedly inhibited TNF- α -induced cell death (Fig. 4c, d). Importantly, we have also detected activation of caspase-3, -8, and -9 in skin keratinocytes of *cpdm* mice (Fig. 4e). Taken together, our results indicate that loss of SHARPIN expression sensitizes cells for TNF- α -induced cell death, in part dependent on a caspase-8 pathway. This phenomenon might be an underlying mechanism for the development of inflammatory skin lesions in *cpdm* mice.

In conclusion, this study provides physiological evidence for a novel LUBAC complex composed of HOIP, the major catalytic subunit, and the adaptor protein SHARPIN. Together, SHARPIN and HOIP mediate linear ubiquitination of NEMO *in vivo* (Fig. 2a–e and Supplementary Figs 4 and 5) and activate the NF- κ B pathway following overexpression in cells (Fig. 2f, g). The interaction between multiple ubiquitinated NEMO molecules, via their UBA1 domains, may cause conformational changes promoting the activation of IKK kinases¹¹. In such a model, the dynamics of NF- κ B activation in response to different stimuli may be determined by the distinct ability of NEMO to recognize a variety of ubiquitin signals, including different linkages (linear, K63 and K11)^{4,6,18} and varying lengths of ubiquitin chains¹⁹. SHARPIN and HOIL-1L have overlapping roles in the function of LUBAC as a key activator of the IKK complex and NF- κ B signalling downstream of several physiological stimuli (Fig. 3). On the other hand, SHARPIN, but not HOIL-1L, deficiency in mice results in an increased cell death that is dependent on caspase-mediated apoptosis, evident in MEFs and inflammatory skin lesions (Fig. 4). Given the identified anti-apoptotic function of SHARPIN, this study exposes a putative role for linear ubiquitination in the regulation of cell death and strongly reinforces its impact on NF- κ B signalling and immune responses.

METHODS SUMMARY

Protein purification, apoptosis and biochemical assays. Recombinant proteins were expressed in Rosetta cells (Novagen). Detailed descriptions of immunoprecipitation, immunoblotting, glutathione-S-transferase (GST) pull-downs and apoptotic assays are available as Supplementary Information. ITC measurements were performed using a VP-ITC or ITC200 (GE Healthcare), as described in Supplementary Methods.

Mice and isolation of primary cells. C57BNL/KaLawRij-*Sharpin*^{*cpdm*}/RijSunJ mice (JR7599, The Jackson Laboratory) were raised in a pathogen-free environment. Resting mature B cells were isolated using negative selection by CD43-coated magnetic beads (Miltenyi Biotec), thioglycollate-induced macrophages were harvested from the peritoneal cavity and MEFs were immortalized using SV40 large T-antigen transfection and dilution passaging.

Apoptosis assays. Quantitative apoptosis assays were performed in real time using a non-invasive impedance-based real-time cell analyser (Roche).

Full Methods and any associated references are available in the online version of the paper at www.nature.com/nature.

Received 6 April 2010; accepted 11 January 2011.

- Grabbe, C. & Dikic, I. Functional roles of ubiquitin-like domain (ULD) and ubiquitin-binding domain (UBD) containing proteins. *Chem. Rev.* **109**, 1481–1494 (2009).
- Seymour, R. E. *et al.* Spontaneous mutations in the mouse Sharpin gene result in multiorgan inflammation, immune system dysregulation and dermatitis. *Genes Immun.* **8**, 416–421 (2007).
- Hayden, M. S. & Ghosh, S. Shared principles in NF- κ B signaling. *Cell* **132**, 344–362 (2008).
- Wertz, I. E. & Dixit, V. M. Ubiquitin-mediated regulation of TNFR1 signaling. *Cytokine Growth Factor Rev.* **19**, 313–324 (2008).
- Ikeda, F. & Dikic, I. Atypical ubiquitin chains: new molecular signals. Review series 'Protein modifications: beyond the usual suspects'. *EMBO Rep.* **9**, 536–542 (2008).
- Iwai, K. & Tokunaga, F. Linear polyubiquitination: a new regulator of NF- κ B activation. *EMBO Rep.* **10**, 706–713 (2009).
- Pasparakis, M. Regulation of tissue homeostasis by NF- κ B signalling: implications for inflammatory diseases. *Nature Rev. Immunol.* **9**, 778–788 (2009).
- Vallabhapurapu, S. & Karin, M. Regulation and function of NF- κ B transcription factors in the immune system. *Annu. Rev. Immunol.* **27**, 693–733 (2009).
- Kirisako, T. *et al.* A ubiquitin ligase complex assembles linear polyubiquitin chains. *EMBO J.* **25**, 4877–4887 (2006).
- Lim, S. *et al.* Sharpin, a novel postsynaptic density protein that directly interacts with the shank family of proteins. *Mol. Cell. Neurosci.* **17**, 385–397 (2001).
- Rahighi, S. *et al.* Specific recognition of linear ubiquitin chains by NEMO is important for NF- κ B activation. *Cell* **136**, 1098–1109 (2009).
- Wagner, S. *et al.* Ubiquitin binding mediates the NF- κ B inhibitory potential of ABIN proteins. *Oncogene* **27**, 3739–3745 (2008).
- Haas, T. L. *et al.* Recruitment of the linear ubiquitin chain assembly complex stabilizes the TNF-R1 signaling complex and is required for TNF-mediated gene induction. *Mol. Cell* **36**, 831–844 (2009).
- Tokunaga, F. *et al.* Involvement of linear polyubiquitylation of NEMO in NF- κ B activation. *Nature Cell Biol.* **11**, 123–132 (2009).
- Gijbels, M. J. J., HogenEsch, H., Blauw, B., Roholl, P. & Zurcher, C. Ultrastructure of epidermis of mice with chronic proliferative dermatitis. *Ultrastruct. Pathol.* **19**, 107–111 (1995).
- Micheau, O. & Tschopp, J. Induction of TNF receptor I-mediated apoptosis via two sequential signaling complexes. *Cell* **114**, 181–190 (2003).
- Wilson, N. S., Dixit, V. & Ashkenazi, A. Death receptor signal transducers: nodes of coordination in immune signaling networks. *Nature Immunol.* **10**, 348–355 (2009).
- Dynek, J. N. *et al.* c-IAP1 and UbcH5 promote K11-linked polyubiquitination of RIP1 in TNF signalling. *EMBO J.* **29**, 4198–4209 (2010).
- Ikeda, F., Crosetto, N. & Dikic, I. What determines the specificity and outcomes of ubiquitin signaling? *Cell* **143**, 677–681 (2010).

Supplementary Information is linked to the online version of the paper at www.nature.com/nature.

Acknowledgements We thank E. Kim, K. Rajalingham and H.-J. Kreienkamp for reagents used in this study, I. Matic for initial MS analysis of HOIP/HOIL-1L samples, S. Wahl for sample preparation, and V. Dötsch and members of the Dikic lab for discussions and comments. This work was supported by grants from the Deutsche Forschungsgemeinschaft (DI 931/3-1), the Cluster of Excellence “Macromolecular Complexes” of the Goethe University Frankfurt (EXC115) to I.D., Landesstiftung Baden-Württemberg to B.M., the Medical Research Council UK to K.R. and B.S., JSPS Postdoctoral Fellowships for Research Abroad to F.I., EMBO long-term fellowship to S.S. and The National Institutes of Health (AR049288 to J.P.S.). V.N. was supported by the Unity Through Knowledge Fund, 3B Grant. C.G. acknowledges support from The International Human Frontier Science Program Organization.

Author Contributions F.I., Y.L.D., S.S.S., B.S., C.G., S.J.L.v.W., B.M., V.N., M.F.-W. and P.G. performed the experiments. F.T., A.A. and T.N. contributed with reagents used throughout the study. F.I., Y.L.D., S.S.S., C.G., M.P., J.T., K.I., J.P.S., L.F., B.M. and K.R. contributed to the project by co-ordination of experimental work and writing the manuscript. I.D. provided ideas, co-ordinated the entire project and wrote the manuscript.

Author Information Reprints and permissions information is available at www.nature.com/reprints. The authors declare no competing financial interests. Readers are welcome to comment on the online version of this article at www.nature.com/nature. Correspondence and requests for materials should be addressed to I.D. (Ivan.Dikic@biochem2.de).

METHODS

cDNA, antibodies and cells. Full-length *SHARPIN*, *NZF* (340–387) or *UBL* (233–314) from HeLa cDNA were subcloned into pGEX-4T1 (GE Healthcare), pEGFP-C1 (Novagen) or pBabe-puro by standard PCR methods. Mutants of *SHARPIN* T358L, F359V, *SHARPIN* Δ NZF (Δ 350–374), *SHARPIN* I272A, *SHARPIN* Δ C (1–232), *SHARPIN* Δ UBL, and insertion of 6 \times His-tag in C terminus of pGEX plasmid were introduced by site-directed mutagenesis. pcDNA3-Myc-human HOIP, pcDNA3-HA-human HOIL-1L Δ RBR-C, pcDNA3-HA-human HOIL-1L Δ UBL, pcDNA3-HA-human HOIL-1L Δ NZF, pGEX-6P1-HOIP NZF1 (350–379), pGEX-6P1-HOIP NZF2 (408–438), and pGEX-6P1-HOIP NZF1+2 (350–438) were described previously¹⁴. pGEX-4T1-Ubiquitin, pGEX-4T1-diUbiquitin, and pGEX-4T1-mouse NEMO-UBAN were described elsewhere¹¹. pMALc2x-human NEMO was generated by a standard PCR method. pGEX-4T2-tetra-Ubiquitin was a gift from C. Guo and E. Friedberg. pGEX-4T1-mouse ABIN1-UBAN was described previously¹². pcDNA3-Myc-human HOIP RING mutant (C699/702S, C871/874S) and pGEX-4T1-mouse ABIN1-UBAN D485A were generated by standard site directed mutagenesis. pMSCV-GFP, pMSCV-Flag-DN-FADD-IRES-GFP, and pMSCV-Flag-Crma-IRES-GFP were gifts from J. Silke.

Anti-His (Novagen, Madison, WI), anti-Ubiquitin (P4D1; Santa Cruz Biotechnology, Santa Cruz, CA), anti-GFP (B-2; Santa Cruz Biotechnology), anti-HA (HA.11; Covance, Berkeley, CA), anti-Myc (9E10; Santa Cruz Biotechnology), anti-Flag (M2, Covance), anti-Cleaved Caspase 3 (Cell Signaling), anti-Caspase 8 (Cell Signaling), anti-Tubulin (Sigma), anti-Vinculin (Sigma), anti-PARP (Cell Signaling), anti-p65 (Santa Cruz Biotechnology), anti-IkB α (Cell Signaling and Santa Cruz Biotechnology), anti-pIkB α (Cell Signaling), anti-IKK α (Imgenex), anti-NEMO (Santa Cruz Biotechnology), anti-pJNK (Cell Signaling), anti-pp38 (Cell signaling), anti-NUP62 (BD Transduction), anti-GAPDH (Abcam), and anti-Flag M2 agarose (Sigma) were purchased and used according to the manufacturers recommendations. Anti-HOIP and anti-HOIL-1L were described previously¹⁴. The anti-SHARPIN antibody was raised against a fragment representing the N-terminal region (1–162 amino acids) of human SHARPIN and affinity-purified using the antigen affinity matrix.

Human Embryonic Kidney (HEK) 293T cells (ATCC) were maintained at 37 °C, in 5% CO₂ condition in DMEM (Gibco) supplemented with 10% Fetal calf serum (Gibco) and 100 U/ml penicillin and streptomycin (Invitrogen). Murine TNF- α , IL-1 β , and CD40L were purchased from PreproTech, while LPS was from Enzo Life Sciences. zVAD-FMK and cycloheximide were purchased from Bachem and R&D, respectively.

SILAC cells. HEK 293T cells were cultured in a custom-made SILAC-DMEM medium (lacking the amino acids lysine and arginine, PAA). The medium was supplemented with dialysed serum (PAA), L-Glutamine, penicillin, streptomycin and amino acids L-lysine and L-arginine. The 'light' culture was supplemented with Lys0 and Arg0 (Sigma); the 'medium-heavy' culture with Lys4 (²H₄) and Arg6 (¹³C₆); and the 'heavy' culture with Lys8 (¹³C₆¹⁵N₂) and Arg10 (¹³C₆¹⁵N₄). All labelled amino acids were purchased from Cambridge Isotope Laboratories.

GST protein purification. Transformed *Escherichia coli* were grown in LB/ampicillin at 37 °C until OD = 0.3–0.5, induced with 1 mM IPTG and grown over night at 16 °C. The bacteria were harvested by centrifugation and resuspended in GST buffer (20 mM Tris, pH 8.0, 100 mM NaCl) supplemented with complete protease inhibitors (Roche Diagnostics), sonicated, and lysed in 1% Triton X-100. The cleared lysate was incubated with Glutathione Sepharose beads (GE Healthcare) for 2 h at 4 °C with continuous rolling. The beads were subsequently washed with buffer 1 (0.1 M Tris, pH 7.8, 0.5 M NaCl), GST-buffer containing 0.35% Triton X-100 and GST buffer alone. The purified GST-fusions were separated by SDS-PAGE and analysed by Coomassie staining.

GST-Pull down and Immunoprecipitation assays. HEK293T cells were transfected with the indicated constructs using FuGene6 (Roche Diagnostics, Mannheim, Germany) or GeneJuice (Novagen) according to the manufacturer's protocol. Cells were treated before lysis (lysis buffer; 50 mM HEPES, 150 mM NaCl, 1 mM EDTA, 1 mM EGTA, 25 mM NaF, 10 μ M ZnCl₂, 10% glycerol, 1% Triton X-100, supplemented with complete protease inhibitors (Roche)). Cleared lysates were subjected to immunoprecipitation by incubation with the indicated antibodies, followed by Protein A/G Agarose (Santa Cruz Biotechnology) or Protein A-agarose (Roche). Similarly, total cell lysates were incubated with GST-proteins conjugated to Glutathione Sepharose beads at 4 °C. After washing three times with lysis buffer, the immunoprecipitates were separated by SDS-PAGE and analysed by western blot.

Purification of proteins for ITC measurements. All constructs for ITC studies have been cloned into pGEX-4T1 or pGEX-6P1 and were expressed using *E. coli* BL21 as host strain. 5 to 10 l expression culture was grown to an OD of 0.8 in LB/ampicillin media supplemented with 100 μ M ZnCl₂ at 37 °C before induction with 0.1 mM IPTG for 12 h at 25 °C. Cells were resuspended in buffer PX (100 mM

HEPES pH 7.4, 500 mM NaCl, 1 mM DTT) and lysed by sonication. The lysate was cleared by centrifugation and loaded onto GSH Sepharose column (GE Healthcare). Bound GST fusion protein was eluted using buffer PX containing 20 mM glutathione, cleaved with thrombin or 3C protease, and further purified by anion exchange chromatography using a Q Sepharose column (GE Healthcare). Fractions containing the protein of interest were polished by size exclusion chromatography on a Superdex 75 or Superdex 200 column (GE Healthcare). Protein concentrations were determined by UV spectrometry at 280 nm using calculated extinction coefficients. K48 and K63-linked ubiquitin chains were prepared essentially as described²⁰.

Isothermal titration calorimetry. ITC measurements were performed using a VP-ITC or ITC200 (GE Healthcare). Typically 50–100 μ M of SHARPIN, HOIL-1L, the isolated NZF domains and the NZF1 of HOIP were loaded into the cell and 500–1,000 μ M of ubiquitin or ubiquitin chains into the syringe. Samples were dialyzed into buffer containing 50 mM HEPES pH 7.4, 150 mM NaCl, and 1 mM TCEP. SHARPIN titrations were performed at 10 °C, HOIL-1L, and HOIP titrations at 20 °C. ITC data were analysed with Origin7 (Micro Cal) supplied by the manufacturer.

Luciferase assay. HEK293T cells were plated on 48-well plates at a density of 20,000 cells per well 24 h before transfection. pNF- κ B-Luc plasmid (Stratagene) and β -GAL plasmid were transfected together with the indicated plasmids using FuGene6. After 36 h of transfection, lysates were prepared and subjected to luciferase assays following the manufacturer's protocol (Roche). Internal control was measured by β -Gal activity using its substrate (Roche). All experiments were done using quadruple samples.

In vitro ubiquitination assay. Ubiquitin (10 μ g), His-tag E1 (150 ng), UbcH7 (300 ng) (Boston Biochem), and the indicated E3 ligase complexes (1 μ g) were incubated with or without 2 mM ATP (Sigma) for the indicated time at 37 °C in ubiquitin assay buffer (20 mM Tris-HCl pH 7.5, 5 mM MgCl₂, 2 mM DTT). Methylated ubiquitin was used as a negative control. To stop the reaction, SDS-loading buffer was added and the samples were boiled at 95 °C for 1 min. The samples were subsequently analysed by SDS-PAGE followed by western blotting using a PVDF membrane.

In vitro kinase assay. MEFs of wild-type, *cpdm* or *cpdm* HOIL-1L shRNA were treated by TNF- α (20 ng ml⁻¹) for indicated times. IKK complex was immunoprecipitated by anti-NEMO antibody from the total cell lysates prepared from treated MEFs. Kinase assays were performed using γ -(³²P)ATP (5 μ Ci), GST-IkB α 1–54 (1 μ g), and the IKK complex, incubated in the kinase buffer (25 mM Tris-HCl pH 7.5, 10 mM MgCl₂, 0.1 mM sodium orthovanadate, 5 mM β -glycerophosphate, 2 mM DTT, 20 μ M ATP) at 30 °C for 30 min.

Protein separation, digestion, and mass spectrometry. Complete protein eluates of the three pull-down experiments were combined and separated by 1D SDS PAGE (NuPAGE 12% precast Bis/Tris gels, Invitrogen). The proteins were visualized by staining using the Novex Colloidal Blue Staining Kit (Invitrogen) according to the manufacturer's instructions and the corresponding gel lane was cut into eleven pieces. In gel trypsin digestion of the proteins was performed as described previously²¹. Chloroacetamide was used for alkylation to prevent formation of lysine modifications isobaric to Gly-Gly²². Prior to LC-MS peptides were desalted using C₁₈ StageTips²³. LC-MS analysis was performed using a Proxeon Easy-LC system (ProxeonBiosystems) coupled to an LTQ-Orbitrap XL mass spectrometer (Thermo Fisher Scientific) equipped with a nano-electrospray ion source (ProxeonBiosystems), as described previously²⁴. Peptides were eluted using a segmented gradient of 5–80% of solvent B (80% ACN in 0.5% acetic acid) with a constant flow of 200 nl min⁻¹ over 118 min. Full scan MS spectra were acquired in a mass range from *m/z* 380 to 920 with a resolution of 60,000 in the Orbitrap mass analyser using the lock mass option for internal calibration²⁵. The ten most intense ions were sequentially isolated for CID fragmentation in the linear ion trap. Inclusion list containing 27 ions of special interest (ubiquitinated NEMO and ubiquitin peptides) was used and up to 500 precursor ion masses selected for MS/MS were dynamically excluded for 90 s. Mass spectra were processed and quantified using the MaxQuant software suite²⁶ (version 1.0.14.3) and the data were searched using Mascot search engine (Matrix Science) against a decoy human database (ipi.HUMAN.v3.64) containing 168,584 protein entries. Carbamidomethylation (Cys) was defined as fixed-, and protein N-terminal acetylation, oxidation (Met), Gly-Gly (Lys), and Gly-Gly (N-terminal) were defined as variable modifications. Initial mass tolerance for the precursor ions was set to 7 p.p.m., and for the fragment ions to 0.5 Da. The Gly-Gly (Lys) modification sites were considered localized if the localization probability (calculated by MaxQuant software) was higher than 0.75.

Absolute quantification of ubiquitin in whole cell lysate. For absolute quantification (AQUA¹¹) proteins were precipitated from crude cell lysates of 'light' (SHARPIN/HOIP) and 'medium-heavy' (SHARPIN TF_LV/HOIP RING mutant) SILAC-labelled HEK293T cells by chloroform/methanol precipitation. Protein concentration was measured by Bradford before and after precipitation to

determine protein recovery. Equal amounts of protein extracts were mixed and in-solution digested by trypsin as described previously²⁴ and chloroacetamide was used for alkylation as described above. Four synthetic AQUA peptides (Thermo Fisher Scientific), labelled with either Lys8 or Arg10 on the C terminus, were added to 100 µg of digested protein in the following amounts: GGM(ox)QIFVK (1 pmol), TLDYNIQK (10 pmol), ESTLHLVLR (10 pmol), and TITLVEPSDTIENVK (100 pmol). The peptide mixtures were further fractionated using isoelectric focusing on an OffGel 3100 Fractionator (Agilent). Focusing was done on 13-cm (12-well) ImmobilineDryStrips pH 3-10 (GE Healthcare) at a maximum current of 50 µA for 23 kVh. Peptide fractions were collected and desalted using C₁₈ StageTips²⁷. LC-MS analysis was performed as described above with the exception that full scan MS spectra were acquired in a mass range from *m/z* 420 to 920. Inclusion list containing 17 ions of special interest (ubiquitin peptides, 'light', 'medium-heavy' and 'heavy'-labelled) was applied and no additional masses were allowed for fragmentation. The five most intense ions from the inclusion list were sequentially isolated for CID fragmentation in the linear ion trap. Mass spectra were processed and searched as described above. The ESTLHLVLR peptide was discarded from final quantification because of an interference caused by the overlapping isotopic distribution of another peptide. The final AQUA results are reported per 100 µg of the crude protein extract considering the protein loss during precipitation and sub-stoichiometric oxidation of the GGMQIFVK peptide. The latter was estimated from the intensities of the modified (oxidized) and unmodified forms of the GGMQIFVK peptide.

Mouse, MEF and primary cells. *cpdm* mice from the C57BL/KaLawRij colony were raised in the specific pathogen-free breeding facility at the Goethe University animal facility. Breeding was made by crossing heterozygous female and male mice. Immortalized mouse embryonic fibroblasts (MEFs) were established using SV40 large T-antigen transfection and serial passaging. Mature resting primary B-cells were isolated from the spleen of 12-week-old mice of indicated genotypes by negative selection using CD43-coated magnetic beads (Miltenyi Biotec). Peritoneal macrophages were isolated by washing the peritoneal cavity with growth media 5 days after intra-peritoneal injection of thioglycollate. MEFs and primary cells were treated with CD40L (250 ng ml⁻¹), LPS (100 ng ml⁻¹), TNF-α (20 ng ml⁻¹) or IL-1β (1 ng ml⁻¹ or 10 ng ml⁻¹) for the indicated times and subjected to SDS-PAGE and western blot analysis. The supernatant of macrophages was assessed for secreted TNF-α and MCP-1 by classical sandwich ELISA using ELISA kits from R&D systems.

Immunohistochemistry. Skin tissue samples from wild type and *cpdm* (male, 10 weeks after birth) mice were fixed in Fekete's acid alcohol formalin solution and subjected to histological analysis by H&E staining, or immunohistochemical analysis using antibodies recognizing cleaved caspase 3, 8 and 9.

Retroviral production. pMSCV-control-GFP, pMSCV-Flag-DN-FADD IRES-GFP, and pMSCV-Flag-CrmA IRES-GFP vectors were transfected into ecotropic phoenix cells (ATCC) using Gene Juice (Novagen). After 36 h of transfection, released retroviruses were filtered and used for infection of target cells using polybrene (4 µg ml⁻¹). Expression of infected protein was monitored by GFP expression.

Subcellular fractionation. To obtain nuclear and cytoplasmic fractions, cells were washed and sampled in 500 µl of cold PBS. Pelleted cells (500g) were resuspended in hypotonic buffer (10 mM Tris-HCl, pH 7.4, 10 mM sodium iodide, 5 mM MgCl₂, 1 mM PMSF) and homogenized with 20 strokes in a tissue grinder. The

supernatant (600g) was designated the cytoplasmic fraction. The pellet, representing the nuclear fraction, was washed with hypotonic buffer containing 0.1% NP-40 (Calbiochem).

Apoptosis assays. Wild type, *Sharpin*^{+/+}/*Sharpin*^{cpdm} or *cpdm* MEFs were plated on 6-well or 24-well plates. After 24 h of sub-culturing, cells were treated with CHX (1 µM) or TNF-α (10 ng ml⁻¹) for the indicated times. Depending on the experimental set-up, the caspase inhibitor zVAD-FMK (50 nM) and retroviral infection were combined. After the treatment, cells were harvested for SDS-PAGE followed by western blot analysis. In parallel, a highly sensitive, non-invasive and quantitative device, an impedance based real-time cell analyser (Roche), was used to study the dynamics of cell death. This device continuously monitors the impedance to electric current flow by cells attaching on gold electrode-plated cell culture dishes. The area covered by cells is quantified and plotted as cell index as a function of time. 10,000 to 20,000 cells were plated per well of a 96-well E-plate. 24 to 36 h later, cells were treated as indicated with TNF-α (10 ng ml⁻¹) alone or in combination with cycloheximide (1 µg ml⁻¹), followed by continuous recordings of cell index in real-time and plotted by normalizing cell indices to one just before treatment of cells with the respective reagents.

Stable shRNA cell lines. Wild type or *cpdm* MEFs were transduced with lentiviral particles (5 MOI) containing non-targeting (control) or HOIL-1L shRNA (sequence: 5'-CCGGCCTACCAGATACCTGCTTCATCTCGAGATGAAGCAGGTATCTGGTAGGTTTTTG-3') (Sigma). 48 h post-transduction, cells were selected with medium containing 4 µg ml⁻¹ puromycin. After two weeks, selected cells were maintained with medium containing 1 µg ml⁻¹ puromycin.

Confocal fluorescence microscopy. Cells were grown on glass coverslips and treated as indicated in the figure legends. The cells were then fixed with 2% paraformaldehyde solution (Sigma), permeabilized with 0.2% Triton X-100 in PBS and immunostained with appropriate antibodies. Fluorophore-labelled secondary antibodies were from Jackson ImmunoResearch. DAPI was used to stain the nuclei. The cells were mounted in Mowiol (Calbiochem) and examined by the laser scanning confocal microscope LSM 510 META (Carl Zeiss). Images were prepared and analysed with the LSM Image Browser software (Carl Zeiss).

20. Pickart, C. M. & Raasi, S. Controlled synthesis of polyubiquitin chains. *Methods Enzymol.* **399**, 21–36 (2005).
21. Shevchenko, A., Tomas, H., Havlis, J., Olsen, J. V. & Mann, M. In-gel digestion for mass spectrometric characterization of proteins and proteomes. *Nature Protocols* **1**, 2856–2860 (2007).
22. Nielsen, M. L. *et al.* Iodoacetamide-induced artifact mimics ubiquitination in mass spectrometry. *Nature Methods* **5**, 459–460 (2008).
23. Ishihama, Y., Rappsilber, J. & Mann, M. Modular stop and go extraction tips with stacked disks for parallel and multidimensional peptide fractionation in proteomics. *J. Proteome Res.* **5**, 988–994 (2006).
24. Borchert, N. *et al.* Proteogenomics of *Pristionchus pacificus* reveals distinct proteome structure of nematode models. *Genome Res.* **20**, 837–846 (2010).
25. Olsen, J. V. *et al.* Parts per million mass accuracy on an Orbitrap mass spectrometer via lock mass injection into a C-trap. *Mol. Cell. Proteomics* **4**, 2010–2021 (2005).
26. Cox, J. & Mann, M. MaxQuant enables high peptide identification rates, individualized p.p.b.-range mass accuracies and proteome-wide protein quantification. *Nature Biotechnol.* **26**, 1367–1372 (2008).
27. Rappsilber, J., Mann, M. & Ishihama, Y. Protocol for micro-purification, enrichment, pre-fractionation and storage of peptides for proteomics using StageTips. *Nature Protocols* **2**, 1896–1906 (2007).

Aberrant chromosome morphology in human cells defective for Holliday junction resolution

Thomas Wechsler^{1†}, Scott Newman² & Stephen C. West¹

In somatic cells, Holliday junctions can be formed between sister chromatids during the recombinational repair of DNA breaks or after replication fork demise. A variety of processes act upon Holliday junctions to remove them from DNA, in events that are critical for proper chromosome segregation. In human cells, the BLM protein, inactivated in individuals with Bloom's syndrome, acts in combination with topoisomerase III α , RMI1 and RMI2 (BTR complex) to promote the dissolution of double Holliday junctions^{1,2}. Cells defective for BLM exhibit elevated levels of sister chromatid exchanges (SCEs) and patients with Bloom's syndrome develop a broad spectrum of early-onset cancers caused by chromosome instability³. MUS81–EME1 (refs 4–7), SLX1–SLX4 (refs 8–11) and GEN1 (refs 12, 13) also process Holliday junctions but, in contrast to the BTR complex, do so by endonucleolytic cleavage. Here we deplete these nucleases from Bloom's syndrome cells to analyse human cells compromised for the known Holliday junction dissolution/resolution pathways. We show that depletion of MUS81 and GEN1, or SLX4 and GEN1, from Bloom's syndrome cells results in severe chromosome abnormalities, such that sister chromatids remain interlinked in a side-by-side arrangement and the chromosomes are elongated and segmented. Our results indicate that normally replicating human cells require Holliday junction processing activities to prevent sister chromatid entanglements and thereby ensure accurate chromosome condensation. This phenotype was not apparent when both MUS81 and SLX4 were depleted from Bloom's syndrome cells, suggesting that GEN1 can compensate for their absence. Additionally, we show that depletion of MUS81 or SLX4 reduces the high frequency of SCEs in Bloom's syndrome cells, indicating that MUS81 and SLX4 promote SCE formation, in events that may ultimately drive the chromosome instabilities that underpin early-onset cancers associated with Bloom's syndrome.

Our current understanding of the way in which Holliday junctions are processed in somatic cells suggests the three potential pathways illustrated in Supplementary Fig. 1. These include the dissolution of double Holliday junctions by BLM–TOPIII α –RMI1–RMI2 (BTR), which suppresses crossover formation between sister chromatids¹, and the nucleolytic resolution of Holliday junctions by MUS81–EME1 (ref. 7) or GEN1 (ref. 12) that can lead to crossover or non-crossover products depending on the orientation of Holliday junction cleavage. Recently, it was shown that SLX4, a component of the SLX1–SLX4 nuclease complex that can also cleave Holliday junctions, associates with MUS81–EME1 and may provide a 'scaffold' function for several nuclease activities^{8–11}.

The relative contribution of each Holliday junction processing pathway is currently unknown. However, given that intact Holliday junctions are a relatively poor substrate for MUS81–EME1 (refs 4, 5), it is likely that the BTR complex provides the primary mechanism for the resolution of double Holliday junctions in human somatic cells at S phase. A further possibility is that resolution events mediated by MUS81–EME1, SLX1–SLX4 and/or GEN1 could substitute for the loss

of BTR activity in Bloom's syndrome cells, either by cleaving the double Holliday junctions or other recombination intermediate structures (such as nicked Holliday junctions^{14,15}), and thereby contribute to their viability.

Because nucleolytic cleavage mechanisms may be responsible for the elevated frequency of SCEs observed in Bloom's syndrome cells, we analysed SCE formation in metaphase spreads from the SV40-transformed Bloom's syndrome cell line GM08505 after short interfering RNA (siRNA)-mediated depletion of MUS81, SLX4 or GEN1. In all cases, efficient gene silencing was achieved, as measured by western blotting or quantitative reverse transcription PCR (RT-PCR) (Supplementary Fig. 2). Because depletion of SLX4 also decreases the levels of SLX1 (ref. 10), as the stabilities of SLX1 and SLX4 are interdependent, the SLX4 depletion should be viewed as an SLX1–SLX4 depletion. Depletion of SLX4 does not affect the levels of MUS81 or EME1 (ref. 10), or GEN1 (data not shown). We found that siRNA treatment against MUS81 or SLX4, but not GEN1, significantly reduced the frequency of SCEs (Fig. 1a, b), as well as the formation of harlequin chromosomes (that is, chromosomes exhibiting more than five SCEs) (Supplementary Fig. 3).

Although the SCE frequency in cells depleted for both MUS81 and GEN1 did not appear significantly different from MUS81-depleted cells, at least in metaphases that could be easily scored, many metaphase chromosomes looked abnormal after treatment with these siRNAs. Because these metaphases could not be scored for SCEs, it is possible that our scoring was biased towards those with only mild GEN1 and/or MUS81 depletion. We also observed decreased cell viability after dual siRNA treatment against GEN1 and MUS81, MUS81 and SLX4, or GEN1 and SLX4 (Fig. 1c), indicating that loss of multiple Holliday junction processing pathways can lead to cell death even in the absence of exogenous DNA damage. Depletion of GEN1 with SLX4, or MUS81 with SLX4, had a greater impact upon cell viability than GEN1 and MUS81 siRNA treatment, suggesting that SLX4 might have a broader role than either of the other nucleases.

When the chromosome aberrations seen in the metaphase spreads prepared from GEN1- and MUS81-depleted cells were analysed, we observed a high percentage of cells in which the chromosomes were elongated and segmented (Fig. 2a, compare left and right panels with enlargements below). Indeed, most chromosomes exhibited a 'beads-on-a-string' morphology. Similar results were obtained when the untransformed Bloom's syndrome fibroblast line GM01492 was treated with MUS81 and GEN1 siRNAs (Fig. 2b and Supplementary Fig. 4). Careful analysis of these spreads revealed the occasional appearance of single chromosomes that had an extreme defect in chromosome condensation (Fig. 2b, arrows).

These observations, with measurements showing that the total number of chromosomes in these metaphases was comparable to control spreads (data not shown), indicated that the beads-on-a-string morphology might result from an aberrant chromosome condensation defect rather than break-induced chromosome rearrangements. To confirm this, we performed whole chromosome painting on chromosomes 4, 8

¹London Research Institute, Cancer Research UK, Clare Hall Laboratories, South Mimms, Hertfordshire EN6 3LD, UK. ²Department of Pathology, University of Cambridge, Tennis Court Road, Cambridge CB2 1QP, UK. [†]Present address: Stanford University School of Medicine, Clark Center, 318 Campus Drive, Stanford, California 94305, USA.

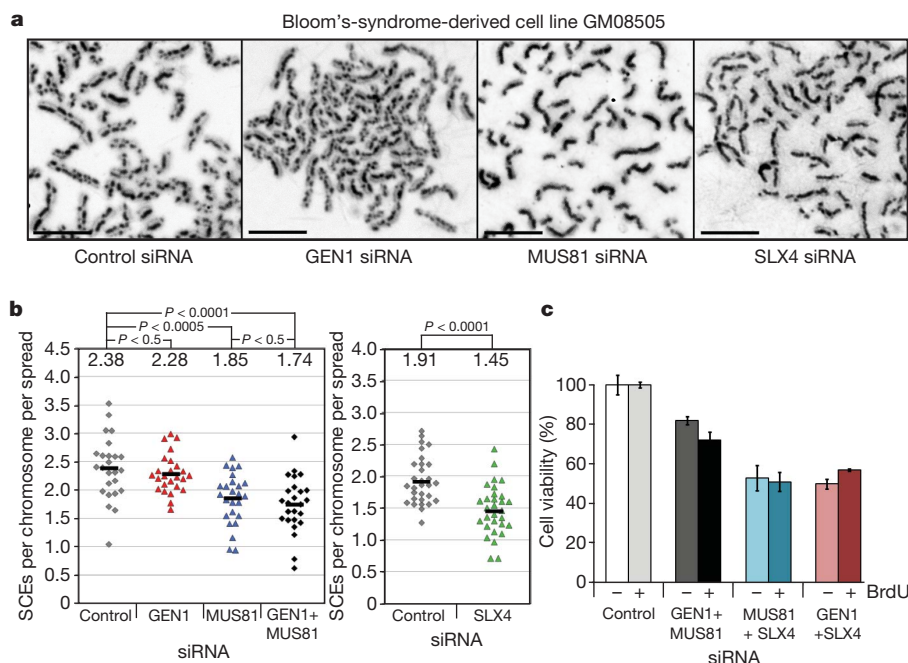


Figure 1 | Contribution of GEN1, MUS81 and SLX4 to SCE frequency in Bloom's syndrome cells. **a**, Representative images of metaphase spreads prepared from BLM-deficient GM08505 cells treated with the indicated siRNAs. Scale bars, 10 μ m. **b**, Quantification of SCE frequency after siRNA treatment. Each data point represents a single cell/metaphase that was scored

and X in GM01492 Bloom's syndrome cells after GEN1 and MUS81 siRNA targeting. We found that segmentation occurred within intact chromosomes and was not due to translocation events (Fig. 2c). Indeed, although some chromosomal regions looked compact, others were more

blind for SCEs per chromosome per spread (for each condition 25 cells, more than 1,700 chromosomes, were analysed). *P* values were determined using a two-tailed *t*-test. **c**, Relative cell viability measured 96 h after siRNA treatment that targeted two genes as indicated. Analyses were performed with and without BrdU treatment. Error bars, s.d.

elongated and appeared as though held together by a thread of (non-staining) DNA. Our interpretation of the extended and segmented chromosome structure is that regions showing normal condensation are linked to uncondensed regions of DNA. Generally, the uncondensed

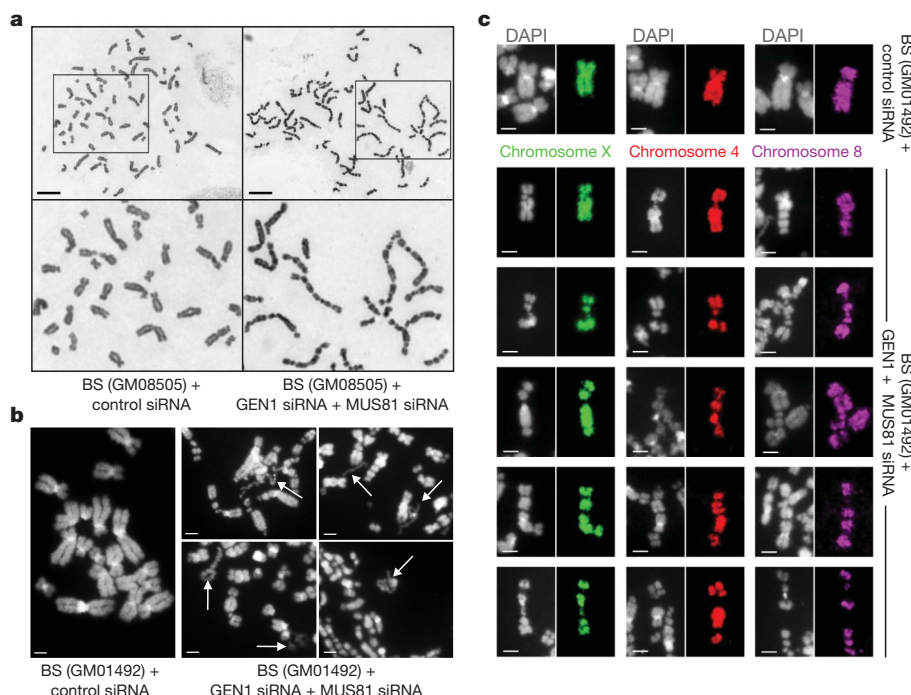


Figure 2 | Chromosome abnormalities in Bloom's syndrome (BS) cells after siRNA-mediated depletion of GEN1 and MUS81. **a**, Giemsa-stained metaphase spreads of GM08505 BLM-defective cells treated with control siRNA or siRNAs against both GEN1 and MUS81. The upper panels show whole chromosome spreads whereas the lower panels show the indicated sections at higher magnification. Scale bars, 10 μ m. **b**, 4',6-Diamidino-2-phenylindole (DAPI)-stained metaphase spreads of GM01492 BLM-defective

cells treated with control siRNA or siRNAs against both GEN1 and MUS81 as indicated. White arrows indicate chromosomes with extreme condensation defects. Scale bars, 2 μ m. **c**, Metaphase spreads from the experiment described in **b** were stained with whole chromosome paints specific for chromosome 4, 8 or X, as indicated. The selected chromosomes are representative of those from a total of nine metaphase spreads. Scale bars, 2 μ m.

regions were observed at equivalent positions on each of the two sister chromatids, which themselves remained tightly associated along their entire length. One possibility is that the loss of Holliday junction processing activity results, either directly or indirectly, in sister chromatid entanglements that prohibit normal chromosome condensation.

To quantify the observed segmentation phenotype, we counted chromosomes with more than three segments ($S > 3$) and scored metaphases with two or more segmented chromosomes as ' $S > 3$ positive' (Fig. 3a). Using this scoring method, a baseline of 2% was observed with the control GM08505 Bloom's syndrome cells, whereas cells depleted for MUS81 or GEN1 contained 6% and 8% of $S > 3$ chromosomes, respectively (Fig. 3b). In contrast, 56% of the Bloom's syndrome metaphases depleted for both GEN1 and MUS81 exhibited two or more $S > 3$ chromosomes (Fig. 3b, c). Moreover, in 13% of these cells, the $S > 3$ phenotype was so severe that virtually all chromosomes in the spread were affected (Fig. 2a). To enable the most simple quantification, these severely affected cells were designated '>9'. The abnormal phenotype was not influenced by the presence or absence of BrdU (an agent used in the earlier SCE analyses) (Supplementary Fig. 5). When the same scoring method was applied to the Bloom's syndrome cell line GM01492 after GEN1- and MUS81-depletion, we found that 46% of the cells (compared with 7% in control cells) showed an $S > 3$ phenotype, ruling out any cell-line-specific effects (Supplementary Fig. 4).

Importantly, the chromosome abnormalities observed in Bloom's syndrome cells depleted for both GEN1 and MUS81 were suppressed by exogenous expression of BLM protein, as shown by comparison of the BLM-defective cell line PSNG13 with its isogenic BLM-complemented cell line PSNF5 after GEN1 and MUS81 siRNA treatment (Fig. 3d–f and Supplementary Fig. 6). We also failed to observe

an increase in $S > 3$ chromosomes in the BLM-proficient cell line U2OS, despite a high depletion efficiency of GEN1 and MUS81 (Supplementary Fig. 7). These results show that BLM is critical for the maintenance of genome stability, and that loss of Holliday junction processing activity caused by disruption of BLM, MUS81 and GEN1 leads to aberrant chromosome morphology.

In yeast, it has been shown that *yen1 mus81* double mutants (Yen1 is the yeast orthologue of GEN1) are considerably more sensitive to DNA damage than the *mus81* single mutant^{16,17} and that Mus81 and Yen1 can promote crossover formation during mitotic recombination¹⁸. These studies indicate that recombination intermediates normally resolved by Mus81 can also serve as substrates for Yen1. In mammalian cells, however, we currently have little information relating to the interplay between GEN1 and MUS81, or with SLX4 with which MUS81 interacts^{8–11}. Therefore, to gain our first insights into the genetic interactions between these proteins, we depleted combinations of either MUS81 + SLX4, GEN1 + SLX4 or, as before, GEN1 + MUS81, and measured the extent of chromosome aberrations. We found that depletion of GEN1 and SLX4 in Bloom's syndrome cells resulted in an extremely severe phenotype, as measured by the formation of segmented chromosomes (Fig. 4). The next most severe combination was caused by depletion of GEN1 and MUS81. In contrast, the chromosome abnormalities observed after siRNA treatment against both MUS81 and SLX4 were considerably less severe. These results favour the view that SLX4 plays a broad role, not only in a nuclease complex with SLX1, but also as a scaffold for the cooperative actions of other nucleases.

The severe phenotype observed after GEN1 and SLX4 depletion allowed us to perform two further experiments. First, time-course analyses revealed that $S > 3$ chromosomes were detectable 36 h after

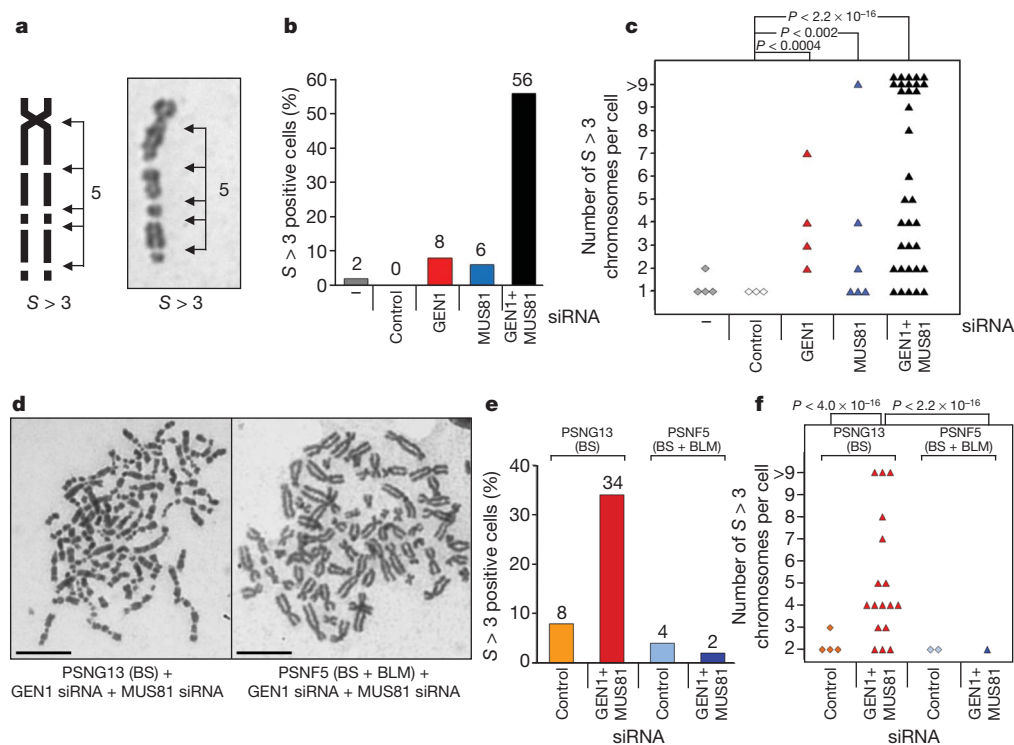


Figure 3 | Quantification of the chromosome segmentation phenotype observed in Bloom's syndrome cells after GEN1 and MUS81 depletion. **a**, Schematic illustration (left) and Giemsa staining (right) of an abnormal metaphase chromosome showing more than three indentations ($S > 3$). The definition $S > 3$ was used in all subsequent experiments. **b**, After the treatment of GM08505 Bloom's syndrome cells with the indicated siRNAs, metaphases ($n = 50$) were scored. The percentage of cells with at least two $S > 3$ chromosomes is shown. **c**, As **b** but to illustrate phenotypic severity, the number of $S > 3$ chromosomes in each metaphase ($n = 50$) was plotted in a

scatter graph. Only metaphases with at least one $S > 3$ chromosome are shown, and those with more than nine segmented chromosomes were termed '>9'. **d**, Complementation of Bloom's syndrome cells with BLM restores chromosome stability. BLM-deficient PSNG13 and the BLM-complemented PSNF5 cell lines were treated with siRNA against GEN1 and MUS81, and analysed for abnormal metaphases using Giemsa staining. Scale bars, 10 μ m. **e**, **f**, Metaphases ($n = 50$) were analysed after control or GEN1 + MUS81 siRNA treatment of PSNG13 and PSNF5 cells. Quantifications were performed as in Fig. 3b.

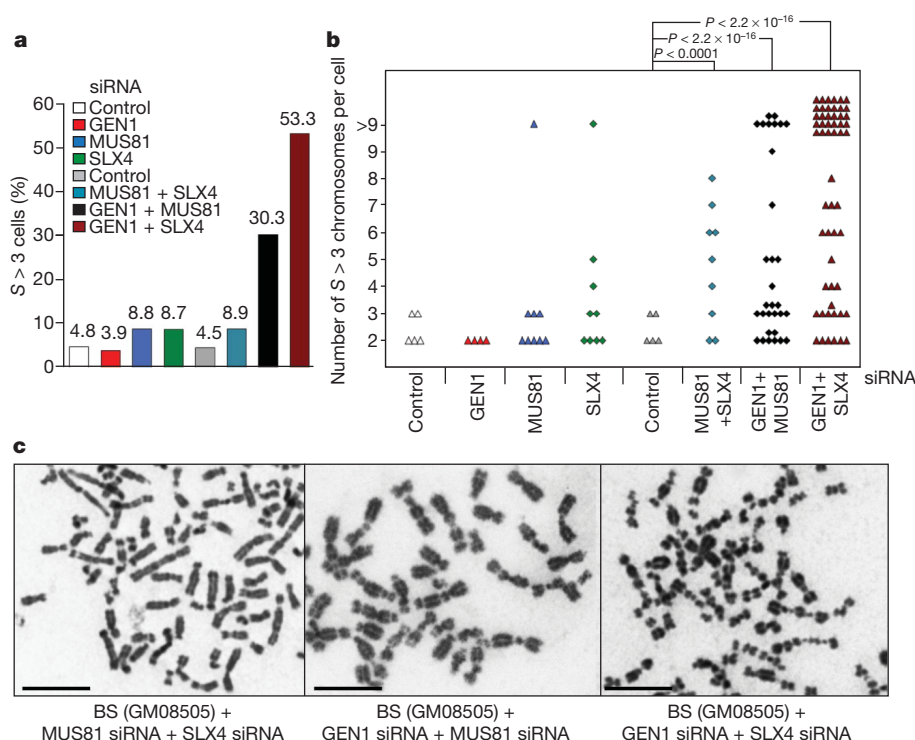


Figure 4 | Synthetic interactions between GEN1, MUS81 and SLX4.

GM08505 Bloom's syndrome cells were depleted for GEN1, MUS81 or SLX4, or for the indicated pairs of proteins. Cells were collected 60 h after the second

transfection and metaphase cells ($n > 100$) were scored (**a**, **b**) and visualized (**c**) as in Fig. 3. Scale bars, 10 μ m.

siRNA treatment, and that the severity of the abnormal chromosome phenotype continued into the second mitotic division (Supplementary Fig. 8). After this point, high levels of cell inviability were observed (Fig. 1c). Second, we found that the chromosome indentations were effectively free of SMC2 protein, confirming that the unusual phenotype was indeed due to a defect in proper chromosome condensation (Supplementary Fig. 9).

These results begin to define the relative contributions of GEN1, MUS81 and SLX4 to Holliday junction processing in human mitotic cells already defective for BLM. Inactivation of MUS81, together with GEN1, effectively produces BLM-defective cells compromised for the known Holliday junction dissolution/resolution pathways. The resulting phenotype was the formation of highly segmented chromosomes with severe condensation defects. Similar results were observed by inactivation of GEN1 and SLX4, supporting the notion that SLX4 and MUS81 might work in the same pathway. Although this is the first time that such an aberrant chromosome morphology has been associated with defects in Holliday-junction processing, similar defects have been observed in human and mouse cells in response to ionizing radiation which causes a delay in DNA replication timing that, in turn, affects mitotic chromosome condensation¹⁹. Similarly, defects in DNA replication due to the mutation of key replication factors such as ORC2 also lead to segmented chromosome condensation morphology. Together, these studies indicate a potential link between DNA replication and the establishment of proper chromosome condensation, and it has been suggested that the timely completion of replication impacts upon the lateral condensation of a metaphase chromosome by helping to remove entanglements²⁰. In our study, we suggest that sister chromatid entanglements, caused instead by defects in Holliday junction processing pathways, might lead to a related aberrant condensation phenotype. The beads-on-a-string chromosome morphology seen here, and the absence of significant break-induced chromosome translocations, indicates that the regions of under-condensed chromatin retain fine DNA threads that link the normally condensed regions.

Moreover, the tight side-by-side alignment of sister chromatids is suggestive of the persistence of unresolved bridges that accumulate after disruption of the three cellular Holliday junction processing pathways.

It has been shown that BLM protein localizes to ultrafine bridges at anaphase, and that these sites represent unresolved entanglements that occur at fragile sites after replication stress^{21–23}. However, many ultrafine bridges derive from centromeric regions^{21,24}, whereas our work shows that the indentations corresponding to regions of under-condensed chromatin are distributed randomly along the length of each chromosome.

The aberrant chromosome morphology seen in the current experiments was suppressed by expression of the BLM protein, leading us to suggest that Holliday junction dissolution, a system that avoids SCEs, provides the primary mechanism for the processing of Holliday junctions in somatic cells. In the absence of this pathway, such as in cells derived from patients with Bloom's syndrome, elevated levels of SCEs are observed and we have shown that these can arise through the actions of MUS81 or SLX4. The precise role of SLX4 is currently unknown, as it may function either as a junction-specific nuclease with SLX1, or it may provide a scaffold for the cooperation of multiple nucleases within a multi-functional DNA processing complex. Loss of both BLM and MUS81 (or SLX4), however, did not result in a severe condensation phenotype, because mitotic cells possess a third pathway of Holliday junction resolution mediated by GEN1, for which we present the first functional evidence *in vivo*. It is likely that MUS81–EME1, SLX1–SLX4 and GEN1 can resolve Holliday junctions that persist in BLM-defective cells, although the bi-directional nature of their cleavage mechanism will, in contrast to the BTR complex, produce SCEs. We therefore suggest that the nucleolytic processing pathways provide additional mechanisms of resolution that can act upon intermediates that escape the attention of the BTR complex, thereby allowing chromosome segregation. Use of these alternatives may, however, come at a price because Bloom's syndrome cells exhibit genomic instability and patients suffer a broad spectrum of early-onset cancers.

METHODS SUMMARY

The human osteosarcoma cell line U2OS, SV40-transformed Bloom's syndrome fibroblasts GM08505 (ref. 25) and untransformed Bloom's syndrome fibroblasts GM01492 (ref. 26) were provided by CRUK Cell Services (Clare Hall). The cell line PSNF5 constitutively expresses BLM protein, whereas the isogenic control PSNG13 contains pcDNA3 vector DNA²⁷. Cells were transfected twice with siRNA within 24 h. For a single gene, 3×10^5 cells were transfected with 400–500 pmol of siRNA (Dharmacon) using 10 μ l of Lipofectamine RNAiMAX (Invitrogen). For double-gene targeting, up to 800 pmol of siRNA was mixed and transfected with 20 μ l Lipofectamine. Control non-targeting siRNAs were used at equivalent concentrations. The efficiency of each siRNA treatment was monitored by western blotting 60 h after the first, or 36 h after the second, transfection, or by quantitative RT-PCR 48 h after the first treatment. SCEs and metaphase chromosomes were monitored as described^{28,29}. The SCE technique relies upon the differential staining of the sister chromatids after replication in the presence of BrdU, followed by staining with Hoechst dye and Giemsa. Cell viability assays were performed 12 h after the second transfection with various siRNA combinations (MUS81 + SLX4; GEN1 + MUS81; GEN1 + SLX4). The cells were then seeded in equal numbers (2,000 per well) in a 96-well plate (in triplicates), grown for a further 84 h and tested using the Cell-Titre Glo assay system (Promega). Chromosome painting was performed as described³⁰.

Full Methods and any associated references are available in the online version of the paper at www.nature.com/nature.

Received 26 July 2010; accepted 5 January 2011.

Published online 13 March 2011.

1. Wu, L. & Hickson, I. D. The Bloom's syndrome helicase suppresses crossing over during homologous recombination. *Nature* **426**, 870–874 (2003).
2. Mankouri, H. W. & Hickson, I. D. The RecQ helicase-topoisomerase III-Rmi1 complex: a DNA structure-specific 'dissolvosome'? *Trends Biochem. Sci.* **32**, 538–546 (2007).
3. Bachrati, C. Z. & Hickson, I. D. RecQ helicases, suppressors of tumorigenesis and premature aging. *Biochem. J.* **374**, 577–606 (2003).
4. Chen, X. B. *et al.* Human MUS81-associated endonuclease cleaves Holliday junctions *in vitro*. *Mol. Cell* **8**, 1117–1127 (2001).
5. Ciccia, A., Constantinou, A. & West, S. C. Identification and characterization of the human MUS81/EME1 endonuclease. *J. Biol. Chem.* **278**, 25172–25178 (2003).
6. Ciccia, A., McDonald, N. & West, S. C. Structural and functional relationships of the XPF/MUS81 family of proteins. *Annu. Rev. Biochem.* **77**, 259–287 (2008).
7. Taylor, E. R. & McGowan, C. H. Cleavage mechanism of human MUS81-EME1 acting on Holliday-junction structures. *Proc. Natl Acad. Sci. USA* **105**, 3757–3762 (2008).
8. Andersen, S. L. *et al.* *Drosophila* MUS312 and the vertebrate ortholog BTBD12 interact with DNA structure-specific endonucleases in DNA repair and recombination. *Mol. Cell* **35**, 128–135 (2009).
9. Fekairi, S. *et al.* Human SLX4 is a Holliday junction resolvase subunit that binds multiple DNA repair/recombination endonucleases. *Cell* **138**, 78–89 (2009).
10. Munoz, I. M. *et al.* Coordination of structure-specific nucleases by human SLX4/BTBD12 is required for DNA repair. *Mol. Cell* **35**, 116–127 (2009).
11. Svendsen, J. M. *et al.* Mammalian BTBD12/SLX4 assembles a Holliday junction resolvase and is required for DNA repair. *Cell* **138**, 63–77 (2009).
12. Ip, S. C. Y. *et al.* Identification of Holliday junction resolvases from humans and yeast. *Nature* **456**, 357–361 (2008).
13. Rass, U. *et al.* Mechanism of Holliday junction resolution by the human GEN1 protein. *Genes Dev.* **24**, 1559–1569 (2010).
14. Osman, F., Dixon, J., Doe, C. L. & Whitby, M. C. Generating crossovers by resolution of nicked Holliday junctions: a role of Mus81-Eme1 in meiosis. *Mol. Cell* **12**, 761–774 (2003).
15. Gaillard, P.-H. L., Noguchi, E., Shanahan, P. & Russell, P. The endogenous Mus81-Eme1 complex resolves Holliday junctions by a nick and couter-nick mechanism. *Mol. Cell* **12**, 747–759 (2003).

16. Blanco, M. G., Matos, J., Rass, U., Ip, S. C. Y. & West, S. C. Functional overlap between the structure-specific nucleases Yen1 and Mus81-Mms4 for DNA damage repair in *S. cerevisiae*. *DNA Repair (Amst.)* **9**, 394–402 (2010).
17. Tay, Y. D. & Wu, L. Overlapping roles for Yen1 and Mus81 in cellular Holliday junction processing. *J. Biol. Chem.* **285**, 11427–11432 (2010).
18. Ho, C. K., Mazón, G., Lam, A. F. & Symington, L. S. Mus81 and Yen1 promote reciprocal exchange during mitotic recombination to maintain genome integrity in budding yeast. *Mol. Cell* **40**, 988–1000 (2011).
19. Breger, K. S., Smith, L., Turker, M. S. & Thayer, M. J. Ionizing radiation induces frequent translocations with delayed replication and condensation. *Cancer Res.* **64**, 8231–8238 (2004).
20. Hearst, J., Kauffman, L. & McClain, W. A simple mechanism for the avoidance of entanglement during chromosome replication. *Trends Genet.* **14**, 244–247 (1998).
21. Chan, K. L., North, P. S. & Hickson, I. D. BLM is required for faithful chromosome segregation and its localization defines a class of ultrafine anaphase bridges. *EMBO J.* **26**, 3397–3409 (2007).
22. Chan, K. L., Palmai-Pallag, T., Ying, S. M. & Hickson, I. D. Replication stress induces sister-chromatid bridging at fragile site loci in mitosis. *Nature Cell Biol.* **11**, 753–760 (2009).
23. Naim, V. & Rosselli, F. The FANCD pathway and BLM collaborate during mitosis to prevent micro-nucleation and chromosome abnormalities. *Nature Cell Biol.* **11**, 761–768 (2009).
24. Baumann, C., Korner, R., Hofmann, K. & Nigg, E. A. PICH, a centromere-associated SNF2 family ATPase, is regulated by Plk1 and required for the spindle checkpoint. *Cell* **128**, 101–114 (2007).
25. Wu, L., Davies, S. L., Levitt, N. C. & Hickson, I. D. Potential role for the BLM helicase in recombinational repair via a conserved interaction with RAD51. *J. Biol. Chem.* **276**, 19375–19381 (2001).
26. Ellis, N. A., Proytcheva, M., Sanz, M. M., Ye, T.-Z. & German, J. Transfection of BLM into cultured Bloom syndrome cells reduced the sister-chromatid exchange rate toward normal. *Am. J. Hum. Genet.* **65**, 1368–1374 (1999).
27. Gaymes, T. J. *et al.* Increased error-prone non homologous DNA end-joining – a proposed mechanism of chromosomal instability in Bloom's syndrome. *Oncogene* **21**, 2525–2533 (2002).
28. Bender, C. F. *et al.* Cancer predisposition and hematopoietic failure in *Rad50*^(S/S) mice. *Genes Dev.* **16**, 2237–2251 (2002).
29. Bayani, J. & Squire, J. A. Sister chromatid exchange. *Curr. Protoc. Cell Biol.* **22**, 7, (2005).
30. Alsop, A. E., Teschendorff, A. E. & Edwards, P. A. W. Distribution of breakpoints on chromosome 18 in breast, colorectal, and pancreatic carcinoma cell lines. *Cancer Genet. Cytogenet.* **164**, 97–109 (2006).

Supplementary Information is linked to the online version of the paper at www.nature.com/nature.

Acknowledgements We thank I. Hickson for providing the Bloom's syndrome cell lines and advice, P. Edwards for help and providing facilities for chromosome painting, S. Horswell for the statistical analysis, S. Ip for the GEN1 antibody, M.G. Blanco for assistance with SCE scoring and our laboratory colleagues for their encouragement and suggestions. We further thank K. Cimprich, the Cimprich laboratory members, and C. Wang, W. Johnson and A. Straight. This work was supported by Cancer Research UK, the Louis-Jeantet Foundation, the European Research Council, the Swiss Bridge Foundation and the Breast Cancer Campaign. S.N. was supported by a studentship from the UK Medical Research Council.

Author Contributions T.W. and S.C.W. designed the project that was undertaken entirely by T.W. Expertise for the chromosome paints was provided by S.N. The manuscript was written by S.C.W. with help from T.W.

Author Information Reprints and permissions information is available at www.nature.com/reprints. The authors declare no competing financial interests. Readers are welcome to comment on the online version of this article at www.nature.com/nature. Correspondence and requests for materials should be addressed to S.C.W. (stephen.west@cancer.org.uk).

METHODS

Antibodies. Affinity-purified anti-GEN1 rabbit polyclonal antibody was raised against a carboxy (C)-terminal peptide (CLDSPLPLRQLKLRFSQT) corresponding to GEN1^{890–908}. Mouse monoclonal antibodies against MUS81 (2G10/3) and RAD51 (14B4) were purchased from Abcam, and rabbit polyclonal antibody against SMC2 (A300-058A) was from Bethyl Labs.

siRNA transfections, quantitative RT-PCR and western blotting. For siRNA transfections, 3×10^5 cells were seeded in 60 mm cell culture dishes 8 h before transfection. In general, the cells were transfected twice within 24 h and the cell culture medium was changed after the first transfection. For depletion of a single protein, 3×10^5 cells were transfected with 400–500 pmol of siRNA using 10 μ l of Lipofectamine RNAiMAX (Invitrogen). For double targeting, up to 800 pmol of siRNA was mixed and transfected with 20 μ l Lipofectamine RNAiMAX; ON TARGET-plus siRNAs specific for each gene and control non-targeting siRNAs were purchased from Dharmacon and were used at the same concentrations. The efficiency of each siRNA treatment was monitored by western blotting 60 h after the first transfection, or 36 h after the second, or by quantitative RT-PCR 48 h after the first transfection. The siRNA sequences, indicated 5' to 3', were as follows. Control siRNA: ON-TARGETplus non-targeting siRNA #3. GEN1/FLJ40869 oligonucleotides 1–4: (1) GCGUAAUCUUGGUGGAAA; (2) UCUAAGACCUUUGCUAUA; (3) UAUGCAAACACUCGAAA; (4) GCCCUAAGAUACAUAUUA. SLX4 (oligonucleotides 1–2)^{9–11}: (1) AAACGUGAAUGAAGCA GAAUU; (2) CGGCAUUUGAGUCUGCAGGUGAA. MUS81 (oligonucleotides 1–2): (1) CAGCCUGGUGGAUCGAUA; (2) CAUUAAGUGUGGCGUCUA.

Owing to the lack of specificity of SLX4 antibodies, the efficiency of depletion of SLX4 was determined by quantitative RT-PCR. For this, total RNA was isolated using the RNeasy kit (Qiagen) according to the manufacturer's instructions with the following modifications: cell lysis was achieved using QIAshredder columns (Qiagen) and DNase I treatment was performed before total RNA was eluted from the RNeasy column. Then 1 μ g of total RNA was reverse transcribed using a TaqMan Reverse Transcription Kit (Applied Biosystems) in a 20- μ l reaction and used for three quantitative RT-PCR reactions in a 96-well format using the EXPRESS SYBR GreenER qPCR SuperMix with Premixed ROX (Invitrogen) and a Real-Time PCR System (Applied Biosystems). The ribosomal protein L23 mRNA was used as a standard. Depletion of SLX4 (or SLX1) by siRNA treatment results in a loss of both SLX1 and SLX4, as their stabilities are interdependent¹⁰. Use of siRNAs against either is therefore considered to be equivalent to SLX1–SLX4 depletion.

Primers for quantitative RT-PCR of GEN1: forward, CCACATGACTATG AATACTGCTGTCCTT; backward, TGGAATCCCTCACAACAGCAAGC.

Primers for quantitative RT-PCR of SLX4: forward, CCTGGAGGAAAA GGGTTTGT; backward, AGCTTCATCCAAGCACCTGT.

Primers for quantitative RT-PCR of L23: forward, TTCCTGGTCCACA ACGTCAAG; backward, TTGTGAAGCGATCTCGGCA.

Cell viability assays. Cells were collected 12 h after the second siRNA transfection with various siRNA combinations (MUS81 + SLX4; GEN1 + MUS81; GEN1 + SLX4). They were then seeded in equal numbers (2,000 per well) in 96-well plates in triplicates (with or without 66 μ M BrdU) and incubated for 84 h. Cell viability was determined using the Cell-Titre Glo assay (Promega).

Analysis of metaphase chromosomes. For the SCE assay, 3×10^5 cells were seeded in 60-mm plates before siRNA transfection. After 8 h, the cells were transfected with siRNA, grown for a further 24 h and then transfected again. After 18 h growth, BrdU (100 μ M) was added and the cells were grown for a further 60–72 h. Metaphase chromosomes were prepared and assayed for SCEs by a modification of published procedures^{28,29}. Briefly, cells were incubated for 1 h with 0.2 μ g ml⁻¹ colcemid and metaphase cells were harvested by mitotic shake-off. The cells were then swollen in 75 mM KCl for 20 min, fixed with methanol:acetic acid (3:1) and spread. After treatment with Hoechst 33258 and ultraviolet treatment, images were acquired using a Zeiss Axio Imager M1 microscope using a Plan-Neofluar $\times 60$, 0.4 numerical aperture oil objective lens, and captured using an ORCA-ER camera (Hamamatsu) controlled by Volocity 4.3.2 software (Improvision). At least 25 images were taken randomly from each condition. The files were renamed and each image (at least 1,700 chromosomes per condition) was scored blind to determine both the number of SCEs per chromosome and the number of harlequin chromosomes per metaphase spread.

To visualize the segmented chromosome phenotype, the same procedure was performed except that BrdU was omitted and the cells were stained in 7% Giemsa for 7 min immediately after spreading and drying. The $S > 3$ phenotype was scored, and spreads with two or more chromosomes exhibiting the $S > 3$ phenotype were considered positive. For the most severely affected metaphases, the count was stopped at 10 and designated '>9'.

SMC2 staining. Metaphase cells were collected as above, swollen in 1 \times PME (5 mM Pipes/NaOH pH 7.2, 5 mM NaCl, 5 mM MgCl₂, 1 mM EGTA), resuspended in lysis buffer (1 \times PME supplemented with protease inhibitors, 0.1% Triton-X, 1 mM ATP, 0.2 mM spermine, 0.5 mM spermidine and 10 μ g ml⁻¹ cytochalasin B) and lysed on ice using a dounce homogenizer. Lysates were layered onto sucrose gradients (30, 40, 50 and 60% sucrose in 1 \times PME) and spun for 30 min at 2,000g. The chromosomes were taken from the 40/50% and 50/60% interfaces, and fixed in 3.7% formaldehyde and then centrifuged (20 min at 4,000g) through a 40% glycerol cushion onto polylysine-treated coverslips. Then chromosomes were stained with anti-SMC2 antibody (1:300) and Alexa Fluor 488-coupled goat anti-rabbit secondary antibody (1:1,000) and mounted in Vectashield containing DAPI.

Statistical analysis. Sister chromatid exchange data was subjected to a Student's two-tailed *t*-test. For $S > 3$ data, the counts were analysed by analysis of deviance using the generalized linear model fitting function glm() with a Poisson approximation to the multinomial, followed by analysis of deviance using the anova() function with the χ^2 test, both performed in R 2.10.1 (for details see <http://www.R-project.org>).

The complete biosynthesis of the genetically encoded amino acid pyrrolysine from lysine

Marsha A. Gaston¹, Liwen Zhang², Kari B. Green-Church² & Joseph A. Krzycki^{1,3}

Pyrrolysine, the twenty-second amino acid found to be encoded in the natural genetic code^{1–4}, is necessary for all of the known pathways by which methane is formed from methylamines^{5,6}. Pyrrolysine comprises a methylated pyrroline carboxylate in amide linkage to the ϵ -amino group of L-lysine^{2,7,8}. In certain Archaea, three methyltransferases initiate methanogenesis from the various methylamines^{9–11}, and these enzymes are encoded by genes with an in-frame amber codon^{12,13} that is translated as pyrrolysine^{2,7,8}. *Escherichia coli* that has been transformed with the *pylTSBCD* genes from methanogenic Archaea can incorporate endogenously biosynthesized pyrrolysine into proteins¹⁴. The decoding of UAG as pyrrolysine requires *pylT*^{1,6}, which produces tRNA^{Pyl} (also called tRNA_{CUA}), and *pylS*¹, which encodes a pyrrolysyl-tRNA synthetase^{4,15,16}. The *pylB*, *pylC* and *pylD* genes¹ are each required for tRNA-independent pyrrolysine synthesis¹⁴. Pyrrolysine is the last remaining genetically encoded amino acid with an unknown biosynthetic pathway. Here we provide genetic and mass spectrometric evidence for a *pylBCD*-dependent pathway in which pyrrolysine arises from two lysines. We show that a newly uncovered UAG-encoded amino acid, desmethylpyrrolysine, is made from lysine and exogenous D-ornithine in a *pylC*-dependent process followed by a *pylD*-dependent process, but it is not further converted to pyrrolysine. These results indicate that the radical S-adenosyl-L-methionine (SAM) protein PylB mediates a lysine mutase reaction that produces 3-methylornithine, which is then ligated to a second molecule of lysine by PylC before oxidation by PylD results in pyrrolysine. The discovery of lysine as the sole precursor to pyrrolysine will further inform discussions of the evolution of the genetic code and amino acid biosynthetic pathways. Furthermore, intermediates of the pathway may provide new avenues by which the *pyl* system can be exploited to produce recombinant proteins with useful modified residues.

In previously proposed pathways of pyrrolysine biosynthesis, lysine is ligated to a ring precursor derived from other cellular metabolites such as ornithine, glutamic acid, proline or isoleucine^{5,14,17}. The results presented here instead support the pathway shown in Fig. 1. We used *E. coli* transformed with the genes from the *Methanosarcina acetivorans* gene cluster *pylTSBCD* and the *Methanosarcina barkeri* gene *mtmB1* (ref. 16), demonstrating, by stable isotopic labelling and mass spectrometry (MS) experiments, that lysine is the only precursor to pyrrolysine. The gene *mtmB1* encodes the pyrrolysine-containing protein MtmB, which is the predominant monomethylamine methyltransferase of *M. barkeri*¹³. Pyrrolysine in MtmB is proposed to bind to, and activate, methylamines for methyl group transfer to a cognate corrinoid protein^{2,5}. There is no known pathway by which *E. coli* degrades lysine into central metabolites, and *E. coli* strain BL21 mainly incorporates lysine into proteins or decarboxylates it to cadaverine¹⁸. Using this strain of *E. coli* therefore allows analysis of the incorporation of lysine into pyrrolysine-containing peptides without the need for extensive time courses, because peptide ions that do not contain lysine will be unlabelled.

Chymotryptic digests of MtmB after incubation with ¹³C₆¹⁵N₂-labelled lysine at 99% enrichment were analysed by MS, using protocols for accurate peptide mass determination, as well as tandem MS for determining peptide sequences and residue masses (Table 1 and Supplementary Tables 1–3). The MtmB peptide 194-AGRPGMGVOGPETSL-208, where O (at amino acid position 202) is pyrrolysine, has been studied previously⁸ and was readily observed as multiple ions in unlabelled controls. By contrast, digests of labelled MtmB contained no detectable unlabelled pyrrolysine-containing peptide, but a single labelled peptide was observed as multiple ions with *m/z* values within 2.5–5.4 p.p.m. of the theoretical value for the pyrrolysine-containing peptide, but with a 15-Da mass shift (equivalent to 12 atoms of ¹³C and 3 of ¹⁵N). Tandem spectra revealed that the

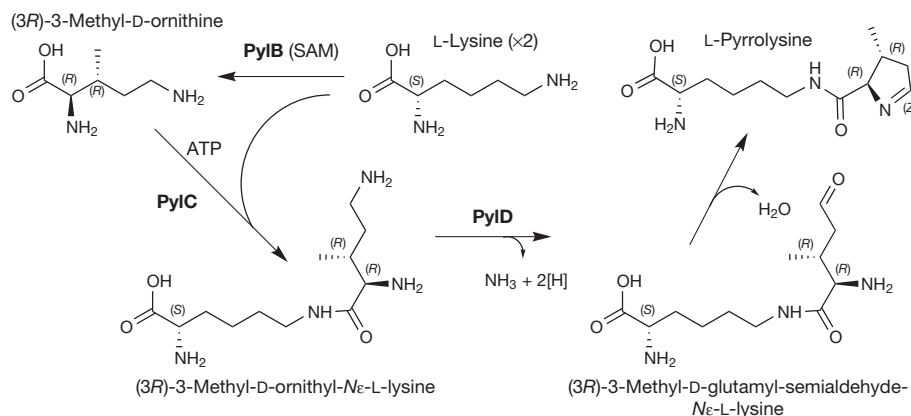


Figure 1 | Proposed pathway of pyrrolysine biosynthesis from two molecules of lysine by the products of *pylB*, *pylC* and *pylD*. The radical SAM enzyme PylB first uses lysine to make (3R)-3-methyl-D-ornithine. After ligation

to a second molecule of lysine by PylC, the terminal amine of the methyl-D-ornithyl-N ϵ -lysine intermediate is oxidized to an aldehyde by PylD. Spontaneous elimination of water results in the formation of pyrrolysine.

¹Department of Microbiology, 484 West 12th Avenue, Ohio State University, Columbus, Ohio 43210, USA. ²CCIC/Mass Spectrometry and Proteomics Facility, 460 West 12th Avenue, Ohio State University, Columbus, Ohio 43210, USA. ³The Ohio State University Biochemistry Program, 484 West 12th Avenue, Columbus, Ohio 43210, USA.

Table 1 | Effect of labelled lysine and D-ornithine on MtmB-derived pyrrolysine-containing peptide ions

Lysine isotope*	D-Ornithine	Observed m/z †	UAG residue formula assigned*	m/z error (p.p.m.)‡	UAG residue mass (Da)§	Residue identity (mass shift, Da)
C_6N_2	–	783.4080 ²⁺	$C_{12}H_{19}N_3O_2$	0.77	237.05	O
$^{13}C_6^{15}N_2$	–	790.9225 ²⁺	$^{13}C_{12}H_{19}^{15}N_3O_2$	2.53	252.05	O (+15)
$\alpha\text{-}^{15}N$	–	792.4031 ²⁺ ¶	$C_{12}H_{19}^{15}N_2NO_2$	0.25	239.14	O (+2)
$\epsilon\text{-}^{15}N$	–	783.9084 ²⁺ ¶	$C_{12}H_{19}^{15}NN_2O_2$	1.27	238.16	O (+1)
C_6N_2	+	783.4065 ²⁺	$C_{12}H_{19}N_3O_2$	3.06	237.15	O
C_6N_2	+	776.3993 ²⁺	$C_{11}H_{17}N_3O_2$	2.19	223.12	O*
$^{13}C_6^{15}N_2$	+	790.9224 ²⁺	$^{13}C_{12}H_{19}^{15}N_3O_2$	0.12	252.19	O (+15)
$^{13}C_6^{15}N_2$	+	780.4099 ²⁺	$^{13}C_6C_5H_{17}^{15}N_2N_1O_2$	0.26	231.16	O* (+8)
$C_6N_2\#$	+	776.4025 ²⁺	$C_{11}H_{17}N_3O_2$	1.93	223.13	O*

The peptide ions are from 194-AGRPGMGVO/O*GPETSL-208 from the chymotryptic digestion of MtmB produced by *E. coli* transformed with *pylTSBCD* (except where indicated) and *mtmB1* and then grown in medium supplemented with the listed isotopic form of lysine in the presence or absence of D-ornithine.

*Isotopic composition denotes the most abundant natural isotope, unless otherwise indicated.

†Accurate mass measured with an LTQ Orbitrap XL mass spectrometer.

‡Difference between the observed and theoretical m/z calculated according to the indicated elemental formula for the UAG-encoded residue.

§Mean calculated mass using y-series and b-series ions from MS/MS analysis.

||Mass shift of the pyrrolysyl or desmethylpyrrolysyl residue produced in the presence of heavy lysine relative to the residue mass produced in the presence of light lysine.

* M_{ox} replaces M.

#Only *pylTSCD* present, not *pylB*.

increased mass was due to the pyrrolysyl residue uniformly labelled with ^{13}C and ^{15}N .

As the experiment described above shows, the pyrrolysyl residue ($C_{12}H_{19}N_3O_2$) is made solely from lysine; one amine group must be eliminated from one of the two lysines that form the lysyl chain and ring. To identify which of the two amine groups of lysine is lost, the way in which 95%-enriched [$\alpha\text{-}^{15}N$]lysine or [$\epsilon\text{-}^{15}N$]lysine is incorporated into the pyrrolysyl residue was ascertained. With [$\alpha\text{-}^{15}N$]lysine, both the accurate peptide mass and residue mass indicated incorporation of two ^{15}N nuclei into pyrrolysine. By contrast, with [$\epsilon\text{-}^{15}N$]lysine, the data supported incorporation of a single ^{15}N atom into pyrrolysine (Table 1 and Supplementary Tables 4 and 5). In directed searches, these labels were not observed to be incorporated into the pyrrolysine-containing peptide at different levels. Therefore, the ϵ -amine group from one lysine must be eliminated to make pyrrolysine, presumably to form the ring with its single imine bond.

The biosynthesis of pyrrolysine with lysine as a sole precursor led us to examine a report in which D-ornithine was shown to stimulate UAG read-through in *E. coli* carrying *pylTSBCD* and in which it was proposed to be an intermediate in pyrrolysine formation¹⁹. In the presence of *pylTSBCD*, D-ornithine but not L-ornithine increased UAG read-through in *mtmB1* RNA (Supplementary Fig. 1), indicating that the formation of D-ornithine or a derivative might limit UAG translation, possibly through limiting the biosynthesis of UAG-encoded residues. Strains lacking any one of *pylB*, *pylC* or *pylD* cannot synthesize pyrrolysine¹⁴,

but this proved untrue for D-ornithine-mediated stimulation of UAG translation. *E. coli* that had *pylC* and *pylD* but not *pylB* was capable of significant D-ornithine-dependent synthesis of full-length MtmB (Fig. 2), indicating that the effect of the lack of *pylB* on UAG-encoded residue formation could be overcome by the addition of D-ornithine.

Chymotryptic digests of MtmB, from *E. coli* carrying *pylTSBCD* and grown in media supplemented with D-ornithine, contained ions of 194-AGRPGM/ M_{ox} GVOGPETSL-208 (where M_{ox} is methionine sulfoxide), with O202 having the pyrrolyl residue mass of 237 Da (Table 1 and Supplementary Tables 6 and 7). However, ions corresponding to 194-AGRPGMGVXGPETSL-208, where X202 corresponds to a new UAG-encoded residue, were also observed (Table 1, Supplementary Table 6 and Supplementary Fig. 2). The observed peptide masses averaged 14.0185 ± 0.0027 Da (mean \pm s.d.) less than the theoretical mass of corresponding pyrrolysine-containing peptides, and tandem MS corroborated a UAG-encoded residue mass of 14 Da less than that of pyrrolysine (Table 1, Supplementary Table 6 and Supplementary Fig. 2). This mass difference is equivalent to the substitution of a proton for a methyl group, indicating that the residue is desmethylpyrrolysine (Fig. 3). Using the desmethylpyrrolysyl residue elemental formula ($C_{11}H_{17}N_3O_2$) yields a peptide theoretical m/z value of 776.4010^{2+} , which is within 1.8–3.7 p.p.m. of observed m/z values. This assignment explains the significant charging of tRNA^{Pyl}

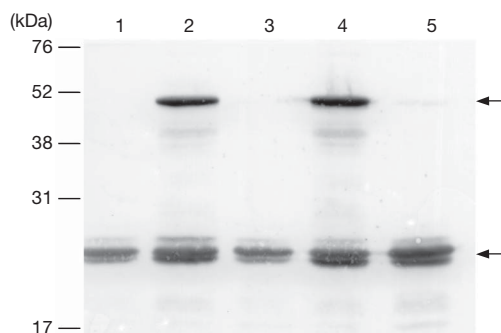


Figure 2 | UAG translation dependent on D-ornithine requires *pylTSCD* but not *pylB*. *E. coli* carrying the plasmids indicated below were induced to express the *mtmB1* and *pyl* genes and then analysed by immunoblotting for the full-length (50 kDa) *mtmB1* product (upper arrow) and the amber-codon-terminated (23 kDa) *mtmB1* product (lower arrow). Bacteria were grown in the presence of D-ornithine after being transformed with pDLBADHis and one of the following vectors: the pK parent vector pACYCDuet-1 (lane 1), pK13 (which carries *pylB*, *pylC* and *pylD*; lane 2), pK14 (which carries *pylB* and *pylD*; lane 3), pK15 (which carries *pylC* and *pylD*; lane 4) or pK16 (which carries *pylB* and *pylC*; lane 5).

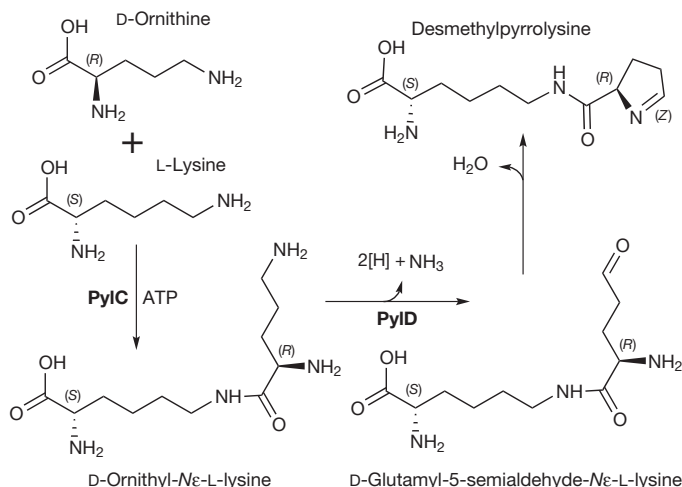


Figure 3 | Pathway of desmethylpyrrolysine biosynthesis. In contrast to the *pylB*-dependent pathway shown in Fig. 1, *pylC* and *pylD* can synthesize desmethylpyrrolysine when given D-ornithine and L-lysine. The amide of the two amino acids, D-ornithyl-Nε-L-lysine, is formed in an ATP-dependent reaction by *PylC*. *PylD* oxidizes the terminal amine of the amide, resulting in the elimination of water and the formation of desmethylpyrrolysine.

with desmethylpyrrolysine *in vivo*, as lysylated ring compounds are necessary for substantial charging of tRNA^{Pyl} by PylS^{20–22}.

Ions corresponding to 194-AGRPGMGVO*GPETSL-208, where O*202 is desmethylpyrrolysine, were readily detected in digests of MtmB synthesized in *E. coli* carrying *pylTSCD* (lacking *pylB*), and the residue mass of desmethylpyrrolysine was observed on tandem MS of this ion (Table 1 and Supplementary Table 6). However, a pyrrolysine-containing peptide ion could not be detected in digests of MtmB from cells lacking *pylB*, confirming that *pylB* is required for producing pyrrolysine but not desmethylpyrrolysine.

If D-ornithine and desmethylpyrrolysine are intermediates in pyrrolysine formation, both desmethylpyrrolysine and pyrrolysine should incorporate D-ornithine. Isotopically labelled DL-ornithine and D-ornithine could not be obtained; therefore, isotopic dilution experiments were undertaken using ¹³C₆¹⁵N₂-labelled lysine and D-ornithine (Table 1, Supplementary Table 8 and Supplementary Fig. 2). Recombinant MtmB produced in the presence of heavy lysine and D-ornithine was subjected to chymotryptic digestion and MS analysis. The labelled pyrrolysine-containing peptide was readily identified, having a mass shift of 15 Da owing to complete biosynthesis of the pyrrolysyl residue from lysine. Ions indicating that pyrrolysine was unlabelled, or was labelled with fewer than 15 heavy nuclei, were sought but were not observed. The 8-Da mass shift of the desmethylpyrrolysine-containing peptide ion and the desmethylpyrrolysyl residue in tandem MS revealed incorporation of the equivalent of an intact ¹³C₆¹⁵N₂-labelled lysine skeleton. The observed *m/z* values for the peptide fit the theoretical value for this assignment with an error of less than 0.8 p.p.m. No desmethylpyrrolysine-containing peptides with different contributions from labelled lysine could be identified. Thus, unlike pyrrolysine, desmethylpyrrolysine is synthesized with the equivalent of only one lysine, consistent with the formation of the amide linkage between lysine and the ring precursor made from D-ornithine.

As PylC is a member of the carbamoyl phosphate synthetase family of proteins, which forms amides between carbon dioxide (or carboxyl groups) and ammonia (or amine groups)^{1,23}, we proposed that PylC ligates the Nε of lysine to the carboxyl group of D-ornithine as the first step in the formation of desmethylpyrrolysine (Fig. 3). To test this idea, extracts of *E. coli* transformed with the plasmid pK18 (which carries *pylC* but no other *pyl* genes) were examined, and an ion with a *m/z* of 261.1915 was detected. The corresponding mass is 2.3 p.p.m. removed from the theoretical mass predicted for C₁₁H₂₄N₄O₃, which is the empirical formula of D-ornithyl-Nε-lysine (Supplementary Fig. 3). This signal was undetectable in *pylC*-carrying cells that had not been incubated with D-ornithine and was also dependent on the presence of *pylC* in the recombinant strain as shown by a comparison with vector-only controls. Similar experiments with *E. coli* carrying *pylD* (but no other *pyl* genes) yielded no evidence of D-ornithine oxidation (data not shown). However, PylD contains a region that is highly similar to the NAD-binding folds of several dehydrogenases²³, and iterative PSI-BLAST (National Center for Biotechnology Information) uncovered significant similarity between PylD and several amino acid dehydrogenases, yielding alignments with expect (*E*) values as low as 10^{−95}. Given that *pylD* is required for desmethylpyrrolysine synthesis, the relationship between PylD and amino acid dehydrogenases is consistent with PylD having a function in oxidation of the δ-amine of the D-ornithyl residue of D-ornithyl-Nε-lysine, leading to spontaneous dehydration to form desmethylpyrrolysine (Fig. 3).

If desmethylpyrrolysine is an intermediate in pyrrolysine formation, then methylation of the ring would be the last step of synthesis. As pyrrolysine can be formed entirely from lysine, this possibility implies that lysine would first be used to make D-ornithine to form the pyrroline ring, which would then be lysylated to form desmethylpyrrolysine, which would, in turn, be methylated with a methyl group also derived from lysine. This is unprecedented and unlikely biochemistry, and no data support D-ornithine being a precursor of pyrrolysine. Furthermore, as an intermediate, desmethylpyrrolysine would function as a competitor for

pyrrolysine ligation to tRNA^{Pyl}, resulting in a mixture of O and O*, but this mixture is not found in native MtmB⁸. Desmethylpyrrolysine is thus likely to be a pyrrolysine analogue that is made with an analogue (D-ornithine) of an intermediate in the pathway.

A much more tenable model for the conversion of lysine to the methylated pyrroline ring of pyrrolysine is the rearrangement of lysine to (3*R*)-3-methyl-D-ornithine via a lysine mutase reaction, thus generating the D-ornithine derivative that is a substrate for ligation to lysine by PylC (Fig. 1). PylB is a radical SAM protein²³, and such proteins are known to function as lyases, reductases and mutases²⁴. As the PylB requirement for production of a residue for UAG translation in *E. coli* can be overcome with D-ornithine, PylB is proposed to function *in vivo* as the lysine mutase in the above model. Certain vitamin-B₁₂-dependent enzymes carry out amino acid mutase reactions with inversion of the configuration of chiral centres²⁵, and PylB operating as a lysine mutase could potentially give rise to the *R* chiral centres of the pyrroline ring, even using L-lysine as substrate, in a radical mechanism dependent on SAM. The pathway explains the loss of the Nε amine from one lysine during pyrrolysine biosynthesis, as the Nε of one lysine would become the δ-amino group of the methylornithine intermediate that is oxidized to form the imine bond of the ring.

Hypotheses of how the genetic code evolved are sometimes interwoven with those of how biosynthetic pathways evolved. For example, the co-evolution theory considers that families of amino acids arising from a common precursor have non-randomly similar codon assignments²⁶. The finding that pyrrolysine is entirely a derivative of lysine firmly identifies it as part of the aspartic acid family in Bacteria and Archaea and places its codon within those of that family of amino acids²⁶. The identification of the precursor and intermediate analogues of the pyrrolysine and desmethylpyrrolysine pathways may have a more applied outcome. In recent years, the *pylS* and *pylT* genes have been used to introduce useful modified residues into recombinant proteins^{22,27–29}. Synthetic analogues of pyrrolysine intermediates, such as D-ornithine derivatives, may provide a route by which wild-type or modified PylC and PylD can endogenously biosynthesize pyrrolysine derivatives with desired properties for incorporation into tailored recombinant proteins.

METHODS SUMMARY

E. coli BL21 Tuner(DE3) (Novagen) was transformed with the plasmid pK13, pK14, pK15 or pK16 (ref. 14) or with the parent vector pACYCDuet-1 (Novagen). These transformed *E. coli* were then transformed with the plasmid pDLBADHis¹⁴ carrying the *M. barkeri* gene encoding MtmB with a carboxy-terminal hexahistidine sequence. For labelling, exponential phase cultures grown in defined medium containing the 20 common amino acids were resuspended in fresh medium with or without 5 mM D-ornithine and with isotopic forms of lysine. Then, expression of *pylTSCD* and *mtmB1* was induced, and MtmB was detected by immunoblotting¹⁴. Urea-solubilized MtmB was purified by affinity chromatography before in-gel chymotryptic digestion^{4,8}. Capillary liquid chromatography and tandem MS were carried out using an LTQ Orbitrap XL mass spectrometer (Thermo Scientific). Tandem MS data were acquired with a microspray source (Michrom Bioresources) with a spray voltage of 2 kV and a capillary temperature of 175 °C. The scan sequence of the mass spectrometer was based on the Top10 method with an MS scan between 300 Da and 2,000 Da followed by ten consecutive MS/MS scans of the ten most abundant peaks to generate product ion spectra. The resolution of the full scan on the LTQ Orbitrap was set at 30,000 for determinations of high mass accuracy. MS/MS scans were then performed in ion trap mode to obtain higher signal intensity, which allows better peptide sequencing but reduces mass accuracy. The RAW data files collected by the mass spectrometer were converted to mzXML and MGF files using MassMatrix tools³⁰ (<http://www.massmatrix.net>). Data were later searched with MassMatrix³⁰ for peptides containing pyrrolysine or its derivatives. For detection of D-ornithyl-Nε-lysine, *E. coli* carrying pK18 (derived by *EagI* digestion of pK16 and religation to delete *pylB*) was grown to the exponential phase in the presence of 10 mM D-ornithine and lysine and was then induced with isopropyl-β-D-thiogalactoside¹⁴ before extraction with hot aqueous methanol at 70 °C. The clarified extract was acidified before microspray ionization and introduction into the LTQ Orbitrap.

Full Methods and any associated references are available in the online version of the paper at www.nature.com/nature.

Received 18 August 2010; accepted 9 February 2011.

1. Srinivasan, G., James, C. M. & Krzycki, J. A. Pyrrolysine encoded by UAG in Archaea: charging of a UAG-decoding specialized tRNA. *Science* **296**, 1459–1462 (2002).
2. Hao, B. *et al.* A new UAG-encoded residue in the structure of a methanogen methyltransferase. *Science* **296**, 1462–1466 (2002).
3. Atkins, J. F. & Gesteland, R. The 22nd amino acid. *Science* **296**, 1409–1410 (2002).
4. Blight, S. K. *et al.* Direct charging of tRNA_{CUA} with pyrrolysine *in vitro* and *in vivo*. *Nature* **431**, 333–335 (2004).
5. Krzycki, J. A. Function of genetically encoded pyrrolysine in corrinoid-dependent methylamine methyltransferases. *Curr. Opin. Chem. Biol.* **8**, 484–491 (2004).
6. Mahapatra, A. *et al.* Characterization of a *Methanosarcina acetivorans* mutant unable to translate UAG as pyrrolysine. *Mol. Microbiol.* **59**, 56–66 (2006).
7. Hao, B. *et al.* Reactivity and chemical synthesis of L-pyrrolysine—the 22nd genetically encoded amino acid. *Chem. Biol.* **11**, 1317–1324 (2004).
8. Soares, J. A. *et al.* The residue mass of L-pyrrolysine in three distinct methylamine methyltransferases. *J. Biol. Chem.* **280**, 36962–36969 (2005).
9. Burke, S. A. & Krzycki, J. A. Reconstitution of monomethylamine:coenzyme M methyl transfer with a corrinoid protein and two methyltransferases purified from *Methanosarcina barkeri*. *J. Biol. Chem.* **272**, 16570–16577 (1997).
10. Ferguson, D. J. Jr, Gorlatova, N., Grahame, D. A. & Krzycki, J. A. Reconstitution of dimethylamine:coenzyme M methyl transfer with a discrete corrinoid protein and two methyltransferases purified from *Methanosarcina barkeri*. *J. Biol. Chem.* **275**, 29053–29060 (2000).
11. Ferguson, D. J. Jr & Krzycki, J. A. Reconstitution of trimethylamine-dependent coenzyme M methylation with the trimethylamine corrinoid protein and the isozymes of methyltransferase II from *Methanosarcina barkeri*. *J. Bacteriol.* **179**, 846–852 (1997).
12. Burke, S. A., Lo, S. L. & Krzycki, J. A. Clustered genes encoding the methyltransferases of methanogenesis from monomethylamine. *J. Bacteriol.* **180**, 3432–3440 (1998).
13. Paul, L., Ferguson, D. J. & Krzycki, J. A. The trimethylamine methyltransferase gene and multiple dimethylamine methyltransferase genes of *Methanosarcina barkeri* contain in-frame and read-through amber codons. *J. Bacteriol.* **182**, 2520–2529 (2000).
14. Longstaff, D. G. *et al.* A natural genetic code expansion cassette enables transmissible biosynthesis and genetic encoding of pyrrolysine. *Proc. Natl Acad. Sci. USA* **104**, 1021–1026 (2007).
15. Polycarpo, C. *et al.* An aminoacyl-tRNA synthetase that specifically activates pyrrolysine. *Proc. Natl Acad. Sci. USA* **101**, 12450–12454 (2004).
16. Krzycki, J. A. The direct genetic encoding of pyrrolysine. *Curr. Opin. Microbiol.* **8**, 706–712 (2005).
17. Ambrogelly, A., Palioura, S. & Soll, D. Natural expansion of the genetic code. *Nature Chem. Biol.* **3**, 29–35 (2007).
18. Jeong, H. *et al.* Genome sequences of *Escherichia coli* B strains REL606 and BL21(DE3). *J. Mol. Biol.* **394**, 644–652 (2009).
19. Namy, O. *et al.* Adding pyrrolysine to the *Escherichia coli* genetic code. *FEBS Lett.* **581**, 5282–5288 (2007).
20. Li, W. T. *et al.* Specificity of pyrrolysyl-tRNA synthetase for pyrrolysine and pyrrolysine analogs. *J. Mol. Biol.* **385**, 1156–1164 (2009).
21. Polycarpo, C. R. *et al.* Pyrrolysine analogues as substrates for pyrrolysyl-tRNA synthetase. *FEBS Lett.* **580**, 6695–6700 (2006).
22. Yanagisawa, T. *et al.* Multistep engineering of pyrrolysyl-tRNA synthetase to genetically encode N^ε-(o-azidobenzoyloxycarbonyl) lysine for site-specific protein modification. *Chem. Biol.* **15**, 1187–1197 (2008).
23. Rother, M. & Krzycki, J. A. Selenocysteine, pyrrolysine, and the unique energy metabolism of methanogenic archaea. *Archaea* **2010**, 453642 (2010).
24. Frey, P. A., Hegeman, A. D. & Ruzicka, F. J. The radical SAM superfamily. *Crit. Rev. Biochem. Mol. Biol.* **43**, 63–88 (2008).
25. Banerjee, R. Radical carbon skeleton rearrangements: catalysis by coenzyme B12-dependent mutases. *Chem. Rev.* **103**, 2083–2094 (2003).
26. Wong, J. T. Coevolution theory of the genetic code at age thirty. *Bioessays* **27**, 416–425 (2005).
27. Fekner, T., Li, X., Lee, M. M. & Chan, M. K. A pyrrolysine analogue for protein click chemistry. *Angew. Chem. Int. Edn Engl.* **48**, 1633–1635 (2009).
28. Chen, P. R. *et al.* A facile system for encoding unnatural amino acids in mammalian cells. *Angew. Chem. Int. Edn* **48**, 4052–4055 (2009).
29. Neumann, H., Peak-Chew, S. Y. & Chin, J. W. Genetically encoding N^ε-acetyllysine in recombinant proteins. *Nature Chem. Biol.* **4**, 232–234 (2008).
30. Xu, H. & Freitas, M. A. A mass accuracy sensitive probability based scoring algorithm for database searching of tandem mass spectrometry data. *BMC Bioinformatics* **8**, 133 (2007).

Supplementary Information is linked to the online version of the paper at www.nature.com/nature.

Acknowledgements This work was supported by a grant from the National Institutes of Health to K.B.G.-C. and by grants from the US Department of Energy and the National Institutes of Health to J.A.K. The authors are grateful to D. Longstaff for preparing the tagged *mtmB1* version of pDLBAD.

Author Contributions M.A.G. planned experiments, labelled and purified MtmB samples from recombinant cells, made recombinant strains, carried out immunoblotting, analysed data and prepared figures. L.Z. carried out proteolytic digestion of MtmB, determined peptide and residue masses, analysed data and helped prepare data for presentation. K.B.G.-C. oversaw data acquisition and primary data analysis. J.A.K. planned and advised on experiments, analysed and interpreted data, prepared figures and wrote the manuscript.

Author Information Reprints and permissions information is available at www.nature.com/reprints. The authors declare no competing financial interests. Readers are welcome to comment on the online version of this article at www.nature.com/nature. Correspondence and requests for materials should be addressed to J.A.K. (krzycki.1@osu.edu).

METHODS

Plasmid and strain construction. *E. coli* BL21 Tuner(DE3) (Novagen) was transformed with the plasmid pK13, pK14, pK15 or pK16 (ref. 14) or the parent vector pACYCDuet-1 (Novagen), in addition to pDLBADHis (for recombinant expression of MtmB with a C-terminal GGGHHHHH tag). The pDLBADHis plasmid was constructed from pDLBAD¹⁴. The *M. barkeri* *mtmB1* gene was amplified from pDLBAD using the primers MtmBNdeIF (5'-CATATGACATTAGAAAATCA TTTG) and MtmBCHisXhoI (5'-CTCAGATTATTATTATTAGTGGTGG TGGTGGTGGTGTCTCCGAATACAAGTCCCAGGTCTTCGAGCTTCTTC CT). The altered *mtmB1* PCR fragment and pDLBAD were digested with NdeI and XhoI to replace the unmodified *mtmB1* gene, creating pDLBADHis. Plasmids pK17 and pK18 were created from pK14 and pK16, respectively, by excision of the EagI fragment, containing *pylB*, from each plasmid. Following religation of the plasmid backbone, pK17 contained only *pylD*, and pK18 only *pylC*.

Production of recombinant MtmB in *pyl*-transformed *E. coli*. Overnight cultures of *E. coli* carrying pDLBADHis and pK13 (or pK14, pK15 or pK16 as appropriate) were grown in M9 minimal medium supplemented with 0.2% glucose, 1 mM of each of the canonical 20 amino acids, 2 mM MgSO₄, 80 μM CaCl₂, 36 μM FeSO₄, 100 μg ml⁻¹ ampicillin and 34 μg ml⁻¹ chloramphenicol. These cultures were then used to inoculate 1 l of the same medium. At an optical density (OD)₆₀₀ of 0.4–0.6, cells were pelleted and then resuspended in 1 l of the same medium containing 80 μM isopropyl-β-D-thiogalactoside for induction of *pylTSBCD*. For labelling experiments, 1 mM isotopically labelled lysine (Cambridge Isotope Laboratories) was substituted for unlabelled lysine. Where noted, the cultures were further supplemented with 5 mM D-ornithine. After cells were grown for 1 h at 37 °C with shaking, *mtmB1* expression was induced with 0.02% L-arabinose. After 2 h MtmB production was assessed by immunoblotting with polyclonal anti-MtmB antibody¹⁴. **Purification of recombinant MtmB.** Cells suspended in 50 mM MOPS, pH 7.0, were lysed by using a French pressure cell, then centrifuged at 1,000 g for 5 min. The supernatant was centrifuged at 25,000 g for 25 min. The pellet was resuspended in 3.5 M urea containing 50 mM MOPS, pH 7.0, and then centrifuged, and this pellet was, in turn, resuspended in 7 M urea containing 50 mM MOPS, pH 7.0, before application to a Ni-activated HiTrap Chelating HP column (GE Healthcare BioSciences) equilibrated in 10 mM imidazole, 500 mM NaCl, 7 M urea in 20 mM sodium phosphate buffer, pH 7.2. MtmB was then eluted with an imidazole gradient up to 500 mM in the same buffer. Aliquots of fractions were assessed for MtmB (by immunoblotting with anti-MtmB antibody), which was found to elute at approximately 220 mM imidazole.

MS analysis of peptides. MtmB-containing fractions were subjected to SDS-PAGE. The 50-kDa MtmB protein was excised and subjected to in-gel chymotryptic digestion before analysis¹⁸. Capillary liquid chromatography–tandem MS (capillary-LC/MS/MS) was used for protein/peptide identification, with an LTQ Orbitrap XL mass spectrometer (Thermo Scientific) operated in positive ion

mode. Samples were separated on a capillary column (3 μm, 200 Å Magic C18AQ, 0.2 mm × 150 mm, Michrom Bioresources) using an UltiMate 3000 HPLC system (LC Packings). Each sample was injected into the trapping column (LC Packings) and desalted with 50 mM acetic acid for 10 min before column injection. Mobile phase A was 0.1% formic acid in water, and 0.1% formic acid in acetonitrile was used as mobile phase B. The flow rate was set at 2 μl min⁻¹. Mobile phase B was increased from 2% to 15% over 30 min and again from 30% to 50% over 45 min. Mobile phase B was then increased from 50% to 90% over 5 min and kept at 90% for another 5 min before being brought back quickly to 2% over 1 min. The column was equilibrated at 2% mobile phase B (or 98% mobile phase A) for 25 min before the next sample injection. The MS/MS spectra were acquired with a microspray source (Michrom Bioresources) operated with a spray voltage of 2 kV and a capillary temperature of 175 °C. The scan sequence of the mass spectrometer was based on the data-dependent Top10 method: the analysis was programmed for a full MS scan recorded between 300 Da and 2,000 Da, followed by ten consecutive MS/MS scans of the ten most abundant peaks in the spectrum to generate product ion spectra for the determination of the amino acid sequence. The resolution of the full scan on the LTQ Orbitrap was set at 30,000 to achieve high mass accuracy determination. MS/MS scans were then performed in ion trap mode to obtain higher signal intensity, which allows better peptide sequencing but reduces mass accuracy. The CID fragmentation energy was set to 35%. Multiple MS/MS detection of the same peptide was excluded after detecting it three times. The RAW data files collected by the mass spectrometer were converted to mzXML and MGF files with the use of MassMatrix data conversion tools (version 1.3, <http://www.massmatrix.net>). Data were later searched with MassMatrix³⁰ for peptides containing pyrrolysine or its derivatives. The mass accuracy of the precursor ions was set to 1.2 Da to accommodate accidental selection of the natural ¹³C ion, and the fragment mass accuracy was set to 0.8 Da. Possible hits were manually verified.

D-Ornithine metabolite analysis. *E. coli* transformed with pK17 (carrying *pylD*), pK18 (carrying *pylC*) or the parent vector pACYCDuet-1 was grown in 500 ml Luria-Bertani medium supplemented with 10 mM lysine in the presence or absence of 10 mM D-ornithine. At an OD₆₀₀ of 0.6, 80 μM isopropyl-β-D-thiogalactoside was added to induce *pylC* or *pylD* expression. After 2 h, cells were pelleted by centrifugation, washed twice in 50 mM MOPS, pH 7.2, resuspended in 3 ml deionized water, then extracted with 9 ml 66% methanol at 70 °C for 30 min. The extract was then centrifuged at 16,100 g for 10 min, and the resultant supernatant was concentrated to 250 μl by vacuum centrifugation. The sample was then diluted with 50% methanol in 2% acetic acid and infused into the micro-electrospray source set as described above. Data were recorded between 100 Da and 300 Da, and the resolution of the full scan was set at 30,000 to achieve high mass accuracy determination. Data were acquired in continuum mode until well-averaged data were obtained.

Crystal structure of metarhodopsin II

Hui-Woog Choe^{1,2*}, Yong Ju Kim^{1*}, Jung Hee Park^{1*}, Takefumi Morizumi^{1†}, Emil F. Pai³, Norbert Krauß⁴, Klaus Peter Hofmann^{1,5}, Patrick Scheerer¹ & Oliver P. Ernst^{1†}

G-protein-coupled receptors (GPCRs) are seven transmembrane helix (TM) proteins that transduce signals into living cells by binding extracellular ligands and coupling to intracellular heterotrimeric G proteins (Gαβγ)¹. The photoreceptor rhodopsin couples to transducin and bears its ligand 11-*cis*-retinal covalently bound via a protonated Schiff base to the opsin apoprotein². Absorption of a photon causes retinal *cis/trans* isomerization and generates the agonist all-*trans*-retinal *in situ*. After early photoproducts, the active G-protein-binding intermediate metarhodopsin II (Meta II) is formed, in which the retinal Schiff base is still intact but deprotonated. Dissociation of the proton from the Schiff base breaks a major constraint in the protein and enables further activating steps, including an outward tilt of TM6 and formation of a large cytoplasmic crevice for uptake of the interacting C terminus of the Gα subunit^{3–5}. Owing to Schiff base hydrolysis, Meta II is short-lived and notoriously difficult to crystallize. We therefore soaked opsin crystals with all-*trans*-retinal to form Meta II, presuming that the crystal's high concentration of opsin in an active conformation (Ops*)^{6,7} may facilitate all-*trans*-retinal uptake and Schiff base formation. Here we present the 3.0 Å and 2.85 Å crystal structures, respectively, of Meta II alone or in complex with an 11-amino-acid C-terminal fragment derived from Gα (GαCT2). GαCT2 binds in a large crevice at the cytoplasmic side, akin to the binding of a similar Gα-derived peptide to Ops* (ref. 7). In the Meta II structures, the electron density from the retinal ligand seamlessly continues into the Lys 296 side chain, reflecting proper formation of the Schiff base linkage. The retinal is in a relaxed conformation and almost undistorted compared with pure crystalline all-*trans*-retinal. By comparison with early photoproducts we propose how retinal translocation and rotation induce the gross conformational changes characteristic for Meta II. The structures can now serve as models for the large GPCR family.

To obtain crystals of Meta II alone or in complex with the GαCT2 peptide, we followed previous approaches using low pH to obtain crystals of opsin in the active Ops* conformation^{6,7} for subsequent soaking with all-*trans*-retinal. GαCT2 was derived from the transducin Gα C terminus and contained two substitutions which improved crystal diffraction quality compared with crystals containing the native peptide fragment (see Methods). Reversible formation of Meta II is indicated by (1) the 380-nm absorption obtained before and after dissolving the all-*trans*-retinal-soaked opsin or opsin-GαCT2 crystals, respectively, (2) formation of an opsin-retinal Schiff base bond as determined by acid denaturation of the reconstituted pigments (Supplementary Fig. 1), (3) the X-ray crystallographic evidence for the Schiff base bond between all-*trans*-retinal and Lys 296^{7,43} of opsin (see below), and (4) the high activity of the reconstituted pigment towards the G protein (Supplementary Fig. 2). In addition, soaking of the opsin crystals with all-*trans*-retinal for an optimized soaking time had only little effect on the diffraction quality of the opsin crystals,

indicating that the Ops* conformation present in the crystal is compatible with the all-*trans*-retinal agonist. In contrast, soaking of opsin crystals with the inverse agonist 11-*cis*-retinal led to a reddish colour indicative of rhodopsin formation. Soaking was accompanied by severe loss of crystal diffraction quality, indicating disintegration of crystal packing, consistent with the expected larger conformational changes induced in the protein by 11-*cis*-retinal.

The structures of Meta II and Meta II-GαCT2 were solved at 3.0 and 2.85 Å resolution, respectively, by molecular replacement techniques using opsin in the Ops* conformation (PDB accession 3DQB) as search model. For crystallization, data collection, structure determination and refinement statistics, see Methods and Supplementary Table 1. The structures comprise amino acids 1–326 of the opsin protein moiety, lacking 22 C-terminal amino acids, which are not resolved in the corresponding electron density maps, presumably because of high mobility^{6,7}. Each model also includes one molecule all-*trans*-retinal, oligosaccharyl chains at Asn 2^{NT} (for superscripts see Methods Summary) and Asn 15^{NT}, several water and two *n*-octyl-β-D-glucopyranoside molecules, and in addition in the case of Meta II-GαCT2, the 11-amino-acid GαCT2 peptide. The models further comprise one molecule palmitic acid covalently bound to Cys 323^{H8}; a second palmitic acid residue at Cys 322^{H8} is lacking in each model because of weak electron density. The overall structure of Meta II and Meta II-GαCT2, comprising seven TMs connected by cytoplasmic and extracellular loops (CL1–CL3 and EL1–EL3) which are followed by the cytoplasmic helix H8, is similar to the previously solved Ops* and Ops*-GαCT structures^{6,7}, but quite different from inactive rhodopsin^{8–10}. The Cα root mean squared deviation (r.m.s.d.) values in Å are 0.51 (Ops*/Meta II), 0.44 (Ops*-GαCT/Meta II-GαCT2), 0.35 (Meta II/Meta II-GαCT2) and 2.85 (Rhodopsin/Meta II) (Fig. 1 and Supplementary Fig. 3)^{6,7,9}. Both Meta II and Meta II-GαCT2 display the open cytoplasmic receptor surface: due to a rotational tilt of TM6 and motion of TM5 a crevice in the cytoplasmic surface is created into which the Gα C terminus or its mimic, the GαCT2 peptide, can bind^{4,5,7}.

The Meta II structures now provide insight into retinal-protein interactions in the ligand binding site. The initial electron density map calculated with omitted retinal ligand could readily be interpreted with the relaxed all-*trans*-retinal conformation represented by the model obtained from the Cambridge Structural Database (reference code TRETAL02; Supplementary Figs 4 and 5). There is strong electron density connecting the retinal into the side chain of Lys 296^{7,43} consistent with the presence of a Schiff base bond between carbon atom C15 of retinal and the ε-amino group of Lys 296^{7,43} (Fig. 2 and Supplementary Fig. 4). The refinement of the Meta II structures only slightly changed the initial conformation of all-*trans*-retinal, indicating that retinal in a relaxed conformation is bound in the ligand binding site of Ops*, in agreement with spectroscopic studies on Meta II (ref. 11). Both structures, Meta II and Meta II-GαCT2, show an almost identical retinal conformation (Supplementary Fig. 5). The

¹Institut für Medizinische Physik und Biophysik - CC2, Charité - Universitätsmedizin Berlin, Charitéplatz 1, D-10117 Berlin, Germany. ²Department of Chemistry, College of Natural Science, Chonbuk National University, 561-756 Chonju, South Korea. ³Departments of Biochemistry, Molecular Genetics and Medical Biophysics, University of Toronto, 1 King's College Circle, Toronto, Ontario M5S 1A8, Canada. ⁴Queen Mary University of London, School of Biological and Chemical Sciences, London E1 4NS, UK. ⁵Zentrum für Biophysik und Bioinformatik, Humboldt-Universität zu Berlin, Invalidenstrasse 42, D-10115 Berlin, Germany. [†]Present addresses: Department of Biochemistry, University of Toronto, 1 King's College Circle, Toronto, Ontario M5S 1A8, Canada (T.M.); Departments of Biochemistry and Molecular Genetics, University of Toronto, 1 King's College Circle, Toronto, Ontario M5S 1A8, Canada (O.P.E.).

*These authors contributed equally to this work.

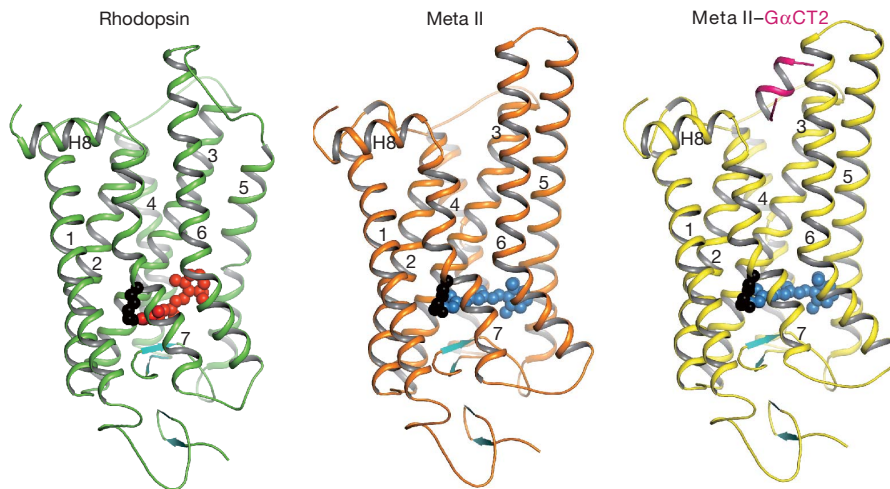


Figure 1 | Structures of inactive rhodopsin, active Meta II and Meta II in complex with a Gα fragment. Side view of cartoon model of rhodopsin (PDB accession 1U19), Meta II and Meta II–GαCT2, that is, Meta II in complex with an 11-amino-acid C-terminal peptide derived from the transducin Gα subunit, representing the key binding site on the heterotrimeric G protein. Inactive rhodopsin consists of the apoprotein opsin in its inactive conformation and the inverse agonist 11-*cis*-retinal (shown as red spheres), which is covalently bound to Lys 296 (shown as black spheres) via a Schiff base. In Meta II, the agonist all-

trans-retinal (shown as blue spheres) is covalently linked to Lys 296. The G-protein-interacting conformation of Meta II (right panel) is identified by the bound G α fragment (shown in purple). Transmembrane helices (numbered 1–7) are followed by a cytoplasmic helix H8. The Meta II models lack 22 C-terminal residues, the C terminus of rhodopsin is not shown. The extracellular domain contains four β -strands (coloured in cyan). Glycosylation at Asn 2 and Asn 15 and palmitoylation at Cys 322 and Cys 323 (at the end of H8) are not shown.

binding site for all-*trans*-retinal appears to be preformed in Ops* because the presence of retinal causes only a small adjustment of side chains (Trp 265^{6,48}, Tyr 268^{6,51}, Met 207^{5,42}, His 211^{5,46} and Glu 122^{3,37}) while the Lys 296^{7,43} side chain, which is more flexible in ligand-free Ops* (ref. 6), becomes ordered due to its linkage with retinal (Supplementary Fig. 6). The Meta II-G α CT2 structure reveals a potential

hydrogen bonding network in which a water molecule links the Schiff base nitrogen with the side chains of Ser 186^{EL2} and Glu 181^{EL2}, the latter hydrogen-bonded to the side chain of Tyr 268^{6,51} (Fig. 2 and Supplementary Fig. 7). A further water molecule constrains the main chain carbonyl of Glu 181^{EL2}, the side chain of Ser 186^{EL2} and the NH-groups of Ser 186^{EL2} and Cys 185^{EL2}. From Cys 185^{EL2} the hydrogen bonding

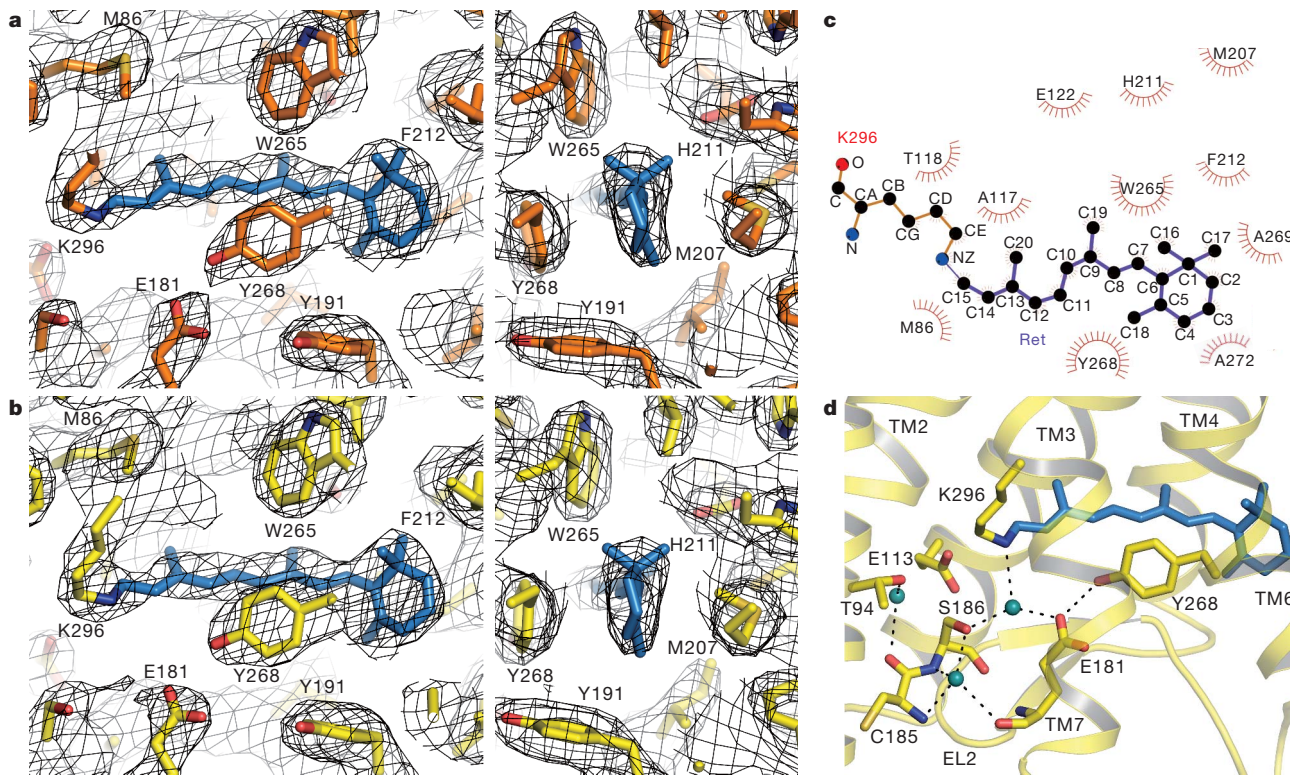


Figure 2 | Retinal binding pocket of Meta II. **a, b,** Retinal and neighbouring residues shown as stick model for Meta II (orange) and Meta II-G α CT2 (yellow), respectively, with $2F_o - F_c$ electron density map contoured at 1.0σ (grey mesh). View from within the membrane, right panel rotated 90° with respect to the left. Retinal is shown as blue stick model. **c,** Hydrophobic

interactions between all-*trans*-retinal and residues in the ligand binding pocket of the opsin protein moiety. Residues with closest distances less than 4 Å are considered to be in van der Waals contact. **d**, Potential hydrogen bonding interactions around retinal in Meta II- α CT2. Water molecules are shown as blue spheres.

network extends via a water molecule to the side chain of Thr 94^{2,61}. In the inactive rhodopsin conformation, a different network is found in which the Schiff base nitrogen is within hydrogen-bonding distance to the side chain of Glu 113^{3,28} from which the network can extend to Thr 94^{2,61} and via Ser 186^{EL2} to Glu 181^{EL2} (refs 9, 10). Together Glu 113^{3,28} and Glu 181^{EL2} form the counterion for the protonated Schiff base in inactive rhodopsin. From Fourier transform infrared (FTIR) studies on rhodopsin activation it was predicted that the main contribution to this complex counterion changes from Glu 113^{3,28} to Glu 181^{EL2} during the transition to Meta I (ref. 12). This is also reflected in the Meta II structure. Relative to rhodopsin, the distance between the Schiff base and the side-chain carboxyl group of Glu 113^{3,28} increases from 3.5 to 5.3 Å, whereas for Glu 181^{EL2} the corresponding distance decreases from 7.1 to 5.0 Å.

The Meta II-G α CT2 structure reveals additional structural water molecules next to amino acids in conserved motifs, extending the hydrogen-bonding network from Asn 302^{7,49} of the NPxxY(x)_{5,6}F motif to Glu 134^{3,49} of the E(D)RY motif. The lack of an interaction between Glu 134^{3,49} and Arg 135^{3,50} in Meta II-G α CT2 enables Arg 135^{3,50} to bind G α CT2 by forming a hydrogen bond to the backbone carbonyl oxygen of Val 347 of G α CT2. TM2 and TM7 are linked via a water molecule between Ser 298^{7,45} and highly conserved residues Asp 83^{2,50} and Asn 302^{7,49}. Structural water molecules are conserved in GPCRs¹³ and changes in radiolytic hydroxyl radical labelling have indicated activation-induced alterations in the local structures in which they are embedded¹⁴. Our data provide further insight into how water molecules are rearranged in the course of receptor activation (Supplementary Fig. 7).

In contrast to rhodopsin^{8–10}, but like Ops* (refs 6, 15), the Meta II structures show two openings of the retinal binding pocket (Supplementary Fig. 8). The opening between TM1 and TM7 is caused by a rotamer change of Phe 293^{7,40} relative to rhodopsin, which occurs in the course of a rotational rearrangement of the extracellular part of TM7 below the retinal attachment site Lys 296^{7,43} (Supplementary Fig. 9). The opening between TM5 and TM6 arises mainly from side-chain changes of Phe 208^{5,43}, Phe 212^{5,47} and Phe 273^{6,56} which are also observed in the Ops* structure⁶. The location of retinal in its binding site fulfils most distance constraints obtained from dipolar-assisted rotational resonance (DARR) NMR spectroscopy (Supplementary Table 2)^{16,17}. A few larger distance deviations indicate that perhaps different Meta II sub-states were observed in the NMR and X-ray experiments (see Scheme 1 in the Supporting Information).

Meta II shows, like Ops*, two gross conformational changes with respect to rhodopsin (Supplementary Fig. 3)^{6,7}. Motion of TM5 towards TM6 is linked to a rearrangement of the TM3-TM5 hydrogen bonding network between Glu 122^{3,37}, Trp 126^{3,41} and His 211^{5,46}. In Meta II, the side chains of Glu 122^{3,37} and His 211^{5,46} are close enough to form a hydrogen bond (Supplementary Figs 6 and 7). The second extensive conformational change involves TM6, which undergoes a rotational tilt resulting in a motion of its cytoplasmic end away from TM3 (Figs 3 and 4). For the corresponding structural rearrangement of residues in the conserved motifs E(D)RY (in TM3) and NPxxY(x)_{5,6}F (in TM7-H8) see the Supplementary Discussion.

Unexpectedly, all-*trans*-retinal in the reversibly formed Meta II appears to be rotated around its long axis compared with the dark state^{8–10}, and the early photoproducts Batho¹⁸ and Lumi¹⁹ (Fig. 3). The significant electron density observed for the methyl groups of the retinal polyene chain and β -ionone ring gives a preference for modelling retinal rotated approximately upside-down relative to Lumi (Fig. 3a) and non-satisfactory results when only the polyene chain was rotated but the β -ionone ring was kept as in Lumi (6-*s-trans* conformation). Retinal rotation is unlikely to occur with the packing seen in the Meta II crystal (Fig. 2c), but small TM movements in the receptor activation process, which can occur as early as in Meta I²⁰, may well provide the necessary space. The Meta II structure does neither reflect the proposed ‘toggle switch’ rotational change of Trp 265^{6,48}

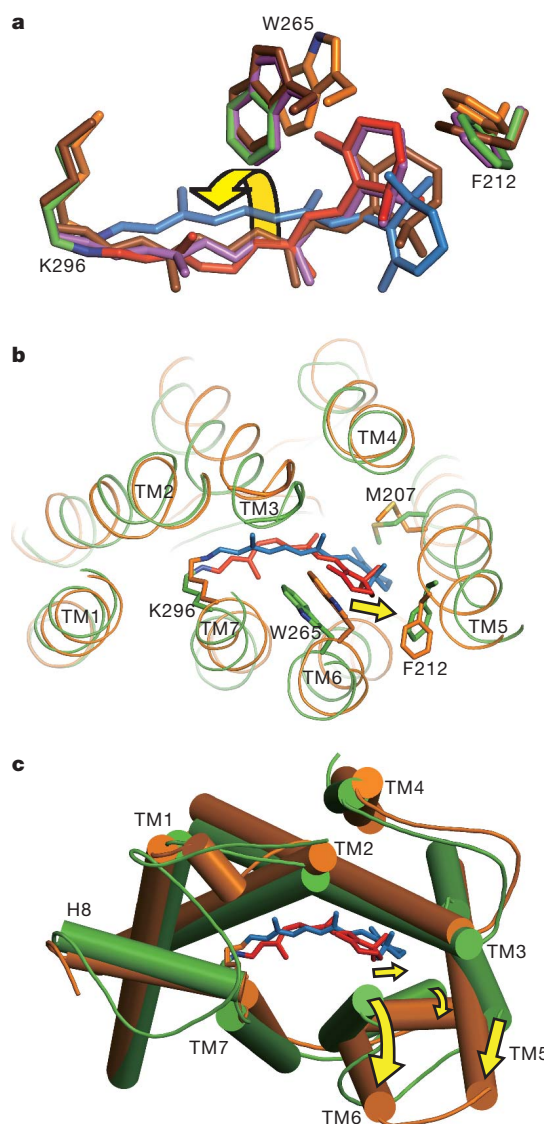


Figure 3 | Superposition of rhodopsin, Batho, Lumi and Meta II. **a**, View from within the membrane on superposition of retinal in rhodopsin (PDB 1U19), Batho (PDB 2G87), Lumi (PDB 2HPY) and Meta II. Amino acid side chains and retinal are shown as stick models. Protein/retinal are coloured green/red (rhodopsin), orange/blue (Meta II), purple/purple (Batho) and brown/brown (Lumi), respectively. The arrow indicates rotation of retinal from Lumi to Meta II. **b**, **c**, Superposition of rhodopsin and Meta II viewed from the cytoplasmic surface. Helices are shown as cartoon or cylinder models, retinal and amino acid side chains as stick models. For clarity, cytoplasmic ends of helices are clipped in **b**. Colours as in **a**. Elongation of retinal and interaction of the β -ionone-ring moiety with TM5/TM6 induces a rigid body-type rotational tilt of TM6 and motion of TM5 (indicated by arrows).

side chain^{17,21–23} nor the displacement of loop EL2 from the retinal binding site¹⁶. An explanation would be that these structural changes are transient and involved in switching to rather than maintaining the active conformation (see Supplementary Discussion and Supplementary Fig. 3). The Meta II structure also shows a positively twisted 6-*s-cis* conformation regarding the bond between carbon atoms C6 and C7 where retinal's β -ionone ring and polyene chain are connected. A negatively twisted 6-*s-cis* conformation as in the rhodopsin dark state, Batho and Lumi, was predicted for Meta I and Meta II by NMR spectroscopy^{17,24–26}, although flexibility of retinal even in the inactive receptor

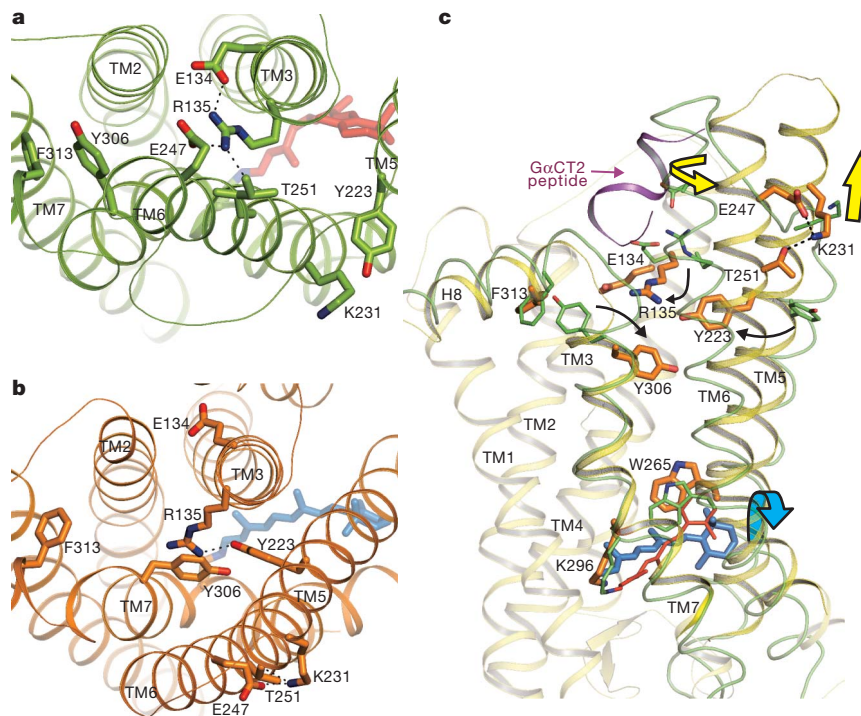


Figure 4 | Conserved E(D)RY and NPxxY(x)_{5,6}F regions. **a**, Rhodopsin and **b**, Meta II viewed from the cytoplasmic surface. Residues in the conserved E(D)RY and NPxxY(x)_{5,6}F motifs in TM3 and TM7/H8, respectively, constrain rhodopsin (green) in the inactive state. A hydrogen bonded network termed ‘ionic lock’ is formed between TM3 and TM6 including Glu 134^{3,49}, Arg 135^{3,50}, Glu 247^{6,30} and Thr 251^{6,34}. Tyr 306^{7,53} and Phe 313^{7,60} show an electrostatic interaction and are part of a functional microdomain between TM7 and H8. In Meta II and Meta II-GαCT2, the conserved residues form a different set of interactions. Glu 247^{6,30}-Lys 231^{5,66}-Thr 251^{6,34} and Tyr 223^{5,58}-Arg 135^{3,50}

state may allow negatively and positively twisted 6-*s-cis* conformations²⁷. An artificial pigment, in which ring rotation about the C6-C7 bond is inhibited, was reported to show lower but still substantial activity towards the G protein²⁸. The positive C5-C6-C7-C8 dihedral angle may thus be preferred but not mandatory to form an active state. Generally, a special status of the retinal in the active Meta II form fits well to previous FTIR spectroscopic results, which have shown that photo-induced back reactions are different between active Meta II and its inactive precursors (Supplementary Discussion).

The X-ray analysis of the reversibly formed Meta II has shown that the ligand fits readily into the binding pocket of Ops* and displays the same relaxed conformation as in pure retinal crystals. Ops* remains in its overall structure almost unchanged when the all-*trans*-retinal ligand binds, and the cytoplasmic G protein interaction domain of Ops* and Meta II carry the same insignia of an active state. On the other hand, comparison of rhodopsin and Meta II structures indicates that the retinal must go through complex elongation and torsional motions of its polyene chain and of the β-ionone ring. The motions of the ligand are likely to correspond to identified intermediates in the light induced pathway. Further structural and spectroscopic analyses may teach us how retinal analogues are less efficiently interrogated by the protein (ref. 29 and references therein), and may open insights into partial agonism and β-arrestin biased ligands at GPCRs. A more general lesson to be learned from this work on rhodopsin is that for reaching the active GPCR state, the receptor can make use of the conformational flexibility of the ligand and the variability of its interaction with the binding site.

METHODS SUMMARY

Opsin was extracted from bovine rod outer segment disc membranes using *n*-octyl-β-D-glucopyranoside and *n*-dodecyl-β-D-maltopyranoside. Solubilized

opsin was crystallized alone or in the presence of GαCT2 peptide (NH₂-ILENLKDVGLF-COOH; Gα₃₄₀₋₃₅₀(K341L,C347V)) by hanging-drop vapour diffusion in a mixture of ammonium sulphate and sodium acetate buffer at pH 5.0–5.8. Hundreds of opsin and opsin-GαCT2 crystals grown within 5 days were systematically soaked with all-*trans*-retinal for up to 30 h in the dark to reconstitute Meta II and Meta II-GαCT2, respectively. Crystals were cryoprotected in 10% trehalose and frozen in liquid nitrogen for screening and X-ray analysis at the synchrotron BESSY II, Berlin. The Meta II structures were solved by molecular replacement using opsin (PDB accession 3DQB) as search model.

The superscript denotes N terminus (NT; for example, Asn 2^{NT}), Helix 8 (H8; for example, Phe 313^{H8}), extracellular loop (EL; for example, Glu 181^{E12}), and GPCR numbering according to Ballesteros and Weinstein³⁰. The most conserved residue in a helix among rhodopsin-like GPCRs is designated x.50, where x is the helix number. All other residues on the same helix are numbered relative to this reference residue. Based on extensive sequence alignment, Smith grouped residues into signature-conserved, group-conserved or subfamily-specific¹⁷. Underlined superscript in GPCR numbering indicates GPCR signature residues (most conserved residues; Asn 55^{1.50}, Asp 83^{2.50}, Glu 134^{3.49}, Arg 135^{3.50}, Trp 161^{4.50}, Pro 215^{5.50}, Tyr 223^{5.58}, Trp 265^{6.48}, Pro 267^{6.50}, Asn 302^{7.49}, Pro 303^{7.50}, Tyr 306^{7.53}). Note that in ref. 17, based on a larger GPCR database, Leu 79 and Tyr 223 were attributed the most conserved residues on TM2 and TM5, respectively.

Full Methods and any associated references are available in the online version of the paper at www.nature.com/nature.

Received 9 September 2010; accepted 5 January 2011.

Published online 9 March 2011.

1. Rosenbaum, D. M., Rasmussen, S. G. & Kobilka, B. K. The structure and function of G-protein-coupled receptors. *Nature* **459**, 356–363 (2009).
2. Palczewski, K. G protein-coupled receptor rhodopsin. *Annu. Rev. Biochem.* **75**, 743–767 (2006).
3. Altenbach, C., Kusnetzow, A. K., Ernst, O. P., Hofmann, K. P. & Hubbell, W. L. High-resolution distance mapping in rhodopsin reveals the pattern of helix movement due to activation. *Proc. Natl Acad. Sci. USA* **105**, 7439–7444 (2008).

4. Hofmann, K. P. *et al.* A G protein-coupled receptor at work: the rhodopsin model. *Trends Biochem. Sci.* **34**, 540–552 (2009).
5. Choe, H.-W., Park, J. H., Kim, Y. J. & Ernst, O. P. Transmembrane signaling by GPCRs: insight from rhodopsin and opsin structures. *Neuropharmacology* **60**, 52–57 (2011).
6. Park, J. H., Scheerer, P., Hofmann, K. P., Choe, H.-W. & Ernst, O. P. Crystal structure of the ligand-free G-protein-coupled receptor opsin. *Nature* **454**, 183–187 (2008).
7. Scheerer, P. *et al.* Crystal structure of opsin in its G-protein-interacting conformation. *Nature* **455**, 497–502 (2008).
8. Palczewski, K. *et al.* Crystal structure of rhodopsin: a G protein-coupled receptor. *Science* **289**, 739–745 (2000).
9. Okada, T. *et al.* The retinal conformation and its environment in rhodopsin in light of a new 2.2 Å crystal structure. *J. Mol. Biol.* **342**, 571–583 (2004).
10. Li, J., Edwards, P. C., Burghammer, M., Villa, C. & Schertler, G. F. Structure of bovine rhodopsin in a trigonal crystal form. *J. Mol. Biol.* **343**, 1409–1438 (2004).
11. Siebert, F. Application of FTIR spectroscopy to the investigation of dark structures and photoreactions of visual pigments. *Isr. J. Chem.* **35**, 309–323 (1995).
12. Lücke, S. *et al.* The role of Glu181 in the photoactivation of rhodopsin. *J. Mol. Biol.* **353**, 345–356 (2005).
13. Angel, T. E., Chance, M. R. & Palczewski, K. Conserved waters mediate structural and functional activation of family A (rhodopsin-like) G protein-coupled receptors. *Proc. Natl Acad. Sci. USA* **106**, 8555–8560 (2009).
14. Angel, T. E., Gupta, S., Jastrzebska, B., Palczewski, K. & Chance, M. R. Structural waters define a functional channel mediating activation of the GPCR, rhodopsin. *Proc. Natl Acad. Sci. USA* **106**, 14367–14372 (2009).
15. Hildebrand, P. W. *et al.* A ligand channel through the G protein coupled receptor opsin. *PLoS ONE* **4**, e4382 (2009).
16. Ahuja, S. *et al.* Helix movement is coupled to displacement of the second extracellular loop in rhodopsin activation. *Nature Struct. Mol. Biol.* **16**, 168–175 (2009).
17. Smith, S. O. Structure and activation of the visual pigment rhodopsin. *Annu. Rev. Biophys.* **39**, 309–328 (2010).
18. Nakamichi, H. & Okada, T. Crystallographic analysis of primary visual photochemistry. *Angew. Chem. Int. Edn Engl.* **45**, 4270–4273 (2006).
19. Nakamichi, H. & Okada, T. Local peptide movement in the photoreaction intermediate of rhodopsin. *Proc. Natl Acad. Sci. USA* **103**, 12729–12734 (2006).
20. Ye, S. *et al.* Tracking G-protein-coupled receptor activation using genetically encoded infrared probes. *Nature* **464**, 1386–1389 (2010).
21. Shi, L. *et al.* $\beta 2$ adrenergic receptor activation. Modulation of the proline kink in transmembrane 6 by a rotamer toggle switch. *J. Biol. Chem.* **277**, 40989–40996 (2002).
22. Crocker, E. *et al.* Location of Trp265 in metarhodopsin II: implications for the activation mechanism of the visual receptor rhodopsin. *J. Mol. Biol.* **357**, 163–172 (2006).
23. Nygaard, R., Frimurer, T. M., Holst, B., Rosenkilde, M. M. & Schwartz, T. W. Ligand binding and micro-switches in 7TM receptor structures. *Trends Pharmacol. Sci.* **30**, 249–259 (2009).
24. Salgado, G. F. *et al.* Solid-state ^2H NMR structure of retinal in metarhodopsin I. *J. Am. Chem. Soc.* **128**, 11067–11071 (2006).
25. Ahuja, S. *et al.* $\beta 2$ -cis conformation and polar binding pocket of the retinal chromophore in the photoactivated state of rhodopsin. *J. Am. Chem. Soc.* **131**, 15160–15169 (2009).
26. Brown, M. F., Salgado, G. F. & Struts, A. V. Retinal dynamics during light activation of rhodopsin revealed by solid-state NMR spectroscopy. *Biochim. Biophys. Acta* **1798**, 177–193 (2010).
27. Lau, P. W., Grossfield, A., Feller, S. E., Pitman, M. C. & Brown, M. F. Dynamic structure of retinylidene ligand of rhodopsin probed by molecular simulations. *J. Mol. Biol.* **372**, 906–917 (2007).
28. Fujimoto, Y. *et al.* On the bioactive conformation of the rhodopsin chromophore: absolute sense of twist around the 6-s-cis bond. *Chem. Eur. J.* **7**, 4198–4204 (2001).
29. Knierim, B., Hofmann, K. P., Gartner, W., Hubbell, W. L. & Ernst, O. P. Rhodopsin and 9-demethyl-retinal analog: effect of a partial agonist on displacement of transmembrane helix 6 in class A G protein-coupled receptors. *J. Biol. Chem.* **283**, 4967–4974 (2008).
30. Ballesteros, J. A. & Weinstein, H. Integrated methods for the construction of three-dimensional models and computational probing of structure-function relations in G-protein coupled receptors. *Methods Neurosci.* **25**, 366–428 (1995).

Supplementary Information is linked to the online version of the paper at www.nature.com/nature.

Acknowledgements We thank J. Engelmann, C. Koch and B. Bauer for technical assistance, and F. Siebert and W. Hubbell for critically reading the manuscript. We are grateful to the European Synchrotron Radiation Facility (ESRF, Grenoble), D. von Stetten and A. Royant of the ID29S-Cryobench (ESRF, Grenoble) and U. Müller and the scientific staff of the BESSY-MX/Helmholtz Zentrum Berlin für Materialien und Energie at beamlines BL 14.1 and BL 14.2, where the data were collected, for continuous support. This work was supported by the DFG Sfb449 (to O.P.E.), Sfb740 (to O.P.E. and K.P.H.) and an Advanced Investigator ERC grant (to K.P.H.) and by the Canada Research Chairs Program (to E.F.P.). H.-W.C. gratefully acknowledges the Basic Science Research Program through the National Research Foundation of Korea (NRF) funded by the Ministry of Education, Science and Technology (2010-0002738) and CBNU funds for overseas research 2009. Y.J.K. thanks the Leibniz Graduate School of Molecular Biophysics, Berlin, for a scholarship.

Author Contributions H.-W.C., Y.J.K. and J.H.P. are joint first authors. H.-W.C., Y.J.K., J.H.P. performed preparation and crystallization of opsin/opsin–G α CT2. H.-W.C. performed the soaking experiment of both crystals. O.P.E. designed G α CT2. H.-W.C., Y.J.K., J.H.P., P.S., O.P.E. performed the data collection. Y.J.K., P.S., N.K. performed the structural analysis of Meta II, and J.H.P., P.S., E.F.P. performed the structural analysis of Meta II•G α CT2. T.M. performed the spectroscopic and biochemical analysis. H.-W.C., N.K., K.P.H., P.S., O.P.E. analysed data and H.-W.C., K.P.H., O.P.E. wrote the paper with contributions from all authors.

Author Information Atomic coordinates and structure factors for the reported structure have been deposited in the Protein Data Bank with the accession codes 3PQR and 3PXO. Reprints and permissions information is available at www.nature.com/reprints. The authors declare no competing financial interests. Readers are welcome to comment on the online version of this article at www.nature.com/nature. Correspondence and requests for materials should be addressed to H.-W.C. (hwchoe@bnu.ac.kr), K.P.H. (klaus_peter.hofmann@charite.de) or O.P.E. (oliver.ernst@utoronto.ca).

METHODS

Crystallization. Opsin was prepared and crystallized by hanging drop vapour diffusion at 277 K essentially as described^{6,7}. The solubilization buffer contained a mixture of 1% *n*-octyl- β -D-glucopyranoside and 0.02% *n*-dodecyl- β -D-maltopyranoside or *n*-octyl- β -D-glucopyranoside alone. The precipitant solution was 3.0–3.4 M $(\text{NH}_4)_2\text{SO}_4$ in 0.1 M sodium acetate buffer (pH 5.0–5.8). A synthetic peptide was used for co-crystallization of opsin with a C-terminal fragment derived from the α -subunit of the G protein transducin. The peptide G α CT2 (sequence NH₂-ILENLKDVGLF-COOH) is a derivative of the high-affinity G α CT peptide³¹ and has a similar affinity. Crystals appeared within 2 days and grew further for 3 days to reach dimensions 0.2 mm \times 0.3 mm \times 0.3 mm. All-*trans*-retinal was purchased from Sigma and further purified by normal phase HPLC using a LiChrosorb Si 60 (5 μ m) 300 mm \times 20 mm column with 5% diethylether in heptane. Opsin crystals were soaked in the dark with all-*trans*-retinal for up to 30 h to reconstitute Meta II. Crystals were then transferred under orange light to cryoprotectant consisting of 10% trehalose in crystallization buffer and immediately frozen in liquid nitrogen.

Structure analysis. Diffraction data collection was performed at 100 K using synchrotron X-ray sources at BESSY II, Berlin, Germany, and ESRF, Grenoble, France. Best diffraction data were collected at beamline BL 14.2 at BESSY II, at $\lambda = 0.91842$ Å. The crystal to MX-225 CCD detector distance was fixed at 230 mm for Meta II and 260 mm for Meta II–G α CT2, respectively. The rotation increment for each frame was 0.5° with an exposure time of 6 s (Meta II) or 12 s (Meta II–G α CT2). All images were indexed, integrated and scaled using the XDS program package³² and CCP4 program SCALA³³. Meta II and Meta II–G α CT2 crystals belong to rhombohedral space group *H*32 ($a = 241.82$ Å, $b = 241.82$ Å, $c = 111.80$ Å, $\alpha = \beta = 90^\circ$, $\gamma = 120^\circ$ and $a = 241.55$ Å, $b = 241.55$ Å, $c = 109.87$ Å, $\alpha = \beta = 90^\circ$, $\gamma = 120^\circ$, respectively). Supplementary Table 1 summarizes the statistics for crystallographic data collection and structural refinement.

Initial phases for Meta II and Meta II–G α CT2 were obtained by conventional molecular replacement protocol (rotation, translation, rigid body fitting) using opsin from the opsin–G α CT structure (PDB accession 3DQB) as initial search model. Molecular replacement was achieved using the CCP4 program PHASER³³ by first placing the opsin monomer (rotation function (RFZ): $Z = 14.5$; translation function (TFZ): $Z = 53.2$ for Meta II and rotation function (RFZ): $Z = 11.7$; translation function (TFZ): $Z = 63.5$ for Meta II–G α CT2, respectively; RFZ and TFZ as defined by PHASER). In subsequent steps, torsion angle molecular dynamics, simulated annealing using a slow-cooling protocol and a maximum likelihood target function, energy minimization, and *B*-factor refinement by the program CNS³⁴ were carried out in the resolution range 33.5–3.0 Å (Meta II) and 34.9–2.85 Å (Meta II–G α CT2). After the first round of refinement, the retinal chromophore was clearly visible in the electron density of both σ_A -weighted $2F_o - F_c$ maps, as well as in the σ_A -weighted simulated annealing omit density maps (Supplementary Fig. 4). Restrained, individual *B*-factors were refined and the crystal structure was finalized by the CCP4 program REFMAC5 and CCP4 (ref. 33). The final models have agreement factors R_{free} and R_{cryst} of 24.5% and 21.6% (Meta II), and 25.0% and 21.7% (Meta II–G α CT2), respectively. Manual rebuilding of the Meta II models and electron density interpretation were performed after each refinement cycle using the program COOT³⁵. Structure validation was performed with the programs PROCHECK³⁶ and WHAT_CHECK³⁷. Potential hydrogen bonds and van der Waals contacts were analysed using the programs HBPLUS³⁸ and LIGPLOT³⁹. All crystal structure superpositions of backbone alpha

carbon traces were performed using CCP4 program LSQKAB³³. All molecular graphics representations were created using PyMol⁴⁰.

Ultraviolet-visible spectroscopy. Ultraviolet-visible spectroscopy of Meta II was performed using a NanoDrop 1000 Spectrophotometer (Thermo Scientific) at room temperature and a CARY 50 Ultraviolet-visible Spectrophotometer (Varian) at 20 °C. Meta II crystals were washed thoroughly three times in crystallization buffer to reduce excess all-*trans*-retinal and were measured immediately in the same buffer. In some cases, Meta II crystals were dissolved in 1% *n*-octyl- β -D-glucopyranoside. Spectra were obtained before and after acid denaturation by addition of 1/10 volume 100 mM sulphuric acid.

Transducin activation assay. As a monitor for Gt activation, changes in intrinsic fluorescence intensity of the G α -subunit upon exchange of GDP to GTP γ S were quantified^{41–43}. All measurements were carried out using a SPEX fluorolog II spectrofluorometer equipped with a 450 W xenon arc lamp. For all activation measurements, settings were $\lambda_{\text{ex}} = 300$ nm and $\lambda_{\text{em}} = 345$ nm with an integration time of 1 s. Gt activation rates were measured with 2.5 nM opsin, 6 μ M GTP γ S, 2 mM DTT, and 0.006% (w/v) *n*-dodecyl- β -D-maltopyranoside in a final volume of 650 μ l (10 mm \times 4 mm cuvette with stirring bar). All samples were equilibrated at 20 °C for 4 min while being irradiated with yellow light (Schott GG 495 long-pass filter). Then reactions were triggered by addition of GTP γ S after recording basic fluorescence levels for 50 s. After recording the fluorescence change at the initial opsin concentration, activation of the whole Gt pool was achieved by adding 10 nM purified rhodopsin to the reaction. The concentration of intact opsin in every sample was calculated from the quantity of reconstituted rhodopsin by 500 nm absorption after addition of excess 11-*cis*-retinal to an aliquot of the sample measured. The 500 nm rhodopsin absorption was determined from difference spectra dark minus light-activated rhodopsin.

31. Herrmann, R. *et al.* Sequence of interactions in receptor-G protein coupling. *J. Biol. Chem.* **279**, 24283–24290 (2004).
32. Kabsch, W. XDS. *Acta Crystallogr. D* **66**, 125–132 (2010).
33. Collaborative Computational Project, Number 4. The CCP4 suite: programs for protein crystallography. *Acta Crystallogr. D* **50**, 760–763 (1994).
34. Brünger, A. T. *et al.* Crystallography & NMR system: a new software suite for macromolecular structure determination. *Acta Crystallogr. D* **54**, 905–921 (1998).
35. Emsley, P. & Cowtan, K. Coot: model-building tools for molecular graphics. *Acta Crystallogr. D* **60**, 2126–2132 (2004).
36. Laskowski, R. A., MacArthur, M. W., Moss, D. S. & Thornton, J. M. PROCHECK: A program to check the stereochemical quality of protein structures. *J. Appl. Cryst.* **26**, 283–291 (1993).
37. Hoof, R. W., Vriend, G., Sander, C. & Abola, E. E. Errors in protein structures. *Nature* **381**, 272 (1996).
38. McDonald, I. K. & Thornton, J. M. Satisfying hydrogen bonding potential in proteins. *J. Mol. Biol.* **238**, 777–793 (1994).
39. Wallace, A. C., Laskowski, R. A. & Thornton, J. M. LIGPLOT: A program to generate schematic diagrams of protein-ligand interactions. *Protein Eng.* **8**, 127–134 (1995).
40. DeLano, W. L. The PyMOL Molecular Graphics System. (DeLano Scientific, San Carlos, California, USA, 2002).
41. Fahmy, K. & Sakmar, T. P. Regulation of the rhodopsin-transducin interaction by a highly conserved carboxylic acid group. *Biochemistry* **32**, 7229–7236 (1993).
42. Ernst, O. P., Bieri, C., Vogel, H. & Hofmann, K. P. Intrinsic biophysical monitors of transducin activation: fluorescence, UV-visible spectroscopy, light scattering, and evanescent field techniques. *Methods Enzymol.* **315**, 471–489 (2000).
43. Ernst, O. P., Gramse, V., Kolbe, M., Hofmann, K. P. & Heck, M. Monomeric G protein-coupled receptor rhodopsin in solution activates its G protein transducin at the diffusion limit. *Proc. Natl Acad. Sci. USA* **104**, 10859–10864 (2007).

The structural basis of agonist-induced activation in constitutively active rhodopsin

Jörg Standfuss^{1,2}, Patricia C. Edwards², Aaron D'Antona³, Maikel Fransen¹, Guifu Xie³, Daniel D. Oprian³ & Gebhard F. X. Schertler^{1,2}

G-protein-coupled receptors (GPCRs) comprise the largest family of membrane proteins in the human genome and mediate cellular responses to an extensive array of hormones, neurotransmitters and sensory stimuli. Although some crystal structures have been determined for GPCRs, most are for modified forms, showing little basal activity, and are bound to inverse agonists or antagonists. Consequently, these structures correspond to receptors in their inactive states. The visual pigment rhodopsin is the only GPCR for which structures exist that are thought to be in the active state^{1,2}. However, these structures are for the apoprotein, or opsin, form that does not contain the agonist all-*trans* retinal. Here we present a crystal structure at a resolution of 3 Å for the constitutively active rhodopsin mutant Glu 113 Gln^{3–5} in complex with a peptide derived from the carboxy terminus of the α -subunit of the G protein transducin. The protein is in an active conformation that retains retinal in the binding pocket after photoactivation. Comparison with the structure of ground-state rhodopsin⁶ suggests how translocation of the retinal β -ionone ring leads to a rotation of transmembrane helix 6, which is the critical conformational change on activation⁷. A key feature of this conformational change is a reorganization of water-mediated hydrogen-bond networks between the retinal-binding pocket and three of the most conserved GPCR sequence motifs. We thus show how an agonist ligand can activate its GPCR.

In the dark, rhodopsin contains a covalently bound 11-*cis* retinal chromophore that preferentially binds to the inactive state and therefore functions as an inverse agonist in the visual system. On exposure to light, the retinal isomerizes to the all-*trans* form, initiating a series of conformational changes leading to the transient signalling state metarhodopsin II.

Crystal structures of bovine rhodopsin have been determined for the inactive state of the native protein bound to 11-*cis* retinal and from crystals of the protein following photoisomerization of the chromophore to the all-*trans* form⁸. However, these structures represent early photointermediates in the activation pathway^{9–11} that have not yet undergone the critical conformational alteration required for activation of the G protein.

Recently, two similar structures have been determined for the apoprotein form opsin^{1,2}. These are thought to represent activated forms of the receptor because one was determined for opsin bound to a peptide derived from the C-terminal tail of the α -subunit of the G protein transducin (the G α CT peptide) known to bind preferentially and stabilize the active intermediate metarhodopsin II¹². Although the opsin structures have been of immense value, a complete understanding of the active state requires structures in which the all-*trans* retinal agonist is included in the ligand-binding pocket of the receptor.

We have obtained such a structure by crystallization of the Glu 113 Gln^{3,28} mutant (superscripts denote Ballesteros–Weinstein general GPCR numbering¹³) that drastically slows hydrolysis and dissociation of all-*trans* retinal from the photoactivated protein by

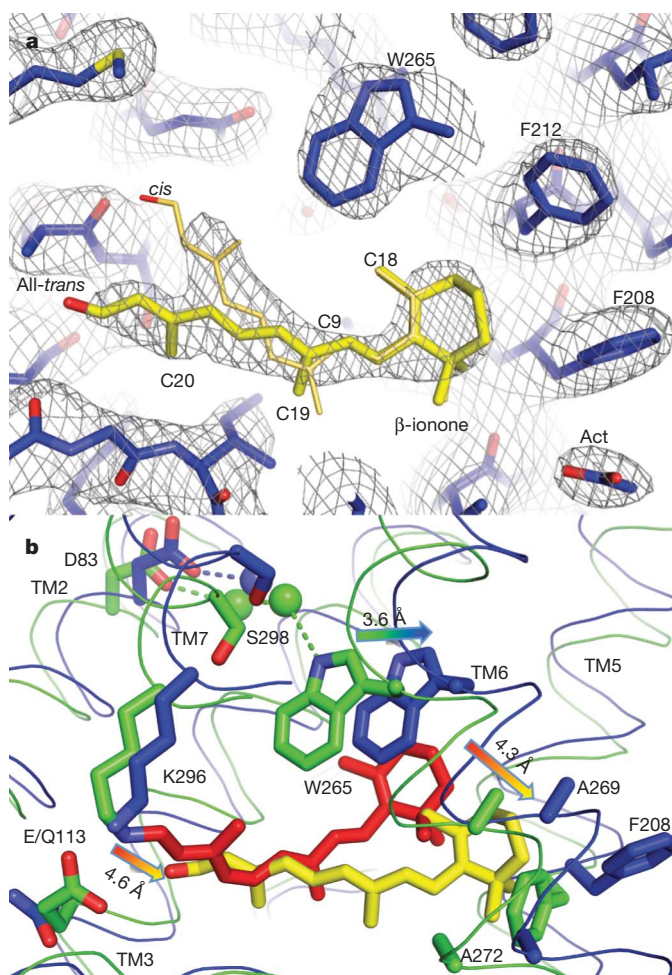


Figure 1 | Conformational changes in the retinal binding pocket.

a, $2F_o - F_c$ map (contoured at 1.5σ) of the retinal-binding pocket. The retinal β -ionone ring is well resolved whereas the density of the polyene chain broadens towards the end facing Lys 296^{7,43}. Occupancy refinements indicated a 60:40 mixture of all-*trans* retinal and a mixed population. An acetate molecule (Act) is packed between Phe 208^{5,43} and Phe 276^{6,59}, blocking a proposed retinal entry/exit channel¹. **b**, Superposition of Glu 113 Gln/G α CT (blue; PDB ID, 2X72) with ground-state rhodopsin (green; PDB ID, 1GZM⁶). The β -ionone ring of all-*trans* retinal (yellow) is shifted 4.3 Å towards the left between TM5 and TM6. This releases Trp 265^{6,48} from its locked position in the ground state and disrupts a water-mediated TM6–TM7 interaction involving Ser 298^{7,45} (ref. 28). The salt bridge between Glu 113^{3,28}, as counterion to the protonated Schiff base, and Lys 296^{7,43} is broken in the Glu 113 Gln/G α CT structure, removing the restraining TM3 and TM7 in the ground state⁵.

¹Paul Scherrer Institut, 5232 Villigen PSI, Switzerland. ²MRC Laboratory of Molecular Biology, Hills Road, Cambridge CB2 0QH, UK. ³Department of Biochemistry and Volen Center for Complex Systems, Brandeis University, Waltham, Massachusetts 02454, USA.

neutralization of the retinal counterion⁴. Furthermore, the mutant shifts the classical metarhodopsin I/metarhodopsin II equilibrium towards active metarhodopsin II and maintains metarhodopsin III in an active conformation¹⁴. Finally, the opsin form of the Glu 113 Gln^{3,28} mutant is constitutively active⁵, and addition of all-*trans* retinal to the apoprotein can activate the mutant to levels comparable to those of light-activated wild-type rhodopsin^{4,15}, essentially turning rhodopsin into a GPCR that is activated by diffusible agonists. However, the Glu 113 Gln^{3,28} mutant is also significantly less stable than wild-type rhodopsin (Supplementary Fig. 1), and for this reason we used the Glu 113 Gln mutation in the context of another rhodopsin mutant, Asn 2 Cys/Asp 282 Cys, which contains an engineered disulphide bond known to enhance thermal stability of the protein without affecting activity^{14,16} or structure¹⁷.

The Glu 113 Gln/Asn 2 Cys/Asp 282 Cys triple mutant (henceforth referred to simply as the Glu 113 Gln^{3,28} mutant) was reconstituted with 11-*cis* retinal during purification and, just before crystallization, was activated by selective illumination of protonated retinal in presence of the G α CT peptide. Crystals used for data collection had a faint yellow colour (Supplementary Fig. 2) indicative of bound retinal.

The structure contains residues 1–326 of the mutant opsin and all eleven residues of the G α CT peptide, including the Lys 341 \rightarrow Leu mutation introduced to increase affinity for the receptor¹⁸. In addition, clear electron density is observed for two partially ordered lipid molecules, one molecule of octylglucoside, several water molecules and, most strikingly, retinal within the ligand-binding pocket of the receptor. With the exception of the missing oligosaccharyl chain at position 2, the recombinantly produced protein contains all post-translational modifications observed with the native protein including acetylation of the amino terminus, palmitoylation of Cys residues at positions 322 and 323, and glycosylation of Asn at position 15. Finally, the engineered disulphide between Cys residues at positions 2 and 282 is clearly visible in the mutant.

The structure of the Glu 113 Gln/G α CT complex deviates significantly from the ground state of rhodopsin (Protein Data Bank ID,

1GZM⁶), but has high similarity to the active-state structure of the opsin/G α CT complex (PDB ID, 3DQB³), with respective C α root mean squared deviations of 2.42 Å and 0.58 Å (Supplementary Fig. 3). The Glu 113 Gln/G α CT structure is also in excellent agreement with the results of high-resolution distance mapping using double electron–electron resonance (DEER) spectroscopy where pairs of nitroxide spin labels (in particular at positions 241 and 252) were used to quantify an outward movement of transmembrane helix 6 (TM6) by 5 Å that is critical to the activation process⁷ (Supplementary Table 1). Other residues not showing significant change in the DEER experiments also do not show significant difference from ground-state rhodopsin in the Glu 113 Gln/G α CT structure.

On the basis of constitutive activity of the Glu 113 Gln^{3,28} mutant, the presence of the G α CT peptide and the agreement with the results of DEER spectroscopy, we conclude that the structure of the Glu 113 Gln/G α CT complex reported here is in fact that of the active state. Electron density for retinal (Fig. 1) is clearly observed in the general area where 11-*cis* retinal is found in ground-state rhodopsin. However, density for the nearby side chain of Lys 296^{7,43} is weak, indicating that retinal is not bound to the protein covalently by a Schiff base, as in the ground state or metarhodopsin II. In addition, density for the β -ionone ring and most of the polyene chain is well defined but shows increasing disorder after position C9. We have modelled retinal in the all-*trans* conformation, but on the basis of occupancy refinement we estimate a 60:40 mixture of all-*trans* retinal and a mixed population. However, we cannot distinguish between a model based on a mixture of *cis* and *trans* isomers, catalysed for example by phosphatidylethanolamine lipids¹⁹ or Lys 296^{7,43}, and one based on a mixture of conformers arising from rotations about single bonds in the polyene chain or one with residual, covalently bound all-*trans* retinal contributing to the density.

Clearly, the structure represents an active conformation but is not identical to metarhodopsin II. We suspect that it probably corresponds to a trapped intermediate in which the retinal is either entering or exiting the ligand-binding pocket. It is well established that wild-type

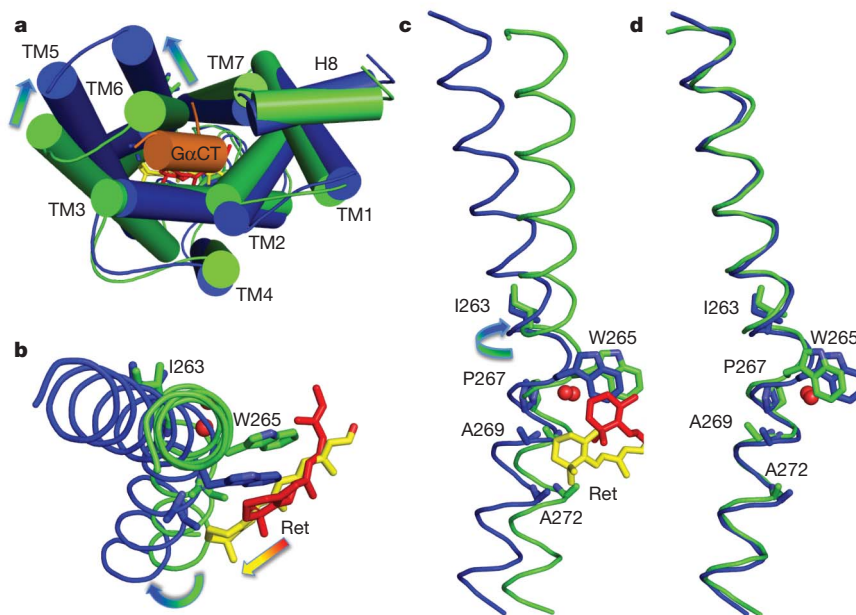
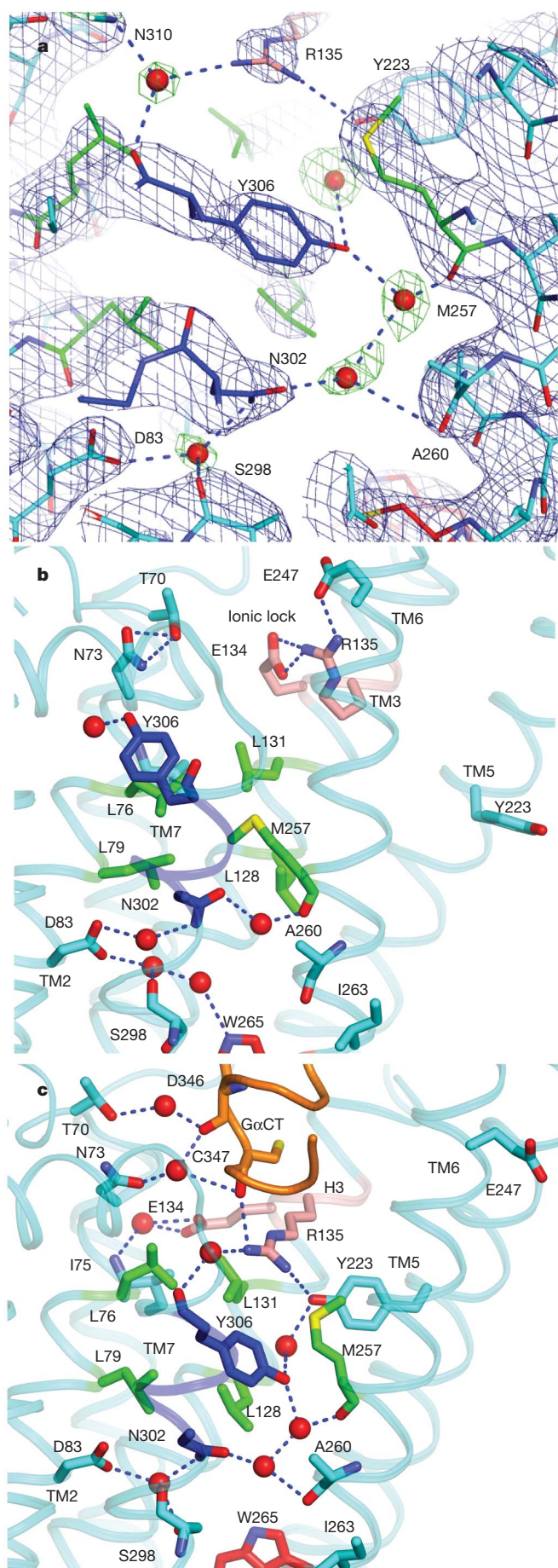


Figure 2 | Rearrangement of the heptahelix bundle and rotation of TM6. **a**, Superposition of C α traces of ground-state rhodopsin (green) and Glu 113 Gln (blue) with bound G-protein peptide (orange). The main rearrangements of transmembrane helices (cylinders) that open the G-protein-binding site are indicated as arrows. The loop regions have been smoothed for clarity. **b**, **c**, Cytoplasmic-side (**b**) and membrane-side (**c**) views of TM6 (C α traces in ribbon representation) from ground-state rhodopsin and the

Glu 113 Gln/G α CT structure illustrate how 11-*cis* (red) to all-*trans* (yellow) isomerization of retinal (Ret) can release Trp 265^{6,48} and lead to rotation of TM6. Resulting conformational changes are amplified towards the cytoplasmic side by the characteristic bend of the helix introduced by Pro 267^{6,50} and water molecule 7. **d**, Superposition of TM6 alone shows that the shape of the helix is preserved during the rearrangements.



opsin transiently activates as retinal enters the binding pocket but before a covalent bond to Lys 296^{7,43} has been formed²⁰, and that both all-*trans* and 11-*cis* retinol can act as potent partial agonists²¹. In this regard, the well-ordered ionone ring end of retinal and part of the polyene chain in the Glu 113 Gln/GαCT structure is probably in the same position that it occupies in metarhodopsin II. With respect to ground-state rhodopsin, the β-ionone ring is shifted by 4.3 Å (Fig. 1) and inserted in the cleft between TM5 (residues Met 207^{5,42}, Phe 208^{5,43} and Phe 212^{5,47}) and TM6 (residues Trp 265^{6,48}, Ala 269^{6,52} and Ala 272^{6,55}). This position is in agreement with two-dimensional dipolar-assisted rotational resonance NMR experiments on the retinal position in metarhodopsin II²².

The transition from inactive to active states evident on comparison of the ground-state and active-state structures is accompanied by a global rearrangement of the helix bundle (Fig. 2) that shifts the cytoplasmic end of TM6 (and to a lesser extent TM5) away from the bundle core (TM1–4 and TM7). This shift is not achieved through a hinge movement but by a rotation of TM6 that leaves the shape of the helix intact. On the cytoplasmic side, the conformational change is amplified by the characteristic bend caused by Pro 267^{6,50}, which is the most conserved residue in TM6 among GPCRs and part of the ubiquitous CWXP motif (where X denotes any amino acid). Pro 267^{6,50} is in close contact with water molecule 7, which is hydrogen-bonded to Cys 264^{6,47}, Tyr 268^{6,51} and Pro 291^{7,38}, an arrangement similar to that observed in ground-state rhodopsin. This water is found also in structures of the β₁-adrenergic²³, β₂-adrenergic²⁴ and adenosine receptors²⁵, and probably forms an important architectural element in formation of the bend in TM6.

Trp 265^{6,48} of the CWXP motif is a highly conserved amino acid that is tightly packed against retinal in ground-state rhodopsin and has been identified as important for GPCR activation through early mutagenesis studies. Trp 265^{6,48} has a central role in the toggle-switch model for activation of GPCRs^{26,27}. Our structure places the indole group of Trp 265^{6,48} 3.6 Å away from its ground-state position as a consequence of rhodopsin activation. However, we do not observe the rotamer change that was originally proposed on the basis of computer simulations. Instead, Trp 265^{6,48} follows the β-ionone ring, maintaining contact with the C18 methyl group. We suggest that the critical movement of TM6 stems from a motion of the β-ionone ring of retinal against TM6 just beneath the CWXP motif, while Trp 265^{6,48} is simultaneously released from its locked ground-state position.

Of special interest in the Glu 113 Gln/GαCT structure is a cluster of densities that indicate the presence of structural water molecules (Fig. 3) between some of the most conserved residues in GPCRs. Although modelling of water is difficult at resolutions around 3 Å, we are confident in their position because omission of water molecules during refinement resulted in clear difference peaks, presumably due to tight hydrogen bonding typical for structural water molecules in the interior of membrane proteins. Our interpretation is further strengthened by the presence of a similar water-mediated hydrogen-bond

Figure 3 | Rearrangement of water-mediated hydrogen-bond networks.

a, Our crystallographic data indicates water molecules that mediate interactions between the retinal-binding region and the GαCT-binding site. Omission of water molecules during simulated annealing results in strong electron density difference peaks (blue mesh, $2F_o - F_c$ map contoured at 2.0σ ; green mesh, $F_o - F_c$ map contoured at 3.0σ), demonstrating a high degree of local order. **b**, The retinal-binding pocket of ground-state rhodopsin is connected with Asn 302^{7,49} of the NPXXY motif (blue) via water-mediated hydrogen-bond networks⁶. A region called the hydrophobic barrier (green) separates this network from the E(D)RY motif (pink) critical for G-protein activation. **c**, In the active Glu 113 Gln/GαCT structure, rotation of TM6 disrupts the water-mediated link between Trp 265^{6,48} and Ser 298^{7,45} in TM7 and reorganizes the ground-state hydrogen-bond network. The hydrophobic barrier opens and Tyr 306^{7,53} of the NPXXY motif (blue) in TM7 and Tyr 223^{5,58} in TM5 rearrange to fill the resulting gap to extend the hydrogen-bond network towards the E(D)RY motif (pink) and the GαCT peptide (orange).

network found in ground-state rhodopsin that begins at Trp 265^{6,48}, involves the conserved Asp 83^{2,50} in TM2 and Ser 298^{7,45} and Asn 302^{7,49} (of the NPXXY motif) in TM7, and ends just below the hydrophobic barrier of six residues between TM2, TM3 and TM6 (Leu 76^{2,43}, Leu 79^{2,46}, Leu 128^{3,43}, Leu 131^{3,46}, Met 253^{6,36} and Met 257^{6,40}), of which many are conserved in rhodopsin-class GPCRs.

The Glu 113 Gln/G α CT structure indicates a rearrangement of this water cluster through rotation of TM6. The water-mediated link between Trp 265^{6,48} in TM6 and Ser 298^{7,45} in TM7 is broken, whereas Ser 298^{7,45}, together with water molecule 16, Asn 55^{1,50}, Asp 83^{2,50} and Asn 302^{7,49}, continues to stabilize the unusual Pro kink introduced in TM7²⁸ by Pro 303^{7,50}. These reorganizations are comparatively minor, but they directly link changes in the CWXP motif in the retinal-binding pocket with the two most conserved residues in TM1 and TM2, and the NPXXY motif in TM7. On the cytoplasmic side, the rotation of TM6 opens the hydrophobic barrier, allowing Tyr 223^{5,58} and Tyr 306^{7,53} of the NPXXY motif to swing into the protein interior from their positions in the ground state. The phenolic side chains provide additional interactions with water molecules 2 and 14, extending the hydrogen-bond network through the opened hydrophobic barrier up to the E(D)RY motif at the cytoplasmic surface of TM3. Residues Glu 134^{3,49} and Arg 135^{3,50} of this motif are released from the warped conformation in the ground state, which opens the ionic lock interactions²⁹ of Glu 134^{3,49}/Arg 135^{3,50} and Glu 247^{6,30} and allows binding of the G α CT peptide in a position that is occupied by TM6 in the ground state. Thus, rotation of TM6 and displacement of Trp 265^{6,48} results in a hydrogen-bond network connecting residues from the protein interior in contact with retinal to those at the cytoplasmic surface critical to activation of the G protein. The

hydrogen-bond network is further extended towards the G α CT peptide by water molecule 13 bridging Tyr 306^{7,53} and Arg 135^{3,50} with Asn 310^{8,47} in the TM7–H8 junction (Fig. 3). Asn 310^{8,47} in turn interacts with water molecule 9, which forms hydrogen bonds to Asn 73^{2,40} of the receptor and the backbone carbonyl of Asp 346 in the peptide. Asp 346 is linked to Thr 70^{2,37} of cytoplasmic loop 1 through water molecule 8, and the side chain is linked to Asn 343 of the peptide and Arg 147^{3,62} of the receptor through water molecule 5. Structural water molecules are thus likely to have a vital role in binding of the G protein to the active receptor.

We have described how translocation of the retinal β -ionone ring can lead to the conformational changes that allow rhodopsin to bind its G protein (Fig. 4). In doing so, we show how an agonist is bound to the active state of a GPCR and how activation is accompanied by a reorganization of hydrogen-bond networks between some of the most conserved residues among GPCRs.

METHODS SUMMARY

We cloned and expressed the rhodopsin gene containing the stabilizing Asn 2 Cys/Asp 282 Cys and Glu 113 Gln counterion mutations in HEK293S cells with restricted and homogenous *N*-glycosylation³⁰. The receptor was purified using a 1D4 immunoaffinity matrix and reconstituted with 11-*cis* retinal under dim red light as previously described¹⁷. Just before crystallization, we mixed purified rhodopsin with an equal weight of brain lipid extract, 10 μ M all-*trans* retinal and a tenfold molar excess of the G α CT/Lys 341 Leu peptide (ILENLKDCGLF). Rhodopsin was light-activated using a >515-nm long-pass filter to prevent exposure of free retinal and metarhodopsin II. The sample was mixed with an equal volume of 3.0–3.4 M ammonium sulphate, 100 mM sodium acetate, pH 4.5, and crystallized by vapour diffusion in the dark. We collected crystals under dim red light and soaked them in crystallization buffer containing 10% trehalose before freezing them. Diffraction data were collected at synchrotron X-ray sources (the Swiss Light Source, the European Synchrotron Radiation Facility and the Diamond Light Source), integrated using XDS and brought onto a common scale using SCALA. We obtained phases by molecular replacement with the opsin structures (PDB IDs, 3CAP¹ and 3DQB²) or ground-state rhodopsin (PDB ID, 1GZM⁶) as search model. The resulting solution was refined using iterative cycles of model building in COOT and refinement with PHENIX.

Full Methods and any associated references are available in the online version of the paper at www.nature.com/nature.

Received 10 March 2010; accepted 5 January 2011.

Published online 9 March 2011.

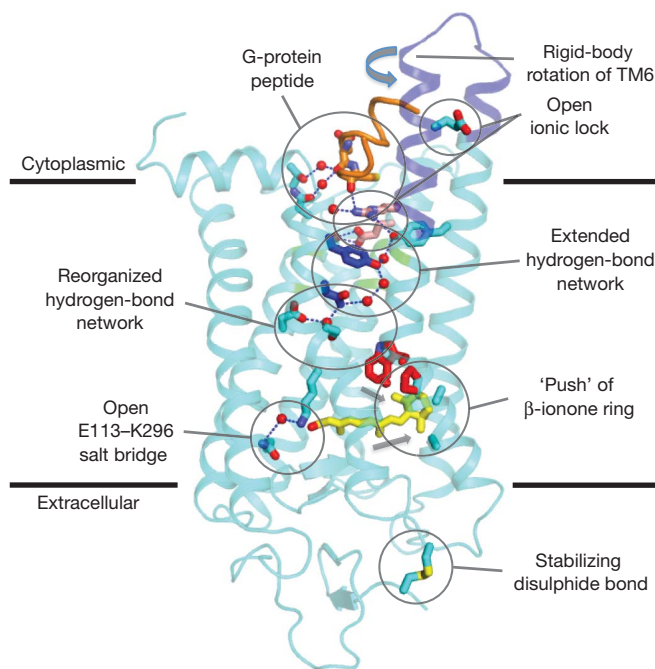


Figure 4 | Activation of rhodopsin by the agonist all-*trans* retinal. The protein backbone of Glu 113 Gln/G α CT is shown in cyan with predominant conformational changes in TM5 and TM6 (root mean squared deviation of C α atoms with respect to ground-state rhodopsin (PDB ID, 1GZM), >3.5 Å) in blue. The key regions involved in rhodopsin activation and discussed in the main text are highlighted. The side chains of the CWXP motif close to the retinal-binding site are coloured red. Side chains of the NPXXY motif (blue) extend the hydrogen-bond network through the hydrophobic barrier (green). Side chains of the E(D)RY motif, as part of the ionic lock and the G-protein-binding site, are coloured pink. The G α CT peptide is shown as an orange ribbon. The engineered disulphide bond in the extracellular domain is well isolated from the structural motifs involved in rhodopsin activation, which explains its neutral stabilizing characteristics^{14,16}.

1. Park, J. H. *et al.* Crystal structure of the ligand-free G-protein-coupled receptor opsin. *Nature* **454**, 183–187 (2008).
2. Scheerer, P. *et al.* Crystal structure of opsin in its G-protein-interacting conformation. *Nature* **455**, 497–502 (2008).
3. Zhukovsky, E. A. & Oprian, D. D. Effect of carboxylic acid side chains on the absorption maximum of visual pigments. *Science* **246**, 928–930 (1989).
4. Sakmar, T. P., Franke, R. R. & Khorana, H. G. Glutamic acid-113 serves as the retinylidene Schiff base counterion in bovine rhodopsin. *Proc. Natl Acad. Sci. USA* **86**, 8309–8313 (1989).
5. Robinson, P. R., Cohen, G. B., Zhukovsky, E. A. & Oprian, D. D. Constitutively active mutants of rhodopsin. *Neuron* **9**, 719–725 (1992).
6. Li, J. *et al.* Structure of bovine rhodopsin in a trigonal crystal form. *J. Mol. Biol.* **343**, 1409–1438 (2004).
7. Altenbach, C. *et al.* High-resolution distance mapping in rhodopsin reveals the pattern of helix movement due to activation. *Proc. Natl Acad. Sci. USA* **105**, 7439–7444 (2008).
8. Hofmann, K. P. *et al.* A G protein-coupled receptor at work: the rhodopsin model. *Trends Biochem. Sci.* **34**, 540–552 (2009).
9. Nakamichi, H. & Okada, T. Local peptide movement in the photoreaction intermediate of rhodopsin. *Proc. Natl Acad. Sci. USA* **103**, 12729–12734 (2006).
10. Ruprecht, J. J. *et al.* Electron crystallography reveals the structure of metarhodopsin I. *EMBO J.* **23**, 3609–3620 (2004).
11. Salom, D. *et al.* Crystal structure of a photoactivated deprotonated intermediate of rhodopsin. *Proc. Natl Acad. Sci. USA* **103**, 16123–16128 (2006).
12. Hamm, H. E. *et al.* Site of G protein binding to rhodopsin mapped with synthetic peptides from the alpha subunit. *Science* **241**, 832–835 (1988).
13. Ballesteros, J. & Weinstein, H. Integrated methods for the construction of three dimensional models and computational probing of structure-function relations in G protein-coupled receptors. *Methods Neurosci.* **25**, 366–428 (1995).
14. Standfuss, J., Zaitseva, E., Mahalingam, M. & Vogel, R. Structural impact of the E113Q counterion mutation on the activation and deactivation pathways of the G protein-coupled receptor rhodopsin. *J. Mol. Biol.* **380**, 145–157 (2008).

15. Cohen, G. B., Oprian, D. D. & Robinson, P. R. Mechanism of activation and inactivation of opsin: role of Glu113 and Lys296. *Biochemistry* **31**, 12592–12601 (1992).
16. Xie, G., Gross, A. K. & Oprian, D. D. An opsin mutant with increased thermal stability. *Biochemistry* **42**, 1995–2001 (2003).
17. Standfuss, J. *et al.* Crystal structure of a thermally stable rhodopsin mutant. *J. Mol. Biol.* **372**, 1179–1188 (2007).
18. Martin, E. L., Rens-Domiano, S., Schatz, P. J. & Hamm, H. E. Potent peptide analogues of a G protein receptor-binding region obtained with a combinatorial library. *J. Biol. Chem.* **271**, 361–366 (1996).
19. Groenendijk, G. W., Jacobs, C. W., Bonting, S. L. & Daemen, F. J. Dark isomerization of retinals in the presence of phosphatidylethanolamine. *Eur. J. Biochem.* **106**, 119–128 (1980).
20. Kefalov, V. J., Crouch, R. K. & Cornwall, M. C. Role of noncovalent binding of 11-*cis*-retinal to opsin in dark adaptation of rod and cone photoreceptors. *Neuron* **29**, 749–755 (2001).
21. Kono, M., Goletz, P. W. & Crouch, R. K. 11-*cis*- and all-*trans*-retinols can activate rod opsin: rational design of the visual cycle. *Biochemistry* **47**, 7567–7571 (2008).
22. Ahuja, S. *et al.* Location of the retinal chromophore in the activated state of rhodopsin. *J. Biol. Chem.* **284**, 10190–10201 (2009).
23. Warne, T. *et al.* Structure of a β_1 -adrenergic G-protein-coupled receptor. *Nature* **454**, 486–491 (2008).
24. Cherezov, V. *et al.* High-resolution crystal structure of an engineered human β_2 -adrenergic G protein-coupled receptor. *Science* **318**, 1258–1265 (2007).
25. Jaakola, V. P. *et al.* The 2.6 angstrom crystal structure of a human A_{2A} adenosine receptor bound to an antagonist. *Science* **322**, 1211–1217 (2008).
26. Shi, L. *et al.* Beta2 adrenergic receptor activation. Modulation of the proline kink in transmembrane 6 by a rotamer toggle switch. *J. Biol. Chem.* **277**, 40989–40996 (2002).
27. Schwartz, T. W. *et al.* Molecular mechanism of 7TM receptor activation—a global toggle switch model. *Annu. Rev. Pharmacol. Toxicol.* **46**, 481–519 (2006).
28. Pardo, L. *et al.* The role of internal water molecules in the structure and function of the rhodopsin family of G protein-coupled receptors. *ChemBioChem* **8**, 19–24 (2007).
29. Vogel, R. *et al.* Functional role of the “ionic lock”—an interhelical hydrogen-bond network in family A heptahelical receptors. *J. Mol. Biol.* **380**, 648–655 (2008).
30. Reeves, P. J., Callewaert, N., Contreras, R. & Khorana, H. G. Structure and function in rhodopsin: high-level expression of rhodopsin with restricted and homogeneous N-glycosylation by a tetracycline-inducible N-acetylglucosaminyltransferase I-negative HEK293S stable mammalian cell line. *Proc. Natl Acad. Sci. USA* **99**, 13419–13424 (2002).

Supplementary Information is linked to the online version of the paper at www.nature.com/nature.

Acknowledgements We thank X. Deupi and R. Vogel for discussions and reading of the manuscript. We thank R. Crouch for the kind gift of 11-*cis* retinal. P. J. Reeves we thank for providing the pACMVtetO vector and the HEK293S-GnT1[−] cells, and for his advice on creating stable cell lines and tetracycline-inducible expression. We also thank the staff at the macromolecular crystallography beamlines at the European Synchrotron Radiation Facility, the Diamond Light Source and the Swiss Light Source. The work was financially supported by NIH grant EY007965 (to D.D.O.), the Human Frontier Science Project programme grant RG/0052 (to D.D.O. and G.F.X.S.), the European Commission FP6 specific targeted research project LSH-2003-1.1.0-1 (to G.F.X.S.), the Marie Curie Intra European Fellowship MEIF-CT-2006-039171 (to J.S.) and the EMBO long-term fellowship ALTF 198-2006 (to J.S.).

Author Contributions The project was initiated by D.D.O. and G.F.X.S. J.S. performed cloning, initial expression and purification using essential experimental protocols and materials contributed by A.D. and D.D.O. Receptor activation and retinal binding studies were contributed by A.D. and G.X. Initial crystallization was by J.S., who also collected data and refined the structures. P.C.E. optimized expression and crystallization, performed crystal cryo-cooling and coordinated data collection. M.F. investigated the stability of mutant proteins. Manuscript preparation was performed by J.S. and D.D.O. The overall project management was by G.F.X.S.

Author Information Coordinates and structure factors have been deposited at the Protein Data Bank under accession code 2X72. Reprints and permissions information is available at www.nature.com/reprints. The authors declare no competing financial interests. Readers are welcome to comment on the online version of this article at www.nature.com/nature. Correspondence and requests for materials should be addressed to G.F.X.S. (gebhard.schertler@psi.ch).

METHODS

Preparation of stable cell line. The rhodopsin gene containing the stabilizing Asn 2 Cys/Asp 282 Cys and Glu 113 Gln counterion mutation was cloned into the pACMVtetO vector for tetracycline-inducible expression in mammalian cells³¹ using NotI and KpnI restriction sites. HEK293S-GnTI[−] cells with restricted and homogenous *N*-glycosylation were stably transfected with this vector as previously described³². Both vector and cells were a kind gift from Philip J. Reeves, University of Essex, UK.

Large-scale expression in wave bag bioreactors. Cells were expanded as adhesion cultures in DMEM/F12 medium supplemented with FBS (10%), PenStrep (Gibco), Geneticin-G418 (200 µg ml^{−1}) and blasticidin (5 µg ml^{−1}). Cells from five fully confluent 75-cm² flasks were collected and further expanded into a 300-ml suspension culture in Freestyle Medium (Invitrogen) supplemented with FBS (5%) and PenStrep. A wave bioreactor (GE Healthcare) was used to further expand the initial suspension cultures to a volume of 9.5 l with a cell density of 2 × 10⁶ cells per millilitre. Protein expression was induced by 0.5 l medium supplemented with tetracycline and sodium butyrate for final concentrations in the wave bag of 2 µg ml^{−1} and 5 mM, respectively. Cells were collected 72 h after induction at a density of (4–5) × 10⁶ cells per millilitre. Cell pellets were washed with PBS buffer containing protease inhibitor cocktail (complete protease inhibitor cocktail tablets, Roche) and stored at −80 °C. The modelled *N*-glycan in the final structure is based on the homogenous glycosylation pattern of the HEK293-GnTI[−] cell line³² used for expression and has been built as GlcNAc₂-Man₃ with two disordered mannose sugars. Crystal contacts between two *N*-glycans and palmitoyl chains that fill the cavity between the two rhodopsin molecules in the crystallographic dimer suggest that the homogeneous post-translational modifications are an important factor in crystal formation.

Purification. Cell pellets were solubilized for 1 h at 4 °C with PBS buffer containing protease inhibitor tablets (complete protease inhibitor cocktail tablets, Roche) and 1.25% DM (β-decylmaltoside). Nuclei and other unsolubilized material were removed by centrifugation and the supernatant incubated with 1D4 antibody coupled to CNBr-activated sepharose (Amersham Biosciences). After 3–4 h the matrix was washed with PBS, pH 7, and 0.125% DM. Ground-state rhodopsin was reconstituted by adding 11-*cis* retinal (50 µM) to the matrix and overnight incubation at 4 °C. All steps involving retinal were performed under dim red light.

The matrix was washed with PBS, pH 7.0, and 0.125% DM, followed by 10 mM Hepes, pH 7.0, and 1% OG (β-octylglycoside). The purified protein was eluted in the same buffer supplemented with an elution peptide resembling the C terminus of rhodopsin (TETSQVAPA, 80 µM). The eluate was reduced to 0.5 ml using a 50-kD cut-off concentrator before gel filtration on a Superdex200 column. The gel filtration step was used to exchange the buffer for 10 mM Mes, pH 5.0, 100 mM NaCl, and 1% OG, which leads to protonation of the Schiff base in the Glu 113 Gln counterion mutant and shifts the absorption maximum from 382 to 498 nm (refs 33–35).

Light activation and crystallization. Reconstituted Glu 113 Gln was concentrated to 5–7.5 mg ml^{−1} (Vivaspin, 50-kD cut-off concentrator) and mixed with dried brain lipid extract (Avanti Polar Lipids, 1 w/w, 10 µM all-*trans* retinal). The sample was briefly sonicated and incubated for 30 min in presence of a tenfold molar excess of peptide resembling the last 11 amino acids of the Gα subunit of the G protein carrying the mutation Lys 341 Leu (ILENLKDCGLF, Advanced Biomedical). The receptor was activated for 5 min using a >515-nm long-pass filter that prevented light exposure of free retinal and metarhodopsin II.

The sample was mixed 1:1 with 3.0–3.4 M ammonium sulphate, 100 mM sodium acetate, pH 4.5, and crystallized by sitting-drop vapour diffusion in the dark. Crystals were collected under dim red light and soaked in crystallization buffer containing 10% trehalose before freezing in liquid nitrogen.

Data collection and structure determination. The diffraction quality of the crystals was assessed at several synchrotron X-ray sources (the Swiss Light Source, the European Synchrotron Radiation Facility and the Diamond Light Source). The best data with a maximum resolution of 2.9 Å was collected at the microfocus beamline ID23eh-2 at the European Synchrotron Radiation Facility by the helical data collection method. Data were integrated using XDS³⁶ and brought onto a common scale using SCALA from the CCP4 program suite³⁷. Data set statistics are given in Supplementary Table 2.

Phases were obtained by molecular replacement using the program PHASER³⁸ and the polypeptide of the opsin structures (PDB IDs, 3CAP³⁹ and 3DQB⁴⁰) or the ground-state rhodopsin structure (PDB ID, 1GZM⁴¹) as search model. The resulting solution was refined using iterative cycles of model building in COOT⁴² and refinement (rigid body, energy minimization, simulated annealing, individual B-factor refinement) with the PHENIX program suite⁴³. Water molecules were added to the model on the basis of five criteria: the presence of clear difference peaks in a 2.5σ-contoured $F_o - F_c$ electron density map calculated after simulated annealing refinement in which water molecules have been omitted (Fig. 3); density above 1σ in 2 $F_o - F_c$ maps refined with the inclusion of water molecules; two or more hydrogen bonds to the protein or other water molecules; a B-factor cut-off within 20% of the average; and interpretable density in maps calculated with both data sets.

Geometric restraints for lipids and heteroatoms were prepared using the PRODRG2 server (<http://davapc1.bioch.dundee.ac.uk/prodrg/>) and HIC-Up database (<http://xray.bmc.uu.se/hicup/>). Coordinates for all-*trans* and 9-*cis* retinal were obtained from the Cambridge Small Molecule Database. Retinal geometry restraints used in the refinement were prepared by carefully adjusting torsion angles and planarity restraints in the retinal parameter file distributed as part of the CCP4 program suite.

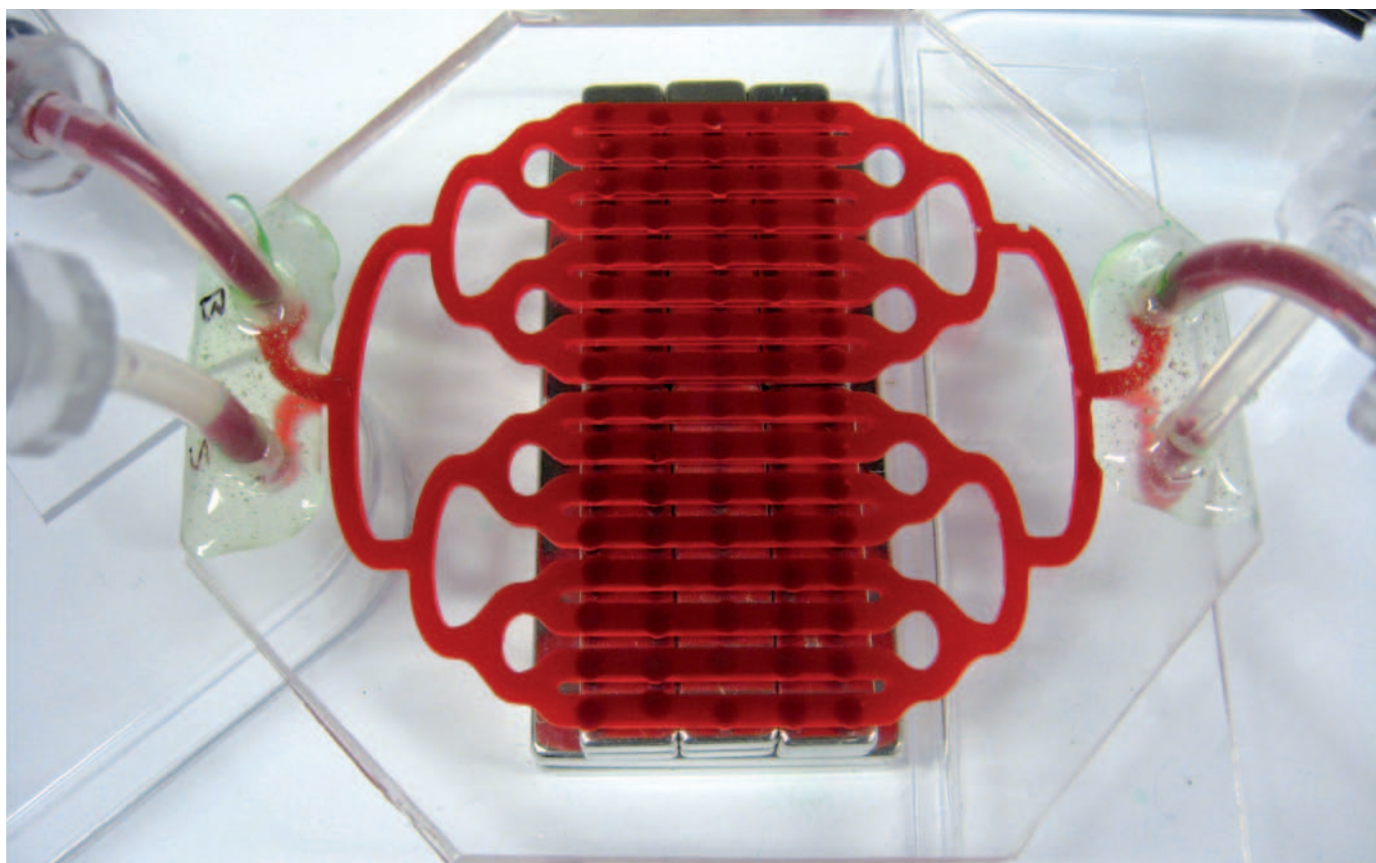
- Reeves, P. J., Kim, J. M. & Khorana, H. G. Structure and function in rhodopsin: a tetracycline-inducible system in stable mammalian cell lines for high-level expression of opsin mutants. *Proc. Natl Acad. Sci. USA* **99**, 13413 (2002).
- Reeves, P. J., Callewaert, N., Contreras, R. & Khorana, H. G. Structure and function in rhodopsin: high-level expression of rhodopsin with restricted and homogeneous *N*-glycosylation by a tetracycline-inducible *N*-acetylglucosaminyltransferase I-negative HEK293S stable mammalian cell line. *Proc. Natl Acad. Sci. USA* **99**, 13419 (2002).
- Sakmar, T. P., Franke, R. R. & Khorana, H. G. Glutamic acid-113 serves as the retinylidene Schiff base counterion in bovine rhodopsin. *Proc. Natl Acad. Sci. USA* **86**, 8309 (1989).
- Zhukovsky, E. A. & Oprian, D. D. Effect of carboxylic acid side chains on the absorption maximum of visual pigments. *Science* **246**, 928 (1989).
- Standfuss, J., Zaitseva, E., Mahalingam, M. & Vogel, R. Structural impact of the E113Q counterion mutation on the activation and deactivation pathways of the G protein-coupled receptor rhodopsin. *J. Mol. Biol.* **380**, 145 (2008).
- Kabsch, W. Automatic processing of rotation diffraction data from crystals of initially unknown symmetry and cell constants. *J. Appl. Cryst.* **26**, 795 (1993).
- Collaborative Computational Project, Number 4. The CCP4 suite: programs for protein crystallography. *Acta Crystallogr. D* **50**, 760–763 (1994).
- McCoy, A. J., Grosse-Kunstleve, R. W., Storoni, L. C. & Read, R. J. Likelihood-enhanced fast translation functions. *Acta Crystallogr. D* **61**, 458–464 (2005).
- Park, J. H. *et al.* Crystal structure of the ligand-free G-protein-coupled receptor opsin. *Nature* **454**, 183 (2008).
- Scheerer, P. *et al.* Crystal structure of opsin in its G-protein-interacting conformation. *Nature* **455**, 497 (2008).
- Li, J. *et al.* Structure of bovine rhodopsin in a trigonal crystal form. *J. Mol. Biol.* **343**, 1409 (2004).
- Emsley, P. & Cowtan, K. Coot: model-building tools for molecular graphics. *Acta Crystallogr. D* **60**, 2126–2132 (2004).
- Adams, P. D. *et al.* PHENIX: building new software for automated crystallographic structure determination. *Acta Crystallogr. D* **58**, 1948–1954 (2002).

TECHNOLOGY FEATURE

A LIVING SYSTEM ON A CHIP

For years, scientists have struggled to reconstruct tissues and organs by combining cells and nanotechnology. These devices are now edging from cool concept to practical application.

WYSS INST.



Researchers are making miniature versions of organs such as the spleen (above). Such organs on chips could speed tests of drugs and toxicity.

BY MONYA BAKER

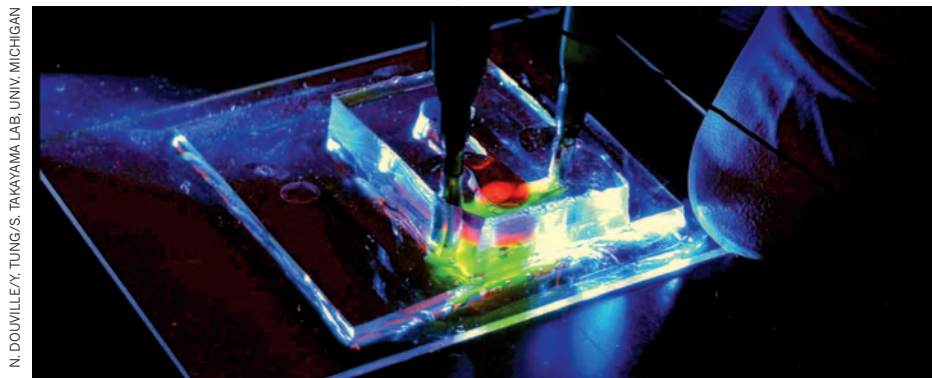
For more than a decade, researchers have been etching grooves into silicon and plastic wafers, filling the spaces with living cells, and hoping that the resulting devices will mimic biological systems such as the liver or gut. Scientists at the Wyss Institute for Biologically Inspired Engineering at Harvard University in Boston, Massachusetts, have created one of the most sophisticated devices so far: a lung on a chip that represents several types of tissue¹. “We started with the simplest embodiment of human airway and capillary cells, and then introduced immune cells,” says Donald Ingber, head of the

institute. The chip holds a pair of microchannels separated by a flexible, porous 10-micrometre membrane. One channel contains air and a layer of epithelial cells such as those lining the tiniest air sacs in the lung; the other holds the type of cell that lines capillaries, along with flowing liquid to simulate blood. The set-up even models breathing: vacuum chambers attached to the channels simulate the mechanical forces that cells encounter as a person’s chest expands and contracts.

The chip showed that the cells’ behaviour changes when they are stretched. To model the effects of air pollution on the lungs, Ingber’s team placed toxic nanoparticles on the surface

of the air-sac cells. More particles moved across the membrane from the air channel to the blood channel when the vacuum-controlled ‘breathing’ apparatus was operating than when the ‘lung’ was at rest, indicating that toxicity tests on static cells underestimate the detrimental effects of airborne particulates. More-complex behaviours could also be monitored: when substances known to provoke an immune response were introduced into the air channel, white blood cells migrated across the membrane, simulating what occurs in actual inflamed lungs.

The goal, says Ingber, is not to make replacement organs for transplant, but to replicate enough of a lung’s functions to make the chips



N. DOUVILLEY, TUNG/S. TAKAYAMA LAB, UNIV. MICHIGAN

An air sac on a chip can mimic the mechanical stress on cells caused by fluid in the lungs.

useful in testing substances for therapeutic and toxic effects. “We are not making a lung,” he says. “We are inspired by design principles of what makes a lung relevant physiologically.”

Although researchers have many ways to study isolated proteins and cultured cells, experimenting on tissues generally requires whole animals or freshly dissected body parts. Such experiments are costly and often unreliable, and can raise ethical issues. Organs on chips are still very much a work in progress, but advances in culturing cells and manufacturing nanomaterials mean that they could eventually supplement or supplant animal studies.

A little-appreciated advantage is that the chips are more consistent than whole mice, says Judith Swain, executive director of the Singapore Institute for Clinical Sciences. “People may say it’s halfway between *in vitro* models and animal models,” she says, “but it goes past that. It endeavours to create the smallest functional unit so that you can control things and you’re not confounded by variability.”

Chips need further validation before they can move from research project to research tool. “We think this is tremendously exciting, but it has a good way to go before it can substitute for some of these animal tests,” says Jesse Goodman, chief scientist at the US Food and Drug Administration (FDA). Nonetheless, the agency is preparing guidelines on how to replace animal tests with chips or related technologies, including computational and cell-based screening. Even if the FDA does not end up considering experiments on chips to make its decisions, says Goodman, the technology can still make drug discovery more efficient by helping companies to decide which drug candidates to prioritize for animal studies. The chips will be especially useful, he says, if they can be used to study toxicity over several days of repeated exposure, or if they can be seeded with cells from different patient groups to reflect varying responses to drugs.

The simulated lung will need to be even more complex than it is at the moment, says Alan Ezekowitz, an immunologist at Merck Research Laboratories in Rahway, New Jersey. “The lung on a chip is the beginning; it’s a very simple prototype,” he says. Modelling how

absorption changes as cells stretch is impressive, but Ezekowitz would like a way to model the lungs’ muscles too, so that screens can assess what might cause effects such as spasms in the bronchial tubes. And the Wyss Institute’s current chip includes only one kind of white blood cell — neutrophils — when in fact the lung is monitored by several types, including dendritic cells, lymphocytes and macrophages, all modulating each other’s effects.

Ingber is adding more types of cell. He foresees the lung on a chip eventually being seeded with cells derived from people with conditions such as asthma, being customized for different assays, or being used to gauge rates of

pulmonary scarring or absorption of inhaled drugs. Chips won’t replace animal testing, says Ingber, but they could reduce it and provide options for diseases for which no good animal models exist.

TACKLING THE WHOLE ANIMAL

Given the difficulty of recreating a single organ, representing the entire body on a chip sounds impossible — but it was actually one of the first biology-on-a-chip projects to be tackled. Michael Shuler, a bioengineer at Cornell University in Ithaca, New York, is credited with coining the phrase ‘animal on a chip’ in the late 1990s, after he and a colleague, Gregory Baxter, began etching silicon wafers to form tiny compartments that would hold gut, liver and fat cells, all linked by microfluidic channels. The approach, which Shuler calls a “microscale cell-culture analogue”, is a physical manifestation of mathematical models used to predict how drugs move through and accumulate in various organs².

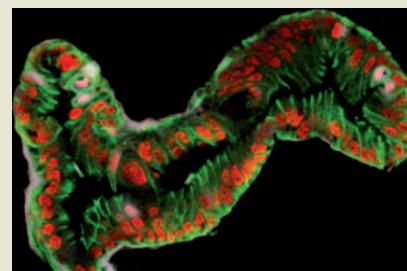
Frank Sonntag, a biosystems technologist at the Fraunhofer Institute for Material and Beam Technology in Dresden, Germany, leads a group that is trying to predict systemic toxicity using what Sonntag calls a chip-based multi-micro-organoid culture system³. His chips hold six identical micro-bioreactors, each containing cells chosen to mimic the liver,

Just cells

The development of simulated tissues on chips has been hindered because researchers couldn’t grow cells that functioned as they would in the body. That may be changing, says Alan Ezekowitz, an immunologist at Merck Research Laboratories in Rahway, New Jersey. “The birth of embryonic stem cells and induced pluripotent stem (iPS) cells has provided a biological opportunity to mesh into bioengineering expertise.” Such cells could be used without chips, because they can develop into complex tissues on their own.

James Wells, a molecular biologist at the Cincinnati Children’s Hospital Medical Center in Ohio, this year showed that iPS cells can form hollow clumps called spheroids. These are made of multiple types of cell, including mucin-secreting goblet cells and nutrient-absorbing enterocytes⁸. Hans Clevers, a molecular geneticist at the Hubrecht Institute in Utrecht, the Netherlands, and his colleagues had previously made similar structures using intestinal stem cells⁹.

Most drugs are swallowed, and enter the bloodstream through the intestines, so scientists hope that reconstructed gut tissue will be useful in medical research. “You can envision a lot of primary drug screens



Pluripotent stem cells form gut tissue *in vitro*.

that are looking not just for toxicity but also absorption and bioavailability,” says Wells. The gut also makes several hormones that influence appetite and obesity, he says, and the structures could be used to hunt for compounds that modulate the secretion of these hormones. But there are several challenges: the cells need to be produced in larger quantities, and they must be adapted to culture conditions amenable to monitoring.

Meanwhile, Wells and others are trying to create structures to represent other organs. “That really is the next step for a lot of tissues, to generate three-dimensionality,” says Wells. Upcoming tissues on chips might not be on chips at all. **M.B.**

J. WELLS LAB

brain and bone marrow. A third team, led by Kiichi Sato, a bioanalytical chemist at the University of Tokyo, has created a chip⁴ to test how cell lines representing breast cancer, liver and intestine interact with drugs.

One difficulty with the chips is the complexity of modelling the proportion and sequence of blood flow to each 'organ'. Shuler says that some devices capture blood distribution at least as well as mathematical models, but they do not model other aspects, such as how blood flows within an organ.

The greater issue, however, is that current devices rely on cell lines that grow readily in culture, rather than the more-finicky cells that better represent organ function. Chips will become more predictive in the next few years as researchers learn to cultivate "more authentic" cells, says Shuler.

FROM ANIMALS TO ORGANS

Shuler is now working on reconstructing better models of the organs through which drugs move. The intestines, a barrier that must be passed by all swallowed drugs, seem surprisingly easy to model (see 'Just cells'): using cell lines representing only the gut epithelium, mucin-secreting cells and lymphocytes, Shuler and his colleagues have been able to recreate the mucoid layer in the gut⁵. With the help of an absorbent polymer gel that can be used to

build microscale scaffolding, the team has even crafted a collagen structure to represent the villi that line the intestinal wall⁶. Meanwhile, the Wyss team is developing a model of the gut that mimics peristalsis using vacuum chambers similar to those in the lung chip. This model



"More complex cultures are needed for more complex questions."

Linda Griffith

allows researchers to observe molecules passing from the gut chamber into the blood chamber, says Ingber.

Several companies are developing chips that can be used as miniature testing systems. Myomics in Providence, Rhode Island, for example, grows models of skeletal muscle in multi-well plates. It is collaborating with pharmaceutical partners to screen drugs that might harm muscles, as well as one that could be used to treat muscle disorders.

It can be difficult to create systems that are robust enough to be shipped and simple enough for most scientists to use, says Robert Freedman, chief executive of Hurel in New Brunswick, New Jersey. The company was

co-founded by Baxter in 2005 and is developing chips to investigate liver toxicity and skin allergies. Part of the product-development process, says Freedman, was switching from opaque silicon chips to transparent plastic ones, to enable microscopy studies. Company researchers also had to put chips packed with living cells on an aeroplane to make sure that they could withstand pressure changes during shipping.

The company's most important task is picking systems that scientists want to buy. For example, a European Union directive to phase out animal testing for cosmetics from 2009 has created a market for *in vitro* evaluation of skin irritants, so Hurel is working with the world's largest cosmetics company, L'Oréal in Paris, to develop a replacement for a test in which a potential allergen is rubbed behind a mouse's ear. The 'allergy test on a chip' holds skin and immune cells. "Once you work out all the kinks, it will be better than the animal test because you'll use all-human materials," says Martin Yarmush, chief scientific adviser at Hurel.

LEARNING ABOUT THE LIVER

Liver toxicity is among the most common biological reasons for drug candidates to be pulled from clinical development, so it is important to be able to predict it. Even if a molecule does not harm the liver, that organ's detoxifying

The real McCoy

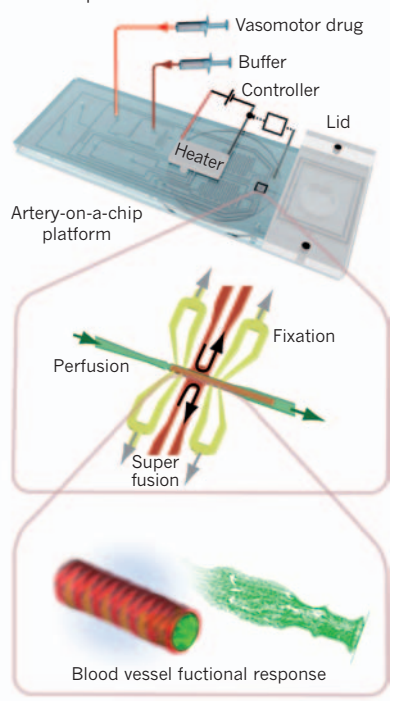
Rather than trying to build an organ from the cells up, some technologists are now turning to microfluidics platforms to help them study actual organs. One example published last year is the artery on a chip¹⁰, engineered by Axel Günther, a bioengineer at the University of Toronto in Canada, and his colleagues. The device is set to be commercialized later this year by Quorum Technologies in Guelph, Canada. It provides a way to study 'resistance arteries', tiny vessels that keep blood from rushing into and damaging capillaries, and so help to regulate blood pressure.

The standard technique for studying such a vessel is to remove one from a mouse and suture it at both ends, manipulating its fluid environment so that the pressure in and around the vessel mimics *in vivo* conditions. The procedure is time-consuming and requires considerable training to master. "It's a very tedious and manual approach," says Günther. Even the most skilled technicians often damage arteries beyond use, and the areas around the sutures become so damaged that they cannot be studied at all.

Günther got the idea for the chip after visiting a collaborator's lab and seeing a similar technique first-hand. "If you had a more scalable approach" than the one he had

ARTERY ON A CHIP

A microfluidics chip positions blood vessels for multiple tests.



seen, he says, "perhaps you could introduce that into drug development, sacrifice fewer animals per screen, and still get better data".

The chip that Günther and his colleagues designed lets researchers place a blood vessel on a microfluidic chip, where a specially designed chamber holds it in place and feeds liquid through it continuously. Not only is it significantly faster to mount vessels onto chips than to suture them for conventional study, says Günther, but imaging and reproducibility are also improved; the same artery can be exposed to different doses of drugs over time, using a computer-controlled system. It could show, for example, whether the artery wall responded when a chemical irritant was applied to the other side.

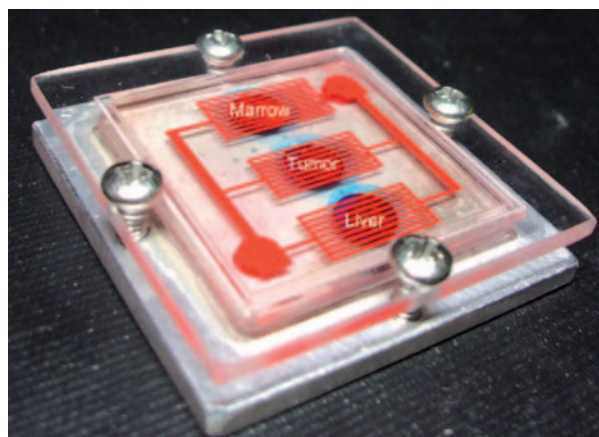
The next step, says Günther, is making chips that can hold more than one artery at a time, so researchers can collect statistical data. Such a set-up would let them compare vessels collected from different parts of the body, from different types of mouse or from clinical biopsies. If the mounting and isolation procedures can be sufficiently simplified, he says, chips could be used with vessels taken from individual patients to help doctors tailor blood-pressure medication regimes. **M.B.**

A. GÜNTHER

actions may harm the molecule, rendering potential drugs ineffective. Compounds can be tested in 'primary' cultures of liver cells, which have been gathered from cadavers, but these are in short supply. Moreover, the cells behave differently and die quickly when grown flat in a dish.

Consequently, several companies and academic labs are developing liver platforms with an eye to drug screening. Hurel plans to launch its liver-cell chips later this year. In 2007, RegeneMed in San Diego, California, began selling three-dimensional liver co-culture plates and screening services as an outgrowth of previous efforts to develop artificial organs for transplantation. Each of the 96 wells in a co-culture plate is set up with what Dawn Applegate, RegeneMed's chief executive, calls a 'jungle gym': nylon scaffolding with openings the right size for cells to pass through. The cells grow over the scaffolding to simulate tissue. "Cells need a third plane to express the extracellular-matrix proteins and growth factors that they would express in the body," says Applegate. Reconstituted tissue can live for up to six months, and the technology supports liver cells from several species, so it can help to resolve conflicting results obtained in different animal models. The plates contain not only hepatocytes, the most common type of cell in the liver, but all the other types as well, says Applegate. Although hepatocytes carry out most drug metabolism, chips must model interaction between different cell types to provide an idea of full liver function.

In March, Hepregen of Medford, Massachusetts, launched HepatoPac: a liver platform based on microfabrication technology developed by Sangeeta Bhatia, a bioengineer at the Massachusetts Institute of Technology (MIT) in Cambridge. A substrate is dotted with collagen, which keeps different types of liver cell in their places and holds colonies of hepatocytes surrounded by supportive cells; the cells can remain functional for 4–6 weeks, says Bhatia. The platform is being developed through a partnership with companies including Boehringer Ingelheim Pharmaceuticals in Ridgefield, Connecticut. At a toxicology meeting this month, scientists from Hepregen and Alnylam Pharmaceuticals in Cambridge, Massachusetts, presented results showing that HepatoPac predicted liver damage from



Channels can simulate blood flow to 'organ chambers' on the chip.

repeated doses of fialuridine, a potential treatment for hepatitis B that failed clinical trials in the early 1990s because it was found to cause severe toxicity in humans — an effect that had not been predicted in animal studies.

In January, CellASIC in Hayward, California, began selling a 96-well sample plate riddled with channels that provide oxygen and a continuous flow of media to hepatocytes in the wells, simulating how blood delivers drugs and toxins to the liver. The cells are assembled in 60-micrometre tubes imprinted with an artificial structure that mimics the effects of cell–cell interactions, and the hepatocytes retain a suite of liver-specific activities for more than four weeks, says Philip Lee, who co-founded CellASIC with Paul Hung in 2005. The two had developed the technology while working in the laboratory of Luke Lee, a bioengineer at the University of California, Berkeley.

The microfluidics technology in the plates relies on gravity rather than a pump system to pull media and test compounds from an inlet well, past the cells and into an outlet well, where the liquid can be collected and analysed for metabolites and other cell products. The goal, says Lee, was to create a robust product that can run on an automated system, minimizing operator-to-operator variability. Researchers can study cells directly by imaging, or collect them and break them up to study gene expression or the induction and inhibition of drug-metabolizing enzymes.

Other systems are still in academic laboratories. Linda Griffith, a bioengineer at MIT, has built silicon scaffolds less than 2 centimetres across and filled them with wells that allow liver cells to grow in three dimensions⁷. These structures are placed inside multiwell plates. Micropumps maintain oxygen and nutrient gradients — similar to those found in the body — between the wells in the silicon scaffolds. Currently, Griffith is comparing how three-dimensional liver tissue containing several cell types compares with flat hepatocyte cultures in predicting drug toxicity. The

goal is to get the most information possible from the simplest culture possible, she says. "You may be able to use the simple cultures as an early screen. More complex cultures are needed for more complex questions."

PUTTING IT TOGETHER

Creating more complex cultures is getting easier, says Shuichi Takayama, a bioengineer at the University of Michigan, Ann Arbor, who has constructed chips that represent bone, liver and lung. The cell types needed for such devices are becoming more accessible, as are the growth factors and extracellular-matrix proteins needed to keep the cells

healthy. But for tissues more than 3 millimetres thick, the chips also need to provide a circulatory system, and many will need to supply some sort of mechanical perturbation: tension on skin and muscles, flow in blood vessels, compression on bone and so on. "Anything that requires dynamic control rather than just static control is a challenge," says Takayama. And of course, each organ represents its own set of challenges: to simulate beating heart tissue, for example, muscle fibres must be aligned on a chip that does not interfere with the mechanical and electrical activity of cells (see 'The real McCoy').

There are other challenges associated with the logistics of the chips, says Shuler: for example, the effects of polymers and microfluidics on cell behaviour are still poorly understood. The very small sample volumes involved make collecting and analysing drug metabolites difficult, and some materials used to build the devices may actually absorb drugs. Not surprisingly, many chips require considerable expertise to operate and troubleshoot, limiting the ease with which they can be adopted by inexperienced labs.

Still, progress is real, says Ali Khademhosseini, a bioengineer at MIT, who is developing ways to create artificial circulatory systems that can keep engineered tissue alive. "The perception of chips being just cute little things is changing, and there is now more of the view that they can make a significant impact," he says ■

Monya Baker is technology editor for *Nature* and *Nature Methods*.

1. Huh, D. *et al. Science* **328**, 1662–1668 (2010).
2. Sung, J. H., Kam, C. & Shuler, M. L. *Lab Chip* **10**, 446–455 (2010).
3. Sonntag, F. *et al. J. Biotechnol.* **148**, 70–75 (2010).
4. Imura, Y., Sato, K. & Yoshimura, E. *Anal. Chem.* **82**, 9983–9988 (2010).
5. Mahler, G. J., Esch, M. B., Glahn, R. P. & Shuler, M. L. *Biotechnol. Bioeng.* **104**, 193–205 (2009).
6. Sung, J. H., Yu, J., Luo, D., Shuler, M. L. & March J. C. *Lab Chip* **11**, 389–392 (2011).
7. Domansky, K. *et al. Lab Chip* **10**, 51–58 (2010).
8. Spence, J. R. *et al. Nature* **470**, 105–109 (2011).
9. Sato, T. *et al. Nature* **459**, 262–265 (2009).
10. Günther, A. *et al. Lab Chip* **10**, 2341–2349 (2010).

"Anything that requires dynamic control rather than just static control is a challenge."

Shuichi Takayama



CAREERS

FUNDING Europe's universities want simpler grant accounting **p.669**

GENDER MIT policies boost number of female science faculty members **p.669**

NATUREJOBS For the latest career listings and advice www.naturejobs.com

B. MELLOR



SOCIAL MEDIA

Self-reflection, online

Some scientists might not like the persona they see when they look online. But they can do something about it.

BY VIRGINIA GEWIN

Michael Tobis has spent years tackling the controversies surrounding climate-related science on his blog 'Only In It For The Gold'. An Earth-system modeller at the University of Texas Institute for Geophysics in Austin, Tobis admits that he may now be more prominent as a blogger than as a published scientist. Although that might not appeal to all researchers, scientists have good reason to take online media seriously. "Scientists have an online persona — whether they like it or not," says Tobis.

Online media offer researchers unique ways to express their interests and goals, foster collaborations and garner invitations and opportunities. But even scientists who don't blog or tweet have an online presence that evolves apace — with or without their intervention. Auto-generated profiles from citation databases, Wikipedia entries, even photos from college can, by virtue of a simple Google search, paint an unwanted portrait of a scientist. If unedited, that portrait can cloud a researcher's work, mar scientific relations and even cost them potential opportunities.

At the very least, scientists should manage their online persona, but they should also consider the pros and cons of doing more. A higher profile can attract both acclaim and scrutiny, so scientists who wish to increase their exposure should consider which media outlets and what level of engagement would best craft an accurate reflection of themselves — and have a positive impact on their career.

CHECK YOURSELF

The Internet is markedly changing how science — and scientists — are perceived. Publications are lauded or rebuked in the Twittersphere (see *Nature* **469**, 286–287; 2011), and leaked e-mails can escalate into political controversy, as in the case of 'climategate' (see *Nature* **468**, 345; 2010). Scientists can also now engage with the public in new and innovative ways, as demonstrated by a researcher who was contacted about his ancestry after publishing his genome on the Internet (see *Nature* **468**, 880–881; 2010). "Even if you never pay attention to the online world and don't want anything to do with it, it's bleeding into your real life," says Liz Neeley, the Seattle-based assistant director of science outreach at the Communication Partnership for Science and the Sea, an organization that helps scientists to engage with the public.

It is important, and fairly easy, for ►

► scientists to check how they are portrayed online, says Michael Habib, product manager at the abstract and citation database Scopus in Amsterdam. First: Researchers should Google themselves. Habib also suggests creating weekly alerts — automated e-mails that send Internet search results for the scientist's name and either their university or a unique phrase describing their research — through Google or Scopus. The researcher then needs to make sure the auto-generated profiles refer to them, and attempt to correct them when they do not. People with common names should take special care to verify their profiles. "There's a 'Wang problem' in China and a 'Smith problem' in the United States," says Habib.

Search-engine results can also reveal information in the public domain that the researcher doesn't want associated with his or her name, and prompt them to alter those results. "Unfortunately, you can't damp down the noise on the Internet; you can only increase the signal," says Neeley. She suggests that users fill in online profiles on Mendeley, LinkedIn, even Facebook, with the information that they do want displayed, such as their specialties, awards and affiliations. The desired details are likely to outweigh the information the researcher does not want known. That said, not all networking sites are easy to navigate, especially when it comes to delineating private and personal lives (see 'Facebook friend or colleague?').

Perhaps most important in keeping an Internet presence positive is making sure that a web page is effective and current. "If you aren't going to keep it up to date, much of the value is lost," says Habib. Prospective students or collaborators want to know about recent activities and initiatives. Publications, grants, project descriptions and upcoming speaking engagements should be routinely updated. Maintaining an additional, personal website, rather than

working with a departmental website and webmaster, may make updating faster and easier.

Those who wish to have a more visible and interactive online presence could also consider setting up a blog. Blogging may prove to be particularly useful for early-career scientists eager to find ways to distinguish themselves in an increasingly competitive job market, and those with professional interests outside their core research. It can also help to strengthen the public outreach component of grant applications, says Kurtis Williams, an astrophysicist at Texas A&M University—Commerce. Williams, known as 'Professor Astronomy' on his blog, says that his blogging helped him during his job search at a teaching institution. Recruiters used it to gain insight into his teaching style and personality. The institutions at which he was interviewed liked his blog activities. "In some cases it helped and in some cases it probably hurt — but that may have been a good thing, to find the best fit for everyone," he says.

WORTH THE EFFORT?

Although early-career scientists arguably have the most to gain by increasing their online exposure, they also have the most to lose. Williams is careful to describe his blog as 'outreach' when talking to colleagues. "If I simply said it was a blog, it may have negative connotations," he says. "Anything that doesn't move you towards publications is still considered by many a waste of time." Blogger Brian Krueger, a molecular-biology postdoc at the University of Florida in Gainesville, says that his former principal investigator viewed the energy that Krueger put into his blog — even though it was on his own time — as energy that should have been channelled into experiments. Krueger's new principal investigator supports his efforts. With his blogging platform 'LabSpaces', Krueger hopes to make science more transparent. For example, he has just begun an 'open notebook' approach, posting pictures of experiments and describing the theory behind techniques.

Some hope their blogging will enhance their career prospects. For instance, Jason Goldman

SELF HELP

Tips for successful blogs

- Have something novel to say.
- If you make a mistake, fix it quickly — and transparently.
- Be radical on one topic only, otherwise your credibility can be undermined.
- Beware of the blurt: don't write things when angry.
- Set a specific amount of time to blog.
- Have an established policy for dealing with rude or abusive comments.
- Register your blog at Scienceblogs.com or Researchblogging.org.
- To get an idea of what it is like to blog, ask to contribute a guest post to an established blog.

— a PhD student in developmental psychology at the University of Southern California in Los Angeles — says that he hopes to mention his blogging efforts in the outreach component of his tenure application when the time comes. Goldman started his blog, 'The Thoughtful Animal', to call attention to animal research that sheds light on the evolution of the mind. "Lots of people write on animals, but there wasn't a blog devoted to the science of animal cognition. I saw a hole I thought I could fill," he says.

Blogger Casey Dunn, an evolutionary biologist at Brown University in Providence, Rhode Island, is not sure whether he'll include his blog in his tenure application. He suspects it may be dangerous to approach blogging with tenure in mind, as blogs are often creative endeavours that may not have relevance to tenure. On his blog, 'Creature Cast', Dunn works with artists to explore creative ways, including the use of original animations, to explain science to the public. He says he'll leave it up to his departmental chair whether or not to mention the blog during Dunn's tenure process. Ultimately, it's difficult to know whether blogging is truly an asset to tenure applications, because committees generally don't share their deliberations.

Many scientists also use blogs as a part of their research programmes. Craig McClain, assistant director of science for the National Evolutionary Synthesis Center in Durham, North Carolina, says that he has gleaned research ideas from writing reviews of publications, found collaborators, opened up new opportunities to write for mainstream media and even received book offers. McClain started his award-winning blog 'Deep-Sea News' in 2005 as a way to reach the public. "Unless you are at a place with a great media-press office, it is hard to reach the public to explain science," he says.

McClain uses irreverent humour in his blog. In one of his posts, McClain capitalized on the public's interest in a video being shared over the Internet that depicted a life form living in a

PRIVACY SETTINGS

Facebook friend or colleague?

Social media sites such as Facebook have started to blur the lines between personal and professional spheres on the Internet. What should professors do when they receive a Facebook 'friend' request from a student?

Scientists should consider whether they prefer a 'filter' or 'firewall' approach — whether they place a barrier between their personal and professional lives or carefully craft a mix of the two. Choosing the firewall approach means not accepting friend requests from students, for example. Filtering

may be appropriate when it's awkward to completely separate the personal and professional. "I filter," says Liz Neeley, the Seattle-based assistant director of science outreach for the Communication Partnership for Science and the Sea, an organization that helps scientists to engage with the public. "I accept friend requests from students and colleagues, but I only post things I would talk about at cocktail parties. It's still me, it's still personal, but it's consistent with my professional side as well." **V.G.**

North Carolina sewer by attempting to identify it — and to therefore dispel the notion that it was “a mysterious alien creature here to suck out our brains”. The humorous style was intentional. “The public has a very narrow view of how scientists act, look and behave, and I wanted a blog that helped dispel the staid stereotype,” says McClain. It worked. His blog gets, on average, 2,000–3,000 hits a day, a lot for an independent blog site. “If people are entertained, they come back for more,” he says.

BLOGGERS BEWARE

Scientists actively cultivating a web presence should, however, tread carefully — it is difficult to remove something once it has been enmeshed in the blogosphere. “The Internet is forever. People should keep in mind that when you blog or tweet something, it becomes Google-able,” says Goldman, who has had guest blogs on *The Guardian* and *Scientific American*’s ‘Mind Matters’ blog.

And not all blogs have the same aims. Dennis Meredith, author of *Explaining Research: How to Reach Key Audiences to Advance Your Work* (Oxford University Press, 2010), says that would-be bloggers should first answer one question: will this blog be useful? The best blogs are those with a unique perspective that draws a readership the blogger deems worthy of the time and energy invested (see ‘Tips for successful blogs’).

Crafting an engaging and appropriate voice is the key to success. John Hawks, a palaeoanthropologist at the University of Wisconsin–Madison, developed rules for his blog through trial and error. After upsetting some colleagues with his cutting criticism of the science in a newly published paper, Hawks learned to rein in his comments. “I realized I had a bigger voice and needed to respectfully air comments and critiques of research,” he says.

Bloggers should realize that readers visit a site to be entertained, but also to engage in conversation, says Teresa Nielsen Hayden, the moderator for Macmillan’s online sites and former editor at the group blog known as BoingBoing. She says the key to self-sustaining conversation is having readers feel a sense of investment in the site. Bloggers might reward insightful comments by highlighting or linking back to them in subsequent posts.

Unfortunately, however, not all comments are useful, or even respectful. In

those instances, Nielsen Hayden opts to ‘disemvowel’, or remove the vowels from, rude posts. Bloggers have every right to remove unhelpful comments, she says. They should also read the comments left on their blog, says Nielsen Hayden. “You can’t throw a party and not attend it.” But that takes time — and that’s where Twitter’s swift tempo can trump a blog.

For some scientists, Twitter serves as a filter whereby respected tweeters post links to studies, articles or conference presentations that might pique scientists’ interest or even help to advance research aims. “It’s the meta-information that Twitter carries that is so important,” says Paul Filmer, programme director for the Inter-American Institute for Global Change Research, based in Arlington, Virginia, part of the National Science Foundation (NSF). Filmer administers the NSF and Voyager2 Twitter feeds. Other scientists may fail to see the point of messages that cannot be longer than Twitter’s limit of 140 characters.

“It’s easy to mock the idea of Twitter,” says Tobis, “with its silly name and teenagers reporting on what they had for lunch. But many scientists underestimate the extent to which casual background communication can help to identify trends and get quick questions answered.” He once used Twitter to find out the relaxation time constant for ocean acidification as a result of a carbon dioxide perturbation, an obscure topic not well-attuned to a simple Google search. McClain says Twitter has helped him to form “an extended journal club in a virtual space with colleagues from all over the world”.

The key is choosing wisely whom to follow. For example, leaders in a particular field often have advance notice of high-impact papers or job advertisements, access to which can be priceless. And scientists not using social media may be missing out on opportunities — without even realizing it. “Grant-making agencies, such as the NSF, are learning how to diffuse opportunities through these types of networks to reach the best and brightest,” says Filmer. An NSF tweet on 14 March, for example, alerted undergraduates to an opportunity to submit a two-minute video describing an original energy-innovation idea; the best will be aired on a special Weather Channel programme. What is more, use of Twitter and other social media can have tangible career-promoting results. “I can’t count the number of conference invitations that have come from people finding me online,” says Hawks.

It is possible to get too immersed, some note — there is no substitute for face time and real-world conversations. “The virtual world doesn’t exist in a vacuum,” says Habib. “The ‘virtual’ world and the ‘real’ world complement each other — and it’s important to tend to both.” ■

Virginia Gewin is a freelance journalist based in Portland, Oregon.



“There wasn’t a blog devoted to the science of animal cognition. I saw a hole I thought I could fill.”

Jason Goldman

EUROPEAN UNION

Funding revamp urged

The next European Union (EU) framework for research funding, which will start in 2014, must adopt simpler scientific and financial reporting processes, says a group of EU universities. In a report out on 14 March, the League of European Research Universities (LERU) in Leuven, Belgium, said that current rules — which require researchers to provide detailed time sheets and financial audits — should be streamlined. Researchers in countries with good accounting practices should be permitted to use those systems. Katrien Maes, LERU chief policy officer, says that the European Commission has been receptive to the recommendations.

GENDER POLICY

Equity rising at MIT

A report from the School of Science at the Massachusetts Institute of Technology (MIT) in Cambridge shows how policies have helped to increase the proportion of women from 8% to 19% of faculty members between 1995 and 2010. Rectifying salary inequities and extending the tenure clock after birth or adoption of a child have helped, says Hazel Sive, an MIT biologist. Most faculty members approved of the efforts, but some worried that women get preferential hiring treatment. Deans have pledged to address the potential for bias. The report, out on 21 March, says that because committees have fewer female than male researchers to draw from, equal-representation policies lead to women’s time being taken up disproportionately. It recommends improved mentoring for junior faculty members, access to childcare and systems to deal with gender-based harassment.

DEVELOPMENT

City seeks facility bids

New York City is looking for a partner for an applied-science facility that will hire hundreds of researchers in nanotechnology and environmental, materials and computer science in the next 10 years. The city, seeking economic benefits and a new talent pool, will donate property and funds. Some 27 universities worldwide have expressed an interest; the city will issue a formal request for proposals by September. Offers can come from single universities or teams, and potential for economic development is the main selection criterion. Mayor Michael Bloomberg says a winner will be chosen by the end of 2011.

North Carolina sewer by attempting to identify it — and to therefore dispel the notion that it was “a mysterious alien creature here to suck out our brains”. The humorous style was intentional. “The public has a very narrow view of how scientists act, look and behave, and I wanted a blog that helped dispel the staid stereotype,” says McClain. It worked. His blog gets, on average, 2,000–3,000 hits a day, a lot for an independent blog site. “If people are entertained, they come back for more,” he says.

BLOGGERS BEWARE

Scientists actively cultivating a web presence should, however, tread carefully — it is difficult to remove something once it has been enmeshed in the blogosphere. “The Internet is forever. People should keep in mind that when you blog or tweet something, it becomes Google-able,” says Goldman, who has had guest blogs on *The Guardian* and *Scientific American*’s ‘Mind Matters’ blog.

And not all blogs have the same aims. Dennis Meredith, author of *Explaining Research: How to Reach Key Audiences to Advance Your Work* (Oxford University Press, 2010), says that would-be bloggers should first answer one question: will this blog be useful? The best blogs are those with a unique perspective that draws a readership the blogger deems worthy of the time and energy invested (see ‘Tips for successful blogs’).

Crafting an engaging and appropriate voice is the key to success. John Hawks, a palaeoanthropologist at the University of Wisconsin–Madison, developed rules for his blog through trial and error. After upsetting some colleagues with his cutting criticism of the science in a newly published paper, Hawks learned to rein in his comments. “I realized I had a bigger voice and needed to respectfully air comments and critiques of research,” he says.

Bloggers should realize that readers visit a site to be entertained, but also to engage in conversation, says Teresa Nielsen Hayden, the moderator for Macmillan’s online sites and former editor at the group blog known as BoingBoing. She says the key to self-sustaining conversation is having readers feel a sense of investment in the site. Bloggers might reward insightful comments by highlighting or linking back to them in subsequent posts.

Unfortunately, however, not all comments are useful, or even respectful. In

those instances, Nielsen Hayden opts to ‘disemvowel’, or remove the vowels from, rude posts. Bloggers have every right to remove unhelpful comments, she says. They should also read the comments left on their blog, says Nielsen Hayden. “You can’t throw a party and not attend it.” But that takes time — and that’s where Twitter’s swift tempo can trump a blog.

For some scientists, Twitter serves as a filter whereby respected tweeters post links to studies, articles or conference presentations that might pique scientists’ interest or even help to advance research aims. “It’s the meta-information that Twitter carries that is so important,” says Paul Filmer, programme director for the Inter-American Institute for Global Change Research, based in Arlington, Virginia, part of the National Science Foundation (NSF). Filmer administers the NSF and Voyager2 Twitter feeds. Other scientists may fail to see the point of messages that cannot be longer than Twitter’s limit of 140 characters.

“It’s easy to mock the idea of Twitter,” says Tobis, “with its silly name and teenagers reporting on what they had for lunch. But many scientists underestimate the extent to which casual background communication can help to identify trends and get quick questions answered.” He once used Twitter to find out the relaxation time constant for ocean acidification as a result of a carbon dioxide perturbation, an obscure topic not well-attuned to a simple Google search. McClain says Twitter has helped him to form “an extended journal club in a virtual space with colleagues from all over the world”.

The key is choosing wisely whom to follow. For example, leaders in a particular field often have advance notice of high-impact papers or job advertisements, access to which can be priceless. And scientists not using social media may be missing out on opportunities — without even realizing it. “Grant-making agencies, such as the NSF, are learning how to diffuse opportunities through these types of networks to reach the best and brightest,” says Filmer. An NSF tweet on 14 March, for example, alerted undergraduates to an opportunity to submit a two-minute video describing an original energy-innovation idea; the best will be aired on a special Weather Channel programme. What is more, use of Twitter and other social media can have tangible career-promoting results. “I can’t count the number of conference invitations that have come from people finding me online,” says Hawks.

It is possible to get too immersed, some note — there is no substitute for face time and real-world conversations. “The virtual world doesn’t exist in a vacuum,” says Habib. “The ‘virtual’ world and the ‘real’ world complement each other — and it’s important to tend to both.” ■

Virginia Gewin is a freelance journalist based in Portland, Oregon.



“There wasn’t a blog devoted to the science of animal cognition. I saw a hole I thought I could fill.”

Jason Goldman

EUROPEAN UNION

Funding revamp urged

The next European Union (EU) framework for research funding, which will start in 2014, must adopt simpler scientific and financial reporting processes, says a group of EU universities. In a report out on 14 March, the League of European Research Universities (LERU) in Leuven, Belgium, said that current rules — which require researchers to provide detailed time sheets and financial audits — should be streamlined. Researchers in countries with good accounting practices should be permitted to use those systems. Katrien Maes, LERU chief policy officer, says that the European Commission has been receptive to the recommendations.

GENDER POLICY

Equity rising at MIT

A report from the School of Science at the Massachusetts Institute of Technology (MIT) in Cambridge shows how policies have helped to increase the proportion of women from 8% to 19% of faculty members between 1995 and 2010. Rectifying salary inequities and extending the tenure clock after birth or adoption of a child have helped, says Hazel Sive, an MIT biologist. Most faculty members approved of the efforts, but some worried that women get preferential hiring treatment. Deans have pledged to address the potential for bias. The report, out on 21 March, says that because committees have fewer female than male researchers to draw from, equal-representation policies lead to women’s time being taken up disproportionately. It recommends improved mentoring for junior faculty members, access to childcare and systems to deal with gender-based harassment.

DEVELOPMENT

City seeks facility bids

New York City is looking for a partner for an applied-science facility that will hire hundreds of researchers in nanotechnology and environmental, materials and computer science in the next 10 years. The city, seeking economic benefits and a new talent pool, will donate property and funds. Some 27 universities worldwide have expressed an interest; the city will issue a formal request for proposals by September. Offers can come from single universities or teams, and potential for economic development is the main selection criterion. Mayor Michael Bloomberg says a winner will be chosen by the end of 2011.

A PERFECT DRUG

What you don't know can help you.

BY DAN ERLANSON

Jeffrey rose slowly, scanned the half-dozen people in the darkly panelled boardroom, and sonorously announced: "You all know the good news. It's the bad news I've gathered you to hear."

Alan carefully maintained a neutral composure, but quietly he seethed. It was bad enough for the head of commercialization to call an emergency executive meeting without informing him, the chief executive, what it was about. Now Jeffrey was going to theatrically draw out whatever he was planning to say — and there was nothing Alan could do. Jeffrey had powerful supporters on the board; after all, he had certainly delivered for the company.

"As you know, the launch of Paxpharma has been one of the most successful product rollouts in the history of our industry," Jeffrey continued. "In the crowded field of antidepressants, our drug stands out with the lowest side-effect profile on the market. Uptake has been phenomenal, and we've gone from a struggling mid-tier pharmaceutical company with a looming patent cliff to the darling of Wall Street.

"As you also know, Paxpharma almost didn't launch. The molecule is a nightmare to synthesize, and the size of the phase III trials necessitated a complete reworking of the manufacturing process. Even with the new synthetic route in place, we barely scraped together enough material for the trials."

Alan remembered that period painfully well. The company was being pounded by analysts and investors for its thin pipeline. A new antidepressant wasn't an obvious home-run, but the phase II data were compelling, and they didn't have much else. Manufacturing spent months validating the new production procedure, and when everything was worked out and signed off with the FDA, the factory went into 24/7 production mode. It was expensive, but it paid off: the phase III trials revealed Paxpharma to be just as effective as existing antidepressants, but with a faster onset of action and milder side-effect profile. In particular, there was no evidence of weight gain or sexual dysfunction, two problems that focus groups had shown to be particularly unpopular with competitor drugs.

The company launched an aggressive and edgy advertising campaign touting Paxpharma. It worked. One of the ads went viral on YouTube, and the drug got the kind of attention from talk-show hosts and celebrities that can only come about through deserved but dumb luck. There were concerns that demand would outstrip supply, but somehow production increased, and profits soared. Stock analysts who had been calling for changes in leadership suddenly became fawning. Alan couldn't help smiling, remembering his change in fortune.

His reverie was broken by Jeffrey, who was still pontificating. "As I said at the outset, the good news is that the trials were positive. Paxpharma was approved and is now a major commercial success. Now the bad news.

"When the drug was approved, we were at a loss as to how we could scale up production even further. We struggled to make enough material for the pivotal trials, let alone for a launch. And, of course, any significant change in manufacturing procedure would have to be approved by the FDA. We realized we couldn't do it in time."

There was silence in the room as people tried to digest what they had just heard. Alan finally blurted: "But you did. Right?"

"No," said Jeffrey. "We tried, but we couldn't do it."

"What do you mean?" asked Alan, his voice rising tremulously. "We've been selling product for the past 18 months!"

"Yes, we've been selling product," Jeffrey repeated slowly. "But we haven't been selling a drug. We've been selling sugar pills for the past six quarters."

Alan felt his stomach hit the floor. Time seemed to stop. "But ... it works," he finally managed, weakly. Jeffrey shrugged. "Yes, we were happily

surprised by that too. The placebo effect is strong with psychoactive drugs. I guess we never realized how strong."

"That's the bad news," Jeffrey continued. "A small team of us have kept this secret until now, and we could probably continue to do so indefinitely, but some new developments require decisions."

"The production difficulties with Paxpharma are well-known, and we've been diligently adding capacity. The new plants are now online, and we believe we can now supply enough active pharmaceutical ingredient to meet demand. The question is, should we?"

Alan shouted: "Of course! Right away — why wouldn't you?"

Jeffrey looked at Alan condescendingly, then gazed slowly around the room. "Think about it. We've been selling a product

with no side effects, and people are clearly benefiting: just read the patient testimonials posted everywhere online. Look at the sales figures.

"If we switch to selling the actual drug molecule, we'll be putting patients at risk. Sure, the side-effect profile is lower than other drugs out there, but there are side effects with any drug. Worse, these will be especially noticeable to the people who are most benefiting from our product — the patients who have been taking it for months without any problems."

"We will of course continue to manufacture the genuine article as a smokescreen for regulators, but, in the interest of our customers and our shareholders, I recommend continuing to sell placebo." Jeffrey paused before adding, "Of course, the decision is not mine to make."

Alan could feel a dozen eyes on him. The seconds ticked into minutes, and by the time he finally replied, his voice was barely audible. ■

Dan Erlanson is a chemist trying to discover non-placebo-based drugs in San Francisco, California. He blogs about a tiny niche of drug discovery at <http://practicalfragments.blogspot.com>.



➔ **NATURE.COM**
Follow Futures on
Facebook at:
go.nature.com/mtoodm

TERRA and hnRNPA1 orchestrate an RPA-to-POT1 switch on telomeric single-stranded DNA

Rachel Litman Flynn¹, Richard C. Centore^{1*}, Roderick J. O'Sullivan^{3*}, Rekha Rai^{4*}, Alice Tse¹, Zhou Songyang⁵, Sandy Chang⁴, Jan Karlseder³ & Lee Zou^{1,2}

Maintenance of telomeres requires both DNA replication and telomere 'capping' by shelterin. These two processes use two single-stranded DNA (ssDNA)-binding proteins, replication protein A (RPA) and protection of telomeres 1 (POT1). Although RPA and POT1 each have a critical role at telomeres, how they function in concert is not clear. POT1 ablation leads to activation of the ataxia telangiectasia and Rad3-related (ATR) checkpoint kinase at telomeres^{1,2}, suggesting that POT1 antagonizes RPA binding to telomeric ssDNA. Unexpectedly, we found that purified POT1 and its functional partner TPP1 are unable to prevent RPA binding to telomeric ssDNA efficiently. In cell extracts, we identified a novel activity that specifically displaces RPA, but not POT1, from telomeric ssDNA. Using purified protein, here we show that the heterogeneous nuclear ribonucleoprotein A1 (hnRNPA1) recapitulates the RPA displacing activity. The RPA displacing activity is inhibited by the telomeric repeat-containing RNA (TERRA) in early S phase, but is then unleashed in late S phase when TERRA levels decline at telomeres³. Interestingly, TERRA also promotes POT1 binding to telomeric ssDNA by removing hnRNPA1, suggesting that the reaccumulation of TERRA after S phase helps to complete the RPA-to-POT1 switch on telomeric ssDNA. Together, our data suggest that hnRNPA1, TERRA and POT1 act in concert to displace RPA from telomeric ssDNA after DNA replication, and promote telomere capping to preserve genomic integrity.

RPA binds ssDNA in a non-sequence specific manner⁴, whereas POT1 specifically recognizes ssDNA consisting of the telomeric repeats⁵. RPA plays a key role in DNA replication and activation of the ATR checkpoint⁶, and POT1 suppresses ATR activation at telomeres^{1,2} (Supplementary Fig. 1). In both yeast and humans, RPA associates with telomeres during S phase of the cell cycle^{7–9}, and is implicated in telomere maintenance^{10–12}. Furthermore, ATR transiently associates with telomeres and suppresses telomere instability^{7,10,13}. These findings raise the question of how the bindings of POT1 and RPA to telomeric ssDNA are orchestrated and, furthermore, how the interplay between POT1 and RPA affects DNA replication and ATR activation at telomeres.

Double-stranded DNA (dsDNA) with ssDNA overhangs activates ATR in human cell extracts¹⁴. To investigate how ATR activation is suppressed at telomeres, we tested whether telomeric ssDNA overhangs affect ATR activation in this assay. Resected dsDNA of random sequences, but not resected telomeric dsDNA, efficiently induced the phosphorylation of RPA2 by ATR (Supplementary Fig. 2)¹⁴, suggesting that telomeric ssDNA overhangs do not support efficient ATR activation in cell extracts.

The absence of ATR activation by telomeric ssDNA suggests that POT1 may prevent RPA binding to telomeric ssDNA². POT1 and TPP1 function as heterodimers in cells, and the complex binds to telomeric ssDNA more efficiently than POT1 alone^{15,16}. In gel-shift assays, the POT1–TPP1 complexes purified from insect or human cells

and the RPA purified from *Escherichia coli* efficiently bound to a telomeric ssDNA probe (Fig. 1a and Supplementary Fig. 3a, b). POT1–TPP1 exhibited lower affinity for telomeric ssDNA than RPA (Supplementary Fig. 3a). When POT1–TPP1 and RPA were co-incubated with the probe, the RPA–ssDNA complex was readily detected, whereas no POT1-containing complexes were observed (Fig. 1a and Supplementary Fig. 3b). In pull-down assays using biotinylated telomeric ssDNA (ssTEL), RPA also outcompeted POT1–TPP1 for binding to ssTEL (Fig. 1b and Supplementary Fig. 3c). Thus, RPA, which is more abundant than POT1–TPP1 in cells^{4,17}, outcompetes POT1–TPP1 for binding to telomeric ssDNA when present at similar concentrations as POT1–TPP1. The *E. coli* ssDNA-binding protein only modestly reduced POT1 binding to ssTEL (Supplementary Fig. 3c), suggesting that the ability to outcompete POT1–TPP1 is unique to RPA.

The ability of RPA to outcompete POT1–TPP1 raises the question of how ATR activation is suppressed in cell extracts. Purified RPA bound to ssTEL and mutated telomeric repeats (ssMUT) efficiently (Fig. 1c). In stark contrast to purified RPA, the endogenous RPA in HeLa whole-cell extracts (WCEs) was largely excluded from ssTEL; however, it still associated with ssMUT (Fig. 1c). The sequence-specific exclusion of RPA from ssTEL in WCEs suggests that RPA may be outcompeted by other proteins or actively displaced from telomeric ssDNA.

To assess if RPA is actively displaced from ssTEL, we pre-coated ssTEL and ssMUT with RPA then incubated them in extracts. The levels of RPA on ssTEL gradually declined with increasing concentrations of WCEs from HeLa, HEK293E, U2OS and MEF cells (Fig. 1d and Supplementary Fig. 4a). In addition, HeLa nuclear extracts, but not the cytoplasmic extracts, efficiently displaced RPA from ssTEL (Supplementary Fig. 4b). In marked contrast to the RPA on ssTEL, the RPA bound to ssMUT remained constant regardless of WCE concentrations (Fig. 1d). When POT1-coated ssTEL was incubated in extracts, POT1 remained stably bound to ssTEL even in high concentrations of WCEs (Fig. 1e). Furthermore, RPA was rapidly displaced from ssTEL within 5 min, whereas no POT1 was displaced after 60 min (Supplementary Fig. 4c). Thus, the activity that displaces RPA from telomeric ssDNA is sequence-specific, protein-specific and localized within the nucleus.

The specific displacement of RPA, but not POT1, from telomeric ssDNA prompted us to test if POT1 is the RPA displacing factor. When incubated with RPA–ssTEL, POT1–TPP1 did not significantly reduce the levels of ssTEL-bound RPA (Supplementary Fig. 5a). To identify the RPA displacing factors, we sought to capture the RPA displacing activity from extracts using RPA–ssTEL as bait. The proteins captured and eluted from RPA–ssTEL, but not RPA–ssMUT, recapitulated the RPA displacing activity (Fig. 2a). Mass spectrometry analysis of the proteins specifically captured by RPA–ssTEL identified hnRNPA1

¹Massachusetts General Hospital Cancer Center, Harvard Medical School, Charlestown, Massachusetts 02129, USA. ²Department of Pathology, Harvard Medical School, Boston, Massachusetts 02115, USA. ³Molecular and Cellular Laboratory, The Salk Institute for Biological Studies, La Jolla, California 92037, USA. ⁴Department of Laboratory Medicine, Yale University School of Medicine, New Haven, Connecticut 06510, USA. ⁵Department of Biochemistry and Molecular Biology, Baylor College of Medicine, Houston, Texas 77030, USA.

*These authors contribute equally to this work.

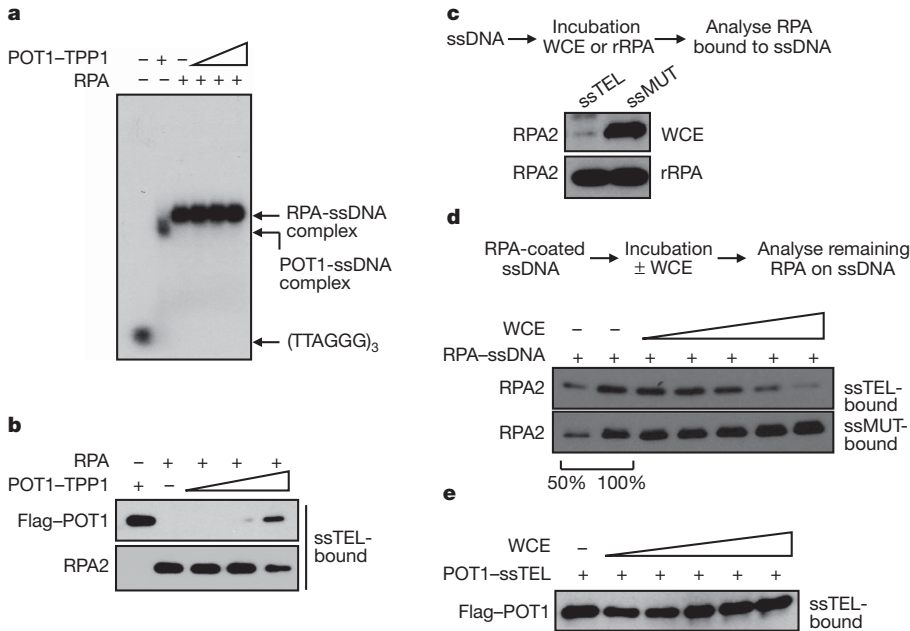


Figure 1 | A novel telomere-specific RPA displacing activity in human cell extracts. **a**, POT1–TPP1 (60 nM; purified from insect cells), RPA (60 nM) and mixtures of POT1–TPP1 and RPA (60, 120, 180 nM of POT1–TPP1 mixed with 60 nM of RPA) were incubated with 20 nM of the ssDNA probe and analysed by gel-shift. **b**, POT1–TPP1 (2.4 nM), RPA (2.4 nM) and mixtures of POT1–TPP1 and RPA (2.4, 4.8, 7.2 nM of POT1–TPP1 mixed with 2.4 nM of RPA) were incubated with 0.8 nM of biotinylated ssTEL (TTTAGG₃). The

and hnRNP A2/B1 (Supplementary Fig. 5b, c), both of which are known to bind telomeric ssDNA^{18,19}. The presence of hnRNP A1 and A2/B1 in the eluted fraction with RPA displacing activity was confirmed by western blot (Fig. 2b). Moreover, hnRNP A1 and A2/B1 gradually bound to ssTEL as RPA was displaced in WCEs (Fig. 2c). These results suggest that hnRNP A1 and A2/B1 may play a role in RPA displacement.

hnRNPA1 has been implicated in telomere maintenance^{20,21}. Extracts from hnRNPA1 knockdown cells exhibited reduced activity

proteins bound to ssTEL were retrieved by streptavidin beads and analysed by western blot. **c**, Biotinylated ssTEL or ssMUT ((TTTGGC)₈) was incubated with WCEs or recombinant RPA (rRPA). **d**, ssTEL or ssMUT pre-coated with RPA was incubated with increasing concentrations of HeLa WCEs (0.08, 0.19, 0.36, 0.8, 1.3 $\mu\text{g } \mu\text{l}^{-1}$). The RPA2 remaining on ssTEL was analysed as in **b**. **e**, ssTEL pre-coated with POT1 was incubated with increasing concentrations of HeLa WCEs (0.07, 0.18, 0.33, 0.66, 1.3 $\mu\text{g } \mu\text{l}^{-1}$).

in RPA displacement (Supplementary Fig. 6a). Purified hnRNPA1 efficiently displaces RPA from ssTEL, but not ssMUT (Fig. 2d). Furthermore, hnRNPA1 did not displace POT1 from ssTEL (Fig. 2e). hnRNPA1 only displaces RPA from ssTEL containing four or more telomeric repeats (Supplementary Fig. 6b), indicating that a DNA length-dependent binding mode of hnRNPA1 may be needed to displace RPA²². Given that hnRNPA1 and A2/B1 are highly homologous in the RRM domains that bind telomeric ssDNA, both of these hnRNPs may contribute to RPA displacement.

hnRNPA1 not only binds telomeric ssDNA but also TERRA^{23–26}. To test if TERRA affects the ability of hnRNPA1 to displace RPA from ssTEL, we added increasing concentrations of TERRA or control RNA to nuclear extracts, then incubated the extracts with RPA–ssTEL. RPA displacement was virtually abolished by TERRA, but not control RNA (Fig. 3a). The RPA displacing activity captured by RPA–ssTEL was also specifically inhibited by TERRA (Fig. 3b). Furthermore, the ability of purified hnRNPA1 to bind ssTEL and to displace RPA from ssTEL was specifically inhibited by TERRA (Fig. 3c and Supplementary Fig. 6c). Thus, TERRA is a potent inhibitor of the RPA displacing activity of hnRNPA1.

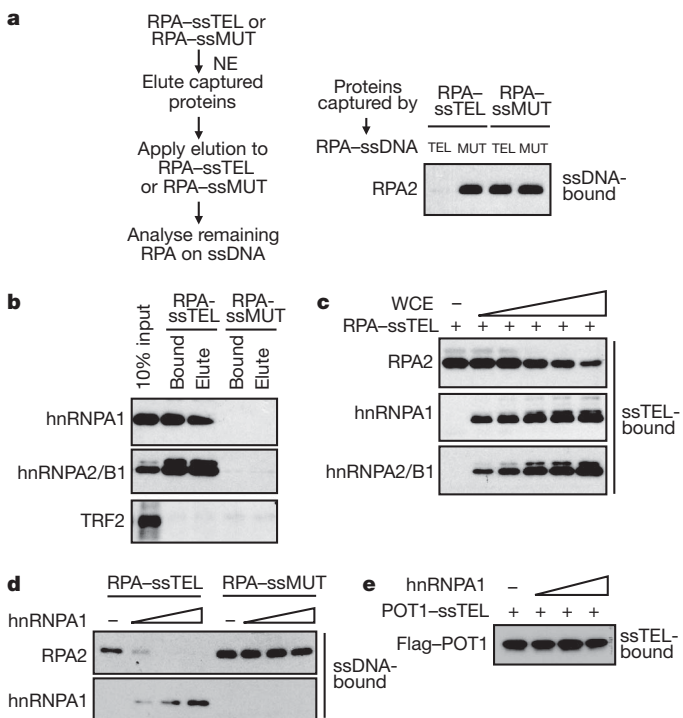


Figure 2 | RPA displacement by hnRNP1. **a**, ssTEL and ssMUT pre-coated with RPA were incubated with nuclear extracts (NE). After the incubation, the proteins bound to DNA were retrieved, eluted and applied to RPA-coated ssTEL or ssMUT (see Supplementary Methods). After the second incubation, the remaining RPA2 on DNA was analysed by western blot. **b**, Proteins captured by RPA–ssTEL or RPA–ssMUT and eluted by salt were analysed by western blot using antibodies to hnRNP1, hnRNP2/B1 and TRF2. **c**, RPA-coated ssTEL (0.8 nM) was incubated with increasing concentrations of WCEs (0.06, 0.24, 0.96 $\mu\text{g } \mu\text{l}^{-1}$). The hnRNP1 and hnRNP2/B1 bound to DNA and the remaining RPA2 on DNA were analysed by western blot. **d**, RPA-coated ssTEL or ssMUT (0.8 nM) was incubated with increasing concentrations of purified hnRNP1 (2.4, 4.8, 7.2 nM). The remaining RPA2 on DNA was analysed as in **a**. **e**, POT1-coated ssTEL (0.8 nM) was incubated with increasing concentrations of purified hnRNP1 (2.4, 4.8, 7.2 nM).

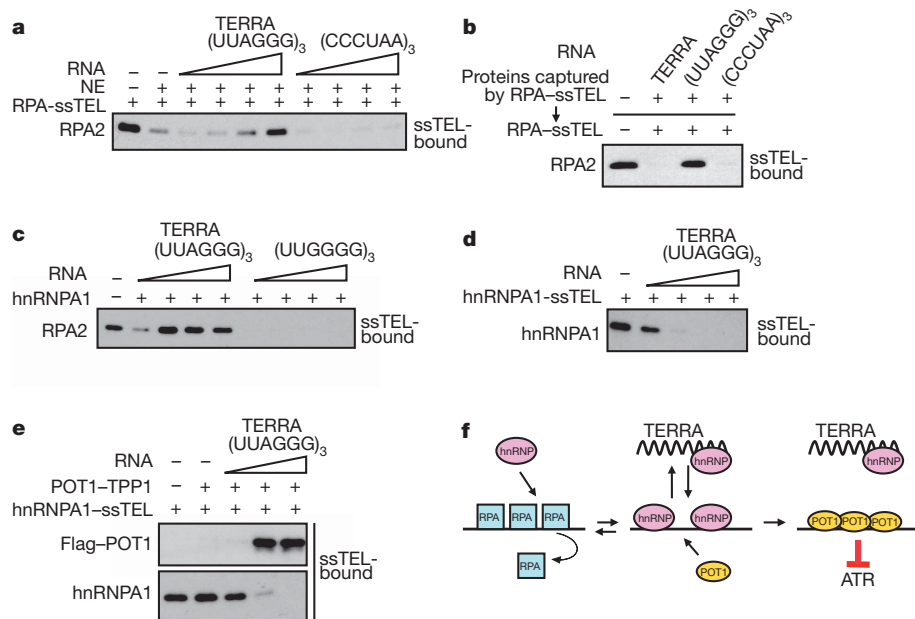


Figure 3 | Regulation of RPA displacement by TERRA. **a**, Nuclear extracts (34 ng μl^{-1}) were treated with increasing concentrations (2, 4, 10, 20 nM) of TERRA (UUAGGG)₃, control RNA (CCCUGA)₃ or mock treated. The treated nuclear extracts were then incubated with RPA-coated ssTEL (2 nM), and the remaining RPA2 on ssTEL was analysed after the incubation. **b**, The RPA displacing factors were captured with RPA-ssTEL as in Fig. 2a. The elution was incubated with TERRA or control RNA, then applied to RPA-ssTEL. **c**, Purified hnRNPA1 (4.8 nM) was incubated with increasing concentrations of

TERRA or control RNA (2, 4, 10, 20 nM), then incubated with RPA-ssTEL (0.8 nM). **d**, hnRNPA1-coated ssTEL (0.8 nM) was incubated with increasing concentrations of TERRA (2, 20, 200, 2,000 nM). The remaining hnRNPA1 on ssTEL was analysed by western blot. **e**, hnRNPA1-coated ssTEL (0.8 nM) was incubated with increasing concentrations of TERRA (2, 20, 200 nM) in the presence of POT1-TPP1 (2.4 nM). The hnRNPA1 and POT1 on ssTEL were analysed by western blot. **f**, A model for RPA displacement.

If hnRNPA1 displaces RPA from telomeric ssDNA, how can POT1 bind to telomeric ssDNA? Given that hnRNPA1 has affinity for both telomeric ssDNA and TERRA, the presence of TERRA at telomeres may promote the dissociation of hnRNPA1 from telomeric ssDNA. Indeed, when hnRNPA1-coated ssTEL was incubated with TERRA, hnRNPA1 was stripped from ssTEL (Fig. 3d), showing that hnRNPA1 binds telomeric ssDNA dynamically. Furthermore, when hnRNPA1-ssTEL was incubated with TERRA and POT1-TPP1, POT1 efficiently bound to ssTEL as hnRNPA1 was removed by TERRA (Fig. 3e).

The *in vitro* results above suggest that the initial displacement of RPA from telomeric ssDNA may be performed by hnRNPs when TERRA levels are low at telomeres (Fig. 3f). However, if TERRA levels rise at telomeres, hnRNPA1 may shuttle between telomeric ssDNA and TERRA dynamically. In this situation, both RPA and POT1 may have the chance to bind telomeric ssDNA. Because hnRNPA1 only displaces RPA, but not POT1, this dynamic process will eventually promote POT1 occupancy at telomeric ssDNA.

This model raises the possibility that the RPA displacing activity may be regulated by TERRA during the cell cycle. To test this, we generated WCEs from cells in G1, early S, late S and M phases of the cell cycle. RPA was more efficiently displaced in the late S- and M-phase extracts than in the G1- and early S-phase extracts (Fig. 4a and Supplementary Fig. 7a, b). Thus, the RPA displacing activity is low in G1 and early S phase, but upregulated in late S phase.

If TERRA inhibits the RPA displacing activity, its levels should inversely correlate with the activity. Furthermore, removal of TERRA in early S phase should alleviate the inhibition. Indeed, a recent study showed that TERRA levels significantly decrease in late S phase and increase again after S phase³. Consistently, telomeric TERRA foci declined as cells progressed from early to late S phase (Fig. 4b and Supplementary Fig. 7c, d). In addition, RNase A treatment of early S-phase extracts significantly enhanced the RPA displacing activity (Supplementary Fig. 7e). Together, these results suggest that TERRA inhibits RPA displacement in early S phase, and its decline in late S phase may provide a window for RPA displacement.

The model above also predicts that hnRNPs are necessary for RPA displacement from telomeres. Depletion of hnRNPA1 using two independent short interfering RNA (siRNAs) significantly increased the fraction of cells displaying RPA foci (Fig. 4c and Supplementary Fig. 8a–d). Notably, a fraction of the RPA foci in hnRNPA1 knockdown cells closely associated with TRF2 foci. Furthermore, increased RPA binding at telomeres was detected in hnRNPA1 knockdown cells by chromatin immunoprecipitation (Fig. 4d). In synchronized hnRNPA1 knockdown cells, RPA binding to telomeres was enhanced in early S phase (Supplementary Fig. 9a, b), indicating that even during this period some hnRNPA1 remains free from TERRA and limits RPA binding to telomeres⁹. In late S/G2, RPA still declined at telomeres in hnRNPA1 knockdown cells, possibly owing to the redundancy among hnRNPs.

If the displacement of RPA by hnRNPA1 is a prerequisite for POT1 binding, POT1 should be needed for RPA exclusion after late S phase. To assess this possibility, we treated cells with POT1 siRNA and synchronized the cells with thymidine as POT1 levels declined (Supplementary Fig. 10a, b). After POT1 knockdown cells and control cells were synchronously released, RPA foci appeared in both cell populations (Fig. 4e). As control cells entered G2, RPA foci rapidly declined. In contrast, the POT1 knockdown cells containing RPA foci that co-localized with TRF2 continued to increase. Concomitantly, modest Chk1 phosphorylation was detected in POT1 knockdown cells (Supplementary Fig. 10c). Thus, reduction of POT1 compromises the exclusion of RPA from telomeres after replication²⁷.

During early to middle S phase, TERRA sequesters hnRNPs and allows RPA to bind telomeric ssDNA at replication forks or telomere ends (Supplementary Fig. 1). When TERRA levels decline in late S phase, hnRNPs are unleashed to displace RPA from telomeric ssDNA. The dynamic binding of hnRNPs to telomeric ssDNA is gradually antagonized by TERRA when TERRA reaccumulates at telomeres, providing a window for both RPA and POT1 to bind. Because only POT1, but not RPA, binds to telomeric ssDNA irreversibly in the presence of hnRNPs, this dynamic process favours the formation of

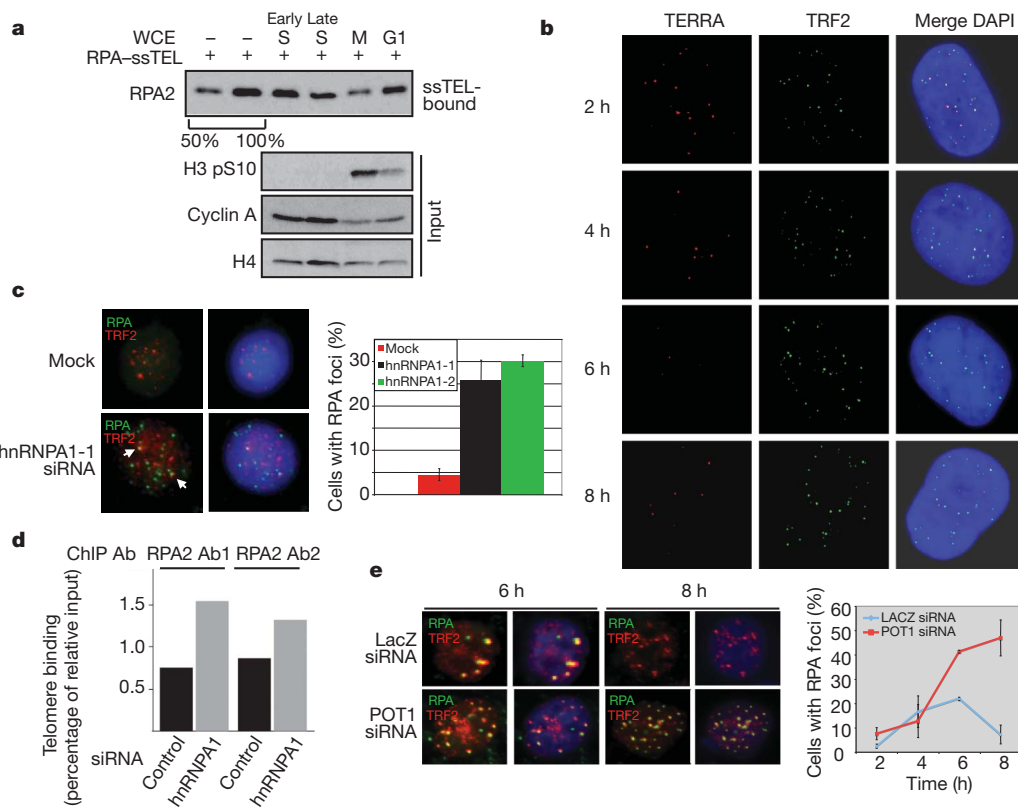


Figure 4 | hnRNPA1 and POT1 suppress the accumulation of RPA at telomeres. **a**, RPA-coated ssTEL was incubated with WCEs from cells in G1, early S, late S and M phases of the cell cycle (see Supplementary Methods). The remaining RPA2 on ssTEL was analysed after incubation. Cyclin A and phospho-histone H3 serve as cell-cycle markers, and histone H4 as a loading control. **b**, TERRA was analysed by RNA fluorescence *in situ* hybridization in HeLa cells after thymidine release. TRF2 serves as a marker of telomeres. **c**, HeLa cells were treated with hnRNPA1 siRNA or mock treated, then immunostained with antibodies to RPA2 and TRF2 (left panel). The cells with

RPA foci (>5) were quantified (right panel). Mean \pm s.d., $n = 3$ for mock and hnRNPA1-1, $n = 2$ for hnRNPA1-2. **d**, Chromatin immunoprecipitation (ChIP) of RPA was performed with two different RPA2 antibodies (Ab). The association of RPA with telomeres was analysed by dot blot using a telomere probe and quantified. **e**, HeLa cells transfected with POT1 or LacZ siRNA were released from a thymidine block. At the indicated times, the G2/M population was determined by FACS (Supplementary Fig. 10c). Cells were immunostained for RPA2 and TRF2 (left panel). The cells with RPA foci (>5) were quantified (right panel). Mean \pm s.d., $n = 3$.

POT1-coated telomeric ssDNA. Unlike RPA, POT1 kinks telomeric ssDNA and induces its self-recognition^{28,29}. These unique properties of POT1 may confer resistance to hnRNP-mediated displacement. The cell-cycle-regulated RPA displacement may allow RPA to transiently associate with telomeric ssDNA during replication, and prevent persistent ATR activation at telomeres after S phase. Once coated by POT1, telomeric ssDNA may remain capped until the arrival of replication forks in the next S phase. Together, TERRA and hnRNPs orchestrate a cell-cycle-regulated RPA-to-POT1 switch on telomeric ssDNA, ensuring orderly telomere replication and capping.

METHODS SUMMARY

To analyse the bindings of RPA and POT1–TPP1 to ssDNA, biotinylated ssDNA was attached to streptavidin-coated magnetic beads. Biotinylated ssDNA (1 pmol) was incubated with purified protein in 500 μ l of binding buffer (10 mM Tris-HCl (pH 7.5), 100 mM NaCl, 10 μ g ml⁻¹ BSA, 10% glycerol, 0.05% NP-40).

Full Methods and any associated references are available in the online version of the paper at www.nature.com/nature.

Received 8 August; accepted 22 December 2010.

Published online 13 March 2011.

- Guo, X. *et al.* Dysfunctional telomeres activate an ATM-ATR-dependent DNA damage response to suppress tumorigenesis. *EMBO J.* **26**, 4709–4719 (2007).
- Denchi, E. L. & de Lange, T. Protection of telomeres through independent control of ATM and ATR by TRF2 and POT1. *Nature* **448**, 1068–1071 (2007).
- Porro, A., Feuerhahn, S., Reichenbach, P. & Lingner, J. Molecular dissection of TERRA biogenesis unveils the presence of distinct and multiple regulatory pathways. *Mol. Cell Biol.* **30**, 4808–4817 (2010).

- Wold, M. S. Replication protein A: a heterotrimeric, single-stranded DNA-binding protein required for eukaryotic DNA metabolism. *Annu. Rev. Biochem.* **66**, 61–92 (1997).
- Baumann, P. & Cech, T. R. Pot1, the putative telomere end-binding protein in fission yeast and humans. *Science* **292**, 1171–1175 (2001).
- Zou, L. & Elledge, S. J. Sensing DNA damage through ATRIP recognition of RPA-ssDNA complexes. *Science* **300**, 1542–1548 (2003).
- Verdun, R. E. & Karlseder, J. The DNA damage machinery and homologous recombination pathway act consecutively to protect human telomeres. *Cell* **127**, 709–720 (2006).
- Moser, B. A. *et al.* Differential arrival of leading and lagging strand DNA polymerases at fission yeast telomeres. *EMBO J.* **28**, 810–820 (2009).
- McGee, J. S. *et al.* Reduced Rif2 and lack of Mec1 target short telomeres for elongation rather than double-strand break repair. *Nature Struct. Mol. Biol.* **17**, 1438–1445 (2010).
- Verdun, R. E., Crabbe, L., Haggblom, C. & Karlseder, J. Functional human telomeres are recognized as DNA damage in G2 of the cell cycle. *Mol. Cell* **20**, 551–561 (2005).
- Kibe, T., Ono, Y., Sato, K. & Ueno, M. Fission yeast Taz1 and RPA are synergistically required to prevent rapid telomere loss. *Mol. Biol. Cell* **18**, 2378–2387 (2007).
- Schramke, V. *et al.* RPA regulates telomerase action by providing Est1p access to chromosome ends. *Nature Genet.* **36**, 46–54 (2004).
- McNees, C. J. *et al.* ATR suppresses telomere fragility and recombination but is dispensable for elongation of short telomeres by telomerase. *J. Cell Biol.* **188**, 639–652 (2010).
- Shiotani, B. & Zou, L. Single-stranded DNA orchestrates an ATM-to-ATR switch at DNA breaks. *Mol. Cell* **33**, 547–558 (2009).
- Wang, F. *et al.* The POT1–TPP1 telomere complex is a telomerase processivity factor. *Nature* **445**, 506–510 (2007).
- Xin, H. *et al.* TPP1 is a homologue of ciliate TEBP-beta and interacts with POT1 to recruit telomerase. *Nature* **445**, 559–562 (2007).
- Takai, K. K., Hooper, S., Blackwood, S., Gandhi, R. & de Lange, T. *In vivo* stoichiometry of shelterin components. *J. Biol. Chem.* **285**, 1457–1467 (2010).
- Ishikawa, F., Matunis, M. J., Dreyfuss, G. & Cech, T. R. Nuclear proteins that bind the pre-mRNA 3' splice site sequence (UUAG/G) and the human telomeric DNA sequence d(TTAGGG)_n. *Mol. Cell Biol.* **13**, 4301–4310 (1993).

19. McKay, S. J. & Cooke, H. hnRNP A2/B1 binds specifically to single stranded vertebrate telomeric repeat TTAGGGn. *Nucleic Acids Res.* **20**, 6461–6464 (1992).
20. LaBranche, H. *et al.* Telomere elongation by hnRNP A1 and a derivative that interacts with telomeric repeats and telomerase. *Nature Genet.* **19**, 199–202 (1998).
21. Zhang, Q. S., Manche, L., Xu, R. M. & Krainer, A. R. hnRNP A1 associates with telomere ends and stimulates telomerase activity. *RNA* **12**, 1116–1128 (2006).
22. Ding, J. *et al.* Crystal structure of the two-RRM domain of hnRNP A1 (UP1) complexed with single-stranded telomeric DNA. *Genes Dev.* **13**, 1102–1115 (1999).
23. Deng, Z., Norseen, J., Wiedmer, A., Riethman, H. & Lieberman, P. M. TERRA RNA binding to TRF2 facilitates heterochromatin formation and ORC recruitment at telomeres. *Mol. Cell* **35**, 403–413 (2009).
24. de Silanes, I. L., d'Alcontres, M. S. & Blasco, M. A. TERRA transcripts are bound by a complex array of RNA-binding proteins. *Nature Commun.* **1**, 1–9 (2010).
25. Azzalin, C. M., Reichenbach, P., Khoraiuli, L., Giulotto, E. & Lingner, J. Telomeric repeat containing RNA and RNA surveillance factors at mammalian chromosome ends. *Science* **318**, 798–801 (2007).
26. Redon, S., Reichenbach, P. & Lingner, J. The non-coding RNA TERRA is a natural ligand and direct inhibitor of human telomerase. *Nucleic Acids Res.* **38**, 5797–5806 (2010).
27. Gong, Y. & de Lange, T. A. Shld1-controlled POT1a provides support for repression of ATR signaling at telomeres through RPA exclusion. *Mol. Cell* **40**, 377–387 (2010).
28. Lei, M., Podell, E. R. & Cech, T. R. Structure of human POT1 bound to telomeric single-stranded DNA provides a model for chromosome end-protection. *Nature Struct. Mol. Biol.* **11**, 1223–1229 (2004).
29. Bochkarev, A., Pfuetzner, R. A., Edwards, A. M. & Frappier, L. Structure of the single-stranded-DNA-binding domain of replication protein A bound to DNA. *Nature* **385**, 176–181 (1997).

Supplementary Information is linked to the online version of the paper at www.nature.com/nature.

Acknowledgements We thank T. de Lange, A. Krainer, B. Chabot and M. Wold for reagents, and members of the Zou laboratory for discussion. L.Z. is an Ellison New Scholar on Aging. R.L.F. is supported by National Institutes of Health (NIH) fellowship 5T32CA009216-28 and American Cancer Society fellowship 0902501. R.C.C. is supported by NIH fellowship F32-GM089150. R.J.O. is supported by the George E. Hewitt Foundation for Medical Research. This work is supported by a Welch Foundation grant (Q-1673) to Z.S., an ACS grant (RSG-08-297) to L.Z., and NIH grants CA133249 to Z.S., CA129037 to S.C., GM06525 and AG025837 to J.K. and GM076388 to L.Z.

Author Contributions R.L.F. and L.Z. conceived the project. R.L.F., R.C.C., R.J.O., R.R., A.T. and L.Z. performed the experiments. Z.S. contributed the POT1–TPP1 complex purified from insect cells. R.R. and S.C. performed the combined RNA-fluorescence *in situ* hybridization and immunostaining analysis. R.J.O. and J.K. performed the RPA chromatin immunoprecipitation and northern blot. R.L.F. and L.Z. wrote the paper.

Author Information Reprints and permissions information is available at www.nature.com/reprints. The authors declare no competing financial interests. Readers are welcome to comment on the online version of this article at www.nature.com/nature. Correspondence and requests for materials should be addressed to L.Z. (zou.lee@mgh.harvard.edu).

METHODS

ATR activation. To generate the 800-base-pair (bp) telomeric dsDNA fragment, the pSTY11 plasmid (a gift from T. de Lange) was digested with EcoRI and the excised fragment was gel purified. The 800-bp random sequence dsDNA was generated by PCR and column purified. These dsDNA fragments were incubated with T7 exonuclease for 15 s at room temperature (approximately 23 °C) and flash frozen in an ethanol-dry-ice bath. T7 was inactivated by subsequent incubation at 70 °C for 20 min and DNA fragments were separated on 2% agarose gel to confirm equal resection. The resected DNA fragments were incubated with nuclear extract as previously described¹⁴. To monitor specifically the phosphorylation of RPA2 by ATR and eliminate the contributions of ataxia telangiectasia mutated (ATM) and DNA-PK to RPA2 phosphorylation, nuclear extracts were pre-treated with 20 μ M KU55933 and NU7026 inhibitors for 15 min at 4 °C. The extracts were mixed with the DNA fragments, incubated for 15 min at 37 °C, and RPA phosphorylation was analysed by western blot.

Protein purification. The POT1–TPP1 complex was either purified from baculovirus-infected Sf9 cells as previously described¹⁶, or purified from HEK293E cells as follows. The pCL–Flag–POT1 and pCL–Flag–TPP1 vectors¹⁶ were individually transfected or co-transfected into HEK293E cells. The cells were collected after 72 h and lysed in the NETN buffer (100 mM NaCl, 1 mM EDTA, 20 mM Tris-HCl (pH 8.0), 0.5% NP-40 and protease inhibitors), sonicated and cleared by centrifugation (10,000g for 10 min). The cleared lysates were incubated with the M2 anti-Flag antibody-conjugated beads at 4 °C for 2 h and eluted with 200 μ g ml^{−1} 3 \times Flag peptide in buffer A (25 mM Tris-HCl (pH 8.0), 100 mM NaCl, 10% glycerol) for 1 h. Recombinant RPA complex was purified from *E. coli* as previously described³⁰. hnRNPA1 pET9d plasmid (a gift from A. Krainer) was transformed into *E. coli* and expression was induced with IPTG (0.4 mM) for 3 h at 37 °C. The cells were then collected and lysed in binding buffer (10 mM Tris-HCl (pH 7.5), 100 mM NaCl, 10 μ g ml^{−1} BSA, 10% glycerol, 0.05% NP-40). Lysates were sonicated, cleared by centrifugation (10,000g for 10 min) and incubated with ssTEL- (50 μ M) conjugated M280 beads (100 μ l) for 30 min at room temperature. The ssTEL and associated protein were captured by magnets, washed in binding buffer and eluted with 1 M NaCl for 10 min at 4 °C. The eluted protein was then diluted in binding buffer without salt to bring the final NaCl concentration down to 100 mM. *E. coli* single-stranded binding protein (SSB) was purchased from Promega.

Gel-shift assay. The 18-nucleotide telomeric ssDNA probe [(TTAGGG)₃] was radiolabelled with γ -³²P using T4 kinase and purified over a G25 column. The labelled ssDNA was incubated with purified RPA or POT1–TPP1 in binding buffer (10 mM Tris-HCl (pH 7.5), 100 mM NaCl, 10 μ g ml^{−1} BSA, 10% glycerol, 0.05% NP-40) for 30 min at room temperature. The resulting protein–DNA complexes were separated by gel electrophoresis using 0.8% agarose at 140 V for 1.5 h and bands were visualized by autoradiography.

DNA–protein binding assay using biotinylated ssDNA. Biotinylated ssTEL [(TTAGGG)₈] or ssMUT [(TTTGCG)₈] were attached to streptavidin-coated magnetic beads in 10 mM Tris-HCl (pH 8.0), 100 mM NaCl at room temperature for 30 min. To analyse the bindings of purified RPA, POT1–TPP1 and POT1 to ssDNA, biotinylated ssDNA (1 pmol) was incubated with various amounts of purified protein in 500 μ l of binding buffer. To analyse the binding of RPA and Flag–POT1 to ssDNA in extracts, biotinylated ssDNA (10 pmol) and various amounts of extracts were added to 500 μ l of binding buffer. After incubation for 30 min, the protein–DNA complexes were retrieved with a magnet and washed three times with binding buffer. In the experiments using RPA or POT1 pre-coated ssDNA, biotinylated ssDNA (1 pmol) was first incubated with purified protein (3.8 pmol) for 30 min at room temperature. The ssDNA pre-coated with RPA or POT1 was retrieved with a magnet and subsequently mixed with increasing concentrations of WCE, nuclear extract or cytoplasmic extract for 30 min at room temperature. For nuclear extract inhibited by addition of TERRA or its derivatives ((UUAGGG)₃, (CCCAUU)₃ and (UUGGCG)₃), extracts were incubated with 1, 2, 5 or 10 pmol RNA for 30 min at 4 °C.

For hnRNPA1 binding, RPA-coated ssTEL or ssMUT (0.8 nM), or Flag–POT1-coated ssTEL (0.8 nM), were incubated with increasing concentrations of hnRNPA1 purified from *E. coli* (2.4, 4.8, 7.2 nM) and the proteins remaining on ssTEL were analysed by western blot. For TERRA inhibition, hnRNPA1 was pre-incubated with increasing concentrations of TERRA (2, 4, 10, 20 nM), or control RNA (UUGGCG)₃. hnRNPA1 was then incubated with RPA coated ssTEL (0.8 nM). Similarly, to demonstrate that TERRA promotes the dissociation of hnRNPA1 from ssTEL, the ssTEL (0.8 nM) was pre-coated with hnRNPA1 (2.4 nM) and subsequently incubated with increasing concentrations of TERRA (2, 20, 200, 2,000 nM). To demonstrate that TERRA enhances POT1 binding, ssTEL (0.8 nM) was pre-coated with hnRNPA1 (2.4 nM) then incubated with both POT1 (2.4 nM) and increasing concentrations of TERRA (2, 20, 200 nM). In all reactions, the proteins remaining on DNA were analysed by western blot.

Cell synchronization. To follow the progression of cells from S to G2 (Fig. 4b, e), HeLa cells were synchronized with 2 mM thymidine for 16 h, washed three times with PBS and once with thymidine-free medium, and released into thymidine-free medium. To enrich HeLa cells in S phase of the cell cycle (Fig. 4a), cells were either collected after treatment for 16 h with 2 mM thymidine (early S), or collected 4 h after thymidine release (late S). To enrich cells in G1 and M phases, cells were either collected after treatment for 16 h with 0.1 μ g ml^{−1} nocodazole (M), or collected 4 h after nocodazole release (G1).

Extract preparation. WCEs were either generated with the NETN buffer as described in the protein purification section, or with the binding buffer used in the DNA binding assays. Nuclear extract and cytoplasmic extract were generated as previously described³. To treat extracts with TERRA or its derivative RNA, RNA was added to WCE or nuclear extract in increasing concentrations (1, 2, 5, 10 pmol) and incubated for 30 min on ice.

Capture of RPA-displacing activity from extracts. To capture the RPA-displacing activity from extracts, RPA-coated ssTEL was incubated with nuclear extract for 30 min at room temperature. The beads were collected, washed three times in binding buffer, and eluted using the binding buffer with 1 M NaCl for 10 min on ice. The eluted material was collected, and diluted with the binding buffer without NaCl to reach a final NaCl concentration of 100 mM. The elution was incubated on ice for 1 h then added to RPA-coated ssDNA and incubated for 30 min at room temperature. For TERRA inhibition, either TERRA (UUAGGG)₃ or its derivative (CCCAUU)₃ were incubated with the eluted proteins before their addition to RPA-coated ssDNA. The proteins remaining bound to DNA were analysed by western blot.

Identification of the RPA-displacing factors from extracts. Biotinylated ssTEL or ssMUT (20 pmol) was attached to streptavidin-coated beads and coated with recombinant RPA. The RPA-coated ssTEL or ssMUT was incubated with 65 μ g of nuclear extract in 500 μ l of binding buffer. Beads with no DNA attached were used as a negative control. After 30 min of incubation, the beads were retrieved and washed three times with binding buffer containing 300 mM NaCl. The proteins associated with the RPA activity were eluted by binding buffer containing 600 mM NaCl for 10 min on ice. The eluted proteins from ssTEL, ssMUT and naked beads were separated by SDS–PAGE. After the gel was silver-stained, the two ~30-kDa bands specifically captured by RPA–ssTEL were excised and analysed by mass spectrometry.

Immunofluorescence analysis. HeLa cells were seeded onto coverslips and cultured overnight. The adhered cells were transfected with POT1 siRNA using oligofectamine (Invitrogen), or with hnRNPA1 siRNA using Lipofectamine RNAi Max (Invitrogen) and cultured for another 48 h. Synchronized cells were treated after 24 h with 2 mM thymidine for 16 h, washed and released, and processed at the indicated time points. Cells were extracted with 0.25% Triton, fixed in 3% paraformaldehyde and further permeabilized with 0.5% Triton. Cells were subsequently incubated with the primary antibodies (diluted in PBS containing 3% BSA and 0.05% Tween 20) for 1 h at 37 °C in a humidified chamber. After extensive washing with PBS, cells were incubated with secondary antibodies for 45 min at room temperature, and washed again with PBS. After incubation for 5 min with DAPI, cells were mounted on slides with Vectashield. Slides were analysed using a Nikon H600L fluorescence microscope.

Combined immunofluorescence–RNA fluorescence in situ hybridization. Cells were grown on coverslips and collected at different time points 17 h after release of single thymidine block. Cells were washed twice with cold PBS for 5 min and treated with cyto buffer (100 mM NaCl, 300 mM sucrose, 3 mM MgCl₂, 10 mM PIPES pH 7, 0.1% Triton X-100, 200 mM vanadyl ribonucleoside complex) for 7 min at 4 °C. Cells were rinsed briefly, fixed with 4% paraformaldehyde in PBS (USB 19943) for 10 min at room temperature. Cells were then washed three times with PBS for 5 min each and permeabilized with 0.5% NP40 in PBS for 10 min. Cells were washed twice with PBS for 5 min each and incubated with blocking solution (0.2% fish gelatin and 0.5% BSA) for 1 h. Cells were then incubated with human TRF2 antibody (clone 4A794 Upstate) at 1:2,000 and diluted in blocking solution for 2 h. After washing three times with PBST (PBS containing 0.1% Triton) for 10 min each, the cells were then incubated with secondary antibody Alexa 488 (Invitrogen A11001) at 1:2,000 dilution in blocking solution for 1 h. Cells were washed three times with PBST for 10 min each and were fixed with 4% paraformaldehyde in PBS for 10 min at room temperature. Cells were rinsed briefly with PBS then incubated with hybridization mix (10 nM PNA–TAMRA–(CCCTAA) probe, 50% formamide, 2 \times SSC, 2 mg ml^{−1} BSA, 10% dextran sulphate, 10 mM vanadyl ribonucleoside complex) for 18 h in a humidified chamber at 39 °C. Cells were washed with 2 \times SSC in 50% formamide three times at 39 °C for 5 min each, three times in 2 \times SSC at 39 °C for 5 min each, and finally once in 2 \times SSC at room temperature for 10 min. Coverslips were then mounted on glass microscope slides with Vectashield mounting medium containing DAPI (H-1200). For RNaseA treatment, coverslips were incubated with 200 μ g ml^{−1} RNase A for

30 min at 37 °C before hybridization. Images were captured with an Endore cooled CCD (charge-coupled device) camera on a Nikon eclipse 80i microscope and the images processed with NIS-Element BR 3.10 software.

Chromatin immunoprecipitation. RPA chromatin immunoprecipitation and the analysis of telomere association were performed as previously described⁷. Cells were transfected twice with hnRNPA1 siRNA (hnRNPA1-1) and synchronized with thymidine for 15 h. The two RPA2 antibodies used were from Abcam and Thermo.

Antibodies and siRNA. The RPA pS33 antibody was from Bethyl. The monoclonal antibody to RPA2 was from Neomarkers. The anti-FLAG M2 antibody was from Sigma. The Chk1 antibody and Cyclin A antibody were from Santa Cruz, and

the phospho-Chk1 Ser345 antibody was from Cell Signaling. The TRF2 antibody was from Bethyl. The phospho-H3 Ser10 antibody was from Millipore. The H4 antibody was from Active Motif. The hnRNPA1 antibody was from Cell Signaling. The POT1 siRNA used in Fig. 4e and Supplementary Fig. 10 was the SMARTPOOL from Dharmacon. The hnRNPA1 siRNAs used in Fig. 4c, d and Supplementary Figs 8 and 9 were CAACUUCGGUC-GUGGAGGA and UCCACGACCACCACCAAAG.

30. Henricksen, L. A. & Wold, M. S. Replication protein A mutants lacking phosphorylation sites for p34cdc2 kinase support DNA replication. *J. Biol. Chem.* **269**, 24203–24208 (1994).

Increasing adult hippocampal neurogenesis is sufficient to improve pattern separation

Amar Sahay^{1,2}, Kimberly N. Scobie^{1,2}, Alexis S. Hill^{1,2}, Colin M. O'Carroll^{1,2}, Mazen A. Kheirbek^{1,2}, Nesha S. Burghardt^{1,2}, André A. Fenton³, Alex Dranovsky^{1,2} & René Hen^{1,2,4}

Adult hippocampal neurogenesis is a unique form of neural circuit plasticity that results in the generation of new neurons in the dentate gyrus throughout life^{1,2}. Neurons that arise in adults (adult-born neurons) show heightened synaptic plasticity during their maturation³ and can account for up to ten per cent of the entire granule cell population⁴. Moreover, levels of adult hippocampal neurogenesis are increased by interventions that are associated with beneficial effects on cognition and mood, such as learning⁵, environmental enrichment⁶, exercise⁶ and chronic treatment with antidepressants^{7–10}. Together, these properties of adult neurogenesis indicate that this process could be harnessed to improve hippocampal functions. However, despite a substantial number of studies demonstrating that adult-born neurons are necessary for mediating specific cognitive functions¹¹, as well as some of the behavioural effects of antidepressants^{8–10,12,13}, it is unknown whether an increase in adult hippocampal neurogenesis is sufficient to improve cognition and mood. Here we show that inducible genetic expansion of the population of adult-born neurons through enhancing their survival improves performance in a specific cognitive task in which two similar contexts need to be distinguished. Mice with increased adult hippocampal neurogenesis show normal object recognition, spatial learning, contextual fear conditioning and extinction learning but are more efficient in differentiating between overlapping contextual representations, which is indicative of enhanced pattern separation. Furthermore, stimulation of adult hippocampal neurogenesis, when combined with an intervention such as voluntary exercise, produces a robust increase in exploratory behaviour. However, increasing adult hippocampal neurogenesis alone does not produce a behavioural response like that induced by anxiolytic agents or antidepressants. Together, our findings suggest that strategies that are designed to increase adult hippocampal neurogenesis specifically, by targeting the cell death of adult-born neurons or by other mechanisms, may have therapeutic potential for reversing impairments in pattern separation and dentate gyrus dysfunction such as those seen during normal ageing^{14,15}.

The dentate gyrus subregion of the hippocampus is a substrate for both cognition and mood regulation. Convergent lines of evidence from neuroanatomical, computational, electrophysiological, behavioural and human brain imaging studies suggest a crucial role for the dentate gyrus in the formation of new episodic memories. The dentate gyrus is thought to transform similar experiences or events into discrete, non-overlapping representations, a process known as pattern separation¹⁶. In addition, overexpression of neurotrophins or transcription factors in the dentate gyrus elicits antidepressant-like behavioural effects^{17,18}. Consistent with these functions of the dentate gyrus, ablation of adult hippocampal neurogenesis impairs pattern separation^{11,19} and blocks some of the behavioural effects of antidepressants^{8–10,12,13}. It is unclear, however, how the converse process, selectively increasing adult hippocampal neurogenesis, affects cognition and mood. Addressing this question has proven difficult owing to a lack of available strategies that selectively increase adult neurogenesis.

Here we developed a genetic gain-of-function strategy to inducibly augment the survival of adult-born neurons in a cell-autonomous manner (Fig. 1a). Because 60–80% of young adult-born neurons undergo programmed cell death, for which the pro-apoptotic gene *Bax* is required²⁰, we used a transgenic mouse line in which the tamoxifen (TAM)-regulatable recombinase CreER^{T2} is expressed under the control of a 5.26-kilobase fragment of the rat nestin (*Nes*) gene promoter (A. Dranovsky *et al.*, manuscript in preparation) together with a *Bax* conditional knockout mouse line²¹ to ablate *Bax* selectively in neural stem cells in the adult brain (Supplementary Fig. 1). Using an inducible reporter, enhanced yellow fluorescent protein (EYFP), as a surrogate marker for *Bax* recombination, we found that $57.5 \pm 3.3\%$ of doublecortin (DCX)-expressing neurons expressed EYFP (Supplementary Figs 1 and 2).

Adult hippocampal neurogenesis was analysed in mice carrying two *loxP*-flanked *Bax* alleles (*Bax*^{fl/fl}) and one *Nes-CreER*^{T2} allele (denoted NCff mice) that had been injected with TAM (referred to as *iBax*^{Nes} mice) or injected with vehicle as a control (Fig. 1b). These mice showed comparable levels of stem cell proliferation in the dentate gyrus (Supplementary Fig. 3). By contrast, we found a marked increase in the survival of adult-born neurons at 8 weeks after TAM injection. Analysis of the population of 1–3-week-old adult-born neurons by DCX immunohistochemistry uncovered a significant (1.8-fold and 2-fold) increase in the total number of DCX⁺ neurons and DCX⁺ neurons that have at least tertiary dendrites, respectively (Fig. 1c).

Quantification of long-term survival by 5-bromodeoxyuridine (BrdU) pulse-chase experiments revealed a 3.6-fold increase in BrdU-labelled cells in the granule cell layer of the dentate gyrus of *iBax*^{Nes} mice, with no change in the proportion of adult-born neurons (BrdU-labelled neuron-specific nuclear protein (NeuN)⁺ cells; Supplementary Fig. 5). In accordance with these findings, there was a 3-fold increase in the population of EYFP-labelled adult-born neurons at 6 weeks after TAM injection (Fig. 1d). The larger increase in the number of DCX⁺ cells in *iBax*^{Nes} mice that was observed at 8 weeks after TAM injection compared with 4 weeks (Supplementary Fig. 4) is consistent with the fact that CreER^{T2}-mediated recombination occurs in both type I neural stem cells (which divide slowly and self-renew) and type II neural progenitors (which are transit amplifying cells) (Supplementary Fig. 1). The expansion of the reservoir of adult-born neurons along the septotemporal axis of the hippocampus in *iBax*^{Nes} mice is comparable to, if not greater than, that observed following chronic antidepressant treatment^{7–10}, environmental enrichment⁶ or exercise⁶. In addition, *iBax*^{Nes} mice show an increase in adult-born cell survival in the olfactory bulb (Supplementary Fig. 5). Control mice and *iBax*^{Nes} mice have a similar body weight, brain architecture and expression of dentate gyrus markers such as calbindin (Supplementary Fig. 6). Surprisingly, the volume of the granule cell layer in the dentate gyrus of both groups is comparable, suggesting that neuronal packing density may be increased in *iBax*^{Nes} mice (Supplementary Fig. 6). In the absence of TAM, no recombination was observed at the

¹Departments of Neuroscience and Psychiatry, Columbia University, New York, New York 10032, USA. ²Division of Integrative Neuroscience, The New York State Psychiatric Institute, New York, New York 10032, USA. ³The Robert F. Furchgott Center for Neural and Behavioural Science, Departments of Physiology and Pharmacology and Neurology, State University of New York, Downstate Medical Center, New York, New York 11203, USA. ⁴Department of Pharmacology, Columbia University, New York, New York 10032, USA.

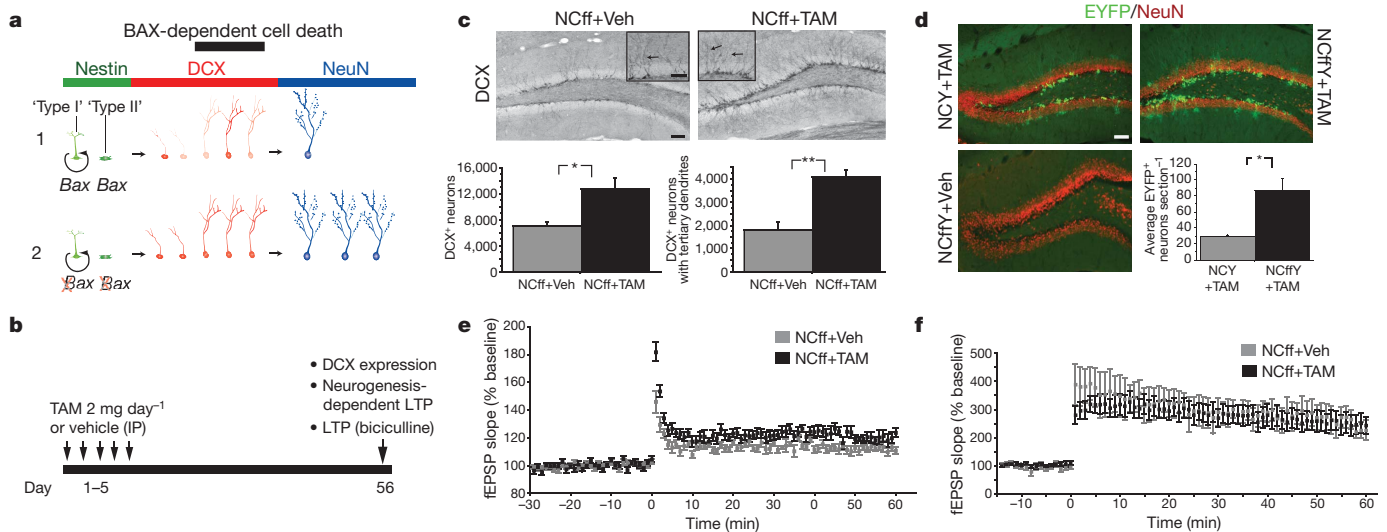


Figure 1 | *Bax* ablation in neural stem cells in the adult brain increases hippocampal neurogenesis and neurogenesis-dependent LTP. **a**, Schematic illustrating genetic gain-of-function strategy to increase adult hippocampal neurogenesis. (1) In the adult dentate gyrus, a substantial fraction of adult-born neurons undergo BAX-dependent programmed cell death (pale red). (2) *Nes-CreER^{T2}*-mediated ablation of *Bax* in type I and type II cells results in the generation of adult-born neurons that lack BAX, thereby preventing their death. **b**, Experimental design. IP, intraperitoneal. **c**, Representative coronal hippocampal sections immunostained for DCX from vehicle (Veh)- and TAM-treated NCff mice (top). Insets are at higher magnification; arrows in insets indicate DCX⁺ neurons with at least tertiary dendrites. Quantification of DCX⁺ population (bottom): total number of DCX⁺ neurons, 6,974 ± 600 (NCff+Veh mice) and 12,636 ± 1764 (NCff+TAM) (*, *P* = 0.038, unpaired two-tailed Student's *t*-test; *n* = 3 mice per group); and total number of DCX⁺ neurons with at least tertiary dendrites, 1,800 ± 340 (NCff+Veh) and 4,090 ± 285 (NCff+TAM) (**, *P* = 0.006; *n* = 3 mice per group). **d**, Representative coronal hippocampal sections immunostained for EYFP and

conditional locus *ROSA26^{fstopEYFP}* in NCffY mice, which are transgenic for *Nes-CreER^{T2}*; *Bax^{fl/fl}*; *ROSA26^{fstopEYFP/+}* (Fig. 1d).

We next examined the morphological maturation of adult-born neurons after *Bax* ablation in neural stem cells in the adult brain. Sholl analysis of genetically labelled 6-week-old adult-born neurons in NCffY mice and NCY mice (which are transgenic for *Nes-CreER^{T2}*; *ROSA26^{fstopEYFP/+}*) indicated that apical dendrite maturation and retraction of basal dendrites were normal (Supplementary Fig. 7). Analysis of the mossy fibres of young adult-born neurons that had been genetically labelled with tau-enhanced green fluorescent protein (EGFP) expressed under the control of the pro-opiomelanocortin- α gene promoter (*Pomc- τ -EGFP*) in *iBax^{Nes}* mice and control mice indicated that there was normal axonal extension and targeting in the CA3 subregion of the hippocampus (Supplementary Fig. 8). To assess the functional integration of adult-born neurons in *iBax^{Nes}* mice, we examined a form of long-term potentiation (LTP) at the synapses of medial perforant path axons onto dentate granule neurons; this form of LTP depends on young adult-born neurons^{22,23} and is enhanced by chronic treatment with fluoxetine²⁴. A significant enhancement in neurogenesis-dependent LTP occurred in *iBax^{Nes}* mice at 4–6 weeks (Supplementary Fig. 9) and at 8 weeks (Fig. 1e) after injection with vehicle or TAM. By contrast, LTP of mature granule neurons in the dentate gyrus, recorded in the presence of bicuculline (Fig. 1f), and basal synaptic transmission (Supplementary Fig. 9) were similar in both groups. These findings suggest that increasing the number of adult-born neurons is sufficient to enhance neurogenesis-dependent LTP and that additional adult-born neurons in *iBax^{Nes}* mice have functionally integrated into the hippocampal network.

To investigate whether there is a causal relationship between increased hippocampal neurogenesis and hippocampus-dependent

NeuN from TAM-treated NCY and NCffY mice and Veh-treated NCffY mice. Quantification of EYFP⁺ neuronal population: mean number of EYFP⁺ neurons per section, whole hippocampus 29.3 ± 2.1 (NCY+TAM) and 87.6 ± 14.3 (NCffY+TAM) (*, *P* = 0.015, unpaired two-tailed Student's *t*-test); septal 28.76 ± 2.3 (NCY+TAM) and 76.3 ± 15.4 (NCffY+TAM) (*, *P* = 0.03) (data not shown); and temporal 30.66 ± 5.7 (NCY+TAM) and 103.6 ± 20 (NCffY+TAM) (*, *P* = 0.02) (data not shown). Mice per group, *n* = 3. **e**, NCff+TAM mice show enhanced medial-perforant-path–dentate-gyrus LTP compared with NCff+Veh mice. Treatment with TAM has a significant effect: *F*_(1,17) = 5, *P* = 0.039 (ANOVA with repeated measures, 50 min). Post-tetanic potentiation differed significantly between the two groups: *P* = 0.003. (NCff+Veh, *n* = 8 slices, six mice; NCff+TAM, *n* = 11 slices, seven mice.) fEPSP, field excitatory postsynaptic potential. **f**, Medial-perforant-path–dentate-gyrus LTP induced in the presence of bicuculline was similar among the groups: *F*_(1,8) < 1 (ANOVA with repeated measures, last 30 min). NCff+Veh, *n* = 4 slices, three mice; NCff+TAM, *n* = 6 slices, three mice. **c–f**, Results are presented as mean ± s.e.m. **c**, **d**, Scale bar, 100 μ m.

learning and memory, we tested *iBax^{Nes}* mice and control mice in object recognition and spatial learning and memory tests. Both *iBax^{Nes}* mice and control mice showed comparable levels of exploration of a novel object, as well as comparable levels for a similar object (Supplementary Fig. 10). Increasing adult hippocampal neurogenesis did not affect spatial learning and memory in the reference version of the Morris water maze, during reversal learning or in the active place avoidance task (Supplementary Figs 11 and 12).

To test whether increased adult hippocampal neurogenesis influences rapid contextual encoding, we subjected *iBax^{Nes}* mice and control mice to a single trial contextual fear-conditioning test (Fig. 2a). Control mice and *iBax^{Nes}* mice showed indistinguishably increased levels of freezing in training context 'A' at 24 h after being trained in A, suggesting that both groups acquired and retained contextual fear conditioning equally well (Fig. 2b and Supplementary Fig. 13) (analysis of variance (ANOVA), *F*_(1,26) < 1; mean freezing, 34.74 ± 7.18% (NCff+Veh) and 35.26 ± 6.6% (NCff+TAM)). Like control mice, *iBax^{Nes}* mice showed negligible levels of freezing behaviour in a distinct context, 'C', that had few features in common with training context A (Fig. 2b) (ANOVA context C, *F*_(1,26) < 1; mean freezing, 4.89 ± 0.78% (NCff+Veh) and 4.03 ± 0.82% (NCff+TAM)); comparison of freezing in contexts A and C, two-way ANOVA (context), *F*_(1,52) = 38.3, *P* < 0.0001). These results indicate that fear conditioning in both groups was specific to the training context and that increasing adult hippocampal neurogenesis does not affect the ability of an animal to distinguish between two markedly different contexts. Control experiments using mice that were homozygous for the *loxP*-flanked *Bax* allele (*Bax^{fl/fl}*; denoted ff mice) showed that TAM treatment alone does not affect contextual fear conditioning (Fig. 2b and Supplementary Fig. 13) (ANOVA, *F*_(1,29) < 1; mean freezing (context A), 33.8 ± 4.9% (ff+Veh) and 28.9 ± 4.7% (ff+TAM);

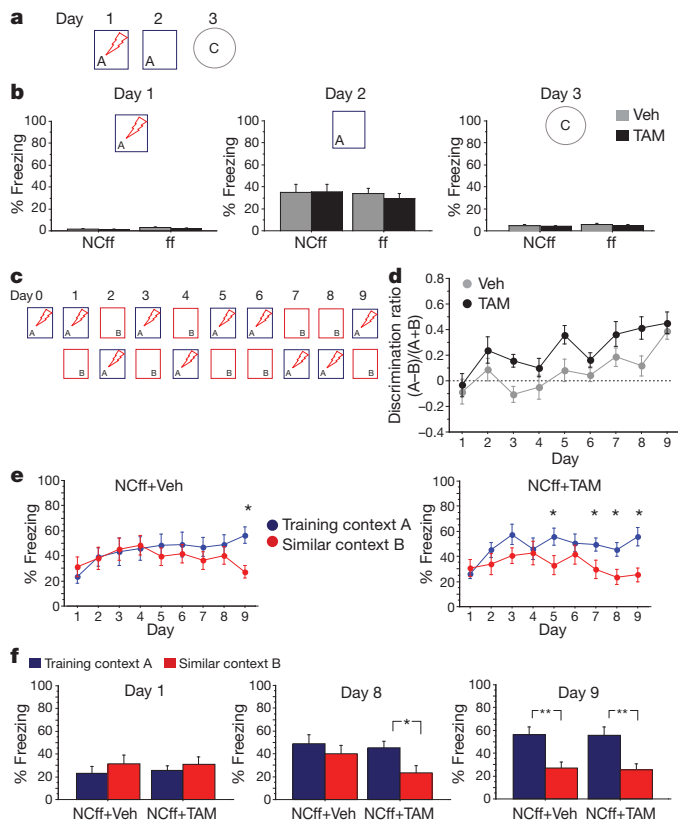


Figure 2 | Increasing adult hippocampal neurogenesis is sufficient to improve discrimination between similar contexts. **a**, Experimental design to test rapid one-trial contextual encoding. **b**, On day 1, both groups showed negligible levels of freezing in context A before a single 2-s, 0.75-mA foot shock (denoted by the red lightning bolt) was delivered. Controls (NCff+Veh) ($n = 14$) and mice with more adult-born neurons (NCff+TAM) ($n = 14$) showed comparable levels of conditioning to training context A and negligible levels of freezing in a distinct context, C. TAM treatment alone did not affect contextual encoding, as reflected in the similar levels of freezing of ff+Veh ($n = 15$) and ff+TAM ($n = 16$) mice in contexts A and C. **c**, Experimental design to test discrimination between two similar contexts, A and B. **d**, Analysis of discrimination ratios. NCff+TAM mice show significantly higher levels of discrimination between the two contexts than do NCff+Veh mice. **e**, Freezing behaviour of mice with increased adult hippocampal neurogenesis (NCff+TAM) and controls (NCff+Veh) over the duration of the experiment. Although both groups show comparable and extensive generalization between the two contexts at the beginning of the experiment, NCff+TAM mice ($n = 11$) distinguished between contexts A and B more rapidly than did NCff+Veh mice ($n = 9$). **f**, NCff+Veh mice were able to discriminate between the two contexts by day 9 of testing: *, $P < 0.05$; **, $P < 0.01$. **b**, **d**–**f**, Results are presented as mean \pm s.e.m.

comparison of freezing in contexts A and C, two-way ANOVA (context), $F_{(1,58)} = 55.23$, $P < 0.0001$).

We next investigated whether increasing the number of adult-born neurons affects a form of learning that requires an animal to distinguish between similar contexts. We chose a contextual fear-discrimination learning task, because it has been proposed to require pattern separation in the dentate gyrus–CA3 circuit²⁵. We first established that this learning task depends on adult hippocampal neurogenesis by testing ff mice in which adult hippocampal neurogenesis, but not subventricular zone neurogenesis, was abolished by X-ray irradiation of the hippocampus. Mice lacking adult-born dentate granule neurons were impaired in their ability to distinguish between two similar contexts (Supplementary Fig. 14).

We then examined whether increasing adult hippocampal neurogenesis is sufficient to improve contextual fear-discrimination learning (Fig. 2c). On day 1, both *iBax*^{Nes} mice and control mice showed

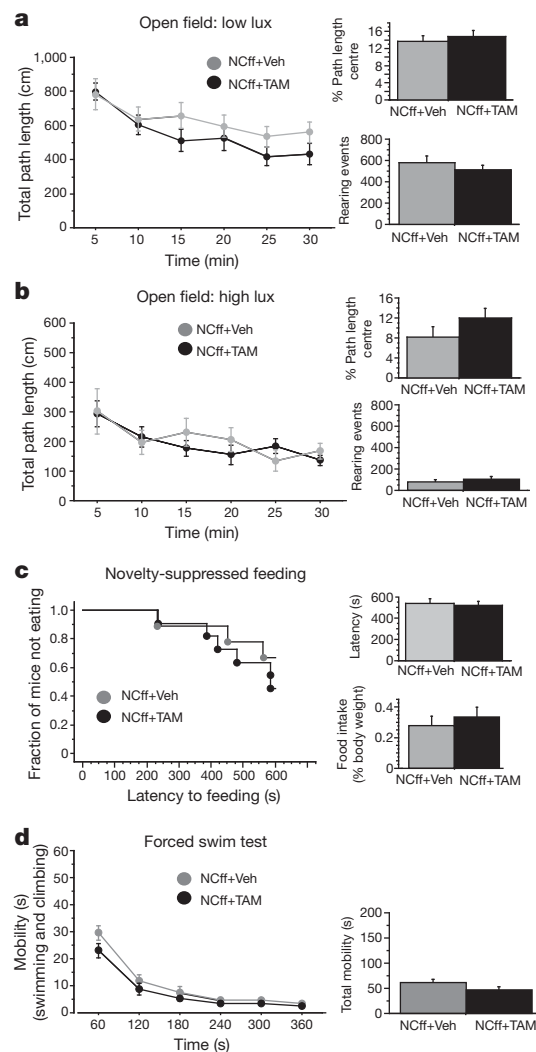


Figure 3 | Increasing adult hippocampal neurogenesis does not produce anxiolytic or antidepressant-like behavioural effects. **a**, **b**, NCff+Veh and NCff+TAM mice showed comparable locomotor activity, rearing events and anxiety-like behaviour in the open field test under two different lighting conditions (with per cent path length centre being the ratio of the distance travelled in the centre of the open field and the total distance travelled in the open field). **c**, NCff+Veh and NCff+TAM mice show similar anxiety-like behaviour in the novelty-suppressed feeding test. **d**, The total mobility of NCff+Veh and NCff+TAM mice did not differ significantly in the forced swim test. Left, swimming and climbing behaviour are shown as a function of time. Right, mobility for the entire session is shown. **a**–**d**, $n = 9$ – 14 mice per group; results are presented as mean \pm s.e.m.

comparable levels of freezing in context A and context B, suggesting that context B shared enough features with context A to elicit generalization of contextual fear in both groups (Fig. 2e, f) (two-way ANOVA of context and treatment, (context) $F_{(1,18)} = 1$, $P = 0.3$; (treatment) $F_{(1,18)} < 1$, $P = 0.85$; (context \times treatment) $F_{(1,18)} < 1$, $P = 0.82$).

Analysis of discrimination ratios for each animal in both groups over the nine days of testing (see Methods), however, revealed that *iBax*^{Nes} mice had significantly higher levels of discrimination between the two contexts than control mice (Fig. 2d) (two-way repeated measures ANOVA of treatment over days, (treatment) $F_{(1,18)} = 6.15$, $P = 0.023$; (day) $F_{(1,18)} = 9.89$, $P < 0.0001$). Analysis of freezing behaviour over days of each group in both contexts showed that NCff+TAM mice had significantly lower levels of freezing in context B than in context A four days earlier than the NCff+Veh group (Fig. 2e, f) (two-way repeated measures ANOVA of context and day followed by Fisher's predicted least-square difference post hoc tests, NCff+Veh (context)

$F_{(1,16)} < 1$, $P = 0.46$; NCff+Veh (day) $F_{(7,112)} < 1$, $P = 0.53$; NCff+Veh (context \times day) $F_{(7,112)} = 3.1$, $P = 0.004$; NCff+TAM (context) $F_{(1,20)} = 3.4$, $P = 0.07$; NCff+TAM (day) $F_{(7,140)} = 4.3$, $P = 0.0002$; NCff+TAM (context \times day) $F_{(7,140)} = 3.8$, $P = 0.0008$). Furthermore, *iBax^{Nes}* mice showed better discrimination than control mice in two other versions of the contextual fear-discrimination learning task (Supplementary Fig. 15).

The enhanced contextual fear-discrimination learning of *iBax^{Nes}* mice was not accompanied by changes in extinction learning (Supplementary Fig. 16), and increasing adult hippocampal neurogenesis did not facilitate the erasure of previously encoded memories¹⁶ (Supplementary Fig. 17). Together, these gain-of-function studies demonstrate that increasing the number of adult-born neurons is sufficient to enhance contextual fear-discrimination learning, which is indicative of improved pattern separation.

Next, we tested a separate cohort of *iBax^{Nes}* mice and control mice in a range of tests that assess anxiety-like and depression-like behaviours and that are used in behavioural screens for antidepressants. Increasing adult hippocampal neurogenesis did not affect exploratory behaviour (as assessed by locomotor activity and rearing events) or anxiety-like behaviour (in the open field, light–dark, elevated plus maze and novelty-suppressed feeding tests) (Fig. 3a–c and Supplementary Fig. 18). No difference in depression-like behaviour was found between *iBax^{Nes}* mice and control mice in the forced swim test (Fig. 3d and Supplementary Fig. 18). As a control, treatment of ff mice with TAM had no effect on anxiety-like and depression-like behaviours (Supplementary Fig. 19). Together with previous studies^{8–10,12,13}, these results suggest that stimulation of adult hippocampal neurogenesis may be necessary, but is not sufficient, to produce the behavioural effects of antidepressants.

To determine whether changes in mood are observed after combining the genetic expansion of adult hippocampal neurogenesis with an environmental intervention that is known to stimulate network activity and hippocampal neurogenesis, we exposed both *iBax^{Nes}* mice and control mice to a voluntary exercise regimen (Fig. 4a). As expected, voluntary exercise increased adult hippocampal neurogenesis in both groups (compare Fig. 4b and Fig. 1c). After voluntary exercise, compared with control mice, *iBax^{Nes}* mice showed a modest increase in the DCX⁺ population and a 4.4-fold increase in the number of surviving

adult-born neurons but similar neuronal and glial ratios (Fig. 4b and Supplementary Fig. 20).

Surprisingly, *iBax^{Nes}* mice showed a marked increase in exploratory behaviours and decreased anxiety-like behaviour in the open field test compared with control mice (Fig. 4c) (for total path length, two-way repeated measures ANOVA, (treatment) $F_{(1,19)} = 11.23$, $P = 0.003$; (treatment \times minute) $F_{(11,209)} = 1.9$, $P = 0.03$; for rearing events, ANOVA, $F_{(1,19)} = 7.54$, $P = 0.01$; for per cent path length centre, ANOVA, $F_{(1,19)} = 4.5$, $P = 0.04$; for time in centre, ANOVA, $F_{(1,19)} = 5.01$, $P = 0.037$). However, in the home cage, *iBax^{Nes}* mice showed similar levels of locomotor activity to control mice (Supplementary Fig. 21). The reduction in anxiety-like behaviour by *iBax^{Nes}* mice in the open field test may result from changes in exploratory behaviour rather than from anxiety itself because *iBax^{Nes}* mice showed normal anxiety-like behaviour in the light–dark and novelty-suppressed feeding tests (Supplementary Fig. 21). Control mice and *iBax^{Nes}* mice showed similar antidepressant-like behaviour in the forced swim test after voluntary exercise (Supplementary Fig. 21). A change in the number of adult-born neurons is unlikely to be solely responsible for the increased exploratory behaviour of *iBax^{Nes}* mice because the increase in survival of adult-born neurons in *iBax^{Nes}* mice after exercise relative to control mice is not much greater than that observed without exercise (Supplementary Fig. 5). Instead, it may be that exercise modifies the properties of the already expanded reservoir of young, excitable adult-born neurons in *iBax^{Nes}* mice.

Determining the impact of increasing adult hippocampal neurogenesis on cognition and mood is pivotal to defining the therapeutic potential of strategies aimed at stimulating the production of new dentate granule neurons in the adult brain. Here we show that selectively increasing the survival of adult-born neurons improves cognitive performance when an animal must distinguish between two similar contexts. By contrast, cognitive gains are not produced when the contexts are markedly different or in other forms of learning, such as object recognition or spatial and reversal learning. Our findings are consistent with the proposed role of the dentate gyrus in pattern separation¹⁶.

Our studies on mood regulation uncover a previously unexpected dissociation between the effect of increased adult hippocampal neurogenesis on learning and on mood. Although *iBax^{Nes}* mice show enhanced pattern

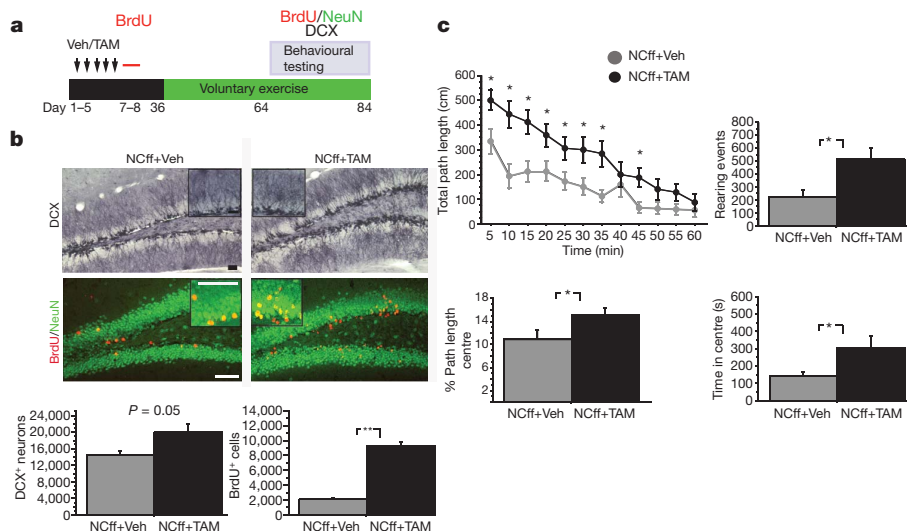


Figure 4 | Mice with more adult-born neurons display increased exploratory behaviour and decreased anxiety-like behaviour in the open field test following a voluntary exercise regimen. **a**, Experimental design. Mice were transferred to cages with running wheels 5 weeks after treatment with Veh or TAM. **b**, Representative images of DCX-immunostained and BrdU- and NeuN-immunostained coronal hippocampal sections from Veh-treated or TAM-treated NCff mice (top). Insets show the granule cell layer at a higher magnification. Scale bars, 100 μ m. Quantification of DCX⁺ neuron population

(bottom, $n = 4–5$ mice per group): total DCX⁺ neurons, 14,527 \pm 987 (NCff+Veh) and 19,893 \pm 2,022 (NCff+TAM) ($P = 0.05$, unpaired two-tailed Student's t -test). Total number of BrdU⁺ cells in the granule cell layer: 2,119 \pm 204 (NCff+Veh) and 9,324 \pm 463 (NCff+TAM) (**, $P < 0.0001$). **c**, NCff+TAM mice showed significantly greater locomotor activity, reduced anxiety-like behaviour and a significant increase in rearing events in the open field test compared with NCff+Veh mice: *, $P < 0.05$ (NCff+Veh, $n = 10$ mice; NCff+TAM, $n = 11$). Results are presented as mean \pm s.e.m.

separation, they do not show anxiolytic or antidepressant-like behaviours. Because *iBax^{Nes}* mice show only a subset of the modifications that are induced by chronic antidepressant treatment (such as enhanced survival of adult-born neurons and increased neurogenesis-dependent LTP)^{7,8,24}, it is probable that other antidepressant-dependent modifications of neural circuitry^{24,26,27} act in concert with increased adult hippocampal neurogenesis to produce the behavioural effects of antidepressants. Consistent with this idea, increasing adult hippocampal neurogenesis enhances exploratory behaviour when combined with voluntary exercise but not under baseline conditions. This result may reflect a role for the dentate gyrus in the modulation of exploratory behaviour²⁸.

Recent studies have found dentate gyrus dysfunction and pattern separation impairments during normal ageing in non-human primates¹⁴ and humans¹⁵, respectively. Deficits in pattern separation may affect not only learning, but also anxiety-related behaviours. In fact, impaired contextual fear discrimination (pattern separation) may result in a bias towards encoding ambiguous cues as threatening and may underlie the excessive generalization that is observed in post-traumatic stress disorder and panic disorder^{29,30}. Stimulating adult hippocampal neurogenesis may therefore be a novel therapeutic strategy for treating such anxiety disorders, as well as age-related memory impairments.

METHODS SUMMARY

Transgenic and conditional knockout mouse lines were used to recombine *Bax* in stem cells in the adult brain (ref. 21 and A. Dranovsky *et al.*, manuscript in preparation). The impact of *Bax* ablation in stem cells on adult hippocampal neurogenesis and on the morphological maturation of adult-born neurons was characterized using various genetic reporter lines in combination with BrdU pulse-chase labelling and standard immunohistochemistry techniques (see Methods). Assessment of LTP at synapses of medial perforant path axons onto dentate granule neurons was performed as described previously²³. Focal X-ray irradiation of the hippocampus was performed²³ using sodium pentobarbital as an anaesthetic agent. Behavioural testing was carried out using hippocampus-dependent learning tests (contextual fear conditioning, contextual fear-discrimination learning²⁵, object recognition, and spatial learning and reversal learning) and tests for anxiety-like and depression-like behaviour. Experimental protocols were approved by the Institutional Animal Care and Use Committee at Columbia University and the New York State Psychiatric Institute. The details of all of the experimental techniques used in this study are available in the Methods.

Full Methods and any associated references are available in the online version of the paper at www.nature.com/nature.

Received 6 November 2009; accepted 10 January 2011.

Published online 3 April 2011.

- Altman, J. & Das, G. D. Autoradiographic and histological evidence of postnatal hippocampal neurogenesis in rats. *J. Comp. Neurol.* **124**, 319–335 (1965).
- Eriksson, P. S. *et al.* Neurogenesis in the adult human hippocampus. *Nature Med.* **4**, 1313–1317 (1998).
- Ge, S., Yang, C. H., Hsu, K. S., Ming, G. L. & Song, H. A critical period for enhanced synaptic plasticity in newly generated neurons of the adult brain. *Neuron* **54**, 559–566 (2007).
- Imayoshi, I. *et al.* Roles of continuous neurogenesis in the structural and functional integrity of the adult forebrain. *Nature Neurosci.* **11**, 1153–1161 (2008).
- Gould, E., Beylin, A., Tanapat, P., Reeves, A. & Shors, T. J. Learning enhances adult neurogenesis in the hippocampal formation. *Nature Neurosci.* **2**, 260–265 (1999).
- van Praag, H., Kempermann, G. & Gage, F. H. Neural consequences of environmental enrichment. *Nature Rev. Neurosci.* **1**, 191–198 (2000).
- Malberg, J. E., Eisch, A. J., Nestler, E. J. & Duman, R. S. Chronic antidepressant treatment increases neurogenesis in adult rat hippocampus. *J. Neurosci.* **20**, 9104–9110 (2000).
- Santarelli, L. *et al.* Requirement of hippocampal neurogenesis for the behavioral effects of antidepressants. *Science* **301**, 805–809 (2003).
- Li, Y. *et al.* TrkB regulates hippocampal neurogenesis and governs sensitivity to antidepressant treatment. *Neuron* **59**, 399–412 (2008).
- David, D. J. *et al.* Neurogenesis-dependent and -independent effects of fluoxetine in an animal model of anxiety/depression. *Neuron* **62**, 479–493 (2009).
- Deng, W., Aimone, J. B. & Gage, F. H. New neurons and new memories: how does adult hippocampal neurogenesis affect learning and memory? *Nature Rev. Neurosci.* **11**, 339–350 (2010).

- Sahay, A. & Hen, R. Adult hippocampal neurogenesis in depression. *Nature Neurosci.* **10**, 1110–1115 (2007).
- Bessa, J. M. *et al.* The mood-improving actions of antidepressants do not depend on neurogenesis but are associated with neuronal remodeling. *Mol. Psychiatry* **14**, 764–773 (2009).
- Small, S. A., Chawla, M. K., Buonocore, M., Rapp, P. R. & Barnes, C. A. Imaging correlates of brain function in monkeys and rats isolates a hippocampal subregion differentially vulnerable to aging. *Proc. Natl Acad. Sci. USA* **101**, 7181–7186 (2004).
- Yassa, M. *et al.* Pattern separation deficits associated with increased hippocampal CA3 and dentate gyrus activity in nondemented older adults. *Hippocampus* doi:10.1002/hipo.20808 (20 May 2010).
- Treves, A., Tashiro, A., Witter, M. E. & Moser, E. I. What is the mammalian dentate gyrus good for? *Neuroscience* **154**, 1155–1172 (2008).
- Shirayama, Y., Chen, A. C.-H., Nakagawa, S., Russell, D. S. & Duman, R. S. Brain-derived neurotrophic factor produces antidepressant effects in behavioral models of depression. *J. Neurosci.* **22**, 3251–3261 (2002).
- Chen, A. C., Shirayama, Y., Shin, K. H., Neve, R. L. & Duman, R. S. Expression of the cAMP response element binding protein (CREB) in hippocampus produces an antidepressant effect. *Biol. Psychiatry* **49**, 753–762 (2001).
- Tronel, S. *et al.* Adult-born neurons are necessary for extended contextual discrimination. *Hippocampus* doi:10.1002/hipo.20895 (3 November 2010).
- Sun, W. *et al.* Programmed cell death of adult-generated hippocampal neurons is mediated by the proapoptotic gene *Bax*. *J. Neurosci.* **24**, 11205–11213 (2004).
- Takeuchi, O. *et al.* Essential role of BAX, BAK in B cell homeostasis and prevention of autoimmune disease. *Proc. Natl Acad. Sci. USA* **102**, 11272–11277 (2005).
- Snyder, J. S., Kee, N. & Wojtowicz, J. M. Effects of adult neurogenesis on synaptic plasticity in the rat dentate gyrus. *J. Neurophysiol.* **85**, 2423–2431 (2001).
- Saxe, M. D. *et al.* Ablation of hippocampal neurogenesis impairs contextual fear conditioning and synaptic plasticity in the dentate gyrus. *Proc. Natl Acad. Sci. USA* **103**, 17501–17506 (2006).
- Wang, J. W., David, D. J., Monckton, J. E., Battaglia, F. & Hen, R. Chronic fluoxetine stimulates maturation and synaptic plasticity of adult-born hippocampal granule cells. *J. Neurosci.* **28**, 1374–1384 (2008).
- McHugh, T. J. *et al.* Dentate gyrus NMDA receptors mediate rapid pattern separation in the hippocampal network. *Science* **317**, 94–99 (2007).
- Schmidt, H. D. & Duman, R. S. The role of neurotrophic factors in adult hippocampal neurogenesis, antidepressant treatments and animal models of depressive-like behavior. *Behav. Pharmacol.* **18**, 391–418 (2007).
- Maya Vetencourt, J. F. *et al.* The antidepressant fluoxetine restores plasticity in the adult visual cortex. *Science* **320**, 385–388 (2008).
- Saab, B. J. *et al.* NCS-1 in the dentate gyrus promotes exploration, synaptic plasticity, and rapid acquisition of spatial memory. *Neuron* **63**, 643–656 (2009).
- Peri, T., Ben-Shakhar, G., Orr, S. P. & Shalev, A. Y. Psychophysiological assessment of aversive conditioning in posttraumatic stress disorder. *Biol. Psychiatry* **47**, 512–519 (2000).
- Lissek, S. *et al.* Overgeneralization of conditioned fear as a pathogenic marker of panic disorder. *Am. J. Psychiatry* **167**, 47–55 (2010).

Supplementary Information is linked to the online version of the paper at www.nature.com/nature.

Acknowledgements We thank J. Gordon, S. Fusi, C. Kellendonk, H. Scharfman and members of the Hen laboratory for comments on the manuscript and discussions about the project. We thank E. Pavlopoulos for consultation on spatial learning, and M. Drew and C. A. Denny for input on the novel object recognition test. A.S. was supported by a 2009 National Institute of Mental Health Grant (1K99MH86615-01), 2006 and 2008 National Alliance for Research on Schizophrenia and Depression (NARSAD) Young Investigator Awards, and a 2008 Sackler Institute of Columbia University Award. K.N.S. was supported by a Ruth L. Kirschstein National Research Service Award for Individual Predoctoral Fellows (F31). R.H. was supported by grants from NARSAD, the New York Stem Cell Initiative (NYSTEM) and the National Institutes of Health (R01 MH068542).

Author Contributions A.S. conceived and designed the experiments, performed the circuitry analysis and behaviour experiments, analysed the data and wrote the manuscript. K.N.S. and A.S.H. contributed to the behavioural testing and circuitry analysis. C.M.O. and M.A.K. performed the electrophysiological experiments. A.D. contributed the *Nes-CreER²* transgenic mouse line used in this study. N.S.B. assisted with focal X-ray irradiation of the mice and performed the active place avoidance experiment in the laboratory of A.A.F. R.H. oversaw the overall execution of the project, contributed to the experimental design and the interpretation of the data, provided financial support and helped to write the manuscript. All authors discussed the results and commented on the manuscript.

Author Information Reprints and permissions information is available at www.nature.com/reprints. The authors declare competing financial interests: details accompany the full-text HTML version of the paper at www.nature.com/nature. Readers are welcome to comment on the online version of this article at www.nature.com/nature. Correspondence and requests for materials should be addressed to A.S. (as2619@columbia.edu) or R.H. (rh95@columbia.edu).

METHODS

Generation of mouse lines. The generation and characterization of the *Nes-CreER^{T2}* transgenic mouse line is described in detail elsewhere (A. Dranovsky *et al.*, manuscript in preparation). The colony of Ncflf mice (that is, *Nes-CreER^{T2}; Bax^{fl/f}* mice) was maintained by interbreeding *Nes-CreER^{T2}; Bax^{fl/f}* mice and *Bax^{fl/f}* mice. The *Bax^{fl/f}* mice generated from these crosses were used to assess the CreER^{T2}-independent effects of TAM on mouse behaviour. An EYFP reporter line (*ROSA26^{fstopEYFP}/+*)³¹ was used in all experiments in which adult-born neurons were inducibly genetically labelled. Specifically, Ncflf and NCY mice were generated as littermates by interbreeding *Nes-CreER^{T2}; Bax^{fl/f}; ROSA26^{fstopEYFP}/+* mice and *Bax^{fl/f}; ROSA26^{fstopEYFP}/+* mice. Ncflf mice were maintained on a mixed (C57BL/6 and 129/SvEv) genetic background. The *Pomc-τ-EGFP* transgenic mouse line was obtained from GENSAT (<http://www.gensat.org>) and used to generate Ncflf; *Pomc-τ-EGFP* mice. To induce CreER^{T2}-mediated recombination of *Bax* and/or *EYFP* in neural stem cells in the adult brain, mice (*Nes-CreER^{T2}; Bax^{fl/f}* mice, *Nes-CreER^{T2}; Bax^{fl/f}; ROSA26^{fstopEYFP}/+* mice, *Nes-CreER^{T2}; ROSA26^{fstopEYFP}/+* mice or *Nes-CreER^{T2}; Bax^{fl/f}; Pomc-τ-EGFP* mice) of at least 8 weeks of age were given 2 mg TAM intraperitoneally, once a day for 5 consecutive days. TAM (10 mg ml⁻¹, Sigma, T-5648) solution was prepared in corn oil containing 10% ethanol. For vehicle, an identical volume of corn oil with 10% ethanol was injected intraperitoneally, once a day for 5 consecutive days. Mice were housed four to five per cage in a 12 h (6 a.m. to 6 p.m.) light–dark colony room at 22 °C and had free access to food and water. For the voluntary exercise regimen, four to five mice were housed per cage (29.2 cm × 19 cm × 12.7 cm), and each cage was equipped with two running wheels. Experimental protocols were approved by the Institutional Animal Care and Use Committee at Columbia University and the New York State Psychiatric Institute.

Electrophysiological recordings. Electrophysiological recordings in the dentate gyrus were performed as previously described^{23,24}. Brains were collected from animals after inducing deep anaesthesia with halothane followed by decapitation, and transverse hippocampal slices (400 µm) were prepared using a vibratome. The slices were incubated in an interface chamber at 32 °C and perfused with oxygenated artificial cerebrospinal fluid (ACSF) (119 mM NaCl, 2.5 mM KCl, 1.3 mM MgSO₄, 2.5 mM CaCl₂, 26.2 mM NaHCO₃, 1 mM NaH₂PO₄ and 11 mM glucose). Slices were allowed to equilibrate for 2 h before positioning the electrodes and beginning stimulation. To record from the dentate gyrus, the medial perforant path (MPP) was stimulated using a stimulation isolation unit and a bipolar tungsten electrode (World Precision Instruments). Evoked potentials were recorded in the molecular layer above the upper blade of the dentate gyrus using a glass capillary microelectrode filled with ACSF (and with a tip resistance of 1–3 MΩ). Isolation of the MPP was confirmed by assessing paired-pulse depression of the MPP–dentate gyrus synaptic connection at 50 ms, which generated the highest level of depression. Input–output curves were obtained after recordings had been stable for 10 min. The stimulation intensity that produced one-third of the maximal response was used for the test pulses and tetanus. After a stable baseline response to test stimulation (once every 20 s) had been observed for 15 min, the ability to elicit LTP was assessed. LTP was induced with a weak stimulation protocol consisting of four trains of 1 s each, at 100 Hz within the train, repeated every 15 s²³. Responses were recorded every 20 s for 60 min after LTP induction. A similar protocol was used to elicit and record LTP of mature dentate granule neurons except that 10 µM bicuculline (bicuculline methobromide, Sigma, B7561) was added to the ACSF to block GABA_A-receptor-mediated inhibition.

Immunohistochemistry and confocal microscopy. To assess the survival of adult-born neurons in the dentate gyrus, BrdU was administered intraperitoneally, once a day in 0.9% NaCl for 2 or 10 days at 150 mg kg⁻¹ body weight. Mice were anaesthetized with ketamine or xylazine (100 and 7 mg kg⁻¹ body weight, respectively) and transcardially perfused (with cold saline, followed by 4% cold paraformaldehyde in PBS). Brains were postfixed overnight in 4% paraformaldehyde at 4 °C, then cryoprotected in 30% sucrose and stored at 4 °C. Coronal serial sections (40 µm) of the entire hippocampus and sagittal sections (40 µm) of the olfactory bulb were obtained using a cryostat and stored in PBS. For BrdU or NeuN immunohistochemistry, sections were mounted onto SuperFrost Plus charged glass slides. Following pretreatment with 10 mM citrate buffer, sections were subjected to antigen retrieval in 10 mM citrate buffer, using a boiling protocol. After cooling to room temperature, sections were rinsed three times in PBS and blocked in PBS with 0.3% Triton X-100 and 10% normal donkey serum (NDS) for 2 h at room temperature. Incubation with primary antibodies was carried out at 4 °C overnight (for BrdU, rat anti-BrdU antibody at 1/100 dilution, Serotec; for NeuN, mouse, 1/500, Chemicon). Fluorescent-label-coupled secondary antibodies (Jackson ImmunoResearch) were used at a final concentration of 1/400 in PBS. For GFAP, NeuN and EYFP triple immunohistochemistry, floating sections were used. Briefly, sections were washed three times in PBS, blocked in PBS buffer containing 0.3% Triton X-100 and 10% NDS, and incubated in primary antibodies overnight, with shaking at 4 °C (GFAP, rabbit, 1/2000, DAKO; NeuN, mouse, 1/500, Chemicon; GFP, chicken, 1/500, Abcam). The next day, sections were washed three times in PBS and incubated with fluorescent-label-coupled secondary

antibodies (Jackson ImmunoResearch) for 2 h at room temperature. For GFP immunohistochemistry alone (rabbit, 1/500, Invitrogen) was used. For calbindin immunohistochemistry, a similar protocol was used (mouse, 1/5,000, Swant). For DCX and Ki67 immunohistochemistry, floating sections were first quenched to remove endogenous peroxidase activity (with 1% H₂O₂ in 1:1 PBS:methanol). Sections were then washed in PBS, blocked (in PBS containing 0.3% Triton X-100 and 10% NDS) and incubated with primary antibody overnight at 4 °C (DCX, goat, 1/500, SantaCruz Biotechnology; Ki67, rabbit, 1/100, Vector Labs). Following washes in PBS, sections were incubated with horse-radish-peroxidase-coupled, biotinylated secondary antibodies. Following incubation with ABC solution (Vector Labs), the colour reaction was carried out using a DAB kit (Vector Labs). An unbiased and blinded quantification protocol was used to quantify DCX⁺ and BrdU⁺ cells in the granule cell layer of the dentate gyrus along the septotemporal axis²⁴. For quantification of survival of adult-born cells in the main olfactory bulb, two high magnification (×20) images of randomly selected regions in the granule cell layer were obtained from six matched sagittal sections for each mouse. BrdU⁺ cells were quantified using a cell counter plug-in for the software ImageJ (NIH), and surface density was computed. Bright-field images were obtained using an Axioplan-2 upright microscope (Zeiss). For quantification of EYFP⁺ neurons in NCY and Ncflf mice, five to six (dorsal) and three (ventral) matched sections were selected, and the mean number of EYFP⁺ neurons per section was computed. Type I neural stem cells expressing EYFP were not included in the analysis. All analyses of mice with the inducible genetic reporter *ROSA26^{fstopEYFP}* were performed at 6 weeks post injection of vehicle or TAM. Phenotyping of BrdU-expressing cells in the granule cell layer of the dentate gyrus entailed the scanning of at least 80 cells from the dorsal and ventral hippocampus of each mouse using an LSM 510 META scanning confocal microscope (Zeiss). To determine the number of BrdU⁺ cells expressing GFAP or NeuN, z-stack analysis was performed using the LSM 510 image browser. To compute the percentage of DCX-expressing cells that also expressed EYFP in Ncflf mice, approximately 120 DCX⁺ neurons per mouse dentate gyrus were scanned using a FluoView 1000 confocal microscope (Olympus) (×40 magnification and numerical aperture (NA) of 1.3). To determine the number of DCX⁺ neurons expressing EYFP, z-stack analysis was performed using FluoView 1000 v1.5 software. Three mice were used for the analysis. A one-in-six series of adjacent sections stained with nuclear fast red (Vector Labs) was used to measure the volume of the granule cell layer in the dentate gyrus.

Quantification of the granule cell layer volume and mossy fibre length in the dentate gyrus. The surface area of the granule cell layer was traced in ImageJ from ×10 images of hippocampal sections spanning the septotemporal axis, and the volume was determined by multiplying the surface area of the granule cell layer by the distance between sections sampled (240 µm). Four mice per group were used for this analysis. To measure the length of axons of young adult-born neurons, we used Ncflf; *Pomc-τ-EGFP* mice, in which axons are genetically labelled with EGFP. Mossy fibre length was determined by tracing the stratum lucidum along the inner edge of the stratum pyramidale. For measurements, the starting point was the intersection of the trace and a line between the tip of the inner and outer blades of the dentate gyrus³². Four dorsal sections from each mouse were used for these measurements.

Sholl analysis. Five to six EYFP⁺ neurons with complex dendritic trees were chosen from each mouse (from both the dorsal and ventral dentate gyrus) and scanned using a FluoView 1000 (Olympus) (×40, 1.3 NA or ×60, 1.42 NA). Images of collapsed z-stacks were imported into Adobe Illustrator CS3, and dendritic trees were reconstructed using the tracing tool. Dendritic complexity was analysed from 8-bit images by using the ImageJ Sholl Analysis plug-in (<http://www-biology.ucsd.edu/labs/ghosh/software/>). The centre of all concentric circles was defined as the centre of the cell's soma. The parameters used were starting radius (10 µm), ending radius (300 µm from the centre) and interval between consecutive radii (10 µm). Three to four mice per group were used.

Focal X-ray irradiation of the hippocampus. Ten-week-old *Bax^{fl/f}* mice were anaesthetized with sodium pentobarbital (administered intraperitoneally at 42 mg kg⁻¹ body weight, once per day on each of three days that were spaced apart by 3–4 days), placed in a stereotaxic frame and exposed to cranial irradiation using a Stabilopan X-ray system (Siemens) operated at 300 kVp and 20 mA. Animals were protected with a lead shield that covered the entire body, but a 3.22 × 11 mm² treatment field above the hippocampus (interaural 3.00 to 0.00) was left unshielded and exposed to X-rays. Dosimetry was done using an electrometer ionization chamber (model PR-06G, Capintec) and Ready Pack Radiographic XV films (Kodak). The corrected dose rate was approximately 1.8 Gy min⁻¹ at a source-to-skin distance of 30 cm. The procedure lasted 2 min 47 s, delivering a total of 5 Gy. Three 5-Gy doses were delivered, on days 1, 4 and 8. Behavioural testing was carried out 4 months after hippocampal X-ray irradiation.

Behavioural testing. Behavioural testing was performed using male and female mice that were 14–18 weeks of age at the time of testing, unless otherwise specified. All experiments and analyses were performed blind to genotype or treatment.

Tests for anxiety-like and depression-like behaviours. Testing in the open field test, light–dark test, elevated plus maze, novelty-suppressed feeding and forced swim tests was carried out at 8 or 10 weeks after vehicle or TAM treatment.

The open field test is a standard test of both anxiety and locomotor behaviour. It consists of a simple square enclosure that is equipped with infrared detectors to track animal movement in the horizontal and vertical planes. Measures of total distance travelled and rearing events are used as an index of exploratory activity³³, whereas the proportion of time or distance spent in the centre is construed as a measure of anxiety-like behaviour. Mice were placed in the corner of the open field, and activity was recorded for 30 or 60 min. Testing took place either under low light (200 lx) or bright light (1,000–1,200 lx) conditions.

The novelty-suppressed feeding test has been validated as a model that is sensitive to chronic, but not acute, antidepressant treatment⁸. Mice were food deprived in their home cages for 24–26 h before testing. The testing apparatus consisted of a plastic arena (45 cm long, 15 cm high and 30 cm wide) whose floor was covered with an approximately 2-cm depth of wood-chip bedding. A single food pellet (familiar laboratory mouse chow) was placed on a circular piece of white filter paper (12 cm in diameter) positioned in the centre of the arena. The test began with a mouse being placed in a corner of the arena, and the latency to approach the pellet and begin feeding was recorded (for a maximum time of 10 min). Testing was carried out under bright light conditions. Each mouse was weighed before food deprivation and just before testing to assess changes in body weight. Immediately after the test, each mouse was transferred to its home cage, and the amount of food consumed within 5 min was measured. When appropriate, survival analysis was performed, and statistical differences between the latencies were determined using the Kaplan–Meier product-limit method.

The elevated plus maze²³ and the light–dark test³⁴ were done as described previously.

For the forced swim test, mice were placed for 6 min in transparent plastic buckets (19 cm in diameter and 23 cm deep) that had been filled with water at 23–25 °C, and their behaviour was recorded using an automated video-tracking system. Testing was carried out over two consecutive days, with the first day serving the purpose of pre-exposure. Mobility (swimming and climbing behaviour) on the second day was analysed using ViewPoint Life Sciences Software.

Object recognition test. At 8 weeks after *Bax* ablation in neural stem cells, separate cohorts of mice were tested for similar and novel object recognition behaviour. NCff mice were tested 8 weeks after TAM or vehicle treatment. Testing entailed placing mice in an arena (45 cm long, 15 cm high and 30 cm wide) with two distinct objects, for seven sessions (each of 7 min) spaced apart by a 3-min intertrial interval. Mice became habituated to the objects during sessions one to six, and one of the objects was then replaced with a novel or a similar object in session seven. Objects and object positions were counterbalanced during testing. The objects that were selected for testing elicited comparable levels of exploration and were categorized as novel or similar based on the exploration levels evoked in NCff mice in pilot experiments. Sessions were video-recorded, and videos were manually scored for locomotion (grid crossings) and object exploration (when an animal's snout was 2 cm or less from the object).

Spatial and reversal learning. A cohort of mice was tested at 8 weeks after *Bax* ablation in neural stem cells. Testing using the reference version of the Morris water maze was performed as described elsewhere³⁵. The task was performed with three training phases executed in succession: visible platform (2 days); acquisition phase (4 days), with a hidden platform in the training quadrant (Q3); and transfer/reversal phase (reversal learning, 4 days), with a hidden platform in the opposite quadrant (Q1). Each phase comprised four trials (120 s maximum and 15-min intertrial interval) per day. The start location was in a different quadrant in each trial so that no single start location was used in consecutive trials. Shaping was carried out before the first trial of the visible platform and the acquisition phases. A probe trial (60 s and no platform) was performed 24 h after the last trial of the acquisition and transfer phase. The animals' trajectories were recorded with a videotracking system (HVS Image Analysing VP-118).

Active place avoidance. Spatial learning was also tested using an active place avoidance task, which is sensitive to hippocampal dysfunction³⁶. The place avoidance training apparatus consists of a slowly rotating (clockwise at 1 r.p.m.) circular platform (40 cm in diameter) within which a non-rotating 60° region of the room is a shock zone (Supplementary Fig. 12, delineated in red). Visual cues are located on the walls of the room. Mice walk freely on the rotating platform and learn to avoid the shock zone based on the visual cues. When the mouse enters the shock zone, it receives a brief foot shock at a constant current (500 ms, 60 Hz, 0.2 mA) that is scrambled across pairs of parallel rods located on the platform floor. Additional shocks of the same intensity and duration are administered every 1.5 s until the mouse leaves the shock zone. The position of the mouse is tracked by PC-based software that analyses images from an overhead camera and delivers shocks appropriately (Tracker, Bio-Signal Group). Track analysis software is used to compute the number of times each animal enters the shock zone and the number of shocks administered. On the first day of the experiment, mice walked freely on the rotating platform for 10 min while the shock device was turned off (pretraining). Then the

shock device was turned on, and mice were given three 10-min training trials with an intertrial interval of 50 min, for two days (trials one to six).

One-trial contextual fear conditioning. Mice were tested at 8 weeks following *Bax* ablation in neural stem cells. Conditioning was conducted on one side of a shuttle box (Med-Associates, ENV-010MC; 20.3 cm × 15.9 cm × 21.3 cm) with a clear plexiglass wall, three aluminium walls and a stainless steel grid as a floor. The chamber was lit from above with a house light (CM1820 bulb), ventilated with a house fan and encased by a sound-dampening cubicle. On the days of testing, mice were brought out of the vivarium and allowed to habituate for 1 h outside the testing room before starting the experiment. Mouse behaviour was recorded by digital video cameras mounted above the conditioning chamber. FreezeFrame and FreezeView software (Actimetrics) were used for recording and analysing freezing behaviour, respectively. The one-trial contextual fear conditioning protocol entailed delivery of a single 2-s foot shock of 0.75 mA at 185 s after placement of the mouse in the training context. The mouse was taken out 15 s after termination of the foot shock and returned to its home cage. For the training context, A, the house fan and lights were switched on; stainless steel grids were exposed; and a mild lemon scent was used as an olfactory cue. Ethanol (70%) was used to clean grids between runs. For the distinct context, C, the stainless steel grid floor was covered with a plastic panel and cage bedding. The chamber walls were covered using plastic inserts, and the house fan and lights were turned off. The chamber door was left ajar during testing. A mild anise scent was used as an olfactory cue, and a non-alcoholic antiseptic was used to clean the chamber between runs. Mice were brought into the testing room in cardboard buckets by a different handler, and the testing room was dimly lit before placement of the mice in the testing chambers. The one-trial contextual fear conditioning protocol was used for extinction learning and memory-clearance experiments. Only males were used for these studies.

Contextual fear-discrimination learning. Mice were tested at 8 weeks after *Bax* ablation in neural stem cells. This test captures an animal's ability to distinguish between two similar contexts, conditions that are most likely to recruit the dentate gyrus²⁵. The shock-associated training context, A, and the similar (no-shock) context, B, shared many features, including an exposed stainless steel grid floor (a salient feature of the context) and roof. The similar context differed from the training context in that two plastic inserts were used to cover the walls; the house fan and lights were turned off; and the chamber door was left ajar during testing. A mild mint scent was used as an olfactory cue, and a non-alcoholic antiseptic was used to clean the grids between runs. Mice were brought into the testing room in buckets by the same experimenter who had handled the mice for the training context. In pilot experiments, the similar context was found to evoke comparable levels of freezing behaviour as that observed in the training context, indicative of extensive generalization (pattern completion) between the two contexts. For discrimination learning, mice were exposed to the training context in which they received a single 2-s foot shock of 0.75 mA at 185 s after placement in the chamber. Mice were taken out of the chamber 15 s after termination of the foot shock and returned to their home cage. After 1 h, mice were placed in the similar context, in which they were left for 180 s and were never shocked. Measurement of the freezing levels in both the training context (3-min pre-shock) and the similar context (3 min) each day allowed the assessment of discrimination between the two contexts and was computed as a discrimination ratio: $(\text{Freezing}_{\text{Training context}} - \text{Freezing}_{\text{Similar context}}) / (\text{Freezing}_{\text{Training context}} + \text{Freezing}_{\text{Similar context}})$. A score of 0 indicates complete lack of discrimination: that is, freezing levels are the same in the similar and training contexts ($\text{Freezing}_{\text{Similar context}} = \text{Freezing}_{\text{Training context}}$). A score of 1 indicates perfect discrimination: that is, freezing level in the similar context is zero ($\text{Freezing}_{\text{Similar context}} = 0$). Only males were used for these experiments.

Home cage activity. Animal behaviour was recorded for 15 min in the home cage, and videos were manually scored for locomotion (grid crossings).

Statistical analysis. Statistical analysis was carried out using StatView software or Microsoft Excel. Statistical significance was assessed by unpaired two-tailed Student's *t*-tests or ANOVA. Significant main effects or interactions were followed up with Fisher's predicted least-square difference post hoc tests where appropriate: *, $P < 0.05$; **, $P < 0.01$.

31. Srinivas, S. et al. Cre reporter strains produced by targeted insertion of *EYFP* and *ECFP* into the *ROSA26* locus. *BMC Dev. Biol.* **1**, 4 (2001).
32. Zhao, C., Teng, E. M., Summers, R. G. Jr, Ming, G. L. & Gage, F. H. Distinct morphological stages of dentate granule neuron maturation in the adult mouse hippocampus. *J. Neurosci.* **26**, 3–11 (2006).
33. Lever, C., Burton, S. & O'Keefe, J. Rearing on hind legs, environmental novelty, and the hippocampal formation. *Rev. Neurosci.* **17**, 111–133 (2006).
34. Scobie, K. N. et al. Kruppel-like factor 9 is necessary for late-phase neuronal maturation in the developing dentate gyrus and during adult hippocampal neurogenesis. *J. Neurosci.* **29**, 9875–9887 (2009).
35. Nicholls, R. E. et al. Transgenic mice lacking NMDAR-dependent LTD exhibit deficits in behavioral flexibility. *Neuron* **58**, 104–117 (2008).

36. Cimadevilla, J. M., Wesierska, M., Fenton, A. A. & Bures, J. Inactivating one hippocampus impairs avoidance of a stable room-defined place during

dissociation of arena cues from room cues by rotation of the arena. *Proc. Natl Acad. Sci. USA* **98**, 3531–3536 (2001).

Crystal structure of inhibitor of κ B kinase β

Guozhou Xu¹*, Yu-Chih Lo¹*, Qiubai Li¹, Gennaro Napolitano², Xuefeng Wu², Xuliang Jiang³, Michel Dreano⁴, Michael Karin² & Hao Wu¹

Inhibitor of κ B (I κ B) kinase (IKK) phosphorylates I κ B proteins, leading to their degradation and the liberation of nuclear factor κ B for gene transcription. Here we report the crystal structure of IKK β in complex with an inhibitor, at a resolution of 3.6 Å. The structure reveals a trimodular architecture comprising the kinase domain, a ubiquitin-like domain (ULD) and an elongated, α -helical scaffold/dimerization domain (SDD). Unexpectedly, the predicted leucine zipper and helix-loop-helix motifs do not form these structures but are part of the SDD. The ULD and SDD mediate a critical interaction with I κ B α that restricts substrate specificity, and the ULD is also required for catalytic activity. The SDD mediates IKK β dimerization, but dimerization per se is not important for maintaining IKK β activity and instead is required for IKK β activation. Other IKK family members, IKK α , TBK1 and IKK-i, may have a similar trimodular architecture and function.

Nuclear factor κ B (NF- κ B) transcription factors are master regulators of inflammatory, immune and apoptotic responses^{1,2}. In the canonical pathway, NF- κ B dimers are held in the cytoplasm through binding to I κ B proteins, which mask their nuclear localization signals. When cells are stimulated by NF- κ B inducers, I κ B proteins are phosphorylated by the Ser/Thr-specific IKK, a modification that triggers their Lys-48-linked polyubiquitination and subsequent proteasomal degradation³. Freed NF- κ B dimers enter the nucleus to regulate gene transcription². In the non-canonical pathway, activated IKK phosphorylates the I κ B-like domain in the NF- κ B family member NF- κ B2 (p49/p100)³ (NFKB2 in humans). NF- κ B signalling pathways are associated with a vast number of human diseases including inflammatory disorders and cancer, which renders IKK a potentially important therapeutic target⁴ (see, for example, <http://www.nf-kb.org>).

IKK was originally purified from HeLa cells as a multiprotein complex that contains the kinase subunits IKK α (CHUK) and/or IKK β (IKKBK), and the regulatory protein NEMO^{5–11} (IKK γ , or IKBK γ). IKK α and IKK β both contain an amino-terminal kinase domain (KD), predicted leucine zipper (LZ) and helix-loop-helix (HLH) domains, and a carboxy-terminal NEMO-binding domain (Fig. 1a). IKK β seems to have an additional ULD following the KD, which is not predicted in the corresponding region of IKK α ³. The IKK-related kinases TBK1 (NAK) and IKK-i (IKK- ϵ , or IKBKE) seem to have a similar domain organization¹². Whereas IKK β mediates activation of the canonical NF- κ B pathway in response to pro-inflammatory stimuli, IKK α has an indispensable role in non-canonical NF- κ B signalling by phosphorylating NF- κ B2 (p49/p100). Protein kinase assays suggest that IKK β accounts for nearly all of the catalytic activity of the IKK holoenzyme towards I κ B α ^{3,13} (NFKBIA).

The activation loop in both the IKK α and the IKK β KD contains the mitogen-activated protein (MAP)-kinase kinase consensus motif SXXXS, where X is any amino acid^{6–8,10} (Ser 177 and Ser 181 in human IKK β). Some MAP-kinase kinase family members, such as TGF- β -activated kinase 1 (MAP3K7, previously TAK1) and NF- κ B-inducing kinase (MAP3K14, or NIK), were shown to phosphorylate IKKs^{3,14,15}. IKK α and IKK β can also undergo autophosphorylation and activation as a result of overexpression or signal-dependent NEMO clustering^{10,16}. Ala substitutions of the activation-loop Ser residues prevent IKK activation whereas the phosphomimetic, double

Glu mutation S177E/S181E (EE) of IKK β renders it constitutively active^{7,13}.

Trimodular arrangement of IKK β

We determined the crystal structure of *Xenopus laevis* IKK β (ikkbk) EE (residues 4–675; Fig. 1a) in complex with either inhibitor Cmpd1 or inhibitor Cmpd2 (Supplementary Fig. 1) at resolutions of 4.0 and 3.6 Å in the *I*₄22 and *P*1 space groups, respectively (Supplementary Tables 1 and 2 and Supplementary Fig. 2). Eight IKK β molecules in *P*1 and the single molecule in *I*₄22 are highly similar to each other (Supplementary Fig. 3 and Supplementary Table 3) and show conserved dimerization (see below). Our structural description will use the first dimer (chains A and B) in *P*1. The sequences of human and *Xenopus* IKK β (henceforth hIKK β and xIKK β , respectively) have 74% identity with no gaps within the region of the structure; residue numbers designated for xIKK β are also true for hIKK β .

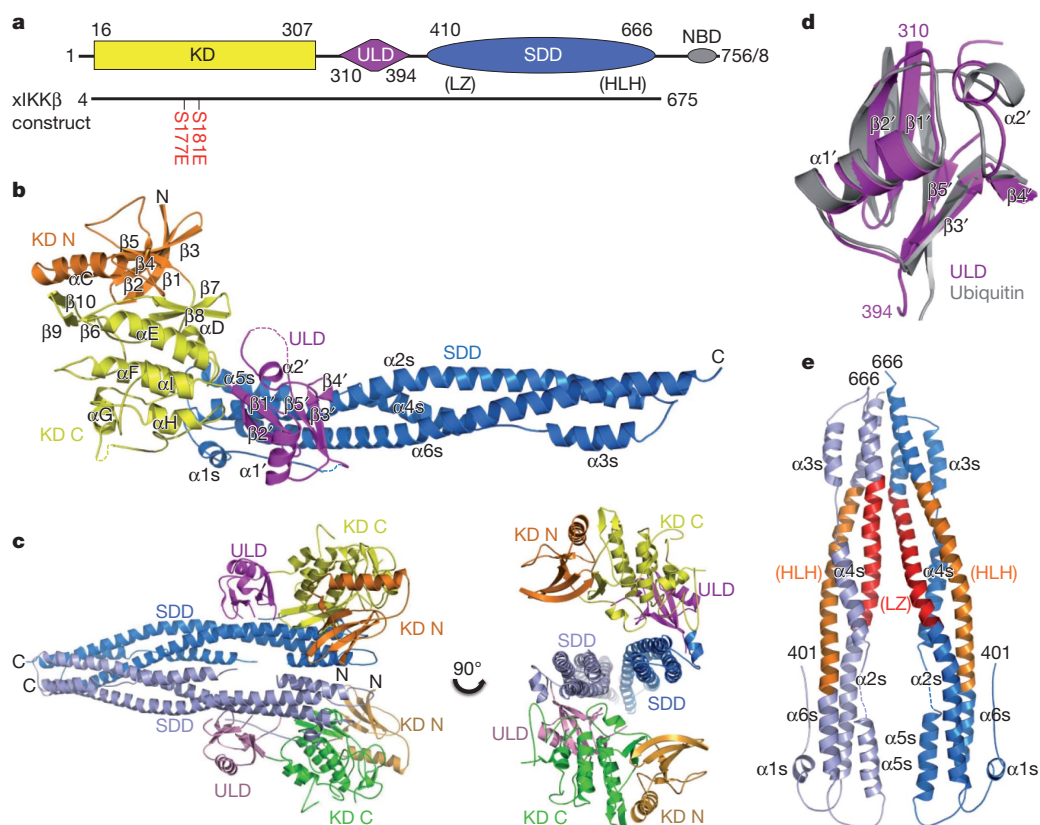
The IKK β dimer structure resembles a pair of shears and has the overall dimensions of approximately 100 Å × 130 Å × 60 Å (Fig. 1b, c). It contains the KD (residues 16–307), the ULD (310–394) and the SDD (410–666) (Fig. 1a and Supplementary Fig. 4). The KD and the ULD form the 'handle' of the shears, and the SDD is the 'blade'. Both the KD and the ULD intimately associate with the SDD, suggesting that the KD does not function independently. Instead, the structure indicates that IKK β is an integral trimodular unit.

The IKK β KD in complex with either Cmpd1 or Cmpd2 has the typical bilobal kinase fold¹⁷. Although it has only 21.1% sequence identity with human ubiquitin, the ULD of IKK β indeed has the ubiquitin fold (Fig. 1d). A major difference is the presence of an eight-residue insertion (373–380) that forms part of the loop connecting β -strands β 4' and β 5' in the ULD, which is mostly disordered. The hydrophobic surface patch of ubiquitin¹⁸, which is often recognized by ubiquitin-binding proteins, is conserved in the ULD, with residues Val 318, Leu 354 and Leu 389 equivalent to Leu 8, Ile 44 and Val 70 of ubiquitin (Supplementary Fig. 5).

The SDD comprises six α -helices (α 1s– α 6s), of which α 2s and α 6s contain 70 and 77 residues, respectively. They twist together with a stretch of three shorter helices between them to fold as an elongated structural ensemble. The C lobe of the KD sits on the N-terminal end

¹Department of Biochemistry, Weill Cornell Medical College, New York, New York 10021, USA. ²Department of Pharmacology, University of California at San Diego, La Jolla, California 92093, USA. ³EMD Serono Research Institute, Billerica, Massachusetts 01821, USA. ⁴Merck Serono, Geneva 1211, Switzerland.

*These authors contributed equally to this work.

**Figure 1 | Structure of xIKKβ.**

a, Linear representation of IKKβ showing the boundaries for the KD, the ULD and the SDD. Sequences of hIKKβ and xIKKβ are of 756 and 758 residues, respectively, and differ only at the most C-terminal region. The crystallized xIKKβ construct is shown. The previously designated LZ and HLH regions are shown in parentheses. **b**, Ribbon diagram of an xIKKβ protomer in the P1 crystal form. The N and C termini, KD N lobe (orange) and C lobe (yellow), ULD (magenta) and SDD (blue) are labelled. Secondary structural elements are labelled, with those in the ULD indicated with a prime and those in the SDD indicated with an 's'. **c**, Ribbon diagram of an xIKKβ dimer. **d**, Superposition of the ULD (magenta) with ubiquitin (grey). **e**, Ribbon diagram of an SDD dimer, showing locations of the previously designated LZ (red) and HLH (orange) regions.

of the SDD, and the ULD binds close to the middle of the SDD. Unexpectedly, formerly designated LZ (458–485) and HLH domains^{7,8,10} (605–644) do not exist as such in the structure and are both part of the SDD (Fig. 1e). Most of the hydrophobic residues in the predicted LZ point inwards and are not available for mediating dimerization as previously proposed.

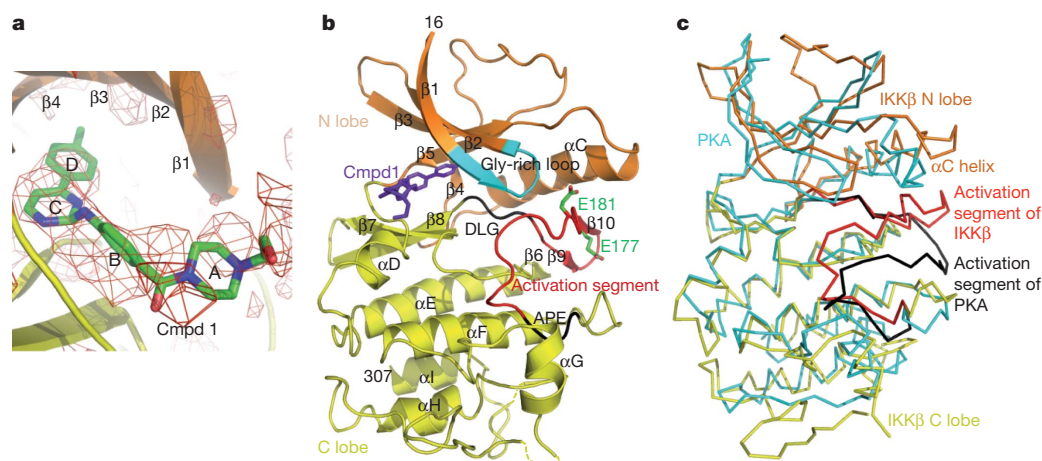
Structure of inhibitor-bound IKKβ KD

The inhibitor binds to the IKKβ KD at the hinge loop connecting the N and C lobes, a region that recognizes the adenine in ATP^{19,20} and is often used for inhibitor binding^{21–23} (Fig. 2a and Supplementary Fig. 6). The KD conformation is incompatible with that of an active kinase^{17,24,25} (Fig. 2b, c). The activation segment, which begins from Asp 166–Leu 167–Gly 168 as the conserved DFG triad and extends to Ala 190–Pro 191–Glu 192 in the conserved APE motif, is fully ordered, including

phosphomimetic residues Glu 177 and Glu 181 (Fig. 2b). However, the C-terminal anchor of the activation segment, including the APE motif, is completely out of place, with the result that essential interactions with the catalytic centre are lost (Fig. 2c). The gross conformation of the N-terminal anchor of the activation segment is preserved, with β9 paired with the β6 strand that precedes the catalytic loop. Part of the activation loop (175–177) contains an additional β-strand (β10), which sits between the lobes to form a three-stranded β-sheet with β9 and β6. The αC helix is tilted up and outwards (Fig. 2c) to make room for β10, which also disrupts its productive interactions with the DFG motif in active kinase structures.

Interactions among the KD, ULD and SDD

The KD, ULD and SDD interact mutually, with the ULD–SDD interaction being the most extensive, followed by the KD–SDD and KD–ULD

**Figure 2 | Inhibitor-bound xIKKβ**

kinase domain. **a**, $F_o - F_c$ electron density map for Cmpd1 in the I4/22 structure, contoured at 2.0σ . Carbon, nitrogen and oxygen atoms are shown in green, blue and red, respectively. The four ring structures in Cmpd1 are labelled A, B, C and D, respectively. **b**, Structure of the xIKKβ KD. Gly-rich loop, cyan; activation segment, red (except that the DLG and APE sequences are in black); Cmpd1, purple. Side chains of phosphomimetic residues Glu 177 and Glu 181 are shown. **c**, Superposition of xIKKβ (orange and yellow) and protein kinase A (PKA, cyan; Protein Data Bank ID, 1ATP). The activation segments of xIKKβ and PKA are shown in red and black, respectively.

interactions. The ULD binds close to the middle of the SDD, contacting helices $\alpha 2s$ and $\alpha 6s$ (Fig. 3a). The interaction buries $\sim 700 \text{ \AA}^2$ of surface area per partner. There are substantial hydrophobic contributions, supplemented by electrostatic interactions. Residues Met 315, Met 317, Leu 354, Ile 387, Leu 389 and Phe 390 on one side of the ULD pack against Leu 612, Tyr 609, Leu 447 and the main chain of $\alpha 2s$ of the SDD to form the central hydrophobic core of the interface. This hydrophobic patch of the ULD is immediately adjacent to and overlaps the conserved hydrophobic patch in the ubiquitin fold. Electrostatic interactions are observed between Glu 352 and Lys 619 and between Lys 394 and Asp 610. Additional interfacial residues include Ser 319 and Ser 357 of the ULD and Thr 453, Gln 449 and Val 616 of the SDD.

Consistent with an important role of the ULD in interacting with the SDD, mutations in residues that are not at the interface, P347A, L361A and Q351A, had minimal effects on NF- κ B activation²⁶. In contrast, mutation in a residue within a ULD surface loop that contacts the SDD, G358A (Fig. 3a), affected IKK β -induced NF- κ B activity²⁶. It was also shown that Leu 353 is required for IKK β activity²⁶; however, Leu 353 is buried in the ULD core and the L353A mutation may have disrupted IKK β structural integrity. Double substitutions of hIKK α and hIKK β , which are equivalent to I608R/Y609P of the SDD of α IKK β , did not affect their interaction with wild-type IKK β but negatively impacted kinase activity¹⁰; Ile 608 is buried in the SDD core and Tyr 609 directly interacts with the ULD (Fig. 3a).

Like the ULD, the KD also makes contact with the N terminal end of the SDD (Fig. 3b), burying a surface area of $\sim 650 \text{ \AA}^2$ of each interface. The binding forces are mainly van der Waals in nature. Limited hydrophobic interactions are observed between residues Ala 252 and Val 253 of the KD and Tyr 423 of the SDD, and between Phe 111 of the KD and the hydrophobic portions of Arg 572, Arg 575 and Glu 576 of $\alpha 5s$ of the SDD. The KD is linked to the ULD through a two-amino-acid linker between αI of the KD and $\beta 1'$ of the ULD (Fig. 3c), burying only $\sim 350 \text{ \AA}^2$ of surface area. Side-chain contacts between Leu 311 of the ULD and Ile 268 of the KD are observed, and together form the small hydrophobic patch at the KD–ULD junction

consisting also of Leu 269 and Ile 306 of the KD and Leu 309 of the linker. Together with the ionic interaction between Asp 373 of the ULD and Arg 123 of αE of the KD, these interactions may confer rigidity to the KD–ULD junction despite the small buried surface area.

Structural comparison with other kinase structures revealed a similarity between the locations of the SDD and ULD and those of several known docking sites for substrates and regulatory proteins²⁷. In the crystal structure of the Ser/Thr kinase SRPK1 in complex with a docking motif in its substrate, ASF/SF2²⁷ (SRSF1), the peptide motif interacts with the kinase at the location of the SDD (Fig. 3d). In the structure of the TAK1 KD fused with the C-terminal region of its binding protein, TAB1²⁸, TAB1 interacts with the C lobe of the kinase at a position analogous to both the SDD and the ULD, presumably to activate the kinase (Fig. 3d).

ULD–SDD binds the I κ B α C-terminal region

Previous studies have suggested that the ULD in TBK1 and IKK-i is involved in substrate recognition because its deletion impaired activity of the respective kinases and a glutathione *S*-transferase (GST)–ULD fusion protein interacted with the specific substrate, IRF3 or IRF7²⁹. Because ULD deletion in IKK β also abolished its activity²⁶, we proposed that the ULD may recognize its specific substrate, I κ B α . However, we were surprised to find that GST–I κ B α (1–317 and 54–317) pulled down only a minute amount of the ULD (Fig. 4a, lanes 9 and 13) and GST alone did not pull down any (Fig. 4a, lane 4), suggesting that the interaction of I κ B α with the ULD is specific, but very weak. In contrast, GST–I κ B α robustly pulled down full-length IKK β or IKK β lacking C-terminal NEMO-binding domain (Fig. 4a, lanes 15 and 16).

I κ B α has an N-terminal region (1–54) that contains cognate phosphoacceptor sites at Ser 32 and S 36, followed by a C-terminal region (55–317) that contains multiple ankyrin repeats and the PEST region^{30,31}. Strikingly, the N-terminal region of I κ B α did not pull down any IKK β constructs (Fig. 4a, lanes 5–8), and the C-terminal region of I κ B α interacted robustly with full-length IKK β as well as its ULD–SDD region (Fig. 4a, lanes 9–12), and very weakly with the ULD alone (Fig. 4a, lane 9). Further mapping on I κ B α showed that both

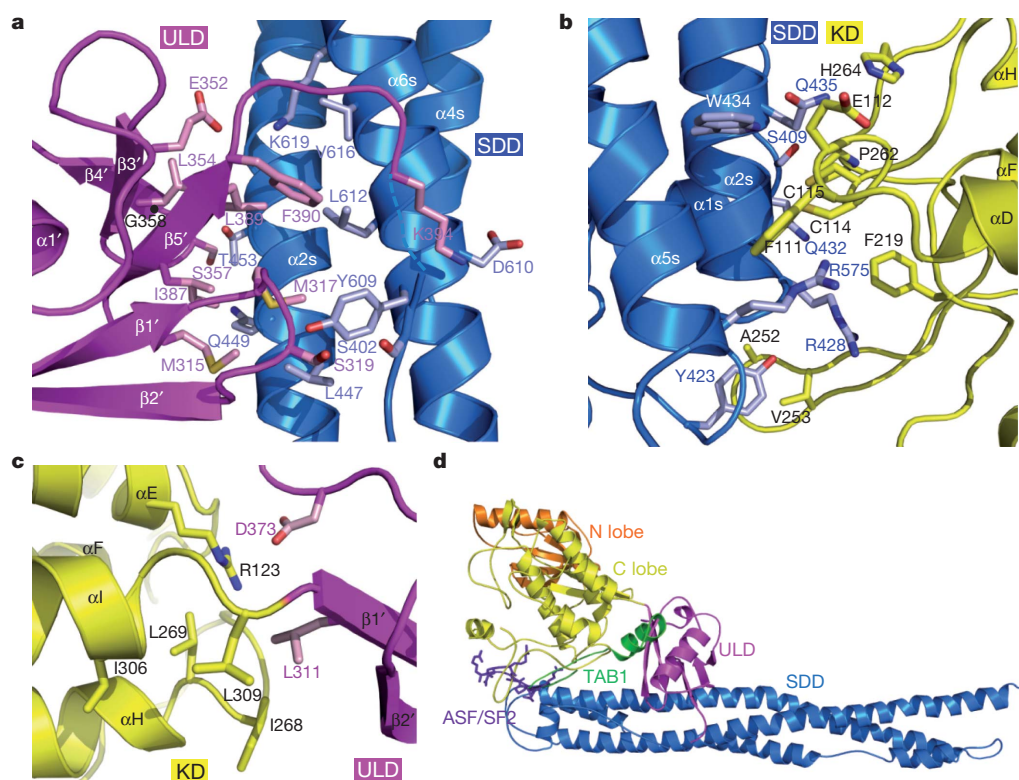


Figure 3 | Interactions among the KD, ULD and SDD. **a**, Interaction between the ULD (magenta) and SDD (blue). Important interfacial side chains are shown with nitrogen atoms in blue, oxygen atoms in red, sulphur atoms in orange and carbon atoms in either pink (ULD) or light blue (SDD). Gly 358 is marked with a black ball on the main chain. **b**, Interaction between the KD (yellow) and SDD (blue). **c**, Interaction between the KD (yellow) and ULD (magenta). **d**, Locations of the TAB1 peptide (green ribbon; PDB ID, 2EVA) and the ASF/SF2 peptide (purple stick model; PDB ID, 1WBP) relative to the IKK β structure after superposition of the corresponding kinase domains.

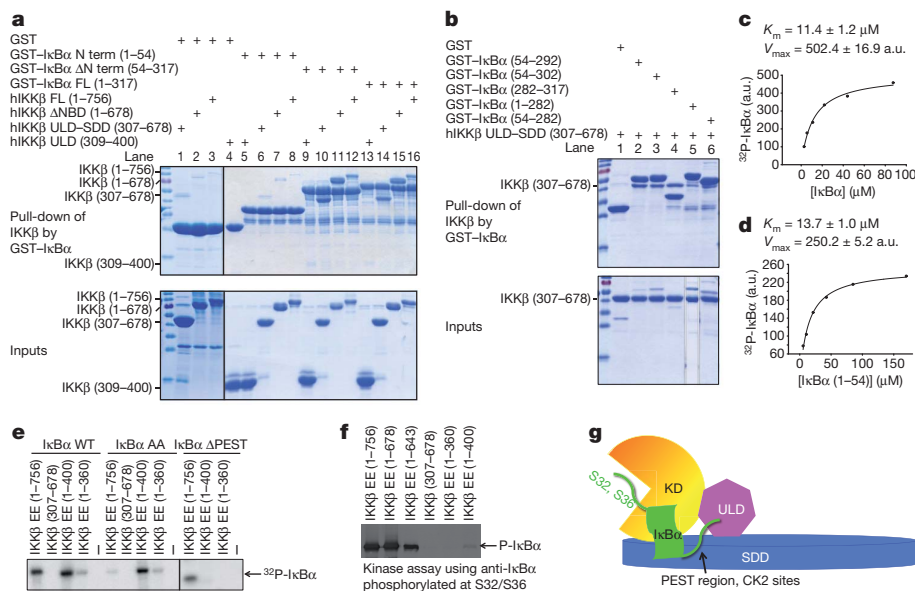


Figure 4 | ULD-SDD restricts IKKβ specificity and ULD is required for catalytic activity.

a, b, Pull-down of hIKKβ constructs using GST-IκBα constructs, showing the reciprocal interaction between ULD-SDD of IKKβ and the C-terminal region of IκBα containing ankyrin repeats and the PEST region. FL, full length. **c, d**, Measurement of K_m and the relative V_{max} of IKKβ against full-length IκBα (**c**) and the N-terminal region of IκBα (1-54) (**d**). a.u., arbitrary units. **e**, Kinase assay of purified hIKKβ proteins against IκBα, its S32A/S36A mutant (AA) and its PEST-deletion construct (ΔPEST, 1-282) using [γ - 32 P]ATP. WT, wild type. **f**, Kinase assay of purified hIKKβ proteins using antibody against IκBα phosphorylated at Ser 32 and Ser 36. **g**, Interaction between the SDD of IKKβ and the C-terminal region of IκBα may position the N-terminal cognate phosphorylation sites of IκBα at the active site of IKKβ. CK2, casein kinase 2.

ankyrin repeats (1-282 or 54-282) and the PEST region (282-317) interacted with IKKβ ULD-SDD (Fig. 4b, lanes 4-6). The extent of pull-down suggests that the PEST region contributes more to IKKβ interaction than do the ankyrin repeats. Despite trying multiple constructs, we could not obtain soluble protein for IKKβ SDD to test its interaction with IκBα. However, the pull-down data suggest a dominant role for SDD in IκBα interaction. In any case, it is clear that the mutual interaction between IKKβ and IκBα is mediated by their ULD-SDD and C-terminal domains, respectively.

ULD-SDD limits specificity and the ULD aids catalysis

The specific interaction between ULD-SDD of IKKβ and IκBα suggests that the Michaelis constant, K_m , of phosphorylation by IKKβ might be lower for full-length IκBα than for its N-terminal region (1-54) alone. We performed kinase kinetics analysis of IKKβ EE against the two different substrates. Unexpectedly, the measured apparent K_m values were 11.4 and 13.7 μM for full-length IκBα and the N-terminal region alone, respectively (Fig. 4c, d), suggesting that binding at the SDD, an exosite, does not alter the K_m of the reaction drastically. This could be due to opposing effects of the SDD-IκBα interaction, which increases substrate interaction but slows down product dissociation. The relative maximum velocity, V_{max} values were 502.4 and 250.2, respectively, suggesting that the SDD-IκBα interaction moderately enhances catalysis.

Casein kinase 2 phosphorylates the C-terminal PEST region of IκBα around residues 283-299^{30,31}. To determine whether the SDD-IκBα interaction restricts substrate specificity, we compared the kinase activity of purified IKKβ EE proteins against either IκBα or its S32A/S36A mutant (AA) using [γ - 32 P]ATP (Fig. 4e). Although the KD-ULD (1-400) construct gave rise to a small amount of protein, it produced robust phosphorylation of wild-type IκBα, comparable to full-length IKKβ (1-756), suggesting that it is catalytically competent. Remarkably, KD-ULD effectively phosphorylated the AA mutant, which, in contrast, was a poor substrate for full-length IKKβ. The C-terminal PEST region seemed to harbour the major sites of phosphorylation by KD-ULD because a construct lacking PEST (1-282) was not significantly phosphorylated by KD-ULD but was phosphorylated by full-length IKKβ (Fig. 4e). In addition, when IκBα phosphorylation was detected by antibody against IκBα phosphorylated at Ser 32/Ser 36, only very weak phosphorylation was seen for the KD-ULD construct in comparison with full-length IKKβ (Fig. 4f). These experiments suggest that although the KD-ULD construct is active, it possesses an altered substrate specificity causing preferential

phosphorylation of the C-terminal PEST sequence, consistent with a previous observation³². Hence, ULD-SDD seems to position IκBα specifically such that only its N-terminal region is accessible to the IKKβ catalytic pocket (Fig. 4g).

We expressed three kinase domain constructs, 1-301, 1-310 and 1-360, in insect cells and obtained only small amount of protein for the 1-360 construct. Kinase assay showed that IKKβ EE (1-360) had very low residual activity against IκBα or its AA mutant (Fig. 4e), suggesting that KD activity is compromised in the absence of the ULD. Without an isolated KD structure, we cannot deduce the molecular mechanism by which the ULD acts. However, in analogy to TAK1 activation by TAB1²⁸ (Fig. 3d), it may be speculated that this KD-ULD interaction allosterically potentiates kinase activity. Further kinase assay using antibody against IκBα phosphorylated at Ser 32/Ser 36 showed no detectable activity of the KD alone (Fig. 4f), confirming that the low residual activity may also be directed towards the C-terminal PEST region, similar to KD-ULD. Therefore, whereas ULD-SDD is critical for IKKβ specificity, ULD is required for its catalytic activity.

SDD mediates IKKβ dimerization

Full-length hIKKβ (1-756) and its KD-ULD-SDD region (1-678) are dimers in solution as determined by gel-filtration chromatography (Fig. 5a). In the P1 and I4122 crystals, two conserved dimerization interfaces exist, one mediated by the SDD and the other mediated by the KD. Because hIKKβ (1-643) that truncates into the SDD is a monomer in solution (Fig. 5a), SDD-mediated dimerization (Fig. 5b) is probably of greater importance than KD-mediated dimerization.

SDD in an IKKβ dimer does not form extensive interactions along the entire length dimension of the helical bundle. Rather, interactions are mostly localized at the end of the bundle (Fig. 5b), distal from the KD and ULD and burying $\sim 1,000 \text{ \AA}^2$ of surface area of each monomer. The interaction is mostly hydrophobic. Residues that contribute significantly to dimerization include Gln 478, Lys 482, Phe 485, Ile 492, Lys 496, Ile 505, Gln 651, Leu 654, Trp 655, Leu 658 and Ile 660, with residues Leu 654, Trp 655 and Leu 658 from helix $\alpha 6$ burying the most surface area (Fig. 5b). This dimerization interface is entirely unexpected as it was predicted earlier that the LZ mediates IKKβ dimerization. The structure now explains that failed dimerization of the LZ-defective L462S/L469S mutant of IKKα¹⁰ is due to the structural role of Leu 469, whose equivalent residue of IKKβ, Met 472, is buried in the SDD core. Superposition of four IKKβ dimers in P1

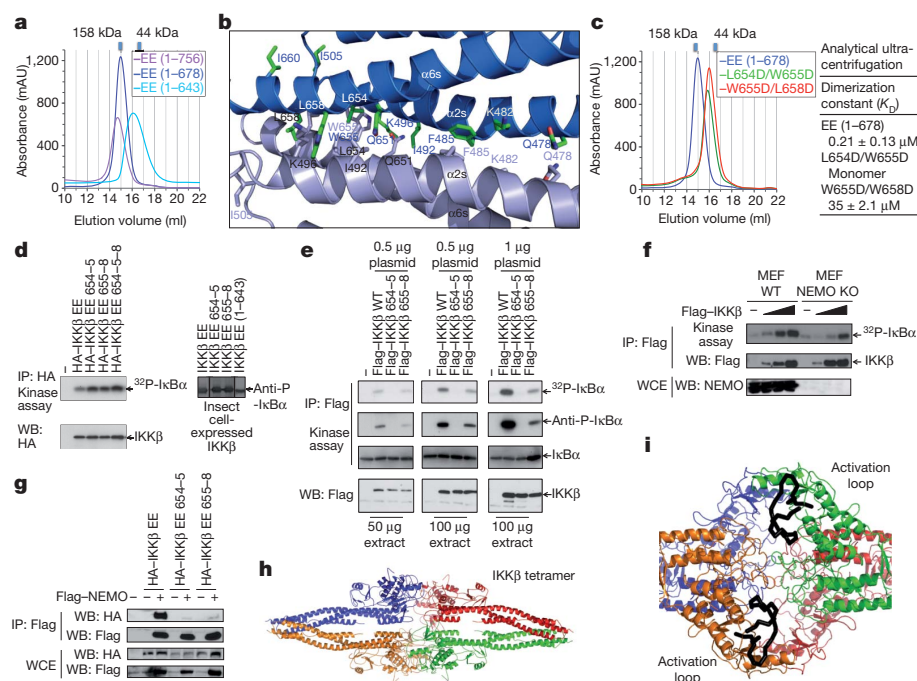


Figure 5 | Dimerization is critical for IKK β activation but not for its activity. **a**, Gel filtration profiles of various hIKK β constructs showing that those containing the KD–ULD–SDD region (1–756, 1–678) are dimeric and that a further truncated construct (1–643) is monomeric. mAU, milliabsorbance unit. **b**, The dimerization interface of xIKK β . **c**, Structure-based mutations disrupt hIKK β dimerization as shown by gel filtration and analytical ultracentrifugation. **d**, Kinase activity of HEK293T-cell-transfected or insect-cell-purified hIKK β EE and dimerization-defective mutants L654D/W655D (654–655), W655D/L658D (655–658) and L654D/W655D/L658D (654–655–658). **e**, Autoactivation of HEK293T-cell-transfected wild-type hIKK β and its dimerization-defective mutants. **f**, Transfection of hIKK β into wild-type and NEMO $^{-/-}$ mouse embryonic fibroblasts (MEFs), showing reduced IKK β activation in the absence of NEMO. **g**, Dimerization mutants of IKK β showing reduced interaction with NEMO. **h**, Tetramer of xIKK β in the P1 structure. **i**, Close-up view of the tetramer interface, showing that the activation loops of neighbouring protomers (black) face each other.

and the single IKK β dimer in *I4,22* shows that IKK β dimers are conserved (Supplementary Fig. 7). In *I4,22*, the distal part of the SDD is not visible, owing to a lack of crystal packing in this region and dynamic disorder, not degradation (Supplementary Fig. 8).

To confirm the observed interface in IKK β dimerization, we performed structure-based mutagenesis on residues that bury the most surface area, Leu 654, Trp 655 and Leu 658. These residues are not within the predicted LZ region. Two purified double mutants, L654D/W655D and W655D/L658D, failed to dimerize, as shown by the considerable shift in gel filtration positions (Fig. 5c). Furthermore, equilibrium analytical ultracentrifugation experiments showed that wild-type IKK β is indeed a dimer whereas one of the IKK β mutants is a monomer and the other has a 167-fold weaker dimerization affinity (Fig. 5c).

Dimerization in IKK β activation but not activity

The geometry of the IKK β dimer with KDs facing away from each other suggests that each IKK β protomer is independent in its kinase activity. To confirm this, we transfected HEK293T cells with hIKK β EE mutants, L654D/W655D (654–655), W655D/L658D (655–658) and L654D/W655D/L658D (654–655–658), and found that all mutants had robust kinase activity (Fig. 5d). Dimerization mutants expressed in insect cell and purified showed the same results. In addition, a purified IKK β construct with truncation into the SDD (1–643) that is monomeric in solution (Fig. 5a) was active in phosphorylating I κ B α (Fig. 5d).

Previous studies have shown that IKK β can undergo *trans*-autophosphorylation and activation on transfection^{13,16}. This autophosphorylation and phosphorylation by TAK1 probably both contribute to IKK β activation on cell stimulation. To determine whether the observed dimerization interface is critical for this activation, we tested dimerization mutations in IKK β activation on overexpression in HEK293T cells (Fig. 5e). Whereas wild-type IKK β was robustly activated, the L654D/W655D and W655D/L658D mutants completely and partly lost this activation, respectively, in a manner that correlates with the degree of impairment in dimerization (Fig. 5c, e). Overexpression of IKK β in NEMO-deficient mouse embryonic fibroblasts resulted in its activation, but to a lesser extent than in wild-type mouse embryonic fibroblasts (Fig. 5f). We found that IKK β dimerization mutants failed to interact with NEMO efficiently (Fig. 5g), perhaps owing to reduced

avidity for oligomeric NEMO. Therefore, although IKK β kinase activity does not depend on dimerization once its activation loop is phosphorylated, IKK β activation requires dimerization and is probably enhanced by interaction with NEMO.

Discussion

The IKK β structure presented here predicts that IKK α , TBK1 and IKK-i all have an overall structural organization that comprises KD, ULD and SDD. Although a ULD was not predicted in IKK α , conservation of buried residues in this region and of the ULD–SDD interface suggests that IKK α also has this domain (Supplementary Fig. 4). The ULD and SDD probably have the same structural role but may have evolved additional, differential functions in the individual kinases. SDD-mediated dimerization may also be conserved. In particular, residues at the observed IKK β dimerization interface are highly conserved in IKK α (Supplementary Fig. 4), explaining how IKK α and IKK β can form both homo- and heterodimers^{8,13}. Given our structure of IKK β and the previously determined structures of NEMO fragments^{33–37}, we may speculate that the full IKK complex is also a dimer, or a dimer of dimers with a molecular mass of around 270 or 540 kD. The apparent 700–900-kD molecular mass of the IKK holoenzyme on gel filtration^{5–10} may be due to the elongated nature of NEMO and the complex (Supplementary Fig. 9).

Because the conserved IKK β dimer structure does not place the KDs close to each other for *trans*-autophosphorylation, we wondered whether higher-order oligomerization, which is probably enhanced by NEMO and its ability to bind ubiquitin^{33,34}, is responsible for this autoactivation. In both *P1* and *I4,22*, IKK β exists as dimers of dimers (Fig. 5h and Supplementary Fig. 10). In particular, active sites of two neighbouring protomers in the tetramer face each other such that an activation loop from one protomer might reach into the active site of the other (Fig. 5i), which may mimic an autophosphorylation state.

The ULD–SDD region of IKK β directly interacts with the C-terminal portion of I κ B α . This interaction may serve several purposes. First, it probably orients I κ B α such that its N-terminal cognate phosphorylation sites are presented to the KD active site (Fig. 4g). Without this interaction, IKK β preferentially phosphorylates the C-terminal PEST motif of I κ B α . Second, the interaction seems to enhance IKK β activity. Third, phosphorylation at the PEST by casein kinase 2 or other kinases may regulate I κ B α interaction with IKK β

and hence affect phosphorylation at the cognate sites. Fourth, the interaction may allow concerted phosphorylation at both Ser 32 and Ser 36 of I κ B α without intervening dissociation. In MAP-kinase cascades that involve dual phosphorylations, specific docking interactions occur between the kinases and their substrates^{27,38,39}. The β -catenin protein in the Wnt signalling pathway contains the same dual-phosphorylated destruction box motif as I κ B α (ref. 40). Consistent with this, β -catenin is brought to the responsible kinase, GSK-3, by means of the adaptor protein axin, allowing both specificity and concerted phosphorylation^{41,42}. Therefore, in a general statement that structure serves function, the IKK β structure seems to fit its function as the I κ B α kinase perfectly, being poised to turn on the important NF- κ B pathway specifically, efficiently and concertedly in response to cellular physiology.

METHODS SUMMARY

Xenopus laevis IKK β was expressed in insect cells and purified to homogeneity using nickel affinity chromatography, ion exchange and gel filtration chromatography. We crystallized the P1 and I4,22 forms at 4 °C in polyethylene glycol 6000 and potassium/sodium phosphate, respectively. The structure was determined by multiwavelength anomalous diffraction of the selenomethionyl protein.

Full Methods and any associated references are available in the online version of the paper at www.nature.com/nature.

Received 27 September 2010; accepted 17 January 2011.

Published online 20 March 2011.

- Hayden, M. S. & Ghosh, S. Shared principles in NF- κ B signaling. *Cell* **132**, 344–362 (2008).
- Vallabhupurapu, S. & Karin, M. Regulation and function of NF- κ B transcription factors in the immune system. *Annu. Rev. Immunol.* **27**, 693–733 (2009).
- Scheidereit, C. I κ B kinase complexes: gateways to NF- κ B activation and transcription. *Oncogene* **25**, 6685–6705 (2006).
- Karin, M. Nuclear factor- κ B in cancer development and progression. *Nature* **441**, 431–436 (2006).
- Chen, Z. J., Parent, L. & Maniatis, T. Site-specific phosphorylation of I κ B α by a novel ubiquitination-dependent protein kinase activity. *Cell* **84**, 853–862 (1996).
- DiDonato, J. A. *et al.* A cytokine-responsive I κ B kinase that activates the transcription factor NF- κ B. *Nature* **388**, 548–554 (1997).
- Mercurio, F. *et al.* IKK-1 and IKK-2: cytokine-activated I κ B kinases essential for NF- κ B activation. *Science* **278**, 860–866 (1997).
- Woronicz, J. D. *et al.* I κ B kinase- β : NF- κ B activation and complex formation with I κ B kinase- α and NIK. *Science* **278**, 866–870 (1997).
- Yamaoka, S. *et al.* Complementation cloning of NEMO, a component of the I κ B kinase complex essential for NF- κ B activation. *Cell* **93**, 1231–1240 (1998).
- Zandi, E. *et al.* The I κ B kinase complex (IKK) contains two kinase subunits, IKK α and IKK β , necessary for I κ B phosphorylation and NF- κ B activation. *Cell* **91**, 243–252 (1997).
- Rothwarf, D. M., Zandi, E., Natoli, G. & Karin, M. IKK- γ is an essential regulatory subunit of the I κ B kinase complex. *Nature* **395**, 297–300 (1998).
- Hacker, H. & Karin, M. Regulation and function of IKK and IKK-related kinases. *Sci. STKE* **2006**, re13 (2006).
- Zandi, E., Chen, Y. & Karin, M. Direct phosphorylation of I κ B by IKK α and IKK β : discrimination between free and NF- κ B-bound substrate. *Science* **281**, 1360–1363 (1998).
- Sato, S. *et al.* Essential function for the kinase TAK1 in innate and adaptive immune responses. *Nature Immunol.* **6**, 1087–1095 (2005).
- Liu, H. H., Xie, M., Schneider, M. D. & Chen, Z. J. Essential role of TAK1 in thymocyte development and activation. *Proc. Natl Acad. Sci. USA* **103**, 11677–11682 (2006).
- Tang, E. D. *et al.* Roles for homotypic interactions and transautophosphorylation in I κ B kinase (IKK β) activation. *J. Biol. Chem.* **278**, 38566–38570 (2003); erratum **278**, 49661 (2003).
- Knighton, D. R. *et al.* Crystal structure of the catalytic subunit of cyclic adenosine monophosphate-dependent protein kinase. *Science* **253**, 407–414 (1991).
- Dikic, I., Wakatsuki, S. & Walters, K. J. Ubiquitin-binding domains — from structures to functions. *Nature Rev. Mol. Cell Biol.* **10**, 659–671 (2009).
- Zheng, J. *et al.* 2.2 Å refined crystal structure of the catalytic subunit of cAMP-dependent protein kinase complexed with MnATP and a peptide inhibitor. *Acta Crystallogr. D* **49**, 362–365 (1993).
- Bossemeyer, D. *et al.* Phosphotransferase and substrate binding mechanism of the cAMP-dependent protein kinase catalytic subunit from porcine heart as deduced from the 2.0 Å structure of the complex with Mn²⁺ adenylyl imidodiphosphate and inhibitor peptide PKI(5–24). *EMBO J.* **12**, 849–859 (1993).
- Xu, R. M., Carmel, G., Kuret, J. & Cheng, X. Structural basis for selectivity of the isoquinoline sulfonamide family of protein kinase inhibitors. *Proc. Natl Acad. Sci. USA* **93**, 6308–6313 (1996).
- Sicheri, F., Moarefi, I. & Kuriyan, J. Crystal structure of the Src family tyrosine kinase Hck. *Nature* **385**, 602–609 (1997).
- Noble, M. E., Endicott, J. A. & Johnson, L. N. Protein kinase inhibitors: insights into drug design from structure. *Science* **303**, 1800–1805 (2004).
- Nolen, B., Taylor, S. & Ghosh, G. Regulation of protein kinases; controlling activity through activation segment conformation. *Mol. Cell* **15**, 661–675 (2004).
- Jeffrey, P. D. *et al.* Mechanism of CDK activation revealed by the structure of a cyclinA-CDK2 complex. *Nature* **376**, 313–320 (1995).
- May, M. J. *et al.* A novel ubiquitin-like domain in I κ B kinase β is required for functional activity of the kinase. *J. Biol. Chem.* **279**, 45528–45539 (2004).
- Goldsmith, E. J. *et al.* Substrate and docking interactions in serine/threonine protein kinases. *Chem. Rev.* **107**, 5065–5081 (2007).
- Brown, K. *et al.* Structural basis for the interaction of TAK1 kinase with its activating protein TAB1. *J. Mol. Biol.* **354**, 1013–1020 (2005).
- Ikeda, F. *et al.* Involvement of the ubiquitin-like domain of TBK1/IKK-i kinases in regulation of IFN-inducible genes. *EMBO J.* **26**, 3451–3462 (2007).
- Kato, T. Jr, Delhase, M., Hoffmann, A. & Karin, M. CK2 is a C-terminal I κ B kinase responsible for NF- κ B activation during the UV response. *Mol. Cell* **12**, 829–839 (2003).
- Barroga, C. F., Stevenson, J. K., Schwarz, E. M. & Verma, I. M. Constitutive phosphorylation of I κ B α by casein kinase II. *Proc. Natl Acad. Sci. USA* **92**, 7637–7641 (1995).
- Shaul, J. D., Farina, A. & Huxford, T. The human IKK β subunit kinase domain displays CK2-like phosphorylation specificity. *Biochem. Biophys. Res. Commun.* **374**, 592–597 (2008).
- Lo, Y. C. *et al.* Structural basis for recognition of diubiquitins by NEMO. *Mol. Cell* **33**, 602–615 (2009).
- Rahighi, S. *et al.* Specific recognition of linear ubiquitin chains by NEMO is important for NF- κ B activation. *Cell* **136**, 1098–1109 (2009).
- Rushe, M. *et al.* Structure of a NEMO/IKK-associating domain reveals architecture of the interaction site. *Structure* **16**, 798–808 (2008).
- Bagnéris, C. *et al.* Crystal structure of a vFlip-IKK γ complex: insights into viral activation of the IKK signalosome. *Mol. Cell* **30**, 620–631 (2008).
- Cordier, F. *et al.* Solution structure of NEMO zinc finger and impact of an anhidrotic ectodermal dysplasia with immunodeficiency-related point mutation. *J. Mol. Biol.* **377**, 1419–1432 (2008).
- Remenyi, A., Good, M. C. & Lim, W. A. Docking interactions in protein kinase and phosphatase networks. *Curr. Opin. Struct. Biol.* **16**, 676–685 (2006).
- Kallunki, T., Deng, T., Hibi, M. & Karin, M. c-Jun can recruit JNK to phosphorylate dimerization partners via specific docking interactions. *Cell* **87**, 929–939 (1996).
- Wu, G. *et al.* Structure of a β -TrCP1-Skp1- β -catenin complex: destruction motif binding and lysine specificity of the SCF(β -TrCP1) ubiquitin ligase. *Mol. Cell* **11**, 1445–1456 (2003).
- Ikeda, S. *et al.* Axin, a negative regulator of the Wnt signaling pathway, forms a complex with GSK-3 β and β -catenin and promotes GSK-3 β -dependent phosphorylation of β -catenin. *EMBO J.* **17**, 1371–1384 (1998).
- Hart, M. J. *et al.* Downregulation of β -catenin by human Axin and its association with the APC tumor suppressor, β -catenin and GSK3 β . *Curr. Biol.* **8**, 573–581 (1998).

Supplementary Information is linked to the online version of the paper at www.nature.com/nature.

Acknowledgements We thank K. Rajashankar and N. Sukumar for data collection at the NE-CAT of APS, B. Schwer for help with the kinase assay, P. Gaillard for help with the chemistry and G. Ahlsen, L. Shapiro and B. Honig for the ultracentrifugation experiments. This work was supported by the National Institutes of Health (H.W. and M.K.), the American Heart Association (G.X. and Y.-C.L.) and the Cancer Research Institute (Y.-C.L.). M.K. is an American Cancer Society Research Professor.

Author Contributions G.X. cloned, expressed, purified, crystallized and determined the crystal structure of xIKK β and performed experiments to determine K_m . Y.-C.L. cloned, expressed, purified and crystallized hIKK β and performed pull-down experiments and kinase assays using phospho-I κ B α antibody. Q.L. expressed the hIKK β mutants in insect cells. G.N. and X.W. performed transfection, immunoprecipitation and kinase assays and M.K. supervised these experiments. H.W. supervised the project. G.X. and H.W. made the figures and wrote the manuscript.

Author Information Atomic coordinates and structure factors have been deposited in the Protein Data Bank under accession codes 3QA8 and 3QAD. Reprints and permissions information is available at www.nature.com/reprints. The authors declare no competing financial interests. Readers are welcome to comment on the online version of this article at www.nature.com/nature. Correspondence and requests for materials should be addressed to H.W. (haowu@med.cornell.edu).

METHODS

Protein expression and purification. To elucidate the molecular basis of IKK β function, we expressed IKK β from a number of species using baculovirus-mediated insect cell expression. The xIKK β sequence in the NCBI database starts at a Met residue that is equivalent to Met 17 of both the hIKK β and the mouse IKK β (mIKK β) sequence. Translation of the DNA sequence preceding the ATG codon of Met 17 revealed sequences that are almost identical to residues 9–16 of hIKK β and mIKK β . These were taken as part of the xIKK β sequence and residues 1–8 were taken from the corresponding mIKK β sequence. This reconstructed xIKK β sequence has the same residue numbering as the hIKK β sequence until after the SDD.

Various constructs of IKK β wild type and the phosphomimetic S177E/S181E mutant were designed with an N-terminal polyhistidine tag and a tobacco etch virus protease-cutting site between the tag and the protein. Recombinant IKK β baculoviruses were made in DH10BAC cells, amplified and used to infect Hi5 insect cells in serum-free media (Invitrogen). The cells were cultured in suspension and harvested 48 h after infection. The recombinant proteins were purified by nickel affinity chromatography, anion exchange and gel filtration chromatography. For crystallization, the polyhistidine tag was cleaved by the tobacco etch virus protease during protein purification.

All IkB α proteins were expressed in *Escherichia coli* using pET28a, pGEX4T3 and pET-SUMO vectors and purified by their respective affinity tags. For kinase assays, the SUMO tag was cleaved from IkB α proteins. His-ULD and His-ULD-SDD of hIKK β were also expressed in *E. coli* using the pET28a vector.

Crystallization and data collection. Unlike many protein kinases, the IKK β KD cannot be recombinantly expressed as a well-behaved biochemical entity for structural studies. In addition, after mapping a compact region by limited proteolysis, IKK β was still refractory to crystallization, both alone and in the presence of various ATP analogues. To overcome this obstacle, we used several IKK β inhibitors, including Cmpd1 and Cmpd2 (Supplementary Fig. 1), which were identified against the S177E/S181E (EE) mutant, in co-crystallization. A hIKK β EE construct (1–678) lacking only the C-terminal NBD did crystallize; however, these crystals only diffracted to a resolution of ~ 7.5 Å. Searching IKK β orthologues that may give better crystals led to success in crystallizing the analogous region of xIKK β EE (4–675; Fig. 1a).

The xIKK β (S177E/S181E) protein containing residues 4–675 was concentrated by ultrafiltration (Amicon) to about 15 mg ml^{-1} in 20 mM Tris-HCl (pH 8.0), 150 mM NaCl and 10 mM dithiothreitol (DTT). It was mixed with an inhibitor compound in a 1:2 molar ratio before crystallization. Cmpd1 is 4-((4-(4-chlorophenyl)pyrimidin-2-yl)amino)phenyl(4-(2-hydroxyethyl)piperazin-1-yl)methanone and Cmpd2 is 1-(4-(4-((4-(pyridin-4-ylsulfonyl)phenyl)pyrimidin-2-yl)amino)benzoyl)piperazin-1-yl)ethanone. The P1 crystals were grown using hanging-drop vapour diffusion at 4 °C by mixing equal volumes of the purified protein and the crystallization condition of 100 mM *N*-(2-acetamido)iminodiacetic acid at pH 6.5, 10% (w/v) polyethylene glycol 6000, 50 mM Li₂SO₄, 300 mM NaCl and 10 mM DTT. The I4₁22 crystals were grown at 4 °C with well solution containing 1.8 M K/Na phosphate at pH 5.6 and 10 mM DTT. For data collection, all crystals were flash frozen in the respective crystallization conditions supplemented with 25% (v/v) ethylene glycol. Diffraction data were collected at the 24ID-C beam line of the Advanced Photon Source. Multiwavelength anomalous diffraction (MAD) data on heavy-atom derivative crystals or selenomethionyl crystals were collected near the respective absorption edges. All diffraction data were processed using the HKL2000 suite⁴³ and their statistics are shown in Supplementary Table 1 and Supplementary Table 2.

Structure determination, refinement and analysis. The initial xIKK β crystals grew in the P1 space group in the presence of the inhibitor Cmpd1 or Cmpd2 and diffracted to a resolution of 3.6 Å. Selenomethionyl crystals were obtained, but we failed to locate the large number of expected selenium sites. Among the extensive heavy-atom searches, an ytterbium-derivative was obtained, with eight well-defined sites, which probably correspond to eight IKK β molecules in the asymmetric unit. However, the electron density map calculated from a three-wavelength ytterbium-anomalous diffraction data set was insufficient for tracing, and phase combination with the selenomethionyl data set could not be performed, owing to non-isomorphism.

The structure determination was eventually successful in the alternative crystal form, I4₁22, which contains one molecule of IKK β in complex with Cmpd1 and diffracted to a resolution of 4.0 Å, using MAD of the selenomethionyl crystals (Supplementary Tables 1 and 2 and Supplementary Fig. 2). Twelve selenium sites were determined using the program SHELXD⁴⁴ and refined with the program MLPHARE in the CCP4 suite⁴⁵. MAD phases were calculated at a resolution of 4.0 Å with data from I4₁22 crystals using the program SHARP⁴⁶. A few cycles of model building and refinement were carried out with the program O⁴⁷ and REFMAC with TLS parameterization⁴⁸. The I4₁22 crystals contain one monomer in the asymmetric unit and 80% solvent when calculated with the entire IKK β construct and 84% solvent when considering only the ordered part of the structure. The inhibitor Cmpd1 has density in the MAD experimental map and the $F_o - F_c$

omit map. The Dundee PRODRG2 Server was used to generate topology and restraint files of the compound for refinement. The refined model contains residues 16–236, 243–286, 290–376, 384–394, 401–475 and 528–637 and Cmpd1.

The structure of the P1 form was determined by molecular replacement using the refined model of the I4₁22 crystal form as the search model, in which eight molecules were located. Selenium sites of the single-wavelength anomalous diffraction data set of a selenomethionyl crystal in the P1 space group was calculated by difference Fourier analysis and used to verify residue registration in the P1 structure. Refinement in the P1 structure was conducted at a resolution of 3.6 Å and incorporated tight non-crystallographic symmetry restraints (root mean squared deviation of 0.02 Å in atom positions). After several rounds of refinement at a resolution of 3.6 Å, new electron densities appeared in the P1 crystal form to complete the model building. Although Cmpd2 was in the crystallization condition, it did not have clear density and was not included in the refinement. The refined model of the P1 crystal form contains four IKK β dimers in the asymmetric unit. Three of the dimers encompass residues 16–236, 243–286, 290–376, 384–394, 401–551 and 559–666. One dimer contains the same residues as the structure in I4₁22. The structures were analysed using the CCP4 suite⁴⁵ and the Dali server⁴⁹, and the figures were made using PYMOL⁵⁰.

GST pull-down. The tagged proteins were first purified with glutathione or Ni-NTA beads and their expression levels were assessed by SDS–polyacrylamide gel electrophoresis (SDS–PAGE). Beads containing estimated equivalent quantities of the tagged proteins were mixed with the cell lysates or the purified versions of the interaction partners. The mixtures were incubated at room temperature (20 °C) for 1 h with rotation. After centrifugation, the supernatants were removed. The beads were then washed twice, eluted and subjected to SDS–PAGE analysis. All pull-down experiments were repeated two to four times with consistency.

Kinase assays using anti-phospho-IkB α antibody. The hIKK β proteins ($0.1 \mu\text{g} \mu\text{l}^{-1}$) were incubated with recombinant IkB α ($1 \mu\text{g} \mu\text{l}^{-1}$) in 50 mM Tris-HCl at pH 8.0, 100 mM NaCl, 10 mM MgCl₂ and 2 mM DTT for 30 min at 30 °C. SDS–PAGE sample buffer was used to terminate the reactions. The products were separated on 15% SDS–PAGE and transferred to PVDF membranes. Anti-phospho-IkB α antibody (Cell Signaling Technology) was used to detect phospho-IkB α .

Determination of K_m of hIKK β for IkB α (1–54) and full-length IkB α . To derive the K_m of hIKK β for full-length IkB α , kinase assays were performed at substrate concentrations of 2.8, 5.3, 10.6, 21.3, 42.5 and 85 μM . Similarly, to derive the K_m of hIKK β for IkB α (1–54), kinase assays were performed at substrate concentrations of 5.3, 10.6, 21.3, 42.5, 85 and 170 μM . A time course of the kinase reactions was first performed to select a hIKK β amount and a time point within which the reactions are linear with time. The final selected reactions contain 10 ng baculovirus-expressed hIKK β , 100 mM cold ATP and $1 \mu\text{l}$ [γ -³²P]ATP ($3,000 \text{ Ci mmol}^{-1}$, 1 mCi per 100 μl) in 25 μl of reaction buffer containing 50 mM Tris-HCl at pH 8.0, 100 mM NaCl, 10 mM MgCl₂ and 2 mM DTT. The phosphotransfer reaction was allowed to proceed for 10 min at 30 °C and quenched with SDS–PAGE sample buffer. The products were separated on 15% SDS–PAGE and subjected to autoradiography. The relative amounts of phosphorylated IkB α were quantified using IMAGEJ, plotted against total IkB α concentrations and fitted using nonlinear regression to the Michaelis–Menten equation to obtain K_m using SIGMAPLOT.

Transfection, immunoprecipitation and kinase assay. The constructs Flag-hIKK β EE and its truncation mutants; HA-hIKK β EE and its dimerization mutants L654D/W655D, W655D/L658D and L654D/W655D/L658D; and Flag-hIKK β and its dimerization mutants L654D/W655D and W655D/L658D were generated in the vector pcDNA3 by conventional PCR. All IKK β constructs were transfected in HEK293T cells with Lipofectamine 2000 (Invitrogen). After 24 h, cell extracts were immunoprecipitated with anti-Flag antibodies bound to agarose beads (M2, Sigma) or anti-HA bound to agarose beads (Sigma). IKK β kinase assays were essentially done as previously described^{6,13}. Briefly, immunoprecipitates were incubated with 2 μM full-length IkB α (1–317) in 20 mM HEPES at pH 7.5, 10 mM MgCl₂, 20 mM β -glycerophosphate, 10 mM PNPP, 50 mM Na₃VO₄, 1 mM DTT, 20 mM ATP, and 1–10 mCi [γ -³²P]ATP at 30 °C for 30 min, and subjected to SDS–PAGE and autoradiography. Immunoblotting was performed using anti-Flag (Sigma), anti-HA (Sigma) or anti-IKK β antibodies (Upstate, 05-535).

Equilibrium analytical ultracentrifugation measurements. Experiments were performed in a Beckman XL-A/I analytical ultracentrifuge (Beckman-Coulter), using six-cell centre pieces with straight walls, a 12-mm path length and sapphire windows. Samples were kept and diluted in 50 mM Tris-HCl at pH 8.0 and 300 mM NaCl. Samples from wild-type protein were diluted to 6.9, 4.5 and 2.4 μM , mutant L654D/W655D to 7.4, 4.8 and 2.6 μM and mutant W655D/L658D to 4.9, 3.2 and 1.7 μM for channels A, B and C, respectively. Dilution buffer was used as blank. All samples were run at 4 °C at 9,000 r.p.m. (5,900g; held for 20 h then scanned four times at 1-h intervals), 11,000 r.p.m. (8,800g; held for 10 h then scanned four times at 1-h intervals), 14,000 r.p.m. (14,300g; held for

10 h then scanned four times at 1-h intervals) and 17,000 r.p.m. (21,000g; held for 10 h then scanned four times at 1-h intervals). Detection was by ultraviolet absorption at 280 nm. Solvent density and the protein partial specific volume at each temperature were determined using the program SEDNTERP (Alliance Protein Laboratories). For calculation of K_D and the apparent molecular weight, all useful data were used in a global fit, using the program HETEROANALYSIS, obtained from University of Connecticut (<http://www.biotech.uconn.edu/auf>).

43. Otwinowski, Z. & Minor, W. Processing of X-ray diffraction data collected in oscillation mode. *Methods Enzymol.* **276**, 307–326 (1997).
44. Schneider, T. R. & Sheldrick, G. M. Substructure solution with SHELXD. *Acta Crystallogr. D* **58**, 1772–1779 (2002).
45. Collaborative Computational Project, Number 4. The CCP4 suite: programs for protein crystallography. *Acta Crystallogr. D* **50**, 760–763 (1994).
46. Bricogne, G. *et al.* Generation, representation and flow of phase information in structure determination: recent developments in and around SHARP 2.0. *Acta Crystallogr. D* **59**, 2023–2030 (2003).
47. Jones, T. A., Zou, J.-Y., Cowan, S. W. & Kjeldgaard, M. Improved methods for building models in electron density maps and the location of errors in those models. *Acta Crystallogr. A* **47**, 110–119 (1991).
48. Winn, M. D., Murshudov, G. N. & Papiz, M. Z. Macromolecular TLS refinement in REFMAC at moderate resolutions. *Methods Enzymol.* **374**, 300–321 (2003).
49. Holm, L. & Sander, C. Dali: a network tool for protein structure comparison. *Trends Biochem. Sci.* **20**, 478–480 (1995).
50. DeLano, W. L. PyMOL Molecular Viewer (<http://www.pymol.org>) (2002).

Structural basis for recognition of centromere histone variant CenH3 by the chaperone Scm3

Zheng Zhou^{1*}, Hanqiao Feng^{1*}, Bing-Rui Zhou¹, Rodolfo Ghirlando², Kaifeng Hu³, Adam Zwolak⁴, Lisa M. Miller Jenkins⁵, Hua Xiao¹, Nico Tjandra⁴, Carl Wu¹ & Yawen Bai¹

The centromere is a unique chromosomal locus that ensures accurate segregation of chromosomes during cell division by directing the assembly of a multiprotein complex, the kinetochore¹. The centromere is marked by a conserved variant of conventional histone H3 termed CenH3 or CENP-A (ref. 2). A conserved motif of CenH3, the CATD, defined by loop 1 and helix 2 of the histone fold, is necessary and sufficient for specifying centromere functions of CenH3 (refs 3, 4). The structural basis of this specification is of particular interest. Yeast Scm3 and human HJURP are conserved non-histone proteins that interact physically with the (CenH3–H4)₂ heterotetramer and are required for the deposition of CenH3 at centromeres *in vivo*^{5–13}. Here we have elucidated the structural basis for recognition of budding yeast (*Saccharomyces cerevisiae*) CenH3 (called Cse4) by Scm3. We solved the structure of the Cse4-binding domain (CBD) of Scm3 in complex with Cse4 and H4 in a single chain model. An α -helix and an irregular loop at the conserved amino terminus and a shorter α -helix at the carboxy terminus of Scm3(CBD) wraps around the Cse4–H4 dimer. Four Cse4-specific residues in the N-terminal region of helix 2 are sufficient for specific recognition by conserved and functionally important residues in the N-terminal helix of Scm3 through formation of a hydrophobic cluster. Scm3(CBD) induces major conformational changes and sterically occludes DNA-binding sites in the structure of Cse4 and H4. These findings have implications for the assembly and architecture of the centromeric nucleosome.

Unlike other eukaryotic species that have complex regional centromeres with multiple centromeric nucleosomes¹⁴, budding yeast has a single centromeric nucleosome that is necessary and sufficient to mediate the accurate segregation of chromosomes during mitosis and meiosis^{15–18}. The simple centromeres of budding yeast provide an attractive system for investigating outstanding topics in centromere biology, including the pathway of CenH3 deposition and the architecture of the centromeric nucleosome^{19,20}.

Yeast Scm3 and human HJURP are binding partners of CenH3–H4 and are functionally required for their deposition at centromeres *in vivo*^{5–13}. A conserved domain of Scm3 dictates specific and stoichiometric binding of CenH3–H4 (Fig. 1a), forming a (Scm3–Cse4–H4)₂ hexamer in 2 M NaCl⁵. This CBD of Scm3 is mapped to residues 84–187 (ref. 5). To investigate the structural basis for the recognition of Cse4 by Scm3, we first analysed the CBD of Scm3 by NMR and found that it is intrinsically disordered (Supplementary Fig. 1). To overcome instability inherent in complexes of individual Scm3, Cse4 and H4 fragments (Supplementary Figs 2–4), we engineered a single-chain molecule in which Scm3 is inserted between Cse4 and H4 to assemble a stably folded molecule (Supplementary Fig. 5). For convenience, we termed the single-chain molecule scSCH (Scm3, Cse4, H4).

The structure of scSCH was determined using multidimensional NMR and verified by structural analysis of its mutants (Fig. 1b–d and Supplementary Fig. 6). The structure of the folded core of scSCH, which includes residues 97–135 of Scm3, 157–202 of Cse4 and 50–99 of H4, is

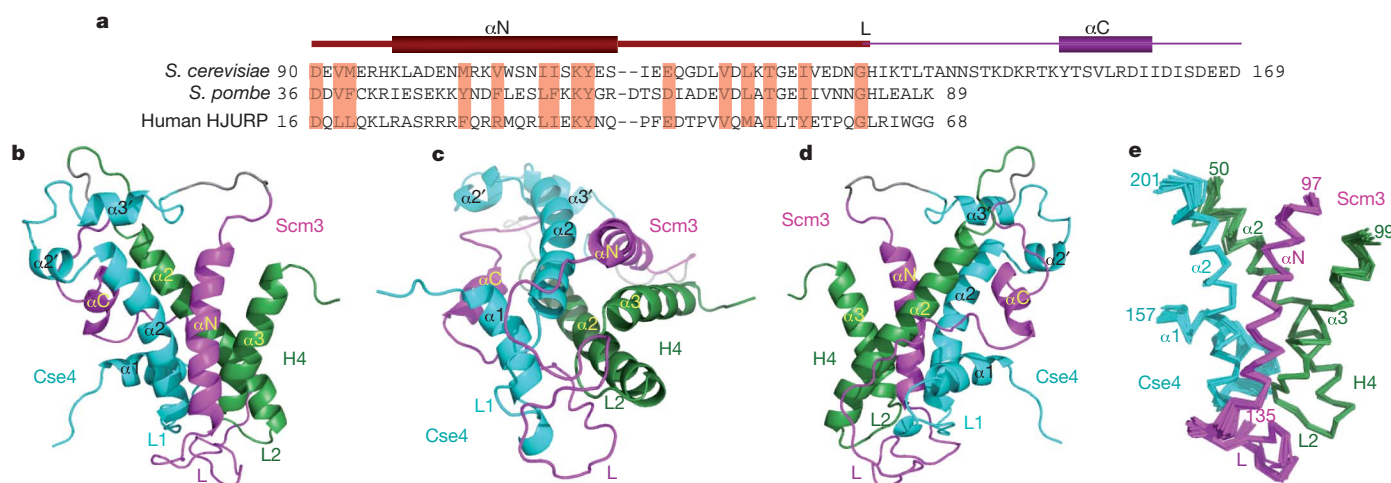


Figure 1 | Overall structure of scSCH. **a**, The amino acid sequence and secondary structures of the Cse4-binding domain of Scm3 in scSCH. Also shown are the conserved regions in Scm3 of *S. pombe* and human HJURP. Highly conserved residues are highlighted in red. The region in the folded core

is shown in dark magenta (see **e**). **b–d**, Front, bottom and back view of the scSCH structure shown in ribbon representation. Scm3, Cse4 and H4 are in magenta, cyan and dark green, respectively. The full sequence of scSCH is M-His₆-KK-Cse4(150–227)-LVPRGS-Scm3(93–169)-GDK-H4(42–103).

¹Laboratory of Biochemistry and Molecular Biology, National Cancer Institute, Bethesda, Maryland 20892, USA. ²Laboratory of Molecular Biology, National Institute of Diabetes and Digestive and Kidney Diseases, Bethesda, Maryland 20892, USA. ³National Magnetic Resonance Facility at Madison, University of Wisconsin, Madison, Wisconsin 53706, USA. ⁴Laboratory of Molecular Biophysics, National Heart, Lung, and Blood Institute, NIH, Bethesda, Maryland 20892, USA. ⁵Laboratory of Cell Biology, National Cancer Institute, NIH, Bethesda, Maryland 20892, USA.

*These authors contributed equally to this work.

well defined with root mean squared deviations (r.m.s.d.) of 0.54 Å for backbone atoms and 1.06 Å for all heavy atoms (Fig. 1e and Supplementary Table 1). Importantly, linker residues inserted between Scm3, Cse4 and H4 do not alter the structure of the folded region. Proteolytic cleavage of the two linkers in the folded scSCH only affects chemical shifts of neighbouring residues close to the cutting sites (Supplementary Fig. 7). Moreover, the folded structure of the above tertiary complex is unchanged by refolding after denaturation in 6 M GdmCl to liberate the three components as individual polypeptides (Supplementary Fig. 8). Backbone amide ^{15}N - $\{^1\text{H}\}$ heteronuclear Overhauser effects (NOE) reflect dynamic motions. The folded core shows small dynamic motions (NOE >0.7) except for loop 1 of Cse4 and the small loop region following the N-terminal α -helix (αN) in Scm3 (Supplementary Fig. 9a, b). In contrast, other regions display larger dynamic motions (NOE <0.7), corresponding to less-well-defined structures (Supplementary Figs 9–11).

In the structure of scSCH, Scm3 interacts broadly with both Cse4 and H4. The αN helix of Scm3 makes close contacts with both the $\alpha 2$ helix of Cse4 and the $\alpha 3$ helix of H4 through multiple hydrophobic interactions (Figs 1b and 2a–d and Supplementary Figs 9c and 13a). Following the αN helix, the loop region of Scm3 (residues 121–144) mainly interacts with loop 1 of Cse4, except that a bulge (Scm3 residues 125–130) in the middle of the loop lies on top of loop 2 of H4 (Fig. 1c and Supplementary Figs 9d and 13b–d). Scm3 loop residues 140–144 also interact with the C-terminal portion of the $\alpha 2$ helix of H4 (Supplementary Figs 9d and 13e). Interestingly, Scm3 residues 145–154 are

completely disordered (Supplementary Figs 9b, e and 10). Finally, the C-terminal α -helix (αC) of Scm3 (155–161) makes interactions with the N-terminal region of the $\alpha 2$ helix of H4 (Supplementary Fig. 13f).

Next, we analysed the effects of mutations on the formation of Scm3–Cse4–H4 complexes with isothermal titration calorimetry. The results reveal that the Scm3 recognition motif resides in the N-terminal region (181–190) of the $\alpha 2$ helix of Cse4. Double mutations Met181Ser/Met184Gly and Ala189Ser/Ser190Val in Cse4 that change the Cse4-specific residues to the corresponding residues in H3 reduced the binding affinity by a factor of 5.5 and 9, respectively (Fig. 2a, b, Supplementary Table 2 and Supplementary Fig. 14). A double mutation Ile110Asp/Ile117Asn in the αN helix of Scm3 decreased the binding affinity by a factor of 85 (Fig. 2a, Supplementary Fig. 14 and Supplementary Table 2). These residues are important for cell growth: mutation of the three residues (Met184, Ala189, and Ser190) in Cse4 to corresponding residues in H3 leads to growth defect (small colony)²¹, and mutation Ile110Asp/Ile117Asn in Scm3 abrogates cell viability⁷, consistent with the effects of these mutations on the binding affinity between Scm3 and Cse4/H4 (Supplementary Table 2). Met 181 should also be important for cell function because it interacts with Ile 117 of Scm3 (Fig. 2a). It is possible that simultaneous mutation of the four residues in Cse4 to the corresponding residues in H3 would abrogate cell viability.

In contrast, deleting the three extra residues Lys 172, Asp 173 and Gln 174 and mutating Thr 170 in loop 1 (to Lys, as in H3), all residues specific to Cse4 (Supplementary Fig. 12), had little effect on the binding affinity (a factor of 1.1) (Supplementary Table 2). Mutation of four residues (Val 165, Thr 166, Asp 167, Glu 168) at the C-terminal region of the $\alpha 1$ helix of Cse4 to corresponding residues in H3 (Ile, Ala, Gln and Asp) also showed little effect on the binding affinity (a factor of 1.4) (Supplementary Table 2). In addition, we found that Scm3 is capable of pulling down the H3^{CATD}–H4 chimera, in which the CATD of Cse4 is swapped to the corresponding region of H3 (ref. 22) (Supplementary Fig. 15). Furthermore, Scm3 can pull down an H3 mutant with only four residues replaced by the corresponding residues in the $\alpha 2$ helix of Cse4 (Met 181, Met 184, Ala 188 and Ser 189) as well (Fig. 2c, d). Importantly, Scm3 residues that interact with the four Cse4-specific residues are well conserved in human HJURP (Fig. 1a). Indeed, Cse4 can also pull down the N-terminal region (residues 2–81) of HJURP (homologous to the Cse4-binding motif of Scm3 (refs 9, 22)) and human H4 (Supplementary Fig. 16). This result is consistent with the ability of Cse4 to replace human CENP-A at centromeres and maintain centromere function in human cells²³. In addition, the CENP-A residues that correspond to the four Cse4-specific residues are reasonably conserved (Fig. 2d).

The structure of scSCH reveals the induction of major local conformational changes in the structure of Cse4 and H4 relative to the (CENP-A–H4)₂ tetramer. First, the packing between the central $\alpha 2$ helices of Cse4 and H4 in the structure of scSCH is loose in comparison to tight hydrophobic interactions in the homology-modelled dimer based on the H3–H4 structure in the nucleosome (Fig. 3a, b), or in the CENP-A–H4 dimer in the (CENP-A–H4)₂ tetramer²⁴. Hydrophobic residues Leu 59, Phe 62 and Val 66 in the $\alpha 2$ helix of H4 lose interacting partners Tyr 193, Ser 192 and Leu 186 in the $\alpha 2$ helix of Cse4 (Fig. 3a, b; Phe 101, Ala 98 and Leu 94 in human CENP-A (ref. 24)). Second, owing to the insertion of the Scm3 loop, loop 1 in Cse4 loses close contact with loop 2 of H4 (Supplementary Fig. 13b) when compared with the corresponding loops in the canonical histone octamer²⁵ (Fig. 3c, d) or in the human (CENP-A–H4)₂ tetramer²⁴ (Supplementary Fig. 17). Third, the $\alpha 2$ helix of Cse4 kinks in the middle in scSCH (Fig. 4a), as forced by the side chain of residue Met 103 of the αN helix of Scm3 (Fig. 4a). In contrast, the $\alpha 2$ helix of CENP-A or H3 is relatively straight in the CENP-A–H4 (ref. 24) (Fig. 4b) or H3–H4 tetramer²⁵ (Supplementary Fig. 18). Fourth, the C-terminal region (94–99) of H4 in scSCH adopts a striking helical conformation and extends the $\alpha 3$ helix of H4. The helical conformation is induced by the side chain

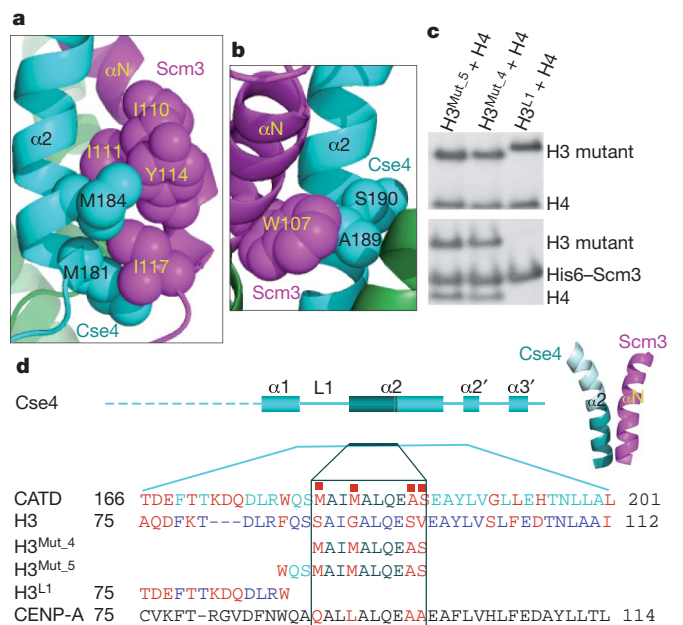


Figure 2 | The N-terminal region (181–190) of the $\alpha 2$ helix of Cse4 is the Scm3 recognition motif. **a**, Ile 110, Ile 111, Tyr 114 and Ile 117 (balls in magenta) in the αN helix of Scm3 form a hydrophobic cluster with Cse4-specific residues Met 181 and Met 184 (balls in cyan) in the $\alpha 2$ helix of Cse4. **b**, Trp 107 (balls in magenta) in the αN helix of Scm3 has close interactions with the Cse4-specific residue Ala 189 (balls in cyan) in the $\alpha 2$ helix of Cse4. Ser 190 is also a Cse4-specific residue (balls in cyan). **c**, SDS-PAGE gels showing the pull-down results with mutants of H3. The top panel shows the input of H3 mutants and H4. The bottom panel shows the molecules eluted from His₆-Scm3 (Scm3(65–169))-bound beads with 250 mM imidazole. H3^{Mut_4}, H3^{Mut_5} and H3^{L1} are the mutants of H3 (see **d**). **d**, Illustration of the secondary structures in Cse4 and the Scm3 recognition motif (dark cyan), CATD, and the mutants used in the pull-down experiments. The red squares indicate the four residues that are sufficient for specific recognition of Cse4 by Scm3. The sequences swapped from Cse4 to H3 in the mutations are shown. The sequences that are not changed in the swap are omitted.

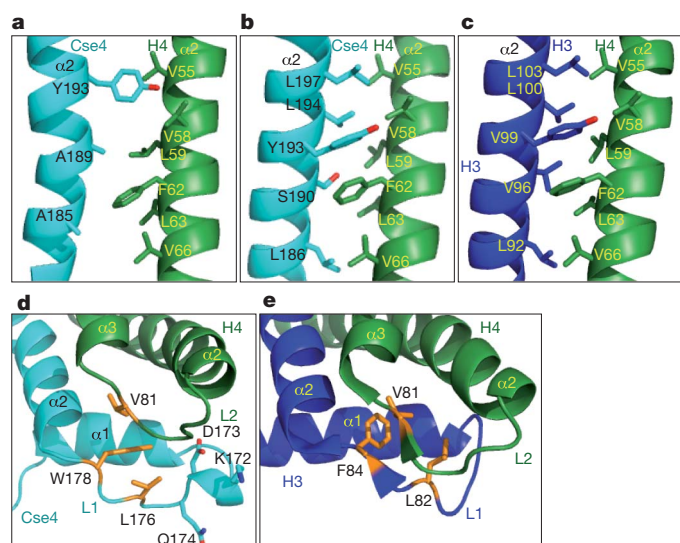


Figure 3 | Altered interactions in the CATD region in scSCH. **a**, The region of the $\alpha 2$ helices of Cse4 and H4 in scSCH, showing that there is little side-chain interaction between the two helices. **b**, The corresponding region of the $\alpha 2$ helices of Cse4 and H4 in the Cse4-H4 dimer structure obtained by homology modelling based on the structures of H3 and H4 in the nucleosome, showing that there are many hydrophobic interactions. **c**, The region of the $\alpha 2$ helices of H3 and H4 in the nucleosome. **d**, Region of loop 1 of Cse4 and the loop 2 of H4. The side chains of the hydrophobic residues are shown in stick representation and orange. The extra three residues in loop 1 of Cse4 are shown in stick representation. **e**, The corresponding loop 1 of H3 and loop 2 of H4 in the nucleosome structure. The hydrophobic residues are shown in stick representation and orange.

of Leu 98 in the αN helix of Scm3 through hydrophobic interactions with the side chains of Leu 98 and Tyr 99 of H4 (Fig. 4a, Supplementary Fig. 14 and Supplementary Table 2). This region is presumably disordered in the (CENP-A-H4)₂ tetramer²⁴ (Fig. 4b). Interestingly, the same region forms a mini β -strand that pairs with a β -strand of H2A in the canonical histone octamer or with a β -strand of histone

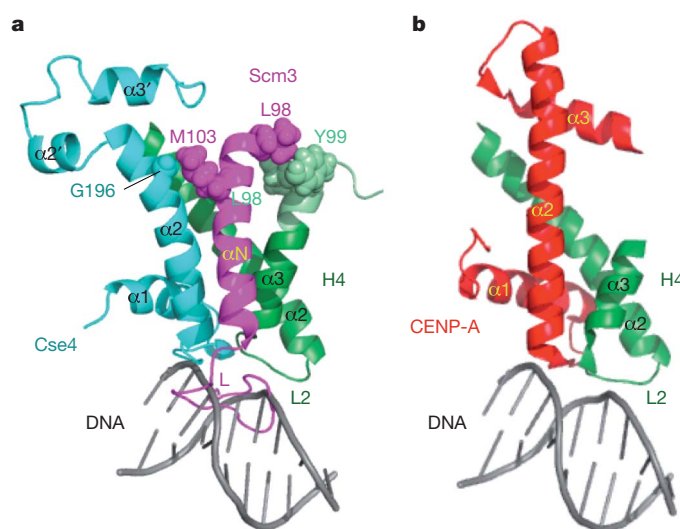


Figure 4 | Scm3 induces large conformational changes in Cse4 and H4 and prevents loop 2 of H4 from binding to DNA. **a**, Cse4-H4 in scSCH. The extended $\alpha 3$ helix in H4 is shown in light green. The loop of Scm3 pushes loop 1 of Cse4 away from loop 2 of H4 and prevents loop 2 of H4 from binding to DNA. DNA is modelled to bind the loop 2 region of H4 based on the canonical nucleosome structure²⁹. **b**, CENP-A-H4 in the (CENP-A-H4)₂ tetramer. DNA is modelled to bind to the loop 2 region of H4 based on the canonical nucleosome structure²⁹.

chaperone Asf1 in the Asf1-H3-H4 complex^{26,27} (Supplementary Fig. 18).

Furthermore, the C-terminal region of Cse4 has considerable disorder in scSCH (Figs 4a, b). The same region is also disordered in the Cse4-H4 dimer and is not required for Cse4-H4 binding to Scm3 (Supplementary Fig. 5 and Supplementary Fig. 19). This 'tetramerization domain' is well folded in the (CENP-A-H4)₂ tetramer. Structure modelling shows that imposing this folded domain on the corresponding region of Cse4 in scSCH allows association as a (Scm3-Cse4-H4)₂ hexamer without major structural incompatibility (Supplementary Fig. 20), consistent with the existence of (Scm3-Cse4-H4)₂ hexamers in 2 M NaCl (ref. 5). However, in this context, histone topography in the scSCH structure outside the tetramerization domain displays dramatic global conformational changes when compared with the (CENP-A-H4)₂ tetramer, making the modelled (Scm3-Cse4-H4)₂ hexamer incompatible with DNA binding (Supplementary Fig. 20). Moreover, the Scm3 loop in the scSCH structure blocks loop 2 of H4, which makes contacts with DNA in the canonical nucleosome (Fig. 4a, b).

Thus, the structure of scSCH indicates that retention of Scm3 in association with centromere DNA is unlikely to occur via binding of Scm3(CBD) to Cse4/H4, as binding of DNA and Scm3(CBD) to Cse4/H4 is mutually incompatible. Instead, Scm3(CBD) behaves as a specific histone chaperone, and the retention of Scm3 with Cse4/H4 on centromeric DNA requires its distinct DNA-binding domain (H. Xiao and C. Wu, manuscript in preparation).

The structure of scSCH reveals that a subregion within the CATD, including four Cse4-specific residues in the N-terminal region of the $\alpha 2$ helix of Cse4, is necessary and sufficient for specific recognition by Scm3. Thus, the remainder of the CATD of Cse4 should be important for association with other proteins for Cse4 functions. The CBD of Scm3 uses both induced histone conformation changes^{26,27} and direct steric occlusion²⁸ to prevent Cse4-H4 in the Scm3-Cse4-H4 complex from DNA binding (Supplementary Fig. 21). Conversely, Cse4-H4, with a conformation similar to that of CENP-A-H4 in the (CENP-A-H4)₂ tetramer, is unfavourable for Scm3(CBD) binding but favours DNA binding, indicating a competition mechanism for Scm3 and HJURP as CenH3-specific chaperones²².

METHODS SUMMARY

All the proteins used in the present study were overexpressed in *Escherichia coli* and purified using Ni-NTA column (Qiagen), ion exchange, gel filtration and reverse-phase HPLC (Waters). Uniformly isotope-labelled proteins were produced using M9 medium with ¹⁵NH₄Cl, ¹³C-D-glucose and D₂O as the sole source of the isotopes. The molecular weight and stoichiometry of the complex were determined by velocity and equilibrium sedimentation experiments on a Beckman Coulter Proteome XL-I analytical ultracentrifuge at 20.0 °C. The multi-dimensional NMR spectra were collected on Bruker 500, 600, 800 and 900 MHz and Varian 600 and 800 MHz instruments. The structure was calculated using the distance constraints measured by NMR and the program Xplor-NIH. Mutations were made using a quick-change kit. The binding constants were measured on the MicroCal VP-ITC instrument.

Full Methods and any associated references are available in the online version of the paper at www.nature.com/nature.

Received 21 October 2010; accepted 17 January 2011.

Published online 16 March 2011.

- Cleveland, D. W., Mao, Y. & Sullivan, K. F. Centromeres and kinetochores: From epigenetics to mitotic checkpoint signaling. *Cell* **112**, 407–421 (2003).
- Henikoff, S., Ahmad, K. & Malik, H. S. The centromere paradox: stable inheritance with rapidly evolving DNA. *Science* **293**, 1098–1102 (2001).
- Black, B. E. *et al.* Structural determinants for generating centromeric chromatin. *Nature* **430**, 578–582 (2004).
- Black, B. E. *et al.* Centromere identity maintained by nucleosomes assembled with histone H3 containing the CENP-A targeting domain. *Mol. Cell* **25**, 309–322 (2007).
- Mizuguchi, G., Xiao, H., Wisniewski, J., Smith, M. M. & Wu, C. Nonhistone Scm3 and histones CenH3-H4 assemble the core of centromere-specific nucleosomes. *Cell* **129**, 1153–1164 (2007).

6. Camahort, R. *et al.* Scm3 is essential to recruit the histone H3 variant Cse4 to centromeres and to maintain a functional kinetochore. *Mol. Cell* **26**, 853–865 (2007).
7. Stoler, S. *et al.* Scm3, an essential *Saccharomyces cerevisiae* centromere protein required for G2/M progression and Cse4 localization. *Proc. Natl Acad. Sci. USA* **104**, 10571–10576 (2007).
8. Camahort, R. *et al.* Cse4 is part of an octameric nucleosome in budding yeast. *Mol. Cell* **35**, 794–805 (2009).
9. Sanchez-Pulido, L., Pidoux, A. L., Pointing, C. P. & Allshire, R. C. Common ancestry of the CENP-A chaperones Scm3 and HJURP. *Cell* **137**, 1173–1174 (2009).
10. Williams, J. S., Hayashi, T., Yanagida, M. & Russell, P. Fission yeast Scm3 mediates stable assembly of Cnp1/CENP-A into centromeric chromatin. *Mol. Cell* **33**, 287–298 (2009).
11. Pidoux, A. L. *et al.* Fission yeast Scm3: A CENP-A receptor required for integrity of subkinetochore chromatin. *Mol. Cell* **33**, 299–311 (2009).
12. Foltz, D. R. *et al.* Centromere-specific assembly of CENP-A nucleosomes is mediated by HJURP. *Cell* **137**, 472–484 (2009).
13. Dunleavy, E. M. *et al.* HJURP is a cell-cycle-dependent maintenance and deposition factor of CENP-A at centromeres. *Cell* **137**, 485–497 (2009).
14. Malik, H. S. & Henikoff, S. Major evolutionary transitions in centromere complexity. *Cell* **138**, 1067–1082 (2009).
15. Stoler, S., Keith, K. C., Curnick, K. E. & Fitzgerald-Hayes, M. A mutation in CSE4, an essential gene encoding a novel chromatin-associated protein in yeast, causes chromosome nondisjunction and cell cycle arrest at mitosis. *Genes Dev.* **9**, 573–586 (1995).
16. Meluh, P. B., Yang, P., Glowczewski, L., Koshland, D. & Smith, M. M. Cse4p is a component of the core centromere of *Saccharomyces cerevisiae*. *Cell* **94**, 607–613 (1998).
17. Cottarel, G., Shero, J. H., Hieter, P. & Hegemann, J. H. A 125-base-pair CEN6 DNA fragment is sufficient for complete meiotic and mitotic centromere functions in *Saccharomyces cerevisiae*. *Mol. Cell. Biol.* **9**, 3342–3349 (1989).
18. Clarke, L. & Carbon, J. Isolation of a yeast centromere and construction of functional small circular chromosomes. *Nature* **287**, 504–509 (1980).
19. Black, B. E. & Bassett, E. A. The histone variant CENP-A and centromere specification. *Curr. Opin. Cell Biol.* **20**, 91–100 (2008).
20. Furuyama, T. & Henikoff, S. Centromeric nucleosomes induce positive DNA supercoils. *Cell* **138**, 104–113 (2009).
21. Keith, K. C. *et al.* Analysis of primary structural determinants that distinguish the centromere-specific function of histone variant Cse4p from histone H3. *Mol. Cell. Biol.* **19**, 6130–6139 (1999).
22. Shuaib, M., Ouararhni, K., Dimiyrov, S. & Hamiche, A. HJURP binds CENP-A via a highly conserved N-terminal domain and mediates its deposition at centromeres. *Proc. Natl Acad. Sci. USA* **107**, 1349–1354 (2010).
23. Wieland, G., Orthaus, S., Ohndorf, S., Diekmann, S. & Hemmerich, P. Functional complementation of human centromere protein A (CENP-A) by Cse4p from *Saccharomyces cerevisiae*. *Mol. Cell. Biol.* **24**, 6620–6630 (2004).
24. Sekulic, N., Bassett, E. A., Rogers, D. J. & Black, B. E. The structure of (CENP-A–H4)₂ reveals physical features that mark centromeres. *Nature* **467**, 347–351 (2010).
25. Wood, C. M. *et al.* High-resolution structure of the native histone octamer. *Acta Crystallogr.* **61**, 541–545 (2005).
26. English, C. M., Adkins, M. W., Carson, J. J., Churchill, M. E. & Tyler, J. K. Structural basis for the histone chaperone activity of Asf1. *Cell* **127**, 495–508 (2006).
27. Natsume, R. *et al.* Structure and function of the histone chaperone CIA/ASF1 complexed with histones H3 and H4. *Nature* **446**, 338–341 (2007).
28. Zhou, Z. *et al.* NMR structure of chaperone Chz1 complexed with histones H2A.Z–H2B. *Nature Struct. Mol. Biol.* **15**, 868–869 (2008).
29. White, C. L., Suto, R. K. & Luger, K. Structure of the yeast nucleosome core particle reveals fundamental changes in internucleosome interactions. *EMBO J.* **20**, 5207–5218 (2001).

Supplementary Information is linked to the online version of the paper at www.nature.com/nature.

Acknowledgements We thank J. Ying, K. Varney, J. F. Ellena and J. Gruschus for help collecting NMR spectra, A. Bax for discussion, C. Klee and M. Lichten for comments on the manuscript, and D. Cleveland for plasmids of human CENP-A and H4 histones. This work is supported by the intramural research programs of NCI, NIDDK and NHLBI.

Author Contributions Z.Z. and H.F. contributed equally to this work. Z.Z. performed protein engineering, biochemical and ITC studies. B.-R.Z. contributed to protein sample preparation. B.-R.Z. and L.M.M.J. contributed to the analysis of ITC data. H.F., K.H., A.Z. and N.T. collected the NMR spectra. H.F. and Z.Z. analysed the NMR data and H.F. solved the structure. R.G. performed the sedimentation experiments. H.X. provided initial plasmids and guidance in cloning. C.W. proposed the project and participated in manuscript writing. Y.B. contributed to the overall strategy, project management and writing of the manuscript. All authors read and commented on the manuscript.

Author Information The atomic coordinates have been deposited in the Protein Data Bank under accession code 2L5A. Reprints and permissions information is available at www.nature.com/reprints. The authors declare no competing financial interests. Readers are welcome to comment on the online version of this article at www.nature.com/nature. Correspondence and requests for materials should be addressed to Y.B. (yawen@helix.nih.gov).

METHODS

Protein sample preparation. All proteins were expressed in *E. coli* (BL21-codonPlus(DE3)-RIL) with pET vectors (Stratagene). N-terminal His₆-tagged fragments of Cse4 and Scm3 and their mutants were first purified via Ni-NTA (Qiagen) whereas H4 and non-His-tagged fragments of Cse4 and Scm3 were first purified via SP sepharose (GE Healthcare). They were next subjected to reverse-phase HPLC purification using acetonitrile and water as solvents. Purified proteins were lyophilized. Isotope-labelled proteins for NMR studies were produced by growing *E. coli* cells in M9 media with ¹⁵NH₄Cl, U-¹³C₆-glucose, and D₂O as the sole source for nitrogen, carbon and deuterium, respectively. For the measurement of side-chain NOEs, specific methyl labelling (¹³CH₃) for Ile, Leu and Val residues was also made following the protocol of ref. 30.

To prepare the Cse4, H4 and Scm3 complexes, lyophilized proteins were first dissolved in H₂O. Their concentrations were determined by measuring the absorbance at 280 nm. Equal amounts of each species were mixed together and dialysed against 10 mM Tris-HCl and 2 M NaCl at pH 7.4 and 4 °C. After centrifugation, the soluble fractions were subjected to gel filtration on Superdex 75 10/300 GL column (GE Healthcare). The eluted complexes were concentrated with an Amicon with Ultra Ultracel-10 membrane (Millipore) and exchanged to a final buffer of 50 mM MES at pH 5.6. The Cse4-H4 complexes were made in the same way. Scm3(80–211) samples for NMR study were prepared by dissolving them in 8 M urea and dialysis against corresponding buffer. scSCH and all other single-chain molecules derived from scSCH are purified with Ni-NTA (Qiagen) under native conditions (20 mM Tris-HCl and 0.5 M NaCl at pH 8.0), followed by gel filtration with Superdex 200 10/60 column at 4 °C (GE healthcare). The fractions containing the target protein were combined and concentrated and exchanged with the final buffer (50 mM MES at pH 5.4).

Analytical ultracentrifugation. Sedimentation velocity experiments were conducted in duplicate at 20.0 °C on a Beckman Coulter Proteome XL-I analytical ultracentrifuge. 400 µl of the sample of 35 µM in 50 mM MES (pH 5.6) was loaded in a double sector centrepiece cell and analysed at a rotor speed of 50,000 r.p.m. One-hundred scans were acquired as single absorbance measurements ($\lambda = 280$ nm) at 7.1-min intervals using a radial spacing of 0.003 cm. Data were analysed in SEDFIT 11.71 in terms of a continuous $c(s)$ distribution to obtain a sedimentation coefficient, s , and molecular mass M (ref. 31). Solution densities ρ were measured at 20.0 °C on a Mettler Toledo DE51 density meter and solution viscosities η were measured using a Cannon-Ubbelohde viscometer and Cannon-CT 500 constant temperature bath set at 20.00 °C. The partial specific volume v of the complex was calculated in SEDNTERP 1.09 (ref. 32). $c(s)$ analyses were carried out using an s -value range of 0.5 to 6.0 with a linear resolution of 100 and a confidence level (F -ratio) of 0.68. The analyses, implemented using time-independent noise corrections, returned root mean square deviation (r.m.s.d.) values for the best fits of 0.0040 absorbance units. Sedimentation equilibrium experiments were conducted at 20.00 °C on a Beckman Optima XL-A. 135 µl volumes of the complex were studied at loading concentrations of 20, 39 and 78 µM, along with the sample recovered from the sedimentation velocity experiments. Experiments were carried out using six-channel centrepiece cells at rotor speeds ranging from 18,000 to 34,000 r.p.m. In all cases data were acquired as an average of four absorbance measurements at wavelengths of 280 and 250 nm using a radial spacing of 0.001 cm. Sedimentation equilibrium at each speed was achieved within 40 h. Data were analysed globally in terms of a single ideal species using SEDPHAT 6.21 (refs 32, 33).

NMR experiments. NMR experiments were performed on Bruker 500, 600, 800 and 900 MHz and Varian 600 and 800 MHz spectrometers at 35 °C. The following experiments were recorded. 2D: [¹H, ¹H]-NOESY, [¹H, ¹⁵N]-TROSY, [¹H, ¹³C]-HMQC, ¹⁵N-¹H NOE; TROSY version 3D: HNCACB, HNCOCACB, HNCA, HNCOCACB, HNCO, HNCACB; 3D HBHACONH, HCCH-TOCSY, CCH-TOCSY, CCC(CO)NH, [¹H, ¹⁵N]-NOESY-HSQC, [¹H, ¹⁵N]-NOESY-HSQC

([¹³C]methyl-labelled sample), [¹H, ¹³C]-NOESY-HSQC, [¹H, ¹³C]-NOESY-HSQC ([¹³C]methyl-labelled sample). The spectra were processed using NMRPipe³⁴ and analysed with NMRView³⁵.

Structure calculation. Structure calculation was done using the program Xplor-NIH³⁶. The NOE-derived restraints were subdivided into four classes, strong, medium, weak and very weak, by comparison with NOEs of protons separated by known distances as described previously³⁷. Backbone dihedral angle restraints (ϕ and ψ angles) were obtained from analysis of ¹H α , HN, ¹³C α , ¹³C β , ¹³C γ and ¹⁵N chemical shifts by using the program TALOS³⁸. Two constraints per hydrogen bond (dNH-O \leq 2.2 Å and dN-O \leq 3.2 Å) were added in the final structure calculation after initial NOE-derived structures were obtained. The program PROCHECK-NMR³⁹ was used to evaluate the quality of the calculated structures.

Isothermal titration calorimetric experiments. The ITC experiments were performed on a MicroCal VP-ITC by injecting Scm3(83–169) solution (250 µM) to a solution of single-chain Cse4-H4 or their mutants (His₆-KK-Cse4(151–207)-LVPRGS-H4(45–103)) (20 µM) in a chamber of 1.4 ml at 25 °C in 50 mM MES (pH 5.4) and 0.1 M NaCl. Twenty-nine injections (each of 10 µl) were made and the heat released was analysed. The data were analysed as described previously⁴⁰.

Pull-down experiments. Pull-down experiments were carried out in 50 mM sodium phosphate, 25 mM imidazole, 2 M NaCl, pH 8.0 at room temperature. Ni-NTA (Qiagen) beads were mixed with His₆-Scm3(66–169) with a final concentration of 6 µM. Approximately 10-fold excess of (Cse4-H4)₂ or (H3-H4)₂ or their mutants was mixed with beads and incubated. The incubation was at 25 °C for 30 min. The beads were washed with the same buffer three times. The complex formed on the beads was eluted with 250 mM imidazole and analysed by SDS-PAGE. Beads without His₆-Scm3 were also incubated with corresponding (Cse4-H4)₂ under identical conditions to assess background binding and the integrity of the tetramer. No nonspecific binding was identified in 2 M NaCl. For molecules derived from thrombin-digested single-chain proteins, the complex was incubated with Ni-NTA (Qiagen) beads at 25 °C for 30 min and then washed three times. The final complex formed on the beads was eluted with either 8 M urea or 250 mM imidazole. The eluted molecules were analysed by SDS-PAGE.

30. Tugarinov, V., Kanelis, V. & Kay, L. E. Isotope labeling strategies for the study of high-molecular-weight proteins by solution NMR spectroscopy. *Nature Protocols* **1**, 749–754 (2006).
31. Schuck, P. Size-distribution analysis of macromolecules by sedimentation velocity ultracentrifugation and Lamm equation modeling. *Biophys. J.* **78**, 1606–1619 (2000).
32. Cole, J. L., Lary, J. W., Moody, T. P. & Laue, T. M. Analytical ultracentrifugation: sedimentation velocity and sedimentation equilibrium. *Methods Cell Biol.* **84**, 143–179 (2008).
33. Schuck, P. On the analysis of protein self-association by sedimentation velocity analytical ultracentrifugation. *Anal. Biochem.* **320**, 104–124 (2003).
34. Delaglio, F. et al. NMRPipe: a multidimensional spectral processing system based on UNIX pipes. *J. Biomol. NMR* **6**, 277–293 (1995).
35. Johnson, B. A. & Blevins, R. A. NMRView: a computer program for the visualization and analysis of NMR data. *J. Biomol. NMR* **4**, 603–614 (1994).
36. Schwieters, C. D., Kuszewski, J., Tjandra, N. & Clore, G. M. The Xplor-NIH NMR molecular structure determination package. *J. Magn. Reson.* **160**, 65–73 (2003).
37. Zhou, Z. et al. NMR structure of chaperone Chz1 complexed with histones H2A2-H2B. *Nature Struct. Mol. Biol.* **15**, 868–869 (2008).
38. Cornilescu, G., Delaglio, F. & Bax, A. Protein backbone angle restraints from searching a database for chemical shift and sequence homology. *J. Biomol. NMR* **13**, 289–302 (1999).
39. Laskowski, R. A. et al. AQUA and PROCHECK-NMR: programs for checking the quality of protein structures solved by NMR. *J. Biomol. NMR* **8**, 477–486 (1996).
40. Houtman, J. C. et al. Binding specificity of multiprotein signaling complexes is determined by both cooperative interactions and affinity preferences. *Biochemistry* **43**, 4170–4178 (2004).

A Raf-induced allosteric transition of KSR stimulates phosphorylation of MEK

Damian F. Brennan^{1*}, Arvin C. Dar^{2*}, Nicholas T. Hertz², William C. H. Chao¹, Alma L. Burlingame³, Kevan M. Shokat² & David Barford¹

In metazoans, the Ras–Raf–MEK (mitogen-activated protein-kinase kinase)–ERK (extracellular signal-regulated kinase) signalling pathway relays extracellular stimuli to elicit changes in cellular function and gene expression. Aberrant activation of this pathway through oncogenic mutations is responsible for a large proportion of human cancer. Kinase suppressor of Ras (KSR)^{1–3} functions as an essential scaffolding protein to coordinate the assembly of Raf–MEK–ERK complexes^{4,5}. Here we integrate structural and biochemical studies to understand how KSR promotes stimulatory Raf phosphorylation of MEK (refs 6, 7). We show, from the crystal structure of the kinase domain of human KSR2 (KSR2(KD)) in complex with rabbit MEK1, that interactions between KSR2(KD) and MEK1 are mediated by their respective activation segments and C-lobe α G helices. Analogous to BRAF (refs 8, 9), KSR2 self-associates through a side-to-side interface involving Arg 718, a residue identified in a genetic screen as a suppressor of Ras signalling^{1–3}. ATP is bound to the KSR2(KD) catalytic site, and we demonstrate KSR2 kinase activity towards MEK1 by *in vitro* assays and chemical genetics. In the KSR2(KD)–MEK1 complex, the activation segments of both kinases are mutually constrained, and KSR2 adopts an inactive conformation. BRAF allosterically stimulates the kinase activity of KSR2, which is dependent on formation of a side-to-side KSR2–BRAF heterodimer. Furthermore, KSR2–BRAF heterodimerization results in an increase of BRAF-induced MEK phosphorylation via the KSR2-mediated relay of a signal from BRAF to release the activation segment of MEK for phosphorylation. We propose that KSR interacts with a regulatory Raf molecule in *cis* to induce a conformational switch of MEK, facilitating MEK's phosphorylation by a separate catalytic Raf molecule *in trans*.

To understand how KSR regulates Raf-dependent MEK activation^{6,7}, we determined the crystal structure of the KSR2(KD)–MEK1 complex (Fig. 1 and Supplementary Table 1). KSR2(KD)–MEK1 dimers assemble into a tetramer through a KSR2(KD) homodimer interface centred on Arg 718 (Supplementary Fig. 1a). In solution, KSR2(KD)–MEK1 tetramers and dimers exist in dynamic exchange, indicating a relatively weak KSR2(KD) homodimer interaction (Supplementary Fig. 1b). KSR2(KD) and MEK1 molecules interact with their catalytic sites facing each other through their activation segments and α G helices (Fig. 1 and Supplementary Fig. 2a), reminiscent of MEK¹⁰ and Chk2 (ref. 11) homodimers (Supplementary Fig. 2b). MEK's activation segment, incorporating Raf phosphorylation sites Ser 218^M and Ser 222^M (where superscript M indicates MEK1), comprises a short α -helix connected to a segment of extended chain that forms an antiparallel β -sheet with the KSR2 activation segment (Fig. 1b). This mutually constrained interaction of the MEK1 and KSR2 activation segments is stabilized by contacts between non-polar residues. The structural similarity of MEK1 when in complex with KSR2 to isolated MEK1, including those bound to allosteric inhibitors^{10,12,13}

(Supplementary Fig. 3), indicates that MEK inhibitors engage a physiologically relevant conformation of the kinase.

MEK and KSR form constitutive complexes^{14,15} stable to Raf phosphorylation^{16,17}, even though Ser 218^M and Ser 222^M phosphorylation would alter the conformation of the MEK1 activation segment. The integrity of the complex is probably conferred by the more extensive interface created by engagement of their respective α G helices (Fig. 1a, c). This is consistent with studies showing that mutation of MEK within a conserved hydrophobic motif (Met 308^M to Ile 310^M), contiguous with the α G helix, disrupts MEK–KSR1 interactions¹⁷. In the

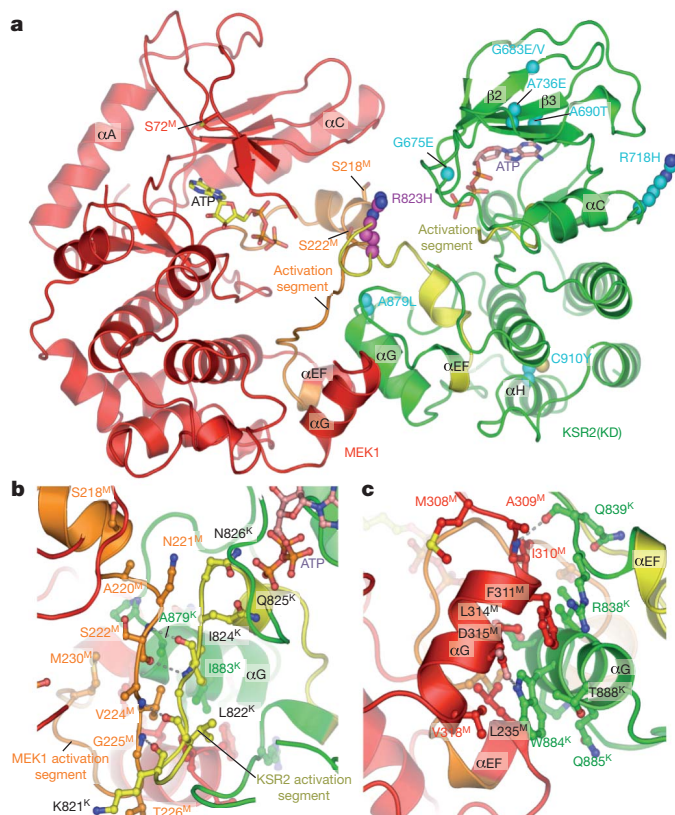


Figure 1 | Structure of the KSR2(KD)–MEK1 heterodimer. **a**, Overall view of the complex showing the face-to-face configuration of KSR2 and MEK1. KSR loss-of-function mutations^{1–3} are shown with C atoms in cyan. A lung adenocarcinoma-associated mutation of KSR2 (R823H)²⁸ is located on the KSR2 activation segment interacting with the MEK1 activation segment. Sites of MEK1 phosphorylation (Ser 72, 218 and 222) are indicated. **b**, Details of the β -sheet formed between the activation segments of MEK1 and KSR2. **c**, Details of α G helix contacts.

¹Section of Structural Biology, Institute of Cancer Research, Chester Beatty Laboratories, 237 Fulham Road, London SW3 6JB, UK. ²Howard Hughes Medical Institute and Department of Cellular and Molecular Pharmacology, University of California San Francisco, San Francisco, California 94107, USA. ³Department of Pharmaceutical Chemistry, University of California San Francisco, San Francisco, California 94107, USA.

*These authors contributed equally to this work.

complex, Ala 309^M and Ile 310^M contact KSR2 directly, whereas Met 308^M helps define the conformation of the α G helix (Fig. 1c). Furthermore, the KSR2(KD)–MEK1 structure rationalizes KSR genetic screens^{2,16,18}. Tyr substitution of Cys 910^K (where superscript K indicates KSR2), a buried residue of the C-lobe α H helix, would destabilize the C-lobe, altering the α G helix conformation (Fig. 1a and Supplementary Fig. 4). In addition, replacement of Ala 879^K within the KSR2 α G helix with a bulky Leu residue in a KSR loss-of-function mutant¹ is not readily accommodated at the KSR–MEK interface (Fig. 1a, b), consistent with our finding that a KSR2(KD) A879L mutant destabilizes MEK1–KSR2(KD) interactions (Supplementary Fig. 5).

The KSR2(KD)–MEK1 crystal structure indicated that KSR has the potential for catalytic activity¹⁹ possibly necessary for KSR function^{6,20}. Electron density maps reveal well-defined density for ATP–Mg²⁺ at the KSR2(KD) catalytic site (Fig. 2a). Although Asp 803^K of the DFG motif is shifted slightly out of position, the metal-coordinating Asn 791^K and the general base Asp 786^K of the catalytic loop adopt conformations typical of conventional protein kinases (Fig. 2b). However, owing to the inactive position of its α C helix, reminiscent of inactive c-Src(KD) (refs 9, 21), KSR2(KD) adopts an inactive conformation (Supplementary Fig. 6). Conservation of ATP-binding-site residues, and the mapping of KSR loss-of-function mutants to the ATP pocket^{2,3}, indicate that ATP binding is necessary for KSR function (Fig. 1a and Supplementary Figs 4 and 7). A Thr substitution for Ala 690^K of β 3, for example, would impede ATP binding, whereas a Glu substitution of Gly 675^K within the Gly-rich loop would disrupt the phosphate-binding site. Whereas *Drosophila* and *Caenorhabditis elegans* KSR share the same catalytic residues as conventional protein kinases, substitution of Arg for the conserved ATP-coordinating Lys residue in mammalian KSRs, the lack of reproducible kinase catalytic activity, and the capacity of kinase-impaired mutants of KSR to mediate MEK phosphorylation and MAP kinase signalling^{16,22}, have implicated KSR as a pseudokinase. Studies of pseudokinases such as HER3 indicate that functions other than catalysis are critical for their role in signal transduction cascades, and that their extremely low kinase activity may

be sufficient to catalyse physiologically relevant transphosphorylation within a protein complex^{23,24}.

To examine putative KSR2 catalytic function we conducted *in vitro* kinase assays using an analogue-specific (as1) mutant of KSR2 (T739^KG) incubated with the modified ATP analogue N6-phenethyl ATP γ S (A*TP γ S). Resultant phosphorylation products include MEK1, specifically within the as1–KSR2(KD)–MEK1 complex (Fig. 2c, lane 4). MEK1 within the wild-type KSR2(KD)–MEK1 complex incubated with unmodified ATP γ S was also reproducibly phosphorylated (Fig. 2d), an activity attributed to KSR2 because purified MEK1 does not autophosphorylate (Supplementary Fig. 8a).

To exclude further the possibility of MEK1 phosphorylation resulting from MEK1 autophosphorylation or by a contaminating kinase, we examined the influence of inhibitors in the KSR2(KD)–MEK1 assay (Fig. 2e and Supplementary Table 2). None of the compounds tested blocked 100% of the MEK1 phosphorylation reaction, including sorafenib, a Raf inhibitor, and PD0325901, a MEK inhibitor. Although the MEK1 inhibitors Sutent and PD0325901 blocked 50% of the reaction, other MEK1 inhibitors (VX680 and dasatinib) showed no inhibition. It is possible that Sutent and PD0325901 are binding to MEK1 and influencing its phosphorylation, an established feature of PD0325901 (ref. 25). The pan-protein kinase inhibitors ASC24 and ASC65 (ref. 26) block 100% of the activity in the KSR2(KD)–MEK1 kinase complex, indicating that KSR2 is a druggable target (Fig. 2e).

We next sought to identify the site(s) of phosphorylation in MEK1 catalysed by KSR2. We did not detect reactivity from activation segment phospho-specific antibodies (Ser 222^M and Ser 218^M/Ser 222^M) or for other MEK1 sites including Thr 286^M or Ser 298^M (data not shown). Using mass spectrometry, we identified Ser 24^M and Ser 72^M as KSR2-dependent phosphorylation sites in MEK1 not previously assigned to any known kinase (Supplementary Fig. 9a, b). KSR2 phosphorylates MEK1 with low discrimination because replacing Ser 24^M and Ser 72^M with alanines only reduced overall MEK1 phosphorylation by ~10% (Supplementary Fig. 8b). Additional KSR2-dependent sites were identified as Ser 18^M and Thr 23^M (Supplementary Fig. 9c). The stoichiometry of KSR2-catalysed MEK1 phosphorylation is 1.25% (data not shown), indicating a very inefficient reaction.

KSR assembles MEK–KSR–Raf ternary complexes responsible for promoting Raf phosphorylation of MEK^{7,8,17,27} in which Raf interacts with the CA1 domain and CA5-kinase domain of KSR (refs 17, 27). The KSR2(KD) homodimer interface has a striking structural resemblance to the homodimer interface of BRAF(KD) (ref. 9), termed the side-to-side dimer interface and proposed to mediate Raf(KD)–KSR(KD) heterodimer interactions⁸ (Fig. 3a, b). Both interfaces are centred on a conserved N-lobe Arg residue (Arg 718^K of KSR2 and Arg 509 of BRAF). Arg 718^K is functionally significant because its replacement with His, a loss-of-function mutation² (Fig. 1a), abolishes the capacity of Raf to activate MEK^{8,22}. Notably, His substitution of Arg, shown to dissociate BRAF(KD) (ref. 8) and KSR2(KD) homodimers (Supplementary Fig. 10), would not be compatible with a Raf(KD)–KSR(KD) heterodimer. KSR2(KD) and BRAF(KD) homodimers adopt different quaternary modes (termed I and A, respectively), and only a subset of intersubunit contacts are common to KSR2(KD) and BRAF(KD) side-to-side dimer interfaces (Fig. 3 and Supplementary Figs 7 and 11). Raf phosphorylation of MEK is promoted by enforced dimerization of Raf and KSR kinase domains through the side-to-side dimer interface⁸. Conservation in KSR of BRAF side-to-side contact residues indicates that KSR and BRAF form heterodimers by means of the BRAF quaternary A mode.

The quaternary structure of the KSR2(KD)–BRAF(KD) heterodimer determines the tertiary structure of the KSR2 α C helix. An inactive conformation of the α C helix is incompatible with the BRAF quaternary A mode. Thus, formation of a KSR2–BRAF heterodimer (A mode) would be accompanied by a shift of the KSR2 α C helix to an active conformation (Supplementary Fig. 12), rationalizing the conservation of Phe 707^K and Glu 710^K of α C (Supplementary Figs 7 and 13). A

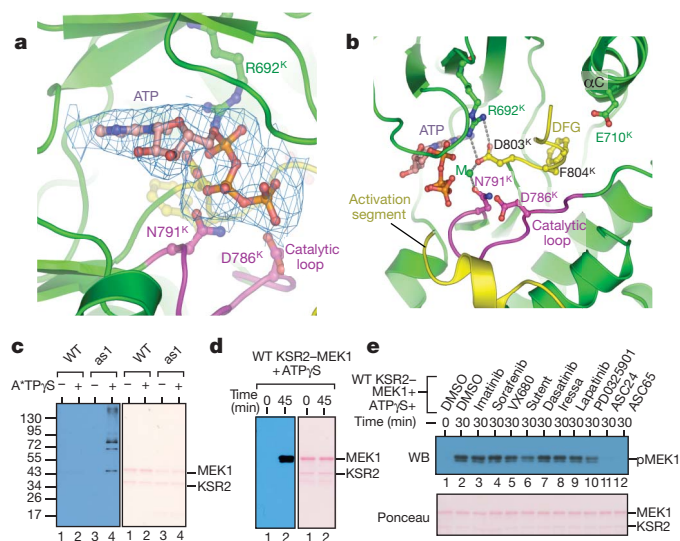


Figure 2 | KSR2 is a protein kinase. **a**, $2|F_o| - |F_c|$ electron density map for ATP bound to KSR2. **b**, Details of the catalytic site of KSR2. M, metal ion. **c**, Wild-type (WT) and T739G KSR2 (as1) KSR2–MEK1 complexes assayed in the presence of A*TP γ S. Molecular mass markers in kDa are indicated along the left side of **c**. Phosphorylated proteins detected by western blot (WB) analysis (left) and total protein stained using ponceau red (right) are shown. **d**, Phosphorylation of MEK1 within wild-type KSR2–MEK1 combined with ATP γ S. Phospho- (left) and total (right) proteins detected as in **c**. **e**, Enzymatic assay as in **d** in the presence of 10 μ M of the listed inhibitors. Phospho-MEK1 is shown.

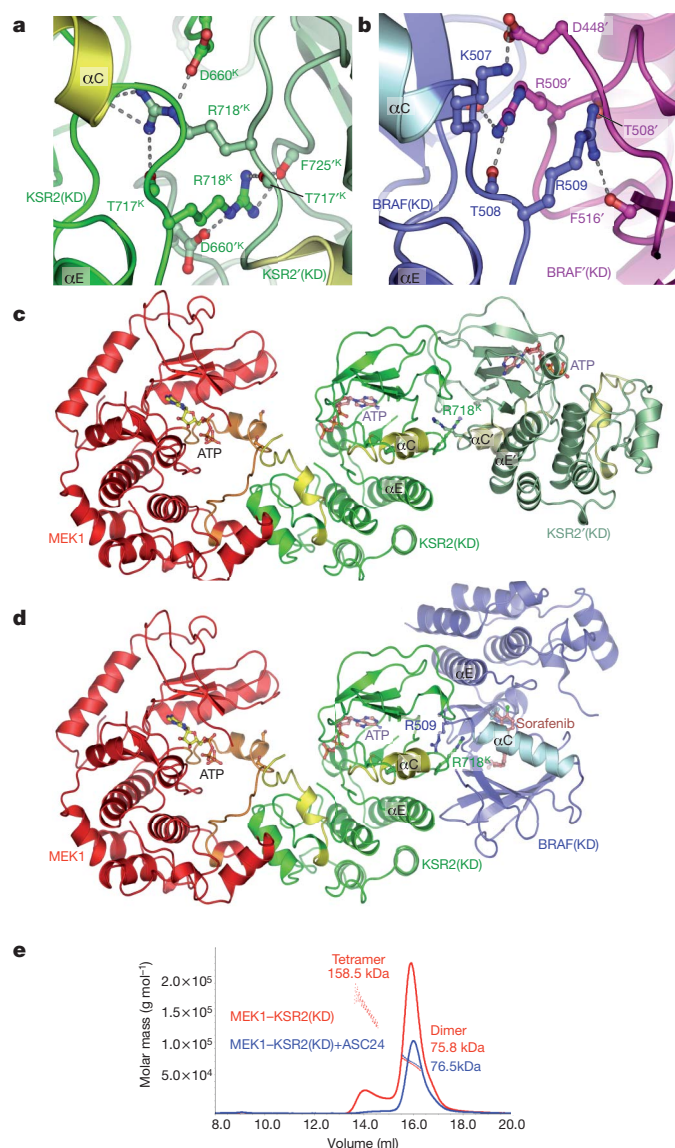


Figure 3 | KSR2 and BRAF homodimerize through a conserved side-to-side interface, but generate different quaternary structures. **a**, Details of the KSR2–KSR2 interface centred on Arg 718. Prime (') denotes residues from the opposite subunit (quaternary mode I). **b**, Details of the BRAF–BRAF interface centred on Arg 509 (quaternary mode A) (Protein Data Bank 1uwh)⁹. **c**, MEK1–KSR2–KSR2 ternary complex. View as in Fig. 1a. **d**, Predicted MEK1–KSR2–BRAF ternary complex (quaternary mode A). **e**, Multiple angle laser light scattering experiment showing that ASC24 dissociates the KSR2(KD)–MEK1 heterotetramer into a heterodimer. The lower peak height in the presence of ASC24 is due to ASC24-induced protein precipitation.

BRAF-induced conformational shift of the KSR2 α C helix into the active position would probably enhance KSR2 kinase activity and influence its interaction with the activation segment of MEK, thereby affecting Raf's capacity to phosphorylate MEK. To test whether KSR2–BRAF heterodimerization stimulates KSR2 and BRAF-dependent MEK phosphorylation, we performed *in vitro* kinase assays. To overcome the weak and transient KSR2–BRAF interactions we immobilized His₆-tagged MEK1, KSR2 and BRAF onto Co²⁺ resin. As shown in Fig. 4a, the addition of kinase-impaired BRAF(K483S) to KSR2(KD)–MEK1 increases total MEK1 phosphorylation 15-fold (compare lanes 1 and 5). Interestingly, most of the increased activity comes from accelerated KSR2 catalytic function (as opposed to activity from additional BRAF). Approximately 70% of total MEK1 phosphorylation and less than 10% of S218/S222-specific activity was blocked by the KSR2 inhibitor ASC24

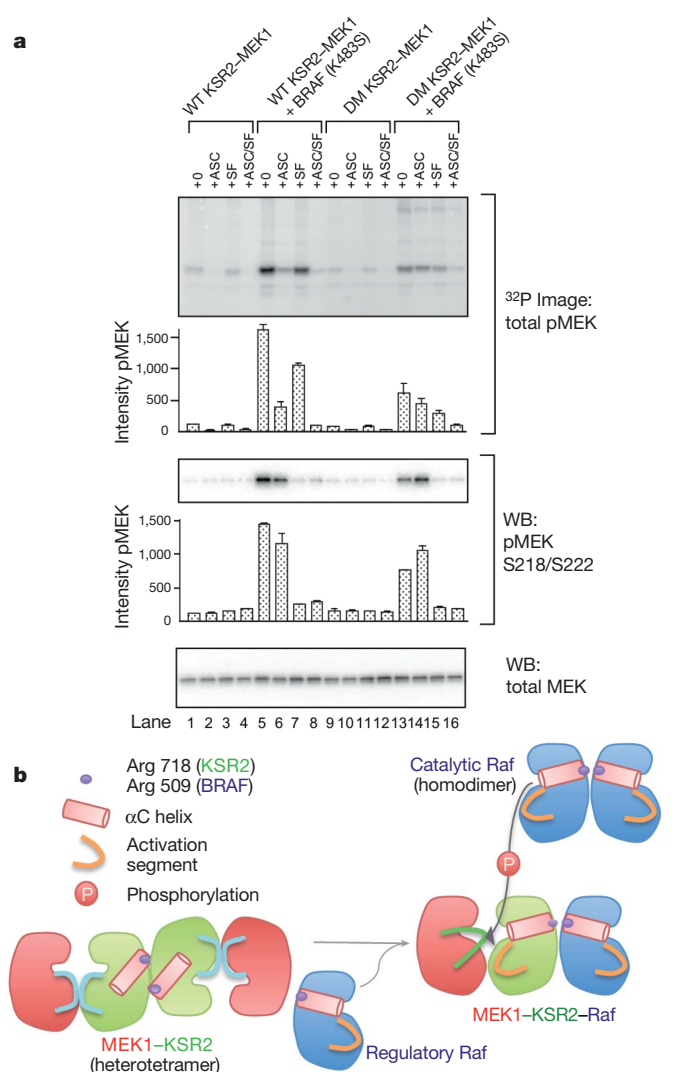


Figure 4 | Stimulation of MEK phosphorylation by an allosteric transition of KSR mediated by BRAF binding to the Arg 718 side-to-side interface.

a, Biochemical reconstitution of KSR–Raf dimerization assessed based on MEK activation. Total phospho-MEK (top), S218/S222 site-specific phospho-MEK (middle), and total MEK (bottom; loading control) are shown. Bands were quantified and phospho-MEK levels were normalized relative to lane 1 in the top and middle panels, respectively. Error bars represent the mean \pm s.d. ($n = 2$). **b**, Schematic of Raf-mediated activation of Raf phosphorylation of MEK. The side-to-side KSR2–Raf heterodimer (mode A) and Raf–Raf homodimer (mode A) are centred on Arg 718 (KSR2) and Arg 509 (BRAF). In the KSR2–MEK1 heterotetramer (left), the inaccessible activation segment of MEK1 is released through the interaction of KSR2 with a regulatory Raf molecule, induced by a conformational change of the α C helix, allowing catalytic Raf to phosphorylate MEK (right). The regulatory Raf molecule could be a catalytically impaired oncogenic mutant BRAF, whereas the catalytic Raf could also be Raf of a MEK1–KSR2–Raf ternary complex. Regulatory and catalytic Raf could be different isoforms (B-Raf or C-Raf). A Raf molecule bound to KSR through a side-to-side heterodimer interface is sterically unable to phosphorylate MEK in *cis*, an activity that therefore must be performed by a different Raf molecule.

(Fig. 4a, lanes 5 and 6). Furthermore, most of the stimulated phosphorylation occurred at non-BRAF sites, as sorafenib only blocked 30% of total MEK1 phosphorylation but over 90% of the S218/S222-specific signal (Fig. 4a, lanes 5 and 7). Thus, KSR2 is the major kinase responsible for stimulated MEK1 phosphorylation in lane 5, and this occurs through a BRAF(K483S)-induced increase in KSR2 catalytic activity. That the R718H dimer interface mutation in KSR2 (KSR2(DM))–MEK1 significantly reduced BRAF-induced stimulation indicates that KSR2 modulation by BRAF(K483S) depends primarily on the Arg 718-mediated

side-to-side interface of KSR2–BRAF heterodimers (Fig. 4a, compare lanes 5 and 13). In the absence of BRAF, the dimer mutation in KSR2 is functionally silent (Fig. 4a, compare lanes 1–4 and 9–12), indicating that wild-type and dimer mutant KSR2 are indistinguishable in a basal state.

Interestingly, BRAF(K483S) retained kinase activity (Supplementary Fig. 14); however, its intrinsic catalytic activity was not modulated through heterodimerization with KSR2. Indeed, with KSR2 inhibited by ASC24, MEK1 phosphorylation by BRAF(K483S) in wild-type and dimer mutant KSR2(KD)–MEK1 was approximately equal (Fig. 4a, lanes 6 and 14; middle panel). Thus, the twofold increase in MEK1 phosphorylation at the BRAF-specific sites, which were upregulated through KSR2–BRAF heterodimerization (lanes 5 and 13; middle panel), more likely resulted from a change in MEK1 structure coupled to allostery in KSR2 rather than an increase in intrinsic BRAF catalytic activity. KSR2(KD) heterodimerization with wild-type BRAF also stimulates BRAF-mediated MEK1 phosphorylation (Supplementary Fig. 15).

Control experiments excluded the possibility that either MEK1 autophosphorylation or contaminating kinases contribute to MEK1 phosphorylation (Supplementary Fig. 16). Thus, our data provide evidence for KSR2 as a protein kinase, stimulated by its interactions with BRAF. The physiological significance of KSR2 kinase activity awaits identification of its cellular substrate(s); however, its BRAF-triggered activation provides an *in vitro* barometer of a conformational change in KSR2. The kinase-independent function of KSR2 modulation of MEK1 is further borne out by the KSR2 inhibitor ASC24, which induces an unexpected increase in MEK1 phosphorylation by BRAF(K483S) (Fig. 4a, lanes 13 and 14; middle panel). Presumably, ASC24 induced a conformational change in KSR2 that partially mimics KSR Arg 718 side-to-side binding by BRAF, thus altering MEK1 and allowing for its increased phosphorylation, consistent with the capacity of ASC24 to disrupt the KSR2(KD) homodimer interface (Fig. 3e). Thus, a KSR inhibitor that binds to the KSR–MEK complex and antagonises the BRAF-induced allosteric switch could function analogously to the Ras suppressor: the KSR(R718H) mutation.

Here we reveal that KSR functions as an effector molecule, receiving a stimulatory signal from an activated regulatory Raf molecule and relaying this to modulate the accessibility of the MEK activation segment for phosphorylation by catalytic Raf (Fig. 4b). Our results highlight the complexity and adaptability of protein kinases, pseudokinases and scaffolding molecules to integrate signal transduction processes.

METHODS SUMMARY

Expression, purification and crystallization of KSR2–MEK1. *Homo sapiens* KSR2 kinase domain (KSR2(KD), residues 634–950) with an N-terminal His₆ tag was co-expressed with full-length MEK1 and the p50^{Cdc37} Hsp90 co-chaperone in the baculovirus/Sf21 insect cell system. The KSR2(KD)–MEK1 complex was purified and crystallized as described in Methods. Crystal structure determination, mutagenesis, compound synthesis, enzyme assays, mass spectrometry and other procedures were performed as described in Methods.

Full Methods and any associated references are available in the online version of the paper at www.nature.com/nature.

Received 4 June 2010; accepted 20 January 2011.

Published online 27 March 2011.

- Kornfeld, K., Hom, D. B. & Horvitz, H. R. The *ksr-1* gene encodes a novel protein kinase involved in Ras-mediated signaling in *C. elegans*. *Cell* **83**, 903–913 (1995).
- Sundaram, M. & Han, M. The *C. elegans ksr-1* gene encodes a novel Raf-related kinase involved in Ras-mediated signal transduction. *Cell* **83**, 889–901 (1995).
- Therrien, M. *et al.* KSR, a novel protein kinase required for RAS signal transduction. *Cell* **83**, 879–888 (1995).
- Clapéron, A. & Therrien, M. KSR and CNK: two scaffolds regulating RAS-mediated RAF activation. *Oncogene* **26**, 3143–3158 (2007).
- Kolch, W. Coordinating ERK/MAPK signalling through scaffolds and inhibitors. *Nature Rev. Mol. Cell Biol.* **6**, 827–837 (2005).

- Therrien, M., Michaud, N. R., Rubin, G. M. & Morrison, D. K. KSR modulates signal propagation within the MAPK cascade. *Genes Dev.* **10**, 2684–2695 (1996).
- Michaud, N. R. *et al.* KSR stimulates Raf-1 activity in a kinase-independent manner. *Proc. Natl Acad. Sci. USA* **94**, 12792–12796 (1997).
- Rajakulendran, T., Sahmi, M., Lefrançois, M., Sicheri, F. & Therrien, M. A dimerization-dependent mechanism drives RAF catalytic activation. *Nature* **461**, 542–545 (2009).
- Wan, P. T. *et al.* Mechanism of activation of the RAF-ERK signaling pathway by oncogenic mutations of B-RAF. *Cell* **116**, 855–867 (2004).
- Ohren, J. F. *et al.* Structures of human MAP kinase kinase 1 (MEK1) and MEK2 describe novel noncompetitive kinase inhibition. *Nature Struct. Mol. Biol.* **11**, 1192–1197 (2004).
- Cai, Z., Chehab, N. H. & Pavletich, N. P. Structure and activation mechanism of the CHK2 DNA damage checkpoint kinase. *Mol. Cell* **35**, 818–829 (2009).
- Fischmann, T. O. *et al.* Crystal structures of MEK1 binary and ternary complexes with nucleotides and inhibitors. *Biochemistry* **48**, 2661–2674 (2009).
- Iverson, C. *et al.* RDEA119/BAY 869766: a potent, selective, allosteric inhibitor of MEK1/2 for the treatment of cancer. *Cancer Res.* **69**, 6839–6847 (2009).
- Denouel-Galy, A. *et al.* Murine Ksr interacts with MEK and inhibits Ras-induced transformation. *Curr. Biol.* **8**, 46–55 (1998).
- Yu, W., Fantl, W. J., Harrowe, G. & Williams, L. T. Regulation of the MAP kinase pathway by mammalian Ksr through direct interaction with MEK and ERK. *Curr. Biol.* **8**, 56–64 (1998).
- Stewart, S. *et al.* Kinase suppressor of Ras forms a multiprotein signaling complex and modulates MEK localization. *Mol. Cell Biol.* **19**, 5523–5534 (1999).
- McKay, M. M., Ritt, D. A. & Morrison, D. K. Signaling dynamics of the KSR1 scaffold complex. *Proc. Natl Acad. Sci. USA* **106**, 11022–11027 (2009).
- Muller, J., Cacace, A. M., Lyons, W. E., McGill, C. B. & Morrison, D. K. Identification of B-KSR1, a novel brain-specific isoform of KSR1 that functions in neuronal signaling. *Mol. Cell Biol.* **20**, 5529–5539 (2000).
- Zhang, Y. *et al.* Kinase suppressor of Ras is ceramide-activated protein kinase. *Cell* **89**, 63–72 (1997).
- Sugimoto, T., Stewart, S., Han, M. & Guan, K. L. The kinase suppressor of Ras (KSR) modulates growth factor and Ras signaling by uncoupling Elk-1 phosphorylation from MAP kinase activation. *EMBO J.* **17**, 1717–1727 (1998).
- Xu, W., Harrison, S. C. & Eck, M. J. Three-dimensional structure of the tyrosine kinase c-Src. *Nature* **385**, 595–602 (1997).
- Douziech, M., Sahmi, M., Laberge, G. & Therrien, M. A KSR/CNK complex mediated by HYP, a novel SAM domain-containing protein, regulates RAS-dependent RAF activation in *Drosophila*. *Genes Dev.* **20**, 807–819 (2006).
- Jura, N., Shan, Y., Cao, X., Shaw, D. E. & Kuriyan, J. Structural analysis of the catalytically inactive kinase domain of the human EGF receptor 3. *Proc. Natl Acad. Sci. USA* **106**, 21608–21613 (2009).
- Shi, F., Telesco, S. E., Liu, Y., Radhakrishnan, R. & Lemmon, M. A. ErbB3/HER3 intracellular domain is competent to bind ATP and catalyze autophosphorylation. *Proc. Natl Acad. Sci. USA* **107**, 7692–7697 (2010).
- Alessi, D. R., Cuenda, A., Cohen, P., Dudley, D. T. & Saltiel, A. R. PD 098059 is a specific inhibitor of the activation of mitogen-activated protein kinase kinase *in vitro* and *in vivo*. *J. Biol. Chem.* **270**, 27489–27494 (1995).
- Statsuk, A. V. *et al.* Tuning a three-component reaction for trapping kinase substrate complexes. *J. Am. Chem. Soc.* **130**, 17568–17574 (2008).
- Roy, F., Laberge, G., Douziech, M., Ferland-McCollough, D. & Therrien, M. KSR is a scaffold required for activation of the ERK/MAPK module. *Genes Dev.* **16**, 427–438 (2002).
- Greenman, C. *et al.* Patterns of somatic mutation in human cancer genomes. *Nature* **446**, 153–158 (2007).

Supplementary Information is linked to the online version of the paper at www.nature.com/nature.

Acknowledgements This work was supported by a Cancer Research UK grant to D.B., ICR studentships to D.F.B. and W.C.H.C. and HHMI grant to K.M.S. We thank staff at the ESRF for help with data collection and K. Wood and V. Good for help with protein production and Z. Zhang for assistance with cloning. Mass spectrometry was made possible by NIH grants NCRR RR015804 and NCRR RR001614. The MEK1/p50^{Cdc37} baculovirus was a gift from C. Vaughan. We thank Cell Signaling Technologies for help with phosphospecific MEK antibodies.

Author Contributions D.F.B. determined and analysed the MEK1–KSR2 structure; A.C.D. conducted biochemical analysis of Raf–KSR–MEK phosphorylation and inhibitor studies; N.T.H. carried out phosphoproteomics mass spectrometry studies; W.C.H.C. helped with protein production; A.L.B. analysed mass spectrometry data; K.M.S. designed and analysed experiments relating to the Raf–KSR–MEK phosphorylation and inhibitor studies; and D.B. designed experiments and analysed data.

Author Information Coordinates and structure factors have been deposited in the RCSB Protein Data Bank with accession numbers 2y4i and 2y4isf, respectively. Reprints and permissions information is available at www.nature.com/reprints. The authors declare no competing financial interests. Readers are welcome to comment on the online version of this article at www.nature.com/nature. Correspondence and requests for materials should be addressed to D.B. (david.barford@ic.ac.uk) or K.M.S. (shokat@cmp.ucsf.edu).

METHODS

Cloning, expression and purification of KSR2(KD)–MEK1. A variety of KSR isoforms were screened for expression and crystallization. *Homo sapiens* KSR2 kinase domain (KSR2(KD), residues 634–950) with an N-terminal His₆ tag was co-expressed with full-length rabbit MEK1 (with 3C Precision-cleavable His₆ tag) and the p50^{Cdc37} Hsp90 co-chaperone in the baculovirus/Sf21 insect cell system (a gift from C. Vaughan). KSR2(KD)–MEK1 was purified using Co²⁺-Talon resin (Clontech) and incubated with GST-tagged Rhinovirus 3C Precision and λ -phosphatase overnight. The protein was then applied to a RESOURCE S column (GE Healthcare) connected to a 5-ml GST column (GE Healthcare) to trap 3C protease. Free MEK1 was either present in the flow through or eluted early. The KSR2(KD)–MEK1 complex eluted as a later peak. Uncleaved protein and λ -phosphatase were removed using Talon resin and the KSR2(KD)–MEK1 complex was applied to a HiPrep 16/60 Superdex 200 gel filtration chromatography column. KSR2(KD)–MEK1 eluted as two peaks, which according to multiple angle light scattering (MALS) corresponded to a heterotetramer and a heterodimer. A smaller third peak is often seen that corresponded to MEK1. Sequential gel filtration has shown that the heterodimer and heterotetramer are dynamic species and so these peaks were pooled. Size exclusion chromatography was performed on mutant KSR2(KD)(R718H)–MEK1 complexes as for wild-type protein.

Crystallization of KSR2(KD)–MEK1. The complex was concentrated to 10 mg ml^{−1} and incubated with 5 mM Mg-ATP. Aggregation was cleared by filtration or by centrifugation for 20 min at 4 °C at 16,000g. Sitting-drop crystallization trials were set up using a Phoenix robot (Art Robbins Instruments) at 4 °C, 14 °C and 20 °C using a variety of commercial screens. Inclusion of 10 mM Pr acetate increased crystal size. Thousands of crystal growth conditions were trialled and in excess of 80 crystals were tested for diffraction. This led to a KSR2(KD)–MEK1 data set with Mg-ATP co-crystallization to 3.8 Å resolution from a crystal grown at 20 °C in 12% (w/v) PEG 3350, 0.2 M Na citrate, 10 mM Pr acetate, Bis-Tris propane pH 6.25. A data set to 3.45 Å was subsequently collected, which was also from a Mg-ATP co-crystallization in a similar condition with Mg acetate in place of Pr acetate. Crystallographic data were collected at beam line ID 14.4 ESRF, Grenoble and processed using MOSFLM and the CCP4 Program suite²⁹.

KSR2(KD)–MEK1 structure determination. BRAF shares ~30% sequence identity with the KSR kinase domain. A systematic approach to solving the structure by molecular replacement was undertaken. The Caspr automated molecular replacement server (<http://www.igs.cnrs-mrs.fr/Caspr2/>) was used³⁰ and is an automated molecular replacement pipeline that generates multiple sequence alignments using TCoffee³¹, before homology model building with MODELLER³², molecular replacement with AMoRe²⁹ and model refinement based on CNS³³. Multiple Caspr runs were performed using all the potential space groups, with data scaled with a 5 Å high-resolution cutoff as well as a 3.8 Å resolution cutoff with both available structures of MEK (Protein Data Bank 1s9j and 2p55) as well as structures of BRAF (Protein Data Bank 1uwf and 3c4c) and with tyrosine kinases. This strategy led to a correct molecular replacement solution found using MEK and a MODELLER produced homology model of KSR based on the N-terminal lobe of BRAF and the C-terminal lobe of ephrin tyrosine kinase. Tyrosine kinases were suggested as search models despite having 15–20% sequence identity by GenTHREADER³⁴. Molecular replacement was used to solve the 3.45 Å data set.

SeMet anomalous difference maps. To obtain independent phase information, we obtained anomalous diffraction data from SeMet incorporated KSR2(KD)–MEK1 crystals. SeMet-labelled KSR2(KD)–MEK1 was prepared in the insect cell system using a procedure modified from ref. 35. Peak data sets were collected for two crystals, although the best of these only diffracted to 7 Å. Anomalous difference maps were useful for confirming the location of Met residues and thus the chain trace of KSR2(KD).

Mutagenesis of BRAF(KD) and KSR2(KD)–MEK1. Point mutations of BRAF kinase-impaired (K483S), gate-keeper KSR2(KD)(T739G) and dimer mutant KSR2(KD)(R718H) were introduced using standard procedures. BRAF mutant and human p50^{Cdc37} were cloned pairwise into a modified pFBDM vector (Z. Zhang). An N-terminally His₆-tagged human KSR2 kinase domain (634–950) was mutated to generate a dimerization-impaired mutant (R718H) in the modified pFBDM vector. In addition the following KSR2(KD) mutants were prepared: (1) dimer mutant KSR2(KD)(R718H); and (2) KSR2 kinase-impaired mutant (catalytic Asp) KSR2(KD)(D786A). Gene-containing pFBDM vectors were converted into bacmids for baculoviral productions. The kinase-dead MEK1 mutant was Lys 97 to Met, and a double phosphosite mutant Ser 24 and Ser 72 to Ala was prepared.

BRAF kinase domain purification. Viruses of BRAF mutants were used to infect Sf9 cells at a multiplicity of infection of 2. Cell pellets were harvested after 3 days of expression. BRAF was expressed and purified according to ref. 9 with minor modifications. Mutant proteins were purified with Talon metal ion affinity and ion-exchange chromatography.

MALS analysis of the KSR2(KD)–MEK1 complex. We used multiple angle laser light scattering at 658 nm using a Dawn Heleos light scattering instrument (Eldan) attached to a UV detector of purified KSR2(KD)–MEK1 complex that was run at room temperature on a 24 ml Superose 6 analytical gel filtration column (GE Healthcare) at a rate of 0.5 ml min^{−1} by HPLC (Varian).

MALS analysis of the KSR2(KD)–MEK1 + ASC24 complex. MALS gel filtration purified KSR2(KD)–MEK1 was concentrated to 2 mg ml^{−1} before multiple angle laser light scattering (MALS) experiments. ASC24 was incubated with KSR2(KD)–MEK1 at a final concentration of 4.5 mM at 4 °C, before the MALS experiment. Protein samples were run at 20 °C on a 24-ml capacity Superdex 200 analytical gel filtration column (GE Healthcare) at a rate of 0.5 ml min^{−1} by HPLC (Varian). MALS was performed on the eluate at 658 nm using a Dawn Heleos light scattering instrument (Eldan) attached to a UV detector.

In vitro kinase assays. Wild-type and mutant forms of KSR2(KD)–MEK1 used for kinase assays were purified as described for the KSR2(KD)–MEK1 used for crystallization, except that the cleavage and gel filtration steps were omitted. Coomassie-blue-stained SDS–PAGE gels of purified proteins are shown in Supplementary Fig. 18.

Thiophosphorylation experiment. For the thiophosphorylation kinase assays, approximately 1 μ M of purified KSR2–MEK1 complex (wild type or the as1 mutant) was pre-incubated for 10 min in reactions containing 10 μ M of the indicated small molecule drugs, 10 mM Tris 7.8, 10 mM MgCl₂ and 2% DMSO. Reactions were initiated by adding ATP γ S or N6-phenethyl ATP γ S (A*TP γ S) as indicated and allowed to proceed for 30 min, before being terminated with EDTA (0.025 mM final concentration). Thiophosphorylated reaction products were alkylated by adding 1.5 μ l of a freshly prepared DMSO solution containing 50 mM para-nitrobenzyl mesylate (PNBM) to the mixtures. After incubation at room temperature for minimally 40 min, SDS-load dye was added, and samples were applied to a 4–20% Tris-HCl gel for SDS–PAGE separation. Proteins were transferred to nitrocellulose membrane, and then in sequence stained with ponceau dye, washed, blocked with 5% milk TBST, and then blotted using a phosphorothioate-specific monoclonal antibody (antibody 51-8; 1:10,000 in 5% milk)³⁶. After removal of excess primary antibody and several washes, the membranes were incubated with HRP-conjugated anti-rabbit IgG secondary antibody (1:10,000 in 5% milk; Promega). Membranes were washed extensively, after which protein bands were visualized on film using enhanced chemiluminescence (Pierce).

Compound synthesis. Sorafenib, ASC24 and ASC65 were synthesized as previously described^{26,37}. All other kinase inhibitors were obtained from Calbiochem or commercially available sources. Drugs were dissolved in DMSO before use.

Kinase assays on Co²⁺-Talon beads. To overcome the weak and transient KSR2–BRAF interactions we immobilized His₆-tagged MEK1, KSR2 and BRAF onto Co²⁺-Talon resin. We used this simplified reconstituted system to promote BRAF dimerization with purified KSR2–MEK1 complexes, and investigated the influence of these interactions on MEK1 phosphorylation. 1 μ M of purified KSR2(KD)–MEK1 complex (wild type or mutants) was premixed with BRAF and then loaded onto Co²⁺-Talon beads (Clontech). Beads were prepared from 50% slurry by washing in water. 2.0 μ l of beads were used per reaction (25 μ l total volume). For reactions containing free MEK1 (recovered), MEK1 isolated as a by-product from the KSR2(KD)–MEK1 complex was used. Free MEK1 (recovered) contains trace levels of KSR2 as detected by mass spectrometry. Kinases were diluted in buffer containing 10 mM Tris 7.8, 10 mM MgCl₂, 2% DMSO and 20 μ M inhibitors as indicated. Reactions were initiated by the addition of 200 μ M cold ATP supplemented with 5 μ Ci γ -³²P-ATP and reactions were incubated at room temperature. After 90 min, reaction samples were mixed with SDS load buffer, heated, and electrophoresed on a 4–20% Tris-HCl SDS gradient gel. Gels were fixed, dried and exposed to a Typhoon phospho-imager to obtain the total MEK1 phosphorylation signal or transferred to nitrocellulose membranes and blotted with pMEK1/2 S217/S221 (Cell Signaling; 1:10,000 in 5% BSA TBST) or total MEK1 (Cell Signaling; 1:10,000 in 5% BSA TBST). Radioactive gels were scanned on a Typhoon imager (GE Healthcare) and bands were quantified using ImageQuant (GE Healthcare). Chemiluminescent signal on western blots was captured on a high-resolution digital camera using the AlphaInnotech system for quantification of pMEK on S218/S222 as shown in Fig. 4a. Graphing and analysis was performed using the program Prism.

Phosphopeptide mapping by tandem mass spectrometry. To identify phosphorylation sites we either enriched for phosphopeptides (ATP-treated KSR2(KD)–MEK1), or ran the whole protein digest directly on the mass spectrometer (A*TP γ S-treated KSR2(KD)–MEK1). Preparations of the indicated kinase reaction were digested as described previously to retain the phosphorylation or thiophosphorylation mark³⁸. The digested peptides were then desalted by using a C₁₈ OMIX 100 μ l Zip Tip. The phosphopeptides were then enriched by IMAC enrichment on a TiO₂ column as done previously³⁹. The thiophosphorylated samples were not enriched. The peptides were run on a nano-LC system before

analysis on both a QSTAR Elite and a LTQ Orbitrap. For both, peptides were separated via a 60 min LC run (0–32% acetonitrile 0.1% formic acid). Separation was achieved by reversed-phase chromatography on a 75 μm \times 15 cm C18 column flowing at 350 nl min⁻¹ applied directly to a LTQ Orbitrap or a QSTAR Elite. For the LTQ Orbitrap, the three most intense ions above 10,000 counts were selected for subsequent fragmentation and MS analysis. Three CID spectra and three ETD spectra (200 = activation energy) were acquired. For the QSTAR Elite, the two most intense multiply charged peaks from each MS spectra were selected for fragmentation by CID, and MS analysis in the TOF mass analyser. For both, a dynamic exclusion window was applied that prevented the same peak from being selected for 1 min. Peak lists were generated by PAVA (in-house LTQ Orbitrap data) or Mascot (QSTAR Elite data) and analysed on Protein Prospector (LTQ Orbitrap: parent mass tolerance, 20 p.p.m., fragment mass tolerance, 0.6 Da, three missed cleavages, max four modifications, no constant modifications, and phospho serine/threonine variable modifications) (QSTAR Elite same as above except: parent mass tolerance, 200 p.p.m., fragment mass tolerance, 300 p.p.m., thiophospho serine/threonine variable modification).

29. Collaborative Computer Project 4. The CCP4 suite: programs for protein crystallography. *Acta Crystallogr. D* **50**, 760–763 (1994).
30. Claude, J. B., Suhre, K., Notredame, C., Claverie, J. M. & Abergel, C. CaspR: a web server for automated molecular replacement using homology modelling. *Nucleic Acids Res.* **32**, W606–W609 (2004).
31. Poirot, O., Suhre, K., Abergel, C., O'Toole, E. & Notredame, C. 3DCoffee@igs: a web server for combining sequences and structures into a multiple sequence alignment. *Nucleic Acids Res.* **32**, W37–W40 (2004).
32. Sali, A. & Blundell, T. L. Comparative protein modelling by satisfaction of spatial restraints. *J. Mol. Biol.* **234**, 779–815 (1993).
33. Brünger, A. T. *et al.* Crystallography & NMR system: A new software suite for macromolecular structure determination. *Acta Crystallogr. D* **54**, 905–921 (1998).
34. McGuffin, L. J. & Jones, D. T. Improvement of the GenTHREADER method for genomic fold recognition. *Bioinformatics* **19**, 874–881 (2003).
35. Cronin, C. N., Lim, K. B. & Rogers, J. Production of selenomethionyl-derivatized proteins in baculovirus-infected insect cells. *Protein Sci.* **16**, 2023–2029 (2007).
36. Allen, J. J. *et al.* A semisynthetic epitope for kinase substrates. *Nature Methods* **4**, 511–516 (2007).
37. Bankston, D. *et al.* A scaleable synthesis of BAY 43-9006: A potent raf kinase inhibitor for the treatment of cancer. *Org. Process Res. Dev.* **6**, 777–781 (2002).
38. Hertz, N. T. *et al.* Chemical genetic approach for kinase-substrate mapping by covalent capture of thiophosphopeptides and analysis by mass spectrometry. *Curr. Prot. Chem. Biol.* **2**, 15–36 (2010).
39. Trinidad, J. C. *et al.* Quantitative analysis of synaptic phosphorylation and protein expression. *Mol. Cell. Proteomics* **7**, 684–696 (2008).

A conserved mechanism of DEAD-box ATPase activation by nucleoporins and InsP₆ in mRNA export

Ben Montpetit^{1,2*}, Nathan D. Thomsen^{2,3†*}, Kara J. Helmke^{1,2}, Markus A. Seeliger^{2,3†}, James M. Berger^{2,3} & Karsten Weis^{1,2}

Superfamily 1 and superfamily 2 RNA helicases are ubiquitous messenger-RNA-protein complex (mRNP) remodelling enzymes that have critical roles in all aspects of RNA metabolism^{1,2}. The superfamily 2 DEAD-box ATPase Dbp5 (human DDX19) functions in mRNA export and is thought to remodel mRNPs at the nuclear pore complex (NPC)^{3–8}. Dbp5 is localized to the NPC via an interaction with Nup159 (NUP214 in vertebrates)^{3–5,8,9} and is locally activated there by Gle1 together with the small-molecule inositol hexakisphosphate (InsP₆)^{10,11}. Local activation of Dbp5 at the NPC by Gle1 is essential for mRNA export *in vivo*^{10,12}; however, the mechanistic role of Dbp5 in mRNP export is poorly understood and it is not known how Gle1_{InsP₆} and Nup159 regulate the activity of Dbp5. Here we report, from yeast, structures of Dbp5 in complex with Gle1_{InsP₆}, Nup159/Gle1_{InsP₆} and RNA. These structures reveal that InsP₆ functions as a small-molecule tether for the Gle1–Dbp5 interaction. Surprisingly, the Gle1_{InsP₆}–Dbp5 complex is structurally similar to another DEAD-box ATPase complex essential for translation initiation, eIF4G–eIF4A, and we demonstrate that Gle1_{InsP₆} and eIF4G both activate their DEAD-box partner by stimulating RNA release. Furthermore, Gle1_{InsP₆} relieves Dbp5 autoregulation and cooperates with Nup159 in stabilizing an open Dbp5 intermediate that precludes RNA binding. These findings explain how Gle1_{InsP₆}, Nup159 and Dbp5 collaborate in mRNA export and provide a general mechanism for DEAD-box ATPase regulation by Gle1/eIF4G-like activators.

Gle1 and InsP₆ robustly activate the ATPase activity of Dbp5 (refs 10, 11), but interactions between Dbp5 and Gle1_{InsP₆} are weak and transient *in vitro*^{10,12}. However, gain-of-function mutations in Dbp5 and Gle1 (Dbp5(L327V) and Gle1(H337R))¹⁰ allowed for the purification of a stable Dbp5–Gle1_{InsP₆} complex for protein crystallography (data not shown). Multiwavelength anomalous diffraction (MAD) phased protein crystal structures were initially obtained for Gle1_{InsP₆} and the carboxy-terminal RecA-like domain (C-terminal domain, CTD) of Dbp5(L327V), both in the presence and absence of the Gle1 H337R mutation at a resolution of 2.6 Å ($R_{\text{work}}/R_{\text{free}}$ of 18.7/21.3%) and 2.5 Å ($R_{\text{work}}/R_{\text{free}}$ of 20.2/23.8%), respectively (Supplementary Table 1). This model allowed us to solve the crystal structure of an amino-terminally truncated $\Delta 90$ Dbp5(L327V) construct containing both RecA-like domains of Dbp5 (residues 91–482) bound to ADP and Gle1(H337R)_{InsP₆} (residues 244–538) by molecular replacement at a resolution of 4.0 Å ($R_{\text{work}}/R_{\text{free}}$ of 21.4/23.9%) (Fig. 1 and Supplementary Table 2). Structures were also obtained for $\Delta 90$ Dbp5(L327V) or $\Delta 90$ Dbp5 wild-type in complex with RNA and ADP•BeF₃ at a resolution of 1.5 Å ($R_{\text{work}}/R_{\text{free}}$ of 16.5/18.9%) and 1.4 Å ($R_{\text{work}}/R_{\text{free}}$ of 16.0/18.0%), respectively (Supplementary Table 2).

The structures reveal that Gle1 comprises an all α -helix HEAT repeat protein that makes contact with both RecA-like domains of

Dbp5 (Fig. 1a, b). The CTD interface buries 2,230 Å² of surface area, and contains a number of residues previously shown to be important for Gle1-mediated activation of Dbp5 (ref. 12). The second interaction surface uses the N-terminal RecA-like domain (N-terminal domain,

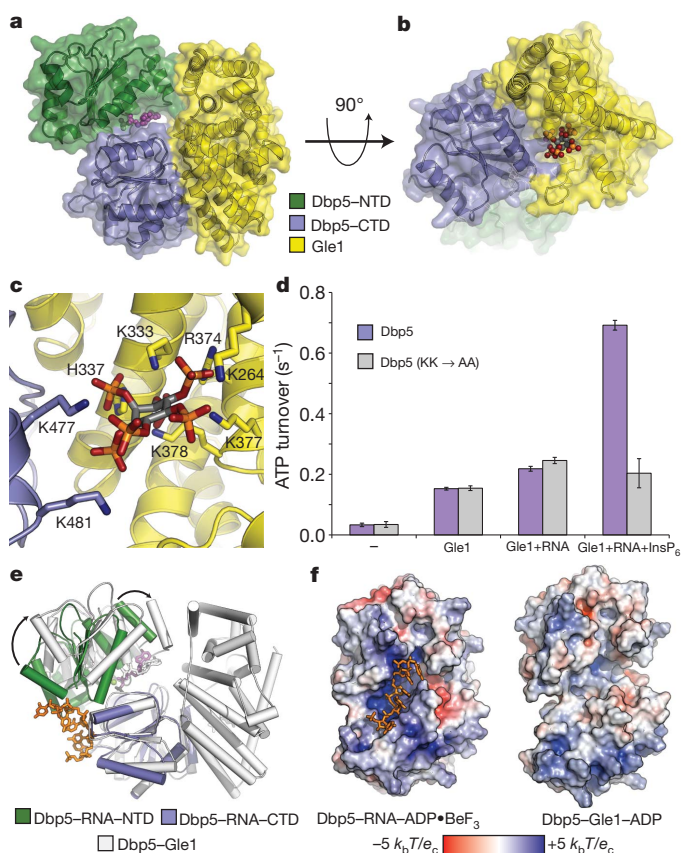


Figure 1 | The Gle1_{InsP₆}– $\Delta 90$ Dbp5–ADP complex. **a**, Structure of Dbp5 bound to ADP (magenta spheres) and Gle1 (see colour key). **b**, Side view showing InsP₆ (coloured spheres) bound at the interface between Gle1 and Dbp5. **c**, Detailed view of the InsP₆ binding interface (see colour key). InsP₆ is shown as grey sticks with orange phosphate and red oxygen atoms. Nitrogen atoms are in dark blue. **d**, InsP₆ binding is required for maximal Dbp5 ATPase stimulation with RNA. Error bars represent standard deviation (s.d.) ($n = 3$). **e**, Structural superposition of the RNA– $\Delta 90$ Dbp5 complex with Gle1_{InsP₆}– $\Delta 90$ Dbp5. Arrows depict the large rigid body movement in Dbp5. **f**, Van der Waals surface view of the RNA– $\Delta 90$ Dbp5 complex and the Gle1_{InsP₆}– $\Delta 90$ Dbp5 complex coloured by solvent accessible electrostatics. k_B , Boltzmann's constant (Joules/Kelvin); T , temperature (310 Kelvin); e , charge of an electron (1.602×10^{-19} Coulombs).

¹Division of Cell and Developmental Biology, University of California, Berkeley, California 94720, USA. ²Department of Molecular and Cell Biology and QB3 Institute, University of California, Berkeley, California 94720, USA. ³Division of Biochemistry and Molecular Biology, University of California, Berkeley, California 94720, USA. [†]Present addresses: Department of Pharmaceutical Chemistry, University of California, San Francisco, California 94158, USA (N.D.T.); Department of Pharmacology, State University of New York at Stony Brook, Stony Brook, New York 11794, USA (M.A.S.).

*These authors contributed equally to this work.

NTD) of Dbp5 and an exposed hydrophobic α -helix of Gle1, which buries an additional 930 Å² of surface area (Fig. 1a). Interestingly, and despite the lack of obvious homology in sequence alignments, a search of the structural database using the DALI server¹³ showed that the Gle1 fold is similar to that of eIF4G (14% identity, 4.1 Å root mean squared deviation (r.m.s.d.)), a co-factor for the superfamily 2 (SF2) DEAD-box ATPase eIF4A^{14–16}, and to that of Upf2 (also known as Nmd2; 8% identity, 3.0 Å r.m.s.d.), which stimulates the superfamily 1 (SF1) protein Upf1 (also known as Nam7)^{17–19}.

A unique feature of the Gle1_{InsP₆}-Dbp5 structures is the presence of InsP₆, which bridges the protein–protein interaction by binding in a positively charged pocket at the interface between Gle1 and the CTD of Dbp5 (Fig. 1b, c). Residues K264, K333, H337, R374, K377 and K378 in Gle1 and K477 and K481 in Dbp5 interact with phosphate groups in InsP₆ (Fig. 1c and Supplementary Fig. 1a, b). Two of these residues in Gle1 (K377 and K378) were recently identified as being involved in InsP₆ binding²⁰. Gle1 residues (H337, R374, K377 and K378) show charge conservation, and Dbp5 residue K477 is conserved as a hydrogen bond donor in most metazoans, indicating an evolutionary pressure to maintain a polar residue that can interact with InsP₆ at these positions. (Supplementary Fig. 1c, d). To our knowledge, this represents the first structural characterization of an endogenous small molecule that localizes at the interface of two heterologous proteins to mediate a protein–protein binding interaction.

To assess the importance of InsP₆ binding by Dbp5, we mutated the InsP₆ contacts K477 and K481 to Ala (Dbp5(KK→AA)). Dbp5(KK→AA) showed no synergistic ATPase activation in the presence of InsP₆, RNA and sub-saturating amounts of Gle1, but was still active as an ATPase and was stimulated by RNA and Gle1 comparable to wild-type protein in the absence of InsP₆ (Fig. 1d). Furthermore, Dbp5(KK→AA) (L327V variant) no longer formed a stable complex with Gle1(H337R) and InsP₆ (Supplementary Fig. 1e). These results demonstrate that InsP₆ stabilizes the Gle1–Dbp5 interaction by acting as a small-molecule tether.

A comparison of the RNA and ADP•BeF₃-bound Δ 90Dbp5 structure with that of Gle1_{InsP₆}-Dbp5 reveals that Gle1_{InsP₆} in the presence

of ADP induces a large rigid body movement in Dbp5, opening the tandem RecA-like domains relative to their positions in the RNA-bound state (Fig. 1e and Supplementary Movie 1). Smaller conformational changes occur at the Gle1_{InsP₆}-CTD interface, and structures obtained with wild-type versus gain-of-function mutations show that these mutations subtly alter Gle1_{InsP₆}-Dbp5 contacts, probably contributing additional binding energy to stabilize the complex (Supplementary Fig. 2). Interestingly, binding to Gle1_{InsP₆} markedly alters the RNA binding site in Dbp5, which opens and loses its localized positive charge (Fig. 1f and Supplementary Movie 2). This indicates that Gle1_{InsP₆} binding leads to the formation of a partially open, catalytically inactive and ADP-bound complex that precludes RNA binding.

Owing to the unexpected similarity between Gle1 and eIF4G, we also compared our structures to the eIF4A/4G complex. The open conformation of Dbp5 induced by Gle1_{InsP₆} is similar to that described for eIF4A in the presence of eIF4G^{14,21,22}, and there is an overall similarity between the interactions of eIF4G and Gle1_{InsP₆} with the CTDs of their DEAD-box ATPase partners (Fig. 2a). However, eIF4G lacks an N-terminal helix that in Gle1 forms part of the binding pocket for InsP₆; instead, eIF4G forms a flexible loop that makes additional contacts with eIF4A, effectively compensating for the lack of InsP₆ (Fig. 2b). The interface between eIF4G and the eIF4A NTD also exhibits interdomain differences when compared to Gle1_{InsP₆}-Dbp5 (Fig. 2c, d), causing eIF4G to stabilize a more open eIF4A intermediate^{14,21}. Thus, the eIF4G–eIF4A complex seems to be more competent for ADP exchange than the Gle1_{InsP₆}-Dbp5 complex. Despite these small differences, both Gle1_{InsP₆} and eIF4G stabilize their DEAD-box binding partner in an open state that is incompatible with RNA binding.

Gle1_{InsP₆} is a potent activator of the overall ATPase activity of Dbp5 (refs 10, 11), but in our structures, Gle1 is not positioned to directly stimulate ATP hydrolysis (Fig. 1). We therefore proposed that Gle1_{InsP₆} activates Dbp5 by enhancing RNA release, a step known to be rate-limiting in the hydrolytic cycle of other DEAD-box ATPases^{23,24}. In such a model, product release would rely on the ability of Gle1_{InsP₆} to induce the structural rearrangement of the two tandem RecA-like

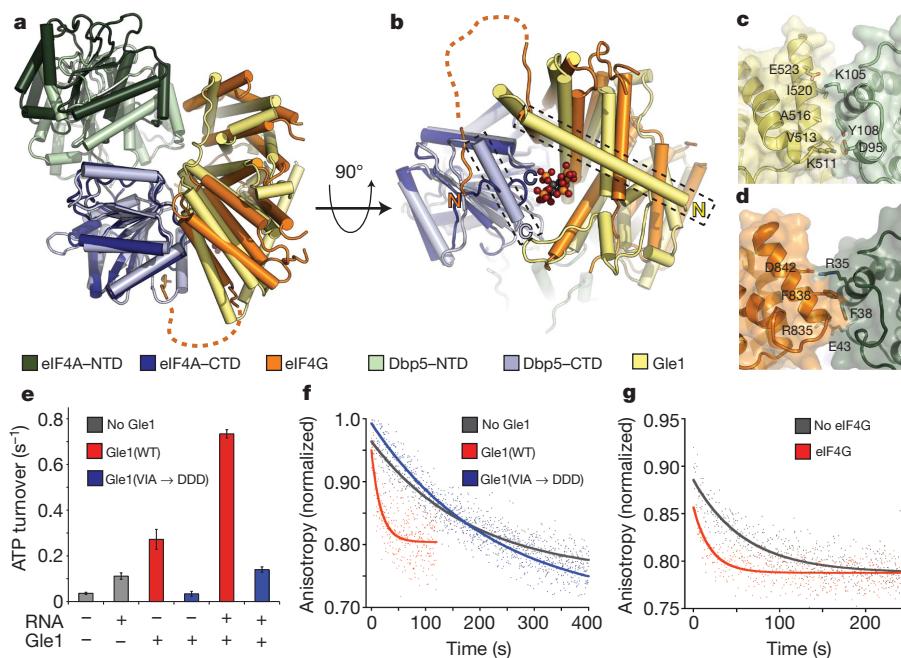


Figure 2 | Comparison of Gle1_{InsP₆}-Δ90Dbp5 and eIF4A-eIF4G.

a, Structural superposition of Gle1_{InsP₆}-Δ90Dbp5 with eIF4G-eIF4A and AMP (PDB accession code 2VSO)²¹ (see colour key). **b**, View of the C-terminal RecA-like domain binding interface. Unique α -helices present in both Dbp5 and Gle1 form the InsP₆ binding pocket (boxed in figure). **c**, **d**, Residues involved in the

formation of the N-terminal RecA-like domain binding interface in Gle1_{InsP₆}-Δ90Dbp5 (**c**) and eIF4A-eIF4G (**d**). **e**, Measured ATPase activity using wild-type (WT) or mutant Gle1. Error bars represent s.d. ($n = 3$). **f**, **g**, RNA release from Dbp5(E240Q) or eIF4A(E172Q) monitored by fluorescence polarization. Representative curves are shown.

domains of Dbp5 (Fig. 1e, f). Thus, loss of contact between Gle1 and the NTD of Dbp5 should impair the ability of Gle1_{InsP₆} to activate Dbp5 without affecting the binding between these proteins, which is primarily mediated by the Gle1_{InsP₆}-CTD interaction (Fig. 1a). To test this idea, residues V513, A516 and I520 on a solvent-exposed helix of Gle1 (Supplementary Fig. 3a) were mutated (Gle1(VAI→DDD)) to disrupt the Gle1-NTD interface (Fig. 2c and Supplementary Fig. 3b). In an ATPase assay, Gle1(VAI→DDD) was unable to activate Dbp5 regardless of the presence of RNA and InsP₆ (Fig. 2e), but still formed a complex with Dbp5(L327V) by gel filtration (Supplementary Fig. 3c), demonstrating that these mutations did not disrupt the primary Gle1_{InsP₆}-CTD association.

Next, we directly assessed the effect of Gle1_{InsP₆} on RNA release from a hydrolysis-deficient Dbp5 mutant, Dbp5(E240Q), bound to both RNA and ATP (Fig. 2f and Supplementary Table 3). Dbp5(E240Q) released RNA very slowly with a $t_{1/2}$ of 180 ± 15 s ($k_{\text{off}} = 0.0039 \text{ s}^{-1}$) and Gle1_{InsP₆} stimulated this release ~ 9 -fold ($t_{1/2}$ of 21 ± 6 s, $k_{\text{off}} = 0.033 \text{ s}^{-1}$). Importantly, no enhancement of RNA release was observed with the Gle1(VAI→DDD) mutant (166 ± 50 s, $k_{\text{off}} = 0.042 \text{ s}^{-1}$). Because mutation of Gle1 at these residues *in vivo* resulted in lethality (Supplementary Fig. 3d) and Gle1_{InsP₆} did not affect the ability of Dbp5 to bind or release ADP (Supplementary Table 3), we conclude that an essential function of Gle1_{InsP₆} is to promote RNA release from Dbp5. This may explain how Gle1_{InsP₆} helps to terminate mRNA export in the cytoplasm.

Given the structural similarities between Gle1_{InsP₆}-Dbp5 and eIF4G-eIF4A, we also tested eIF4G in the same RNA release assay and found that RNA release from eIF4A is similarly stimulated in the presence of its ATPase activator (eIF4A(E172Q) alone = 55 ± 8 s, $k_{\text{off}} = 0.019 \pm 0.03 \text{ s}^{-1}$ compared to eIF4A(E172Q) + eIF4G = 11 ± 3 s, $k_{\text{off}} = 0.091 \pm 0.03 \text{ s}^{-1}$) (Fig. 2g). This behaviour corresponds well with the ~ 3 -fold stimulation of ATPase activity reported for eIF4G²¹. Together with the structural similarity between Gle1, eIF4G and other RNA helicase activators such as Upf2, these findings support a model in which Gle1/eIF4G-like proteins generally activate SF1 and SF2 ATPases by promoting RNA release and enzyme recycling.

Recent structural studies of the human Dbp5 orthologue, DDX19, identified an N-terminal α -helix that lowers basal Dbp5/DDX19 ATPase activity, but that is also required for RNA-stimulated ATP turnover^{9,25}. Our structures lack this N-terminal helix, but structural

alignments show that Gle1_{InsP₆} and a C-terminal helix of Dbp5 would clash with this N-terminal domain in the RNA bound state (Supplementary Fig. 4a, b). This observation indicates that the autoinhibitory N-terminal helix must be displaced on Gle1_{InsP₆} association, and should have little effect on ATPase activity in the presence of Gle1_{InsP₆}. As seen for human DDX19 (ref. 25), the yeast $\Delta 90$ Dbp5 construct lacking this regulatory domain has a basal ATPase rate ~ 3 -fold higher than full-length Dbp5. However, $\Delta 90$ Dbp5 only reaches the same maximum ATPase level as full-length Dbp5 in the presence of Gle1_{InsP₆} (Supplementary Fig. 4c). This result indicates that release of Dbp5 autoregulation accounts for a portion of Gle1_{InsP₆}-mediated ATPase stimulation.

Dbp5 is an ATP-dependent RNA binding protein that dissociates from RNA on each hydrolysis event (Supplementary Fig. 4d), and an interaction between full-length Dbp5 and RNA can only be detected at steady state when turnover is inhibited (Supplementary Table 3)¹⁰. Intriguingly, deletion of the N-terminal regulatory α -helix within Dbp5 allowed for the formation of a steady-state RNA-Dbp5 complex under conditions of hydrolysis (Supplementary Fig. 4e). These data imply that the N-terminal 90 residues of Dbp5 are involved in regulating Dbp5-RNA binding. Furthermore, the observation that $\Delta 90$ Dbp5 binds RNA (Supplementary Fig. 4e), but is not stimulated for hydrolysis by RNA (Supplementary Fig. 4c), indicates that these 90 residues have a critical role in the coupling of RNA binding to ATPase activity. To test whether Gle1_{InsP₆} can alter steady-state RNA binding by displacing this α -helix, we added Gle1_{InsP₆} to RNA binding assays containing full-length Dbp5 and ATP. We observed that addition of Gle1_{InsP₆} allowed for steady-state binding with an apparent affinity for RNA equal to that measured for $\Delta 90$ Dbp5 (Supplementary Fig. 4e and Supplementary Table 3). This observation indicates that the N-terminal extension of Dbp5 regulates RNA association, and that Gle1_{InsP₆} binding can alter this activity. Overall, our results are consistent with a model in which Gle1_{InsP₆} regulates Dbp5 by: (1) altering the regulatory function of an N-terminal helix within Dbp5; and (2) promoting substrate release through separating the Dbp5 RecA-like domains. Together, these findings explain the robust activation of Dbp5 by Gle1 and the small molecule InsP₆.

In addition to Gle1, Dbp5 interacts with the nucleoporin Nup159 (NUP214 in vertebrates)^{3,4,8,9,26}. Nup159 and RNA bind to overlapping

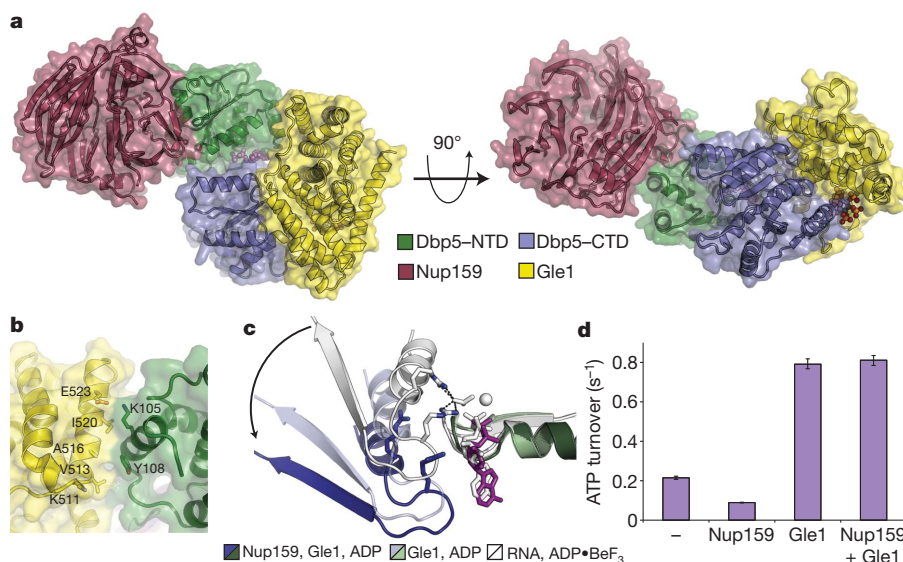


Figure 3 | The Gle1_{InsP₆}-Δ90Dbp5-Nup159 complex. **a**, Two views of the Gle1_{InsP₆}-Dbp5-Nup159 complex (see colour key). **b**, The N-terminal RecA-like domain binding interface between Dbp5-Gle1_{InsP₆} is altered in the presence of Nup159 (compare to Fig. 2c). Residues involved in the binding interface (sticks) are labelled. **c**, Superposition of the N-terminal RecA-domain among the three structural states of Dbp5. Arrow highlights the movement of

the CTD and catalytic arginine finger residues (sticks) among the three states (see colour key). For clarity, the Gle1-ADP intermediate is shown slightly transparent, and both the arginine finger side chains and ADP have been removed. **d**, Inhibition of the RNA-stimulated ATPase activity of Dbp5 by Nup159 is overcome in the presence of Gle1. Error bars represent s.d. (n = 3).

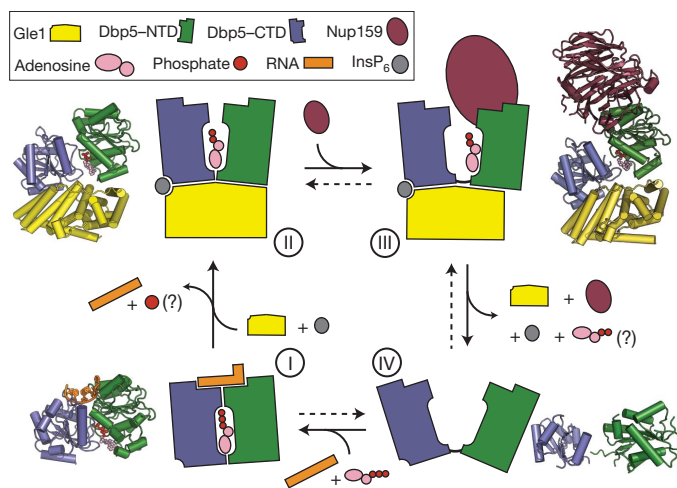


Figure 4 | Model of the Dbp5 mechanochemical cycle. In the presence of ATP, Dbp5 binds RNA causing local destabilization and remodelling of duplexed RNA or RNA–protein complexes (state I). ATP hydrolysis then allows the activator (Gle1) to bind both the C-terminal and N-terminal RecA-like domains, separating the two RecA-like domains and promoting RNA release (state II). For Dbp5 it is currently not known when inorganic phosphate (P_i) is released after hydrolysis, but this will probably occur before the formation of state II. Subsequent release of the bound RNA allows Nup159 to bind Dbp5 causing the two RecA domains to further separate (state III). The formation of this state could then facilitate ADP release, prevent rebinding of the RNA, and aid in enzyme recycling (state IV). Crystal structure model in state IV is PDB accession code 3FH0²⁸. For colour coding details see key.

surfaces on Dbp5, and Nup159 inhibits RNA-dependent ATPase stimulation of Dbp5 *in vitro*⁹. To better understand how this potentially inhibitory role of Nup159 contributes to mRNA export, we solved the crystal structure of a Dbp5(L327V)–Gle1(H337R)–Nup159 complex bound to $InsP_6$ and ADP at a resolution of 2.9 Å (R_{work}/R_{free} of 22.9/26.2%) (Fig. 3a and Supplementary Table 2). Within this structure, Nup159 interacts with Dbp5 in a manner similar to that of DDX19 and NUP214 (ref. 9), occluding the RNA binding site and sterically clashing with the closed, RNA- and ATP-bound state of Dbp5 (Supplementary Fig. 5). Whereas the Gle1 _{$InsP_6$} –CTD interface remains relatively static in all of our structures, the Gle1–NTD interface has distinct structural differences in the presence of Nup159 and now buries only 672 Å² of solvent-exposed surface area (compare Figs 2c and 3b). Furthermore, the two RecA-like domains of Dbp5 become further separated in the Dbp5–Gle1 _{$InsP_6$} –Nup159 structure, and the Dbp5 catalytic centre becomes exposed to solvent as functionally critical arginine fingers are pulled out from the nucleotide binding site (Fig. 3c). A comparison of Dbp5 among all structures reveals that interdomain structural changes proceed along a pair of related arcs, indicating that Nup159 may further assist Gle1 _{$InsP_6$} in stabilizing a post-hydrolysis state of Dbp5 to allow for efficient product release at the cytoplasmic face of the NPC (Supplementary Movie 3).

To test this biochemically, we assayed Dbp5 ATPase activity and found that on addition of Gle1 _{$InsP_6$} , Nup159 no longer inhibits ATP turnover (Fig. 3d) indicating that Gle1 _{$InsP_6$} can overcome the inhibitory effect of Nup159. This indicates that during the hydrolysis cycle in the presence of Gle1, the association of Dbp5 with Nup159 is transient, which is in agreement with the observation that the presence of adenosine nucleotide and/or RNA weakens the Dbp5–Nup159 interaction^{3,9}. This provides for the possibility that Nup159 not only increases the local concentration of Dbp5 at the NPC^{4,8}, but also cooperates with Gle1 to promote mRNA export. Mechanistically, Gle1 and Nup159 may spatially coordinate the loading of Dbp5 onto an mRNP to target the removal of mRNA-bound export factors and contribute to the overall efficiency of mRNA export^{4,8,9}. Alternatively, in a non-mutually exclusive model, the Dbp5–Gle1 _{$InsP_6$} –Nup159 structure may represent a post-mRNA export complex formed

after mRNP remodelling is complete and Dbp5 is removed from the mRNP. In this model, the interactions of Gle1 and Nup159 with Dbp5 would be critical for enzyme recycling and/or preventing spurious rebinding of Dbp5 to an mRNA in the terminal stages of export.

Our study reveals a surprising structural similarity between Gle1 and other helicase regulators including eIF4G and Upf2 (refs 14, 19, 21). Together with our biochemical data, these results indicate a common mode of activation for DEAD-box ATPases and RNA helicases by Gle1/eIF4G-like protein activators. Critical for the activation are a primary stable interaction between the activator and the C-terminal RecA-like domain of the ATPase, and a secondary transient interaction between the activator and the N-terminal RecA-like domain that is required to trigger nucleic-acid release (Fig. 2). For Dbp5, we propose that RNA and Gle1 _{$InsP_6$} /Nup159 promote the formation of closed (ATP binding and hydrolysis) and open (substrate release) conformations of the ATPase, respectively, by influencing the position of the NTD of Dbp5 relative to the CTD (Fig. 4 and Supplementary Movie 3). Complex disassembly may be further promoted by the ~50-fold ATP-dependent lowering of Dbp5 binding affinity for Nup159 observed in the presence of ATP⁹, thus allowing Dbp5 to once again bind an mRNA and re-enter the ATPase cycle. For DEAD-box ATPases in general, such a toggling mechanism of the two RecA-like domains could be used to facilitate recycling of enzymes that have just melted RNA duplexes or remodelled RNA–protein complexes. Furthermore, in the presence of additional RNA-binding domains provided in *cis* or *trans*, this activity might also allow for a processive movement of this class of SF2 proteins along an RNA substrate²⁷.

The unique role of $InsP_6$ as a small molecule tether within the Dbp5–Gle1 complex may allow for $InsP_6$ -dependent fine-tuning of interaction strength. Functionally, this could be used to modulate RNA release/turnover and consequently regulate mRNA export under various growth conditions (for example, in response to stress). Additional experiments will be needed to elucidate the functional importance of $InsP_6$ *in vivo*. However, the structural and biochemical framework presented here should guide future experiments not only to determine how Dbp5 in combination with its interaction partners confers directionality to mRNA export, but also to dissect the cellular functions of other RNA helicases and their activators.

METHODS SUMMARY

Yeast strains and plasmids are listed in Supplementary Tables 4 and 5. RNA binding and ATPase assays were performed as described in Methods. Single-stranded RNA substrates used for binding and release assays carrying a single fluorescein-conjugated UTP were made by *in vitro* transcription. RNA release assays were performed by monitoring the change in fluorescence polarization after rapid 1:1 mixing of DEAD-box protein–RNA-binding reactions with excess polyA-RNA using a stopped-flow apparatus linked to a Fluoromax-3 fluorimeter. For crystallography, protein purification was performed by affinity and ion exchange chromatography followed by affinity tag cleavage and complex formation. Protein complexes were separated by gel filtration over a HiPrep Sephacryl S-200 column. Fractions containing the Dbp5–Gle1 or Nup159–Dbp5–Gle1 complex were used for crystal screening in a hanging-drop format (200 nl) using a Mosquito robotics platform at 18 °C. After 3–7 days of growth, crystals were looped and flash frozen in liquid nitrogen, and diffraction data collected on Beamlime 8.3.1 at the Advanced Light Source. Detailed methods and references related to data processing, structure solution, and model building, plus all other methods used are outlined in Methods.

Full Methods and any associated references are available in the online version of the paper at www.nature.com/nature.

Received 16 October 2010; accepted 19 January 2011.

Published online 27 March 2011.

1. Cordin, O., Banroques, J., Tanner, N. K. & Linder, P. The DEAD-box protein family of RNA helicases. *Gene* **367**, 17–37 (2006).
2. Jankowsky, E. RNA helicases at work: binding and rearranging. *Trends Biochem. Sci.* **36**, 19–29 (2010).
3. Schmitt, C. *et al.* Dbp5, a DEAD-box protein required for mRNA export, is recruited to the cytoplasmic fibrils of nuclear pore complex via a conserved interaction with CAN/Nup159p. *EMBO J.* **18**, 4332–4347 (1999).

4. Hodge, C. A., Colot, H. V., Stafford, P. & Cole, C. N. Rat8p/Dbp5p is a shuttling transport factor that interacts with Rat7p/Nup159p and Gle1p and suppresses the mRNA export defect of *xpo1-1* cells. *EMBO J.* **18**, 5778–5788 (1999).
5. Snay-Hodge, C. A., Colot, H. V., Goldstein, A. L. & Cole, C. N. Dbp5p/Rat8p is a yeast nuclear pore-associated DEAD-box protein essential for RNA export. *EMBO J.* **17**, 2663–2676 (1998).
6. Lund, M. K. & Guthrie, C. The DEAD-box protein Dbp5p is required to dissociate Mex67p from exported mRNPs at the nuclear rim. *Mol. Cell* **20**, 645–651 (2005).
7. Tran, E. J., Zhou, Y., Corbett, A. H. & Wente, S. R. The DEAD-box protein Dbp5 controls mRNA export by triggering specific RNA:protein remodeling events. *Mol. Cell* **28**, 850–859 (2007).
8. Weirich, C. S., Erzberger, J. P., Berger, J. M. & Weis, K. The N-terminal domain of Nup159 forms a β -propeller that functions in mRNA export by tethering the helicase Dbp5 to the nuclear pore. *Mol. Cell* **16**, 749–760 (2004).
9. von Moeller, H., Basquin, C. & Conti, E. The mRNA export protein DBP5 binds RNA and the cytoplasmic nucleoporin NUP214 in a mutually exclusive manner. *Nature Struct. Mol. Biol.* **16**, 247–254 (2009).
10. Weirich, C. S. *et al.* Activation of the DEXD/H-box protein Dbp5 by the nuclear-pore protein Gle1 and its coactivator InsP₆ is required for mRNA export. *Nature Cell Biol.* **8**, 668–676 (2006).
11. Alcázar-Roman, A. R., Tran, E. J., Guo, S. & Wente, S. R. Inositol hexakisphosphate and Gle1 activate the DEAD-box protein Dbp5 for nuclear mRNA export. *Nature Cell Biol.* **8**, 711–716 (2006).
12. Dossani, Z. Y., Weirich, C. S., Erzberger, J. P., Berger, J. M. & Weis, K. Structure of the C-terminus of the mRNA export factor Dbp5 reveals the interaction surface for the ATPase activator Gle1. *Proc. Natl Acad. Sci. USA* **106**, 16251–16256 (2009).
13. Holm, L., Kaariainen, S., Rosenstrom, P. & Schenkel, A. Searching protein structure databases with DaliLite v.3. *Bioinformatics* **24**, 2780–2781 (2008).
14. Oberer, M., Marintchev, A. & Wagner, G. Structural basis for the enhancement of eIF4A helicase activity by eIF4G. *Genes Dev.* **19**, 2212–2223 (2005).
15. Korneeva, N. L., First, E. A., Benoit, C. A. & Rhoads, R. E. Interaction between the NH₂-terminal domain of eIF4A and the central domain of eIF4G modulates RNA-stimulated ATPase activity. *J. Biol. Chem.* **280**, 1872–1881 (2005).
16. Sonenberg, N. & Dever, T. E. Eukaryotic translation initiation factors and regulators. *Curr. Opin. Struct. Biol.* **13**, 56–63 (2003).
17. He, F., Brown, A. H. & Jacobson, A. Upf1p, Nmd2p, and Upf3p are interacting components of the yeast nonsense-mediated mRNA decay pathway. *Mol. Cell Biol.* **17**, 1580–1594 (1997).
18. Chamieh, H., Ballut, L., Bonneau, F. & Le Hir, H. NMD factors UPF2 and UPF3 bridge UPF1 to the exon junction complex and stimulate its RNA helicase activity. *Nature Struct. Mol. Biol.* **15**, 85–93 (2008).
19. Kadlec, J., Guilligay, D., Ravelli, R. B. & Cusack, S. Crystal structure of the UPF2-interacting domain of nonsense-mediated mRNA decay factor UPF1. *RNA* **12**, 1817–1824 (2006).
20. Alcázar-Román, A. R., Bolger, T. A. & Wente, S. R. Control of mRNA export and translation termination by inositol hexakisphosphate requires specific interaction with Gle1. *J. Biol. Chem.* **285**, 16683–16692 (2010).
21. Schutz, P. *et al.* Crystal structure of the yeast eIF4A-eIF4G complex: an RNA-helicase controlled by protein–protein interactions. *Proc. Natl Acad. Sci. USA* **105**, 9564–9569 (2008).
22. Marintchev, A. *et al.* Topology and regulation of the human eIF4A/4G/4H helicase complex in translation initiation. *Cell* **136**, 447–460 (2009).
23. Henn, A., Cao, W., Hackney, D. D. & De La Cruz, E. M. The ATPase cycle mechanism of the DEAD-box rRNA helicase, DbpA. *J. Mol. Biol.* **377**, 193–205 (2008).
24. Henn, A. *et al.* Pathway of ATP utilization and duplex rRNA unwinding by the DEAD-box helicase, DbpA. *Proc. Natl Acad. Sci. USA* **107**, 4046–4050 (2010).
25. Collins, R. *et al.* The DEXD/H-box RNA helicase DDX19 is regulated by an α -helical switch. *J. Biol. Chem.* **284**, 10296–10300 (2009).
26. Napetschnig, J. *et al.* Structural and functional analysis of the interaction between the nucleoporin Nup214 and the DEAD-box helicase Ddx19. *Proc. Natl Acad. Sci. USA* **106**, 3089–3094 (2009).
27. Büttner, K., Nehring, S. & Hopfner, K. P. Structural basis for DNA duplex separation by a superfamily-2 helicase. *Nature Struct. Mol. Biol.* **14**, 647–652 (2007).
28. Fan, J. S. *et al.* Solution and crystal structures of mRNA exporter Dbp5p and its interaction with nucleotides. *J. Mol. Biol.* **388**, 1–10 (2009).

Supplementary Information is linked to the online version of the paper at www.nature.com/nature.

Acknowledgements We thank J. Kirsch, J. Thorner, M. Welch, D. Wemmer, B. Krantz, J. Zorn and all J.M.B. and K.W. laboratory members for discussions and advice. We also thank J. Kuriyan, M. Welch and S. Marqusee for access to equipment and workspace; J. Tanamachi, G. Meigs and J. Holton at ALS beamline 8.3.1; and N. Echols for assistance with programs from the Yale Morph Server. Research was supported by the G Harold and Leila Y Mathers foundation (J.M.B.) and the NIH (K.W., R01GM58065 and RC1GM91533).

Author Contributions B.M., N.D.T., J.M.B. and K.W. designed the experiments. Protein purifications for crystallization and biochemical assays were performed by B.M. Crystal screening, optimization and data collection were performed by B.M. and N.D.T. Data processing, structure solution and model building was performed by N.D.T. *In vivo* tests and *in vitro* RNA binding, ATPase assays and other biochemical assays were performed by B.M. with assistance from M.A.S. and K.J.H. B.M., N.D.T., J.M.B. and K.W. both analysed and interpreted the data and wrote the manuscript.

Author Information Coordinates and structure factors for Dbp5-CTD(L327V)/InsP₆/Gle1(H337R), Dbp5-CTD(L327V)/InsP₆/Gle1(WT), Δ 90Dbp5(L327V)/RNA/ADP•BeF₃, Δ 90Dbp5(RNA/ADP•BeF₃), Δ 90Dbp5(L327V)/InsP₆/Gle1(H337R)/ADP and Δ 90Dbp5(L327V)/InsP₆/Gle1(H337R)/ADP/Nup159 have been deposited in the protein data bank under accession numbers 3PEU, 3PEV, 3PEW, 3PEY, 3PEX and 3PEZ, respectively. Reprints and permissions information is available at www.nature.com/reprints. The authors declare no competing financial interests. Readers are welcome to comment on the online version of this article at www.nature.com/nature. Correspondence and requests for materials should be addressed to K.W. (kweis@berkeley.edu) or J.M.B. (jmberger@berkeley.edu).

METHODS

Protein purification for crystallography. Dbp5, Gle1 (amino acids (a.a.) 244–538), Nup159 (a.a. 2–387), eIF4A and eIF4G (a.a. 572–952) from *Saccharomyces cerevisiae* were expressed as previously described^{8,10,21} in BL21-CodonPlus (DE3)-RIPL cells (Stratagene) using a combination of nickel affinity, ion exchange and size exclusion chromatography. For the production of selenomethionine-labelled protein, Dbp5 and Gle1 proteins were purified as above, except that cells were grown in minimal media supplemented with selenomethionine and β -ME and dithiothreitol (DTT) were replaced with tris(2-carboxyethyl)phosphine (TCEP) throughout the purification. TEV cleavage was done at a 1:50 ratio (w/w) in 30 mM HEPES (pH 7.5), 400 mM NaCl, 1 mM DTT, 0.25 mM InsP₆ and 10% glycerol at 22 °C for 4 h²⁹. After removal of uncleaved protein, by orthogonal purification over a mixture of HIS-Select HF Nickel Affinity Gel (Sigma) and amylose resin (NEB), proteins were mixed in an equimolar ratio, diluted to 150 mM NaCl and concentrated to $\sim 15 \text{ mg ml}^{-1}$ at 4 °C (Amicon Ultra; Millipore). The protein mixture was then further separated by gel filtration over a HiPrep Sephacryl S-200 column (GE Healthcare) at 0.4 ml min^{-1} in 10 mM HEPES (pH 7.5), 100 mM NaCl, 1 mM DTT, 0.50 mM InsP₆ and 5% glycerol at 4 °C. Fractions containing the desired protein complex, in an equimolar ratio (as judged by SDS–PAGE), were then pooled and concentrated to $\sim 25 \text{ mg ml}^{-1}$ at 4 °C.

Protein crystallization. Protein solutions were stored at 4 °C and used for crystallization within 1 week, during which time there was no detectable degradation of the proteins. All crystallization was performed in a hanging drop format using a Mosquito robotics platform (TTP LabTech) at 18 °C.

The Dbp5–CTD(L327V)/InsP₆/Gle1(H337R) crystals were grown by mixing 100 nl of selenomethionine-labelled protein solution at 14 mg ml^{-1} in gel filtration buffer with 100 nl of a solution containing 30% PEG 3350, 100 mM HEPES pH 8.0, 50 mM NaOAc and 200 mM LiSO₄, and incubating for 5 days. Crystals were cryoprotected by dilution into a solution containing 24% PEG 3350, 80 mM HEPES 8.0, 160 mM LiSO₄, 40 mM NaOAc, 20% glycerol, 0.25 mM InsP₆, 1 mM DTT and 100 mM NaCl, and flash frozen in liquid nitrogen.

The Dbp5–CTD(L327V)/InsP₆/Gle1(WT) crystals were grown using the same methods as for Dbp5–CTD(L327V)/InsP₆/Gle1(H337R), but proteins were subjected to gel filtration individually before forming 1:1 complexes by direct mixing. Crystallization was performed by mixing 20 mg ml^{-1} of selenomethionine-labelled protein solution in gel filtration buffer (with NaCl increased to 150 mM) with a solution containing 30% PEG 3350, 100 mM HEPES 7.8 and 200 mM LiSO₄ and incubating for 5 days. Crystals were cryoprotected by diluting into a solution containing 24% PEG 3350, 80 mM HEPES 7.8, 160 mM LiSO₄, 10% glycerol, 0.4 mM InsP₆, 1 mM DTT and 120 mM NaCl, and flash frozen in liquid nitrogen.

The $\Delta 90\text{Dbp5(L327V)/RNA/ADP}\cdot\text{BeF}_3$ complex was formed by mixing a solution containing unlabelled $\Delta 90\text{Dbp5(L327V)}$ in gel filtration buffer (with the addition of 5 mM MgCl₂) with a 1.2:1 molar ratio of rU₁₀ RNA (IDT), incubating for 15 min, and then mixing with ADP $\cdot\text{BeF}_3$ (prepared in a 1:3:15 ratio of ADP:Be:F) to a final concentration of 1 mM, followed by another 15 min of incubation. Crystals of the $\Delta 90\text{Dbp5(L327V)/RNA/ADP}\cdot\text{BeF}_3$ complex were grown by mixing 100 nl of the complex at a protein concentration of 15 mg ml^{-1} with 100 nl of a solution containing 200 mM MgNO₃ and 20% PEG 3350 (The PEGs Suite, condition #64; Qiagen) and incubating for 7 days. Crystals were cryoprotected by diluting in a solution containing 18% PEG 3350, 9 mM HEPES pH 7.5, 180 mM MgNO₃, 4.5% glycerol, 1 mM DTT, 90 mM NaCl, 0.5 mM InsP₆, 4.5 mM MgCl₂ and 1 mM ADP $\cdot\text{BeF}_3$ (prepared in a 1:3:15 ratio of ADP:Be:F), and flash frozen in liquid nitrogen. The $\Delta 90\text{Dbp5/RNA/ADP}\cdot\text{BeF}_3$ crystals were grown in the same manner using wild type $\Delta 90\text{Dbp5}$.

The $\Delta 90\text{Dbp5(L327V)/InsP}_6\text{/Gle1(H337R)/ADP}$ complex was formed by mixing the unlabelled protein solution with ADP to a final concentration of 0.5 mM and incubated for 15 min. Crystals were grown by mixing 200 nl of a solution containing 30% PEG 300 and 100 mM MES pH 6.5 with 50 nl of a 10% MPD additive solution, adding 250 nl of protein–ADP complex at 15 mg ml^{-1} protein in gel filtration buffer (with the addition of 10 mM MgCl₂), and incubating for 9 days. Crystals were cryoprotected by diluting in a solution containing 27% PEG 300, 90 mM MES pH 6.5, 9 mM HEPES pH 7.5, 5.4% MPD, 90 mM NaCl, 9 mM MgCl₂, 0.9 mM DTT, 0.9 mM ADP, 0.45 mM InsP₆ and 4.5% glycerol and flash frozen in liquid nitrogen.

The Nup159/ $\Delta 90\text{Dbp5(L327V)/InsP}_6\text{/Gle1(H337R)/ADP}$ complex was formed by mixing the unlabelled protein solution with ADP to a final concentration of 1.0 mM, and incubating for 15 min. Crystals were grown by mixing 200 nl of a solution containing 20% PEG 33350 and 200 mM KOAc with 50 nl of a 100 mM sarcosine additive solution, adding 250 nl of protein–ADP complex at 15 mg ml^{-1} protein in gel filtration buffer (with the addition of 10 mM MgCl₂), and incubating for 5 days. Crystals were cryoprotected by diluting in a solution

containing 27% PEG 3350, 180 mM KOAc, 90 mM NaCl, 9 mM HEPES pH 7.5, 9 mM sarcosine, 9 mM MgCl₂, 0.9 mM DTT, 0.9 mM ADP, 0.45 mM InsP₆ and 4.5% glycerol and flash frozen in liquid nitrogen.

Data collection, structure solution and refinement. All data were collected at beamline 8.3.1 at the Advanced Light Source at 100 Kelvin³⁰, and processed using either HKL2000 or ELVES^{31,32} (see also later). Structures were solved with the AutoSol or AutoMR components of PHENIX³³. Iterative rounds of manual model building in COOT³⁴, coupled with refinement using PHENIX³³ and stereochemical validation using MOLPROBITY³⁵, resulted in final models displaying excellent geometry and $R_{\text{work}}/R_{\text{free}}$ values for their respective resolutions, as well as no Ramachandran outliers. Rigid body refinement was conducted on Gle1 and Dbp5 RecA-like domains for all structures solved by molecular replacement in order to reveal any rigid-body differences among the structures. Simulated annealing omit maps were calculated to confirm the presence of all ligands (Supplementary Fig. 6). For all structures solved by molecular replacement, simulated annealing composite omit maps and prime and switch maps, both made using the AutoBuild component of PHENIX³³, were calculated to help remove model bias.

MAD data were collected at wavelengths of 0.9796, 0.9798 and 1.020 Å for the Dbp5–CTD(L327V)/InsP₆/Gle1(H337R) crystals in inverse beam mode and processed in HKL2000³¹ (Supplementary Table 1). The structure was solved using PHENIX AutoSol, which found 11 selenium sites and gave figures of merit of 0.5 and 0.7 for phasing and density modification, respectively. An initial model was built using PHENIX AutoBuild³³. For the final model, atomic coordinates, individual atomic displacement parameters (B-factors), translation/libration/screw (TLS) parameters, and f' and f'' parameters for the Se atoms were refined against the unmerged Friedel pairs (F+ and F−) of the remote data set as implemented in PHENIX. Ramachandran statistics are 98.3% preferred, 1.7% allowed and 0% outliers as reported by Molprobit³⁵.

A single low-energy remote data set was collected at a wavelength of 1.116 Å for the Dbp5–CTD(L327V)/InsP₆/Gle1(WT) crystals and processed in HKL2000 with merging of Friedel pairs. The structure was solved using PHENIX AutoMR by searching for a single copy of the fully refined Dbp5–CTD(L327V)/InsP₆/Gle1(H337R) structure³³. For the final model, atomic coordinates, individual atomic displacement parameters (B-factors), and TLS parameters were refined. The refinement test set was copied from the isomorphous Dbp5–CTD(L327V)/InsP₆/Gle1(H337R) data and extended to higher resolution in order to avoid biasing the R_{free} . Ramachandran statistics are 98.0% preferred, 2.0% allowed and 0% outliers as reported by Molprobit³⁵.

Native data were collected on the $\Delta 90\text{Dbp5(L327V)/RNA/ADP}\cdot\text{BeF}_3$ crystals at a wavelength of 1.116 Å and processed in HKL2000. The structure was solved using PHENIX AutoMR by searching for a single copy of a *S. cerevisiae* Dbp5 homology model (SWISS-MODEL^{33,36}, created using the human Ddx19/RNA/AMPPNP structure as a template (PDB accession code 3G0H)²⁵. For the final model, atomic coordinates, B-factors, TLS parameters and occupancies for residues with alternate conformations were refined. Custom bond restraints were used for octahedral Mg²⁺–H₂O clusters and the ADP $\cdot\text{BeF}_3$ molecule. Ramachandran statistics are 99.2% preferred, 0.8% allowed and 0% outliers as reported by Molprobit³⁵.

Native data were collected on the $\Delta 90\text{Dbp5(WT)/RNA/ADP}\cdot\text{BeF}_3$ crystals at a wavelength of 1.116 Å and processed in HKL2000. The structure was solved using PHENIX AutoMR by searching for a single copy of the fully refined $\Delta 90\text{Dbp5(L327V)/RNA/ADP}\cdot\text{BeF}_3$ structure and refined in the same manner³³. Ramachandran statistics are 98.5% preferred, 1.5% allowed and 0% outliers as reported by Molprobit³⁵.

Native data were collected on the $\Delta 90\text{Dbp5(L327V)/InsP}_6\text{/Gle1(H337R)/ADP}$ crystals at a wavelength of 1.116 Å and processed in ELVES. The structure was solved using PHENIX AutoMR by searching for a single copy of the fully refined Gle1(H337R)/InsP₆/Dbp5–CTD(L327V) structure and a single copy of the Dbp5–NTD (residues 101–293) of the fully refined $\Delta 90\text{Dbp5(L327V)/RNA/ADP}\cdot\text{BeF}_3$ structure³³. B-factor sharpening was used throughout model building. Initial $F_o - F_c$ difference density showed that two additional InsP₆ molecules were present in the structure. Although the InsP₆ molecules have high relative B-factors, they mediate crystal-packing contacts and are coordinated by a large number of basic and polar residues. For the final structure, atomic coordinates and TLS parameters were refined. Secondary structure restraints as implemented in PHENIX were used throughout refinement to maintain proper backbone geometry. Ramachandran statistics are 97.6% preferred, 2.4% allowed and 0% outliers as reported by Molprobit³⁵.

Native data were collected on the Nup159/ $\Delta 90\text{Dbp5(L327V)/InsP}_6\text{/Gle1(H337R)/ADP}$ crystals at a wavelength of 1.116 Å and processed in HKL2000. The structure was solved using PHENIX AutoMR by searching for a single copy each of Gle1, the Dbp5–NTD, the Dbp5–CTD and Nup159 (PDB accession code 1XIP)^{8,33}. For the

final model, atomic coordinates and TLS parameters were refined. Ramachandran statistics are 97.3% preferred, 2.7% allowed and 0% outliers as reported by MolProbity³⁵.

Structural analysis. All structural analysis and rendering for figures was performed with PyMOL (Schrödinger, LLC). Solvent accessible electrostatics in Fig. 1 was calculated using ABSP³⁷. Energy minimized linear interpolations shown in Supplementary Movies 1–3 were made using a CNS script written by the Yale Morph Server^{38,39}.

Complex formation and gel filtration. To assay for Dbp5–Gle1 complex formation, 100 µl of a binding reaction was applied to a Superdex 200 gel filtration column (GE Healthcare) in the presence of 30 mM HEPES (pH 7.5), 150 mM NaCl, 1 mM DTT, 0.25 mM InsP₆ and 5% glycerol at 0.4 ml min^{−1}. Binding reactions contained Dbp5 (20 µM) and Gle1 (40 µM) mixed with column buffer.

ATPase assays. ATPase assays using Dbp5 were performed as previously described¹⁰. When present, Nup159 was added to a final concentration of 1 µM.

RNA binding and release assay. The RNA substrate used for the binding and release assays was a 29-nucleotide single-stranded (ss)RNA of the sequence 5'-GGGUAAAAAAAAAAAAAAAAAAAAAAAAA-3' for Dbp5 or a 25-nucleotide ssRNA of the sequence 5'-GGGUACAACGGAAGACAGCAGAGAA for eIF4A carrying a fluorescein-conjugated UTP made by *in vitro* transcription (MEGAscript Kit, Ambion). RNA binding assays were performed as previously described^{10,40}. To perform RNA release assays, Dbp5(E240Q) (1.0 µM) or eIF4A(E172Q) (4.0 µM), FITC-RNA (40 nM), and ATP (2 mM) ± Gle1 (2.0 µM) or eIF4G (8.0 µM) were complexed for 5 min in a buffer containing 50 mM HEPES (pH 7.5), 140 mM KCl, 5 mM MgCl₂, 1 mM DTT, 20% glycerol, 0.1 mg ml^{−1} BSA and 10 µM InsP₆ for Dbp5 or 20 mM MES (pH 6.0), 20 mM KOAc, 5 mM MgCl₂, 1 mM DTT, 20% glycerol, and 0.1 mg ml^{−1} BSA for eIF4A. After rapid 1:1 mixing of DEAD-box-RNA binding reactions with polyA-RNA (1.0 mg ml^{−1}) using a stopped flow apparatus (RX2000; Applied Photophysics) linked to a Fluoromax-3 fluorimeter (Horiba Jobin Yvon), fluorescence intensities were measured every 0.05 to 0.2 s depending on the reaction. To measure fluorescent polarization, samples were excited with vertically polarized light (492 nm), and emission (521 nm) of vertically (I_{VV}) and horizontally (I_{VH}) polarized light was measured independently in two consecutive runs. Anisotropy (r) was then calculated using the equation: $r = (I_{VV} - (G \times I_{VH})) / (I_{VV} + (2 \times G \times I_{VH}))$, where $G = I_{HV} / I_{HH}$. Reported $t_{1/2}$ values are an average of three independent experiments ± standard deviation. Release curves were fit to a first order exponential decay curve using Kaleidagraph (Synergy Software).

ADP binding and release assays. 2'-(or-3')-O-(N-methylanthraniloyl)adenosine 5'-diphosphate (MANT-ADP) (Invitrogen) was used for the binding and

release assays with Dbp5(E240Q). MANT-ADP binding assays were performed in a manner similar to the RNA binding assay¹⁰. Briefly, Dbp5(E240Q) (0–2 µM) and MANT-ADP (100 nM) were mixed with buffer (50 mM HEPES pH 7.5, 140 mM KCl, 5 mM MgCl₂, 1 mM DTT, 20% glycerol, 0.1 mg ml^{−1} BSA and 10 µM InsP₆) and RNA (1 mg ml^{−1}) or Gle1 (2 µM) as indicated. After mixing, anisotropy was measured using a Fluoromax-3 fluorimeter (Horiba Jobin Yvon). To perform the release assay, Dbp5(E240Q) (1 µM) was complexed with MANT-ADP (100 nM) for 5 min ± Gle1 (2 µM) and/or RNA (1 mg ml^{−1}) in a buffer containing 50 mM HEPES pH 7.5, 140 mM KCl, 5 mM MgCl₂, 1 mM DTT, 20% glycerol, 0.1 mg ml^{−1} BSA and 10 µM InsP₆. After rapid 1:1 mixing of Dbp5-MANT-ADP reactions with excess ADP (2 mM) using a stopped flow apparatus (RX2000; Applied Photophysics) linked to a Fluoromax-3 fluorimeter (Horiba Jobin Yvon), fluorescence intensities were measured every 0.01 s using 370 nm (excitation) and 445 nm (emission) light. Fluorescent polarization and $t_{1/2}$ values were calculated as described earlier for the RNA release assays.

29. Kapust, R. B. & Waugh, D. S. Controlled intracellular processing of fusion proteins by TEV protease. *Protein Expr. Purif.* **19**, 312–318 (2000).
30. MacDowell, A. A. *et al.* Suite of three protein crystallography beamlines with single superconducting bend magnet as the source. *J. Synchrotron Radiat.* **11**, 447–455 (2004).
31. Otwinowski, Z. & Minor, W. in *Methods in Enzymology* (eds Carter, W. C. & Sweet, R. M.) 307–326 (Academic, 1997).
32. Holton, J. & Alber, T. Automated protein crystal structure determination using ELVES. *Proc. Natl Acad. Sci. USA* **101**, 1537–1542 (2004).
33. Adams, P. D. *et al.* PHENIX: a comprehensive Python-based system for macromolecular structure solution. *Acta Crystallogr. D* **66**, 213–221 (2010).
34. Emsley, P. & Cowtan, K. Coot: model-building tools for molecular graphics. *Acta Crystallogr. D* **60**, 2126–2132 (2004).
35. Davis, I. W. *et al.* MolProbity: all-atom contacts and structure validation for proteins and nucleic acids. *Nucleic Acids Res.* **35**, W375–W383 (2007).
36. Arnold, K., Bordoli, L., Kopp, J. & Schwede, T. The SWISS-MODEL workspace: a web-based environment for protein structure homology modelling. *Bioinformatics* **22**, 195–201 (2006).
37. Baker, N. A., Sept, D., Joseph, S., Holst, M. J. & McCammon, J. A. Electrostatics of nanosystems: application to microtubules and the ribosome. *Proc. Natl Acad. Sci. USA* **98**, 10037–10041 (2001).
38. Flores, S. *et al.* The Database of Macromolecular Motions: new features added at the decade mark. *Nucleic Acids Res.* **34**, D296–D301 (2006).
39. Brünger, A. T. *et al.* Crystallography & NMR system: a new software suite for macromolecular structure determination. *Acta Crystallogr. D* **54**, 905–921 (1998).
40. Lorsch, J. R. & Herschlag, D. The DEAD box protein eIF4A. 1. A minimal kinetic and thermodynamic framework reveals coupled binding of RNA and nucleotide. *Biochemistry* **37**, 2180–2193 (1998).

Neuronal activity is required for the development of specific cortical interneuron subtypes

Natalia V. De Marco García^{1*}, Theofanis Karayannis^{1*} & Gord Fishell¹

Electrical activity has been shown to regulate development in a variety of species and in various structures¹, including the retina^{2–4}, spinal cord^{5,6} and cortex⁵. Within the mammalian cortex specifically, the development of dendrites and commissural axons in pyramidal cells is activity-dependent^{7,8}. However, little is known about the developmental role of activity in the other major cortical population of neurons, the GABA-producing interneurons. These neurons are morphologically and functionally heterogeneous and efforts over the past decade have focused on determining the mechanisms that contribute to this diversity^{9–11}. It was recently discovered that 30% of all cortical interneurons arise from a relatively novel source within the ventral telencephalon, the caudal ganglionic eminence (CGE)^{11,12}. Owing to their late birth date, these interneurons populate the cortex only after the majority of other interneurons and pyramidal cells are already in place and have started to functionally integrate. Here we demonstrate in mice that for CGE-derived reelin (Re)-positive and calretinin (Cr)-positive (but not vasoactive intestinal peptide (VIP)-positive) interneurons^{12,13}, activity is essential before postnatal day 3 for correct migration, and that after postnatal day 3, glutamate-mediated activity controls the development of their axons and dendrites. Furthermore, we show that the engulfment and cell motility 1 gene (*Elmo1*)¹⁴, a target of the transcription factor distal-less homeobox 1 (*Dlx1*)¹⁵, is selectively expressed in Re⁺ and Cr⁺ interneurons and is both necessary and sufficient for activity-dependent interneuron migration. Our findings reveal a selective requirement for activity in shaping the cortical integration of specific neuronal subtypes.

Experimental evidence indicates that interneurons are electrically active shortly after their birth and participate in the early network activity that may contribute to circuit maturation in the neonatal cortex^{16–18}. However, the role of activity in developing interneuron subtypes has not been addressed. Here we demonstrate that altering the level of neuronal excitability *in vivo* within genetically targeted CGE-derived interneurons has profound consequences on multiple aspects of the development of select subtypes within this population, as well as their associated gene expression (Supplementary Fig. 1).

To suppress neuronal excitability within CGE-derived interneurons, we electroporated *in utero* the inward rectifying potassium channel Kir2.1 under the control of the *Dlx5/6* enhancer element¹⁹ at embryonic day (E)15.5, which results in selective expression within CGE-derived interneuron populations (Supplementary Fig. 2). Kir2.1-overexpression has been shown to affect activity by lowering the resting membrane potential (V_{rest}), therefore altering neuronal excitability²⁰. We detected expression of this channel by *in situ* hybridization (Supplementary Fig. 3a, b). To functionally assess the presence of membrane-targeted channels, we performed whole-cell patch-clamp recordings from *Dlx5/6-Kir2.1*, *Dlx5/6-eGFP* co-electroporated interneurons in voltage clamp at P8–P9. Current/voltage (I/V) curve analysis indicated the presence of an inward rectifying potassium conductance that was active at V_{rest} and was blocked by 300 μM barium, a concentration that

preferentially blocks Kir2.1 channels (Supplementary Fig. 3d–g). Consistent with these observations, the V_{rest} of Kir2.1-electroporated interneurons was significantly more hyperpolarized than that of interneurons electroporated with eGFP alone (Supplementary Fig. 3c).

By postnatal day (P)8, subsets of the interneurons expressing the Kir2.1 channel showed pronounced defects in their morphologies (Fig. 1 and Supplementary Figs 4a, b, 5). To quantify alterations in dendrites and axons, we reconstructed interneuron morphologies from cortical slices at P8–P9, the earliest stages at which interneuron subtypes can be consistently delineated by expression of immunochemical markers. Our analysis revealed that the total length of axonal arborizations was significantly reduced in multipolar and bipolar Cr⁺ interneurons, as well as neurogliaform and dense plexus Re⁺ subtypes, whereas those of multipolar VIP⁺ interneurons remained unaltered (Fig. 1 and Supplementary Fig. 4a, b). Quantification of axonal nodes and ends (see Methods) also revealed scantily branched axons in Cr⁺ and Re⁺ subtypes but not in VIP⁺ interneurons (Fig. 1b and Supplementary Fig. 5a–c). Although total dendritic length was not significantly decreased in Re⁺ interneurons (Fig. 1c), this subtype exhibited less complex dendritic trees (Fig. 1c and Supplementary Fig. 5f). In contrast, VIP⁺ and Cr⁺ interneurons showed normal dendritic morphologies (Fig. 1c and Supplementary Fig. 5d, e). To assess whether the morphological defects observed in Cr⁺ and Re⁺ interneurons were due to a developmental delay, we analysed the electrophysiological properties and morphology of these interneurons at P15–19. Despite possessing mature intrinsic properties, Cr⁺ and Re⁺ interneurons at P15–19 showed morphological defects similar to those found at P8 (Supplementary Fig. 4c–h). These findings indicate that the observed defects are unlikely to be simply a result of a developmental delay in maturation.

Although neuronal activity has been shown to be dispensable for the migration of pyramidal cells⁷, we noticed a pronounced overall shift in the laminar positioning of CGE subtypes expressing Kir2.1. CGE-derived interneurons migrate tangentially from the ventral telencephalon to the cortex where they then undergo radial migration to reach stereotypic positions in cortical laminae by P7. To assess the role of neuronal activity during interneuron migration, we used a *tetO-Kir2.1.ires.LacZ* transgenic mouse line in which Kir2.1 and LacZ are expressed on binding of the tet transactivator (Tta) to the *tetO* element²⁰. We electroporated a *Dlx5/6-Tta* plasmid together with *Dlx5/6-eGFP*, again at E15.5 (Supplementary Fig. 6a), to induce Kir2.1 expression selectively in CGE-derived interneurons. These experiments revealed that the tangential migration of interneurons expressing Kir2.1 was indistinguishable from control populations at early developmental stages (Fig. 2a). However, after P5, and in agreement with the constitutive *Dlx5/6-Kir2.1* electroporation experiment, interneurons that expressed Kir2.1 were found to occupy deeper cortical layers than control populations (Fig. 2a). To analyse the selectivity of this defect, we quantified the distribution of Cr⁺, Re⁺ and VIP⁺ interneurons across all cortical layers. We detected a significantly higher percentage of Kir2.1 Cr⁺ interneurons in layer IV and a concomitant

¹Smilow Neuroscience Program, Departments of Cell Biology and Neural Science, New York University Langone Medical Center, New York, New York 10016, USA.

*These authors contributed equally to this work.

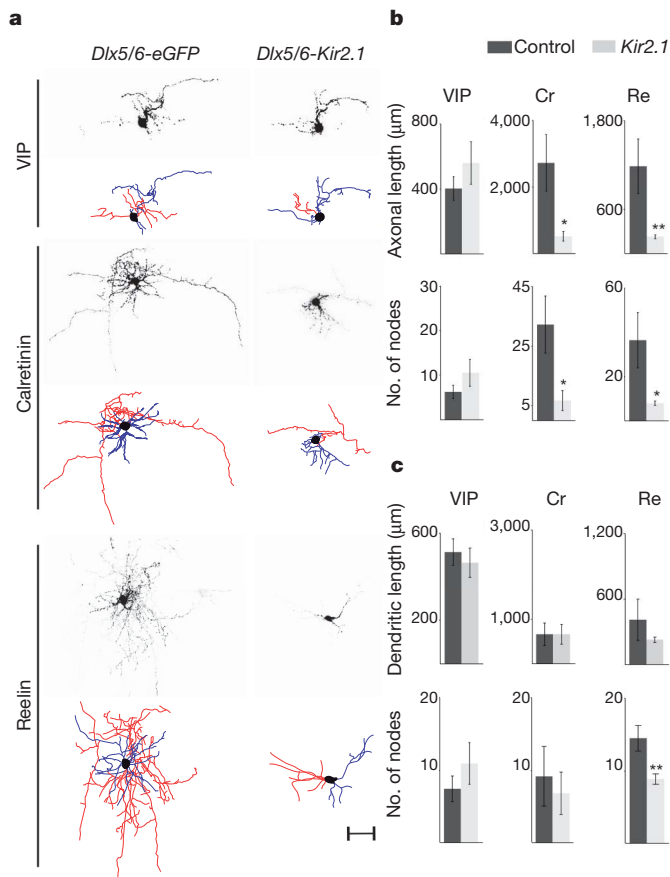


Figure 1 | Defective morphology of Cr⁺ and Re⁺ interneuron subtypes resulting from Kir2.1 expression. **a**, Representative examples of P8 VIP⁺, Cr⁺ and Re⁺ interneurons in mice electroporated at E15.5 with *Dlx5/6-eGFP* (control) or *Dlx5/6-eGFP, Dlx5/6-Kir2.1* plasmids at E15.5. Photomicrographs of eGFP expression and corresponding neuroLucida reconstructions depicting axons (red), dendrites (blue) and somata (black). Scale bar, 50 μm. **b**, Morphometric analysis of control and Kir2.1-expressing VIP⁺, Cr⁺ and Re⁺ subtypes including the total length of axonal arborizations (top) and number of axonal nodes (bottom). **c**, Total length of dendritic trees (top) and number of dendritic nodes (bottom) in the same subtypes. Mean values (± s.e.m.) were obtained from >4 reconstructed interneurons each in *Dlx5/6-eGFP* and *Dlx5/6-eGFP, Dlx5/6-Kir2.1* electroporated mice. Paired *t*-test: **P* < 0.05, ***P* < 0.01.

reduction in the percentage of this population in layers II/IIIIt (where II/IIIIt refers to II/III, top, as layers II and III have not sorted out by this developmental timepoint) compared to controls (Fig. 2b). Similarly, in electroporated *tetO-Kir2.1.ires.LacZ* mice we observed a significantly lower percentage of Re⁺ interneurons in layer II/IIIIt and a subsequent increase in layer II/IIIb (where II/IIIb refers to II/III, bottom) compared to controls (Fig. 2b). In contrast, the distribution of VIP⁺ interneurons in electroporated *tetO-Kir2.1.ires.LacZ* mice was similar to that observed in controls (Fig. 2b). Our results indicate that neuronal activity is a determinant in the allocation of Cr⁺ and Re⁺ subtypes to defined cortical layers.

One interpretation of our results is that the morphological defects observed in Cr⁺ and Re⁺ Kir2.1-expressing interneurons are an indirect consequence of the laminar mispositioning in the cortex. Alternatively, neuronal activity may regulate laminar migration and morphological maturation independently. To distinguish between these two possibilities, we took advantage of the ability of doxycycline to suppress Kir2.1 expression from the *tetO-Kir2.1.ires.LacZ* transgenic line²⁰ and administered it at different developmental time points (Supplementary Fig. 6a). We were able to monitor the expression of the Kir2.1 transgene by assessing β-galactosidase activity (Fig. 3b). To determine whether

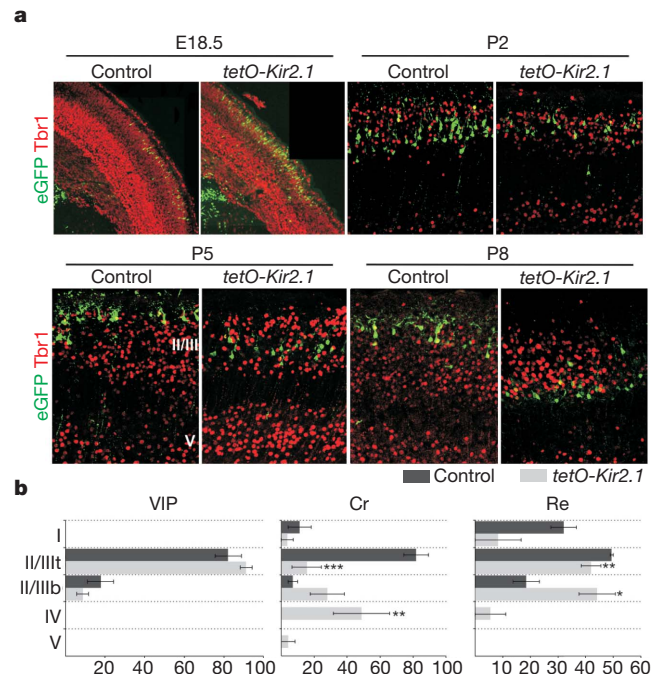


Figure 2 | Neuronal activity is essential for the proper laminar migration of selective interneuron subtypes. **a**, Laminar positioning of electroporated interneurons in wild-type mice (control) and *tetO-Kir2.1.ires.LacZ* littermates both co-electroporated with *Dlx5/6-Tta* and *Dlx5/6-eGFP* plasmids at E15.5. Tbr1 expression delineates layers II/III and V at P5–P8. Representative examples taken from the analysis of four control and six *tetO-Kir2.1.ires.LacZ* electroporated mice for each developmental stage. **b**, Quantification of the distribution of VIP⁺, Cr⁺ and Re⁺ interneuron subtypes across cortical layers at P8. Owing to the lack of selective molecular markers to distinguish between cortical layer II and III at P8–P9, we divided these layers collectively into II/IIIIt and II/IIIb (where II/IIIIt and II/IIIb refer to II/III top and II/III bottom, respectively). Mean percentage values (± s.e.m.) were obtained from four wild-type and six *tetO-Kir2.1.ires.LacZ* electroporated mice. Paired *t*-test: **P* < 0.05, ***P* < 0.01, ****P* < 0.001.

Kir2.1 expression had any effects on early interneuron differentiation, we treated *Dlx5/6-Tta* and *Dlx5/6-eGFP* E15.5-electroporated pregnant mice with doxycycline at E16.5. As it takes approximately three days for doxycycline administration to fully and irreversibly suppress the expression of Kir2.1 and LacZ (Supplementary Fig. 7), in these experiments Kir2.1 expression is shut off from P0 onwards. We found that Kir2.1 expression before P0 had no effect on the laminar position, immunochemical profile, morphology or intrinsic physiological properties of CGE-derived interneurons analysed at P8–P9 (Fig. 3a, data not shown). Thus, interneuron specification and maturation proceed normally if Kir2.1 is shut off by P0.

In contrast, migration defects persisted when Kir2.1 expression was shut off at P3 (Fig. 3a). Remarkably, despite their abnormal laminar position under these conditions, the morphology of Cr⁺ and Re⁺ subtypes was unperturbed (Fig. 3c, d). The total length and complexity of Cr⁺ and Re⁺ interneuron axonal arborizations was not significantly different in doxycycline-treated *tetO-Kir2.1.ires.LacZ* mice compared to wild-type controls (Fig. 3d and Supplementary Fig. 6b, d). Similarly, the complexity of the dendritic trees in Kir2.1-expressing Re⁺ interneurons after doxycycline treatment was similar to that observed in controls (Fig. 3d and Supplementary Fig. 6c). In contrast, both morphological and migratory defects persisted in *tetO-Kir2.1.ires.LacZ* mice in which Kir2.1 expression was turned off from P5 onwards (Supplementary Fig. 8, data not shown). Together these findings revealed that neuronal activity is independently required between P0 and P3 to regulate laminar position and after P3 to control the morphological development of specific interneuron subtypes.

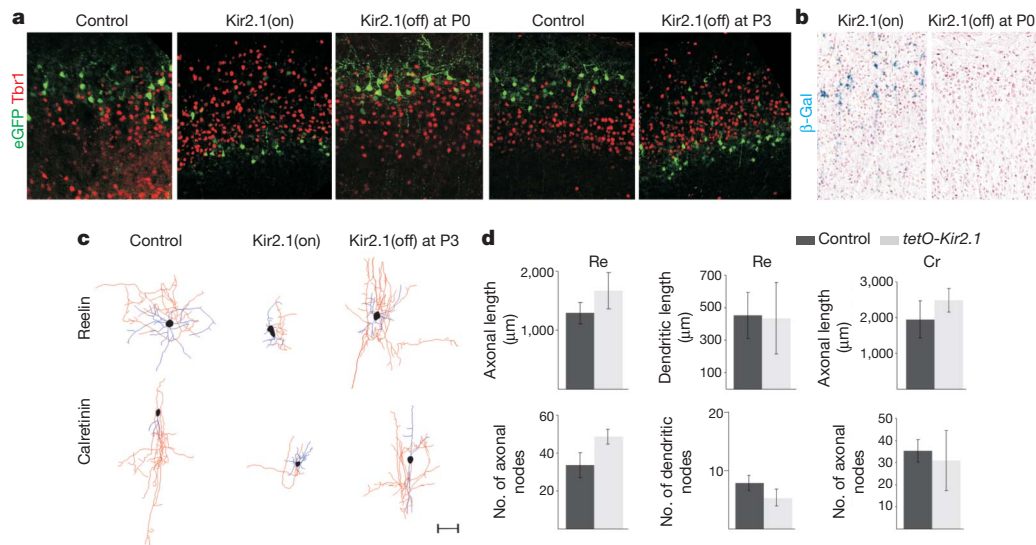


Figure 3 | Specific interneuron subtypes require activity for migration and morphological maturation at two distinct stages of development. **a**, Laminar positioning of P8 electroporated interneurons in wild-type mice (control) and *tetO-Kir2.1.ires.LacZ* mice both co-electroporated with *Dlx5/6-Tta* and *Dlx5/6-eGFP* plasmids at E15.5. Mice received either no treatment (Kir2.1(on)); or were treated with doxycycline at E16.5 (Kir2.1(off) at P0 onwards); or with doxycycline at P0 (Kir2.1(off) at P3 onwards). **b**, β -Galactosidase (β -Gal) activity in P8 *tetO-Kir2.1.ires.LacZ* mice co-electroporated with *Dlx5/6-Tta* and *Dlx5/6-eGFP* plasmids either untreated or treated with doxycycline at E16.5 (Kir2.1(off) at P0 onwards). **c**, Neurolucida reconstructions of Cr⁺ and Re⁺

interneurons in wild-type (control) and *tetO-Kir2.1.ires.LacZ* mice both co-electroporated with *Dlx5/6-Tta* and *Dlx5/6-eGFP* plasmids. Mice received either no doxycycline treatment (Kir2.1(on)) or doxycycline at P0 (Kir2.1(off) at P3 onwards). Axons are shown in red, dendrites in blue and somata in black. Scale bar, 50 μ m. **d**, Quantification of dendritic and axonal morphology in control and experimental Cr⁺ and Re⁺ interneurons in *tetO-Kir2.1.ires.LacZ* mice after doxycycline administration at P0. Mean percentage values (\pm s.e.m.) were obtained from >3 reconstructed interneurons each in doxycycline-treated wild-type and *tetO-Kir2.1.ires.LacZ* mice for each subtype analysed at P8.

It is unclear what kinds of activity might be responsible for controlling these distinct aspects of subtype-specific integration at different developmental stages. Experimental evidence indicates that a large proportion of developing neurons in the central nervous system show correlated spontaneous activity^{21–23}. This activity results in prominent cortical activity patterns apparent during the first postnatal week such as glutamate-dependent cortical early network oscillations¹⁶. Interestingly, cortical interneurons have the ability to participate in such activity as they express glutamate receptors at early stages of development²⁴. To explore the possibility that interneuron maturation is regulated by glutamate-driven ionotropic receptor activity, we used kynurenic acid, an NMDA and AMPA/kainate receptor blocker²⁵. We applied either kynurenic acid diluted in PBS or PBS alone (control) subdurally to the brains of *Dlx5/6-eGFP* electroporated mice at P0, P1, P2 and P3 and analysed interneuron migration and morphology at P8–P9 (Supplementary Fig. 9a and Fig. 4). Migration of all subtypes was normal after kynurenic acid injections at all ages tested (see Supplementary Information). In contrast, we observed morphological defects in Cr⁺ and Re⁺ subtypes in mice injected with kynurenic acid at P3 (but not after administration at earlier ages, that is, P0, P1, P2). These subtype-specific defects were reminiscent of those found in the Kir2.1 experiments (Fig. 4). Specifically, the total axonal length and complexity of Cr⁺ and Re⁺ interneurons was significantly reduced after kynurenic acid treatment (Fig. 4b and Supplementary Fig. 9d, f). Dendritic trees of Re⁺ interneurons in kynurenic-acid-treated mice also showed a trend towards a reduction in overall length and a simplified morphology compared to controls (Fig. 4c and Supplementary Fig. 9g). In contrast, VIP⁺ interneurons were not affected by kynurenic acid treatment (Fig. 4 and Supplementary Fig. 9b, c). These results indicate that ionotropic glutamate receptor-mediated activity is required after P3 to regulate the subtype-specific development of neuronal morphology but does not control their selection of cortical laminae.

To explore the molecular mechanism underlying the activity-dependent maturation of CGE-derived interneuron subtypes, we examined transcriptional programs that operate in these interneurons at early developmental stages^{26,27}. Previous experimental evidence

indicates that *Dlx1* is essential for both proper cortical migration and morphological development of GABAergic interneurons^{15,26,28}. To determine whether *Dlx1* expression is modulated by activity, we analysed the expression of the DLX protein in control and Kir2.1-electroporated interneurons. We found that Kir2.1-expressing interneurons show lower levels of DLX expression compared to controls at P5 (Fig. 5a, c). Reduced levels of DLX expression are likely to represent attenuated *Dlx1* and/or *Dlx2* expression (see Methods). To confirm that the *Dlx1* transcriptional program is downregulated in Kir2.1-expressing interneurons, we assessed the expression of the neuronal PAS domain protein 1 (NPAS1), a previously described *Dlx1* target²⁸. Consistent with a downregulation of *Dlx1*, we found that levels of NPAS1 in Re⁺ subtypes were reduced upon Kir2.1 expression (Supplementary Fig. 10).

Another gene that was also shown to be a target of *Dlx* genes is *Elmo1*¹⁵, which encodes an evolutionarily conserved Rac-activator protein¹⁴. We assessed ELMO1 expression in developing GABAergic interneurons (Fig. 5b), because it has been implicated in cytoskeletal reorganization and migration in the immune system^{14,29}. It is also significantly downregulated in *Dlx1/2* knockout mice¹⁵, which show severe interneuron migration defects. We found that ELMO1 is expressed by Re⁺ and Cr⁺ but not VIP⁺ subtypes and is downregulated upon Kir2.1 expression (Fig. 5b, c). To investigate whether loss of ELMO1 function can lead to defects in interneuron migration and morphological maturation, we co-electroporated E15.5 CGE-derived interneurons with a dominant-negative form of the ELMO1 protein that impairs Rac activation, *Dlx5/6-Elmo1_TN558.Flag*³⁰, and *Dlx5/6-eGFP*. At P9, we detected immunoreactivity against the Flag epitope, indicating that there is robust expression of the dominant-negative protein in electroporated interneurons (Fig. 5d, inset). Interestingly, whereas electroporated Re⁺ and Cr⁺ interneurons show normal morphological development, these interneurons were found to be distributed within deeper layers compared to *Dlx5/6-eGFP* controls (Fig. 5d, f; data not shown). In agreement with the lack of ELMO1 expression in VIP⁺ interneurons, neither their migration nor their morphology was affected by overexpression of the dominant-negative protein (data not

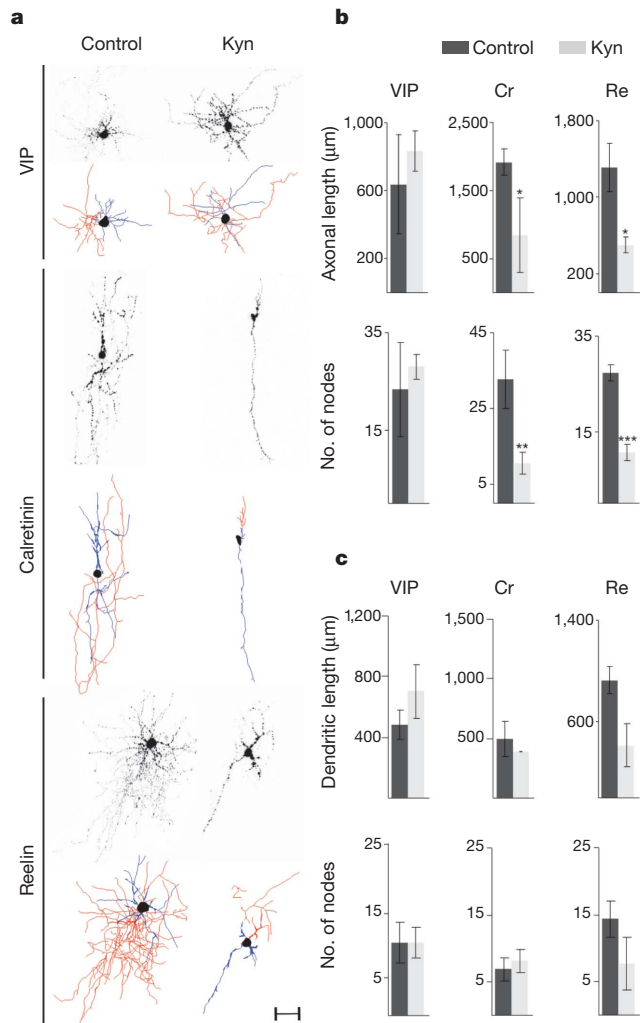


Figure 4 | Ionotropic glutamate receptor blockade mimics the effects of Kir2.1 expression on Cr⁺ and Re⁺ interneuron morphology. **a**, Representative examples of P8 VIP⁺, Cr⁺ and Re⁺ interneurons in *Dlx5/6-eGFP* electroporated mice at E15.5 injected with PBS (control) or kynurenic acid (Kyn) at P3 and corresponding neuroLucida reconstructions depicting axons (red), dendrites (blue) and somata (black). Scale bar, 50 μ m. **b**, **c**, Morphometric analysis of control and kynurenic-acid-treated neurons including the total length of axonal arborizations (**b**, top) and the number of axonal nodes (**b**, bottom), and the total length of dendritic trees (**c**, top) and the number of dendritic nodes (**c**, bottom) in VIP⁺, Cr⁺ and Re⁺ subtypes. Mean percentage values (\pm s.e.m.) were obtained from three electroporated interneurons each in control and kynurenic-acid-treated mice for each subtype. Paired *t*-test: **P* < 0.05, ***P* = 0.05, ****P* < 0.01.

shown). Our observations indicate that ELMO1 is necessary for the proper radial migration of Re⁺ and Cr⁺ subtypes.

To address whether the reduction in ELMO1 expression is responsible for the abnormalities in laminar migration observed in Kir2.1-expressing Re⁺ interneurons, we co-electroporated E15.5 interneurons with a *Dlx5/6-Elmo1* construct together with *Dlx5/6-Kir2.1* and *Dlx5/6-eGFP* plasmids. We reasoned that if so the recovery of ELMO1 expression in Re⁺ and Cr⁺ Kir2.1-electroporated interneurons would rescue their migratory defects. Remarkably, the migration but not the morphology of these subtypes appeared normal in Kir2.1-electroporated interneurons that co-expressed ELMO1 at P9 (Fig. 5e, f, data not shown). As expected, neither migratory nor morphological defects were detected in VIP⁺ interneurons. In contrast, expression of *Dlx5/6-Elmo1* plasmid in the absence of *Dlx5/6-Kir2.1* did not affect migration or the morphological maturation of Re⁺, Cr⁺ and VIP⁺ subtypes (data not shown). These results indicate that ELMO1 is necessary and sufficient for the proper

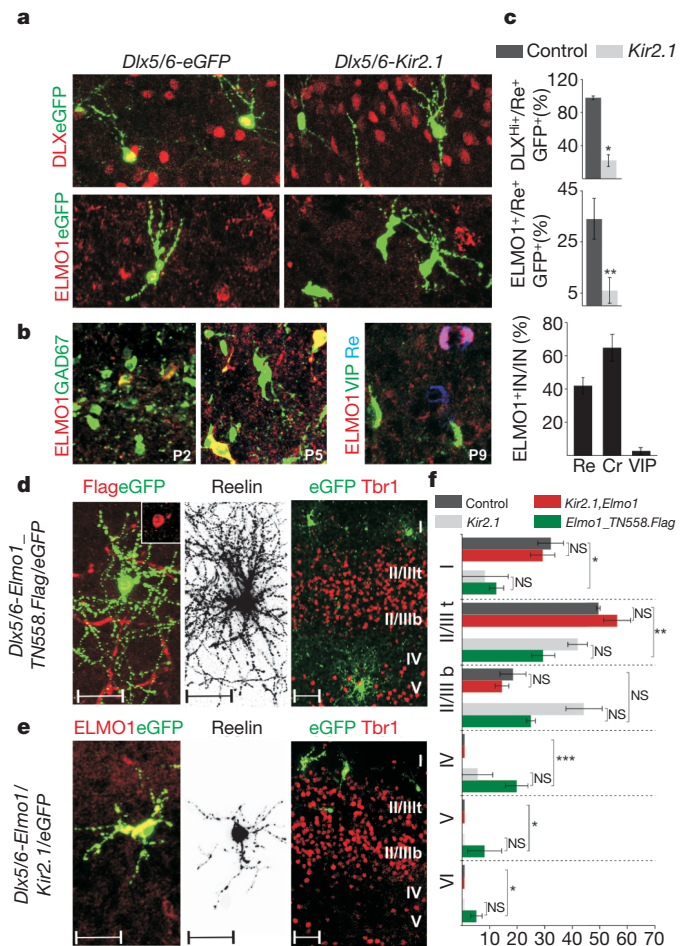


Figure 5 | Activity-dependent expression of ELMO1 regulates CGE-derived interneuron migration. **a**, Expression of *Dlx* genes and ELMO1 at P5 in *Dlx5/6-eGFP* and *Dlx5/6-Kir2.1* electroporated interneurons at E15.5. **b**, Expression of ELMO1 in *GAD67-GFP* transgenic mice at P2 and P5. Selective expression of ELMO1 in CGE-derived interneuron subtypes at P9. Quantification of ELMO1 expression in Re⁺, Cr⁺ and VIP⁺ interneurons (IN) at P9 (right). Mean percentage values (\pm s.e.m.) were obtained from >70 interneurons for each subtype. **c**, Quantification of DLX^{Hi} (where Hi refers to high level of DLX protein expression) and ELMO1 expression in *Dlx5/6-eGFP* (control) and *Dlx5/6-Kir2.1* Re⁺ E15.5 electroporated interneurons at P5. Mean percentage values (\pm s.e.m.) were obtained from >20 interneurons each in control and Kir2.1 electroporated mice for each quantification. **d**, Electroporation of *Dlx5/6-Elmo1-TN558.Flag* plasmid at E15.5. Flag immunoreactivity is detected in electroporated interneurons at P9 (inset). Neuronal morphology of a Re⁺ interneuron and laminar distribution of electroporated interneurons at P9. Representative examples from four electroporated mice. **e**, Co-electroporation of *Dlx5/6-Elmo1* and *Dlx5/6-Kir2.1* plasmids at E15.5. ELMO1 expression in electroporated interneurons at P9. Morphological defects of an electroporated Re⁺ interneuron and laminar distribution of electroporated interneurons. Representative examples from six electroporated mice. Scale bars for **d** and **e**, 50 μ m. **f**, Quantification of the distribution of Re⁺ interneurons across cortical layers at P9 on expression of different plasmids. Mean percentage values (\pm s.e.m.) were obtained from >80 interneurons for each group. Values for control and *Dlx5/6-Kir2.1* alone groups are repeated from Fig. 2 to facilitate comparison between groups. The large bracket indicates comparison between the control and *Dlx5/6-Elmo1-TN558.Flag* electroporated interneurons. Paired *t*-test: **P* < 0.05, ***P* < 0.01, ****P* < 0.0001.

activity-dependent migration of select interneuron subtypes. Taken together, our results indicate that the molecular machinery directing the maturation of Re⁺ and Cr⁺ interneurons, including *Dlx1*, *Npas1* and *Elmo1*, has evolved to be controlled by activity during development.

A role for *Dlx* genes in both interneuron migration and morphological development has been previously reported¹⁵; however, a link between *Dlx*

expression and neuronal activity has not been established. Our studies indicate that *Dlx1* expression and associated downstream targets are selectively regulated by activity in at least some interneuron subtypes. Specifically, *Dlx* genes induce the expression of *Elmo1*¹⁵, which is required for proper laminar migration of Re^+ and Cr^+ subtypes. Although we currently provide only correlative evidence for the link between activity-regulated expression of *Dlx1* and morphological development, the alteration in interneuron morphology observed in *Dlx1* null mutants supports this contention²⁸. These findings indicate that genetic programs initiated at the progenitor stage are modulated during development by activity. Thus, our studies indicate that the role of early network activity in shaping the development of specific neuronal subtypes in the central nervous system is greater than is presently appreciated.

METHODS SUMMARY

Mouse strains and *in utero* electroporation. Pregnant wild-type and genetically modified mice (see Methods) were electroporated at 15 days of gestation (E15.5) using a standard *in utero* electroporation technique³¹. The plasmids used in the electroporation experiments were generated using standard cloning techniques.

***In situ* hybridization and immunohistochemistry.** *In situ* hybridization and immunohistochemistry were performed as previously described³². For morphological reconstruction, vibratome sections were fixed and incubated overnight at 4 °C with selected antibodies.

Quantification of interneuron layer distribution. The proportion of Cr^+ , Re^+ and VIP^+ interneurons over the total number of electroporated interneurons across cortical layers was calculated in all cryostat tissue sections from individual brains. Tbr1 immunolabelling was used to delineate cortical layers II/III and V at P5–P8.

Kynurenic acid treatment. *Dlx5/6-eGFP* electroporated pups were anaesthetized by hypothermia. Kynurenic acid (300 nM, Sigma-Aldrich) diluted in PBS or pure PBS (controls) were injected at P0, P2 and P3. Treated brains in which electroporated interneurons were found in the vicinity of the injection site were used for analysis to minimize variability due to drug diffusion.

Electrophysiology. Whole-cell patch-clamp electrophysiological recordings were performed on eGFP-expressing cells in acute brain slices prepared from P8–P18 animals. Whole-cell recordings were made from randomly selected eGFP-positive neurons located in the upper layers (I–III) of the somatosensory cortex. Experiments were performed in both current-clamp and voltage-clamp modes.

Neuronal morphology analysis. Images of interneurons were obtained with a confocal microscope, analysed with LSM Image Browser, and reconstructed with NeuroLucida software (Version 9). To assess the length and complexity of dendritic and axonal arborizations, we quantified the number of nodes (points from which two or more branches arose) and ends (terminal branches) in each of these trees with NeuroLucida Explorer.

Statistical analysis. Statistical analysis was performed by using Student's *t*-test (two-tailed distribution, homoscedastic) unless otherwise stated.

Detailed methods on the mouse strains, animal surgery and electrophysiology protocols can be found in Methods.

Full Methods and any associated references are available in the online version of the paper at www.nature.com/nature.

Received 28 July 2010; accepted 18 January 2011.

Published online 3 April 2011.

- Blankenship, A. G. & Feller, M. B. Mechanisms underlying spontaneous patterned activity in developing neural circuits. *Nature Rev. Neurosci.* **11**, 18–29 (2010).
- Wong, R. O., Chernjavsky, A., Smith, S. J. & Shatz, C. J. Early functional neural networks in the developing retina. *Nature* **374**, 716–718 (1995).
- Penn, A. A., Riquelme, P. A., Feller, M. B. & Shatz, C. J. Competition in retinogeniculate patterning driven by spontaneous activity. *Science* **279**, 2108–2112 (1998).
- Huberman, A. D. *et al.* Architecture and activity-mediated refinement of axonal projections from a mosaic of genetically identified retinal ganglion cells. *Neuron* **59**, 425–438 (2008).
- Spitzer, N. C. Electrical activity in early neuronal development. *Nature* **444**, 707–712 (2006).
- Root, C. M., Velazquez-Ulloa, N. A., Monsalve, G. C., Minakova, E. & Spitzer, N. C. Embryonically expressed GABA and glutamate drive electrical activity regulating neurotransmitter specification. *J. Neurosci.* **28**, 4777–4784 (2008).
- Cancedda, L., Fiumelli, H., Chen, K. & Poo, M. M. Excitatory GABA action is essential for morphological maturation of cortical neurons *in vivo*. *J. Neurosci.* **27**, 5224–5235 (2007).

- Wang, C. L. *et al.* Activity-dependent development of callosal projections in the somatosensory cortex. *J. Neurosci.* **27**, 11334–11342 (2007).
- McBain, C. J. & Fisahn, A. Interneurons unbound. *Nature Rev. Neurosci.* **2**, 11–23 (2001).
- Ascoli, G. A. *et al.* Petilla terminology: nomenclature of features of GABAergic interneurons of the cerebral cortex. *Nature Rev. Neurosci.* **9**, 557–568 (2008).
- Batista-Brito, R. & Fishell, G. The developmental integration of cortical interneurons into a functional network. *Curr. Top. Dev. Biol.* **87**, 81–118 (2009).
- Miyoshi, G. *et al.* Genetic fate mapping reveals that the caudal ganglionic eminence produces a large and diverse population of superficial cortical interneurons. *J. Neurosci.* **30**, 1582–1594 (2010).
- Karube, F., Kubota, Y. & Kawaguchi, Y. Axon branching and synaptic bouton phenotypes in GABAergic nonpyramidal cell subtypes. *J. Neurosci.* **24**, 2853–2865 (2004).
- Gumienny, T. L. *et al.* CED-12/ELMO, a novel member of the Crkl/Dock180/Rac pathway, is required for phagocytosis and cell migration. *Cell* **107**, 27–41 (2001).
- Cobos, I., Borello, U. & Rubenstein, J. L. *Dlx* transcription factors promote migration through repression of axon and dendrite growth. *Neuron* **54**, 873–888 (2007).
- Allene, C. & Cossart, R. Early NMDA receptor-driven waves of activity in the developing neocortex: physiological or pathological network oscillations? *J. Physiol. (Lond.)* **588**, 83–91 (2010).
- Garaschuk, O., Linn, J., Eilers, J. & Konnerth, A. Large-scale oscillatory calcium waves in the immature cortex. *Nature Neurosci.* **3**, 452–459 (2000).
- Dupont, E., Hanganu, I. L., Kilb, W., Hirsch, S. & Luhmann, H. J. Rapid developmental switch in the mechanisms driving early cortical columnar networks. *Nature* **439**, 79–83 (2006).
- Stenman, J., Toresson, H. & Campbell, K. Identification of two distinct progenitor populations in the lateral ganglionic eminence: implications for striatal and olfactory bulb neurogenesis. *J. Neurosci.* **23**, 167–174 (2003).
- Yu, C. R. *et al.* Spontaneous neural activity is required for the establishment and maintenance of the olfactory sensory map. *Neuron* **42**, 553–566 (2004).
- Yang, J. W., Hanganu-Opatz, I. L., Sun, J. J. & Luhmann, H. J. Three patterns of oscillatory activity differentially synchronize developing neocortical networks *in vivo*. *J. Neurosci.* **29**, 9011–9025 (2009).
- Khazipov, R. & Luhmann, H. J. Early patterns of electrical activity in the developing cerebral cortex of humans and rodents. *Trends Neurosci.* **29**, 414–418 (2006).
- McCabe, A. K., Chisholm, S. L., Picken-Bahrey, H. L. & Moody, W. J. The self-regulating nature of spontaneous synchronized activity in developing mouse cortical neurones. *J. Physiol. (Lond.)* **577**, 155–167 (2006).
- Manent, J. B., Jorquera, I., Ben-Ari, Y., Aniksztejn, L. & Represa, A. Glutamate acting on AMPA but not NMDA receptors modulates the migration of hippocampal interneurons. *J. Neurosci.* **26**, 5901–5909 (2006).
- Stone, T. W. Neuropharmacology of quinolinic and kynurenic acids. *Pharmacol. Rev.* **45**, 309–379 (1993).
- Anderson, S. A., Eisenstat, D. D., Shi, L. & Rubenstein, J. L. Interneuron migration from basal forebrain to neocortex: dependence on *Dlx* genes. *Science* **278**, 474–476 (1997).
- Wonders, C. P. & Anderson, S. A. The origin and specification of cortical interneurons. *Nature Rev. Neurosci.* **7**, 687–696 (2006).
- Cobos, I. *et al.* Mice lacking *Dlx1* show subtype-specific loss of interneurons, reduced inhibition and epilepsy. *Nature Neurosci.* **8**, 1059–1068 (2005).
- Ravichandran, K. S. & Lorenz, U. Engulfment of apoptotic cells: signals for a good meal. *Nature Rev. Immunol.* **7**, 964–974 (2007).
- Park, D. *et al.* BAI1 is an engulfment receptor for apoptotic cells upstream of the ELMO/Dock180/Rac module. *Nature* **450**, 430–434 (2007).
- Saito, T. *In vivo* electroporation in the embryonic mouse central nervous system. *Nature Protocols* **1**, 1552–1558 (2006).
- Butt, S. J. *et al.* The requirement of *Nkx2-1* in the temporal specification of cortical interneuron subtypes. *Neuron* **59**, 722–732 (2008).

Supplementary Information is linked to the online version of the paper at www.nature.com/nature.

Acknowledgements We are grateful to R. Batista-Brito, E. Chiappe, R. Cossart, J. Dasen, J. Kaltschmidt, S. Lee, J. Hjerling-Lefler, M. Long, D. Pisapia and B. Rudy for comments on the manuscript. We thank L. Yin for technical assistance. We are indebted to K. Ravichandran for providing the ELMO1 constructs. N.V.D.G. and T.K. are both supported by grants from The Patterson Trust. Research in the Fishell laboratory is supported by the National Institutes of Health, National Institute of Mental Health (5R01MH068469-08 and 2R01MH071679-09), National Institute of Neurological Disorders and Stroke (5R01NS039007-1), New York Stem Cell Science State (NGSG-130) and the Simons Foundation.

Author Contributions N.V.D.G. and G.F. conceived the project. N.V.D.G. and T.K. designed and carried out the experiments. N.V.D.G. wrote the manuscript with the help of all authors.

Author Information Reprints and permissions information is available at www.nature.com/reprints. The authors declare no competing financial interests. Readers are welcome to comment on the online version of this article at www.nature.com/nature. Correspondence and requests for materials should be addressed to G.F. (fisheg01@nyumc.org).

METHODS

Mouse strains. Pregnant Swiss Webster mice (Taconic) were electroporated at 15 days of gestation (E15.5). The *tetO-Kir2.1.ires.LacZ* transgenic mouse line was provided by J. Gogos²⁰. Doxycycline was administered in mouse feed (20 g per kg of feed) at selected time points (E16.5, P0, P3). The *Gad67-GFP* (gift from Y. Yanagawa) mouse line³³ was available in the G.F. laboratory. Details on the genotyping of the mouse strains have been described elsewhere¹².

In utero electroporation. Pregnant mice were electroporated using a standard *in utero* electroporation technique³¹. In brief, a timed pregnant mouse was anaesthetized and embryos were injected through the uterine wall in one lateral ventricle with 1–2 μ l of DNA (3 μ g μ l⁻¹). Fast green was used for visualization of the DNA solution. DNA was delivered by a glass needle operated with a mouth pipette. Five square 50-ms pulses at 40 mV with a 950 ms interval were delivered with a 5-mm paddle electrode (CUY650P5, Protech International) using an electroporator (CUY21, Protech International). After electroporation, the uterus was placed back in the abdominal cavity and the mouse was sutured. The mice were kept on a warm plate (Fine Science Tools) through surgery to minimize hypothermia. After surgery, mice recovered in a humidified chamber at 30 °C for 2–3 h. Mouse colony maintenance and handling was performed in compliance with the protocols approved by the Institutional Animal Care and Use Committee of the New York University School of Medicine.

The plasmids used in the electroporation experiments were generated using standard cloning techniques. The mouse *Kir2.1*, *Tta*, *mCherry*, *eGFP*, *Elmo1* and *Elmo1.TN558.Flag* cDNAs were each individually cloned into a *Dlx5/6-Pmin-polyA* plasmid. Because eGFP expression was not detected in brains electroporated with a *Dlx-5/6-Kir2.1.ires.eGFP* polycistronic plasmid, the *Dlx5/6-eGFP* plasmid was co-electroporated with *Dlx5/6-Kir2.1*, *Dlx5/6-Tta*, *Dlx5/6-Elmo1* or *Dlx5/6-Elmo1.TN558.Flag* plasmids at equivalent molar concentrations to ensure high levels of co-expression. The detection of similar levels of eGFP expression in *Dlx5/6-eGFP* and *Dlx5/6-eGFP/Dlx5/6-Kir2.1* electroporated interneurons indicates that transcription driven by this enhancer is not affected by *Kir2.1* expression. For generation of *CAG-mCherry*, the *mCherry* cDNA was cloned into a *CAG-MCS* vector. Expression of the *tetO-Kir2.1.ires.LacZ* transgene in interneurons electroporated with the *Dlx5/6-Tta* plasmid was detected by processing tissue sections for β -galactosidase staining²⁰.

In situ hybridization and immunohistochemistry. *In situ* hybridization was performed as described³² using a full-length *Kir2.1* dig-labelled probe. Immunohistochemistry on 20- μ m tissue cryostat sections was previously described³⁴. For morphological reconstruction, 250- μ m-thick vibratome sections were fixed for 2 h and incubated overnight at 4 °C with selected antibodies. Sections were washed in PBS for several hours and incubated at 4 °C overnight with donkey secondary antibodies (Jackson laboratories). Primary antibodies used in the experiments include rat anti-GFP (1:2,000; Nacalai Tesque), mouse anti-Reelin (CR50) (1:500; MBL), rabbit anti-VIP (1:1,000; Immunostar), mouse anti-calretinin (1:1,500; Millipore Bioscience Research Reagents), rabbit anti-Tbr1 (1:1,000; Abcam), goat anti-Tbr1 (1:1,000; Abcam), rabbit anti-Pan-DLX (a gift from J. Kohtz), rabbit anti-NPAS1 (a gift from M. Masayuki), goat anti-ELMO1 (1:250; Millipore) and mouse anti-Flag (1:200; Sigma-Aldrich).

Quantification of cell death. Caspase 3 activity (Clontech) was assessed on cryostat sections of P8 brains electroporated with *Dlx5/6-eGFP* or *Dlx5/6-eGFP* and *Dlx5/6-Kir2.1* plasmids. The percentage of Caspase3 immunoreactive interneurons that co-express eGFP over the total number of eGFP-expressing interneurons was counted on five *Kir2.1*-electroporated mice and five control mice.

Quantification of interneuron layer distribution. The proportion of Cr⁺, Re⁺ and VIP⁺ interneurons over the total number of electroporated interneurons across cortical layers was calculated in all cryostat tissue sections from individual brains. Analysis was performed on four wild-type (74 interneurons) and six *tetO-Kir2.1.ires.LacZ* (150 interneurons) mice co-electroporated with *Dlx5/6-Tta* and *Dlx5/6-eGFP* plasmids.

Kynurenic acid treatment. *Dlx5/6-eGFP* electroporated pups were anaesthetized by hypothermia on ice for two minutes. The pups were protected with cloth to prevent frostbite. Kynurenic acid²⁵ (300 nM, Sigma-Aldrich) diluted in PBS and pure PBS (controls) was injected at P0, P2 and P3. Fast green was used for visualization. A small window was opened in the skull with needles and solution was injected in the subdural space on the electroporated side. The skull opening was closed with cyanoacrylate adhesive. Pups were allowed to recover in a humidified chamber at 34 °C for 5–10 min and another 20 min at room temperature (18 °C) before putting them back in their cages. Treated brains in which electroporated interneurons were found in the vicinity of the injection site were used for analysis to minimize variability due to drug diffusion. Kynurenic acid injections at P0, P1, P2 and P3 had no effect on interneuron migration. Therefore, we averaged

the values obtained for laminar distribution in six control (110 interneurons) and six kynurenic-acid-treated (165 interneurons) mice electroporated with a *Dlx5/6-eGFP* plasmid. Analysis was performed at P8–P9.

Electrophysiology. Whole-cell patch-clamp electrophysiological recordings were performed on eGFP-expressing cells in acute brain slices prepared from P8–P18 animals. Briefly, animals were decapitated and the brain was dissected out and transferred to physiological artificial cerebrospinal fluid (ACSF) cooled down to 4 °C of the following composition: 125 mM NaCl, 2.5 mM KCl, 25 mM NaHCO₃, 1.25 mM NaH₂PO₄, 1 mM MgCl₂, 2 mM CaCl₂ and 20 mM glucose. The brain was then glued to a stage and 250- μ m-thick slices were cut using a vibratome (Vibratome 3000 EP). The slices were allowed to recover in recording ACSF at room temperature for at least 45 min before recording. They were then placed in a recording chamber mounted on the stage of an upright microscope (Axioscope, Zeiss) equipped with immersion differential interference contrast objectives (\times 5, \times 40) coupled to an infrared camera system (Zeiss), superfused at a rate of 1–2 ml min⁻¹ with oxygenated recording ACSF and maintained at a temperature of 31 °C. An eGFP filter was used to visualize the fluorescent interneurons in epifluorescence.

Whole-cell recordings were made from randomly selected eGFP-positive neurons located in upper layers (I–III) of the somatosensory cortex. Patch electrodes were made from borosilicate glass (Harvard Apparatus), had a resistance of 4–8 M Ω and were filled with a solution containing: 128 mM K-gluconate, 4 mM NaCl, 0.3 mM Na-GTP, 5 mM Mg-ATP, 0.0001 mM CaCl₂, 10 mM HEPES, 1 mM glucose and 5 mg ml⁻¹ biocytin (Sigma). Experiments were performed in current-clamp mode using the Axoclamp 2B (Molecular Devices) or the Axopatch 200B amplifier and in voltage clamp using the latter.

Access resistance was always monitored to ensure the stability of recording conditions. Cells were only accepted for analysis if the initial series resistance was less than or equal to 40 M Ω and did not change by more than 20% throughout the recording period. The series resistance was compensated online by at least \sim 50% in voltage-clamp mode to reduce voltage errors. No correction was made for the junction potential between the pipette and the ACSF.

For *Kir2.1* conductance assessment a series of voltage steps in 10-mV increments were applied every 1–5 s in voltage clamp from –140 mV to 0 mV starting from –70 mV after a prepulse down to –90 mV so as to deactivate any *Kir2.1* channels that had entered inactivated states.

Active firing and passive membrane properties were recorded in current-clamp mode by applying a series of sub- and suprathreshold current steps. The resting membrane potential (V_{rest}) was ascertained in current clamp right after rupturing the patch by applying zero current.

All drugs were applied to the recording preparation through the bath. Salts used in the preparation of the intracellular recording solution and ACSF were obtained from Sigma-Aldrich. Kynurenic acid and SR95531 were also purchased from Sigma-Aldrich.

Neuronal morphology analysis. Images of interneurons were obtained with a Zeiss (LSM 510 Meta) confocal microscope, analysed with LSM Image Browser, and reconstructed with Neurolucida software (v.9). Morphological defects were observed in >50 interneurons (>10 brains) of each subtype (Cr⁺ and Re⁺) after *Kir2.1* electroporation and kynurenic acid treatment. In addition, analysis of morphology after doxycycline administration in *tetO-Kir2.1.ires.LacZ* mice co-electroporated with *Dlx5/6-Tta* and *Dlx5/6-eGFP* plasmids was performed in >20 interneurons (>4 brains). Similarly, >70 interneurons (>10 brains) were analysed in control experiments. A few of these interneurons were chosen for reconstruction. The total length and complexity of axonal arborizations and dendritic trees was scored in confocal stacks (optical slice thickness, 4 μ m; stack size 50–100 μ m) including all the neuronal processes. Interneurons are oriented such that the top of the figure panel points towards the pia and the bottom to the lateral ventricle. To assess the length and complexity of dendritic and axonal arborizations, we quantified the number of nodes (points from which two or more branches arose) and ends (terminal branches) in each of these trees with Neurolucida Explorer. Total length and complexity of neuronal processes were scored in the same set of reconstructed interneurons for each experiment. eGFP labelling in electroporated interneuron was indistinguishable from that of streptavidin fills.

Statistical analysis. Statistical analysis was performed by using Student's *t*-test (two-tailed distribution, homoscedastic) unless otherwise stated.

33. Tamamaki, N. *et al.* Green fluorescent protein expression and colocalization with calretinin, parvalbumin, and somatostatin in the GAD67-GFP knock-in mouse. *J. Comp. Neurol.* **467**, 60–79 (2003).

34. Miyoshi, G., Butt, S. J., Takebayashi, H. & Fishell, G. Physiologically distinct temporal cohorts of cortical interneurons arise from telencephalic Olig2-expressing precursors. *J. Neurosci.* **27**, 7786–7798 (2007).

Genome-wide analysis reveals novel molecular features of mouse recombination hotspots

Fatima Smagulova^{1*}, Ivan V. Gregoret^{2*}, Kevin Brick², Pavel Khil², R. Daniel Camerini-Otero² & Galina V. Petukhova¹

Meiotic recombination predominantly occurs at discrete genomic loci called recombination hotspots, but the features defining these areas are still largely unknown (reviewed in refs 1–5). To allow a comprehensive analysis of hotspot-associated DNA and chromatin characteristics, we developed a direct molecular approach for mapping meiotic DNA double-strand breaks that initiate recombination. Here we present the genome-wide distribution of recombination initiation sites in the mouse genome. Hotspot centres are mapped with approximately 200-nucleotide precision, which allows analysis of the fine structural details of the preferred recombination sites. We determine that hotspots share a centrally distributed consensus motif, possess a nucleotide skew that changes polarity at the centres of hotspots and have an intrinsic preference to be occupied by a nucleosome. Furthermore, we find that the vast majority of recombination initiation sites in mouse males are associated with testis-specific trimethylation of lysine 4 on histone H3 that is distinct from histone H3 lysine 4 trimethylation marks associated with transcription. The recombination map presented here has been derived from a homogeneous mouse population with a defined genetic background and therefore lends itself to extensive future experimental exploration. We note that the mapping technique developed here does not depend on the availability of genetic markers and hence can be easily adapted to other species with complex genomes. Our findings uncover several fundamental features of mammalian recombination hotspots and underline the power of the new recombination map for future studies of genetic recombination, genome stability and evolution.

The vast majority of homologous recombination takes place in recombination hotspots—discrete regions of the genome with a recombination frequency significantly above the frequency in adjacent areas. Extensive studies of several individual hotspots in mammals have greatly advanced our understanding of hotspot biology (reviewed in refs 1–6), but some critical features may be missed without examining the full ensemble of hotspots in a genome. Recently, remarkable progress has been made that culminated in the identification of more than 30,000 recombination hotspots in human^{7–11}. Nevertheless, the relatively low resolution of the human map and the high variability of the recombination pattern between individuals still hinders fine structural analysis of hotspots. At the same time, it is clear that the primary DNA structure per se is a poor predictor of recombination activity and that hotspot position depends on additional factors, including epigenetic marks and most probably others^{1–4}. Therefore, defining the complete set of variables that ultimately determine hotspot sites in mammals would be greatly facilitated if a hotspot map of a genetically homogeneous and malleable organism were available. We therefore embarked on generating a high-resolution physical map of recombination hotspots in the mouse using a direct molecular approach for identification of recombination initiation sites.

Meiotic recombination is initiated by the introduction of DNA double-stranded breaks (DSBs) by the protein SPO11, followed by resection of the ends to produce long, single-stranded overhangs¹². Proteins RAD51 and DMC1 form nucleoprotein filaments at the ends

of the breaks and search for a homologous chromosome that is used for repair¹². We used anti-DMC1 antibodies to localize recombination initiation sites in the male mouse genome by chromatin immunoprecipitation followed by high-throughput sequencing (ChIP-Seq). To enrich for DSB-stage spermatocytes, we used *Hop2*^{-/-} mice (*Hop2* also known as *Psmc3ip* or *Tbpi*) that lack the cells of later spermatogenic stages owing to meiotic arrest after DSB formation¹³ (Supplementary Text). Hotspots identified by our approach in wild-type and in *Hop2*^{-/-} mice correlate extensively (Supplementary Fig. 1), but four times more hotspots can be identified using *Hop2*^{-/-} mice, owing to a higher signal-to-noise ratio.

Consistent with co-localization of RAD51 and DMC1 to DSB sites¹², we found that tag coverage in anti-RAD51 ChIP-Seq was highly correlated with that in anti-DMC1 ChIP-Seq (Fig. 1). Furthermore, the mapping data were highly reproducible between biological replicates ($R = 0.71$ – 0.97 (correlation coefficient); Fig. 1c). We were able to identify 9,874 recombination hotspots ($P = 10^{-4}$, FDR = 6.7% (false-discovery rate); Supplementary Data and Supplementary Figs 2 and 3), although the number of hotspots could be higher when less restrictive parameters are used (Supplementary Fig. 4). Confirmation of several identified hotspots was carried out by two approaches including direct physical detection of DSBs as previously described¹⁴ (Supplementary Fig. 5). Furthermore, we found that the correlation of our DSB map with available genetic maps^{15,16} is almost as high as the correlation between the genetic maps themselves (Fig. 1d, Supplementary Fig. 6 and Supplementary Text). The correlation of these genetic maps with the DSB hotspot distribution from this study is an important validation of our hotspot mapping approach. Additional supporting evidence comes from our finding that the ‘hottest’ cluster of DSB hotspots in the mouse genome is located in the PAR—the only homologous region between the X and Y chromosomes (Fig. 1e and Supplementary Fig. 3). Despite the very short length of the PAR, each spermatocyte undergoes an obligatory crossover in this area¹⁷. Estimates from our analysis show that this cluster is probably sufficient to ensure that there is at least one DSB in the PAR of every spermatocyte (Supplementary Text).

The centres of the hotspots in our map are defined with an approximate precision of 200 nucleotides, which is at least an order of magnitude higher than that of other available recombination maps in multicellular organisms (Supplementary Methods). More than 250 of the identified hotspots are hotter than one of the hottest previously known hotspots, *H2Ex* (Fig. 2a). On the basis of the estimated maximum recombination frequency of the *H2Ex* hotspot, 2 cM (ref. 18), the strength of the hottest hotspot in the mouse might be as high as 6 cM. Most of the hotspots lie 60–330 kb apart, with only a few recombination deserts more than 3 Mb in length (Supplementary Fig. 7). The average strengths of individual hotspots on different autosomes are similar, and on a chromosome scale the slight variation in hotspot density between autosomes does not correlate with the density of genes, chromosomal GC content, abundance of DNA repeats or chromosome length (not shown).

¹Uniformed Services University of the Health Sciences, Bethesda, Maryland 20814, USA. ²National Institute of Diabetes, Digestive and Kidney Diseases, NIH, Bethesda, Maryland 20892, USA.

*These authors contributed equally to this work.

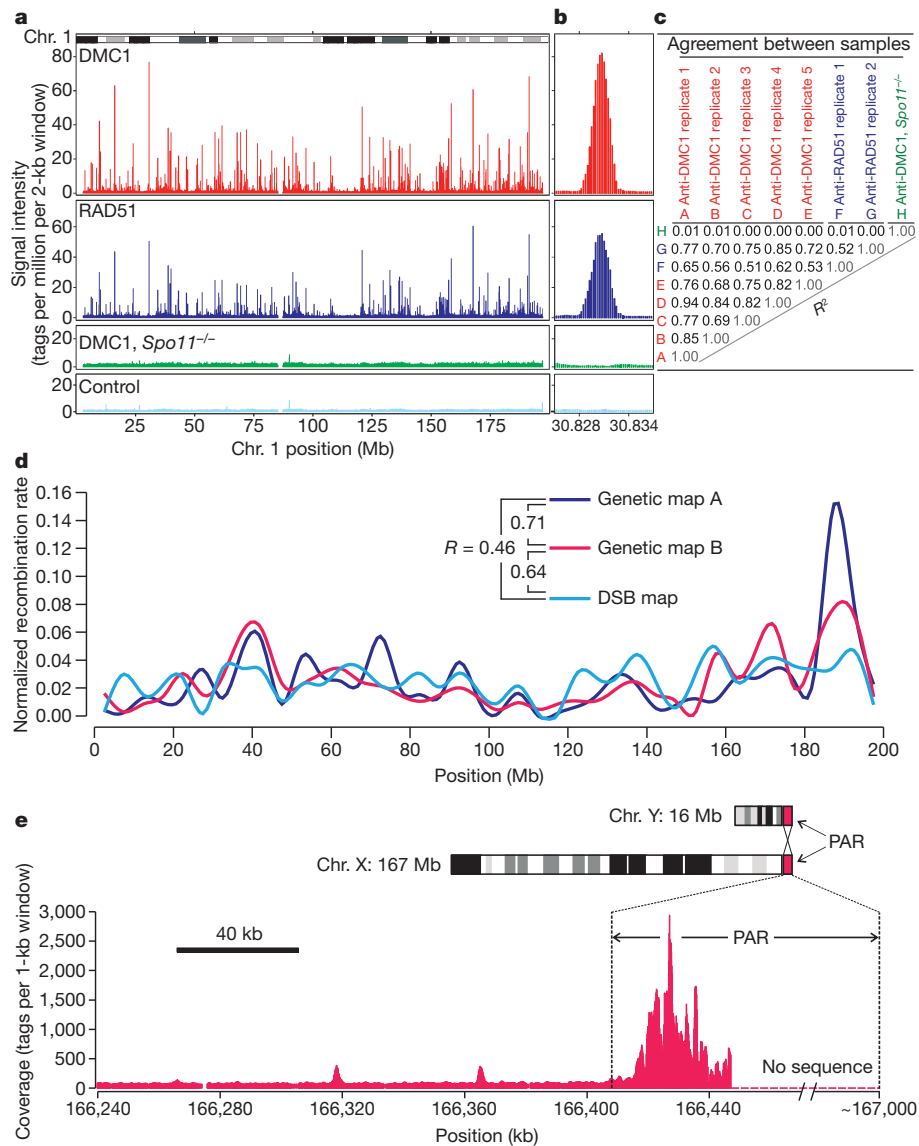


Figure 1 | DSB hotspots in the mouse genome. **a**, ChIP-Seq tag density profiles. DMC1: anti-DMC1 ChIP; RAD51: anti-RAD51 ChIP; DMC1, *Spo11*^{-/-}: anti-DMC1 ChIP from *Spo11*^{-/-} mice that do not form DSBs; Control: IgG ChIP and input DNA pool. **b**, Close-up of a representative hotspot. **c**, Agreement between ChIP-Seq samples (correlations in 2-kilobase (kb) bins across genome). **d**, Correlation between the DSB hotspot map and the

published genetic maps A¹⁵ and B¹⁶ for chromosome 1. The DSB map is generated from hotspot strengths (Supplementary Methods). All maps are generated in 5-megabase (Mb) windows and normalized by area of the map. **e**, The pseudoautosomal region (PAR) contains a large cluster of overlapping hotspots. DMC1 ChIP-Seq tag coverage is shown (smoothing window, 1 kb; step size, 100 bp).

We found that mouse hotspots have a tendency to overlap genes (Fig. 2b), although only the hottest 40% of the hotspots contribute significantly to this correlation (Supplementary Fig. 8). We next examined the association of DSB hotspots with different classes of DNA repeats and other genomic features. Significant correlations were found with GC content, short and long interspersed nuclear elements, long terminal repeats and other repeats, in agreement with those found in previous work^{1,2,4,5} (Supplementary Table 1 and Supplementary Text).

In searching for additional features that might define hotspot locations, we analysed the nucleotide composition of the hotspot regions, as characteristic nucleotide skews have been found at some functional genomic elements including replication origins and transcription start sites¹⁹. Examination of either single strand of the double-stranded DNA in the 5'-to-3' direction reveals that the sequence 5' to the centre of a hotspot is enriched in purines but that the polarity of the bias changes in the middle of the hotspot, such that the sequence 3' to the hotspot centre is more rich in pyrimidines (Fig. 2c and Supplementary Fig. 9). Replication- and transcription-related skews have been

attributed to mutational biases acting asymmetrically on complementary DNA strands. It is conceivable that the skew detected at hotspots is the result of mutational asymmetry as well (Supplementary Text and Supplementary Fig. 9c). It is also possible that the skew represents some unknown functional feature of the genome that favours DSB formation. Importantly, we were able to detect the same signature of nucleotide usage in human hotspots (Supplementary Fig. 9d), suggesting that the purine-pyrimidine skew is an intrinsic property of recombination hotspots in mammals. We also noticed a slight increase in the overall GC content in the middle of hotspots (not shown), which might indicate the presence of a gene conversion bias²⁰.

The protein PRDM9 is a meiosis-specific methyltransferase responsible for trimethylation of lysine 4 on histone H3²¹ (H3K4me3). In addition to its well-known role in transcription²², this histone modification is associated with increased recombination activity in yeast and in mouse^{23,24}. PRDM9 is highly polymorphic in its multi-Zn²⁺-finger DNA-binding domain, and recent studies have implicated PRDM9 in determining the positions of recombination hotspots through the

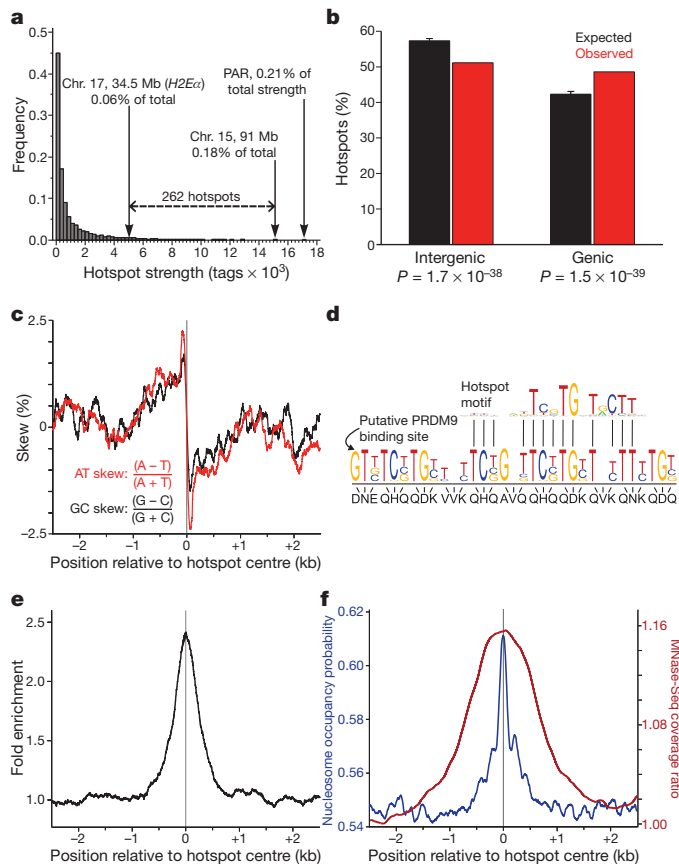


Figure 2 | Characteristics of mouse DSB hotspots. **a**, The *H2Ex* hotspot and the PAR hotspot cluster are among the strongest in the mouse genome. The strength of the hottest individual hotspot identified in this study (chromosome 15, ~91 Mb) is also indicated. **b**, Mouse DSB hotspots are significantly enriched in genes (one-sided binomial tests). Genic regions are defined from start to stop codons including introns. Error bars, 5th to 95th percentiles of the expected value distributions ($n = 10,000$ iterations). **c**, A purine–pyrimidine skew is apparent at DSB hotspots. Skew is calculated in 100-bp windows with a step size of 1 bp. **d**, The consensus hotspot motif is similar to the predicted binding site of PRDM9. **e**, The consensus motif is present in the centres of DSB hotspots. The distribution of hits to the consensus motif is shown in the 5-kb regions around hotspots (window size, 200 bp; step size, 1 bp). **f**, Both predicted (blue) and experimentally determined (red) nucleosome occupancy profiles peak at the centres of DSB hotspots. MNase-Seq coverage ratio is plotted as the whole-fragment coverage ratio of micrococcal-nuclease-digested chromatin to randomly fragmented chromatin in sliding, 500-bp windows (step size, 1 bp).

different binding specificities of its alleles^{25–27}. Approximately 40% of human recombination hotspots possess a consensus motif²⁸ that matches the predicted binding site of human PRDM9. We were able to identify a consensus motif specific to mouse hotspots (Fig. 2d, e). Sequences with better alignment scores to the motif consensus are more strongly over-represented in the hotspot regions, with the best hits showing almost 180-fold enrichment (Supplementary Fig. 10). Overall, hotspots containing consensus sequences are stronger than those without, and the quality of the motif alignment within hotspots is positively correlated with hotspot strength (Supplementary Fig. 11). Importantly, the motif shows a strong match to the predicted binding site of the *Prdm9* allele present in our mouse strain (Fig. 2d and Supplementary Fig. 12), and it is present at the centre of at least 73% of hotspots. This indicates that PRDM9 is a determinant for many more hotspots than previously thought and can explain the stronger-than-expected correlation between hotspot activity and *Prdm9* allelic variation found in recent association²⁷ and sperm typing²⁹ studies.

Because post-translational histone modification has been implicated in the regulation or maintenance of recombinational activity,

we asked whether DNA in the hotspot regions is assembled into nucleosomes. Strikingly, we found that both the predicted³⁰ and the actual nucleosomal occupancies are co-centred with recombination hotspots (Fig. 2f), reflecting a previously unknown, intrinsic ability of hotspot DNA to assemble a nucleosome. We next examined the distribution of the H3K4me3 marks in germ (testis) and somatic (liver) tissues. We found that 94% of hotspots overlap H3K4me3, with the majority of hotspots overlapping testis-specific H3K4me3 marks (87%) and practically none overlapping the marks specific to the liver (Fig. 3a and Supplementary Fig. 13). Although the association of H3K4me3 with DSB hotspots is not surprising in light of recent work^{23–27}, the extent of the overlap revealed here is such that H3K4me3 can be considered a global feature of DSB sites in multicellular organisms. Importantly, unlike in *Saccharomyces cerevisiae*²³, where gene promoters and hotspots seem to share the same H3K4me3 mark, H3K4me3 marks at mouse hotspots are hotspot specific (Fig. 3b). Even when a hotspot is located very close to a transcription start site, the corresponding H3K4me3 marks are clearly spatially distinct (Fig. 3c), indicating that different mechanisms are involved in the histone modifications at these sites (Fig. 3c, Supplementary Fig. 13 and Supplementary Text).

Importantly, H3K4me3 per se is not a sufficient mark for DSB formation. Why meiotic DSBs are correlated with only a small fraction (16.7%) of the ~55,000 H3K4me3 marks in testis remains a mystery. An attractive possibility is that some component of the DSB machinery directly associates with PRDM9 or a PRDM9-containing complex and is therefore delivered to the potential DSB sites. Subsequent trimethylation of H3K4 might be required to set the stage for recombination initiation and progression. Other possibilities may also be considered: (i) in addition to H3K4me3, other epigenetic marks may be present that require H3K4me3 to allow DSB formation; (ii) H3K4me3 introduced

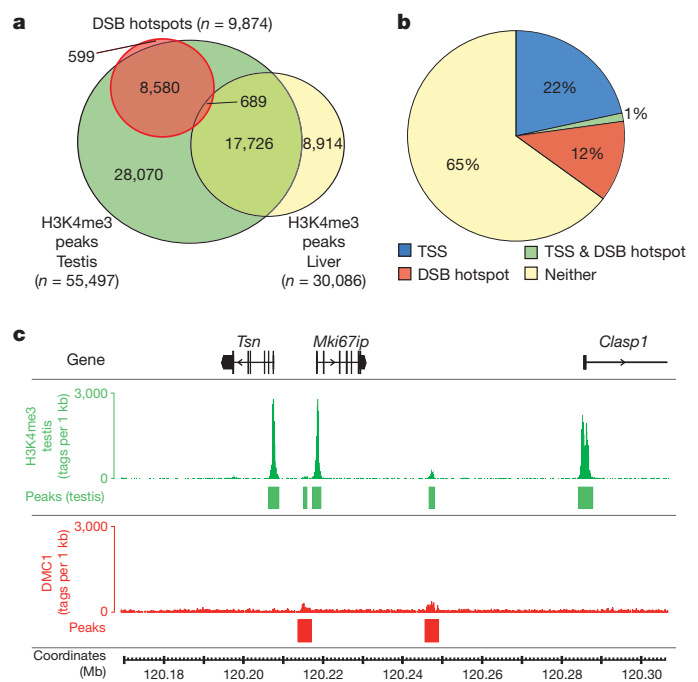


Figure 3 | Specific H3K4me3 marks are associated with DSB hotspots. **a**, The vast majority (93.9%) of DSB hotspots overlap H3K4me3 marks, most of which (86.9%) are testis specific. The six DSB hotspots that overlap liver-specific H3K4me3 marks are not shown. Peak calling for each data set was performed using an equal number of tags. **b**, DSB hotspots are associated with a set of H3K4me3 marks that are distinct from those at transcription start sites (TSSs). The fraction of H3K4me3 marks overlapping TSSs and/or DSB hotspots, or neither, is shown. **c**, H3K4me3 marks at DSB hotspots are generally weaker than TSS-associated marks, and are also spatially distinct despite being sometimes in very close proximity. Tag coverage is displayed in 100-bp steps.

by PRDM9 may be different from other H3K4me3 marks (for example, PRDM9, unlike other methyltransferases, might modify one rather than both H3 histones in the same nucleosome, or the other way around); (iii) specific histone variants could be present in the PRDM9-modified nucleosomes or could be substrates of PRDM9; (iv) transcription factors or other proteins bound to 'non-PRDM9' trimethylation marks may interfere with the DSB machinery.

METHODS SUMMARY

We used *Hop2*^{-/-} mice¹³ on a [C57BL/10.S × C57BL/10.F] F₁ genetic background and wild-type mice on the same background to make a map of DSB hotspots. ChIP and high-throughput sequencing were performed according to manufacturer-provided protocols (Upstate and Illumina, respectively) with minor modifications. For each sample, 36-bp end sequences were aligned to the mm9 reference genome using the Illumina GAT analysis pipeline. Only quality-filtered reads that mapped uniquely to the genome were retained for downstream analyses. We identified DSB hotspots and H3K4me3 peaks by comparing the sequence tag coverage for each ChIP sample with that of tag-count-matched control samples using the MACS algorithm. The hotspot consensus motif was identified from nonamers enriched near hotspot centres using a bespoke analysis pipeline. Additional details are available in Supplementary Information.

Received 5 October 2010; accepted 24 January 2011.

Published online 3 April 2011.

1. Arnheim, N., Calabrese, P. & Tiemann-Boege, I. Mammalian meiotic recombination hot spots. *Annu. Rev. Genet.* **41**, 369–399 (2007).
2. Buard, J. & de Massy, B. Playing hide and seek with mammalian meiotic crossover hotspots. *Trends Genet.* **23**, 301–309 (2007).
3. Lichten, M. Meiotic chromatin: the substrate for recombination initiation. *Genome Dynam. Stab.* **3**, 165–193 (2008).
4. Paigen, K. & Petkov, P. Mammalian recombination hot spots: properties, control and evolution. *Nature Rev. Genet.* **11**, 221–233 (2010).
5. Clark, A. G., Wang, X. & Matisse, T. Contrasting methods of quantifying fine structure of human recombination. *Annu. Rev. Genom. Hum. Genet.* **11**, 45–64 (2010).
6. Kauppi, L., May, C. A. & Jeffreys, A. J. Analysis of meiotic recombination products from human sperm. *Methods Mol. Biol.* **557**, 323–355 (2009).
7. The International HapMap Consortium. A haplotype map of the human genome. *Nature* **437**, 1299–1320 (2005).
8. Durbin, R. M. *et al.* A map of human genome variation from population-scale sequencing. *Nature* **467**, 1061–1073 (2010).
9. Frazer, K. A. *et al.* A second generation human haplotype map of over 3.1 million SNPs. *Nature* **449**, 851–861 (2007).
10. Kong, A. *et al.* Fine-scale recombination rate differences between sexes, populations and individuals. *Nature* **467**, 1099–1103 (2010).
11. Myers, S., Bottolo, L., Freeman, C., McVean, G. & Donnelly, P. A fine-scale map of recombination rates and hotspots across the human genome. *Science* **310**, 321–324 (2005).
12. Neale, M. J. & Keeney, S. Clarifying the mechanics of DNA strand exchange in meiotic recombination. *Nature* **442**, 153–158 (2006).
13. Petukhova, G. V., Romanienko, P. J. & Camerini-Otero, R. D. The Hop2 protein has a direct role in promoting interhomolog interactions during mouse meiosis. *Dev. Cell* **5**, 927–936 (2003).
14. Qin, J., Richardson, L. L., Jasin, M., Handel, M. A. & Arnheim, N. Mouse strains with an active H2-Ea meiotic recombination hot spot exhibit increased levels of H2-Ea-specific DNA breaks in testicular germ cells. *Mol. Cell. Biol.* **24**, 1655–1666 (2004).
15. Paigen, K. *et al.* The recombinational anatomy of a mouse chromosome. *PLoS Genet.* **4**, e1000119 (2008).
16. Cox, A. *et al.* A new standard genetic map for the laboratory mouse. *Genetics* **182**, 1335–1344 (2009).
17. Burgoyne, P. S. Genetic homology and crossing over in the X and Y chromosomes of mammals. *Hum. Genet.* **61**, 85–90 (1982).
18. Khambata, S., Mody, J., Modzelewski, A., Heine, D. & Passmore, H. C. Ea recombination hot spot in the mouse major histocompatibility complex maps to the fourth intron of the Ea gene. *Genome Res.* **6**, 195–201 (1996).
19. Francino, M. P. & Ochman, H. Strand asymmetries in DNA evolution. *Trends Genet.* **13**, 240–245 (1997).
20. Duret, L. & Galtier, N. Biased gene conversion and the evolution of mammalian genomic landscapes. *Annu. Rev. Genom. Hum. Genet.* **10**, 285–311 (2009).
21. Mihola, O., Trachtulec, Z., Vlcek, C., Schimenti, J. C. & Forejt, J. A mouse speciation gene encodes a meiotic histone H3 methyltransferase. *Science* **323**, 373–375 (2009).
22. Wang, Z., Schones, D. E. & Zhao, K. Characterization of human epigenomes. *Curr. Opin. Genet. Dev.* **19**, 127–134 (2009).
23. Borde, V. *et al.* Histone H3 lysine 4 trimethylation marks meiotic recombination initiation sites. *EMBO J.* **28**, 99–111 (2008).
24. Buard, J., Barthès, P., Grey, C. & de Massy, B. Distinct histone modifications define initiation and repair of meiotic recombination in the mouse. *EMBO J.* **28**, 2616–2624 (2009).
25. Parvanov, E. D., Petkov, P. M. & Paigen, K. *Prdm9* controls activation of mammalian recombination hotspots. *Science* **327**, 835 (2010).
26. Myers, S. *et al.* Drive against hotspot motifs in primates implicates the PRDM9 gene in meiotic recombination. *Science* **327**, 876–879 (2010).
27. Baudat, F. *et al.* PRDM9 is a major determinant of meiotic recombination hotspots in humans and mice. *Science* **327**, 836–840 (2010).
28. Myers, S., Freeman, C., Auton, A., Donnelly, P. & McVean, G. A common sequence motif associated with recombination hot spots and genome instability in humans. *Nature Genet.* **40**, 1124–1129 (2008).
29. Berg, I. L. *et al.* PRDM9 variation strongly influences recombination hot-spot activity and meiotic instability in humans. *Nature Genet.* **42**, 859–863 (2010).
30. Kaplan, N. *et al.* The DNA-encoded nucleosome organization of a eukaryotic genome. *Nature* **458**, 362–366 (2009).

Supplementary Information is linked to the online version of the paper at www.nature.com/nature.

Acknowledgements We thank M. Lichten (NCI, NIH) and P. Hsieh (NIDDK, NIH) for comments and discussion. We are grateful to S. Sharmeen for her help with high-throughput sequencing. This work was supported in part by Basil O'Connor Starter Scholar Research Award Grant No. 5-FY07-667 from the March of Dimes Foundation (G.V.P.); NIH grant 1R01GM084104-01A1 from NIGMS (G.V.P.); New Investigator Start-up Grants FS71HU, R071HU and CS71HU from USUHS (G.V.P.); and the NIDDK (NIH) Intramural Research Program (R.D.C.-O.).

Author Contributions F.S. performed all experiments. I.V.G., K.B. and P.K. performed computational data analyses. All authors contributed to experimental design. G.V.P. and R.D.C.-O. designed and supervised the study. G.V.P. wrote the manuscript. All authors discussed the results and commented on the manuscript.

Author Information ChIP-Seq data have been deposited in the Gene Expression Omnibus under accession number GSE24438. *Prdm9* complementary DNA sequences have been deposited in GenBank under accession numbers HQ704390 and HQ704391. Reprints and permissions information is available at www.nature.com/reprints. The authors declare no competing financial interests. Readers are welcome to comment on the online version of this article at www.nature.com/nature. Correspondence and requests for materials should be addressed to G.V.P. (gpetukhova@usuhs.mil) or R.D.C.-O. (rdcamerini@mail.nih.gov).

Amyloid-binding compounds maintain protein homeostasis during ageing and extend lifespan

Silvestre Alavez¹, Maithili C. Vantipalli¹, David J. S. Zucker^{1,2}, Ida M. Klang^{1,3} & Gordon J. Lithgow¹

Genetic studies indicate that protein homeostasis is a major contributor to metazoan longevity¹. Collapse of protein homeostasis results in protein misfolding cascades and the accumulation of insoluble protein fibrils and aggregates, such as amyloids². A group of small molecules, traditionally used in histopathology to stain amyloid in tissues, bind protein fibrils and slow aggregation *in vitro* and in cell culture^{3,4}. We proposed that treating animals with such compounds would promote protein homeostasis *in vivo* and increase longevity. Here we show that exposure of adult *Caenorhabditis elegans* to the amyloid-binding dye Thioflavin T (ThT) resulted in a profoundly extended lifespan and slowed ageing. ThT also suppressed pathological features of mutant metastable proteins and human β -amyloid-associated toxicity. These beneficial effects of ThT depend on the protein homeostasis network regulator heat shock factor 1 (HSF-1), the stress resistance and longevity transcription factor SKN-1, molecular chaperones, autophagy and proteosomal functions. Our results demonstrate that pharmacological maintenance of the protein homeostatic network has a profound impact on ageing rates, prompting the development of novel therapeutic interventions against ageing and age-related diseases.

The longevity of the nematode *Caenorhabditis elegans* is influenced by hundreds of genes including an insulin-like signalling pathway (ILS) that regulates the activities of the transcription factors FOXO-like DAF-16 (ref. 5) and Nrf2-like SKN-1 (ref. 6). Together with the stress response transcription factor HSF-1, DAF-16 also regulates protein homeostasis and influences lifespan^{7–9}, indicating that chemical modulation of protein homeostasis might slow ageing. We reasoned that compounds that have protein-fibril- and protein-aggregate-binding properties may affect age-related changes to protein homeostasis and tested a series of amyloid-binding proteins for lifespan effects. We found that exposing sterilized wild-type (N2) nematodes to the fibril-binding flavonoid ThT (4-(3,6-dimethyl-1,3-benzothiazol-3-ium-2-yl)-N,N-dimethylaniline chloride)¹⁰ at either 50 or 100 μ M throughout adult life leads to an increase in median (60%) and maximal lifespan (43–78%; Fig. 1a, b, Supplementary Fig. 2 and Supplementary Table 1). The compound reduced age-specific mortality at all ages ($P < 0.001$, Fig. 1c) and slowed age-related decline in spontaneous movement (Fig. 1d), indicating improved health throughout adulthood. At higher doses (500 μ M) ThT is toxic and shortens lifespan (Fig. 1a, b). Other compounds with protein-aggregate-binding properties, including curcumin and rifampicin, increased lifespan to a lesser extent (up to 45%) (Supplementary Figs 3, 4). When ThT and curcumin treatments were combined, we did not observe additive effects on lifespan (Supplementary Fig. 5).

We then tested several compounds with similar structural features to ThT, but with different pharmacological properties: 2-(2-hydroxyphenyl)-benzoxazole (HBX), 2-(2-hydroxyphenyl) benzothiazole (HBT) and 2-(2-aminophenyl)-1H-benzimidazole (BM)¹¹ (Supplementary Fig. 6). These compounds also extended the lifespan of adult nematodes (up to 40%) but at concentrations significantly lower than ThT (Fig. 1e–g),

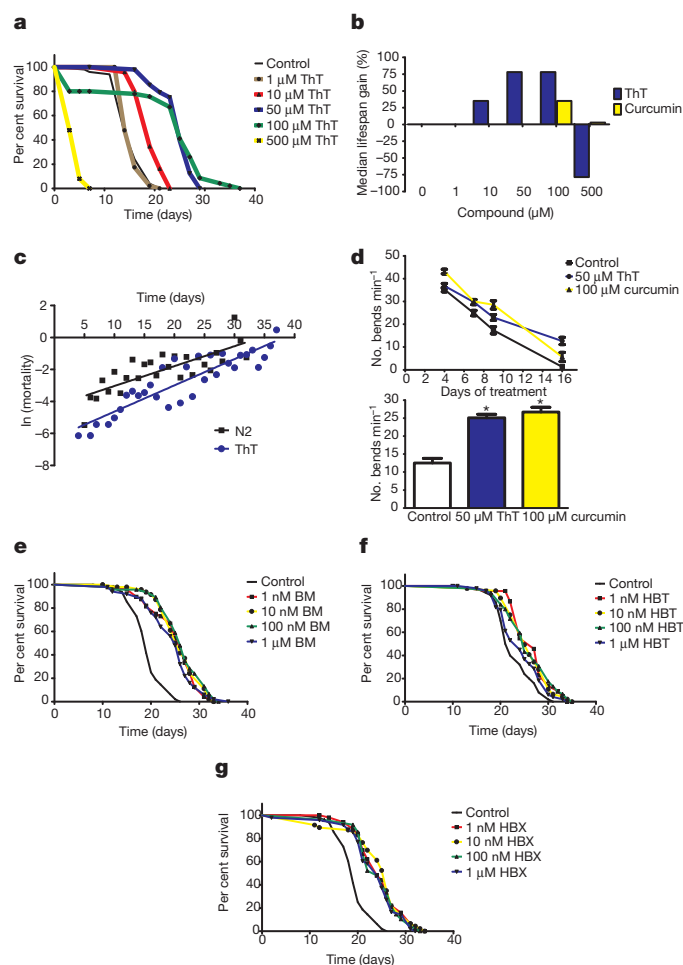


Figure 1 | Amyloid-binding compounds extend *C. elegans* lifespan.

a, Dose-response Kaplan-Meier survival curves of synchronously ageing hermaphrodite wild-type (N2) populations exposed to 0 μ M (control) to 500 μ M ThT at 20 °C. **b**, Per cent change in median lifespan of N2 populations cultured on 0–500 μ M ThT and curcumin. **c**, ln-linear plot of age-specific mortality rate with age for control and 50 μ M ThT-treated *C. elegans*. **d**, Effect of 50 μ M ThT and 100 μ M curcumin on motility of N2 worms evaluated as the mean number of body bends in a 20-s period in 15 individual worms throughout life (upper panel) and after 12 days of treatment (lower panel) with ThT and curcumin. Data are presented as bends min^{-1} and represent the average of three independent experiments. * $P < 0.0001$. **e–g**, Dose-response Kaplan-Meier survival curves of synchronously ageing hermaphrodite N2 populations exposed to 0 μ M (control) to 1 μ M of BM (**e**), HBT (**f**) and HBX (**g**) at 20 °C. Plots are representative of three independent experiments.

¹Buck Institute for Research on Aging, 8001 Redwood Blvd, Novato, California 94945, USA. ²Department of Natural Sciences and Mathematics, Dominican University of California, San Rafael, California 94901, USA. ³Karolinska Institute, Center for Biosciences at NOVUM, Department of Biosciences and Nutrition, Hålsövägen 7, S-141 83 Huddinge, Sweden.

indicating that the bioavailability and/or pharmacological properties of ThT-like compounds influence lifespan.

To test the effects of ThT on protein homeostasis we exploited two *C. elegans* models of human proteotoxic disease: the strain CL4176 (*dvIs27[myo-3::A β ₃₋₄₂ let 3' UTR(pAF29); pRF4 (rol-6(su1006))*)¹², which expresses an aggregating amyloid- β (3–42) peptide (A β (3–42)) in muscle tissue¹³ and AM140 (*rmls132[P(unc-54) Q35::YFP]*), which expresses a polyglutamine (polyQ) protein. Amyloid- β aggregates are associated with lesions in Alzheimer's disease, and polyQ aggregation is a feature in several neurological conditions¹⁴. When raised at 25 °C, nematodes expressing these proteins in muscle accumulate protein aggregates and become paralysed. We found that 50 μ M ThT and 100 μ M curcumin decreased the proportion of paralysed worms (Fig. 2a, b). By immunohistochemistry we found that ThT reduced A β (3–42) aggregation *in vivo* and preserved muscle integrity in CL4176 (Fig. 2e). We also found that ThT rescued A β (3–42) aggregation-induced paralysis even when nematodes were treated 18 h after the induction of aggregate formation, indicating that ThT can ameliorate detrimental effects during the development of the aggregate-related pathology (Supplementary Fig. 7).

If amyloid-binding compounds extended lifespan through improved protein homeostasis, then we expected that they would influence not only heterologous disease-related models but also nematode proteins. We tested ThT and curcumin on mutant worms that express metastable proteins previously exploited as indicators of the protein homeostatic network capacity¹⁵. Strains carrying mutations in the genes *unc-52* (HE250 [*unc-52(e669su250)II*]) and *unc-54* (CB1157 [*unc-54(e1157)I*]) produce temperature-sensitive muscle proteins UNC-52 (perlecan) and UNC-54 (myosin class II heavy chain), respectively, that exhibit altered structure and cause paralysis at 25 °C^{15,16,17}. We found that ThT suppressed paralysis of these mutants (Fig. 2c), prevented the disruption of the muscle sarcomeres (Supplementary Fig. 8) and restored perlecan organization (Fig. 2d). We extended these observations to other temperature-sensitive missense protein-folding mutations expressed in the neuromuscular junction and in the nervous system¹⁸. We found that ThT suppressed ethanol sensitivity in a strain carrying the *gas-1(fc21)* mutation in a subunit of mitochondrial complex I and levamisole resistance in a strain carrying *unc-63(x26)*, an α -subunit of the nicotinic acetylcholine receptor (Supplementary Fig. 9), indicating that ThT could act in a variety of tissues including the nervous system.

Because certain forms of dietary restriction suppress protein aggregation and increase lifespan, we asked whether ThT acts as a dietary restriction mimetic. We observed that ThT produces a small decrease in pharyngeal pumping rate (~15%) after 3 days of treatment, which could slightly decrease food intake. No difference was detected after 6 days of ThT treatment (Supplementary Fig. 16a). It is very unlikely that this small difference could promote the major ThT-mediated lifespan extension we observe. ThT also increased the lifespan of a strain carrying the *eat-2(ad1116)* mutation (Fig. 4c) that causes a major defect in pharyngeal pumping, thereby inducing a dietary restriction lifespan extension¹⁹. Dilution of the bacterial food source also leads to lifespan extension by dietary restriction²⁰. ThT at 50 μ M was detrimental to lifespan in this dietary restriction model but 1 and 10 μ M ThT increased lifespan by 24% (Supplementary Fig. 16b). As ThT increases lifespan in both genetic and nutrient-based models of dietary restriction, ThT-induced lifespan extension is at least in part independent from dietary restriction.

We then considered whether ThT was interacting more directly with homeostatic mechanisms. We exploited ThT fluorescence to visualize the compound *in vivo* and observed a variable co-distribution of ThT with A β (3–42) aggregates detected by immunolocalization, indicating a direct interaction between ThT protein misfolding cascades (Supplementary Fig. 10). Consequently, we tested for the presence of amino acid sequence-independent oligomers of protein or peptides prone to aggregation. We found that protein detected by an

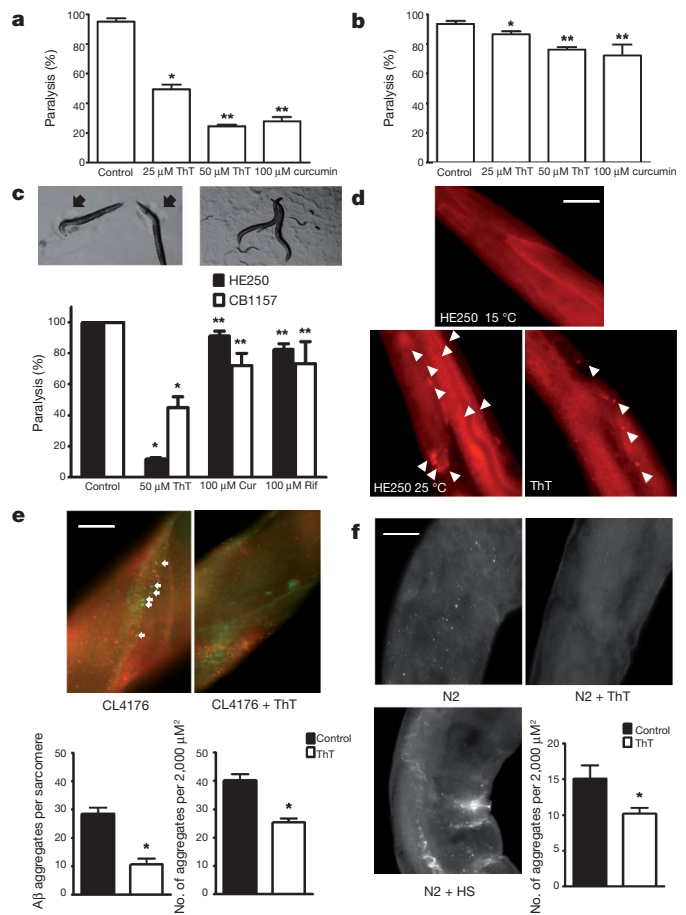


Figure 2 | ThT and curcumin rescue a paralysis phenotype and slow protein aggregation *in vivo*.

a, b, The paralysis phenotype associated with protein aggregation is suppressed by 25 μ M ThT, 50 μ M ThT, 100 μ M curcumin in CL4176 (* P < 0.001, ** P < 0.0001) expressing A β (3–42) (**a**) and AM140 (* P < 0.05, ** P < 0.01) expressing polyQ (**b**) after 1 and 8 days at 25 °C, respectively. Error bars represent the mean \pm s.e.m. of four independent experiments. **c**, Temperature-sensitive strain HE250 [*unc-52(e669su250)II*] after 36 h at 25 °C showing the typical paralysis phenotype (left upper panel) and the rescue elicited by 50 μ M ThT (right upper panel). Arrows indicate the halos of clearance in the bacterial lawn characteristic of paralysed worms. Lower panel shows protection (\pm s.e.m.) of the HE250 paralysis phenotype by 50 μ M ThT, 100 μ M curcumin (Cur) and 100 μ M rifampicin (Rif). * P < 0.0001, ** P < 0.01. n = 4 independent experiments. **d**, Perlecan immunolocalization showing disruption/aggregation pattern after 24 h at 25 °C, as compared with worms raised at the permissive temperature (upper panel), and the suppression of disruption by 50 μ M ThT treatment. Sixteen of twenty worms showed similar perlecan distribution in three independent experiments. Arrows indicate perlecan aggregates. Scale bar, 30 μ m.

e, Immunolocalization of aggregation-prone soluble oligomeric protein (A11 antibody, red) and A β (3–42) (green) in the presence or absence of 50 μ M ThT in CL4176. Scale bar, 10 μ m. Error bars represent the mean \pm s.e.m., 11 worms per group in 3 independent experiments. * P < 0.0001. **f**, Immunolocalization of aggregation-prone soluble oligomeric protein (A11 antibody) in the presence or absence of 50 μ M ThT and under heat shock (HS) in 11 days old wild-type N2 worms. Scale bar, 20 μ m. Error bars represent the mean \pm s.e.m., 11 worms per group, of 3 independent experiments. * P < 0.0001. Scale bar, 10 μ m.

antibody specific for such oligomers (A11) accumulated during normal ageing and after heat shock, but was significantly decreased in both CL4176 (Fig. 2e) and N2 strains (Fig. 2f) after ThT treatment, consistent with ThT affecting protein misfolding cascades.

We reasoned that ThT may also require components of the protein homeostatic network activated by DAF-16 and HSF-1 to influence protein aggregation and lifespan^{8,21}. We undertook a targeted pharmacogenetic RNA interference (RNAi) screen of genes encoding several

components of the ubiquitin/proteasome system, autophagy/lysosomal machinery and molecular chaperones. First, we asked whether reducing the expression of genes encoding these proteins modulated the paralysis of metastable perlecan mutant in the absence of ThT (Fig. 3). RNAi of small chaperones known to positively modulate lifespan in *C. elegans*, HSP-16.2 and HSP-16.41 (refs 8, 22), and the mitochondrial HSP-70 (*hsp-6*) increased paralysis of the HE250 strain. An autophagy gene (*vps-34*) also influenced the HE250 mutant paralysis phenotype (Fig. 3). Interestingly, RNAi targeting *rle-1*, an E3 ubiquitin ligase that influences lifespan in *C. elegans* by determining the rate of DAF-16 degradation²³, produced a remarkable reduction in the paralysis phenotype. This led us to test *daf-16* (RNAi), but no change in the paralysis phenotype was observed, indicating that other proteins regulated by *rle-1* can influence protein homeostasis.

We then tested for interactions between these protein homeostasis factors and the protective effect elicited by ThT on the HE250 paralysis phenotype, and found that ThT protection was decreased when combined with RNAi for several stress genes (for example, *hsp-16.2*, *hsp-16.41*), consistent with a concerted action between chaperones and ThT to maintain protein conformation. Similarly, ubiquitin/proteasome (*aip-1*) and autophagy/lysosomal (*atg-9* and *vps-34*) functions were required for the beneficial effects of ThT. Interestingly, LMP-2, a protein involved in lysosome function, suppresses the ThT effect on paralysis. As *lmp-2* knockdown itself has no effect on paralysis it is possible that ThT is cleared from the cell by a lysosomal mechanism, such that *lmp-2* RNAi results in increased ThT bioactivity.

Next, we explored the dependency of DAF-16 for ThT action. The ThT suppression of the paralysis phenotype was potentiated by *daf-16* (RNAi), indicating that some proteins activated by DAF-16 interfere with the mechanism elicited by ThT to promote protein homeostasis. This is consistent with the previous report of a reduction of amyloid- β aggregation by *daf-16* (RNAi)⁹. In contrast, *skn-1* (RNAi), encoding a transcription factor that positively modulates stress resistance and longevity, was required for the ThT effect on the HE250 paralysis phenotype (Fig. 3), indicating that some SKN-1 target genes are necessary for ThT action. However, ThT does not seem to induce constitutive nuclear localization of a SKN-1 fusion protein CF2189 [Is001(*skn-1::GFP*; *rol-6(su1006)*)] as occurs with certain toxins (Supplementary Fig. 15).

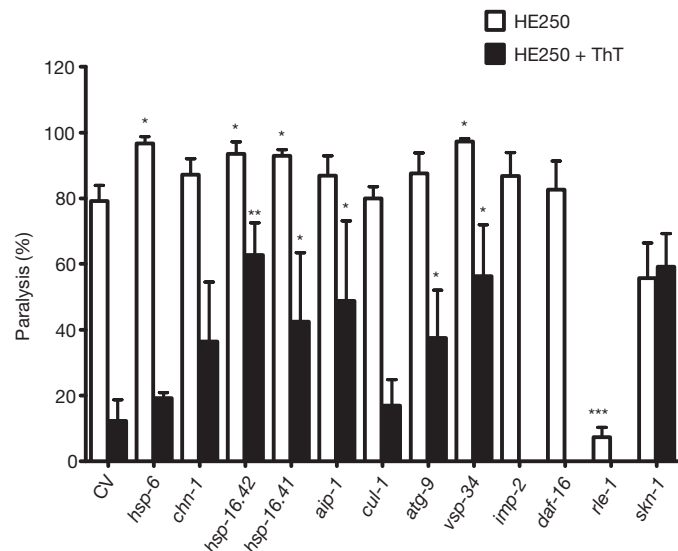


Figure 3 | Dependency of ThT suppression of protein aggregation-associated paralysis on protein homeostasis factors. RNAi by feeding was used to knockdown the expression of genes encoding proteostatic factors in HE250 in the presence or absence of 50 μ M ThT and the paralysis phenotype was scored after 36 h. Proportion of worms paralysed is plotted (mean \pm s.e.m.). * P < 0.01, ** P < 0.001, *** P < 0.0001 versus control vector (CV).

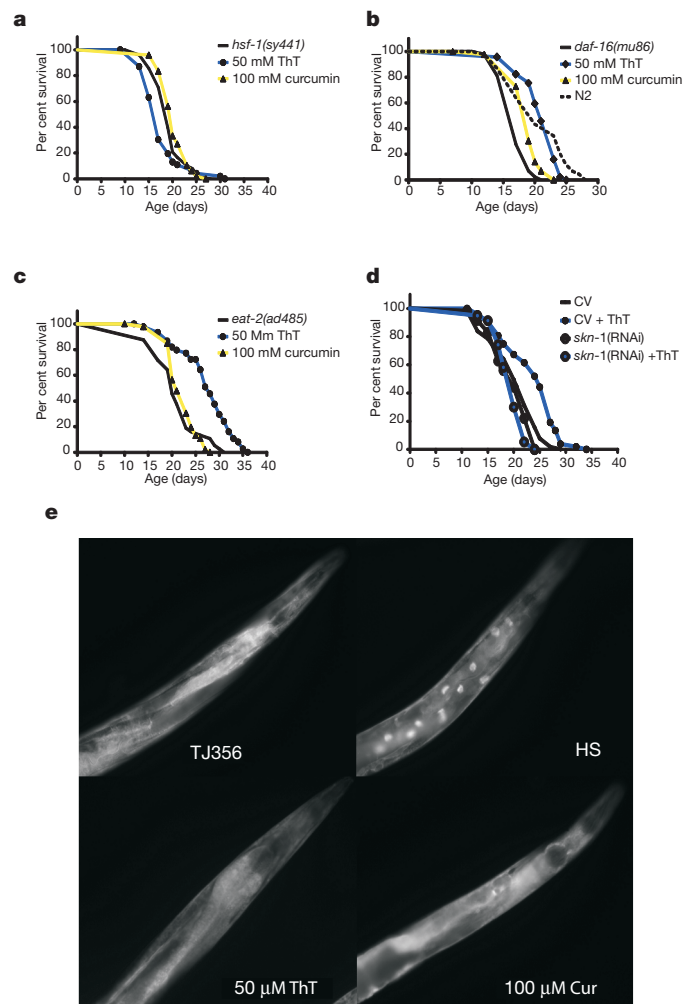


Figure 4 | ThT enhancement of lifespan depends on HSF-1 and SKN-1 transcription factors but not on DAF-16. **a–c**, Effect of 50 μ M ThT and 100 μ M curcumin on Kaplan–Meier survival curves of synchronously ageing PS3551 [*hsf-1(sy441)*] (**a**), CF1038 [*daf-16(mu86)*] (**b**) and DA465 [*eat-2(ad485)*] (**c**) lifespan. **d**, Effect of reducing SKN-1 by *skn-1* RNAi on the increase in lifespan elicited by ThT. Plots are representative of three independent experiments. **e**, ThT and curcumin (Cur) treatment does not result in DAF-16::GFP relocalization as compared to control strain [*daf-16::daf-16-gfp* + *rol-6*] (upper left). Control strain under heat shock (HS) produces a clear relocalization of DAF-16::GFP to the nuclei of intestinal cells.

We returned then to the question of whether ThT was extending lifespan by a mechanism related to protein homeostasis and initially focused on the transcription factor genes *hsf-1* and *daf-16*; mutation of either one shortens normal lifespan and suppresses the beneficial effects of a *daf-2* mutation on the amyloid- β -aggregation model in *C. elegans*⁹. We found that ThT does not increase lifespan in a strain carrying the *hsf-1(sy441)* mutation—resulting in non-functional HSF protein (Fig. 4a and Supplementary Fig. 11)—indicating that the ThT effect on lifespan requires the participation of HSF-1-regulated machinery. Consistent with this idea, we found that the protein levels of HSP-16.2 and HSP-70, the mRNA levels of a mitochondrial (*hsp-6*) and a cytosolic (*chn-1*) *hsp-70* isoform are upregulated by ThT treatment (Supplementary Fig. 12a). We also detected a slight increase in the levels of HSF-1 protein under ThT treatment (Supplementary Fig. 12b).

ThT treatment did extend the lifespan of *daf-16(mu86)* worms lacking functional DAF-16 (Fig. 4b) and in a long-lived ILS mutant, *age-1(hx546)*, which is hypomorphic for the p110 catalytic subunit of a phosphoinositide 3-kinase (Supplementary Fig. 13). In addition, ThT treatment did not alter the localization of a DAF-16 fusion protein TJ356 (zIs356 IV [*daf-16::daf-16-gfp*; *pRF4(rol-6(su1006))*]), in contrast

to the effect of stress (Fig. 4e; Supplementary Fig. 14). We conclude that ThT lifespan extension is independent of ILS.

Because ThT suppression of the paralysis phenotype on the HE250 strain required the *skn-1* transcription factor, we tested if it was required for lifespan extension. We found that ThT does not increase the lifespan of nematodes exposed to *skn-1* RNAi and conclude that this transcription factor is, along with HSF-1, required for the increase in lifespan elicited by ThT (Fig. 4d).

We have observed that compounds traditionally used to stain amyloid- β deposits confer a large increase in lifespan to *C. elegans*. ThT is capable of suppressing protein-aggregation-associated paralysis in toxic protein models in multiple tissues. ThT reduces A β (3–42) aggregation, decreases the levels of soluble aggregation-prone oligomeric proteins and localizes with these aggregates *in vivo*. The mechanism of aggregation suppression depends on molecular chaperones, autophagy and proteosomal functions. Finally, the extent of the ThT-mediated lifespan increase depends on the transcription factors HSF-1 and SKN-1. We propose that amyloid-binding compounds act as stress response mimetics and activate the *C. elegans* stress-response pathways regulated by the HSF-1 and SKN-1 transcription factors, leading to stabilization of misfolded proteins and increased lifespan. Given the known ability of these compounds to bind to amyloid, we propose that they may also directly interact with aggregating proteins, promoting proper folding and possibly activating stress response pathways by an unknown mechanism (Supplementary Fig. 1). This modulation of protein homeostasis and protein aggregation pathways has beneficial effects for healthspan and lifespan. Small stress response mimetic molecules that target protein homeostatic mechanisms may provide opportunities for intervention in ageing and age-related disease.

METHODS SUMMARY

Lifespan assays were performed on nematode growth media plates with the compounds spread over the surface of the plates and 60 μ l of a concentrated suspension of *Escherichia coli* OP50 in the presence of FUDr (75 μ M) at 20 °C. Nematodes were scored as alive, dead or lost every other day. Nematodes that failed to display touch-provoked movement were scored as dead. For dietary restriction experiments, bacterial concentration was adjusted to 1.0×10^9 c.f.u. ml $^{-1}$, spotted on peptone-free 2% agar in the presence or absence of the specified compounds. Estimates of initial mortality rate, rate of increase with age and model fitting to Gompertz mortality curves were made using WinModest. Scoring for paralysis was initiated 1, 2 and 8 days after temperature upshift for HE250, CL4176 and AM140, respectively. Nematodes were scored as paralysed if they exhibited 'halos' of cleared bacteria around their heads, eggs accumulated close to the body or if they failed to respond to a touch-provoked movement. For fluorescence microscopy, strains were paralysed with 1 mM levamisole, mounted on 1% agarose pads and imaged. For immunofluorescence, worms were collected after treatment, rinsed, fixed in 4% paraformaldehyde overnight, permeabilized by 24 h exposure to β -mercaptoethanol at 37 °C followed by collagenase treatment and processed for different antigens. RNAi bacterial strains expressing double-stranded RNA that inactivates specified genes were used to knockdown the expression of specific genes of interest. For real-time quantitative PCR with reverse transcription (RT-qPCR) analysis, RNA from individual worms was extracted and the sample was added to the reverse transcription reaction and reversed transcribed at 50 °C for 20 min. mRNAs were found to have invariant steady-state levels across treatments and were used to derive calibrated normalized relative quantities (CNRQs) for each gene of interest. Differences in relative mRNA transcript levels were identified using pair-wise *t*-tests.

Full Methods and any associated references are available in the online version of the paper at www.nature.com/nature.

Received 19 October 2009; accepted 26 January 2011.

Published online 30 March 2011.

1. Morimoto, R. I. Proteotoxic stress and inducible chaperone networks in neurodegenerative disease and aging. *Genes Dev.* **22**, 1427–1438 (2008).

2. Balch, W. E., Morimoto, R. I., Dillin, A. & Kelly, J. W. Adapting proteostasis for disease intervention. *Science* **319**, 916–919 (2008).
3. Porat, Y., Abramowitz, A. & Gazit, E. Inhibition of amyloid fibril formation by polyphenols: structural similarity and aromatic interactions as a common inhibition mechanism. *Chem. Biol. Drug Des.* **67**, 27–37 (2006).
4. Frid, P., Anisimov, S. V. & Popovic, N. Congo red and protein aggregation in neurodegenerative diseases. *Brain Res. Brain Res. Rev.* **53**, 135–160 (2007).
5. Kenyon, C. The plasticity of aging: insights from long-lived mutants. *Cell* **120**, 449–460 (2005).
6. Tullet, J. M. *et al.* Direct inhibition of the longevity-promoting factor SKN-1 by insulin-like signaling in *C. elegans*. *Cell* **132**, 1025–1038 (2008).
7. Morley, J. F. & Morimoto, R. I. Regulation of longevity in *Caenorhabditis elegans* by heat shock factor and molecular chaperones. *Mol. Biol. Cell* **15**, 657–664 (2004).
8. Hsu, A. L., Murphy, C. T. & Kenyon, C. Regulation of aging and age-related disease by DAF-16 and heat-shock factor. *Science* **300**, 1142–1145 (2003).
9. Cohen, E., Bieschke, J., Perciavalle, R. M., Kelly, J. W. & Dillin, A. Opposing activities protect against age-onset proteotoxicity. *Science* **313**, 1604–1610 (2006).
10. Groenning, M. Binding mode of Thioflavin T and other molecular probes in the context of amyloid fibrils—current status. *J. Chem. Biol.* **3**, 1–18 (2009).
11. Rodríguez-Rodríguez, C. *et al.* Design, selection, and characterization of thioflavin-based intercalation compounds with metal chelating properties for application in Alzheimer's disease. *J. Am. Chem. Soc.* **131**, 1436–1451 (2009).
12. Drake, J., Link, C. D. & Butterfield, D. A. Oxidative stress precedes fibrillar deposition of Alzheimer's disease amyloid β -peptide (1–42) in a transgenic *Caenorhabditis elegans* model. *Neurobiol. Aging* **24**, 415–420 (2003).
13. McColl, G. *et al.* The *Caenorhabditis elegans* A β _{1–42} model of Alzheimer's disease predominantly expresses A β _{3–42}. *J. Biol. Chem.* **284**, 22697–22702 (2009).
14. Temussi, P. A., Masino, L. & Pastore, A. From Alzheimer to Huntington: why is a structural understanding so difficult? *EMBO J.* **22**, 355–361 (2003).
15. Gidalevitz, T., Ben-Zvi, A., Ho, K. H., Brignull, H. R. & Morimoto, R. I. Progressive disruption of cellular protein folding in models of polyglutamine diseases. *Science* **311**, 1471–1474 (2006).
16. Zengel, J. M. & Epstein, H. F. Identification of genetic elements associated with muscle structure in the nematode *Caenorhabditis elegans*. *Cell Motil.* **1**, 73–97 (1980).
17. Anderson, P. & Brenner, S. A selection for myosin heavy chain mutants in the nematode *Caenorhabditis elegans*. *Proc. Natl Acad. Sci. USA* **81**, 4470–4474 (1984).
18. Ben-Zvi, A., Miller, E. A. & Morimoto, R. I. Collapse of proteostasis represents an early molecular event in *Caenorhabditis elegans* aging. *Proc. Natl Acad. Sci. USA* **106**, 14914–14919 (2009).
19. Lakowski, B. & Hekimi, S. The genetics of caloric restriction in *Caenorhabditis elegans*. *Proc. Natl Acad. Sci. USA* **95**, 13091–13096 (1998).
20. Chen, D., Thomas, E. L. & Kapahi, P. HIF-1 modulates dietary restriction-mediated lifespan extension via IRE-1 in *Caenorhabditis elegans*. *PLoS Genet.* **5**, e1000486 (2009).
21. Murphy, C. T. *et al.* Genes that act downstream of DAF-16 to influence the lifespan of *Caenorhabditis elegans*. *Nature* **424**, 277–283 (2003).
22. Walker, G. A. & Lithgow, G. J. Lifespan extension in *C. elegans* by a molecular chaperone dependent upon insulin-like signals. *Aging Cell* **2**, 131–139 (2003).
23. Li, W., Gao, B., Lee, S. M., Bennett, K. & Fang, D. RLE-1, an E3 ubiquitin ligase, regulates *C. elegans* aging by catalyzing DAF-16 polyubiquitination. *Dev. Cell* **12**, 235–246 (2007).

Supplementary Information is linked to the online version of the paper at www.nature.com/nature.

Acknowledgements We thank A. A. Gerencser for expert assistance with the confocal microscopy; A. M. Cuervo, M. S. Gill, M. Lucanic, J. Campisi, S. Melov, V. Lunyak and P. Kapahi for suggestions on the manuscript, members of the G.J.L. and P. Kapahi laboratories for helpful discussion and members of the Paper Polishing Club. Nematode strains were provided by the *Caenorhabditis* Genetics Center, funded by the National Institutes of Health (NIH) National Center for Research Resources. CF2189 was a gift from C. Kenyon's laboratory. This work was supported by grants from the Larry L. Hillblom Foundation and the NIH (UL1024917, supporting the Interdisciplinary Research Consortium on Geroscience and 1R01AG029631-01A1). G.J.L. is supported by the NIH AG21069, AG22868, AG029631-01A1, ES016655, the Larry L. Hillblom Foundation and UL1 RR024917. S.A. was supported by the U19AG0231222 from the Longevity Consortium.

Author Contributions S.A. planned and designed the project with consultation and support from G.J.L. All the data were collected by S.A. and M.C.V., with assistance from D.J.S.Z. and I.M.K. S.A. and G.J.L. wrote the paper with contribution from all authors.

Author Information Reprints and permissions information is available at www.nature.com/reprints. The authors declare no competing financial interests. Readers are welcome to comment on the online version of this article at www.nature.com/nature. Correspondence and requests for materials should be addressed to G.J.L. (glithgow@buckinstitute.org) or S.A. (salavez@buckinstitute.org).

METHODS

Nematode growth and strains. Strains were cultured under standard laboratory conditions in USP agar. Strains used in this work include N2, HE250 [*unc-52(e669su250)*], CB1157 [*unc-54(e1157)*], CF1038 [*daf-16(mu86)*], DA465 [*eat-2(ad465)*], TJ1052 [*age-1(hx546)*], PS3551 [*hsf-1(sy441)*], TJ356 [*zIs356 IV (daf-16::daf-16-gfp; pRF4 (rol-6(su1006)))*], CL4176 [*dIs27[myo-3::Aβ₍₃₋₄₂₎-let 3'UTR(pAF29); pRF4 (rol-6(su1006))*], AM140 [*rmls132[P(unc-54) Q35::YFP]*], ZZ26 [*unc-63(x26)*], CW152 [*gas-1(fc21) X*], CF2189 [*Is001[skn-1::gfp rol-6(su1006)]*].

Lifespan assay. Lifespan assays were performed as described previously²⁴. Briefly, the nematode growth media (NGM, USP agar) plates were prepared under sterile conditions. One-hundred microlitres of concentrated stocks of each of the compounds used in this study were added onto a previously prepared NGM small plate (3 ml volume) immediately spread over the surface of the plate. The final concentrations quoted in the text assume an even distribution of compound throughout the 3 ml of agar in the plate. The plates were then placed in a laminar flow hood at room temperature (22 °C) for 30 min and then 60 µl of a concentrated suspension of *E. coli* OP50 was spotted to form a circular lawn on the centre of each plate. Thirty late L4 larvae growing at 20 °C were transferred to fresh NGM plates with FUDR (75 µM, unless otherwise stated) in the presence or absence of the specified compounds and incubated at 20 °C. The first day of adulthood is day 3 in survival curves. We noted between-experiment variation in the magnitude of the lifespan extension observed with ThT, which appeared to correlate with different suppliers and batches. ThT concentration should be optimized depending on batch and purity and stability of the compound. We noted that a darkening in the appearance of the stock resulted in loss of lifespan extension activity and even early death. The optimal range for lifespan extension was between 25 and 75 µM.

Nematodes were scored as alive, dead or lost every second day. Nematodes that failed to display touch-provoked movement were scored as dead. Nematodes that died from causes other than ageing, such as sticking to the plate walls, internal hatching of eggs ('bagging') or gonadal extrusion were censored as were lost worms. Nematodes were transferred to fresh plates every 3–6 days. All lifespan experiments were performed at 20 °C unless otherwise stated. Survival curves were plotted and statistical analyses (log-rank test) were performed using Prism 4 software (Graphpad Software). **Dietary restriction.** Plates were prepared as described²⁵ but bacterial concentration was adjusted to 1.0×10^{12} c.f.u. ml⁻¹ and diluted to achieve a bacterial concentration of 1.0×10^9 c.f.u. ml⁻¹. Diluted bacterial cultures were spotted onto dietary restriction agar plates, which were modified from the standard nematode growth media (NGM) plates by excluding peptone and increasing agar from 1.7% to 2.0%. Carbenicillin (50 mg ml⁻¹) was added to the agar plates to further prevent bacterial growth. Synchronized L4 larvae grown under standard laboratory conditions (NGM plates with OP50 food, 20 °C) were transferred to fresh dietary restriction agar plates in the presence or absence of 1, 10, 25, 50 and 100 µM ThT, and lifespans scored as described earlier.

Demographic analysis. Estimates of initial mortality rate and rate of increase with age and model fitting were made using WinModest. Gompertz mortality curves, $\ln(ux) = \ln(a) + bx$, where ux defines the age-specific hazard, were fitted with log-likelihood ratios used to examine the effects of constraining the intercept (a) or gradient (b) variables.

Worm paralysis assays. Populations of CL4176 *dIs27[pCL12(unc-54/human Aβ₃₋₄₂ minigene) + pRF4]* or AM140 [*rmls132[P(unc-54) Q35::YFP]*] worms were grown at 20 °C for 48 h and then exposed to 50 µM ThT and 100 µM curcumin at 25 °C in presence of FUDR (10 µg ml⁻¹) for AM140. Scoring for paralysis was initiated 2 and 8 days after temperature upshift for CL4176 and AM140, respectively. Nematodes were scored as paralysed if they failed to move during observation and exhibited 'halos' of cleared bacteria around their heads (indicative of insufficient body movement to access food), eggs accumulated close to the body or if they failed to respond to a touch-provoked movement with a platinum wire. For sensitivity to ethanol or levamisole resistance, CW152 *gas-1(fc21) X* and ZZ26 [*unc-63(x26)*] worms were picked into 0.4 M ethanol or 50 µM levamisole, respectively, equilibrated for 5 min, and scored for paralysis as described earlier. Treated and untreated worms were compared with an unpaired *t*-test (implemented in Prism 4, Graphpad Software).

Immunostaining and photomicroscopy. For fluorescent microscopy, TJ356 [*zIs356 IV (daf-16::daf-16-gfp; pRF4 (rol-6(su1006)))*] or CF2189 *Is001[skn-1::gfp + rol-6(su1006)]* nematodes were paralysed with 1 mM levamisole mounted on 1% agarose pads and imaged using Olympus BX51 (×60 objective) and HCLImage software (Hamamatsu). For positive controls, TJ356 worms were exposed for 3 h to 33 °C and CF2189 worms were exposed to 5 mM NaAsO₂ for 15 min. For immunofluorescence, N2, HE250 *unc-52(e669su250)*, CB1157 *unc-54(e1157)* or CL4176 *dIs27[myo-3::Aβ₍₃₋₄₂₎-let 3'UTR(pAF29); pRF4 (rol-6(su1006))*] worms were treated for 24–36 h with or without 50 µM ThT at 25 °C. After this period the worms were collected, rinsed and fixed in 4% paraformaldehyde overnight. After fixation, worms were rinsed twice with 1 ml of 10 mM Tris-HCl pH 7.5 and then permeabilized by 24 h exposure to β-mercaptoethanol at 37 °C followed by collagenase treatment (2 mg ml⁻¹ for 1–1.5 h at 37 °C) to allow for digestion of the cuticle. Paramyosin and perlecan were detected with primary monoclonal antibodies 5-23 and MH3

(developed by H. Epstein and R. H. Waterston and obtained from the Developmental Studies Hybridoma Bank developed under the auspices of the NICHD and maintained by The University of Iowa, Department of Biology) and AlexaFluor 633 goat anti-mouse (Molecular Probes) as secondary antibody. Soluble oligomers and amyloid-β peptide were detected with anti polyclonal A11 (Invitrogen) and 6E10 monoclonal (Covance) primary antibodies, respectively, with AlexaFluor 568 goat anti-rabbit and AlexaFluor 488 goat anti-mouse (Molecular Probes) as secondary antibodies. Image analysis was performed in Image Analyst MKII 2.0.49 (Image Analyst Software) as follows. Aggregates were counted by image segmentation. To this end, wide-field epifluorescence and confocal micrographs were pre-processed by high pass Butterworth filtering at $\omega_{\text{cutoff}} = 0.85 \text{ cycles } \mu\text{m}^{-1}$ (order 1.5) to amplify small (<1.2 µm) punctate details, smoothed by Wiener filtering and rescaled with a gamma level 0.7. Image segmentation was performed by a modified Watershed method from seeds defined by being brighter than the 99.9 percentile of the rescaled image. Pixels brighter than 10% of the peak intensity for each aggregate were taken as positive. Because the high-pass filtering subtracts local mean, the segmentation resulted in objects outlined close to their original half maximal intensities, and therefore the size of segmented objects truly reflected the size of the aggregates. Objects larger than 30 pixels (0.56 µm²) were rejected. The high-pass filtering also eliminated the blur of wide-field images, therefore these images were handled in the same way as confocal images. Images of different conditions were handled with the same algorithm, and no subjective threshold levels were applied. The number of aggregates was determined in same-size areas close to the vulva of at least 10 worms under the same conditions.

We explored ThT distribution and potential colocalization with proteins prone to aggregate by using two-photon excitation of ThT at 800 nm and emission at 435–485 nm in combination with anti-oligomers and amyloid-β peptide immunodetection described earlier. In this spectral range worms exhibited negligible autofluorescence, therefore the signal was highly specific for ThT. Considering that image acquisition was performed after immunostaining probably only the protein-bound form of ThT was imaged. Pearson's coefficient values for ThT and amyloid-β were calculated by using Image Analyst MKII 2.0.49 (Image Analyst Software).

Western blot. Peptide corresponding to amino acids 110–145 (NLSGKGLSIEAPKKEAVQGRSIPQQAIVEEKSAE) of HSP-16.2 was used to commercially synthesize antiserum (Invitrogen). Briefly, KLH-peptide was emulsified by mixing with an equal volume of Freund's adjuvant and injected into three subcutaneous dorsal sites for a total of 0.1 mg of peptide for immunization. The animals (rabbits) were bled, the blood allowed to clot and the serum collected by centrifugation. Monoclonal HSP-70 and polyclonal HSF-1 primary antibodies were from Stressgen (N27F3-4 and SPA-901, respectively).

For immunoblot analysis, 3-day-old adult hermaphrodites were treated with 50 µM ThT or 100 µM curcumin as described earlier and replicates of 25 nematodes were collected for each treatment. Worms were transferred to siliconized eppendorf tubes, washed once in S-basal and frozen in liquid N₂. Standard SDS-PAGE was performed using (4–12%) NOVEX gels and MES running buffer. Following transfer PVDF (BioRad) membranes were incubated with antisera (1:10,000) or primary antibodies (1:1,000) diluted in blocking buffer and then with secondary, goat anti-rabbit IgG antibody/horseradish peroxidase conjugate (Pierce), diluted 1:25,000. Detection was undertaken with chemiluminescent reagents (SuperSignal, Pierce) and standard autoradiography.

RNAi knockdown of gene expression. RNAi bacterial strains expressing double-stranded RNA that inactivates specified genes were cultured and used as previously described²⁶. Briefly, eggs isolated from synchronous populations of cultures were placed on fresh RNAi plates and allowed to grow at 15 °C; 3 days later, L4 moult nematodes were transferred to new plates seeded with the same bacteria in the presence or absence of compounds and switched to 25 °C. In all cases, 1 mM isopropyl-β-D-thiogalactopyranoside (IPTG) was used for induction of double-stranded RNA. In all cases the identity of the clones was confirmed by sequencing.

Real-time qPCR analysis. Twelve single adults from control or 50 µM ThT populations were picked after 3, 6 and 12 days of treatment into 5 µl of distilled water and flash frozen until extraction. Individual worms were extracted and analysed on the QIAcube robot as described previously²⁷. The housekeeping genes *gpd-1* and *gpd-4* were found to have invariant steady-state levels across treatments and were used to derive calibrated normalized relative quantities (CNRQs) for each gene of interest as previously described²⁷.

24. McColl, G. *et al.* Pharmacogenetic analysis of lithium-induced delayed aging in *Caenorhabditis elegans*. *J. Biol. Chem.* **283**, 350–357 (2008).
25. Chen, D., Thomas, E. L. & Kapahi, P. HIF-1 modulates dietary restriction-mediated lifespan extension via IRE-1 in *Caenorhabditis elegans*. *PLoS Genet.* **5**, e1000486 (2009).
26. Timmons, L., Court, D. L. & Fire, A. Ingestion of bacterially expressed dsRNAs can produce specific and potent genetic interference in *Caenorhabditis elegans*. *Gene* **263**, 103–112 (2001).
27. McColl, G. *et al.* Insulin-like signaling determines survival during stress via posttranscriptional mechanisms in *C. elegans*. *Cell Metab.* **12**, 260–272 (2010).

Ephrin Bs are essential components of the Reelin pathway to regulate neuronal migration

Aycan Sentürk¹, Sylvia Pfennig¹, Alexander Weiss^{1†}, Katja Burk^{1†} & Amparo Acker-Palmer¹

Coordinated migration of neurons in the developing and adult brain is essential for its proper function. The secreted glycoprotein Reelin (also known as RELN) guides migration of neurons by binding to two lipoprotein receptors, the very-low-density lipoprotein receptor (VLDLR) and apolipoprotein E receptor 2 (ApoER2, also known as LRP8)¹. Loss of Reelin function in humans results in the severe developmental disorder lissencephaly² and it has also been associated with other neurological disorders such as epilepsy, schizophrenia and Alzheimer's disease³. The molecular mechanisms by which Reelin activates its receptors and controls cellular functions are largely unknown. Here we show that the neuronal guidance cues ephrin B proteins are essential for Reelin signalling during the development of laminated structures in the brain. We show that ephrin Bs genetically interact with Reelin. Notably, compound mouse mutants (*Reln*^{+/-}; *Efnb3*^{-/-} or *Reln*^{+/-}; *Efnb2*^{-/-}) and triple ephrin B1, B2, B3 knockouts show neuronal migration defects that recapitulate the ones observed in the neocortex, hippocampus and cerebellum of the *reeler* mouse. Mechanistically, we show that Reelin binds to the extracellular domain of ephrin Bs, which associate at the membrane with VLDLR and ApoER2 in neurons. Clustering of ephrin Bs leads to the recruitment and phosphorylation of Dab1 which is necessary for Reelin signalling. Conversely, loss of function of ephrin Bs severely impairs Reelin-induced Dab1 phosphorylation. Importantly, activation of ephrin Bs can rescue the *reeler* neuronal migration defects in the absence of Reelin protein. Together, our results identify ephrin Bs as essential components of the Reelin receptor/signalling pathway to control neuronal migration during the development of the nervous system.

The mammalian neocortex has characteristic laminations, containing different neuron types arranged in stereotypical patterns. Formation of this layered structure is possible only with proper migration of neurons from proliferative zones to their final position⁴⁻⁶. In recent years the extracellular protein Reelin has emerged as an important factor that affects several steps of neuronal migration and layering in the cerebral cortex (reviewed in ref. 7). Reelin exerts its function by binding to the lipoprotein receptors VLDLR and ApoER2 and inducing the phosphorylation of the adaptor protein Dab1 (refs 1, 8) by Src-family kinases (SFKs)^{9,10}. Despite the importance of the Reelin signalling pathway for proper nervous system development and that disruption of this pathway results in the severe developmental disorder lissencephaly² and is associated with epilepsy, schizophrenia and Alzheimer's disease^{3,11,12}, molecular characterization of the activation of this pathway at the cell membrane remains poorly understood. Because VLDLR and ApoER2 do not possess intrinsic kinase activity the existence of a co-receptor that locally activates Src kinases has been proposed for at least a decade. We have previously shown that ephrin Bs, transmembrane ligands for Eph receptors, have signalling capabilities that are required for synaptic plasticity and sprouting angiogenesis by regulating the activity of other transmembrane receptors such as α -amino-3-hydroxy-5-methyl-4-isoxazolepropionic acid (AMPA) receptor and vascular endothelial

growth factor (VEGF) receptor 2, respectively¹³⁻¹⁵. Moreover, stimulation of cultured cortical neurons with soluble Eph B receptors leads to the recruitment and activation of SFKs in ephrin B-membrane patches¹⁶. Therefore, we proposed that ephrin Bs might control Reelin signalling *in vivo*.

To study whether ephrin B and Reelin signalling genetically interact *in vivo* we generated compound mutant mice null for ephrin B3 or ephrin B2 and heterozygous for Reelin (*Reln*^{+/-}; *Efnb3*^{-/-} and *Reln*^{+/-}; *Efnb2*^{-/-}). *Reeler* is an autosomal recessive mutant mouse and in heterozygosity (*Reln*^{+/-}) does not show any overt phenotypes¹⁷. Gross morphology of the cortex assessed by DAPI staining on coronal cortical sections showed alterations in cell layering in the *Reln*^{+/-}; *Efnb3*^{-/-} compound mice compared to control littermates (Supplementary Fig. 1a). NeuN staining revealed a small but significant increase in neurons in the marginal zone of the ephrin B3 compound mutant mice (*Reln*^{+/-}; *Efnb3*^{-/-}), one of the hallmarks of the *reeler* phenotype¹⁸ (Supplementary Fig. 1b, c). To characterize the cortical defects in detail we analysed the distribution of postmitotic migrating neurons in the cortex of *Reln*^{+/-}; *Efnb3*^{-/-} compound mutant mice using different layer-specific markers. In wild-type mice, Tbr1 is expressed in some cortical plate neurons in layer II and most abundantly in neurons in layer VI (Fig. 1a, b) and therefore is a typical marker for early born glutamergic neocortical neurons (lower layers)¹⁹. Analysis of the *Reln*^{+/-}; *Efnb3*^{-/-} compounds revealed the presence of abundant Tbr1-positive (Tbr1⁺) neurons instead in the superficial layers of the cortex (Fig. 1a, b). We confirmed the aberrant presence of large pyramidal neurons expressing green fluorescent protein (GFP) in upper cortical layers by crossing the *Reln*^{+/-}; *Efnb3*^{-/-} compound mutant or the *reeler* mice with Thy1-GFP M-line (Supplementary Fig. 2). Conversely, markers for late cortical plate neurons (upper layers II–IV), Brn1 (also known as POU3F3) and SatB2 (ref. 20) showed an aberrant distribution in *Reln*^{+/-}; *Efnb3*^{-/-} compound mice with an accumulation of late born neurons in the lower cortical layers (Fig. 1c and Supplementary Fig. 3). At embryonic day 17.5 (E17.5), *Reln*^{+/-}; *Efnb3*^{-/-} compound mice mimicked the aberrant cortical plate splitting of the *reeler* mice²¹ with a striking accumulation of the extracellular matrix component chondroitin sulphate proteoglycan (CSPG) throughout the neocortex (Supplementary Fig. 4). To confirm that the observed defects in cortex lamination in the *Reln*^{+/-}; *Efnb3*^{-/-} compound mice are due to neuronal migration impairment we performed additional 5-bromodeoxyuridine (BrdU) pulse experiments (Supplementary Fig. 5). BrdU is incorporated in dividing progenitor cells and therefore reflects the migratory behaviour of newly born neurons at the time of injection. Quantification of cell distribution in the different cortical layers showed the characteristic *reeler* inverted cortical layering in the ephrin B3 compound mice (Supplementary Fig. 5). Loss of ephrin Bs does not cause defects in differentiation of Reelin-positive Cajal–Retzius cells or the level of expression of Reelin and components of the Reelin pathway (Supplementary Fig. 6). Therefore, all these results confirm a *reeler* outside-in cortex layering in

¹Frankfurt Institute for Molecular Life Sciences (FMLS) and Institute of Cell Biology and Neuroscience, Goethe University Frankfurt, Max-von-Laue-Str. 9, D-60438, Frankfurt am Main, Germany. †Present addresses: Samuel Lunenfeld Research Institute, Mount Sinai Hospital, Room 1078, 600 University Avenue, Toronto, Ontario M5G 1X5, Canada (A.W.); IBDML-UMR6216-CNRS, Case 907- Parc Scientifique de Luminy, 13288 Marseille Cedex 9, France (K.B.).

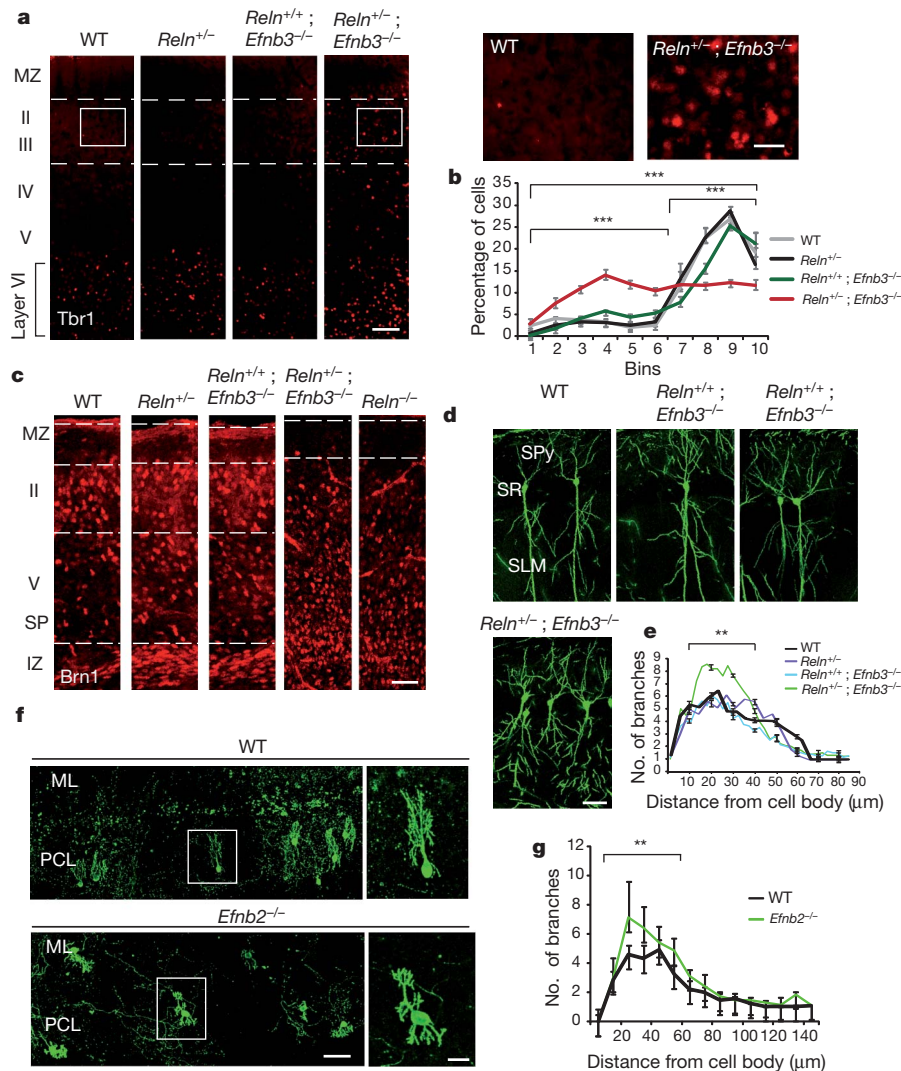


Figure 1 | Ephrin B3 and ephrin B2 deficiency differentially phenocopy *reeler*-like defects. **a**, Tbr1 staining of cerebral cortex of adult mice. Tbr1⁺ cells accumulated in the upper cortical layers (II–III, dashed lines) of the compound mice (*Reln*^{+/-}; *Efnb3*^{-/-}) compared to wild-type (WT), heterozygous *reeler* (*Reln*^{+/-}) and ephrin B3 knockout (*Efnb3*^{-/-}) mice. Magnification pictures show accumulation of cells in layer II–III of *Reln*^{+/-}; *Efnb3*^{-/-} compound mice compared to control littermates (WT). **b**, Quantification based on the distribution of the Tbr1⁺ cells in the cerebral cortex (s.e.m., *n* = 10–30). **c**, Immunostaining for Brn1 of E17.5 mice cortex showed late born neurons accumulated in lower layers in ephrin B3 compound mice similar to *reeler* cortex. **d**, Pyramidal neurons projecting towards the stratum lucosum

molecular (SLM) show misorientation and branching defects in the ephrin B3 compound mice (*Reln*^{+/-}; *Efnb3*^{-/-}, Thy1–GFP⁺). **e**, Sholl analysis showed increased branching close to the cell body (s.e.m., *n* = 90–120). **f**, **g**, Dendrite structure of Purkinje cells in the Purkinje cell layer was visualized by GFP electroporation of P6 organotypic cerebellar cultures and analysed by Sholl analysis. Increased arborization was observed in the single ephrin B2 knockout mice (*Efnb2*^{-/-}) (s.e.m., *n* = 30–40). Scale bars, 100 μm (**f**); 75 μm (**a**, **c**); 50 μm (higher magnifications in **f**), 25 μm (**d**, higher magnifications of **a**). IZ, intermediate zone; ML, molecular layer; MZ, marginal zone; PCL, Purkinje cell layer; SLM, stratum lacunosum moleculare; SP, sub-plate, SPy, stratum pyramidale; SR, stratum radiatum. ***P* < 0.01; ****P* < 0.001.

the *Reln*^{+/-}; *Efnb3*^{-/-} compound mice and suggest that these lamination defects are in fact a result of an impaired neuronal migration.

Hippocampal laminated structures were also found to be abnormal in *Reln*^{+/-}; *Efnb3*^{-/-} compound mice. In these mice, the CA1 region of the hippocampus showed significant increase in thickness and invasion of pyramidal cells into the stratum oriens (Supplementary Fig. 7a, b). Moreover, the abnormalities observed in *Reln*^{+/-}; *Efnb3*^{-/-} compound mice in the dendritic branching of pyramidal neurons of the CA1 region strikingly resembled the ones observed in the *reeler* mutants (Fig. 1d, e and Supplementary Fig. 8). Reelin also controls differentiation and position of GFAP⁺ radial glial cells for the proper migration of newly generated granule cells²². In *Reln*^{+/-}; *Efnb3*^{-/-} compound mice this radial glial scaffold network was severely affected (Supplementary Fig. 9) and this also resulted in a loose organization of the granule cell layers in the dentate gyrus (Supplementary Fig. 10). We have also observed defects in the cortex and hippocampus of

compound *Reln*^{+/-}; *Efnb2*^{-/-} mice (data not shown) indicating that both ephrin B2 and ephrin B3 might be involved and be redundant in their function to control Reelin signalling during neuronal migration in both brain structures.

Ataxia in *reeler* mice results from a severe disorganization of the cerebella in those mutants⁷. Interestingly, in *Reln*^{+/-}; *Efnb3*^{-/-} compound mice we found only mild defects in the cerebellar structures (Supplementary Fig. 11a–d, g). Instead, ephrin B2 is highly expressed in the Purkinje cells in the cerebellum²³ and although no major defects on the migration of these cells were observed (Supplementary Fig. 11h), *Efnb2*^{-/-} mice showed striking defects in the arborization of Purkinje cells analysed by electroporation of GFP in acute cerebellar slices (Fig. 1f, g) as well as by using calbindin staining (Supplementary Fig. 11e, f). Importantly, arborization defects that were already visible in the single ephrin B2 mutants (*Efnb2*^{-/-}) were significantly increased in the *Reln*^{+/-}; *Efnb2*^{-/-} compound mice (Supplementary Fig. 11e, f),

indicating that, in the cerebellum, Reelin functions in the arborization of Purkinje cells require specifically ephrin B2 and not ephrin B3.

Analysis of the compound mice revealed that ephrin B2 and ephrin B3 might have compensatory, but also specific functions in controlling Reelin signalling in the different brain structures. Importantly, a triple ephrin B1, B2, B3 mutant displayed severe migration phenotypes that resembled the *reeler* mouse (Fig. 2a–c and Supplementary Fig. 12), indicating a major role for ephrin Bs in the Reelin signalling pathway *in vivo*. However, some phenotypes in the cerebellum and hippocampus of the ephrin B1, B2, B3 mutant are not as strong as in the *reeler* mouse, suggesting compensation by ephrin B-independent functions of Reelin. In agreement with an important role of ephrin Bs controlling Reelin functions in the developing brain we find ephrin Bs colocalizing with Reelin receptors and Dab1 in migrating neurons in the cerebral cortex (Fig. 2d, e), hippocampus (Supplementary Fig. 13a, b) and in Purkinje cell neurons in the developing cerebellum (Supplementary Fig. 13c).

In order to get mechanistic insights on how ephrin Bs can crossstalk to Reelin signalling we next assessed the biochemical interaction of these two pathways. We performed a directed proteomic analysis of ephrin B-binding proteins from a neuroblastoma cell line using the tandem affinity purification–mass spectrometry methodology²⁴ and identified Reelin as a putative ephrin B-interacting protein (data not shown). We first confirmed the ability of Reelin to associate with ephrin Bs by co-immunoprecipitation of both endogenous proteins from brain lysates (Fig. 3a). Reelin extracellular domain bound directly to the extracellular domain of ephrin B3 and also to ephrin B2 (Fig. 3b), suggesting that both ephrins Bs could influence the *in vivo* functions of Reelin signalling. Importantly, stimulation of cortical neurons with Reelin leads to the clustering of ephrin Bs (Fig. 3c) and effective tyrosine phosphorylation of the adaptor Dab1 (Supplementary Fig. 14). We have previously shown that activation of ephrin Bs leads to the recruitment and activation of Src kinases in ephrin B clusters¹⁶. Therefore, we propose that ephrin Bs could recruit and activate Src kinases in VLDLR and ApoER2 receptor clusters. In agreement, we find that phosphorylated Dab1 co-immunoprecipitates with ephrin Bs at E16.5 when the neuronal migration and layering of the brain structures takes place (Fig. 3d and Supplementary Fig. 15a). Activation of ephrin Bs by a soluble receptor Eph B3–Fc leads to the recruitment and phosphorylation of Dab1 in ephrin B clusters in cortical and hippocampal neurons (Fig. 3e and Supplementary Fig. 15b). Importantly, we find that ephrin

Bs co-immunoprecipitate with both Reelin receptors, ApoER2 and VLDLR, (Fig. 3f, g) and activation of ephrin B by Eph B3–Fc clusters these receptors in ephrin B3 membrane patches in cortical and hippocampal neurons (Supplementary Fig. 15c–f) without affecting their level of expression (Supplementary Fig. 16). Co-stimulation of ephrin Bs by Eph B receptors and Reelin in cortical neurons resulted in increased Dab1 phosphorylation (Supplementary Fig. 17a–c). This function of ephrin Bs requires Src kinases (Supplementary Fig. 17d) and fully functional Reelin receptors because VLDLR knockouts and ApoER2 knockouts both showed a reduction in the activation of Dab1 following Eph B3–Fc treatment in cortical neurons (Fig. 3h and Supplementary Fig. 17e–h).

We next addressed the requirement of ephrin B-mediated recruitment and activation of Src kinases for Reelin signalling by loss-of-function studies both in cortical neurons in culture and *in vivo* in mice. Cortical neurons isolated from ephrin B3 and ephrin B2 double knockouts showed a significant impairment of Reelin-mediated phosphorylation of Dab1 (Fig. 4a, b). Ephrin B3 mouse mutants also showed *in vivo* a reduction in Dab1 phosphorylation that correlated with increased levels of Dab1 proteins (Fig. 4c–e) as it has been already shown for different mouse mutants in Reelin signalling components^{8,9,25}. More importantly, the levels of phosphorylation of Dab1 in triple ephrin B1, B2, B3 mouse mutants were greatly reduced to the same extent as in *reeler* mutants (Fig. 4c–e). We next set up a series of rescue experiments both in neuronal cultures as well as during neuronal migration in the cortex *in vivo*. Phosphorylation of Dab1 in cortical neurons isolated from *reeler* mice could be rescued as expected by stimulation with exogenous Reelin (Fig. 4f and Supplementary Fig. 18). More importantly, Dab1 phosphorylation in *reeler* neurons was rescued solely by activation of ephrin Bs with Eph receptors. To underline the importance of ephrin B for Reelin signalling during neuronal migration in the cerebral cortex we set up similar rescue experiments of the *reeler* phenotype in organotypic slice cultures. *Reeler* slices showed the typical *reeler* phenotype in the cerebral cortex with BrdU⁺ cells accumulated strongly in the lower layers. Importantly, ephrin B activation by Eph receptors was able to rescue the migratory defects in *reeler* slices guiding the BrdU⁺ cells to their proper location on layers II–III (Fig. 4g, h).

Taken together, our genetic analysis together with a strong biochemical analysis of the ephrin B mutant mice identify ephrin Bs as

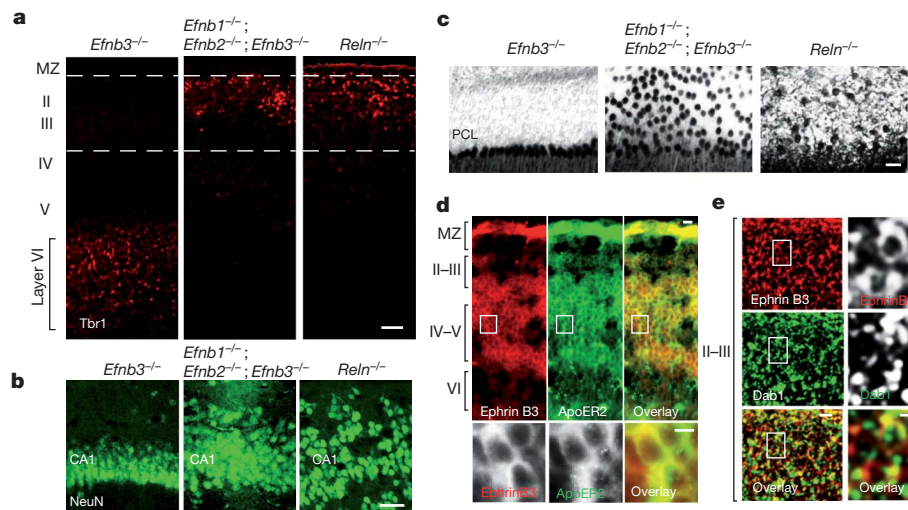


Figure 2 | Ephrin B1, B2, B3 triple mutants show a *reeler*-like phenotype. **a**, Cortical layering is inverted in the triple ephrin B1, B2, B3 mice shown in coronal cortical sections of P2 mice immunostained for Tbr1 for early born neurons (layers defined with dashed lines). **b**, NeuN analysis of adult hippocampus of *Efnb3*^{−/−}, *Efnb1*^{−/−}; *Efnb2*^{−/−}; *Efnb3*^{−/−} and *Reln*^{−/−} mice showing an expansion of the CA1 region. **c**, Calbindin immunostaining of P2

cerebellum of *Efnb3*^{−/−}, *Efnb1*^{−/−}; *Efnb2*^{−/−}; *Efnb3*^{−/−} and *Reln*^{−/−} showed severe migration defects in the Purkinje cell layer (PCL) in the *Efnb1*^{−/−}; *Efnb2*^{−/−}; *Efnb3*^{−/−}. **d**, **e**, Colocalization of ephrin B3 with ApoER2 and Dab1 detected by immunostaining in the cerebral cortex of E17.5 mice. Scale bars: 75 μ m (**d**, **e**), 50 μ m (**a**, **b**, **c**), 25 μ m (higher magnifications of **d**, **e**). CA1, Hippocampal area; MZ, Marginal zone; PCL, Purkinje cell layer.

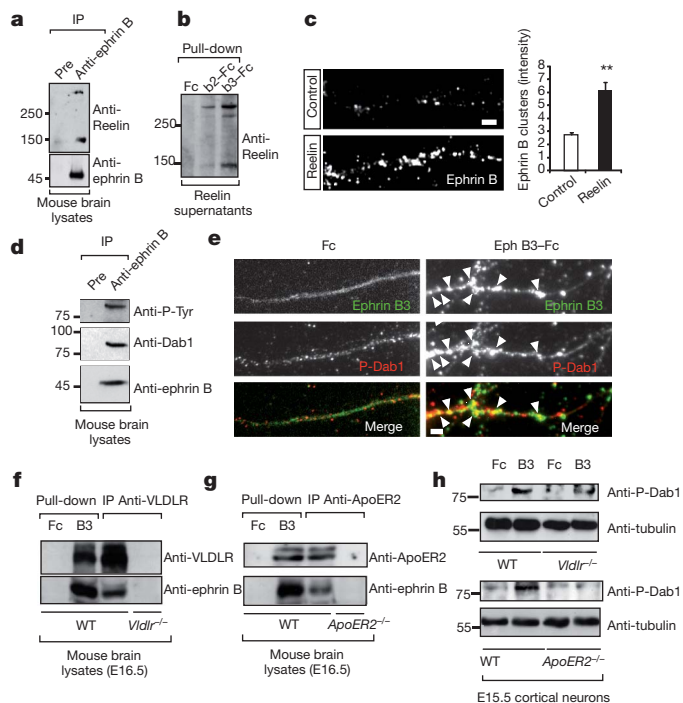


Figure 3 | Ephrin B2 and ephrin B3 ligands bind to Reelin and cluster VLDLR and ApoER2 signalling machinery. **a**, Reelin co-precipitates with ephrin B from embryonic mouse brain (E16.5) lysates. Pre, pre-immune serum. **b**, The extracellular domain of ephrin B2 and ephrin B3 binds to Reelin. Supernatants of 293 cells expressing Reelin were incubated with ephrin B2-Fc, ephrin B3-Fc or Fc as a control. **c**, Reelin clusters ephrin Bs in cortical neurons (E16.5 + 5 days in culture (DIC)). Quantification is based on signal intensity on dendritic branches (s.e.m., $n = 100-150$). **d**, Dab1 is in complex with ephrin B. Lysates from E16.5 brain were immunoprecipitated with anti-ephrin B antibody and analysed with anti-Dab1, anti-P-Tyr and anti-ephrin B antibodies. **e**, Stimulation of ephrin B3 with Eph B3-Fc induces clustering and phosphorylation of Dab1 in ephrin B3 patches in primary cortical neurons (E16.5 + 5 DIC) (arrowheads). **f**, **g**, Ephrin B3 co-immunoprecipitates with VLDLR and ApoER2. Lysates from E16.5 brains were used for Eph B3-Fc pull-downs and immunoprecipitation with anti-VLDLR or anti-ApoER2 antibodies. Fc, *Vldlr*^{-/-} and *ApoER2*^{-/-} brains were used as negative controls. **h**, *Vldlr*^{-/-} and *ApoER2*^{-/-} cortical neurons (E15.5 + 5 DIC) showed reduced P-Dab1 levels upon stimulation with Eph B3-Fc. The reduction in P-Dab1 was assessed by western blot analysis. Scale bars, 2 μ m. ** $P < 0.01$.

crucial components of the Reelin signalling machinery (Fig. 4i) that are required for the function of Reelin in neuronal migration. The regulation of Reelin signalling by ephrin Bs represents a further example of how ephrin Bs regulate the action of other membrane receptors. Ephrin Bs regulate cerebellar granule cell migration by controlling SDF-1-mediated activation of the G protein-coupled chemokine receptor CXCR4 (ref. 26). We have shown previously that ephrin B2 regulates the trafficking of AMPA receptors at the synapse, thereby controlling synaptic transmission¹⁵. In the vasculature our recent study has unravelled that ephrin B2 controls the internalization and activation of VEGFR2 during vascular development and tumour angiogenesis¹³. Now we provide evidence that ephrin Bs induce the formation of a macromolecular complex required for Src recruitment/activation and Reelin signalling. Taken together, ephrin Bs emerge now as general regulators of cellular signalling involved in the physical recruitment of signalling machineries to achieve proper spatial and temporal activation of other receptors implicated in a broad array of functions. Reelin signalling is required for proper nervous system function not only during development, but also during synaptic plasticity in the adult brain³. Importantly, we show that the activation of ephrin Bs is sufficient to rescue the absence of Reelin, indicating a

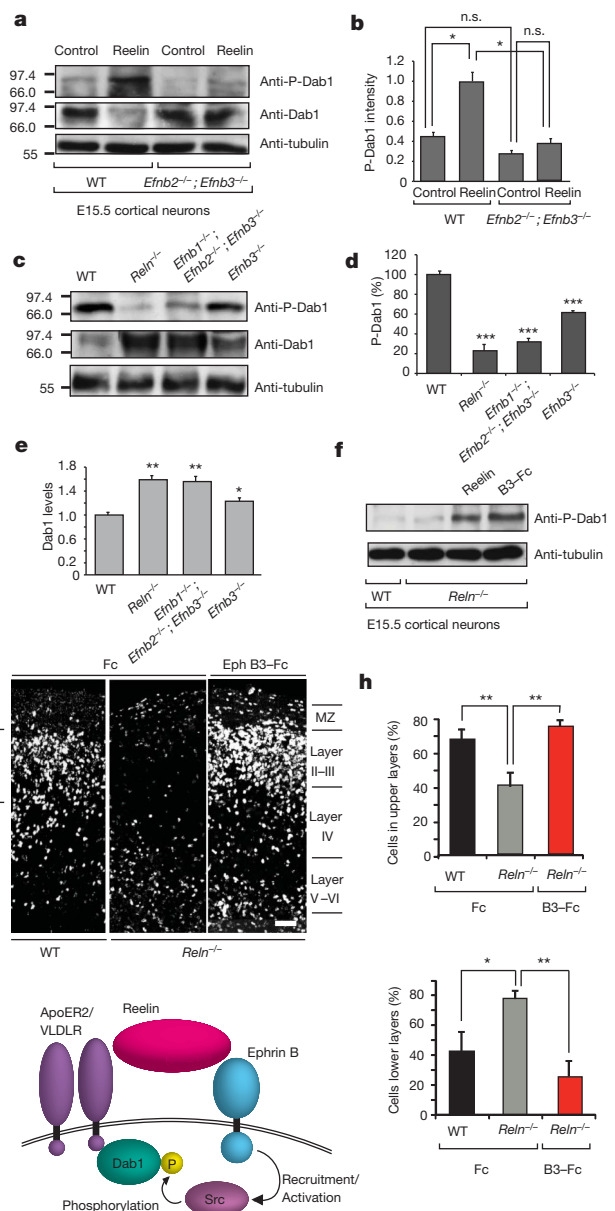


Figure 4 | Ephrin Bs are required for Reelin signalling *in vivo* and rescue the reeler defects. **a**, Ephrin Bs are required for Reelin-induced Dab1 phosphorylation. Mouse cortical neurons (E15.5) from double ephrin B2 and ephrin B3 knockouts are not able to phosphorylate Dab1 following stimulation with Reelin. **b**, Quantification of P-Dab1 signal intensity is shown. **c**, Dab1 phosphorylation is impaired *in vivo* in the *Efnb3*^{-/-} and *Efnb1*^{-/-}; *Efnb2*^{-/-}; *Efnb3*^{-/-} mice. **d**, **e**, Quantification of percentage of P-Dab1 signal (**d**) as well as Dab1 levels (**e**) is shown. **f**, Stimulation of *Reln*^{-/-} cortical neurons (E15.5) with Eph B3-Fc is sufficient to induce Dab1 phosphorylation. Levels of Dab1 phosphorylation were assessed by western blot analysis. **g**, **h**, Activation of ephrin B3 in *Reln*^{-/-} organotypic cortical cultures is sufficient to rescue the reeler phenotype. Pregnant females were injected with BrdU at E16.5 to label later born neurons that will constitute layers II–III. The correct positioning of BrdU⁺ neurons was re-established following stimulation of slice cultures during 2 days with Eph B3-Fc. Distribution of BrdU⁺ neurons is quantified both in the upper and lower cortical layers (s.e.m., $n = 24-36$) (**h**). **i**, Model for the function of ephrin Bs on Reelin signalling. Reelin binds to ephrin Bs and to the Reelin receptors. Ephrin Bs recruit and activate Src kinases which in turn phosphorylate the Dab1 associated to VLDLR and ApoER2 at the membrane. Scale bar, 50 μ m. MZ, marginal zone; n.s., not significant. * $P < 0.05$; ** $P < 0.01$; *** $P < 0.001$.

major role of ephrin Bs regulating Reelin signalling and opening avenues to explore further potential therapeutic targets for neurological disorders associated with the loss of Reelin protein.

METHODS SUMMARY

Animals. Compound mice were generated as described in Methods. All the animal experiments were conducted under the institutional guidelines and were approved by the Hessen Animal Ethics Committees.

BrdU injection and immunohistochemistry. Pregnant mice were injected intraperitoneally with BrdU (Roche Diagnostics) in 0.9% NaCl (50 mg per kg) at E12.5, E15.5 and E17.5. Postnatal mice were perfused transcardially under anaesthesia with 4% paraformaldehyde (PFA) in PBS. Embryonic brains were immersion fixed in 4% PFA at 4 °C overnight. To characterize the migrating cells sections were treated for BrdU labelling as described previously²⁷. Coronal sections of fixed brains were subjected to immunohistochemistry as described in Methods and images were acquired using a confocal microscope (Leica TCS SP2). Quantitative measurements were performed using MetaMorph software (Molecular Devices).

Stimulation of neurons. Cortical neurons from E14.5 were grown for 5 days *in vitro* and stimulated either with Eph B3–Fc chimaeras or with Reelin, using Fc or GFP as control conditions, respectively. Reelin and GFP were obtained from stable 293–HEK cell lines, as explained in Methods. Images were acquired using a digital camera (SpotRT; Diagnostic Instruments) attached to an epifluorescence microscope (Zeiss) equipped with a $\times 63$ objective (Plan-Apochromat; Zeiss). All quantitative measurements were performed using MetaMorph (Molecular Devices).

Organotypic cultures. Cortical slices were prepared from embryonic mice (E14–E16) and cerebellar slices from P5 mice as described previously^{28,29} and mounted onto porous nitrocellulose filters (0.45 μ m; pore size, Millipore). Cortical and cerebellar sections were incubated in a humidified incubator supplied with 5% CO₂ at 35 °C. After 2–4 h recovery, stimulation and staining of cultured cortical slices were performed as described previously³⁰. Cerebellar slices were electroporated (CUY21, NepaGene) with pGFP (Clontech), incubated 4 days and mounted for imaging.

Full Methods and any associated references are available in the online version of the paper at www.nature.com/nature.

Received 10 May 2010; accepted 25 January 2011.

Published online 3 April 2011.

- D'Arcangelo, G. *et al.* Reelin is a ligand for lipoprotein receptors. *Neuron* **24**, 471–479 (1999).
- Hong, S. E. *et al.* Autosomal recessive lissencephaly with cerebellar hypoplasia is associated with human *RELN* mutations. *Nature Genet.* **26**, 93–96 (2000).
- Herz, J. & Chen, Y. Reelin, lipoprotein receptors and synaptic plasticity. *Nature Rev. Neurosci.* **7**, 850–859 (2006).
- Rakic, P. Specification of cerebral cortical areas. *Science* **241**, 170–176 (1988).
- Bystron, I., Blakemore, C. & Rakic, P. Development of the human cerebral cortex: Boulder Committee revisited. *Nature Rev. Neurosci.* **9**, 110–122 (2008).
- Walsh, C. A. & Goffinet, A. M. Potential mechanisms of mutations that affect neuronal migration in man and mouse. *Curr. Opin. Genet. Dev.* **10**, 270–274 (2000).
- Tissir, F. & Goffinet, A. M. Reelin and brain development. *Nature Rev. Neurosci.* **4**, 496–505 (2003).
- Howell, B. W., Herrick, T. M. & Cooper, J. A. Reelin-induced tyrosine phosphorylation of Disabled 1 during neuronal positioning. *Genes Dev.* **13**, 643–648 (1999).
- Bock, H. H. & Herz, J. Reelin activates SRC family tyrosine kinases in neurons. *Curr. Biol.* **13**, 18–26 (2003).
- Arnaud, L., Ballif, B. A., Forster, E. & Cooper, J. A. Fyn tyrosine kinase is a critical regulator of disabled-1 during brain development. *Curr. Biol.* **13**, 9–17 (2003).
- Costa, E. *et al.* *REELIN* and schizophrenia: a disease at the interface of the genome and the epigenome. *Mol. Interv.* **2**, 47–57 (2002).
- Botella-Lopez, A. *et al.* Reelin expression and glycosylation patterns are altered in Alzheimer's disease. *Proc. Natl Acad. Sci. USA* **103**, 5573–5578 (2006).
- Sawamiphak, S. *et al.* Ephrin-B2 regulates VEGFR2 function in developmental and tumour angiogenesis. *Nature* **465**, 487–491 (2010).
- Segura, I., Essmann, C. L., Weinges, S. & Acker-Palmer, A. Grb4 and GIT1 transduce ephrinB reverse signals modulating spine morphogenesis and synapse formation. *Nature Neurosci.* **10**, 301–310 (2007).
- Essmann, C. L. *et al.* Serine phosphorylation of ephrinB2 regulates trafficking of synaptic AMPA receptors. *Nature Neurosci.* **11**, 1035–1043 (2008).
- Palmer, A. *et al.* EphrinB phosphorylation and reverse signaling: regulation by Src kinases and PTP-BL phosphatase. *Mol. Cell* **9**, 725–737 (2002).
- Caviness, V. S. Jr & Rakic, P. Mechanisms of cortical development: a view from mutations in mice. *Annu. Rev. Neurosci.* **1**, 297–326 (1978).
- Caviness, V. S. Jr. Neocortical histogenesis in normal and reeler mice: a developmental study based upon [³H]thymidine autoradiography. *Brain Res.* **256**, 293–302 (1982).
- Hevner, R. F. *et al.* Tbr1 regulates differentiation of the preplate and layer 6. *Neuron* **29**, 353–366 (2001).
- Britanova, O. *et al.* Satb2 is a postmitotic determinant for upper-layer neuron specification in the neocortex. *Neuron* **57**, 378–392 (2008).
- Sheppard, A. M. & Pearlman, A. L. Abnormal reorganization of preplate neurons and their associated extracellular matrix: an early manifestation of altered neocortical development in the reeler mutant mouse. *J. Comp. Neurol.* **378**, 173–179 (1997).
- Forster, E. *et al.* Reelin, Disabled 1, and β_1 integrins are required for the formation of the radial glial scaffold in the hippocampus. *Proc. Natl Acad. Sci. USA* **99**, 13178–13183 (2002).
- Liebl, D. J., Morris, C. J., Henkemeyer, M. & Parada, L. F. mRNA expression of ephrins and Eph receptor tyrosine kinases in the neonatal and adult mouse central nervous system. *J. Neurosci. Res.* **71**, 7–22 (2003).
- Angrand, P. O. *et al.* Transgenic mouse proteomics identifies new 14-3-3-associated proteins involved in cytoskeletal rearrangements and cell signaling. *Mol. Cell. Proteomics* **5**, 2211–2227 (2006).
- Trommsdorff, M. *et al.* Reeler/Disabled-like disruption of neuronal migration in knockout mice lacking the VLDL receptor and ApoE receptor 2. *Cell* **97**, 689–701 (1999).
- Lu, Q., Sun, E. E., Klein, R. S. & Flanagan, J. G. Ephrin-B reverse signaling is mediated by a novel PDZ-RGS protein and selectively inhibits G protein-coupled chemoattraction. *Cell* **105**, 69–79 (2001).
- Hack, I. *et al.* Divergent roles of ApoER2 and Vldlr in the migration of cortical neurons. *Development* **134**, 3883–3891 (2007).
- Alifragis, P., Parnavelas, J. G. & Nadarajah, B. A novel method of labeling and characterizing migrating neurons in the developing central nervous system. *Exp. Neurol.* **174**, 259–265 (2002).
- Ghoumari, A. M., Wehrle, R., Bernard, O., Sotelo, C. & Dusart, I. Implication of Bcl-2 and Caspase-3 in age-related Purkinje cell death in murine organotypic culture: an *in vitro* model to study apoptosis. *Eur. J. Neurosci.* **12**, 2935–2949 (2000).
- Nadarajah, B., Brunstrom, J. E., Grutzendler, J., Wong, R. O. & Pearlman, A. L. Two modes of radial migration in early development of the cerebral cortex. *Nature Neurosci.* **4**, 143–150 (2001).

Supplementary Information is linked to the online version of the paper at www.nature.com/nature.

Acknowledgements We would like to thank R. Klein for the ephrin B2^{lox/lox} and ephrin B1^{lox/lox} mice, N. Gale for the ephrin B3^{-/-} mouse, J. Herz for the ApoER2^{-/-} mouse, M. Goetz for 293-cells expressing Reelin or GFP, I. Segura for help with the ephrin B triple mutants, U. Bauer, O. Yildiz, C. Saygi, F. Kasikci, F. Voss and K. Happich for technical support, K. Hong and A. Griciuc for early contributions to this project, M. Frotscher for helpful discussions and I. Dikic and T. Acker for critically reading the manuscript. We acknowledge the Max Planck Institute of Neurobiology in Martinsried (Germany) for support and the use of equipment and animal facilities in the early stages of this project. This work was supported by grants from the Deutsche Forschungsgemeinschaft (AC180/2-1, 2-2 to A.A.-P.) and the Clusters of Excellence “Macromolecular Complexes (CEF)” (EXC115) and ECCPS (EXC147) at the University Frankfurt.

Author Contributions A.S. designed experiments and performed all the phenotypic characterization of the mouse mutants, the cortical neuron culture, organotypic slice culture rescue experiments and electroporation of cerebellar acute slice cultures. S.P. performed some of the neuronal culture experiments, organotypic slice culture rescue experiments and the biochemistry. A.W. and K.B. performed biochemistry for panels **d** and **a** in Fig. 4. A.A.-P. performed the initial biochemistry on the binding of ephrin B ligands to Reelin, designed experiments, interpreted results and wrote the manuscript.

Author Information Reprints and permissions information is available at www.nature.com/reprints. The authors declare no competing financial interests. Readers are welcome to comment on the online version of this article at www.nature.com/nature. Correspondence and requests for materials should be addressed to A.A.-P. (Acker-Palmer@bio.uni-frankfurt.de).

METHODS

Animals and genotyping. Heterozygous Thy1–GFP, VLDLR and *reeler* mice were obtained from Jackson Laboratories and genotyped as suggested by the distributor. Single ephrin B3 knockout mice were provided by N. Gale (Regeneron Pharmaceuticals) and genotyped as described previously³¹. ApoER2 knockout mice were kindly provided by Joachim Herz and genotyped as described previously³². The generation of conditional ephrin B2^{lox/lox} and the ephrin B1^{lox/lox} knockout mice has been described^{33,34}. To generate ephrin B3 or ephrin B2 compound mice, heterozygous *reeler* (*Reln*^{+/-}) mice were crossed with homozygous ephrin B3 knockout animals or Nes-cre⁺; ephrin B2^{lox/lox} and also with Thy1–GFP mice. Triple ephrin B1, B2, B3 knockout mice were generated by genetic crosses performed using single ephrin B1^{lox/lox}, ephrin B2^{lox/lox} and ephrin B3 mouse lines. All the animal experiments were conducted under the institutional guidelines and were approved by the Hessen Animal Ethics Committees.

Immunohistochemistry (IHC) and tissue preparation. Postnatal mice were perfused transcardially under anaesthesia with 0.1 M phosphate buffered saline (PBS) containing 4% paraformaldehyde (PFA). Brains of young postnatal (P) mice (P0–P5) were immersion fixed in 4% PFA at 4 °C overnight. Coronal sections (50 µm) were cut using a vibratome (VT 1200S, Leica Instruments). Embryonic brains were fixed overnight in 4% PFA, cryoprotected in 30% sucrose in PBS, embedded in TissueTek OCT compound (Sakura Finetek Europa) and cut frozen coronally on a sliding microtome (Leica Instruments) at 20 µm thickness. For IHC, vibratome sections were washed in PBS, blocked in 1% BSA/0.5% Tween-20/PBS for 1 h at room temperature and incubated with primary antibodies (rabbit anti-calbindin D-28K (1:1,000), rabbit anti-Calretinin (1:1,000), rabbit anti-Dab1 (1:1,000), mouse anti-Reelin (1:1,000), mouse anti-NeuN (1:1,000), rabbit anti-Tbr1 (1:1,000) (all from Chemicon), rabbit anti-ApoER2 (1:500, Abcam), mouse anti-CSPG (1:400, Sigma), rabbit anti-GFAP (1:1,000, DAKO), goat anti-Brn1 (C-17) (1:100, Santa Cruz), rabbit anti-Dab1 (1:500, Chemicon), rabbit anti-Phospho-Dab1 (Tyr232) (1:1,000; Cell Signaling), rabbit anti-ApoER2 (1:1,000, Abcam), goat anti-VLDLR (1:200, R&D), human Eph B3–Fc, Eph B2–Fc chimaeras (1:100, R&D Systems), rat anti-BrdU (1:200, AbD Serotec), rabbit anti-SATB2 (1:500, Abcam)) for 24–48 h at 4 °C in the same solution. Sections were then washed and incubated for 2 h with either biotinylated secondary antibodies that were viewed by the ABCkit (Vector Laboratories) with diaminobenzidine (DAB) or with fluorescence-conjugated secondary antibodies (1:200, Jackson ImmunoResearch). Cryosections, collected on gelatin coated glass microscope slides, were first washed with PBS for 5 min, then boiled in 0.1% sodium citrate buffer (pH 8.0) 15 min in a microwave for antigen retrieval and placed in a humidified chamber for the rest of the staining procedure. Sections were blocked for 1 h at room temperature in 10% serum, 0.2% Triton X-100 PBS and incubated overnight with primary antibody at 4 °C in the same solution. After washing three times with PBS for 10 min, slices were incubated with fluorescent-labelled secondary antibody for 2 h at room temperature. All sections were coverslipped with Vectashield mounting medium with DAPI (Vector Laboratories).

BrdU injection and staining. For birth dating studies, the day of the vaginal plug was considered embryonic day (E) 0.5. The timed-pregnant female mice ($n = 2-4$ for each developmental point) were injected intraperitoneally at E12.5, E15.5 and E17.5 with a single pulse (50 mg per kg body weight) of 5-bromodeoxyuridine (BrdU) (5 mg ml⁻¹ dissolved in 0.9% NaCl). The mice were perfused at P20 and BrdU staining was performed on 50-µm sections as described previously²⁷. Briefly, sections were treated with 2 M HCl for 1 h, rinsed in 0.1 M sodium borate buffer (pH 8.4) to neutralize the residual acid for 10 min and after blocking 1 h in blocking solution (5% serum, 0.2% Triton X-100 PBS) at room temperature, incubated for two nights with monoclonal mouse anti-BrdU (1:500, Chemicon) at 4 °C. After washing the sections were incubated with Alexa-Fluor-488 secondary antibodies at room temperature for 2 h and embedded in fluorescent mounting medium (Dako).

Immunocytochemistry. Cortical and hippocampal neuron cultures were prepared from embryonic mouse brains (E15.5–E17.5) as described^{15,35}. Briefly, cortices or hippocampi were removed and digested with 0.25% trypsin containing 1 mM EDTA (Invitrogen) for 20 min at 37 °C with gentle shaking. 30,000 to 70,000 (24-well plates) or 10⁶ (6-cm plates) neurons were plated on coverslips or tissue culture plates, respectively, coated with poly-D-lysine (1 mg ml⁻¹) and laminin (5 µg ml⁻¹), in neurobasal medium supplemented with B27 containing 0.5 mM L-glutamine (all reagents from Invitrogen). Neurons were grown 5 days *in vitro* (DIV) and stimulated. Stimulation and staining of neuronal cortical and hippocampal cultures were performed as described³⁵. For stimulation, unclustered recombinant mouse Eph B3–Fc, Eph B2–Fc chimaeras (R&D Systems) or Fc (Jackson ImmunoResearch) were pre-clustered for 1 h at room temperature using goat anti-human IgG (Jackson ImmunoResearch) as described previously¹⁶. For colocalization of P-Dab1, VLDLR and ApoER2 with ephrin clusters neurons were stimulated with Fc or Eph B3–Fc for 1 h. For inhibition of Src family kinases 10 µM

SU6656 (Calbiochem) was added to the medium 1 h before the stimulation with Eph B3–Fc. The neurons were then fixed with 4% PFA and 4% sucrose in PBS for 12 min at 4 °C, rinsed twice with PBS, incubated with 50 mM NH₄Cl in PBS for 10 min at 4 °C and rinsed twice again before permeabilization for 5 min with ice cold 0.1% Triton X-100 in PBS. After washing with PBS, cells were blocked for 30 min at room temperature in blocking solution (2% bovine serum albumin, 4% serum (Jackson ImmunoResearch)) and incubated with primary (rabbit anti-ephrin B (C18) (1:100, Santa Cruz), rabbit anti-Phospho-Dab1 (Tyr 232) (1:1,000, Cell Signaling), goat anti-VLDLR (1:20, R&D), rabbit anti-ApoER2 (1:500, Sigma), goat anti-human Fc (1:50, Jackson Immuno Research)) and secondary antibodies for 60 and 30 min at room temperature, respectively. Samples were mounted using the Gel/Mount anti-fading medium (Biomed).

Immunoblotting, immunoprecipitation and pull-down experiments. For immunoblotting, protein samples were separated by 7.5% SDS-PAGE and transferred to 0.45-µm nitrocellulose membranes (Schleicher & Schuell). For immunoprecipitation and direct western blot analysis cells or tissue from mouse brain were lysed in LBA lysis buffer (50 mM Tris HCl buffer, pH 7.5, 0.5% Triton X-100, 150 mM NaCl, 10 mM sodium pyrophosphate, 20 mM NaF, 1 mM sodium orthovanadate and 1% Complete (Roche)) and centrifuged at 10,000g for 10 min. Antibodies were pre-bound for 1 h to 10 µl protein A- or protein G-Sepharose beads (Pharmacia) and incubated with the lysates for 2 h at 4 °C and then applied to the gels. For western blot analysis, the following primary antibodies were used: rabbit anti-ephrin B (C-18) (1:200, Santa Cruz), mouse anti-phosphotyrosine 4G10 (1:1,000, Upstate), mouse anti-Reelin (1:1,000, Chemicon), rabbit anti-Dab1 (1:1,000, Chemicon), goat anti-Dab1 (1:200, Santa Cruz), rabbit anti-phospho-Dab1 (Tyr 232) (1:1,000; Cell Signaling), rabbit anti-ApoER2 (1:1,000, Abcam), goat anti-VLDLR (1:500, R&D), mouse anti-tubulin (1:50,000, Molecular Probes). The secondary antibodies used were horseradish peroxidase-conjugated goat anti-mouse, donkey anti-goat and goat anti-rabbit IgG (1:3,000, Jackson ImmunoResearch). Ephrin B2–Fc and ephrin B3–Fc pull-down experiments were performed as described¹⁶. Western blots are representative of at least three independent experiments. For stimulation, we used recombinant mouse Eph B3–Fc (R&D Systems), human Fc (Jackson ImmunoResearch) and Reelin and GFP (as a control) from supernatants from 293 cells expressing Reelin and GFP respectively.

Preparation of Reelin-containing and control supernatants. To obtain Reelin-enriched supernatants and control supernatants, the incubation medium (DMEM, 10% fetal calf serum, 0.360 g l⁻¹ G418, 2 mM L-glutamine (all from Invitrogen), 0.1 g l⁻¹ penicillin/streptomycin (PAA)) from Reelin-transfected 293-HEK cells or GFP-transfected control 293-HEK cells (a gift from M. Goetz) was replaced by serum-free medium (Optimem-1 with GlutaMAX (Gibco), 0.1 g l⁻¹ penicillin/streptomycin (PAA), 2 mM L-glutamine (Invitrogen)) and cells were incubated for 2 days at 37 °C, 5% CO₂. The conditioned medium was collected and concentrated ~ 20-fold by centrifugation using Amicon Ultra filters (100K, Millipore) and the Reelin content (absence of Reelin in control cell supernatants) was confirmed by western blotting using mouse anti-Reelin antibody (1:1,000, Chemicon).

Organotypic cultures. Cerebellar slices from P6 mice and brain slices from embryonic mice (E14–E16) were prepared as described previously^{28,29}. Briefly, brains were dissected out and embedded in 3% low melting point agarose (Sigma) and sectioned immediately in ice-cold preparation medium (MEM (Invitrogen), 0.1 g l⁻¹ penicillin/streptomycin (PAA), 25 mM HEPES (Invitrogen), 2 mM L-glutamine (Invitrogen), 0.45% glucose and 1 N NaOH, pH 7.4), at 300 µm using a vibratome (VT 1200S, Leica Instruments). Coronal slices of embryonic brains and cerebellar sections were mounted onto porous nitrocellulose filters (0.45 µm; Millipore) and transferred to 6-well culture plates. Slices were allowed to recover for 1 h in defined culture medium with DMEM (Invitrogen), 5% heat-inactivated horse serum (Sigma), 1 × N-2 (Gibco), 100 µM L-glutamine (Invitrogen), 2.4 g l⁻¹ glucose, and 0.1 g l⁻¹ penicillin/streptomycin (PAA) 1 × B27 (Gibco), 25% BME (Gibco) and 25 mM HEPES, with 5% CO₂ and 35 °C. The amount of medium added to each well was that required to cover the slices with a meniscus of fluid. Organotypic cultures of embryonic brains were stimulated with Eph B3–Fc or with Fc, as control, at 35 °C in a humidified incubator with 5% CO₂ for 2–4 days. We performed electroporation on cerebellar organotypic cultures. Green fluorescent protein (pGFP; Clontech) expression vector was dissolved in PBS at a concentration of 0.5 µg µl⁻¹. Immediately before use, Fast Blue solution (0.1% in PBS, Sigma) was added to the plasmid solution at a ratio of 1:10 to monitor the injection. Plasmid solution (~ 1 µl) was applied onto the cerebellar cultures using a glass micropipette. The electronic pulses (20 V, 50 ms, five times, 950 ms intervals) were then delivered using a sequence wave electroporator (CUY21, Nepa Gene). Cultured cortical and cerebellar slices were fixed with 4% PFA in 0.1 M PBS and 5% sucrose, washed several times with TBS and processed for IHC as described previously³⁰. To characterize the phenotype of migrating cells, sections were treated for BrdU labelling as described previously²⁷.

Imaging and quantifications. Images of immunocytochemical staining were acquired using a digital camera (SpotRT; Diagnostic Instruments) attached to an epifluorescence microscope (Zeiss) equipped with a $\times 63$ objective (Plan-Apochromat; Zeiss). Immunohistochemical staining done on vibratome sections were acquired using confocal microscope (Leica TCS SP2) equipped with $\times 20$ and $\times 40$ objectives. Immunohistochemical staining performed using ABCkit were acquired using a stereomicroscope (Leica M165 FC). All quantitative measurements were performed using MetaMorph software (Molecular Devices). In the cerebellum the branching defects of the Purkinje cells were analysed by setting a radial line from the Purkinje cell soma to the granular cell layer in the cerebellum. The distance was measured from the first branching point that occurs in the dendritic tree of every secondary branch of a Purkinje cell to the radial line. BrdU experiments were performed on a total number of 34 embryonic brains coming from injected females at time points E12.5, E15.5 and E17.5. From the different genotypes between 23 and 58 sections were counted with a total number of neurons that ranged between 448 and 1,022 per genotype. The images were taken consistently from all the genotypes from the S1 (primary somatosensory cortex) and the PPTA (posterior parietal association area). Quantification of Dab1 phosphorylation was based on fluorescence intensities. The intensity of P-Dab1 was calculated for dendrite stretches of 100–200 μm imaged on at least 10 different treated neurons ($n = 50$ –100). All the analysis of cortex, hippocampus and cerebellum was performed in 3–4 animals per group. Quantification of cell densities at

various areas of cortex was calculated for 100–200 μm^2 cortical area in 10–30 sections per animal. Sholl analysis was performed to characterize the morphological characteristics of neurons by counting the number of dendrite intersections for concentric circles starting at the centre of the cell body, from 20–30 neurons from each pyramidal layer of 3–4 animals. Rescue experiments in organotypic slice cultures were performed with four slices per condition in three different experiments. Quantification of western blots was performed by measuring band sizes and intensities using Photoshop (Adobe). Statistical analysis was performed using Microsoft Excel and student's *t*-tests were used to assess statistical significance of the differences between measurements.

31. Kullander, K. *et al.* Ephrin-B3 is the midline barrier that prevents corticospinal tract axons from recrossing, allowing for unilateral motor control. *Genes Dev.* **15**, 877–888 (2001).
32. Trommsdorff, M. *et al.* Reeler/Disabled-like disruption of neuronal migration in knockout mice lacking the VLDL receptor and ApoE receptor 2. *Cell* **97**, 689–701 (1999).
33. Grunwald, I. C. *et al.* Hippocampal plasticity requires postsynaptic ephrinBs. *Nature Neurosci.* **7**, 33–40 (2003).
34. Compagni, A., Logan, M., Klein, R. & Adams, R. H. Control of skeletal patterning by ephrinB1-EphB interactions. *Dev. Cell* **5**, 217–230 (2003).
35. Zhang, Y. & Bhavnani, B. R. Glutamate-induced apoptosis in primary cortical neurons is inhibited by equine estrogens via down-regulation of caspase-3 and prevention of mitochondrial cytochrome c release. *BMC Neurosci.* **6**, 13 (2005).

Structure of mammalian AMPK and its regulation by ADP

Bing Xiao^{1*}, Matthew J. Sanders^{2†*}, Elizabeth Underwood^{1*}, Richard Heath^{1*}, Faith V. Mayer^{2*}, David Carmena², Chun Jing¹, Philip A. Walker¹, John F. Eccleston^{1‡}, Lesley F. Haire¹, Peter Saiu^{1†}, Steven A. Howell¹, Rein Aasland^{1†}, Stephen R. Martin¹, David Carling² & Steven J. Gambin¹

The heterotrimeric AMP-activated protein kinase (AMPK) has a key role in regulating cellular energy metabolism; in response to a fall in intracellular ATP levels it activates energy-producing pathways and inhibits energy-consuming processes¹. AMPK has been implicated in a number of diseases related to energy metabolism including type 2 diabetes, obesity and, most recently, cancer^{2–6}. AMPK is converted from an inactive form to a catalytically competent form by phosphorylation of the activation loop within the kinase domain⁷: AMP binding to the γ -regulatory domain promotes phosphorylation by the upstream kinase⁸, protects the enzyme against dephosphorylation, as well as causing allosteric activation⁹. Here we show that ADP binding to just one of the two exchangeable AXP (AMP/ADP/ATP) binding sites on the regulatory domain protects the enzyme from dephosphorylation, although it does not lead to allosteric activation. Our studies show that active mammalian AMPK displays significantly tighter binding to ADP than to Mg-ATP, explaining how the enzyme is regulated under physiological conditions where the concentration of Mg-ATP is higher than that of ADP and much higher than that of AMP. We have determined the crystal structure of an active AMPK complex. The structure shows how the activation loop of the kinase domain is stabilized by the regulatory domain and how the kinase linker region interacts with the regulatory nucleotide-binding site that mediates protection against dephosphorylation. From our biochemical and structural data we develop a model for how the energy status of a cell regulates AMPK activity.

At the whole-body level, AMPK is regulated by a diverse range of hormones—for example, leptin¹⁰, adiponectin¹¹, ciliary neurotrophic factor¹² and ghrelin¹³—and it has a role in appetite^{13,14}, glucose, lipid and protein metabolism^{1,3,15}, cell growth, and cell polarity^{2,4}. AMPK is a heterotrimeric complex comprising an α -catalytic subunit and two regulatory subunits (β and γ)¹. Activation of AMPK requires phosphorylation of Thr 172, which lies in the activation segment of the amino-terminal kinase domain of the α -subunit⁷. Phosphorylation of Thr 172 leads to a several-hundred-fold increase in activity^{9,16}. In mammals, calcium/calmodulin-dependent protein kinase kinase- β (CaMKK β) and LKB1 are the predominant kinases upstream of AMPK, although there is some evidence implicating other upstream kinases^{17,18}. Previous studies have shown that AMP protects against the dephosphorylation of Thr 172 (refs 16, 19) and we recently provided evidence that protection against dephosphorylation is the major physiological mechanism for activation of AMPK⁹. In addition to activation by phosphorylation, AMP causes a 2–5-fold allosteric activation of AMPK depending on the nature of the isoforms present in the AMPK complex²⁰. To address this issue we previously investigated the nucleotide-binding properties of the γ 1 subunit of AMPK and determined the structure of the regulatory core of mammalian

AMPK (C-terminal domain of α -subunit, C-terminal domain of β -subunit, full-length γ -subunit; hereafter referred to as the regulatory fragment) in complex with nucleotides²¹. Notably, our studies revealed that three of the four potential nucleotide-binding sites are occupied²¹. One of these sites contains a permanently bound AMP molecule (site 4, following nomenclature proposed by ref. 22), whereas AMP and Mg-ATP compete for binding at the other two sites²¹ (site 1 and site 3).

Unlike AMP, ADP has no significant allosteric effect on AMPK isolated from rat liver²³. Consistent with this, we also found that ADP does not activate recombinant AMPK under conditions where AMP produces a twofold activation (Fig. 1a). However, our studies show that ADP provides protection of AMPK from dephosphorylation across a similar range of concentrations as AMP (Fig. 1b). We have also shown the same effect using AMPK purified from rat liver (Supplementary Fig. 2a). Although Mg-ATP does not protect against dephosphorylation (Fig. 1c), it does compete with the protective effect of both AMP and ADP on dephosphorylation (Fig. 1d). We have also shown that the protective effect of ADP is lost in a Wolff–Parkinson–White syndrome mutation (Supplementary Fig. 2b). We propose that AMP or ADP (AMP/ADP) binding shifts the equilibrium between dephosphorylation-sensitive and -insensitive states, and thus slows, but does not abolish, dephosphorylation of the enzyme by phosphatases.

Extending our earlier work looking at nucleotide binding to the regulatory fragment, we characterized binding of nucleotides to active full-length AMPK. For these studies we used CaMKK β to stoichiometrically phosphorylate Thr 172 on the activation loop of recombinant full-length AMPK, we used the coumarin adducts of ATP and ADP as fluorescent reporters of nucleotide binding, and derived the binding parameters for the unlabelled nucleotides by competition experiments (Fig. 2a). We verified that the two species bind at the same sites by determining the crystal structures of the regulatory fragment in complex with coumarin-ADP and with ADP (Supplementary Fig. 3). The results show (Table 1) that the two exchangeable sites have markedly different affinities for nucleotides. Binding at the tighter of the two sites is at least 30-fold stronger than at the weaker site. Given that under physiological conditions most of the ATP is coordinated to Mg²⁺, and that the majority of AMP and ADP is not, we also measured nucleotide binding in the presence of this cation. The data show that Mg-ATP binds up to tenfold weaker than ATP. Thus, active AMPK binds AMP/ADP significantly more strongly than it does Mg-ATP at both exchangeable sites. There are two lines of evidence that lead us to conclude that it is AMP/ADP binding at the weaker of the two exchangeable sites that accounts for the protection of the enzyme against dephosphorylation. The first is that the dose-response curve for AMP/ADP-mediated protection against phosphorylation correlates with the binding curves for these nucleotides at the weaker, rather than the stronger, of the two binding sites (Fig. 1b). The second comes from our discovery that NADH binds to AMPK.

¹MRC National Institute for Medical Research, The Ridgeway, Mill Hill, London NW7 1AA, UK. ²MRC Clinical Sciences Centre, Hammersmith Hospital Campus, Imperial College, DuCane Road, London W12 0NN, UK. [†]Present addresses: MRC National Institute for Medical Research, The Ridgeway, Mill Hill, London NW7 1AA, UK (M.J.S.); Department of Molecular Biology, University of Bergen, Thormøhlensgt. 55, N5020 Bergen, Norway (R.A.); Cancer Research UK, 44 Lincoln's Inn Fields, PO Box 123, London WC2A 3PX, UK (P.S.).

*These authors contributed equally to this work.

‡Deceased.

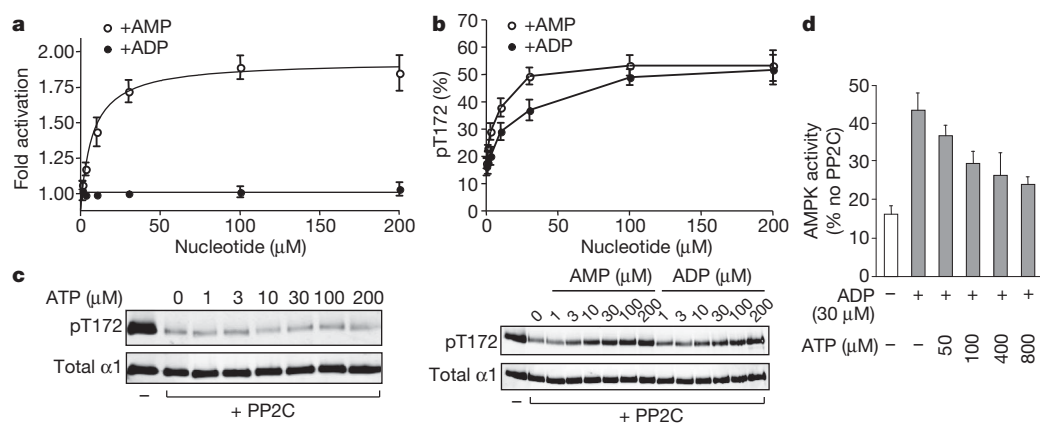


Figure 1 | Role of ADP in regulation of AMPK activity. **a**, AMP, but not ADP, allosterically activates AMPK. **b**, AMP and ADP protect AMPK from dephosphorylation. **c**, ATP does not protect against dephosphorylation. **d**, Mg-ATP competes with the protective effect of ADP on dephosphorylation. All results are displayed as the mean \pm s.e.m. determined from at least three independent experiments. Where appropriate a representative blot ($n = 3$) showing Thr 172 phosphorylation and total α -subunit levels is shown.

NADH undergoes a significant change in fluorescence upon binding to AMPK. We used this property to establish that the cofactor binds to a single site on the enzyme, with a dissociation constant (K_d) of about 50 μM (Fig. 2b, inset). NADH binding is competed by AXPs binding to the stronger, but not the weaker, of the two exchangeable sites (Fig. 2b and Table 1). When we repeated the ADP protection against dephosphorylation experiments using a range of NADH concentrations, we found no evidence for NADH competing with the protective effect of ADP on dephosphorylation, whereas NADH and ADP both compete with AMP for allosteric activation of the enzyme (Supplementary Fig. 4). This observation indicates that it is AMP/ADP binding at the weaker of the two exchangeable sites, the one that does not bind NADH, that is responsible for protection against dephosphorylation. We also carried out co-crystallization of the regulatory fragment with one molar equivalent of ADP (Supplementary Fig. 5). The resulting electron density map showed full occupancy of ADP at site 1 and no detectable density at site 3, identifying site 3 as the weaker binding site. We can therefore assign the allosteric effect to AMP binding at the tighter site 1, and protection against dephosphorylation is mediated by AMP/ADP binding at the weaker site 3.

Previous studies on the regulation of AMPK have focused on the role of AMP because it allosterically activates the enzyme¹⁵ whereas ADP does not. However, phosphorylation remains central to AMPK regulation as the enzyme is inactive in the absence of Thr 172 phosphorylation^{7,16}. Under optimal conditions, mammalian cells maintain ATP at a high level relative to ADP and AMP. Typical concentrations

of free adenine nucleotides in mammalian cells lie in the range of 3,000–8,000 μM for ATP, 50–200 μM for ADP and 0.5–5 μM for AMP^{24–26}. Because the free concentration of ADP is between 10- to 400-fold higher than AMP, and their binding constants are similar, ADP will be more successful at competing with Mg-ATP than AMP. Therefore, the fact that ADP protects AMPK from dephosphorylation is likely to represent an important physiological mechanism for regulating the activity of the enzyme.

We have also determined the crystal structure of an active form of the enzyme that encompasses the whole of the catalytic α -subunit. The construct used is shown in Fig. 3a (details of its design are given in Supplementary Fig. 6). From the best samples we collected a data set to 3.3 Å Bragg spacing, after screening about 100 crystals, and solved the structure by molecular replacement using independent models for the regulatory fragment (Protein Data Bank 2V8Q)²¹ and the kinase domain (Protein Data Bank 2H6D)²⁷. Although the data set is at medium resolution, the molecular replacement solution was robust and yielded initial electron density that revealed the location of many components that were not present in the original model. As might be expected for a structure of this complexity and resolution, some parts of the molecule are better defined than others. For example, the activation loop of the kinase domain, which is packed against the regulatory fragment, has better defined electron density than loops on the surface of the complex, which often show continuous main-chain density but lack side-chain features. Overall, the most important features of the current structure concern the architecture of the complex, particularly the relationships between the α -kinase domain and the α -linker with the regulatory fragment (omit maps for these regions are presented in Supplementary Fig. 7).

The structure is shown in Ribbons representation (Fig. 3b, c and Supplementary Fig. 8) and in space-filling representation before and after the kinase domain and the linker region have been rotated away from the complex to display their contact regions (Fig. 3d). The first of these interfaces involves the kinase domain and has a surface area of about 1,100 Å². This relatively modest contact area is consistent with the observation that specific protease cleavage of the linker between the kinase domain and the C-terminal domain of the α -subunit leads to material that separates into two components (kinase domain plus regulatory fragment) after gel filtration. A significant part of the

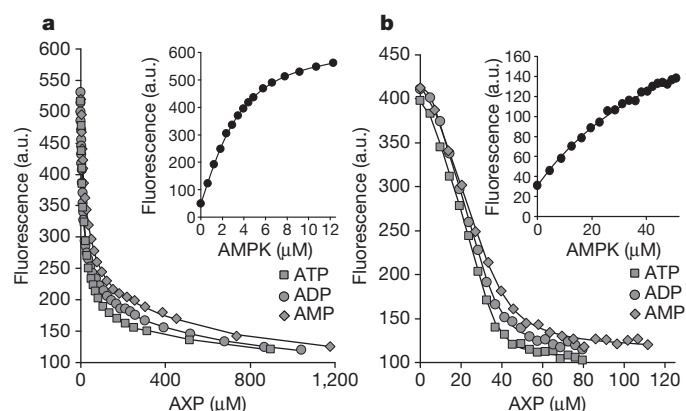


Figure 2 | Measurement of equilibrium dissociation constants for the binding of AXPs to phosphorylated AMPK. **a**, Displacement of coumarin-ATP (C-ATP) from the AMPK–(coumarin-ATP)₂ complex by AXPs monitored using fluorescence at 470 nm. Solid lines are the computed best fits with $K_{d,I}$ and $K_{d,II}$ for C-ATP binding to AMPK fixed at 1.1 and 4.2 μM . Inset: titration of coumarin-ATP with AMPK. **b**, Displacement of NADH from the AMPK–NADH complex by AXPs monitored using fluorescence at 435 nm. The solid line is the computed best fit with the K_d for NADH fixed at 65 μM . Inset: fluorescence titration of NADH with AMPK.

Table 1 | Equilibrium K_d values for the binding of AXPs to phosphorylated AMPK

Ligand	K_d (μM) versus NADH	$K_{d,I}$ (μM)	$K_{d,II}$ (μM)
		versus C-AXPs	
AMP	1.6 (0.5)	2.5 (0.6)	80 (25)
ADP	1.3 (0.5)	1.5 (0.4)	50 (15)
ATP	0.9 (0.3)	1.7 (0.5)	65 (15)
Mg-ATP	32 (12)	18 (7.5)	230 (80)

Dissociation constants (K_d) were determined at 20 °C by competition against NADH or coumarin-ATP (C-AXPs) in 25 mM Tris, 1 mM TCEP, 100 mM NaCl (pH 8) with and without 5 mM MgCl₂. The K_d values are reported as the mean (\pm s.d.) determined from at least three independent measurements.

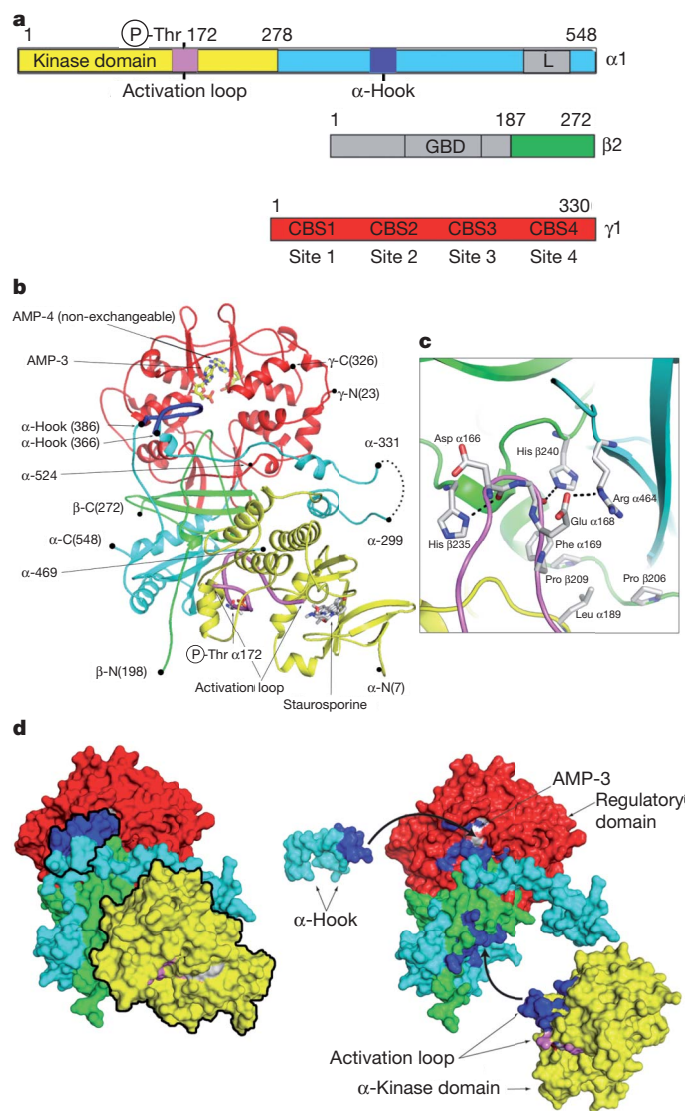


Figure 3 | Crystal structure of active mammalian AMPK. **a**, Schematic representation of the components of the heterotrimer; the parts of the complex missing from the crystallized protein are shown in grey. The domains, including the activation loop (pink) and α -hook (dark blue), are coloured the same in all panels. GBD, glycogen-binding domain. **b**, Ribbon representation of the crystallized complex with two bound AMPs, stauroporine and phosphorylated Thr 172 shown in stick representation. The α -hook and activation loop of the kinase domain are shown in heavier lines and coloured dark blue and pink, respectively. **c**, The interface between the activation loop and the regulatory fragment is shown in more detail in a similar orientation as **b**; potential electrostatic interactions are indicated by dashed lines. **d**, The complex is shown in two space-filling representations. The left panel represents the same view as **b** with the α -hook and kinase domain outlined in black. In the right-hand panel these two components have been rotated away from the regulatory domain to show the interaction surfaces in an 'open-book' representation, where the contacting residues have been coloured in dark blue. With the α -hook removed, AMP-3 becomes visible. The black arrows indicate the rotations that would reassemble the complex.

contact area involves the activation loop of the kinase interacting predominantly with the C terminus of the β -domain (Fig. 3c). Unlike previous structures of the isolated and non-phosphorylated kinase domain, the phosphorylated activation loop in our structure is well ordered, as evidenced by electron density maps (Supplementary Fig. 7). The small lobe of the kinase is in a more closed conformation relative to the unphosphorylated (and thus inactive) isolated kinase domain structure²⁷ (Supplementary Fig. 9). The fact that the activation loop mediates the interaction of the kinase domain with the regulatory

fragment means that, in this conformation, Thr 172 is protected from access by phosphatases. This idea is strongly supported by site-directed mutagenesis experiments: mutation of β 1 His 233 (corresponding to His-235 in β 2) at the interface with the kinase domain (Fig. 3c) results in an enzyme that is activatable by phosphorylation but that has a significantly increased rate of dephosphorylation in phosphatase assays (Fig. 4a, b).

Another component of the α -subunit-regulatory fragment interaction is provided by a part of the segment of the α -chain that links the N-terminal kinase domain to the C-terminal regulatory fragment, involving residues between α 373 and α 382 that are largely conserved between α 1 and α 2 in vertebrates (Supplementary Fig. 10) and which we have called the α -hook structure (Fig. 3b, d). The α -hook interacts with the γ -subunit at the exchangeable binding site 3, with AMP bound, which we have assigned as the weaker of the two sites responsible for mediating AMP/ADP protection against dephosphorylation. The hook makes a lid over the nucleotide-binding site that accounts for a buried surface area of about 500 Å². We obtained crystals of this construct with AMP added to the crystallization mixture, and an AMP molecule is clearly identifiable in the electron density maps at site 3, as well as at the non-exchangeable site. Although we did not see AMP at site 1 in the initial crystals, we subsequently achieved good occupancy at this site by maintaining a higher concentration of AMP during crystallization and handling procedures (data not shown). In contrast, we think that the AMP at site 3 is held in place by the arrangement of the α -hook and that it would have to dissociate before the bound AMP could be released and then exchanged. On the basis of superposition of our earlier structures of the regulatory fragment of AMPK in complex with ADP and Mg-ATP and the structure presented here, we think that the α -hook sequence cannot interact with site 3 when Mg-ATP is bound, mainly

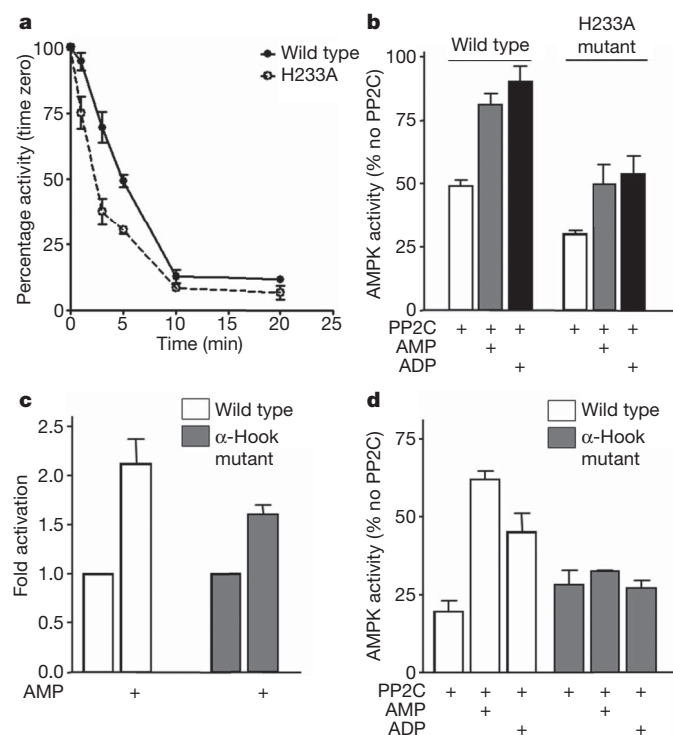


Figure 4 | Mutational analysis of AMPK regulation. **a**, Dephosphorylation rate of the wild type or β -His 233 to alanine kinase domain interface mutant (H233A, corresponding to H235A in β 2). **b**, Protection of dephosphorylation of wild type or H233A mutant by AMP (30 μ M) or ADP (30 μ M) after incubation for 5 min. **c**, Allosteric activation of wild type or α -hook mutant (harbouring mutation of residues R375Q, T377A, D379A and E380A within α 1) by AMP (100 μ M). **d**, AMP (30 μ M) and ADP (30 μ M) protection of wild type or α -hook mutant from dephosphorylation after incubation for 20 min. All results are the mean \pm s.e.m. from at least three independent experiments.

due to the change in conformation of Arg 69 of the γ -subunit, which would generate a steric clash with the α -hook (Supplementary Fig. 11). To test the role of the α -hook in mediating protection against dephosphorylation we generated a mutant in this region (R375Q/T377A/D379A/E380A). The resulting enzyme was allosterically activated by AMP but was not subject to protection against dephosphorylation by AMP or ADP (Fig. 4c, d). Interestingly, the mutation at His 233 described above does retain some protective effect of AMP/ADP (Fig. 4a, b). Given that this mutation would be expected to weaken the interaction between the kinase domain and the regulatory fragment, but not block it, it seems reasonable that AMP/ADP binding would still help to order the α -hook and thus facilitate the recruitment of the kinase domain.

Taking our biochemical and structural data together, we propose the following model for how AMP/ADP, but not Mg-ATP, protects AMPK against dephosphorylation, and thus inactivation (Supplementary Fig. 1). We have demonstrated that the protective effect of AMP/ADP is mediated by its binding to the weaker of the two exchangeable sites, which we have identified as site 3. We have also shown that the α -hook region binds into this site in the presence of AMP and predict that the same situation would occur with ADP. We further suggest that binding of the α -hook acts to restrict the flexibility of the preceding α -linker region (residues 300–370) and, in so doing, promotes the interaction of the kinase domain with the regulatory fragment seen in our crystal structure. This interaction, which mostly involves contacts between the activation loop and the C-terminal domain of β , would therefore act to protect Thr 172 against dephosphorylation. Because the interaction surface of the α -hook with the regulatory fragment is relatively small it is likely that there is a dynamic equilibrium between the α -hook-bound and α -hook-unbound species. If, as our structure indicates, AMP/ADP binding favours the α -hook-bound species but Mg-ATP binding drives formation of the α -hook-unbound species, then the competitive binding of AMP/ADP versus Mg-ATP would control the extent to which the enzyme was protected from dephosphorylation and inactivation.

METHODS SUMMARY

AMPK complexes were expressed in *Escherichia coli* BL21 (DE3) cells, purified by affinity chromatography using nickel-Sepharose and phosphorylated by incubation with CaMKK β as described previously⁹. AMPK activity was determined using 0.2 mM SAMS peptide⁹, 0.2 mM ATP and 5 mM MgCl₂. Dephosphorylation of AMPK by recombinant PP2C- α was monitored either by measuring AMPK activity using the SAMS peptide assay or by western blotting of phospho-T172. Western blot signals for phospho-T172 and total AMPK α -subunit (determined using sheep anti- α 1 or anti- α 2 antibodies) were quantified using the Li-Cor Odyssey infrared imaging system. Uncorrected fluorescence spectra of the nucleotides (3'-(7-diethylaminocoumarin-3-carboxylamino)-3'-deoxy-ADP (C-ADP), and 3'-(7-diethylaminocoumarin-3-carboxylamino)-3'-deoxy-ATP (C-ATP) (both gifts from M. Webb)) and NADH and their complexes were recorded at 20 °C using a Jasco FP-6300 fluorimeter. Binding of nucleotides was monitored by titrating nucleotide (4–10 μ M) with AMPK. Dissociation constants for AMP, ADP and ATP were determined using competition assays. The engineered crystallization construct was expressed as a His-tag fusion protein in *E. coli*. Purified protein was phosphorylated using CaMKK β before mixing with AMP and staurosporine. Crystals were grown by the hanging-drop method using isopropanol and MPD as precipitant. Diffraction data were collected on the Diamond Light Source, Oxford and processed using Denzo and Scalepack²⁸. The structure was solved by molecular replacement using Amore²⁹ and standard refinement was carried out with Refmac³⁰ with manual model building with COOT. Figures were created with Pymol (<http://pymol.sourceforge.net/>).

Received 30 July 2010; accepted 16 February 2011.

Published online 13 March 2011.

- Carling, D. The AMP-activated protein kinase cascade—a unifying system for energy control. *Trends Biochem. Sci.* **29**, 18–24 (2004).
- Hardie, D. G. AMP-activated/SNF1 protein kinases: conserved guardians of cellular energy. *Nature Rev. Mol. Cell Biol.* **8**, 774–785 (2007).
- Kahn, B. B., Alquier, T., Carling, D. & Hardie, D. G. AMP-activated protein kinase: ancient energy gauge provides clues to modern understanding of metabolism. *Cell Metab.* **1**, 15–25 (2005).
- Shackelford, D. B. & Shaw, R. J. The LKB1-AMPK pathway: metabolism and growth control in tumour suppression. *Nature Rev. Cancer* **9**, 563–575 (2009).

- Cool, B. *et al.* Identification and characterization of a small molecule AMPK activator that treats key components of type 2 diabetes and the metabolic syndrome. *Cell Metab.* **3**, 403–416 (2006).
- Huang, X. *et al.* Important role of the LKB1-AMPK pathway in suppressing tumorigenesis in PTEN-deficient mice. *Biochem. J.* **412**, 211–221 (2008).
- Stein, S. C., Woods, A., Jones, N. A., Davison, M. D. & Carling, D. The regulation of AMP-activated protein kinase by phosphorylation. *Biochem. J.* **345**, 437–443 (2000).
- Oakhill, J. S. *et al.* β -Subunit myristoylation is the gatekeeper for initiating metabolic stress sensing by AMP-activated protein kinase (AMPK). *Proc. Natl Acad. Sci. USA* **107**, 19237–19241 (2010).
- Sanders, M. J., Grondin, P. O., Hegarty, B. D., Snowden, M. A. & Carling, D. Investigating the mechanism for AMP activation of the AMP-activated protein kinase cascade. *Biochem. J.* **403**, 139–148 (2007).
- Minokoshi, Y. *et al.* Leptin stimulates fatty-acid oxidation by activating AMP-activated protein kinase. *Nature* **415**, 339–343 (2002).
- Yamauchi, T. *et al.* Adiponectin stimulates glucose utilization and fatty-acid oxidation by activating AMP-activated protein kinase. *Nature Med.* **8**, 1288–1295 (2002).
- Watt, M. J. *et al.* CNTF reverses obesity-induced insulin resistance by activating skeletal muscle AMPK. *Nature Med.* **12**, 541–548 (2006).
- Andersson, U. *et al.* AMP-activated protein kinase plays a role in the control of food intake. *J. Biol. Chem.* **279**, 12005–12008 (2004).
- Minokoshi, Y. *et al.* AMP-kinase regulates food intake by responding to hormonal and nutrient signals in the hypothalamus. *Nature* **428**, 569–574 (2004).
- Hardie, D. G., Carling, D. & Sim, A. T. R. The AMP-activated protein kinase: a multisubstrate regulator of lipid metabolism. *Trends Biochem. Sci.* **14**, 20–23 (1989).
- Suter, M. *et al.* Dissecting the role of 5'-AMP for allosteric stimulation, activation, and deactivation of AMP-activated protein kinase. *J. Biol. Chem.* **281**, 32207–32216 (2006).
- Carling, D., Sanders, M. J. & Woods, A. The regulation of AMP-activated protein kinase by upstream kinases. *Int. J. Obes.* **32** (Suppl. 4), S55–S59 (2008).
- Momcilovic, M., Hong, S. P. & Carlson, M. Mammalian TAK1 activates Snf1 protein kinase in yeast and phosphorylates AMP-activated protein kinase *in vitro*. *J. Biol. Chem.* **281**, 25336–25343 (2006).
- Davies, S. P., Helps, N. R., Cohen, P. T. & Hardie, D. G. 5'-AMP inhibits dephosphorylation, as well as promoting phosphorylation, of the AMP-activated protein kinase. Studies using bacterially expressed human protein phosphatase-2C α and native bovine protein phosphatase-2AC. *FEBS Lett.* **377**, 421–425 (1995).
- Cheung, P. C., Salt, I. P., Davies, S. P., Hardie, D. G. & Carling, D. Characterization of AMP-activated protein kinase γ -subunit isoforms and their role in AMP binding. *Biochem. J.* **346**, 659–669 (2000).
- Xiao, B. *et al.* Structural basis for AMP binding to mammalian AMP-activated protein kinase. *Nature* **449**, 496–500 (2007).
- Kemp, B. E., Oakhill, J. S. & Scott, J. W. AMPK structure and regulation from three angles. *Structure* **15**, 1161–1163 (2007).
- Carling, D., Clarke, P. R., Zammit, V. A. & Hardie, D. G. Purification and characterization of the AMP-activated protein kinase. Copurification of acetyl-CoA carboxylase kinase and 3-hydroxy-3-methylglutaryl-CoA reductase kinase activities. *Eur. J. Biochem.* **186**, 129–136 (1989).
- Veech, R. L., Lawson, J. W., Cornell, N. W. & Krebs, H. A. Cytosolic phosphorylation potential. *J. Biol. Chem.* **254**, 6538–6547 (1979).
- Hellsten, Y., Richter, E. A., Kiens, B. & Bangsbo, J. AMP deamination and purine exchange in human skeletal muscle during and after intense exercise. *J. Physiol.* **520**, 909–920 (1999).
- McConnell, G. K. *et al.* Short-term exercise training in humans reduces AMPK signalling during prolonged exercise independent of muscle glycogen. *J. Physiol. (Lond.)* **568**, 665–676 (2005).
- Little, D. R. *et al.* A conserved mechanism of autoinhibition for the AMPK kinase domain: ATP-binding site and catalytic loop refolding as a means of regulation. *Acta Crystallogr. F* **66**, 143–151 (2010).
- Otwinowski, Z. & Minor, W. Data Collection and Processing. *Proc. CCP4 Study Weekend* 556–562 (SERC, 1993).
- Navaza, J. AMoRe: an Automated Package for Molecular Replacement. *Acta Crystallogr. A* **50**, 157–163 (1994).
- CCP4. The CCP4 suite: programs for protein crystallography. *Acta Crystallogr. D* **50**, 760–763 (1994).

Supplementary Information is linked to the online version of the paper at www.nature.com/nature.

Acknowledgements We thank M. Webb for gift of coumarin nucleotides, J. Skehel for comments on the manuscript and S. Smerdon for discussion and assistance. Work in both laboratories is supported by the MRC and we gratefully acknowledge Diamond Light Source for synchrotron access.

Author Contributions B.X., M.J.S., E.U., R.H., F.V.M., D. Carmina, C.J., P.A.W., J.F.E., L.F.H., P.S., S.A.H., R.A. and S.R.M. performed experiments. All authors contributed to data analysis, experimental design and manuscript writing.

Author Information Coordinates and structure factors have been deposited in the Protein Data Bank with accession codes 2Y8L, 2Y8Q, 2Y94 and 2YA3. Reprints and permissions information is available at www.nature.com/reprints. The authors declare no competing financial interests. Readers are welcome to comment on the online version of this article at www.nature.com/nature. Correspondence and requests for materials should be addressed to D.C. (david.carling@csc.mrc.ac.uk) or S.J.G. (sgambli@nimr.mrc.ac.uk).

Dynamic regulation of 5-hydroxymethylcytosine in mouse ES cells and during differentiation

Gabriella Ficiz^{1*}, Miguel R. Branco^{1*}, Stefanie Seisenberger¹, Fátima Santos¹, Felix Krueger², Timothy A. Hore¹, C. Joana Marques^{1,†}, Simon Andrews² & Wolf Reik^{1,3}

Methylation at the 5' position of cytosine in DNA has important roles in genome function and is dynamically reprogrammed during early embryonic and germ cell development¹. The mammalian genome also contains 5-hydroxymethylcytosine (5hmC), which seems to be generated by oxidation of 5-methylcytosine (5mC) by the TET family of enzymes that are highly expressed in embryonic stem (ES) cells^{2–4}. Here we use antibodies against 5hmC and 5mC together with high throughput sequencing to determine genome-wide patterns of methylation and hydroxymethylation in mouse wild-type and mutant ES cells and differentiating embryoid bodies. We find that 5hmC is mostly associated with euchromatin and that whereas 5mC is under-represented at gene promoters and CpG islands, 5hmC is enriched and is associated with increased transcriptional levels. Most, if not all, 5hmC in the genome depends on pre-existing 5mC and the balance between these two modifications is different between genomic regions. Knockdown of *Tet1* and *Tet2* causes downregulation of a group of genes that includes pluripotency-related genes (including *Esrrb*, *Prdm14*, *Dppa3*, *Klf2*, *Tcl1* and *Zfp42*) and a concomitant increase in methylation of their promoters, together with an increased propensity of ES cells for extraembryonic lineage differentiation. Declining levels of TETs during differentiation are associated with decreased hydroxymethylation levels at the promoters of ES cell-specific genes together with increased methylation and gene silencing. We propose that the balance between hydroxymethylation and methylation in the genome is inextricably linked with the balance between pluripotency and lineage commitment.

5hmC occurs in ES cells (in 5% of CpGs), Purkinje cells in the mouse brain, and in other adult mouse tissues^{2–5}. The TET1 and TET2 enzymes, which can oxidise 5mC thus generating 5hmC, are highly expressed in ES cells and regulate the expression of pluripotency-related genes together with the potential of ES cells to differentiate into the embryonic and extraembryonic lineages^{4,6}. The genomic distribution of 5hmC in the ES cell genome and during differentiation and its relation to the distribution to 5mC is unknown. Because bisulphite conversion and high throughput sequencing (BS-Seq) does not distinguish between 5mC and 5hmC⁷, we used specific antibodies (Fig. 1a and Supplementary Fig. 1) to determine the genomic distribution of both 5mC and 5hmC by MeDIP-Seq⁸ and hMeDIP-Seq (methylated DNA immunoprecipitation and hydroxymethylated DNA immunoprecipitation followed by high throughput sequencing, respectively) in two different ES cell lines (J1, E14), *Np95*^{−/−} ES cells (lacking maintenance methylation), *Tet1/2* knockdown ES cells, and embryoid bodies (EBs). We obtained 19–33 million paired-end reads for each sample; all samples were sequenced in two biological replicates which were found to be highly reproducible (Supplementary Table 1 and Supplementary Fig. 2). Note that (h)MeDIP-Seq profiles (as chromatin immunoprecipitation (ChIP)-Seq profiles) reveal only the relative distribution of the respective modification within a sample and therefore cannot be used to infer absolute quantitative differences between samples or antibodies.

By immunofluorescence we found strong nuclear staining for 5hmC in ES cells (and in other cell types) that broadly overlapped in euchromatic regions with staining for 5mC, whereas DAPI-dense heterochromatic regions are highly enriched for 5mC but not 5hmC (Fig. 1b and

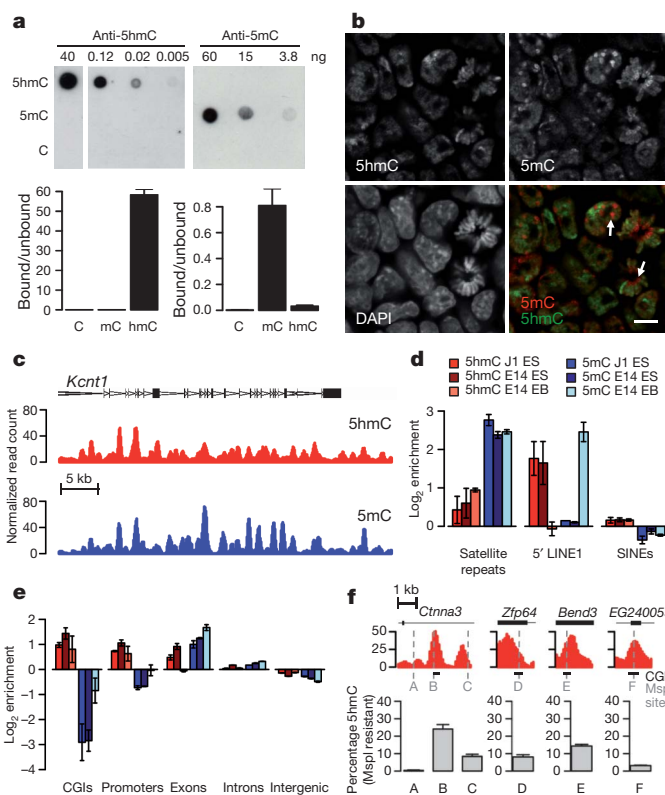


Figure 1 | Distribution of 5-hydroxymethylcytosine in the mouse genome.

a, The specificities of the antibodies used in this study were confirmed by dot blot and (h)MeDIP using PCR fragments containing 5hmC, 5mC or C. **b**, Immunofluorescence co-staining of J1 ES cells with antibodies against 5hmC (green) and 5mC (red). Grey scale images of the two modifications are shown separately. Staining for 5mC is particularly strong in pericentromeric heterochromatin (arrows), contrary to 5hmC. Scale bar, 10 μ m. **c**, Examples of hMeDIP-Seq and MeDIP-Seq profiles at a genomic region on Chr2 in J1 ES cells. **d**, Relative enrichment (\log_2 bound/unbound) of 5hmC and 5mC in repetitive sequences in J1 and E14 ES cells and E14 EBs. **e**, Enrichment of 5hmC and 5mC in single-copy genomic features. Values in **d** and **e** represent means of two biological replicates with the ends of the error bars corresponding to the individual data points. **f**, Validation of the presence of 5hmC in CGIs using glucMS-qPCR (grey bars represent mean \pm s.d.). Selected CGIs (black bars, upper panel) were tested for the presence of 5hmC at particular MspI sites (grey vertical line). Genomic coordinates of the left-most base pairs of each region: *Cttna3* (chr10, 63044495); *Zfp64* (chr2, 168750875); *Bend3* (chr10, 43230661); *EG240055* (also known as *Neur11b*: chr17, 26567975).

¹Laboratory of Developmental Genetics and Imprinting, The Babraham Institute, Cambridge CB22 3AT, UK. ²Bioinformatics Group, The Babraham Institute, Cambridge CB22 3AT, UK. ³Centre for Trophoblast Research, University of Cambridge, Cambridge CB2 3EG, UK. [†]Present address: Genetics Department, Faculty of Medicine, University of Porto, 4200-319 Porto, Portugal.

*These authors contributed equally to this work.

Supplementary Fig. 3). (h)MeDIP-Seq confirmed that 5hmC is widely distributed throughout non-repetitive regions (see example in Fig. 1c) and substantially overlaps with the distribution of 5mC, whereas satellite repeats (which are located in heterochromatin) are highly enriched for 5mC but substantially less for 5hmC (Fig. 1d and Supplementary Fig. 4). In single-copy regions the distribution of 5hmC in ES cells follows a broadly similar pattern to that of 5mC in intergenic regions, exons and introns, with a higher enrichment in exons over introns (Fig. 1e). Notably, whereas 5mC is relatively depleted from CpG islands (CGIs), gene promoters, the 5' ends of LINE1 elements (their promoters), CTCF and pluripotency transcription factor binding sites in accordance with previous work⁹, 5hmC is relatively enriched in all of these (Fig. 1d, e and Supplementary Figs 5 and 6). Furthermore, upon differentiation into EBs 5hmC enrichment decreases in these regions, concomitant with a gain of 5mC. Consistent with the distinct 5mC and 5hmC patterns at CGIs, whereas 5mC is depleted from high CpG density promoters (as described previously¹⁰), 5hmC remains enriched (Supplementary Fig. 7), indicating that the ratio of 5hmC to 5mC is higher here than in low CpG density promoters. To independently and quantitatively verify the presence of 5hmC in CGIs we carried out glucosylation of 5hmC in genomic DNA followed by MspI digestion (which does not digest glucosylated 5hmC) and quantitative PCR (qPCR) across MspI sites (glucMS-qPCR)¹¹. We found significant levels of 5hmC (3–24%) in selected CGIs (Fig. 1f and Supplementary Fig. 8). We also determined the corresponding 5mC levels (see Methods) and found them to be comparable to those of 5hmC at these CGIs, whereas elsewhere 5mC can be several fold higher than 5hmC (Supplementary Fig. 8, compare regions B and C). These measurements suggest that 5hmC is still derived from 5mC at CGIs, but that a high proportion of 5mC is converted to 5hmC in these regions. We also confirmed the presence of cytosine modifications in these regions by bisulphite conversion followed by Sequenom MassARRAY analysis (Supplementary Fig. 8).

We found by thin layer chromatography analysis that 5hmC was reduced in *Tet1/2* knockdown cells and *Np95*^{-/-} cells, and eliminated in *Dnmt1*^{-/-}/*Dnmt3a*^{-/-}/*Dnmt3b*^{-/-} triple knockout (TKO) ES cells (Fig. 2a). We confirmed this by glucMS-qPCR on selected regions and all were found to display lower levels of both modifications in *Np95*^{-/-} ES cells and only vestigial amounts in TKO cells (Fig. 2b). We find losses of 5hmC enrichment at exons, 5' regions of LINE1 elements and CTCF binding sites in *Np95*^{-/-} and *Tet1/2* knockdown ES cells (Fig. 2d and Supplementary Fig. 6). Enrichment of 5hmC is also reduced at promoters in *Np95*^{-/-} but not in *Tet1/2* knockdown cells. However, maintenance of relative enrichment levels at promoters upon *Tet1/2* knockdown means that its absolute 5hmC levels follow the observed genome-wide reduction in 5hmC (see Supplementary Fig. 9). Overall these results suggest that most 5hmC in mouse ES cells is dependent on pre-existing 5mC (although we cannot exclude that 5hmC may also be generated by an independent mechanism¹²), but that the kinetics of generating and maintaining 5mC and converting it to 5hmC are likely to be different for different genomic elements.

Our protocol for (h)MeDIP-Seq conserves information on strand-specificity of hydroxymethylation and methylation (Supplementary Fig. 10). Extensive occurrence of strand-biased regions was found in both 5mC and 5hmC methylomes, and these regions were enriched for CpH (where H is C, A, or T) dinucleotides (Fig. 3a), indicating that strand-specific (hydroxy)methylation occurs largely in non-CpG context. The strand specificity and sequence context of asymmetric (hydroxy)methylation were confirmed by analysis of a BS-Seq ES cell data set¹³ (Fig. 3c) and by bisulphite sequencing of selected asymmetric regions, showing that modification occurred predominantly in CpH context, where it was entirely strand-specific (Fig. 3d). Overall strand bias in 5hmC profiles was increased in *Np95*^{-/-} and *Tet1/2* knockdown cells (Fig. 3b), consistent with the dependence of 5hmC on pre-existing 5mC at CpGs and suggesting that TET1 and TET2 may have a preference for oxidizing 5mC in CpG context.

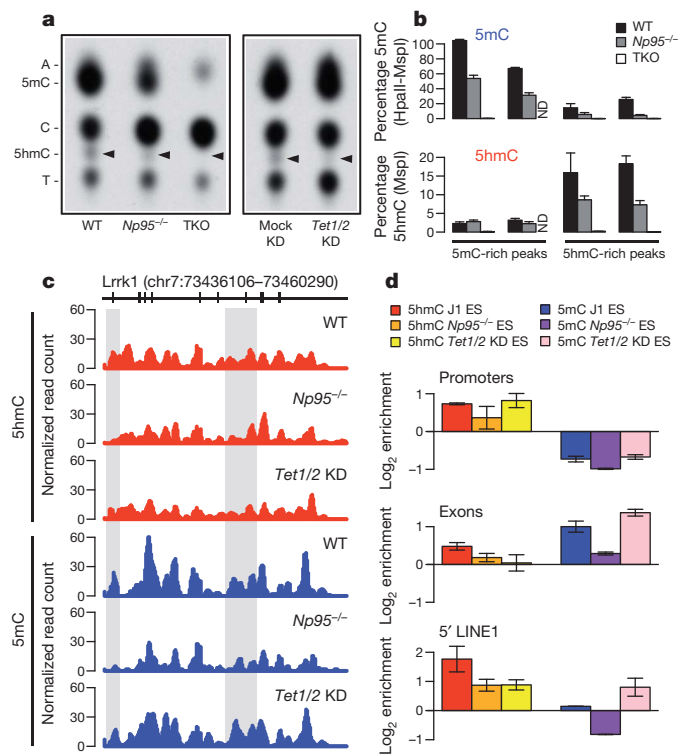


Figure 2 | Genetic relationship between methylation and hydroxymethylation.

a, Thin layer chromatography separation of radioactively end-labelled bases from MspI-digested genomic DNA, showing reduced levels of 5hmC (arrowheads) in methylation- and TET-deficient ES cells. **b**, glucMS-qPCR validation of genomic regions specifically enriched for 5mC or 5hmC in wild-type (WT) J1, *Np95*^{-/-} and TKO ES cells (bars represent mean \pm s.d.). Genomic regions were selected on the basis of (h)MeDIP-Seq profiles of wild-type ES cells. **c**, Examples of (h)MeDIP-Seq profiles in wild type, *Np95*^{-/-} and *Tet1/2* KD ES cells. 5hmC profiles are relatively similar, whereas 5mC distribution is significantly altered in *Np95*^{-/-} cells, but less so in *Tet1/2* knockdown (*Tet1/2* KD) cells. Shadowed areas highlight regions of altered 5hmC and/or 5mC enrichment. **d**, Relative enrichment at promoters, exons and 5' regions of LINE1 elements in J1, *Np95*^{-/-} and *Tet1/2* KD ES cells. *Np95* deficiency causes depletion of both 5hmC and 5mC in all three regions, whereas *Tet1/2* KD causes preferential reduction of 5hmC at exons and LINE1 promoters, which leads to increased 5mC enrichment in these regions. Values represent means of two biological replicates with the ends of the error bars corresponding to the individual data points.

We asked if there was a relationship between hydroxymethylation at gene promoters in ES cells and their transcription levels (Fig. 4a and Supplementary Fig. 11). We generated an ES cell transcriptome by RNA-Seq and classified promoters with respect to enrichment of 5mC and 5hmC. Whereas the presence of 5mC in the promoter region was associated with low levels of transcription as expected, 5hmC was associated with high levels of transcription. In fact, genes specifically enriched for 5hmC were more highly transcribed than those with neither of the modifications (Fig. 4a); this effect is also partially dependent on promoter CpG density (Supplementary Fig. 11). Promoters enriched for both 5hmC and 5mC were also associated with higher levels of transcription than promoters specifically enriched for 5mC, suggesting that presence of 5hmC partially overcomes the silencing effect of 5mC. Consistent with these observations, promoters that are high in 5hmC are enriched in the activating histone mark H3K4me3, whereas those enriched in 5mC are depleted of H3K4me3 (Fig. 4b; data from ref. 14). 5hmC in exons was also found associated with increased levels of transcription (Supplementary Fig. 11), consistent with what has been found in mouse cerebellum¹⁵.

RNA-Seq of *Tet1/2* knockdown ES cells identified 107 genes that were downregulated in knockdown cells (18 out of 22 validated by

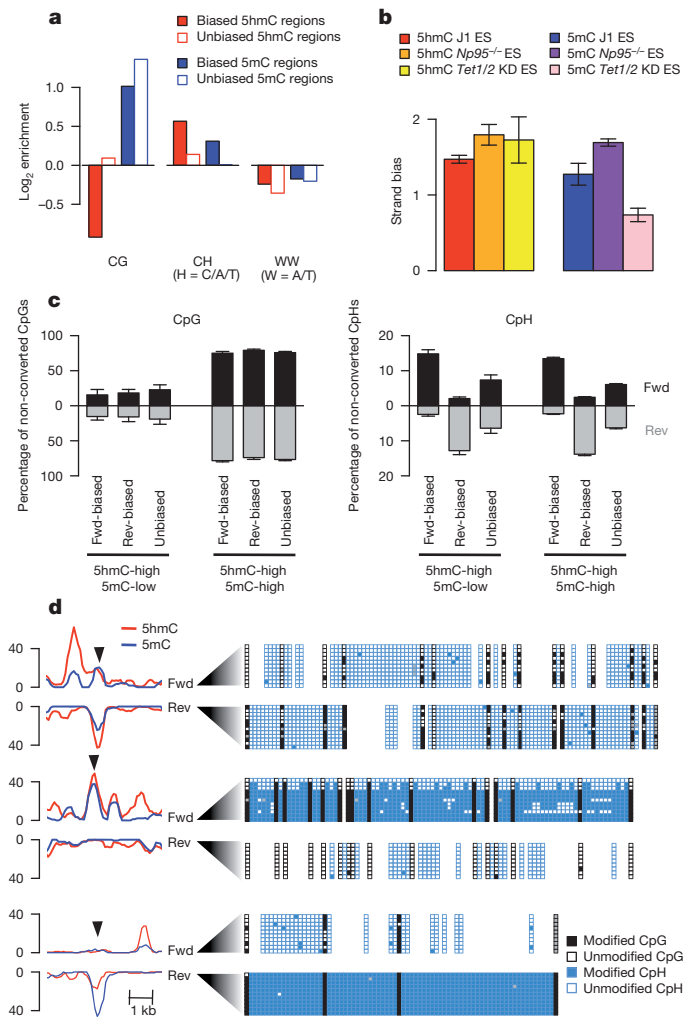


Figure 3 | Strand specificity and sequence context of methylation and hydroxymethylation. **a**, Enrichment of dinucleotide sequences present in the central 200 bp of 5hmC and 5mC regions separated into biased and unbiased fragments. CG dinucleotides are enriched in unbiased regions, as expected from its symmetric nature. Biased regions are enriched for CH dinucleotides, indicating extensive non-CpG (hydroxy)methylation. **b**, Strand bias measurements, which represent the overall level of asymmetric methylation in the genome. Depletion of NP95 increases strand bias in the 5hmC and 5mC profiles due to reduced CpG methylation. Knockdown of *Tet1/2* decreases strand bias in the 5mC profile, as expected if reduction of 5hmC at CpGs leads to an accumulation of 5mC at the same sites. Values represent means of two biological replicates with the ends of the error bars corresponding to the individual data points. **c**, BS-Seq¹³ validation of the (h)MeDIP data. Percentages of methylated CpGs present in 5hmC-enriched peaks containing low or high 5mC levels are plotted (left) showing the symmetrical nature of CpG methylation (in both biased and unbiased peaks). Conversely, CpH methylation in biased peaks is asymmetric in nature (right). Error bars represent 95% confidence intervals. **d**, Validation of asymmetric methylation by bisulphite sequencing of biased and unbiased (h)MeDIP-Seq peaks. Filled squares represent methylated/hydroxymethylated cytosines and empty squares represent unmodified cytosines. Bisulphite sequencing confirms the asymmetric nature of methylation in biased regions (middle and bottom) and reveals extensive non-CpG methylation, whereas the unbiased region (top) contains mostly CpG methylation.

quantitative PCR with reverse transcription (qRT-PCR); Fig. 4c and Supplementary Fig. 12). We also carried out *Tet1* knockdown on its own and found all 18 validated genes consistently downregulated by qRT-PCR (Supplementary Fig. 12), indicating that TET1 has the major role in the observed expression changes. This was confirmed in a stable ES cell line containing a doxycycline-inducible shRNA

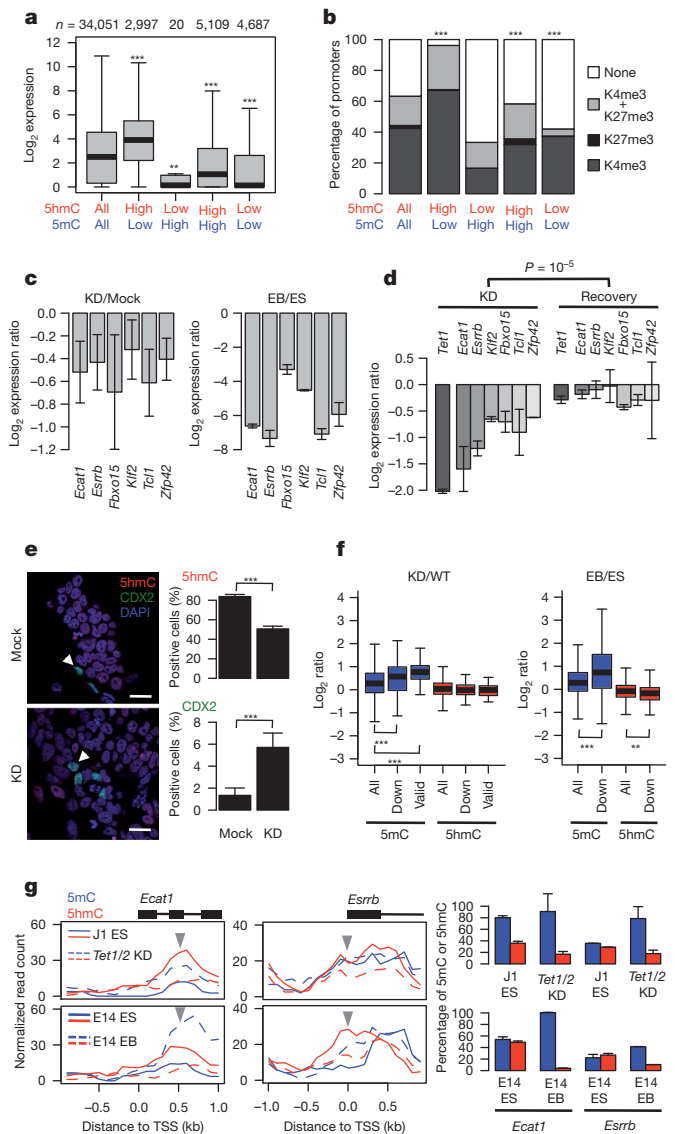


Figure 4 | Gene expression and promoter methylation in ES cells and during differentiation. **a**, Relationship between 5hmC and 5mC levels at gene promoters and expression of downstream genes measured by RNA-Seq in J1 ES cells. Significance levels are relative to all promoters (** $P < 0.001$, *** $P < 0.0001$ throughout the figure). **b**, Relationship between 5hmC, 5mC and presence/absence of H3K4me3 and H3K27me3 at gene promoters (data from ref. 14). **c**, qRT-PCR validation of genes downregulated upon *Tet1/2* KD across three biological replicates and expression level changes in the same genes from ES to EB differentiation (values are mean \pm s.d.). **d**, Induction of a shRNA targeting *Tet1* in a stable ES cell line also results in the downregulation of the genes in **c**. Restoring TET1 expression leads to recovery in expression of these genes (values are mean \pm s.d.). **e**, Co-immunostaining of mock and *Tet1/2* KD ES cells for 5hmC (red) and CDX2 (green). Scale bar, 20 μm. Cells were scored for presence of 5hmC and CDX2 expression ($n = 1,120$ and 1,209 for mock and *Tet1/2* KD cells, respectively; values are percentage of cells \pm 95% confidence interval). **f**, KD/WT ratios for promoter 5mC and 5hmC shows that downregulated genes, and in particular qRT-PCR-validated ones, suffer methylation changes different from the pool of all genes. Genes downregulated upon ES to EB differentiation have increased 5mC enrichment levels and decreased 5hmC. **g**, Examples of 5hmC and 5mC profiles of two genes in J1 and E14 ES cells, *Tet1/2* KD and E14 EBs, and corresponding quantification of 5mC and 5hmC levels by glucMS-qPCR (the *MspI* site used is indicated by the grey arrowhead). A considerable reduction in 5hmC levels is detected upon both *Tet1/2* KD and differentiation into EBs, with a concomitant increase in 5mC.

against *Tet1* in which we found again downregulation of the same set of genes (Fig. 4d). Removal of doxycycline led to recovery of TET1 and 5hmC levels back to normal and we found that gene expression changes were restored to wild-type levels (Fig. 4d and Supplementary Fig. 13).

The genes that were downregulated in response to *Tet1/2* knockdown included pluripotency-related genes such as *Esrrb*, *Klf2*, *Tcl1*, *Zfp42*, *Dppa3*, *Ecat1* (also known as *2410004A20Rik*) and *Prdm14* (by contrast *Nanog*, *Oct4* (also known as *Pou5f1*) and *Sox2* were not downregulated). These are amongst the earliest genes to be downregulated upon ES cell differentiation¹⁶, and include genes that undergo epigenetically regulated transcriptional fluctuations in ES cells, such as *Dppa3* and *Zfp42* (refs 17, 18). It remains to be seen whether such fluctuations are associated with stochastic patterning of 5hmC at these promoters across a cell population. Consistent with a role in regulating transcription of pluripotency-associated genes, the upstream region of the *Tet1* gene contains a large cluster of binding sites for core pluripotency transcription factors (Supplementary Fig. 14), and both TET1 and TET2 are rapidly downregulated upon differentiation to EBs (Supplementary Fig. 15). Indeed, we found a 23-fold enrichment ($P < 2.2 \times 10^{-16}$) for transcripts downregulated upon *Tet1/2* knockdown to also be substantially downregulated during ES cell differentiation¹⁹, 16 of which we validated by qRT-PCR (Fig. 4c and Supplementary Fig. 12).

Although ES cells subjected to *Tet1/2* knockdown did not appear to differentiate spontaneously, we found that markers of extraembryonic endoderm differentiation (*Gata6* and *Sox17*) were precociously expressed when *Tet1/2* knockdown ES cells were differentiated with retinoic acid (Supplementary Fig. 16). This is consistent with downregulation of *Esrrb* and *Prdm14*, which safeguard ES cells from commitment to endoderm cell fate^{20,21}. We also found a significant increase of CDX2-positive cells concomitant with the decrease in the number of 5hmC-positive cells upon *Tet1/2* knockdown (all CDX2-positive cells were particularly low in 5hmC, Fig. 4e). These results are in agreement with recent studies using *Tet1* knockdown ES cells^{4,6}.

Promoters of genes that were downregulated during ES cell differentiation had a marked decrease of 5hmC enrichment levels, which was accompanied by a significant increase in 5mC levels (Fig. 4f, g). Notably, genes that were downregulated in *Tet1/2* knockdown cells had robustly increased levels of 5mC in their promoters (Fig. 4f, g; see also Supplementary Fig. 17), suggesting that decline of TET levels during differentiation leads, at least in part, to gene silencing through methylation of promoters. Enrichment of 5hmC in these promoters was unchanged, that is, its absolute levels accompanied the genome-wide loss of 5hmC. Importantly, we confirmed the reduction of 5hmC levels by glucMS-qPCR of selected promoters (Fig. 4g).

Our study shows that 5hmC is relatively enriched in euchromatic parts of the genome, including in CGIs and promoters, and its presence in promoters and exons is associated with increased levels of transcription. This may in part be explained by the removal of the repressive effects of 5mC, but it is also possible that 5hmC itself has a positive effect on transcription. Furthermore, the TET proteins may have roles in transcriptional regulation in addition to their ability to convert 5mC to 5hmC. The core pluripotency network is connected with TET1/2 which regulate genes with established roles in pluripotency and epigenetic reprogramming such as *Esrrb*, *Dppa3*, *Klf2*, *Zfp42* and *Prdm14*, thus safeguarding ES cells against commitment to extraembryonic cell fate (Supplementary Fig. 19). On the basis of these results, we suggest that hydroxymethylation and the TET proteins could also have a role in erasing methylation marks from promoters of pluripotency-related genes during fusion of ES cells with somatic cells^{22,23}, and during the generation of induced pluripotent stem cells for which erasure of DNA methylation seems critical²⁴. Hydroxymethylation may also have a role in the large-scale erasure of methylation in primordial germ cells and early embryos^{25,26}.

METHODS SUMMARY

All immunofluorescence and (h)MeDIP-Seq data were produced using a rabbit anti-5hmC polyclonal antibody (Active Motif, catalogue no. 39769) and a mouse

anti-5mC monoclonal antibody (Eurogentec, MMS-900P-B). J1, E14, *Np95*^{-/-} and TKO ES cells were grown under standard conditions in the presence of serum and leukaemia inhibitory factor (LIF). Differentiation of E14 ES cells into embryoid bodies was done by removal of LIF and suspension culture for 13 days. RNA interference (RNAi) experiments were performed as described² with modifications. A2lox.cre ES cells²⁷ were targeted with a short hairpin RNA-micro RNA (shRNA-mir) sequence against *Tet1* cloned into p2Lox; induction of *Tet1* knockdown and recovery were achieved by the addition and later removal of doxycycline. Cells were either fixed for immunofluorescence or collected for DNA and/or RNA extraction. MeDIP-Seq and hMeDIP-Seq were based on the MeDIP method²⁸ using either the anti-5mC or anti-5hmC antibodies, respectively, but incorporating the ligation of Illumina adaptors for paired-end sequencing, which was performed on a Illumina Genome Analyzer GAII-X. RNA-Seq was performed as described previously²⁹ with modifications. Bioinformatic analyses were performed using SeqMonk (<http://www.bioinformatics.bbsrc.ac.uk/projects/seqmonk/>) and custom Perl or R scripts.

Full Methods and any associated references are available in the online version of the paper at www.nature.com/nature.

Received 28 June 2010; accepted 18 March 2011.

Published online 3 April 2011.

- Feng, S., Jacobsen, S. E. & Reik, W. Epigenetic reprogramming in plant and animal development. *Science* **330**, 622–627 (2010).
- Tahilian, M. et al. Conversion of 5-methylcytosine to 5-hydroxymethylcytosine in mammalian DNA by MLL partner TET1. *Science* **324**, 930–935 (2009).
- Kriaucionis, S. & Heintz, N. The nuclear DNA base 5-hydroxymethylcytosine is present in Purkinje neurons and the brain. *Science* **324**, 929–930 (2009).
- Ito, S. et al. Role of Tet proteins in 5mC to 5hmC conversion, ES-cell self-renewal and inner cell mass specification. *Nature* **466**, 1129–1133 (2010).
- Szwagierczak, A. et al. Sensitive enzymatic quantification of 5-hydroxymethylcytosine in genomic DNA. *Nucleic Acids Res.* **38**, e181 (2010).
- Koh, K. P. et al. Tet1 and Tet2 regulate 5-hydroxymethylcytosine production and cell lineage specification in mouse embryonic stem cells. *Cell Stem Cell* **8**, 200–213 (2011).
- Huang, Y. et al. The behaviour of 5-hydroxymethylcytosine in bisulfite sequencing. *PLoS ONE* **5**, e8888 (2010).
- Down, T. et al. A Bayesian deconvolution strategy for immunoprecipitation-based DNA methylome analysis. *Nature Biotechnol.* **26**, 779–785 (2008).
- Lister, R. et al. Human DNA methylomes at base resolution show widespread epigenomic differences. *Nature* **462**, 315–322 (2009).
- Weber, M. et al. Distribution, silencing potential and evolutionary impact of promoter DNA methylation in the human genome. *Nature Genet.* **39**, 457–466 (2007).
- Davis, T. & Vaisvila, R. High sensitivity 5-hydroxymethylcytosine detection in Balb/C brain tissue. *J. Vis. Exp.* **48**, doi:10.3791/2661 (2011).
- Liutkeviciūtė, Z. et al. Cytosine-5-methyltransferases add aldehydes to DNA. *Nature Chem. Biol.* **5**, 400–402 (2009).
- Popp, C. et al. Genome-wide erasure of DNA methylation in mouse primordial germ cells is affected by AID deficiency. *Nature* **463**, 1101–1105 (2010).
- Ku, M. et al. Genomewide analysis of PRC1 and PRC2 occupancy identifies two classes of bivalent domains. *PLoS Genet.* **4**, e1000242 (2008).
- Song, C. X. et al. Selective chemical labeling reveals the genome-wide distribution of 5-hydroxymethylcytosine. *Nature Biotechnol.* **29**, 68–72 (2011).
- Glover, C. H. et al. Meta-analysis of differentiating mouse embryonic stem cell gene expression kinetics reveals early change of a small gene set. *PLoS Comput. Biol.* **2**, e158 (2006).
- Hayashi, K., Lopes, S. M., Tang, F. & Surani, M. A. Dynamic equilibrium and heterogeneity of mouse pluripotent stem cells with distinct functional and epigenetic states. *Cell Stem Cell* **3**, 391–401 (2008).
- Toyooka, Y. et al. Identification and characterization of subpopulations in undifferentiated ES cell culture. *Development* **135**, 909–918 (2008).
- Cloonan, N. et al. Stem cell transcriptome profiling via massive-scale mRNA sequencing. *Nature Methods* **5**, 613–619 (2008).
- Ivanova, N. et al. Dissecting self-renewal in stem cells with RNA interference. *Nature* **442**, 533–538 (2006).
- Ma, Z. et al. Sequence-specific regulator Prdm14 safeguards mouse ESCs from entering extraembryonic endoderm fates. *Nature Struct. Mol. Biol.* **18**, 120–127 (2011).
- Tada, M. et al. Nuclear reprogramming of somatic cells by *in vitro* hybridization with ES cells. *Curr. Biol.* **11**, 1553–1558 (2001).
- Bhutani, N. et al. Reprogramming towards pluripotency requires AID-dependent DNA demethylation. *Nature* **463**, 1042–1047 (2010).
- Meissner, A. et al. Genome-scale DNA methylation maps of pluripotent and differentiated cells. *Nature* **454**, 766–770 (2008).
- Iqbal, K., Jin, S. G., Pfeifer, G. P. & Szabo, P. E. Reprogramming of the paternal genome upon fertilization involves genome-wide oxidation of 5-methylcytosine. *Proc. Natl Acad. Sci. USA* **108**, 3642–3647 (2011).
- Wossidlo, M. et al. 5-Hydroxymethylcytosine in the mammalian zygote is linked with epigenetic reprogramming. *Nature Commun.* **2**, 241 (2011).
- Mallanna, S. K. et al. Proteomic analysis of Sox2-associated proteins during early stages of mouse embryonic stem cell differentiation identifies Sox21 as a novel regulator of stem cell fate. *Stem Cells* **28**, 1715–1727 (2010).

28. Weber, M. *et al.* Chromosome-wide and promoter-specific analyses identify sites of differential DNA methylation in normal and transformed human cells. *Nature Genet.* **37**, 853–862 (2005).
29. Marioni, J. C. *et al.* RNA-seq: an assessment of technical reproducibility and comparison with gene expression arrays. *Genome Res.* **18**, 1509–1517 (2008).

Supplementary Information is linked to the online version of the paper at www.nature.com/nature.

Acknowledgements We would like to thank A. Bird for discussions and input, K. Tabbada for help with epigenomics and transcriptomics sequencing, and M. Okano for providing the TKO ES cells. We would like to thank H. Stuart for her dedicated contribution to gene expression analyses, and all Reik lab members for advice and discussion. This work was funded by the BBSRC, MRC and the EU NoE The Epigenome.

Author Contributions G.F. and M.R.B. designed and performed experiments and analysed data. S.S. established the (h)MeDIP-Seq protocol and performed bisulphite sequencing. F.S. performed immunostainings. T.A.H. carried out qRT-PCR and glucMS-qPCR analyses. C.J.M. established the inducible *Tet1* shRNA ES cell line. F.K. and S.A. performed bioinformatic analyses. W.R. designed and directed the study. G.F., M.R.B. and W.R. wrote the manuscript.

Author Information All sequencing files have been deposited at the EBI Sequence Read Archive under the accession number ERP000570 (<http://www.ebi.ac.uk/ena/data/view/ERP000570>). Reprints and permissions information is available at www.nature.com/reprints. The authors declare no competing financial interests. Readers are welcome to comment on the online version of this article at www.nature.com/nature. Correspondence and requests for materials should be addressed to W.R. (wolf.reik@bbsrc.ac.uk).

METHODS

Antibody validation by dot blot and methylated/hydroxymethylated DNA immunoprecipitation assay (MeDIP/hMeDIP). All immunofluorescence and (h)MeDIP-Seq data were produced using a rabbit anti-5hmC polyclonal antibody (Active Motif, catalogue no. 39769) and a mouse anti-5mC monoclonal antibody (Eurogentec, MMS-900P-B). To generate control templates, PCR fragments were amplified from M13mp18 DNA or custom oligonucleotides using either dCTP, d5mCTP or d5hmCTP. For dot blot, analysis DNA samples were denatured at 99 °C for 5 min and spotted onto Hybond-N+ nitrocellulose membranes (GE Healthcare). After ultraviolet cross-linking membranes were blocked overnight with 10% non-fat milk and 1% BSA in PBT (PBS + 0.1% Tween20) at 4 °C followed by >1 h incubation with either the 5mC or 5hmC antibodies (1:500 in blocking solution) at room temperature. Membranes were washed four times with PBT, incubated for 30 min with horseradish peroxidase (HRP)-conjugated goat anti-mouse or anti-rat antibodies (GE Healthcare; 1:10,000 in blocking solution), washed with PBT, and developed using the ECL+ detection system (GE Healthcare). For (h)MeDIP, three control templates with different sequences (~200-bp products containing C, 5mC or 5hmC; 15 pg each) were mixed with sonicated genomic DNA (1.5 µg) followed by denaturation (10 min at 95 °C) and immunoprecipitation as described previously for MeDIP²⁸ using 2 µg of anti-5mC or anti-5hmC antibody and 8 µl Dynabeads (coupled with M-280 sheep anti-mouse IgG for the 5mC antibody or with Protein G for the 5hmC antibody, Invitrogen). Pulled-down products were detected by qPCR and normalized to the unbound fraction.

Cell lines and other biological samples. J1 ES cell line (129S4/SvJae) was purchased from ATCC (catalogue no. SCRC-1010) and grown on a γ -irradiated pMEF feeder layer at 37 °C and 5% CO₂ in complete ES medium (DMEM 4,500 mg l⁻¹ glucose, 4 mM L-glutamine and 110 mg l⁻¹ sodium pyruvate, 15% fetal bovine serum, 100 U of penicillin/100 µg of streptomycin in 100 ml medium, 0.1 mM non-essential amino acids, 50 µM β -mercaptoethanol, 10³ U LIF ESGRO). E14 ES cells were grown either in complete ES medium or differentiated for 13 days into embryoid bodies via LIF removal and suspension culture. Retinoic acid (RA) differentiation of the mock siRNA treated and *Tet1/2* knockdown ES cells was done with 2 µM end concentration of RA in complete ES medium without LIF for 24 h. *Np95*^{-/-} ES cells (129/Ola derived) and TKO ES cells (*Dnmt3a*^{-/-}, *Dnmt3b*^{-/-} and *Dnmt1*^{-/-}, J1-derived, gift from M. Okano³⁰) were grown in complete ES medium. Primary mouse embryonic fibroblasts were derived from E11.5 embryos (B6CBAF1 \times B6) and grown for three passages in DMEM 4,500 mg l⁻¹ glucose, 4 mM L-glutamine and 110 mg l⁻¹ sodium pyruvate, 10% fetal bovine serum, 100 U of penicillin/100 µg of streptomycin in 100 ml medium, 50 µM β -mercaptoethanol. Cerebellum sections were a gift from E. Ivanova and G. Kelsey.

RNAi knockdown of *Tet1* and *Tet2* in ES cells. RNA interference experiments were performed as described² with modifications. Transfections of Dharmacon siGENOME siRNA duplexes (Thermo Fisher Scientific) against mouse *Tet1* (catalogue no. D-062861-01; caacuugcauccagauua), siGENOME SMARTpool against *Tet2* (catalogue no. M-058965-01; gaaagcagcucgaaagcg, ccucagauuuuaggaga, acucuaacuccaccuua, uagcaacguuuucuccua) and siGENOME non-targeting siRNA#2 (catalogue no. D-001210-02; sequence not available) were done with Lipofectamine 2000 according to the manufacturer's instructions. Cells were harvested after three rounds of transfection for DNA/RNA isolation.

Stable shRNA *Tet1* knockdown and recovery. The pSM2 retroviral vector containing the shRNA-mir sequence targeting the *Tet1* messenger RNA (tgctgttgac agtgagcgcgtagctatagatagatagatgaagccagatgtattactatctatagctagcttgcctactgc ctgga) was purchased from Open Biosystems. shRNA-mir sequences were amplified by PCR using primers that created restriction sites for HindIII and NotI (atacaagcttcaggtaattgtttgaatgagc and agcgccgcgtctccaattgaaaaagtgta), cloned into p2Lox³¹ and subsequently transfected into A2Lox.cre ES cells²⁷ (derived from the E14 cell line strain 129P2/OlaHsd, provided by M. Kyba). One day before transfection, Cre expression was induced by adding doxycycline (0.5 µg ml⁻¹) to the complete ES cell medium to promote the stable site-specific integration of the shRNA-mir sequence, following inducible cassette exchange recombination, which renders the cells resistant to neomycin.

ES cells were transfected using Lipofectamine 2000 (Invitrogen) at a concentration of 5×10^5 cells ml⁻¹. One day after transfection, selection medium containing geneticin (G418, Melford; 300 µg ml⁻¹ active concentration) was added to the cells and selection was maintained for 10 days. Resistant colonies were then individually picked into 96-well plates and expanded for freezing of stable cell lines. Integration was confirmed by PCR using Loxin primers³². shRNA-mir expression was induced by adding 2 µg ml⁻¹ of doxycycline (Sigma) to the culture medium during 5 days followed by removal of the doxycycline from the ES medium for an additional 7 days. RNA and DNA were isolated before removing the doxycycline to evaluate

knockdown effects and after 7 days of recovery, using a Qiagen AllPrep DNA/RNA isolation kit.

Immunofluorescence, microscopy and image analysis. Antibody staining of DNA methylation and hydroxymethylation was performed as previously described³³ with modifications. Briefly, cells were fixed with 4% PFA for 15 min and, after permeabilization with 0.5% Triton X-100, the samples were treated with 4 N HCl for 10 min at room temperature, washed in PBS Tween and blocked overnight; simultaneous incubation with both primary antibodies followed by simultaneous secondary detection was used. Antibody staining against CDX2 was performed as previously described³⁴. Mouse cerebellum cryosections (30 µm) were fixed with methanol (20 min at -20 °C) before staining with anti-calbindin D28K (CBP; gift from P. Emson) and post-fixing with 2% PFA after which same protocol as above was used for 5hmC staining. Single optical sections were captured with a Zeiss LSM510 Meta microscope ($\times 63$ oil-immersion objective) and the images pseudo-coloured using Adobe Photoshop. Semi-quantification of signals was performed on single optical sections using Velocity5.2 (Improvision).

DNA/RNA extraction. Genomic DNA was prepared using the Qiagen AllPrep DNA/RNA mini kit. RNA was extracted using either the Qiagen AllPrep DNA/RNA mini kit or RNeasy mini kit and subjected to DNase treatment using the Ambion DNA-free kit according to the manufacturers' instructions.

(h)MeDIP and next generation sequencing. The (h)MeDIP-Seq protocol was performed as described above with the following modifications: after sonication of gDNA the ends of the DNA fragments were repaired and paired-end sequencing specific adaptors (Illumina) were ligated using either a Paired-End DNA Sample Preparation Kit (Illumina) or NEBNext DNA Sample Prep Reagent Set 1 (NEB). Following adaptor ligation, DNA was immunoprecipitated and purified. Fragments were amplified with 12–18 cycles using adaptor specific primers (Illumina); fragments ranging between 300 and 500 bp in size were gel-purified before cluster generation and sequencing. Sequencing was done on an Illumina Genome Analyzer GAIIX using Cluster Generation v2 and 4 chemistries as well as Sequencing by Synthesis Kits v3 and v4. Data collection was performed using Sequencing Control Software v2.5 and 2.6. Real-time Analysis (RTA) 1.5–1.8 were used for base calling. Genomic mapping of short reads was performed using the sequence_pair mode of ELAND in the Illumina CASSAVA pipeline v1.5–1.8. Details on the number of sequencing reads obtained for each run are shown in Supplementary Table 1.

Bisulphite sequencing. J1 ES cell genomic DNA was bisulphite-treated using the Qiagen Epitect Kit and amplified using either Qiagen Hotstar Taq DNA Polymerase or Roche High Fidelity DNA Polymerase (primer sequences in Supplementary Table 2). A single amplification band was excised from the agarose gel and cloned into pGEM-T Easy vector (Promega) for sequencing.

Sequenom MassARRAY. Genomic DNA was bisulphite treated using the Qiagen Epitect Kit. PCR amplification of target regions (primer sequences in Supplementary Table 2), *in vitro* transcription and cleavage of the products for MassARRAY analysis were performed according to the manufacturer's instructions.

Glucosylation of genomic 5hmC followed by methylation sensitive qPCR (glucMS-qPCR). Genomic DNA (1 µg) was treated with T4 Phage β -glucosyltransferase (T4-BGT, NEB M0357S) according to the manufacturer's instructions. Glucosylated genomic DNA (100 ng) was digested with 10 U of either HpaII, MspI or no enzyme (mock digestion) at 37 °C overnight, followed by inactivation for 20 min at 80 °C. The HpaII- and MspI-resistant fraction was quantified by qPCR using primers designed around at least one HpaII/MspI site, and normalizing to the mock digestion control and two regions lacking HpaII/MspI sites (Supplementary Table 2). Resistance to MspI directly translates into percentage of 5hmC, whereas 5mC levels were obtained by subtracting the 5hmC contribution from the total HpaII resistance¹¹.

5hmC detection using thin layer chromatography (TLC). Detection of 5hmC within MspI sites was done as described previously². Briefly, 1 µg of genomic DNA was restriction-enzyme-digested with 20 U MspI and 10 µg RNase A overnight at 37 °C, followed by inactivation of the enzyme at 65 °C for 20 min. DNA fragments were dephosphorylated with shrimp alkaline phosphatase and purified using QIAquick PCR purification kit followed by radioactive end labelling with ³²P-ATP (10 µCi, 3.3 pmol) using T4 Polynucleotide kinase for 1 h at 37 °C. Radioactively labelled DNA was precipitated, resuspended in 18 µl DNase I buffer and fragmented to single nucleotides with 1 µl DNase I (10 U µl⁻¹; Roche) and 1 µl SVPD (10 µg µl⁻¹; Worthington) for 3 h at 37 °C. Samples of 1–5 µl were spotted onto PEI cellulose F TLC plates and developed with isobutyric acid:H₂O:NH₃ (66:20:1 v/v/v) overnight followed by drying of the plate and exposure of radioactivity on an imaging film.

mRNA library preparation for next generation sequencing (RNA-Seq). mRNA was isolated from 3 µg total RNA using Dynabeads mRNA DIRECT (Invitrogen) and fragmented with RNA fragmentation reagent (Ambion). First strand cDNA synthesis was done with SuperScript III First-Strand Synthesis System and 3 µg µl⁻¹

random hexamers (Invitrogen) followed by second strand synthesis with DNA Polymerase I and RNase H. After purification, a sequencing library was generated from the double stranded cDNA using paired-end adaptors (Illumina) and NEBNext DNA Sample Prep Reagent Set 1 (NEB), and sequenced following a single-end sequencing protocol²⁹. Sequencing was done on an Illumina Genome Analyzer GAII-X using Cluster Generation v4 chemistry and Sequencing by Synthesis Kit v4. Data collection was performed using Sequencing Control Software v2.6. Real-time Analysis (RTA) 1.6 was used for data monitoring. Spliced mapping of RNA-Seq data was performed with TopHat v1.0.14 using default parameters³⁵. Details on the number of sequencing reads obtained for each run are shown in Supplementary Table 1.

Quantitative reverse transcription PCR. RNA was extracted using the Qiagen RNeasy Mini kit and subjected to DNase treatment using the Ambion DNA-free kit according to the manufacturers' instructions. cDNA was constructed from 2 µg of this RNA using the SuperScript III First-Strand Synthesis System for RT-PCR using random hexamers to prime the reaction. This cDNA was diluted 1:50 and used as template for quantitative real-time PCR reactions in combination with Brilliant II SYBR Green QPCR Master Mix and primers designed to specifically amplify a small product (intron-spanning where possible) for each gene of interest (Supplementary Table 2). Cycling reactions were performed in duplicate and cycle threshold (C_t) fluorescence data recorded on a Stratagene Mx3000P thermal cycler and Bio-Rad C1000 Thermal Cycler. The relative abundance of each gene of interest was calculated on the basis of the $\Delta\Delta C_t$ method³⁶, where results were normalized to the average C_t of two housekeeping genes with consistent C_t values over all samples (*Atp5b* and *Hsp90ab1*).

Bioinformatics. Analysis of gene region enrichment. An initial identification of enriched clusters was performed on a data group, which combined the reads from all of the individual data sets. Clusters were identified where the density of reads represented an enrichment of >1 fold (equating to 19 reads) over at least 50 bp. Where adjacent clusters were within 20 bp of each other they were combined. All clusters were then quantified with \log_2 -transformed count of the number of overlapping reads. The read counts were normalized both to the total count of the largest data set by applying a linear scaling factor, and by the length of the cluster. Clusters with a quantified value of more than 12 in any sample were removed because these represented an unrealistically high level of enrichment which was most likely due to mismapping of data. Each cluster was then called as present or absent in each sample. A cutoff of 5 (approximately equivalent to the median in most samples) in the corrected counts was taken as the point above which a cluster would be said to be present. All clusters were divided into groups based on the position of the centre of the cluster falling into a promoter, gene, exon, intron or intergenic region. Finally counts were made for the number of present clusters per kilobase of sequence in each of the different genomic region classes. Final enrichment values were calculated as the \log_2 ratio of the clusters per kb in the selected genomic region compared to the whole genome cluster density. Similar results were obtained when normalizing the data to an unbound fraction of a MeDIP experiment subjected to sequencing, ruling out any potential mapping effects.

Strand bias analysis. Clusters were generated as for the region enrichment analysis. For each cluster a count was made for the number of forward and reverse reads overlapping with that cluster in every sample. A cluster was discarded in a sample if the total count of forward plus reverse was less than 20 or greater than 200. For each valid cluster a bias value was calculated as $\text{abs}(\log_2((f+1)/(r+1))) - c(f+r)$ where $c(f+r)$ represents an averaged value from a simulation of observed strand biases from clusters with different numbers of reads, but where the probability of reads being either forward or reverse was exactly 0.5. The valid bias values were then attributed to whichever genomic regions they fell into and an average value for each genomic region for each sample was calculated. High values would indicate a higher than expected level of asymmetry in individual clusters and a zero value would

indicate a completely symmetrical sample. A control sample of sonicated input DNA showed a mean bias of +0.021 (data not shown).

Repeat analysis. For non-directional repeat analysis all currently known instances of repeats were retrieved from the Ensembl database (totalling nearly 9.5 million), and the sequence information for the major types of repeats were concatenated to form individual repeat genomes. The repeat content of different samples was determined using in-house developed software that aligns all sequences of Illumina sequence files to the entire repeatome employing multiple instances of Bowtie³⁷. The number of aligning sequences was counted for each repeat type individually.

RNA-Seq analysis. Initial RNA-Seq quantification was performed over each exon and was expressed as the number of overlapping bases of sequence per base of exon. The values were normalized to total read count between samples and an overall expression level was calculated for each transcript by normalizing the total expression value of the exons in that transcript to its total exon length. On the *Tet1/2* knockdown experiment we found that effects in expression were proportional to the amount of measured knockdown, and the first of three biological replicates had considerable lower amounts of *Tet1* and *Tet2* transcripts when compared with the remaining. We therefore classified a transcript as differentially expressed if: (1) its expression level was above 2.5; (2) it was up- or downregulated in the first replicate by >1.5-fold relative to both untransfected and mock KD controls; (3) it was up- or downregulated by >1.15-fold in the other two replicates. Despite these low thresholds 18 out of 22 downregulated genes were validated by qRT-PCR in five biological replicates. For the comparison of the published ES and EB data sets¹⁹, we classified transcripts as differentially expressed if their expression ratio was larger than fourfold. For correlation of expression with 5mC and 5hmC levels, promoters were classified as 5mC- or 5hmC-high if their normalized read count (\log_2) was above 5.5 and 5mC- or 5hmC-low if it was below 4.5 (medians were between 4.2 and 5.5). Similar results were obtained with a large range of threshold values or by using quantile-based thresholds.

BS-Seq analysis. A mouse ES cell shotgun BS-Seq data set¹³ was obtained from GEO (accession number GSE19960) and remapped to the mouse genome (build NCBI37) using Bismark (<http://www.bioinformatics.bbsrc.ac.uk/projects/bismark>). Prior to performing alignments the first 5 bp of all reads in the mouse ES cell shotgun data were clipped off to remove adaptor sequence. To validate our results with the above mentioned publically available BS-Seq data set, clusters were generated as described for the region enrichment analysis. In addition, peaks identified in (h)MeDIP-Seq were further subdivided into '5hmC regions with low 5mC' and '5hmC regions with high 5mC'. Peaks with an abnormally high coverage of bisulphite reads were identified with a box-whisker distribution filter and extreme outliers (ratio of >threefold above median) were excluded from the analysis. The read coverage and methylation levels underlying these peaks or different genomic features were analysed using SeqMonk.

30. Tsumura, A. *et al.* Maintenance of self-renewal ability of mouse embryonic stem cells in the absence of DNA methyltransferases Dnmt1, Dnmt3a and Dnmt3b. *Genes Cells* **11**, 805–814 (2006).
31. Iacovino, M. *et al.* A conserved role for Hox paralog group 4 in regulation of hematopoietic progenitors. *Stem Cells Dev.* **18**, 783–792 (2009).
32. Ting, D. T. *et al.* Inducible transgene expression in mouse stem cells. *Methods Mol. Med.* **105**, 23–46 (2005).
33. Santos, F. *et al.* Epigenetic marking correlates with developmental potential in cloned bovine preimplantation embryos. *Curr. Biol.* **13**, 1116–1121 (2003).
34. Ng, R. K. *et al.* Epigenetic restriction of embryonic cell lineage fate by methylation of *Elf5*. *Nature Cell Biol.* **10**, 1280–1290 (2008).
35. Trapnell, C., Pachter, L. & Salzberg, S. L. TopHat: discovering splice junctions with RNA-Seq. *Bioinformatics* **25**, 1105–1111 (2009).
36. Livak, K. J. & Schmittgen, T. D. Analysis of relative gene expression data using real-time quantitative PCR and the $2^{-\Delta\Delta C_t}$. *Methods* **25**, 402–408 (2001).
37. Langmead, B., Trapnell, C., Pop, M. & Salzberg, S. L. Ultrafast and memory-efficient alignment of short DNA sequences to the human genome. *Genome Biol.* **10**, R25 (2009).